Parallel Monte Carlo Algorithms for Flowsheet Simulations based on the Population Balance Equation

Von der Fakultät für Ingenieurwissenschaften,
Abteilung Elektrotechnik und Informationstechnik
der Universität Duisburg-Essen

zur Erlangung des akademischen Grades

Doktor der Ingenieurwissenschaften

genehmigte Dissertation

von

Gregor Kotalczyk
aus
Laurahütte

1. Gutachter: Prof. Dr.-Ing. Frank Einar Kruis
2. Gutachter: Prof. Dr.-Ing. Andreas Kempf
Tag der mündlichen Prüfung: 20. Januar 2023

Danksagung

Die im folgenden Präsentierte Arbeit wurde durch die Deutsche Forschungsgemeinschaft (DFG) im Rahmen des Schwerpunktprogramms (SPP) 1679 *Dynamische Simulation vernetzter Feststoffprozesse* gefördert. Ich betrachte es als großes Privileg, an diesem wunderbaren SPP beteiligt worden zu sein, welcher neben der finanziellen Vergütung der geleisteten Arbeit, ebenfalls die Teilnahme an zahlreichen lehrreichen Workshops, Summerschools, sowie internationalen Konferenzen ermöglichte und so ein Forum geschaffen hat für einen stimulierenden Austausch mit zahlreichen Fachkollegen und Projektpartnern.

Mein besonderer Dank gilt Professor Einar Kruis, dessen offene, stillvolle und charmante Art immer eine sichere Quelle der Inspiration war. Ich bedanke mich für seine Unterstützung and Anleitung bei meinen ersten Schritten im wissenschaftlichen Arbeiten, Publizieren, dem Umgang mit bürokratischen Hürden, sowie für die interessanten Gespräche, die wissenschaftliche Freiheit und das damit verbundene Vertrauen, was mir gegeben wurde.

Diese Arbeit wäre nicht möglich gewesen ohne die kreative und kollegiale Atmosphäre, wie man sie in der Nanostrukturtechnik (NST) vorfindet. Natürlich liegt dies an den wunderbaren Kolleginnen und Kollegen der NST, denen mein großer Dank gilt. Wobei man da selbst verständlich Dennis Kiesler hervorheben muss, dessen viele Fachgebiete umfassendes technisches Wissen und Interesse an den Fragestellungen anderer Kolleginnen und Kollegen zum Gelingen der einen und anderen Doktorarbeit beigetragen hat (hier sind es die Feinheiten bei der logarithmischen Darstellung der Partikelgrößenverteilung).

Zu guter Letzt wäre noch das Interesse und die Begeisterung der Studenten, deren Abschlussarbeiten ich betreuen durfte, zu nennen, welche zum Gelingen dieser Arbeit beigetragen haben. Insbesondere Ivan Skenderović sowie Krishan Lambach wären da zu erwähnen, die mit frischen Ideen und neuen Perspektiven nicht unerheblich zur Entwicklung und Erweiterung der im Folgenden präsentierten Monte Carlo Software beigetragen haben.

Zusammenfassung

Diese Arbeit befasst sich mit der Simulation mit einander verbundenen Grundoperationen, wie sie bei der Verarbeitung und Herstellung von Feststoffen eingesetzt werden. Der Feststoff wird dabei als ein Partikelensemble beschrieben, das möglicherweise in Flüssigkeiten (Kolloide) oder in einem Gas (Aerosole) suspendiert ist. Die Verarbeitung der Partikel beruht auf physikalischen Mechanismen wie Nukleation, Koagulation, Bruch, Verdampfung und Kondensation sowie Partikeltransport zwischen den Grundoperationen. Die entsprechenden Raten dieser Mechanismen hängen dabei von den Eigenschaften der einzelnen Partikel ab: neben der Partikelgröße müssen für eine korrekte Beschreibung ggf. weitere Partikeleigenschaften (wie Porosität, Oberflächenvolumen, elektrische Ladung, usw.) berücksichtigt werden. Die Lösung der sich daraus ergebenden Populationsbilanzgleichung stellt eine anspruchsvolle numerische Aufgabe dar, insbesondere wenn viele Partikeleigenschaften in einem Netzwerk von miteinander verbundenen Kompartimenten oder Geräten modelliert werden.

Herkömmliche Lösungsstrategien für die Populationsbilanzgleichung umfassen 1) die Beschreibung der Partikelpopulation nur durch die Momente der entsprechenden Verteilung oder 2) die Diskretisierung des Partikelgrößenspektrums in eine endliche Anzahl von Größen oder Größenbereichen. Beide Strategien sind auf eine geringe Anzahl von Partikeleigenschaften (maximal 2–3 bei relativ schlechter Auflösung) beschränkt. Stochastische Methoden, auch Monte-Carlo-Methoden genannt, stellen eine attraktive Alternative zu diesen Ansätzen dar. Sie ermöglichen die Modellierung mehrerer Partikeleigenschaften auf Kosten einer deutlich höheren Rechenzeit und eines inhärenten stochastischen Rauschens der generierten Ergebnisse.

Im Rahmen dieser Arbeit werden neuartige Strategien zur Verringerung der erforderlichen Rechenzeit auf zwei Wegen erreicht: 1) der Einsatz von GPUs ermöglicht die Parallelisierung der erforderlichen Berechnungen und 2) die Formulierung neuartiger mathematischer Konzepte ermöglicht eine neue Art von Monte Carlo Simulationen, die ein geringeres inhärentes Rauschen aufweisen und daher die gleiche Genauigkeit (im Vergleich zu konventionellen Methoden) garantieren, wenn weniger Simulationspartikel – und damit Rechenressourcen – eingesetzt werden.

Dazu wird eine Reihe von parallelen Algorithmen vorgestellt und deren Implementierung auf der GPU veranschaulicht. Die Algorithmen sind speziell für die gleichzeitige Behandlung einer großen Anzahl von gewichteten Monte Carlo Simulationspartikeln konzipiert. Im Rahmen dieses Ansatzes wird die parallele stochastische Simulation von Bruchereignissen für jedes Simulationspartikel möglich. Die parallele Beschreibung des Partikelwachstums und der Verdampfung für jedes Partikel ermöglicht – im Gegensatz zu seriellen CPU-Ansätzen – eine effiziente Simulation dieser Prozessschritte und damit des Ostwald-Reifungsprozesses.

Die im Rahmen dieser Arbeit vorgeschlagenen neuartigen mathematischen Formulierungen basieren auf unterschiedlich gewichteten Monte Carlo Simulationspartikeln, die es erlauben, eine Vielzahl von Simulationsszenarien zu modellieren, die durch die Anwendung konventioneller Monte Carlo Techniken, die auf ein Ensemble gleich gewichteter Simulationspartikel zurückgreifen, nicht zugänglich sind. Dies wird explizit durch die Simulationen von Szenarien gezeigt, die 1) den Transport von Partikeln in einem zusammenhängenden Kompartimenten-Netzwerk oder 2) die Nukleation von Partikeln und das anschließende Partikelwachstum durch die Mechanismen der Koagulation und des Kondensationswachstums (bzw. der Verdampfung) beschreiben.

Neben der Formulierung dieser neuartigen Ansätze werden verschiedene relevante Benchmark-Testfälle vorgestellt und die Gültigkeit der neuartigen Schemata wird durch den Vergleich der Simulationsergebnisse mit anderen Simulationstechniken, die auf Diskretisierungsmethoden oder analytischen Ergebnissen basieren, demonstriert. Vergleiche mit anderen vorgeschlagenen modernen MC-Simulationstechniken, die auf gewichteten Simulationspartikeln basieren (sogenannte stochastische gewichtete Algorithmen (SWA)), zeigen 1) ein geringeres inhärentes statistisches Rauschen der neu vorgeschlagenen Techniken für die Simulation der Koagulation und 2) ein erweitertes Partikelgrößen-

spektrum, das durch die Partikelgrößenverteilung für die Simulation des Bruchs dargestellt wird.

Abstract

This work discusses the modeling of interconnected unit operations as used for the processing and production of solid materials. The materials are thereby described as single particles which are possibly suspended in liquids (colloids) or in a gas (aerosols). The processing of the particles is based on physical mechanisms such as nucleation, coagulation, breakage, evaporation and condensation as well as particulate transport between the units. The corresponding rates of these mechanisms depend thereby on the properties of the single particles: next to the particle size, additional particle properties (like porosity, surface volume, electric charge, etc.) might have to be considered for a correct description. The solution of the resulting population balance equation poses a challenging numerical task, especially if many particle properties are modeled in a network of interconnected compartments, or units.

Conventional solution strategies for the population balance equation encompass 1) the description of the particle population only by its moments, or 2) the discretization of the particle size spectrum into a finite number of sizes or size ranges. Both strategies are limited to a low number of particle properties (maximal 2–3 with a low number of sections or points). Stochastic methods, also called Monte Carlo methods, pose an attractive alternative to these approaches, enabling the modeling of several particle properties at the cost of higher computational time and an intrinsic stochastic noise of the generated result.

In the scope of this work, novel strategies for the reduction of the necessary computing time are introduced by two means: 1) the application of GPUs allows the parallelization of the necessary computations and 2) the formulation of novel mathematical concepts allows for a new kind of Monte Carlo simulations which have inherent lower noise levels and guarantee therefore the same accuracy (in comparison with conventional methods) if less computational particles – and thus computational resources – are applied.

A suit of parallel algorithms is introduced and the GPU-implementation is shown. The algorithms are specifically designed for the simultaneous treatment of a large number of weighted Monte Carlo simulation particles. In the scope of this approach, the parallel stochastic simulation of breakage events for each simulation particle becomes possible. The parallel description of particulate growth and evaporation for each particle makes an efficient simulation of these processing steps and thus the Ostwald-ripening process possible – in contrast to serial CPU approaches.

The novel mathematical formulations proposed in the scope of this work are based on weighted Monte Carlo simulation particles which allow the modelling of a variety of simulation scenarios which are not accessible by the application of conventional Monte Carlo techniques recurring to an ensemble of equally weighted simulation particles. This is explicitly shown by the simulations of scenarios describing 1) the transport of particles in an interconnected network of units or 2) the nucleation of particles and subsequent particle growth through the mechanisms of coagulation and condensational growth (resp. evaporation).

Next to the presentation of these novel approaches, different relevant benchmark test cases are formulated and the validity of the novel schemes is demonstrated by the comparison of the simulation results with other simulation techniques based on discretization methods (discrete-sectional methods or the fixed pivot point technique) or analytical results. Comparisons to other proposed state-of-the-art MC simulation techniques based on weighted simulation particles (termed stochastic weighted algorithms (SWA)), shows 1) a lower inherent statistical noise of the novel proposed techniques for the simulation of coagulation, and 2) an extended particle size spectrum rendered by the particle size distribution for the simulation of breakage.

Contents

Notation

Citations

[Paper III]	Refers to the 3rd paper constituting this thesis (beginning on page 129)
[CoPaper II]	Refers to the 2nd paper co-written by the author, but not constituting this thesis (these contributions are listed on page 75)
[3]	Refers to the 3rd entry in the 'Other Publications' subsection of the Bibliography section (starting on page 76)

Abbreviations

AR	Acceptance-Rejection (MC method), page 18
ASPEN	Advanced System for Process ENgineering (Company and Software [1]), page 1
CAPE	Computer Aided Process Engineering (CAPE-OPEN Standard [2]), page 1
CFD	Coputational Fluid Dynamics, page 9
CNMC	Constant Number Monte Carlo, page 18
CPU	Central Processing Unit
CSTR	Continuous Stirred Tank Reactor, page 9
CUDA	Compute Unified Device Architecture, page 21
DNS	Direct Numerical Simulation, page 9
DS	Discrete-Sectional method, page 12
DQMOM	Direct Quadrature Method Of Moments, page 11
FEM	Finite Element Method, page 14
FP	Fictitious Particle theory, page 30
FWTF	Fragmentation Weight Transfer Function, page 35
GPU	Graphic Processing Unit, page 21
GTX	Giga Texel shader eXtreme, GPU brand produced by Nvidia
LV	Low Volume selection scheme for breakage, page 36
LWM	Low Weight Merging, page 39
MC	Monte Carlo, page 15
MFA	Mass Flow Algorithm, page 29 (coagulation) or 34 (breakage)
mMC	multi Monte Carlo, page 29 and Table 4.2
NB	Number Based selection scheme for breakage, page 35
ODE	Ordinary Differential Equation, page 12
PBE	Population Balance Equation, page 5
PDF	probability density function, page 34
PSD	Particle Size Distribution, page 1
QMOM	Quadrature Method Of Moments, page 11
RTX	Ray tracing Texel eXtreme, GPU brand produced by Nvidia
RM	Random Merging, page 39
SM	Streaming Multiprocessor, page 21
SWA	Stochastic Weighted Algorithm, page 29, Table 4.2 and 4.3 define SWA1 – SWA4
URN	Uniformly distributed Random Number, page 24
VB	Volume Based selection scheme for breakage, page 34

Latin Nomenclature

Symbol	Unit	Description
$\breve{a}$	–	parameter for triangular PSD, Eq. (A.4)
$\breve{b}$	–	parameter for triangular PSD, Eq. (A.4)
$b(v_\mathrm{P})$	s^{-1}	breakage rate of a parent particle with volume v_P
b_max	s^{-1}	maximal $b(v_i)$ for all $\mathcal{N}_\mathrm{MC}$ particles i
$B(v_\mathrm{P})$	–	total number of fragments resulting from breakage of parent particle with volume v_P, Eq. (4.4)
$\mathcal{B}_\mathrm{dim}$	–	total number of threads per block, Table 3.1
$\mathcal{B}_\mathrm{id}$	–	unique ID for each CUDA block, Table 3.1
$\breve{c}$	–	parameter for triangular PSD, Eq. (A.4)
$C^\mathrm{B}_\ldots$	various	breakage rate constants Table 2.1b shows units of C^B_l and C^B_q
$C^\mathrm{C}_\ldots$	various	coagulation constants Table 2.1a shows units of C^C_c, $C^\mathrm{C}_\mathrm{sum}$, $C^\mathrm{C}_\mathrm{prod}$, C^C_fm and C^C_co
C^E_w	–	constant coefficients for RK error calculation, Table E.1a
$C^\mathrm{G}_\ldots$	various	growth rate constants Table 2.1d shows units of C^G_c, C^G_l, C^G_d and C^G_fm
$C^\mathrm{I}_{n,k}$	–	constant coefficients for RK interpolation, Table E.1c
$C^\mathrm{RK}_{n,w}$	–	constant coefficients for RK method, Table E.1a
C^N_c	$\mathrm{m}^{-3}\,\mathrm{s}^{-1}$	constant nucleation rate, Table 2.1c
C^T_n	–	constant coefficients for RK time calculation, Table E.1b
$\overline{C}$	–	constant for f_LV in Table 4.6, defined as $C(v_\mathrm{P})$ in [Paper III] Eq. (**14**)
d	m	particle diameter
d^*	m	Kelvin diameter, Eq. (2.5)
$d_i^{(j)}$	m	particle diameter of i-th MC particle of j-th simulation
d_0	m	diameter of particles in monodisperse initial PSD
d_g^PP	m	mean geometric diameter resulting from pivot point method, Eq. (D.8)
$d_\mathrm{g}^{(\mathrm{j})}$	m	mean geometric diameter of j-th MC simulation, Eq. (D.1)
$\overline{d_\mathrm{g}}$	m	mean geometric diameter, mean value for $\mathcal{N}_\mathrm{MC}$ MC simulations, Eq. (D.3)
$\mathrm{d}N/\mathrm{d}\log(d)$	m^{-3}	number-based PSD (short notation for $\mathrm{d}N(d)/\mathrm{d}\log(d)$)
$E_\mathrm{m}(i,j)$	–	merging error, defined in Eq. (4.10)
$\breve{e}$	–	parameter for arcsine PSD, Eq. (A.3)
$\breve{f}$	–	parameter for arcsine PSD, Eq. (A.3)
$f_\ldots(v_\mathrm{F}\|v_\mathrm{P})$	m^{-3}	PDF for selection fragment volume v_F resulting from breakage of parent particle with volume v_P Table 4.6 shows f_Gen, f_VB, f_NB and f_LV Eq. (4.7) shows $f_\mathrm{VB-LV}$ and $f_\mathrm{NB-LV}$
$f_{U_1\to U_2}$	s^{-1}	particle flow rate from unit U_1 to U_2, Eq. (4.11)
$f_\mathrm{sT}^{(i)}(x)$	–	Student's t-test distribution for i degrees of freedom
$\mathscr{F}_{j\to i}(n_j(v,t))$	$\mathrm{m}^{-6}\,\mathrm{s}^{-1}$	on size v dependent rate of change of PSDs due to outflow of particles from compartment j (with PSD $n_j(v,t)$) into compartment i

$G(v,t)$	$\mathrm{m^3\,s^{-1}}$	growth rate of particle with volume v, see Eq. (2.7) Table 2.1d shows definitions for G_c, G_l, G_d and G_fm
$\mathcal{G}_\mathrm{dim}$	$-$	total number launched blocks, Table 3.1
$H(i)$	various	arbitrary function defining SWA3 and SWA4 in Table 4.3
J	$\mathrm{m^{-3}\,s^{-1}}$	nucleation rate J_c, J_cou, J_cls and J_gir are defined in Table 2.1c
$\breve{k}$	$-$	parameter for Pareto PSD, Eq. (A.2)
k_B	$\mathrm{J\,K^{-1}}$	Boltzmann constant
$K(d)$	$-$	Kelvin correction factor, see Table 2.1d
$\breve{m}$	$-$	parameter for log-normal PSD, Eq. (A.1)
m_G	kg	atomic (resp. molecular) mass of the nucleating material
$n(v)$, $n(v,t)$	$\mathrm{m^{-6}}$	number-based PSD (short notation for $\mathrm{d}N(v)/\mathrm{d}v$)
$n_\mathrm{res}(v_\mathrm{F})$	$\mathrm{m^{-6}}$	PSD of breakage fragments in the stochastic mean, Eq. (4.5)
$n_\mathrm{exact}(v_\mathrm{F})$	$\mathrm{m^{-6}}$	exact PSD of breakage fragments described by γ, Eq. (4.6)
$n(d)$	$\mathrm{m^{-4}}$	number-based PSD (short notation for $\mathrm{d}N(d)/\mathrm{d}d$) $n_\mathrm{LN}(d)$, $n_\mathrm{P}(d)$, $n_\mathrm{AS}(d)$ and $n_\mathrm{T}(d)$ are defined in Appendix A.1
$n_l^i(t)$	$\mathrm{m^{-6}}$	i-th linear combination factor in section l for PSD approximation by FEM
$\overline{n_l}(t)$	$\mathrm{m^{-6}}$	number-based PSD resulting from discretization into sections
$N(t)$	$\mathrm{m^{-3}}$	total particle number concentration (i.e.: $N(t) = N_{[0,\infty]}(t)$) particle
$N(t)_l$, N_l	$\mathrm{m^{-3}}$	number concentration of section or pivot point l
N^PP	$\mathrm{m^{-3}}$	total particle number concentration resulting from pivot point method, Eq. (D.8)
$N^{(j)}$	$\mathrm{m^{-3}}$	total particle number concentration for j-th MC simulation, Eq. (D.1)
$\overline{N}$	$\mathrm{m^{-3}}$	total particle number concentration, mean value for $\mathcal{N}_\mathrm{MC}$ MC simulations, Eq. (D.3)
$\overline{N}^{b+}$, $\overline{N}^{b-}$	$\mathrm{m^{-3}}$	bounds of the confidence interval for the total particle number concentration, Eq. (D.5)
N_evap	$\mathrm{m^{-3}}$	correction for N_G resulting from evaporation of MC particles during one RK step, Figure E.1
$N_\mathrm{evap}^\mathrm{I}$	$\mathrm{m^{-3}}$	correction for N_G resulting from evaporation of MC particles during one RK step with subsequent interpolation, Figure E.2
N_G	$\mathrm{m^{-3}}$	concentration of atoms (or molecules) of the nucleating/condensing material
$N_\mathrm{G}^{\mathrm{AP},n}$	$\mathrm{m^{-3}}$	used as N_G in RK calculation of $N_\mathrm{G}^{\mathrm{RK},n}$ and $v_i^{\mathrm{RK},n}$, Eq. (E.1)
$N_\mathrm{G}^{\mathrm{RK},n}$	$\mathrm{m^{-3}}$	RK variable for the calculation of $N_\mathrm{G}^{\mathrm{AP},n}$ and $N_\mathrm{G}^{\mathrm{RK,new}}$, Eq. (E.1)
$\tilde{N}_\mathrm{G}^{\mathrm{RK},n}$	$\mathrm{m^{-3}}$	RK value for interpolation of N_G, (E.15) and Eq. (E.17)
$N_\mathrm{G}^{\mathrm{RK,new}}$	$\mathrm{m^{-3}}$	approximation of N_G after one RK step Eq. (E.3)
$N_\mathrm{G,growth}^{\mathrm{RK},n}$	$\mathrm{m^{-3}}$	growth contribution to $N_\mathrm{G}^{\mathrm{RK},n}$ (if no nucleation is simulated: $N_\mathrm{G}^{\mathrm{RK},n} = N_\mathrm{G,growth}^{\mathrm{RK},n}$), Eq. (E.1)
$N_\mathrm{G}^\mathrm{I}(t)$	$\mathrm{m^{-3}}$	interpolated value of N_G for time t using RK, Eq. (E.14)
N_s	$\mathrm{m^{-3}}$	concentration of atoms (or molecules) of the nucleating/condensing material at saturation pressure, Eq. (2.5) and Eq. (B.10)
N_sp	$\mathrm{m^{-3}}$	surplus concentration of atoms (or molecules) of the nucleating/condensing material (Eq. (B.10))

$\mathcal{N}_{\text{cells}}$	–	number of cells (resp. compartments) used in CFD (resp. compartmental) modeling
$\mathcal{N}_{\text{mc}}^{\text{break}}$	–	number of MC particles with identical properties selected for breakage
$\mathcal{N}_{\text{MC}}$	–	total number of MC particles used for one MC simulation
$\mathcal{N}_{\text{PP}}$	–	number of pivot points used for discrete solution method of PBE
$\mathcal{N}_{\text{sample}}$	–	number of randomly selected particle pairs, used by algorithm shown in section 3.2
$\mathcal{N}_{\text{sec}}$	–	number of sections used in sectional solution methods of PBE
$\mathcal{N}_{\text{sim}}$	–	number of used MC simulations
m_{G}	kg	atomic (or molecule) mass of the nucleating/condensing material
M	$\text{kg}\,\text{m}^{-3}$	total mass concentration of a particle species (e.g. $M_{\text{Fe,p}}$) or of a gaseous material prior to condensation (e.g. $M_{\text{Fe,g}}$) or of the carrier gas (e.g. M_{N_2})
$p_i^{(k)}$	various	k-th property of particle i
p_{s}	Pa	saturation pressure of the nucleating/condensing material
P_{sel}	–	$P_{\text{sel}}(_{(i,j)} \mid _{(i,j)}$ or $_{(j,i)})$ is the selection probability for MC particle pair (i,j) under the condition that either (i,j) or (j,i) are selected for sure for coagulation in scope of SWA, Eq. (C.5) and (C.6)
$P_{i,j}$	–	coagulation probability for MC particles i and j during $\Delta\tau_{\text{MC}}$, Eq. (2.21)
$P_{i,j}(\Delta\tau_{\text{s}}\|\Delta\tau_{\text{MC}})$	–	Conditional probability that coagulation of an AR selected pair takes place within a time smaller than $\Delta\tau_{\text{s}}$ if it takes place for sure within $\Delta\tau_{\text{MC}}$, see Eq. (4.3)
$P_{i,j}^{\text{AR}}$	–	$P_{i,j}$ for randomly selected MC particles i and j in AR approach, Eq. (2.22)
$P_{U_1\to U_2}(i)$	–	probability for particle i in unit 1 for outflow to unit 2, Eq. (4.16)
Q_l	various	general property of a section l (e.g. number concentration), described and only used in the footnote on page 12
r	–	uniformly distributed random number
r_{off}	–	random integer with $0 \le r_{\text{off}} \le \mathcal{N}_{\text{MC}}$, section 4.6.1.4
$R_{i,j}$	s^{-1}	coagulation rate for non weighted MC particles i and j, Eq. (2.17), or for weighted MC particles: $R_{i,j}^{\text{mMC}}$ and $R_{i,j}^{\text{SWA}}$ in Table 4.2, $R_{i,j}^{\text{fp}}$ and $R_{i,j}^{\text{sr}}$ in Table 4.4
R_{max}	s^{-1}	maximum of all possible coagulation rates $R_{i,j}$
R_{mean}	s^{-1}	mean coagulation rate for a sample of randomly selected pairs
R_{sum}	s^{-1}	sum of coagulation rates $R_{i,j}$ for a sample of randomly selected pairs
$\mathcal{R}_{\text{A}}$	–	maximum of ratios of RK errors to tolerance values in actual RK step, Eq. (E.6)
$\mathcal{R}_{\text{L}}$	–	value of $\mathcal{R}_{\text{A}}$ during last accepted RK step
$\breve{s}$	–	parameter for log-normal PSD, Eq. (A.1)
S	–	supersaturation, Eq. (2.5)
t	s	time
t_{end}	s	simulation end time
$t_{\mathcal{I}}$	s	time for RK interpolation, Eq. (E.13)
t_{sim}	s	simulation time increasing from 0 to t_{end}

t_{RK}	s	simulation time during RK routine, section E.1.4
$t_{\mathrm{RK}}^{\mathrm{end}}$	s	simulation end time for RK routine
t_{stop}	s	time interval between two artificial stops of the simulation
$t^{(\mathrm{col})}$	s	time for collision/coagulation of 2 specific particles
$\overline{t^{(\mathrm{col})}}$	s	mean time for collision/coagulation of 2 particles
T	K	temperature
$\mathcal{T}_{\mathrm{id}}$	$-$	unique ID for each thread within a CUDA block, Table 3.1
U_{d}	m	arbitrary constant for normalization of PDFs (e.g. δ functions)
U_{v}	m^3	arbitrary constant for normalization of PDFs (e.g. δ functions)
v	m^3	particle volume
v^*	m^3	Kelvin volume (volume of nucleating particles is $v^* + v_{\mathrm{G}}$), Eq. (2.5)
$v_l^{\dashv}$	m^3	boundary of a section l for sectional method, page 12 and section B.1
$v_i^{\bullet}$	m^3	volume of i-th pivot point
$\overline{v}$	m^3	defined in footnote 1 on page 10
v_0	m^3	volume of particles in monodisperse initial PSD
v_i	m^3	particle volume of i-th MC simulation particle
$v_i^{(\mathrm{new})}$	m^3	v_i after coagulation, see Table 4.2 for SWA, mMC; and Figure 4.2 for SR and FP
$v_{i,U}^{\mathrm{new}}$	m^3	particle volume of i-th MC simulation particle to be inserted in unit U due to transport, Eq. (4.13)
$v_i^{\mathrm{AP},n}$	m^3	value for v_i during n-th part of one RK step, Eq. (E.1)
$v_i^{\mathrm{I}}(t)$	m^3	interpolated value of v_i for time t using RK, Eq. (E.13)
$v_i^{\mathrm{RK},n}$	m^3	RK value for interpolation of v_i, Eq. (E.1)
$\tilde{v}_i^{\mathrm{RK},n}$	m^3	RK value for the calculation of v_i , Eq. (E.12)
$v_i^{\mathrm{RK,new}}$	m^3	new value for v_i after one RK step, Eq. (E.3)
v_{F}	m^3	volume of a fragment resulting from breakage of a parent particle
v_{G}	m^3	atomic (or molecule) volume of the nucleating/condensing material
v_{lim}	m^3	limit volume for f_{LV} selection scheme in Table 4.6
v_{P}	m^3	volume of a parent particle undergoing breakage
$\mathcal{V}_{\mathrm{B}}$	$\mathrm{m}^3/\mathrm{m}^3$	volume concentration within the nucleation buffer, section 4.7.3
$\mathcal{V}_{\mathrm{B}}^{\mathrm{I}}(t)$	$\mathrm{m}^3/\mathrm{m}^3$	interpolated value of $\mathcal{V}_{\mathrm{B}}$ for time t using RK, Eq. (E.14)
$\mathcal{V}_{\mathrm{B}}^{\mathrm{RK},n}$	$\mathrm{m}^3/\mathrm{m}^3$	RK value for the calculation of $\mathcal{V}_{\mathrm{B}}^{\mathrm{RK,new}}$, Eq. (E.11)
$\tilde{\mathcal{V}}_{\mathrm{B}}^{\mathrm{RK},n}$	$\mathrm{m}^3/\mathrm{m}^3$	RK value for interpolation of $\mathcal{V}_{\mathrm{B}}$, Eq. (E.16) and Eq. (E.17)
$\mathcal{V}_{\mathrm{B}}^{\mathrm{RK,new}}$	$\mathrm{m}^3/\mathrm{m}^3$	new value for $\mathcal{V}_{\mathrm{B}}$ after one RK step, Eq. (E.11)
$\mathcal{V}_{\mathrm{T}}$	$\mathrm{m}^3/\mathrm{m}^3$	volume concentration threshold for MC nucleation, section 4.7.3
V_{sys}	m^3	volume of simulated system (representative for larger reactor volume)
W_i	m^{-3}	statistical weight of MC simulation particle i
$W_i^{(j)}$	m^{-3}	statistical weight of i-th MC particle of j-th simulation
$W_{i,U}$	m^{-3}	statistical weight of i-th MC particle in unit U
$W_i^{(\mathrm{new})}$	m^{-3}	W_i after coagulation, see Table 4.2 for SWA, mMC; and Figure 4.2 for SR and FP
$W_{i,U}^{\mathrm{new}}$	m^{-3}	$W_{i,U}$ of novel particle to be inserted in unit U due to transport, Eq. (4.13)
W_{F}	m^{-3}	statistical weight of fragment assigned to MC particle after breakage, Table 4.6 or Eq. (4.8)

W_P	m^{-3}	statistical weight of MC parent particle undergoing breakage
$W_\mathrm{P}^\mathrm{tot}$	m^{-3}	total statistical weight of $\mathcal{N}_\mathrm{mc}^\mathrm{break}$ MC parent particles undergoing breakage
W_MC	m^{-3}	statistical weight of equally weighted MC simulation particles
$\overline{W}$	m^{-3}	mean statistical weight of all MC particles in one simulation, footnote 12 on page 39
$\breve{x}$	–	parameter for Pareto PSD, Eq. (A.2)
x	m	spatial coordinate(s) (1D: scalar / 2D, 3D: two, three component vector), used only in section 2.1.3.
x_u	$\mathrm{m\,s}^{-1}$	velocities at the spatial coordinate; scalar (1D) or vector (2D,3D) used only in section 2.1.3.
z^*	–	interval boundary for Student's t-test distribution, Eq. (D.6)

Greek Nomenclature

Symbol	Unit	Description
α_T	–	tuning factor for time-driven MC time step for breakage, section 4.3.2
$\alpha_{i,j}$	–	factor for weighted MC particles used by SWA with constraint in Eq. (4.1), Table 4.3 lists specific values
$\beta(v,v')$	$\mathrm{m}^3\,\mathrm{s}^{-1}$	coagulation kernel for particles with volumes v and v', as used in Eq. (2.2) explicit definitions are given in Table 2.1a as β_c, β_sum, β_prod, β_fm and β_co
$\beta_{i,j}$	$\mathrm{m}^3\,\mathrm{s}^{-1}$	coagulation kernel for MC particles i and j, short notation for $\beta(v_i,v_j)$
$\overline{\beta_{i,k\to l}}$	$\mathrm{m}^3\,\mathrm{s}^{-1}$	integrated coagulation kernel for sections or pivot points i and k resulting in particles in section (Eq. (B.2)) or pivot point (Eq. (B.7)) l
$\overline{\beta_{l,k\to}}$	$\mathrm{m}^3\,\mathrm{s}^{-1}$	coagulation kernel for coagulation of sections (resp. pivot points) l and k resulting in particles in all other possible sections (Eq. (B.3)) resp. pivot points (Eq. (B.8))
$\gamma(v_\mathrm{F}\|v_\mathrm{P})$	m^{-3}	breakage function described beneath Eq. (2.3)
$\gamma_\mathrm{B}(v_\mathrm{F}\|v_\mathrm{P})$	m^{-3}	binary breakage function defined in Table 2.1b
δ	–	δ - Dirac function [1]
$\delta_{i,j}$	–	discrete form of Dirac function: $\delta_{i,j}=1$,if $i=j$; $\delta_{i,j}=0$, else
Δd_g	m	arithmetic standard deviation for geometric mean diameters resulting from $\mathcal{N}_\mathrm{MC}$ different MC simulations, Eq. (D.4)
ΔN	m^{-3}	arithmetic standard deviation for total number concentrations resulting from $\mathcal{N}_\mathrm{MC}$ different MC simulations, Eq. (D.4)
Δt	s	general time step for MC simulation
Δt_RK	s	adaptive time step for one RK step
$\Delta t_\mathrm{RK}^\mathrm{new}$	s	novel value for Δt_RK calculated in (E.7)
$\Delta t_\mathrm{RK}^\mathrm{ini}$	s	initial value for Δt_RK, section E.1.4
$\Delta t_\mathrm{RK}^{\mathrm{ini},U}$	s	$\Delta t_\mathrm{RK}^\mathrm{ini}$ in unit or compartment U
$\Delta\tau_\mathrm{B}$	s	adaptive time step for time-driven MC simulation of breakage, Figure 4.6
$\Delta\tau_\mathrm{B}^U$	s	$\Delta\tau_\mathrm{B}$ in compartment or unit U
$\Delta\tau_\mathrm{MC}$	s	event-driven MC time step for coagulation, Eq. (2.20)
$\Delta\tau_\mathrm{MC}^U$	s	$\Delta\tau_\mathrm{MC}$ in compartment or unit U

[1] The function $\delta(x)$ has the following properties: $\delta(0)=\infty,\ \delta(x\neq 0)=0,\ \int_{-\epsilon}^{+\epsilon} f(x)\delta(x)\mathrm{d}x=f(0),\ \epsilon>0$.

$\Delta\tau_\mathrm{s}$	s	time step with $\Delta\tau_\mathrm{s} < \Delta\tau_\mathrm{MC}$
$\Delta\tau_\mathrm{Tr}$	s	time step for transport
$\Delta\sigma_\mathrm{g}$	–	arithmetic standard deviation for geometric standard deviations resulting from $\mathcal{N}_\mathrm{MC}$ different MC simulations, Eq. (D.4)
$\Delta^\mathrm{RK} v_i$	m^3	difference between 4th and 5th order RK value for v_i, Eq. (E.4)
$\Delta^\mathrm{RK} N_\mathrm{G}$	m^{-3}	difference between 4th and 5th order RK value for N_G, Eq. (E.4)
$\Delta W_{i,U}$	m^{-3}	change of statistical weight of MC simulation particle i in unit U within one Euler step, Eq. (4.15)
$\epsilon_{..}$	–	relative deviation between MC and pivot point method ϵ_N (concentration), ϵ_{d_g} (mean geometric diameter) and $\epsilon_{\sigma_\mathrm{g}}$ (mean geometric standard deviation) are defined in Eq. (D.10)
ε^G	m^{-3}	RK error tolerance for N_G, Eq. (E.5)
$\varepsilon_\mathrm{g,abs}$	–	absolute RK error tolerance for N_G, used in Eq. (E.5)
$\varepsilon_\mathrm{g,rel}$	m^{-3}	relative RK error tolerance for N_G, used in Eq. (E.5)
$\varepsilon_\mathrm{merge}$	–	maximal allowable merging error in section 4.6.1.3
ε_i^v	m^3	RK error tolerance for particle i, Eq. (E.5)
$\varepsilon_\mathrm{v,abs}$	m^3	absolute RK error tolerance for particle volume, used in Eq. (E.5)
$\varepsilon_\mathrm{v,rel}$	–	relative RK error tolerance for particle volume, used in Eq. (E.5)
η	Pa s	dynamic viscosity of the carrier gas or fluid
θ	–	ratio of time increment for interpolation to full RK time step, Eq. (E.13)
κ_H	–	constant factor describing geometric grid spacing (i.e.: $v_{l+1}/v_l = 2^{\kappa_\mathrm{H}}$)
μ_n	$\mathrm{m}^{3(\mathrm{n}-1)}$	n-th moment of a PSD $n(v)$, defined in Eq. (2.11)
$\mu_{\mathrm{d},n}$	$\mathrm{m}^{(-3+\mathrm{n})}$	n-th moment of a PSD $n(d)$
ρ_p	$\mathrm{kg\,m}^{-3}$	particle density
σ	$\mathrm{J\,m}^{-2}$	surface tension
$\sigma_\mathrm{g}^\mathrm{PP}$	–	geometric standard deviation resulting from pivot point method, Eq. (D.8)
$\sigma_\mathrm{g}^{(j)}$	–	geometric standard deviation of j-th MC simulation, Eq. (D.2)
$\overline{\sigma_\mathrm{g}}$	–	geometric standard deviation, mean value for $\mathcal{N}_\mathrm{MC}$ simulations, Eq. (D.3)
τ_fm	s	characteristic time for coagulation in free-molecule regime, Eq. (A.10)
Υ	–	constant used for combination of breakage schemes, Eq. (4.7)
$\phi(v)$	–	test function for FEM ($\phi(v) = \sum_k \phi_k^l(v)$, for $v \in (v_{l-1}, v_l)$)
$\phi_k^l(v)$	–	k-the part of test function ϕ in section l, used for FEM
χ	–	safety correction factor for calculation of R_max from sample, Eq. (3.2)
$\psi_l^i(v)$	–	i-th Lagrange polynomial in section l used by FEM for PSD approximation
ω_k	–	merging weight for k particle property, described in section 4.4.1

Chapter 1

Introduction

Flowsheet simulations are a crucial tool for controlling and optimization of chemical engineering processes as well as production processes in general - on laboratory and plant scales. Especially the optimization of plant production processes leads to increased profitability and may also improve the ecological footprint of the production. It may also help to understand complex assembly processes and make thus the development of novel materials possible.

Chemical engineering processes in which liquid and gaseous materials have to be considered are well understood and can be simulated to a sufficiently detailed accuracy by commercially available flowsheet simulation software (e.g. ASPEN plus [1, 3], ChemCAD [4], etc. all using a unified standard, CAPE-OPEN [2, 5], for material parameters and unit operations). The processing of solids, on the other hand, is not well understood. This is mainly due to the many properties of the particulate material, which have to be captured, in order to describe its physical and chemical behavior correctly. While it is absolutely sufficient, to monitor only a few parameters, such as the pressure, temperature and chemical composition, in order to describe and control the behavior of a gas or a liquid completely[1], the correct modeling of single particles which form the solid, is necessary in order to process a powder correctly. This is mostly done by means of the particle size distribution (PSD), which describes the amount of the particulate material in dependency of the size of the single particle. Such a description takes into account, that differently sized particles may behave differently in the context of chemical processing steps due to their sizes. It has been noted, however, that size is not the only one property, which has to be taken into account, and there exists a fruitful discussion and research about, how to capture which properties of a given powder, in order to describe its behavior correctly. Depending on the application, different additional particle properties are considered, e.g. porosity and wet (or binder) content for granulation [6, 7], sphericity for sieving[8], fractal dimensions and number of primary particles for particulate production via the aerosol route [9, 10]. The combination of all these different descriptions into one flowsheet simulation framework poses an intriguing research area [11, 12, 13, 14].

Next to the two intriguing questions, of 1.) how to measure these additional properties and 2.) how to formulate a model which describes the influence of these additional properties on the process correctly, there arises a third question, of 3.) how a correct simulation and prediction of the evolution of a PSD with several particle properties is possible. The answer to this question is the main topic of this thesis. But first, an exemplary production process is introduced in order to elaborate the notions of particle properties and sizes a little bit further.

1.1 An Exemplary Production Process

Figure 1.1 shows an exemplary pharmaceutical production process. First the pharmaceutical agent is created in a solid form (as crystals) in a crystallizer, by mixture of two liquid precursors. After the crystallization, the resulting crystals are milled and undergo a granulation process - a binder is used to 'glue' the agent into larger sizes of the product. The resulting particles (or granules) consist of two components: the agent and the binder. In a subsequent step the granules are sorted with respect to

[1] Note that, liquid-liquid mixtures (e.g. emulsions), as well as liquid-gas mixtures (foams) might make more complex descriptions necessary. The correct capture of the behavior of these mixtures treats one liquid (resp. gas) as dispersed in the other, so that the formal approach for the treatment of particles can be applied to these systems (sometimes referred to as colloidal systems).

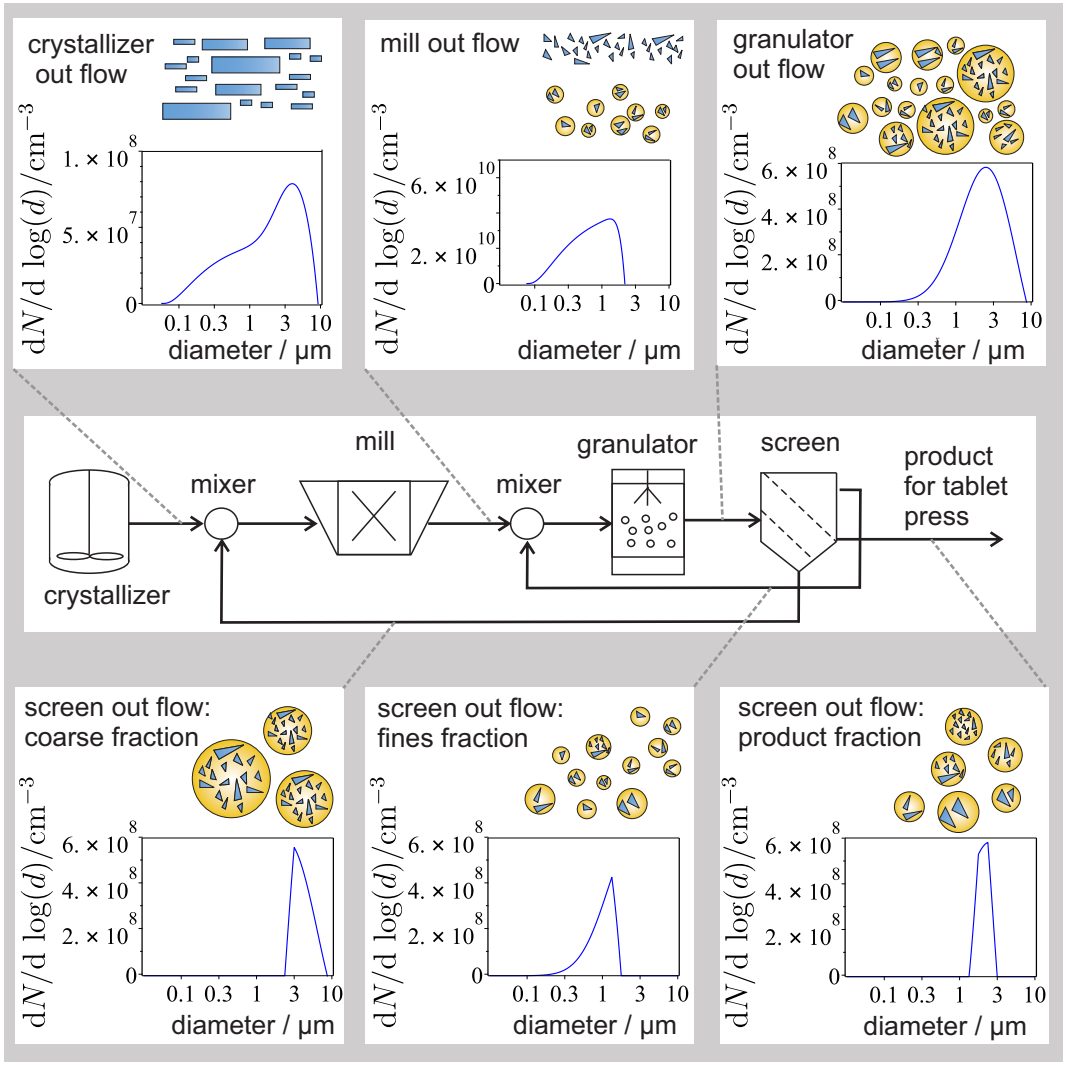

Figure 1.1: Flowsheet of interconnected unit operations of a pharmaceutical production. Exemplary particle size distributions are shown for single streams.

their size - only those in a certain size range are accepted as final product in the tablet press. Those, too small are redirected to the agglomeration process and those which are too large are redirected to the mill.

In order to describe this process correctly, it is necessary to foretell the particle size distributions in every unit (i.e. crystallizer, mill, screen, granulator) at every time. At least two particle properties such as the particle size and the ratio of pharmaceutical agent to binder have to be taken into account (the PSDs in Figure 1.1 take only the particle (i.e. crystal or granule size) into account). At the end, not only the correct amount of the agent in the product (i.e. the tablet) is important - the whole dissolution behavior of the tablet is important - i.e. the agent has to be released after being exposed to a biological ambient (the stomach) for a certain period of time. This dissolution behavior can only be foretold, if the exact composition of the granules in the tablet is predicted. Maybe, an even more detailed description of the particles, taking their shapes or composition out of primary agent crystals with binder shells has to be made in order to describe this dissolution behavior exactly.

1.2 Unit Operations

The separation of the complex production process into single processes (or unit) operations, like shown in Figure 1.1, allows to formulate the production process as the (potentially complex) interplay of single units whose behavior is (more or less) clearly defined with its own models. Hence, dispersions of particles in gaseous or liquid media are of the main interest of this thesis, a classification of unit

operations is presented from the perspective, of how the properties of the dispersion i.e. the properties of the single particles are altered. This perspective leads to the classification of unit operations into chemical, thermal and particulate operations, as is exemplified in the following.

- **Chemical processing:** the chemical composition is changed.

  One unit process can represent one chemical reaction as a processing step [15, 16]. During this step, the chemical composition of the affected particles is changed. Examples are:

  - reactions between different compounds
  - chemical decomposition
  - oxidation

- **Thermal processing:** the chemical composition remains unchanged, the disperse phase (i.e. the particles) remain unchanged, too.

  These unit operations may involve a change of the state of the matter, as long as the particulate dispersion is not changed, examples are:

  - heating or cooling
  - melting of bulk matter

- **Particulate processing:** the chemical composition remains unchanged, the disperse phase is (resp. the particle properties are) changed.

  These unit operations encompass the traditional five mechanical processing steps as articulated by [17] (the first five). Nowadays, 2 additional important particulate unit operations are considered [18], these are the last two on the following list of examples[2]:

  - size enlargement (agglomeration)
  - size reduction (comminution)
  - storage and conveying
  - separation
  - mixing
  - nucleation / crystallization
  - drying or evaporation (of the dispersed particles)

Table 1.1 lists the relevant physical mechanisms for the particulate processing unit operations. The agglomeration of particles can be enhanced due to the addition of the binder, whose nucleation, growth and evaporation has to be taken into account. The breakage of single particles during the size enlargement operation is thereby an unwanted side-effect of the process [19, 20, 21]. For the correct description of the PSD, this side effect has to be considered for certain scenarios. In other cases, the agglomeration is an unwanted side effect of milling of particles and has sometimes also to be taken into account [22].

The mixing of particle streams is assumed to happen instantly in this work. This is the case, if the typical time, which is needed to obtain a homogeneous mixture (e.g. miliseconds), is much shorter than the characteristic times of the other considered processes (e.g. seconds or minutes).[3]

The population balance equation, as it will be introduced in the subsequent chapter 2, can be used to capture all the unit operations in Table 1.1 by the rendering of the corresponding physical mechanism, as it is listed in table 1.1. A discussion of conventional deterministic and stochastic (Monte Carlo) solution strategies for the population balance equation and typical application scenarios is also discussed there. Chapter 3 introduces the concepts of parallel programming methods for acceleration of Monte Carlo simulations. And chapter 4 introduces a general solution framework based on parallel Monte Carlo algorithms for the solution of problems like the one shown in Figure 1.1.

[2] In some classifications, the drying, evaporation and nucleation / crystallization of particles is also regarded as a thermal process. Maybe the finer distinction in thermal particulate processes and mechanical particulate processes would be more accurate.

[3] If such an assumption cannot be made, more complicated mixing models have to be applied. These models also recur to simulations of transport, in which the considered unit would be separated into one mixed compartment (growing in time) and two or more unmixed compartment (shrinking in time) and a particulate flow between the two [23, 24]. An alternative approach – using weighted Monte Carlo particles – would be the attachment of an additional particle property: the mixing degree to each particle, which changes in time and has to be considered in the formulation of the corresponding rates and kernels listed in Table 2.1. The mixing of particles, however, is described as *"one of the oldest and yet one of the least understood of the unit operations of process engineering"* [16].

Table 1.1: Unit operations describing particulate processing with the population balance formalism from chapter 2.

Unit Operation	Mechanism	Equation	Section
size enlargement	coagulation (primary mechanism)	(2.2)	2.1.1.1
	evtl. nucleation (of binder)	(2.4)	2.1.1.3
	evtl. growth/evaporation (of binder)	(2.6)	2.1.1.4
	evtl. breakage (unwanted side effect)	(2.3)	2.1.1.2
size reduction	breakage (primary mechanism)	(2.3)	2.1.1.2
	evtl. coagulation (unwanted side effect)	(2.2)	2.1.1.1
conveying	transport	(2.10)	2.1.3
separation	size (or other property) dependent transport	(2.10)	2.1.3
mixing	transport (mixed and unmixed compartments)	–	–
	instantaneous homogeneous mixing	(2.10)	2.1.3
drying	evaporation (evtl. growth)	(2.6)	2.1.1.4
crystallization	nucleation (primary mechanism)	(2.4)	2.1.1.3
	evtl. growth/evaporation	(2.6)	2.1.1.4
	evtl. coagulation	(2.2)	2.1.1.1

Chapter 2

The Population Balance Equation

The population balance equation (PBE) is applied in a very wide area of natural sciences and different fields of engineering [25]. Some examples are: astrophysics (the formation of small planets or satellites [26, 27]), medicine (the modeling of cancer cells [28] or cell growth in general [29]), environmental sciences (particle formation in the atmosphere [30, 31], or sediment flocculation in marine environments [32, 33]), even the modeling of sociological and political phenomena has been suggested recently [34].

In the field of chemical engineering, the PBE is often used to describe single apparatuses or processes such as: milling [22, 35], crystallization (or precipitation) [36, 37, 38], drying [39], particle production in aerosol reactors [9, 40], granulation in fluidized beds [19, 41] or in general [20, 6].

In the scope of this thesis, the PBE is applied to such diverse problems as particle formation due to aggregation [Paper I] and [Paper II], decomposition of polymers [Paper III], particle formation in aerosol reactors [Paper VI] or in systems mimicking atmospheric conditions [Paper IV]. But first, the equation itself and some common solution strategies will be introduced.

2.1 Formulation of the Population Balance Equation

The main physical processes, which have to be considered in the flow sheet presented in Figure 1.1 are breakage, coagulation, condensational growth (resp. evaporation) and nucleation; as well as particulate transport between the single units. The complex interplay between coagulation, nucleation, growth (resp. evaporation), breakage and transport of particles can be formulated for each of these units as a population balance equation (PBE) [42]. The PBE describes the temporal evolution of the particle size distribution (PSD), $n(v,t)$, where the integral term $N(t) = \int_{v_0}^{v_0+\Delta v} n(v,t)\mathrm{d}v$ denotes the particle concentration (in units m^{-3}) of all particles with the sizes v between v_0 and $v_0 + \Delta v$. Where v might also represent a vector with multiple components (like volume, binder content, etc..), in this case the integration with respect to $\mathrm{d}v$ has to be taken with respect to each of these dimensions.

2.1.1 Mechanisms described by the PBE

In the following the equations will be presented for coagulation $\left(\frac{\mathrm{d}n(v,t)}{\mathrm{d}t}\right)_{\mathrm{coag}}$, condensation / evaporation $\left(\frac{\mathrm{d}n(v,t)}{\mathrm{d}t}\right)_{\mathrm{growth}}$, nucleation $\left(\frac{\mathrm{d}n(v,t)}{\mathrm{d}t}\right)_{\mathrm{nuc}}$ and breakage $\left(\frac{\mathrm{d}n(v,t)}{\mathrm{d}t}\right)_{\mathrm{break}}$. The modeling of all these processes happening simultaneously can be achieved by simple addition of the presented equations as:

$$\frac{\mathrm{d}n(v,t)}{\mathrm{d}t} = \left(\frac{\mathrm{d}n(v,t)}{\mathrm{d}t}\right)_{\mathrm{coag}} + \left(\frac{\mathrm{d}n(v,t)}{\mathrm{d}t}\right)_{\mathrm{growth}} + \left(\frac{\mathrm{d}n(v,t)}{\mathrm{d}t}\right)_{\mathrm{nuc}} + \left(\frac{\mathrm{d}n(v,t)}{\mathrm{d}t}\right)_{\mathrm{break}}. \tag{2.1}$$

The individual mechanisms are explained in the following sections.

2.1.1.1 Coagulation

$$\left(\frac{\mathrm{d}n(v,t)}{\mathrm{d}t}\right)_{\mathrm{coag}} = \underbrace{+\frac{1}{2}\int_0^v \beta(v',v-v')n(v',t)n(v-v',t)\mathrm{d}v'}_{\text{coagulation birth term}} \underbrace{- n(v,t)\int_0^\infty \beta(v,v')n(v',t)\mathrm{d}v'}_{\text{coagulation death term}} . \tag{2.2}$$

The coagulation dynamic is described by the coagulation kernel $\beta(v,v')$ (in units (m^3/s)). The collision frequency per m^3 (units $1/(\mathrm{m}^3\,\mathrm{s})$) between two particle species with the sizes v and v' and concentrations of $N(v)$ and $N(v')$ (in units m^{-3}) is given by: $\beta(v,v')\cdot N(v)\cdot N(v')$. Eq. (2.2) assumes that each collision of two particles with the sizes v and v' leads to the formation of a novel particle with the size $v+v'$. The coagulation birth term describes therefore the formation of novel particles with the size v, resulting from the coagulation of all possible particle pairs with the sizes $v-v'$ and v' (the factor $1/2$ prevents from double counting). The coagulation death term, on the other hand, describes the depletion of particles with the size v due to their coagulation with particles of any other size v'.

A wide range of coagulation kernels β have been suggested and its exact form depends on the considered process. Examples of different kernels are given for granulation in [43], or aerosol processes in [44, 45]. Table 2.1a summarizes all coagulation kernels used in this thesis.

2.1.1.2 Breakage

$$\left(\frac{\mathrm{d}n(v,t)}{\mathrm{d}t}\right)_{\mathrm{break}} = \underbrace{-b(v)\cdot n(v,t)}_{\text{breakage death term}} + \underbrace{\int_v^\infty b(v')\cdot n(v',t)\cdot\gamma(v|v')\mathrm{d}v}_{\text{breakage birth term}} . \tag{2.3}$$

The breakage of particles is described by the breakage rate $b(v)$ (units $1/\mathrm{s}$) which is the rate at which particles of size v break into smaller fragments, forming thus the breakage death term in Eq. (2.3). The (number-based) breakage function $\gamma(v|v')$ (units m^{-3}) allows to formulate the dimensionless term $\gamma(v|v')\mathrm{d}v$ which describes the number of particles (or fragments) of sizes between v and $v+\mathrm{d}v$ resulting from the breakage of the (parent) particle of size v'. The integration over all possible parent particle sizes v' whose breakage may lead to new particles with the size v leads to the breakage birth term in Eq. (2.3).

Several expressions for b and $\gamma(v|v')$ have been proposed for droplet breakage in liquid-liquid dispersions [52], granulation processes [43] or grinding [53]. Two simple examples are shown in Table 2.1b.

2.1.1.3 Nucleation

$$\left(\frac{\mathrm{d}n(v,t)}{\mathrm{d}t}\right)_{\mathrm{nuc}} = \underbrace{+J(t)\cdot\delta(v-v^*(t)-v_{\mathrm{G}})}_{\text{nucleation}} . \tag{2.4}$$

The nucleation rate $J(t)$ (units $1/(\mathrm{m}^3\mathrm{s})$) describes the rate of formation of novel particles per m^3 into the simulated (reactor-)volume. The novel particles have the size $v^*(t)+v_{\mathrm{G}}$, δ describes the delta-Dirac function. In the field of nucleation of aerosol nanoparticles, there exists a variety of proposed theories for the forms of J (as well as v^*) [54], nucleation rates used for crystallization are defined in [36, 37]. The nucleation theories for aerosols discussed in the results section of this thesis are shown in Table 2.1c and resort to the following definition of the Kelvin volume v^*, resp. Kelvin diameter d^*:

$$v^* = \frac{\pi\cdot(d^*)^3}{6}, \qquad d^* = \frac{4\cdot\sigma\cdot v_{\mathrm{G}}}{k_{\mathrm{B}}\cdot T\cdot\ln(S)}, \qquad S = N_{\mathrm{G}}/N_{\mathrm{s}}, \qquad N_{\mathrm{s}} = p_{\mathrm{s}}/(k_{\mathrm{B}}\cdot T), \tag{2.5}$$

Table 2.1: Coagulation kernels β, nucleation rates J, growth rates G, breakage rates b and breakage functions γ.

(a) Definitions of kernels β for coagulation of particles with the volumes v and v'. β_{fm} and β_{co} are discussed in [46].

Model	Coagulation kernel $\beta(v, v')$		Unit of constant	
Constant kernel	β_{c}	$= C_{\mathrm{c}}^{\mathrm{C}}$	$[C_{\mathrm{c}}^{\mathrm{C}}]$	$= \mathrm{m}^3\,\mathrm{s}^{-1}$
Sum kernel	β_{sum}	$= C_{\mathrm{sum}}^{\mathrm{C}} \cdot (v + v')$	$[C_{\mathrm{sum}}^{\mathrm{C}}]$	$= \mathrm{s}^{-1}$
Product kernel	β_{prod}	$= C_{\mathrm{prod}}^{\mathrm{C}} \cdot v \cdot v'$	$[C_{\mathrm{prod}}^{\mathrm{C}}]$	$= \mathrm{m}^{-3}\,\mathrm{s}^{-1}$
Brownian motion: free-molecule regime	β_{fm}	$= \underbrace{\left(\frac{3}{4\pi}\right)^{1/6} \sqrt{\frac{6 k_{\mathrm{B}} T}{\rho_p}}}_{C_{\mathrm{fm}}^{\mathrm{C}}} \sqrt{\frac{1}{v} + \frac{1}{v'}} \cdot \left(v^{1/3} + (v')^{1/3}\right)^2$	$[C_{\mathrm{fm}}^{\mathrm{C}}]$	$= \mathrm{m}^{5/2}\,\mathrm{s}^{-1}$
Brownian motion: continuum regime	β_{co}	$= \underbrace{\frac{2}{3}\frac{k_{\mathrm{B}} T}{\eta}}_{C_{\mathrm{co}}^{\mathrm{C}}} \cdot \left(v^{1/3} + (v')^{1/3}\right) \cdot \left(v^{-1/3} + (v')^{-1/3}\right)$	$[C_{\mathrm{co}}^{\mathrm{C}}]$	$= \mathrm{m}^3\,\mathrm{s}^{-1}$

(b) Examples for breakage rates b and functionsγ for breakage of parent particles with volume v_{P} into fragments with volume v_{F}. Solutions after [47] are listed in Table **2** of [Paper III].

Model	Breakage rate b	Breakage function γ	Unit of constant
Linear binary breakage	$b_{\mathrm{l}}(v_{\mathrm{P}}) = C_{\mathrm{l}}^{\mathrm{B}} \cdot v_{\mathrm{P}}$	$\gamma_{\mathrm{B}}(v_{\mathrm{F}} \vert v_{\mathrm{P}}) = 2/v_{\mathrm{P}}$	$[C_{\mathrm{l}}^{\mathrm{B}}] = \mathrm{m}^{-3}\,\mathrm{s}^{-1}$
Quadratic binary breakage	$b_{\mathrm{q}}(v_{\mathrm{P}}) = C_{\mathrm{q}}^{\mathrm{B}} \cdot v_{\mathrm{P}}^2$	$\gamma_{\mathrm{B}}(v_{\mathrm{F}} \vert v_{\mathrm{P}}) = 2/v_{\mathrm{P}}$	$[C_{\mathrm{q}}^{\mathrm{B}}] = \mathrm{m}^{-6}\,\mathrm{s}^{-1}$

(c) Examples for nucleation rates J.

Model	Nucleation rate J		Unit of constant
Constant rate	J_{c}	$= C_{\mathrm{c}}^{\mathrm{N}}$	$[C_{\mathrm{c}}^{\mathrm{N}}] = \mathrm{m}^{-3}\,\mathrm{s}^{-1}$
Courtney [48]	$J_{\mathrm{cou}}(N_{\mathrm{G}})$	$= N_{\mathrm{G}} \cdot \sqrt{\frac{2\sigma}{\pi \cdot m_{\mathrm{G}}}} \frac{p_{\mathrm{s}}}{k_{\mathrm{B}} \cdot T} \cdot v_{\mathrm{G}} \cdot \exp\left(-\frac{16 \cdot \pi \cdot \sigma^3 \cdot v_{\mathrm{G}}^2}{3 \cdot k_{\mathrm{B}}^3 \cdot T^3 \cdot \ln(S)^2}\right)$	–
Classic [49]	$J_{\mathrm{cls}}(N_{\mathrm{G}})$	$= J_{\mathrm{cou}}(N_{\mathrm{G}}) \cdot S$	–
Girshick [50]	$J_{\mathrm{gir}}(N_{\mathrm{G}})$	$= J_{\mathrm{cou}}(N_{\mathrm{G}}) \cdot \exp\left((36\pi)^{1/3} \cdot \sigma \cdot v_{\mathrm{G}}^{2/3} / (k_{\mathrm{B}} \cdot T)\right)$	–

(d) Examples for growth rates $G(v)$. G_{fm} describes spherical particles with $v = \pi d^3/6$ in the free molecule regime [46].

Model	Growth rate $G(v)$	Unit of constant
Constant	$G_{\mathrm{c}} = C_{\mathrm{c}}^{\mathrm{G}}$	$[C_{\mathrm{c}}^{\mathrm{G}}] = \mathrm{m}^3\,\mathrm{s}^{-1}$
Linear	$G_{\mathrm{l}} = v \cdot C_{\mathrm{l}}^{\mathrm{G}}$	$[C_{\mathrm{l}}^{\mathrm{G}}] = \mathrm{s}^{-1}$
Diameter independent	$G_{\mathrm{d}} = v^{2/3} \cdot C_{\mathrm{d}}^{\mathrm{G}}$	$[C_{\mathrm{d}}^{\mathrm{G}}] = \mathrm{m}\,\mathrm{s}^{-1}$
Free molecule [(i)], [(ii)]	$G_{\mathrm{fm}} = \pi d^2 \cdot \underbrace{\frac{p_s \cdot v_{\mathrm{G}}}{\sqrt{2\pi \cdot m_{\mathrm{G}} \cdot k_{\mathrm{B}} \cdot T}}}_{C_{\mathrm{fm}}^{\mathrm{G}}} \left(S - \underbrace{\exp\left\{\frac{4 \cdot \sigma \cdot v_{\mathrm{G}}}{k_{\mathrm{B}} \cdot T \cdot d}\right\}}_{\text{Kelvin correction } K(d)}\right)$	$[C_{\mathrm{fm}}^{\mathrm{G}}] = \mathrm{m}\,\mathrm{s}^{-1}$

[(i)] This expression is a simplification of the more accurate formula (resulting from Eq. (B.9) in combination with β_{fm}):
$G_{\mathrm{fm,exact}} = \frac{\pi \cdot (6/\pi)^{\frac{2}{3}} \cdot v_{\mathrm{G}} \cdot p_{\mathrm{s}}}{\sqrt{\pi \cdot 2 \cdot k_{\mathrm{B}} \cdot T \cdot \rho_{\mathrm{p}}}} \cdot \sqrt{\frac{1}{v_{\mathrm{G}}} + \frac{1}{v}} \cdot \left(v_{\mathrm{G}}^{\frac{1}{3}} + v^{\frac{1}{3}}\right)^2 \cdot \left(S - \exp\left\{\frac{4 \cdot \sigma \cdot v_m}{k_{\mathrm{B}} \cdot T \cdot d_p}\right\}\right)$.
The simplification shown in the Table is valid, if the particle volume is larger than the monomer volume, i.e. $v \gg v_{\mathrm{G}}$. A discussion of the error can be found in [51].

[(ii)] In the case in which the Kelvin correction might be neglected (for large particles, if $K(d) = 1$), the free molecule growth model is equal to the diameter independent growth model with: $(36\pi)^{1/3} \cdot (S-1) \cdot C_{\mathrm{fm}}^{\mathrm{G}} = C_{\mathrm{d}}^{\mathrm{G}}$.

where S is the supersaturation and N_s the monomer concentration at vapor pressure p_s.

2.1.1.4 Condensation and Evaporation

$$\left(\frac{\mathrm{d}n(v,t)}{\mathrm{d}t}\right)_{\text{growth}} = \underbrace{-\nabla_v\left(G(v,t)n(v,t)\right)}_{\text{growth } (G>0) \text{ / evaporation } (G<0)} \quad . \tag{2.6}$$

The growth rate $G(v,t)$ describes the change of the particle size due to condensation or evaporation of single atoms or molecules forming the particle (or a compound of it). The evolution of the particle size v due to the growth process could be described by a single discrete equation - given the absence of other processes such as coagulation:

$$\frac{\mathrm{d}v}{\mathrm{d}t} = G(v,t) \ . \tag{2.7}$$

The particles grow, if $G(v,t) > 0$ and evaporate for $G(v,t) < 0$. There exist several explicit functions proposed for the growth rate G, see e.g. [55].

The concentration N_G of atoms (or molecules) of the nucleating/condensing material is often included into the modeling, because it directly affects the growth and nucleation rates (i.e. $G = G(v, N_\mathrm{G}, t)$ and $J = J(N_\mathrm{G}, t)$). A mass balance helps to model the depletion of these atoms (or molecules) due to condensation or nucleation:

$$\frac{\mathrm{d}N_\mathrm{G}}{\mathrm{d}t} = -\frac{v^* + v_\mathrm{G}}{v_\mathrm{G}} \cdot J(N_\mathrm{G}, t) - \frac{1}{v_\mathrm{G}} \cdot \int_0^\infty G(v,t)n(v,t)\mathrm{d}v \, , \tag{2.8}$$

where v_G is the atomic (or molecule) volume of the nucleating/condensing substance and $v^* + v_\mathrm{G}$ the volume of the nucleating particle.

2.1.2 Dynamic Kernels and Rates

The dynamic of the system is expressed through the kernels and rates describing the kinetics, which are β in Eq. (2.2), b, γ in Eq. (2.3), J, v^* in Eq. (2.4) and G in Eq. (2.6).

An example for one of these expressions is the coagulation kernel in the free-molecule regime (see e.g. [44, 46]):

$$\beta_\mathrm{fm} = \left(\frac{3}{4\pi}\right)^{\frac{1}{6}} \sqrt{\frac{6k_\mathrm{B}T}{\rho_\mathrm{p}}} \cdot \sqrt{\frac{1}{v_1} + \frac{1}{v_2}} \cdot \left(v_1^{\frac{1}{3}} + v_2^{\frac{1}{3}}\right)^2 \ , \tag{2.9}$$

where k_B is the Boltzmann constant, the other variables in Eq. (2.9) can be separated into three classes:

- Material variables: e.g. the density ρ_p,
- Process variables: e.g. the temperature T, particle concentration $n(v)\mathrm{d}v$ (changed via dilution),
- Particle properties: e.g. the size v.

The process variables can be changed and allow thus a certain level of control over the resulting particle properties and thus the overall process. The explicit form of the rates and kernels β, G, J, v^*, b, γ is, however, dependent on the particular process and several formulations have been proposed for different fields [56, 57, 25]. The attribution of specific values for β, G, J, v^*, b, γ from experimental data is termed 'the inverse problem' [57, 58, 59] - it is, however not clear how well the results from one material class can be transferred to another and whether completely new measurements are necessary, if the material system is changed. A second problem is the dependency of these parameters on the properties v and the question, how many and which of these properties of the particle have to be taken into account. The fractal dimension and number of primary particles of aerosol nanoparticles [60, 61] or the wet-content and porosity in the context of granulation processes [62, 63, 21] are two examples. The inverse problem becomes more complicated, if multiple particle properties are involved [63].

2.1.3 Accounting for Spatial Inhomogeneity

The Eqs. (2.2)-(2.6) model spatial homogeneous systems, which reflect relevant batch production processes, like crystallization [64] or polymerization [65].

In the scope of a more general formulation [42, 66], the PSD is not only dependent on the particle properties v (termed the 'internal coordinates'), but also spacial coordinates, x, (termed 'external coordinates') have to be taken into account: $n(v;x)$. The dynamic can be considered in one dimension (1D: x is a scalar), two dimensions (2D x is a vector consisting of two components) or three dimensions (3D: x is a vector with three components). The dynamic variables β, G, J, v^*, b, γ can in turn model spacial inhomogeneities as well, the coagulation kernel β_{fm} could reflect for example an applied temperature profile $T(x)$ or a position dependent growth rate $G(x)$ in a crystallizer could be modeled. The necessity of additional modeling of the velocity x_u of the particles as an external coordinate has been proposed for the correct modeling of perpendicular particle jets [66] - resulting in the Boltzmann equation [67, 68] instead of Eq. (2.2). Sometimes the addition of diffusion terms to Eq. (2.1) is also proposed [69, 66, 70]. The explicit modeling of external coordinates is not used in this thesis. Instead, spacial inhomogeneities are treated in the two following ways:

- The dynamic variables β, G, J, v^*, b, γ change in time, mimicking thus typical trajectories of a small volume element through the simulated equipment. Such simulation approach is very well suited for plug-flow reactors [71] or laminar flames [72, 73] - where the position of the simulated volume can be transformed to a simulation time. More complicated, turbulent simulation conditions can be treated by direct numerical simulations (DNS) or simplified computational fluid dynamics (CFD) approaches, where Lagrange particle tracking is used to extract one or several (weighted) paths from the simulations, providing thus the temporal evolution of the dynamic variables for the PBE [37]. Steady state considerations allow the integration of such an approach into flowsheet simulations [74].

- An interconnected network of $\mathcal{N}_{\text{cells}}$ compartments (or cells in combination with CFD) is simulated. Each of these compartments has its own PSD, $n_i(v,t)$ and dynamic variables $\beta_{(i)}$, $G_{(i)}$, $J_{(i)}$, $v^*_{(i)}$,$b_{(i)}$,$\gamma_{(i)}$. Particulate flows from compartment i to compartment j can be defined as general functions $\mathscr{F}_{i\to j}(n_i(v,t))$, with $i,j = 1,\dots,\mathcal{N}_{\text{cells}}$ and $i \neq j$. This leads to the following general set of $\mathcal{N}_{\text{cells}}$ coupled equations:

$$\frac{\mathrm{d}n_i(v,t)}{\mathrm{d}t} = \left(\frac{\mathrm{d}n_i(v,t)}{\mathrm{d}t}\right)_{\text{coag}} + \left(\frac{\mathrm{d}n_i(v,t)}{\mathrm{d}t}\right)_{\text{growth}} + \left(\frac{\mathrm{d}n_i(v,t)}{\mathrm{d}t}\right)_{\text{nuc}} + \left(\frac{\mathrm{d}n_i(v,t)}{\mathrm{d}t}\right)_{\text{break}} + \sum_{\substack{\text{all } j \text{ with} \\ \text{out stream to } i}} \mathscr{F}_{j\to i}(n_j(v,t)) - \sum_{\substack{\text{all } j \text{ with} \\ \text{in stream from } i}} \mathscr{F}_{i\to j}(n_i(v,t))\,. \tag{2.10}$$

  - The set of Eqs. (2.10) can be combined with CFD simulations, allowing thus to couple the particle dynamics with the dynamics of the gas flow (see, e.g. [75, 76]). CFD simulations typically require the modeling of a large amount of cells (ranging from ca. 10 000 [77] to 1 000 000 [78]).
  - Due to the computational complexity of such a coupling, the modeling of homogeneous zones of the simulated equipment is often applied, so that a low number of compartments (typically 2 - 16) can be used to render the particle dynamics described by Eqs. (2.10). Such a modeling can still capture spatial differences of single apparatuses, assuming for example several homogeneous spray zones within a granulator [79, 80], different mixing zones within a continuous stirred tank reactor (CSTR) [81], compartments for bioreactors [82] or multiple homogeneous zones within an aerosol particle reactor [83, 84]. This approach also allows to simulate the connections of diverse units like shown in Figure (1.1) by means of a flowsheet simulation [85, 86, 11, 87].

2.2 Solution Methods

Despite the complexity of the integro-differential Eqs. (2.1)–(2.10), analytical solutions can be formulated – for a few special cases, among them the famous solution of Smoluchowski from 1917 [88]. The simplicity of the dynamics of the presented special cases limits the applicability of analytical solutions to the modeling of relevant engineering problems. They pose, however, an important reference which helps to test and validate newly developed techniques for the solution of the PBE (see e.g. [89, 90]). Some examples are listed in Table 2.2 demonstrating the simplicity and thus limitations of possible

Table 2.2: Examples for particulate systems for which analytical solutions can be formulated.

Mechanism	Kernel, rate or function	Source
Coagulation	Constant kernel β_c	[88]
	Sum and the product kernel β_{prod}, β_{sum}	[91]
	Linear combinations of β_c, β_{sum} and β_{prod}	[92]
Breakage	binary breakage γ_B with b_l or b_q	[47]
Breakage and coagulation	β_c with γ_B and b_l	[93, 94, 95]
Transport and breakage	monodisperse feed streams with γ_B and b_l	[96]
Growth	constant or linear growth rates (G_c or G_l)	[97]
Growth and coagulation	G_l or G_c with β_c or β_{sum}	[98]

application scenarios. The subsequent sections will introduce numerical solution methods for the approximation of a solution for the PBE which are applicable to a broad range of problems. These approximations resort to 1) the simulation of the moments of the PSD (section 2.2.1 elaborates the term), 2) discretization of all possible particle sizes into bins (section 2.2.2) and 3) stochastic methods (section 2.2.3).

2.2.1 Method of Moments

Hulburt and Katz [99], the authors which where among the first (with [100] and [101]) to propose to apply Equation (2.1) in order to describe industrial particulate processes, found that the formulation of an explicit form of $n(v)$ is too demanding and not feasible with the mathematics and computers available at the time. They therefore suggested to regard the evolution of the n-th moment of the distribution, μ_n, instead. The mathematical definition of a moment of a distribution is:

$$\mu_n = \int_0^\infty v^n \cdot n(v)\,\mathrm{d}v\,. \tag{2.11}$$

The zeroth moment μ_0 describes the total particle concentration, the first moment μ_1 the total volume concentration of the distribution, the ratio μ_1/μ_0 is the arithmetic mean volume, and the second moment μ_2 can be used to describe the variance[1] given by: $\mu_2/\,\mu_0 - \mu_1^2\,/\,\mu_0^2$.

One can formulate the equations describing the rate of change of the moments by multiplying Eq. (2.2) with v^n from both sides and integrating over the domain $(0,\infty)$ with respect to $\mathrm{d}v$. Hulburt and Katz obtain by applying this method the following system of equations given a size independent coagulation kernel $\beta_c = C_c^C$ in the absence of other processes [99]:

$$\frac{\mathrm{d}\mu_0}{\mathrm{dt}} = -\frac{1}{2}\cdot \mathrm{C}_c^C \cdot \mu_0^2\,, \quad \frac{\mathrm{d}\mu_1}{\mathrm{d}t} = 0\,, \quad \frac{\mathrm{d}\mu_2}{\mathrm{d}t} = +C_c^C \cdot \mu_1^2\,. \tag{2.12}$$

The term $\frac{\mathrm{d}\mu_1}{\mathrm{d}t} = 0$ states that there is no change of the total mass due to coagulation.

Thus the problem of estimating $n(v)$ from the integro–differential Eq. (2.2) has been reduced to a simple set of coupled ordinary differential Eqs. (2.12) for μ_0, μ_1 and μ_2. This problem can be easily solved with available numerical solvers. Such a simplification is - unfortunately - only possible because of the simple form of the postulated coagulation kernel. The application of this method to a more relevant coagulation kernel leads to the so called 'closure problem'. For example, the following set of equations results for the Brownian coagulation kernel in the continuum regime β_{co} - in the absence of other processes [102]:

$$\frac{\mathrm{d}\mu_0}{\mathrm{d}t} = -C_{co}^C \cdot \mu_0^2 - C_{co}^C \cdot \mu_{\frac{1}{3}} \cdot \mu_{-\frac{1}{3}}, \qquad \frac{\mathrm{d}\mu_1}{\mathrm{d}t} = 0, \qquad \frac{\mathrm{d}\mu_2}{\mathrm{d}t} = 2\cdot C_{co}^C \cdot \mu_1^2 + 2\cdot C_{co}^C \cdot \mu_{\frac{4}{3}} \cdot \mu_{\frac{2}{3}}\,. \tag{2.13}$$

Unlike Eq. (2.12), this set of Eqs. (2.13) contains unknown expressions $\mu_{\frac{1}{3}}, \mu_{-\frac{1}{3}}, \mu_{\frac{2}{3}}, \mu_{\frac{4}{3}}$, so that a simple solution by application of a solver for differential equations is not possible.

Many methods (see e.g. [103]) have been proposed in order to obtain a closure for sets of differential equations like Eqs. (2.13), among others:

- **Assumption on PSD shape.** Assuming $n(v)$ to be distributed according to a log normal

[1] The variance of the distribution is defined as: $\int_0^\infty (v-\overline{v})^2 \cdot n(v)\,\mathrm{d}v\,/\,\mu_0$, with $\overline{v} = \int_0^\infty v \cdot n(v)\,\mathrm{d}v\,/\,\mu_0 = \mu_1\,/\,\mu_0$.

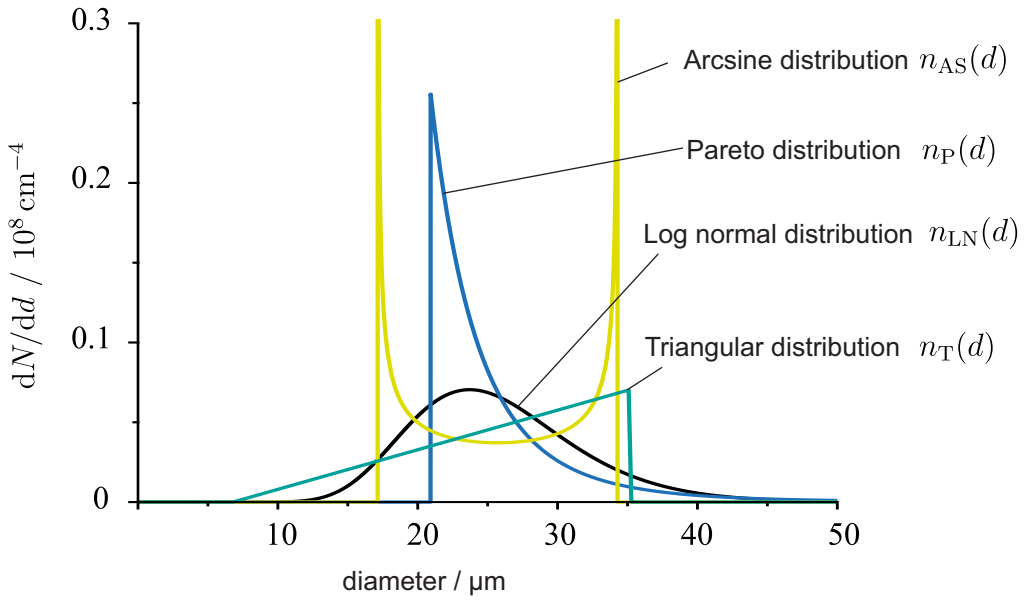

Figure 2.1: Exemplary PSDs with equal zeroth, first and second moments. The explicit definitions of the functions $n(d)$ are described in appendix A.1.

distribution allows to express all moments μ_x in terms of parameters which characterize the log normal distribution [102]. This modeling has been often applied in aerosol sciences [104]. The assumption of a monodisperse distribution [105] (instead of a log normal one) can be also interpreted as a branch of the method of moments.

- **The quadrature method of moments (QMOM)** [106, 107] approximates the integration of Eq. (2.2) with respect to dv using an $n-$point Gaussian quadrature (see e.g. [108]).
- **The direct quadrature method of moments (DQMOM)** [109] goes even a step further than QMOM and formulates instead of differential equations for the moments μ_i, differential equations for weights and abscissas needed for the Gaussian quadrature.[2]

The simplicity of the resulting equations makes methods like QMOM or DQMOM very attractive for simulations where detailed reactor structures and gas flows have to be taken into account. This is mostly done by a coupling of the PBE model with computational fluid dynamics (CFD) simulations, where the number of equations to be solved corresponds to the number of modeled cells times a small number of equations for the moments (i.e. $3-7\cdot\mathcal{N}_{\text{cells}}$), see e.g. [112, 113, 114, 115, 116].

Although the method has been validated on several test cases [110], it is not clear whether the approximations done by the Gaussian quadrature are valid for a large range of applications. Some concerns about the validity of the method have been reported lately for multi-phase flow simulations [117] or for polymer degradation problems involving random scission [118].

The great disadvantage of the moment based methods is that the unequivocal reconstruction of the PSD from a finite set of its moments is not possible. This is demonstrated in figure 2.1: all shown distributions have equal moments μ_0, μ_1 and μ_2, the explicit definitions of the PSDs and the values of the moments are described in appendix A.1.

Several methods have been proposed for a possible reconstruction of the PSD [119]. It is now generally agreed, however, that some theoretical or experimental insight on the form of the PSD is needed prior to the reconstruction [120]. This might be the reason, why the chosen reconstruction method depends on the specific application: different approaches are proposed for depolymerization processes [121], pharmaceutical drying processes [122] or soot formation [123], to name a few.

Thus, the method of moments is a good choice when computational costs have to be kept to a minimum (for example in combination with CFD simulations, e.g. [124]) and a good understanding

[2] The Gaussian quadrature approximates the integral expression $\int v^k n(v)\mathrm{d}v \approx \sum w_i \cdot v_i^k n(v_i)$ with the help of the abscissas v_i and weights w_i. The finding of the correct values of the abscissas v_i and weights w_i poses a major problem for QMOM, especially for multivariate problems. [109, 110, 111] Therefore, DQMOM treats instead the differential equations for the moments, $\frac{\mathrm{d}\mu_n}{\mathrm{d}t}$, differential equations for the abscissas and weights: $\frac{\mathrm{d}w_i}{\mathrm{d}t}$ and $\frac{\mathrm{d}v_i}{\mathrm{d}t}$.

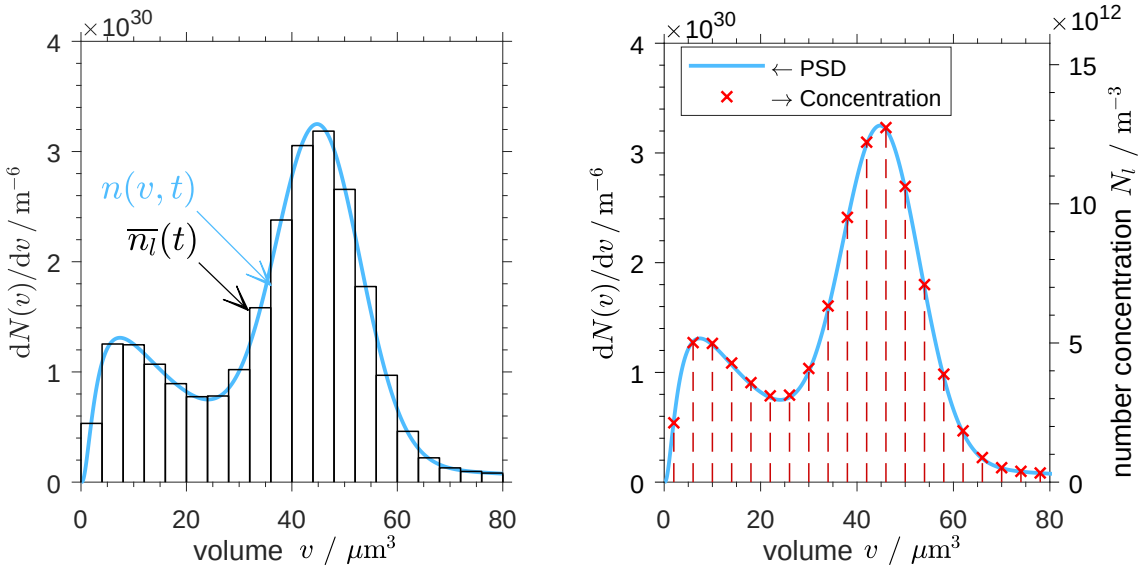

(a) Piece-wise constant functions $\overline{n_l}(t)$. **(b)** Concentrations N_l for $\overline{n_l}(t)$.

Figure 2.2: The approximation of the PSD $n(v,t)$ with piece-wise constant functions $\overline{n_l}(t)$ (shown in 2.2a) resulting in number concentrations N_l (shown in 2.2b) for each section l.

about the shape of the PSD is available prior to the simulation. The method is less applicable in scenarios in which the shape of the PSD cannot be foretold, especially if its shape is crucial for the overall process. For example, the separation-function of a sieve could lead to dramatically different feed-back streams, depending on which of the functions from figure 2.1 is gained as a result of the reconstruction.

2.2.2 Discretization Methods

The most simple discretization method is to allow only discrete volume values v_m and integer multiples of it (i.e $v = v_\mathrm{m}, 2v_\mathrm{m}, 3v_\mathrm{m}, \dots$). Such a modeling would lead, however to a very small particle size spectrum, which could be rendered: a relatively small particle range covering values from 1 nm to 10 nm would already require 1 000 discrete points with the corresponding coupled differential equations for each point.

As examples for more efficient discretization methods, the sectional, the discrete-sectional and the pivot point method are presented in this section.

- **Sectional methods** [125] divide the continuous particle size spectrum v, into a finite number of sections. The shape of the PSD $n(v,t)$ is thereby assumed to take a specific form within the section l. The most simple assumption is a constant distribution to the value $n(v,t) = \overline{n_l}(t)$, for $v_{l-1}^{\dashv} \leq v < v_l^{\dashv}$, like shown in Figure 2.2a.
- **Discrete-sectional (DS) methods** [126] combine the approach of few (e.g. 100) discrete points for the smallest particle volumes (i.e $v = v_\mathrm{m}, 2v_\mathrm{m}, 3v_\mathrm{m}, \dots$) with the continuous grids of the sectional method for larger particle volumes.
- **Pivot point methods** render the PSD as a set of concentrations N_l for fixed [127] or moving [128] particle sizes (termed 'pivot points'). The PSD is thereby approximated by the values of N_l at these specific points, as suggested by Figure 2.2b.

Both discretization techniques allow the transformation of the partial integro-differential (Eq. (2.1)) to a more simplified set of coupled ordinary differential equations (ODEs) for the concentrations N_l [3], with $l = 1, \dots, \mathcal{N}_\mathrm{sec}$.

[3] Instead of the number concentration N_l (number-based model $Q_l(t) = N_l(t) = \int_{v_{l-1}}^{v_l} n(v,t)\mathrm{d}v$, like shown in Figure 2.2b), other, general properties Q_l have been suggested in the scope of sectional methods [126], e. g. the volume concentration (volume-based model $Q_l(t) = V_l(t) = \int_{v_{l-1}}^{v_l} v \cdot n(v,t)\mathrm{d}v$).

In the following two sections, the discretization of two mechanisms, 1) coagulation and 2) growth will be presented in more detail.

2.2.2.1 Coagulation

The piece-wise integration of the PBE for coagulation (Eq. (2.2)) with respect to dv over single sections l (i.e. $v = v_{l-1}^{\dashv} \dots v_l^{\dashv}$) leads to the set of equations described by Eq. (2.14):

$$\left(\frac{\mathrm{d}N_l}{\mathrm{d}t}\right)_{\mathrm{coag}} = \sum_i \sum_{k \le i} N_i \cdot N_k \cdot \overline{\beta_{i,k\to l}} - N_l \cdot \sum_k N_k \cdot \overline{\beta_{l,k\to}} \qquad \text{for } l = 1, 2, 3 \dots \mathcal{N}_{\mathrm{sec}}\,. \tag{2.14}$$

The resulting equation is a PBE for coagulation in a discrete form with the modified coagulation kernel $\overline{\beta_{i,k\to}}$ for coagulation of particles from the sections i and k with each other. All possible coagulations of particles A from section i (i.e. with $v_{i-1}^{\dashv} < v_A \le v_i^{\dashv}$) with particles B from section k (i.e. with $v_{k-1}^{\dashv} < v_B \le v_k^{\dashv}$) resulting in particles within section l (i.e. with $v_{l-1}^{\dashv} < v_A + v_B \le v_l^{\dashv}$) are described by $\overline{\beta_{i,k\to l}}$. Many of the $\overline{\beta_{i,k\to l}}$ values can be determined to be zero prior to the integration, simplifying thus the calculation [129]). The explicit values of $\overline{\beta_{i,k\to l}}$ and $\overline{\beta_{i,k\to}}$ termed 'collision integrals' in [126] are shown as Eq. (B.2) and Eq. (B.3) in appendix B.1.

The integrations necessary for the determination of $\overline{\beta_{i,k\to l}}$ might become computationally expensive to calculate. Some approaches formulate ideal geometric grids (e.g. $v_{l+1}^{\dashv}/v_l^{\dashv} = 2$ [130] or $v_{l+1}^{\dashv}/v_l^{\dashv} = 2^{\kappa_H}$ [131]) and derive the factors $\overline{\beta_{i,k\to l}}$ from considerations that the development of the moments is described correctly.

A much simpler approach was proposed by the group of Ramkrishna [127], which treated instead of constant sections, discrete points, named 'pivot points' (or pivot elements). The coagulation of two particles with the sizes of the pivot points i and j, with the volumes $v_i^{\bullet}$ and $v_j^{\bullet}$ leads to particles with the size $v_{\mathrm{new}} = v_i^{\bullet} + v_j^{\bullet}$. If there is no pivot point, which corresponds to the exact value, the production rate of this new particle is divided between the two adjacent pivot points k and $k+1$ with $v_k^{\bullet} < v_{\mathrm{new}} \le v_{k+1}^{\bullet}$. The splitting is done in such a way that the total change of the number concentration and the volume concentration due to the growth of the nodes k and $k+1$ is the same as it would have been due to the production of novel particles with the size v_{new}. The relatively simple expressions for $\overline{\beta_{i,k\to l}}$ are listed in appendix B.2.1 as Eq. (B.7) in more detail.

Vanni [132] compares these suggested approaches (together with another sectional method proposed by [133]) for aggregation-breakage problems and finds that sectional methods [126, 125] as well as fixed pivot methods are able to produce the most reliable results and favors the fixed pivot approach [127] due to its simplicity.

The main characteristic of these methods is, that the accuracy of the results is dependent on the number of used sections or pivot points [132, Paper I], allowing thus to simply increase the accuracy by applying a finer grid at the cost of additional computational resources and especially computing time.

2.2.2.2 Growth and Numerical Diffusion

One way to include condensational growth into a pivot point method is to model the monomers in the gaseous phase as first pivot points, as proposed by [134], which leads to the following set of equations for positive growth rates ($G(v_j^{\bullet}) > 0$):

$$\left(\frac{\mathrm{d}N_j}{\mathrm{d}t}\right)_{\mathrm{growth}} = -\frac{G(v_j^{\bullet}) \cdot N_j}{v_{j+1}^{\bullet} - v_j^{\bullet}} + \frac{G(v_{j-1}^{\bullet}) \cdot N_{j-1}}{v_j^{\bullet} - v_{j-1}^{\bullet}}\,, \tag{2.15}$$

where $v_j^{\bullet}$ are the volumes and N_j the corresponding concentrations of the j-th pivot points, $j = 2 \dots (\mathcal{N}_{\mathrm{PP}} - 1)$. The closure of these equations (Eq. (B.17) for $j = 1$ and Eq. (B.16) for $j = \mathcal{N}_{\mathrm{PP}}$) as well as the modeling of evaporation are presented in appendix B.2.2. It should be noted, that these equations correspond to the application of a first order upwind scheme [135], if an equidistant grid is used, i.e. $v_{j+1} - v_j = \Delta v$ for all j. The term 'finite differences' is used, if the particle concentration is considered at single (pivot) points (see. e.g. [136, 137]). The term 'finite volume' describes a variant of Eq. (2.15) for sections (see e.g. [138, 139]). Thereby, the values for $G(v_j^{\bullet})$ in Eq. (2.15) have to be replaced with results of integration over single sections j, $\overline{G(v_j^{\dashv})}$.

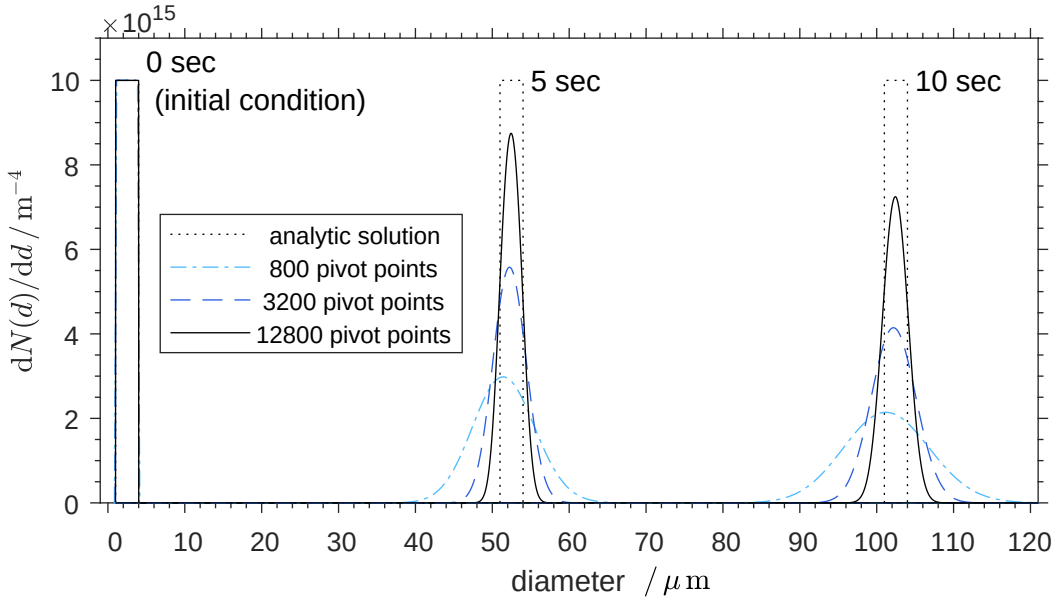

Figure 2.3: The PSDs resulting for a diameter independent growth rate $\frac{\mathrm{d}d}{\mathrm{d}t} = 10\mu\mathrm{m\,s}^{-1}$ in combination with the set of Eqs. (2.15). The explicit simulation conditions are summarized in appendix A.2.

One of the main problems encountered in the application of discretization methods for the simulation of condensational growth is the phenomenon of 'numerical diffusion' [140]. Figure 2.3 shows the artificial broadening of the PSD due to numerical diffusion for an exemplary simulation of a constant growth rate.

Many methods have been proposed in order to avoid the numerical diffusion, the three following approaches seem to be mostly used:

- **Anti diffusion terms and flux limiters.** The application of the Lax-Wendroff method [141] for finite differences and for finite volumes methods [138, 139] introduces an anti-diffusion term to the set of equations (2.15). This leads to spurious oscillations in some relevant test cases [142], so that the additional application of flux limiters (i.e. functions which mitigate the effects of the anti diffusion terms) becomes necessary [138, 139, 142]. Different formulation for the flux limiter have been proposed [143, 144], so that some might perform better for certain simulation conditions than others.

- **Finite elements methods (FEM)** pose an alternative approach, where the PSD $n(v)$ is approximated for each section l, as a linear combination of p Lagrange polynomials ψ_l^i ($i = 1 \dots p$), so that:

$$n(v,t) \approx \sum_{i=1}^{p} \psi_l^i(v) \cdot n_l^i(t) \quad \text{for: } v_{l-1} \le v < v_l \,. \tag{2.16}$$

  Weighted residual statements are formed by multiplying the PBE (2.1) with a weight function $\phi(v)$ and integrating over the domain $(v_{l-1}^{\dashv}, v_l^{\dashv})$ of each section (also called 'element' in the framework of the FEM). This procedure leads to p coupled differential equations ($e = 1 \dots p$) for the values for the factors $n_l^e(t)$ for each element l - instead of only one equation for each section like in the finite volume/differences approach (2.14) and (2.15). In order to obtain these equations, specific functions $\phi(v)$ have to be formulated, mostly in form of: $\phi = \sum \phi_k^l(v)$, if $v_{l-1}^{\dashv} \le v < v_l^{\dashv}$. The use of B-splines as $\phi_k^l(v)$ is reported to lead to oscillations [145], the collocation approach defines $\phi_k^l(v)$ to be delta-Dirac functions [146] and Galerkin formulations use $\phi_k^l(v)$ to be Lagrange polynomials (like $\psi_k^l(v)$) [146, 147]. These formulations are reported not to exhibit numerical diffusion but to be computational costly for time-dependent coagulation kernels and multidimensional problems [29]. Furthermore, additional adjustments have to be made in order to cover discontinuities or singularities of the PSD, which are typically encountered in nucleation processes [59].

- **Moving grid** techniques have been proposed for sectional methods [148, 149] by allowing the section boundaries to change their position $v_l^{\dashv}$ according to the corresponding growth rates, $G(v_l^{\dashv})$, i.e. $\frac{\mathrm{d}v_l^{\dashv}}{\mathrm{d}t} = G(v_l^{\dashv})$. The combination of these approaches with aggregation processes is generally deemed to be difficult [150]. Aggregation and breakage processes can be integrated for moving pivot point grids [128] and combined with particulate growth [97]. This approach as applied for the modeling of soot formation in plug flow reactors [71] or TiO_2 formation in aerosol reactors [151].

2.2.2.3 Discretization Methods: Applications and Modeling of Spatial Inhomogeneities

The main advantage of discretization methods is that no assumptions on the shape of the PSD have to be made and that the accuracy of the method can be increased by an increase of simulated sections (see e.g. [132]). The main drawback of the method is that it is only applicable to a relatively low number of particle properties. The resulting integral expressions for multiple dimensions are complicated [152, 153] and they become even more complicated if strategies to counter numerical diffusion are employed like flux limiters [154, 137] or finite element formulations [155]. The application of moving grids complicates the modeling of particle transport between CFD mesh cells, as the grids of two adjacent mesh cells may have completely different forms.

The main limiting factor, however, is the vast number of resulting differential equations. If, for example, 100 sections are used to represent each dimension, a number of $100^2 = 10\,000$ coupled differential equations results for two dimensional problems, while $100^3 = 1\,000\,000$ coupled differential equations would result for three dimensional problems – this type of problem is no more feasible within acceptable computing times with modern day desktop computers.

Sectional methods are thus very effective, if only one or two particle properties are of interest and if growth due to condensation or evaporation of the particles can be neglected. They are integrated in flowsheet simulation software like Parsival [156, 157] or DynSim [11] – the combination of different sectional methods for different unit operations is often applied in this context [157, 11].

In the context of CFD simulations, the number of sections is limited by the large amount of mesh cells (ranging from ca. 10 000 [77] to 1 000 000 [78] cells). In a typical Euler-Euler approach, the transport of each section l is modeled as an individual phase of the gas, so that typical numbers of sections range between 12 [75] and 30 [76] – while simulations of exemplary flowsheet processes (with a relatively low number of 3 units) make more detailed grid-layouts consisting of more than 1000 sections possible [87]. Some application examples encompass the simulation of bubble columns [75, 158], crystallization reactors [76] or nanoparticle formation via the aerosol route [159].

2.2.3 Monte Carlo Methods

The usage of stochastic methods for the solution of scientific problems can be traced back to the 18th century and Bouffon's needle problem. Laplace suggested that the inherent randomness of the location and orientation of thrown needles could be used to approximate a value for the mathematical constant π [160]. Following this approach, few experiments were carried out in the 19th century, which – indeed – yielded very crude approximations for π [161].

The term 'Monte Carlo' (MC) originated in the mid 20th century [162] and refers to the renowned casino in Monaco and the gambling habits of Stanislaw Ulam's uncle [163]. Building upon the pioneering works of Enrico Fermi and John von Neumann, the authors Stanislaw Ulam and Nicholas Metropolis suggested in 1949 [162, 163] the usage of computing machines for the generation of random numbers.[4] These random numbers allow, in turn, to obtain a stochastic solution of the Boltzmann equation of gases. The authors note, that their statistic method is applicable to a wide range of problems which *"occur in various branches of the natural sciences"* [162].

This prediction should prove to be correct, nowadays the MC method can be found in such diverse fields as biomedicine (modeling of light transport through tissues [164]), computer graphics (ray tracing, i.e. solutions of the render equation [165, 166]), semiconductor device fabrication (modeling of electron transport and scattering [167, 168]) and many more. This leads to a broad variety of suggested methods [169].

All these simulation approaches have in common that the produced results depend upon the specific sequence of used random numbers. Different random number sequences lead to different simulation

[4] The 'random numbers' were generated by deterministic algorithms, mimicking randomness. The resulting numbers, however, were deemed to be enough 'random' for the intended applications.

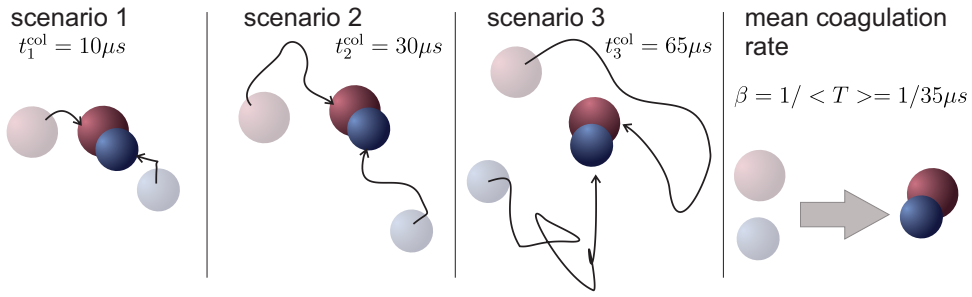

Figure 2.4: Exemplary paths of particles undergoing Brownian motion and the relation to the mean coagulation rate.

results. This stochastic noise makes the repetition of the same simulation with different random number sequences necessary in order to provide a confidence interval as a measure for the accuracy of the gained results.

In the following, the specific application of MC to the solution of the coagulation equation Eq. (2.2) will be sketched. Further solution strategies for breakage, nucleation, transport, growth and evaporation will be discussed in chapter 4 of this thesis.

2.2.3.1 Monte Carlo Simulation of Coagulation

In the scope of the direct simulation Monte Carlo method [89], the PSD $n(v,t)$ is rendered by discrete particles. Figure 2.4 shows exemplary Brownian motions of aerosol particles leading to collisions and thus coagulation. The exact paths depend on the initial positions and velocities of the particles as well as every single gas molecule of the carrier gas. Changes in these initial conditions lead to different paths of the particles and thus different times $t^{(\mathrm{col})}$ for a collision to take place. Analogous to the approach by Boltzmann to calculate the velocity distribution of single gas molecules of a gas as well as the free mean path (see e.g. [170, 171]), the means of statistical physics can be applied in order to calculate the mean collision times, $\overline{t^{(\mathrm{col})}}$, by averaging over all possible situations [172, 173]. For more complex particulate structures, atomistic molecular dynamics simulations might be performed, in order to extract the value of $\overline{t^{(\mathrm{col})}}$ [174, 175, 176].

The collision frequency $1\,/\,\overline{t^{(\mathrm{col})}}$, or coagulation rate $R_{i,j}$, for particles i and j with concentration N_i and N_j and volume (or general property) v_i and v_j defines the coagulation kernel $\beta(v_i, v_j)$ via:

$$R_{i,j} = V_{\mathrm{sys}} \cdot N_i \cdot N_j \cdot \beta(v_i, v_j) = 1\,/\,\overline{t^{(\mathrm{col})}}\,, \tag{2.17}$$

where V_{sys} is the considered system volume. This mean collision frequency subsumes all possible initial positions and velocities, so that the computational expensive tracking of the exact paths of single particles is no longer necessary in the formulation of the PBE for coagulation (2.2).

The same idea is applied by the MC simulation: a finite number of particles is simulated by storing the properties of each of these particles on the computer.

In the scope of conventional (non-weighted) modeling, one MC particle represents one real particle in a small, representative system volume, V_{sys} (i.e. both particles represent the same concentration $W_i = W_j = W_{\mathrm{MC}} = 1/V_{\mathrm{sys}}$). The rate of coagulation between each of the MC particles i and j is therefore given by:

$$R_{i,j} = \beta(v_i, v_j)/V_{\mathrm{sys}}\,. \tag{2.18}$$

If particles coagulate with each other, the particle properties are changed accordingly: one particle is removed from the simulation and the other particle contains now the properties of the particle resulting from the coagulation. For example, if the coagulation of droplet spheres is simulated with the volumes v_1 and v_2, the volume of the new droplet sphere resulting from the coagulation would be $v_{\mathrm{new}} = v_1 + v_2$. Figure 2.5 sketches the main idea of successive changes of the particle population after successive time steps Δt. This kind of modeling makes the method very suitable for the simulation of multiple particle properties: it is only necessary to store all these properties for each of the particles on the computer and update them accordingly after each coagulation. Another advantage of this approach is, that the particles assume their sizes or compositions as described by the simulated dynamics and

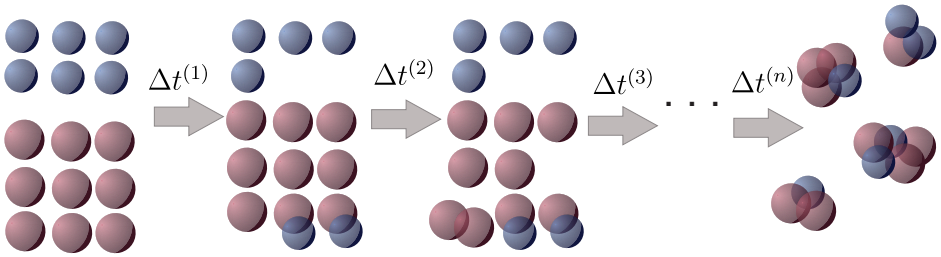

Figure 2.5: Successive changes of a particle population at the beginning and after one, two and n MC steps.

no a priori knowledge is needed on the form of the PSD. Such a priori knowledge might be otherwise necessary, in order to set up an adequate grid for discretization methods or reconstruct the PSD from moment methods.

There are two main simulation approaches for the decision whether particles coagulate within a time frame Δt:

- **Time-driven methods.** It is considered in this approach, see e.g. [177, 178], that each possible particle pair i, j may possibly coagulate within a freely chosen time step Δt. The corresponding coagulation rate $R_{i,j}$ is interpreted as the rate of a Poisson process and it has to be checked for each possible pair, whether this pair coagulates (smart bookkeeping methods [179] might reduce the vast number of all possible checks but are less applicable if the MC simulation is coupled with other processes). Usually, one uniformly distributed random number $r \in (0, 1)$ is generated and particles coagulate, if
$$r < 1 - \exp(-\Delta t \cdot R_{i,j})\,. \tag{2.19}$$
The advantage of this approach is that the time step can be set variably. A reasonable time step should be provided, however, because a too small time step would lead to too many unnecessary comparisons and a too large time step leads to errors [178].

- **Event-driven methods.** The rate at which any coagulation happens is given by the sum of all possible coagulation rates: $\sum_{\text{all } i>j} R_{i,j}$. This defines the mean time at which one coagulation event happens [180], also termed 'the interval of quiescence' [181]:
$$\Delta\tau_{\text{MC}} = 1/\sum_{\text{all } i>j} R_{i,j}\,. \tag{2.20}$$
The deduction of which coagulation pair coagulated during this time frame is done by modeling the probability of each particle pair for coagulation to be proportional to its coagulation rate [182]:
$$P_{i,j} = R_{i,j}/\sum_{\text{all } i>j} R_{i,j}\,. \tag{2.21}$$
After the pair (i, j) has been selected and coagulated, the rates for coagulation of the novel MC particle and the remaining MC particle population, $R_{i,j}$, change and with it changes the time step $\Delta\tau_{\text{MC}}$ in Eq. (2.20). Several of these coagulation steps are performed in this approach to simulate the desired time Δt.
Although this approach offers the advantage of an optimal time step for every condition, it leads to some complications, if a smaller time step $\Delta t < \Delta\tau_{\text{MC}}$ is needed (e.g. due to combination with other processes). A solution strategy for this problem has been developed in the scope of this thesis and will be presented in section 4.2.1.

The strategy with which the particle pair for coagulation is determined according to Eq. (2.21) can be grouped into two classes, so that event-driven methods can be subsumed into:

- **Inverse selection methods.** In the scope of this approach, one uniformly distributed random number $r \in (0, 1)$ is generated. The cumulative sum of all possible coagulation probabilities is

used to determine the coagulation pair [89, 183]. If, for example three particles (1, 2, 3) are simulated, there are only three possible coagulation pairs with the corresponding coagulation probabilities $P_{1,2}$, $P_{1,3}$ and $P_{2,3}$. So that:

$$\begin{aligned} \text{if, } r \leq P_{1,2} &\quad \Rightarrow \text{ the pair } (1,2) \text{ is chosen,} \\ \text{if } P_{1,2} < r \leq P_{1,2} + P_{1,3} &\quad \Rightarrow \text{ the pair } (1,3) \text{ is chosen,} \\ \text{if } P_{1,2} + P_{1,3} < r \leq P_{1,2} + P_{1,3} + P_{2,3} = 1 &\quad \Rightarrow \text{ the pair } (2,3) \text{ is chosen.} \end{aligned}$$

The calculation of these cumulative sums can become very expensive as there exist $\mathcal{N}_{\mathrm{MC}}^2 - \mathcal{N}_{\mathrm{MC}}$ possible coagulation pairs, if $\mathcal{N}_{\mathrm{MC}}$ MC particles are simulated. Special bookkeeping strategies which store and update the cumulative sums in an efficient way have to be applied [179].

- **Acceptance-Rejection (AR) selection methods**. In the scope of this approach [182], two particles i and j are selected randomly by two uniformly distributed random numbers. A third uniformly distributed random number $r \in (0, 1)$ is used to decide whether to accept the selected pair or not. The pair is selected if the random number is smaller than the selection probability $P^{\mathrm{AR}_{i,j}}$:

$$r < (P_{i,j}^{\mathrm{AR}}) = R_{i,j}/R_{\max}\,, \tag{2.22}$$

where $R_{\max}$ is the maximum of all possible values for $R_{i,j}$. If the random number is larger than $P_{i,j}^{\mathrm{AR}}$, than a new pair of particles is randomly selected and condition (2.22) is checked again. Thereby a large number of iterations might be required in order to find a pair for coagulation.

The computation of $R_{\max}$ and $\Delta\tau_{\mathrm{MC}}$ is generally expensive: $\mathcal{N}_{\mathrm{MC}}^2 - \mathcal{N}_{\mathrm{MC}}$ pairs have to be calculated for the simulation based on $\mathcal{N}_{\mathrm{MC}}$ MC particles in order to obtain exact values. There are generally two ways to reduce the complexity of this calculation: 1) majorant kernel approaches in combination with fictitious jumps[184, 185] and 2) the usage of a population sample from which $R_{\max}$ and $\Delta\tau_{\mathrm{MC}}$ is approximated [183, 186]. The latter approach is used for the works presented in this thesis - and presented in more detail in section 3.2.

The second problem encountered in the description of the coagulation by MC particles is the depletion of the MC particles due to coagulation, hence each coagulation event is rendered by introducing one novel particle, which replaces two existing particles, as it is shown in Figure 2.5. The following three approaches are mostly used to treat this problem.

- **Topping up** [177]. If the number of MC particles reaches a critical value (e.g. 500), the existing particles are copied (resulting in 1000 particles) and the simulated system volume V_{sys} is doubled.

- **Constant number Monte Carlo (CNMC)** [187, 180, 188, 189]. In this approach, one randomly selected particle is copied after each coagulation event. The simulated system volume V_{sys} has to be adjusted in such a way that the total mass concentration M of all particles does not change due to the copy operation (i.e. $M^{(\mathrm{old})}/V_{\mathrm{sys}}^{(\mathrm{old})} = M^{(\mathrm{new})}/V_{\mathrm{sys}}^{(\mathrm{new})}$, where the superscripts (old) and (new) refer to the system before and after the copy operation).

- **Weighted simulation particles** [184, 185, 190]. Both above mentioned techniques apply the same statistical weight, $W_{\mathrm{MC}} = 1/V_{\mathrm{sys}}$, for all simulated MC particles[5]. The PSD is thereby approximated by:

$$n(v) \approx \sum_{i=1}^{\mathcal{N}_{\mathrm{MC}}} W_{\mathrm{MC}} \cdot \frac{1}{U_{\mathrm{v}}} \cdot \delta\left(\frac{v - v_i}{U_{\mathrm{v}}}\right)\,, \tag{2.23}$$

where δ is the Dirac-δ function, U_{v} an arbitrary normalization unit (e.g $U_{\mathrm{v}} = 1\,\mathrm{m}^3$) and v_i the volume of the i-th MC particle. MC schemes based on weighted particles attach an additional property to each particle i: the statistical weight W_i. In the scope of this modeling, the PSD is approximated by:

$$n(v) \approx \sum_{i=1}^{\mathcal{N}_{\mathrm{MC}}} W_i \cdot \frac{1}{U_{\mathrm{v}}} \cdot \delta\left(\frac{v - v_i}{U_{\mathrm{v}}}\right)\,. \tag{2.24}$$

[5]This statistical weight changes in the course of the simulation, namely each time a topping-up is performed (the doubling of the system volume V_{sys} leads to: $W_{\mathrm{MC}}^{(\mathrm{new})} = W_{\mathrm{MC}}^{(\mathrm{old})}/2$) or during every time step in the scope of Matsoukas' constant number scheme (here: $W_{\mathrm{MC}}^{(\mathrm{new})} = W_{\mathrm{MC}}^{(\mathrm{old})} \cdot V_{\mathrm{sys}}^{(\mathrm{old})}/V_{\mathrm{sys}}^{(\mathrm{new})}$).

The coagulation of two weighted particles is realized by the change of statistical weights and all other particle properties of both particles (or only for one particle [185]). This avoids the depletion of MC particles and makes constant number schemes possible, as it is described in section 4.1 in more detail.

2.2.3.2 MC Methods: Applications and Modeling of Spatial Inhomogeneities

The main advantage of MC methods is that multiple particle properties can be covered and absolutely no a priori knowledge about the PSD is needed. This makes this method the only possible choice if complex particle morphologies have to be taken into account (for example crystallization in batch conditions [191] or TiO_2 formation in flame processes [192]) or multiple properties describe the particulate dynamics (e.g. during fluidized bed spray drying [62] or granulation [193]).

Compartmental MC methods are often applied and can be found in the modeling of industrial reactors [83, 84], multiphase loop reactors [194], polymerization and gelation [195], granulation processes [196] or reactor networks in general [197].

Long computing times are the main drawback of MC simulations, making a full CFD-PBE coupling costly: The computation time of 47 h (10 h, if a parallel computing cluster with 11 nodes is applied) for the simulation of only 400 cells and 200 000 MC particles (i.e. 500 MC particles per each cell) has been reported [198]. Such a coupling is however, necessary to model the interaction of the particle population with the gas phase [199, 200].

A two step methodology has been proposed by [192]: in a first step a numerically efficient moment based method is used for a coupled CFD-PBE simulation, taking thus the particle gas-phase coupling into account. In a subsequent second step, Lagrangian tracking of a volume element is applied to provide simulation conditions for a detailed MC simulation allowing thus the prediction of complex particle morphologies.

2.3 Summary

This chapter describes the PBE and shows the range of applications in the field of chemical engineering. Specific solution strategies such as the method of moments, discretization methods and MC methods are briefly outlined. The application of these methods for the modeling of reactor networks in combination with CFD simulations has been assessed. It has been found, that while the moment method is the computationally most efficient method, the reconstruction of the PSDs is not unequivocally possible, which might pose a problem for flowsheet simulations with sieve units. The application of discretization methods is computationally more costly but the formulation of the flow equations between compartments or CFD cells is very simple (if non-moving grids are applied). The main limitation of this method is the very low number (2-3) of particle properties it can capture. The MC methods are able to capture a large number of particle properties (even 1000 is computationally feasible for smaller compartment networks, i.e. less than 100 compartments). The introduction of different statistical weights to each MC particle facilitates the modeling of particulate transport between single compartments or CFD cells. The main drawback of the MC method is a high computation time. The reduction of the computation time due to the application of Graphic Processing Units (GPUs) as well as the development of more efficient, weighted MC particle-based methods for single processes like coagulation, nucleation, growth, breakage and transport are the main topics treated in the subsequent chapters of this thesis.

Chapter 3

Parallel Computing for MC-PBE Modeling

The programming of graphic processing units (GPUs) is one alternative approach for parallelization in contrast to the programming of several central processor units (CPU) of larger computing clusters (see e.g. [198]). The main advantage of the GPU is the sheer computing power for a relatively low price. For example, a RTX 2080 Ti (sold since 09/2018) costs ca. 700 €(in the year 2022) and consists of 68 parallel streaming multiprocessors (SMs) [201]. Each of these SMs can perform up to 1024 parallel instructions, so that a total of up to $68 \times 1048 = 69\,632$ instructions (called 'threads') can be executed in parallel.

The application of GPUs for the acceleration of numerical solutions of the PBE poses thus an interesting possibility and different strategies have been proposed for the acceleration of the method of moments [202], discretization methods [203, 87] and MC methods [184, 204, 183].

Many toolkits for different programming languages have been developed, allowing the direct programming of GPUs (e.g. openCL [205], openACC [206]). In the following section 3.1 a quick overview of the Compute Unified Device Architecture (CUDA) programming language [207, 208] - an extension to C++ [209] - is given[1]. The second section 3.2 of this chapter sketches some parallelization strategies for the acceleration of MC simulations.

3.1 GPU Architecture and Programming

The SM of a GPU consists of several vector processors (see e.g. [210]) which can perform 32 arithmetic operations in parallel[2]. The hardware associated with the processing of one operation is given the marketing name 'CUDA core' [211].

Figure 3.1 depicts the relation of the CUDA cores to the processed data. The CUDA cores operate on registers of the Multiprocessors which are grouped in so called warps (another Nvidia marketing name), each warp represents 32 execution threads. In Figure 3.1, only 4 vector processors (or 4 x 32 CUDA cores) are present in each SM, while 64 warps (à 32 execution threads) are arranged for execution[3]. The single vector processor can access registers from different warps (depicted as 'context switch'). If an arithmetic operation consists of many stages, instruction pipelining is used, so that data of different warps is handled at different stages simultaneously.

The threads can access the local registers of each warp and the local memory of each SM - these accesses are very fast compared to an access to values stored in the main memory of the GPU.

Due to the architecture shown in Figure 3.1, the programmer has to arrange the intended parallel threads into so called 'blocks' (up to $2^{31} - 1 \approx 2.15 \cdot 10^9$). Each block consists of up to 1024 threads (or 32 warps) and is executed on one SM - in this way all threads within a block can access local shared variables and can be synchronized (i.e. forced to stop at a specific point of the code). The number of blocks which can be launched on one SM depends on the executed kernel, more specifically: on the amount of needed local memory, the number of needed registers and the number of requested

[1] The presented programming strategies could also be implemented with the OpenCL programming language[205]. This approach is not discussed in this thesis.

[2] The 32 operations are divided in 2 pipelines, each processing 16 elements in parallel.

[3] This example describes a GTX 980 Ti. The SMs of the RTX 2080 Ti, for example, contain each only 2 x 32 CUDA cores and allow the parallel execution of only 1024 threads (or 32 x 32 warps).

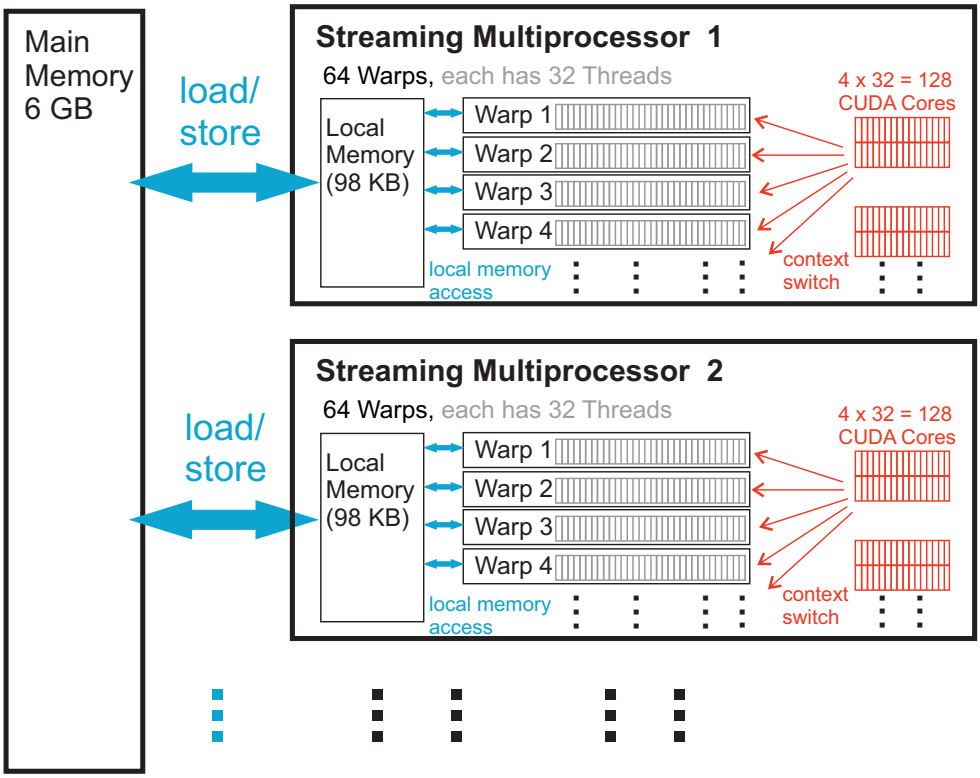

Figure 3.1: Simplified scheme of the components of a GPU and memory access patterns. The number shows the maximal possible number of warps per SM for a GTX 980 Ti.

threads per block. For this reason, different blocks may be launched on different SMs and therefore no synchronization between threads in different blocks is possible. If the programmed kernel requests too many resources (e.g. one block requires more memory than a SM can provide), an error will be issued at run-time and the program has to be terminated.

An exemplary instruction dispatch using CUDA is shown in Algorithm 1, the last line invokes the parallel execution of a kernel with the name `TestKernel`. The variable `Block_No` defines the number of blocks and `Thread_No` the number of threads which will be used, these are set up by the `<<< , >>>` notation syntax. The shown code requests therefore the invocation of 5 984 blocks, each consisting of 256 parallel threads. Assuming that the kernel is so simple that all threads of a SM (2048 (for the GTX 980 Ti) or 1024 (for the RTX 2080 Ti)) can be used for the computation leads to the situation where each SM can process 8 blocks (GTX 980 Ti) resp. 4 blocks (RTX 2080 Ti). Thus, the RTX 2080 Ti (with 68 SM) would need to loop the requested instructions $5\,984 / (4 \times 68) = 22$ times, while a GTX 980 Ti (with only 22 SM) would need to loop the requested instructions $5\,984 / (8 \times 22) = 34$ times.

Algorithm 1 Function call of a predefined CUDA-kernel `TestKernel` shown as Algorithm 2.

```
float* d_input; // pointer to GPU array containing input data
float* d_output; // pointer to GPU array containing output data
...  // Allocation of GPU memory for d_input and d_output not shown
int Block_No = 5984;
int Thread_No = 256;.
TestKernel <<< Block_No, Thread_No >>> (d_input, d_output);
```

An exemplary code for the GPU kernel `TestKernel` is shown in Algorithm 2. The simple calculation $y = x^2 + 10$ is carried out, where y refers to each element of `d_output` arrays and x to the elements of the `d_input` arrays stored in the main memory of the GPU. Each of the launched threads performs the same calculation on a different element of the data following the single instruction multiple data (SIMD) paradigm. The element is defined by its array index and accessed by the `index` variable.

Each launched block has a unique identification number and each thread within a block has also a

Algorithm 2 The keyword `__global__` declares the shown routine to be executed as a CUDA-kernel on the GPU.

```
__global__ void TestKernel(float* d_input, float* d_output) {
    int index = threadIdx.x + blockIdx.x * blockDim.x ;
    d_output[index] = d_input[index]*d_input[index] + 10;
}
```

Table 3.1: Variables used for the calculation of the index of elements in the `d_input` and `d_output` array in algorithm 2. The specific values of `Thread_No` and `Block_No` are passed to the kernel in the last line of algorithm 1.

Symbol	Variable name	Range	Description
$\mathcal{T}_{\text{id}}$	`threadIdx.x`	$0 \ldots$ (`Thread_No` -1)	unique ID for each thread within a block
$\mathcal{B}_{\text{id}}$	`blockIdx.x`	$0 \ldots$ (`Block_No` -1)	unique ID for each block
$\mathcal{B}_{\text{dim}}$	`blockDim.x`	`Thread_No` (one value)	total number of threads per block
$\mathcal{G}_{\text{dim}}$	`gridDim.x`	`Block_No` (one value)	total number of launched blocks

unique number. This allows the calculation of a unique `index` value for each possible (block, thread) pair as it is shown in the second line of Algorithm 2. The variables used for the calculation are described in Table 3.1 in more detail.

The arrays `d_input` and `d_output` are passed to the routine `TestKernel` and it is the responsibility of the programmer to make sure that these pointers point to valid addresses on the GPU. The programmer has also to ensure that enough memory has been allocated, so that the accesses dispatched by the `TestKernel` routine do not lead to run-time errors (i.e. segmentation faults).

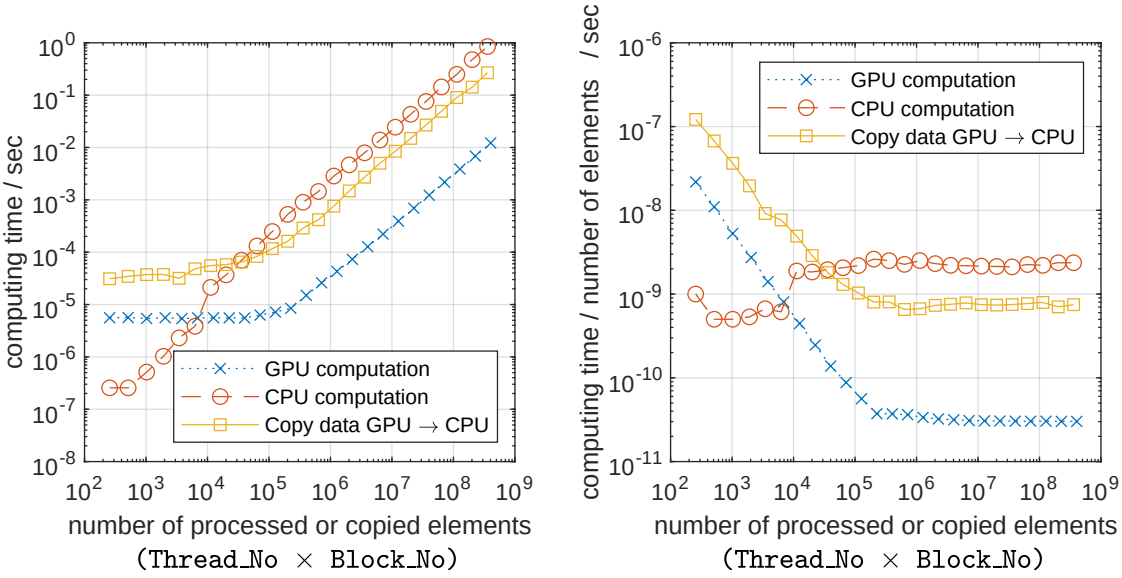

(a) Absolute computing times.

(b) Ratio computing times to number of processed elements.

Figure 3.2: Typical running times (mean of 10 runs) for Algorithm 2 run on a GPU (GTX 980 Ti) compared to a serial CPU (Intel i7-4790K) implementation (Algorithm 3), as well as the data transfer times between GPU and CPU memory. A constant `Thread_No` of 256 has been used, while `Block_No` has been varied.

Figure 3.2 shows a comparison of run-times of the parallel algorithms (Algorithms 1 and 2) to the serial CPU implementation using a simple for-loop (shown as Algorithm 3). It can be seen in Figure 3.2 that for relatively low numbers of processed elements (i.e. $< 7\,000$) the CPU computation is much faster. The CPU times scale linearly with the number of processed elements. The GPU computing

times show also a linear scaling for values greater than $2 \cdot 10^5$, however, the computing times are nearly 100 times smaller than the CPU computation times. It can also be seen that the copies of the calculated values from GPU memory to the CPU are more costly than the simple calculation. For this reason, the application of a GPU is advantageous for applications for which the copy operations between CPU and GPU can be kept to a minimum, forming only a small fraction of the overall computing times. This is the case in the presented algorithms in the following, where - disregarded from copying a few integer values for algorithmic control purposes - the CPU-GPU copy is only used to initiate the particle properties at the beginning of the simulation and export the particle properties to files at 20-100 specific simulation time points for further post-simulation analysis.

Algorithm 3 The serialized version of Algorithm 2 with arrays `output` and `input` allocated on CPU main memory.

```
for(int index = 0; index < Block_No * Thread_No; index++) {
    output[index] = input[index] * input[index] + 10;
}
```

3.2 Parallel Algorithms for Coagulation of MC Particles

Parallel strategies have been proposed for the MC based simulation of coagulation using the inverse method [183] and the acceptance rejection (AR) method [204], both methods have been briefly outlined in section 2.2.3.1 on page 17. A more detailed implementation of the GPU-based AR method is shown in Figure 3.3. The shown algorithm selects 256 (this is the used number of threads per block) random MC particle pairs (i, j) in parallel and calculates the corresponding coagulation rates $R_{i,j}$. A pair will be chosen for coagulation, if a uniformly distributed random number (URN) r satisfies the condition $r < R_{i,j}/R_{\max}$, as stated in Eq. (2.22). By performing all of these checks in parallel, a significant speed-up is gained compared to a serial loop implementation where 200 iteration would be needed in the statistical mean in order to find a coagulation pair (if $\chi = 200$ is used). The second advantage of the presented algorithm is that the randomly selected coagulation pairs can be used as a representative population sample, allowing the parallel addition (as in Figure 3.3 and discussed for example in Chapter 39 of [212] for prefix sums) of $R_{i,j}$ for the fast approximation of $\Delta\tau_{\mathrm{MC}}$ (introduced in Eq. (2.20)) via:

$$\Delta\tau_{\mathrm{MC}} = \frac{1}{\sum_{\text{all } i>j} R_{i,j}} \approx \frac{2 \cdot \mathcal{N}_{\mathrm{sample}}}{\mathcal{N}_{\mathrm{MC}} \cdot (\mathcal{N}_{\mathrm{MC}} - 1) \cdot R_{\mathrm{sum}}}\,, \quad \text{with: } R_{\mathrm{sum}} = \sum_{\substack{\text{all pairs } (i,j) \\ \text{in sample}}} R_{i,j}\,, \tag{3.1}$$

where $\mathcal{N}_{\mathrm{sample}}$ is the size of the selected sample and $\mathcal{N}_{\mathrm{MC}}$ is the number of all simulation particles - thus $(\mathcal{N}_{\mathrm{MC}} \cdot (\mathcal{N}_{\mathrm{MC}} - 1))/2$ is the number of all possible coagulation pairs. The sample size $\mathcal{N}_{\mathrm{sample}}$, as well as R_{sum} increase each time an unsuccessful selection attempt has been performed. This leads to more accurate values for R_{sum} and thus for $\Delta\tau_{\mathrm{MC}}$ due to larger sample sizes. The values are reset to zero if a new coagulation pair is found, in this way the algorithm adjusts to the novel coagulation dynamics.

The maximum possible coagulation rate, $R_{\max}$, can be approximated with the help of a constant safety factor χ:[4]

$$R_{\max} \approx \chi \cdot R_{\mathrm{sum}}/\mathcal{N}_{\mathrm{sample}}\,. \tag{3.2}$$

It could be shown that the parallel implementation of the AR method shown in Figure 3.3 is 20–40 times faster (depending on the number of used simulation particles) than the CPU version [213]. The advantage of handling of thousands of cells in a parallel fashion (by simply launching the algorithm in Figure 3.3 for 1000 blocks in parallel) is also pointed out in [213].

[4] For coagulation scenarios, χ has been reported to be sufficient to be set to constant values between 40 and 200 [204, 186]. For more demanding simulation scenarios values of 10 000 are necessary to obtain accurate results [Paper I] .

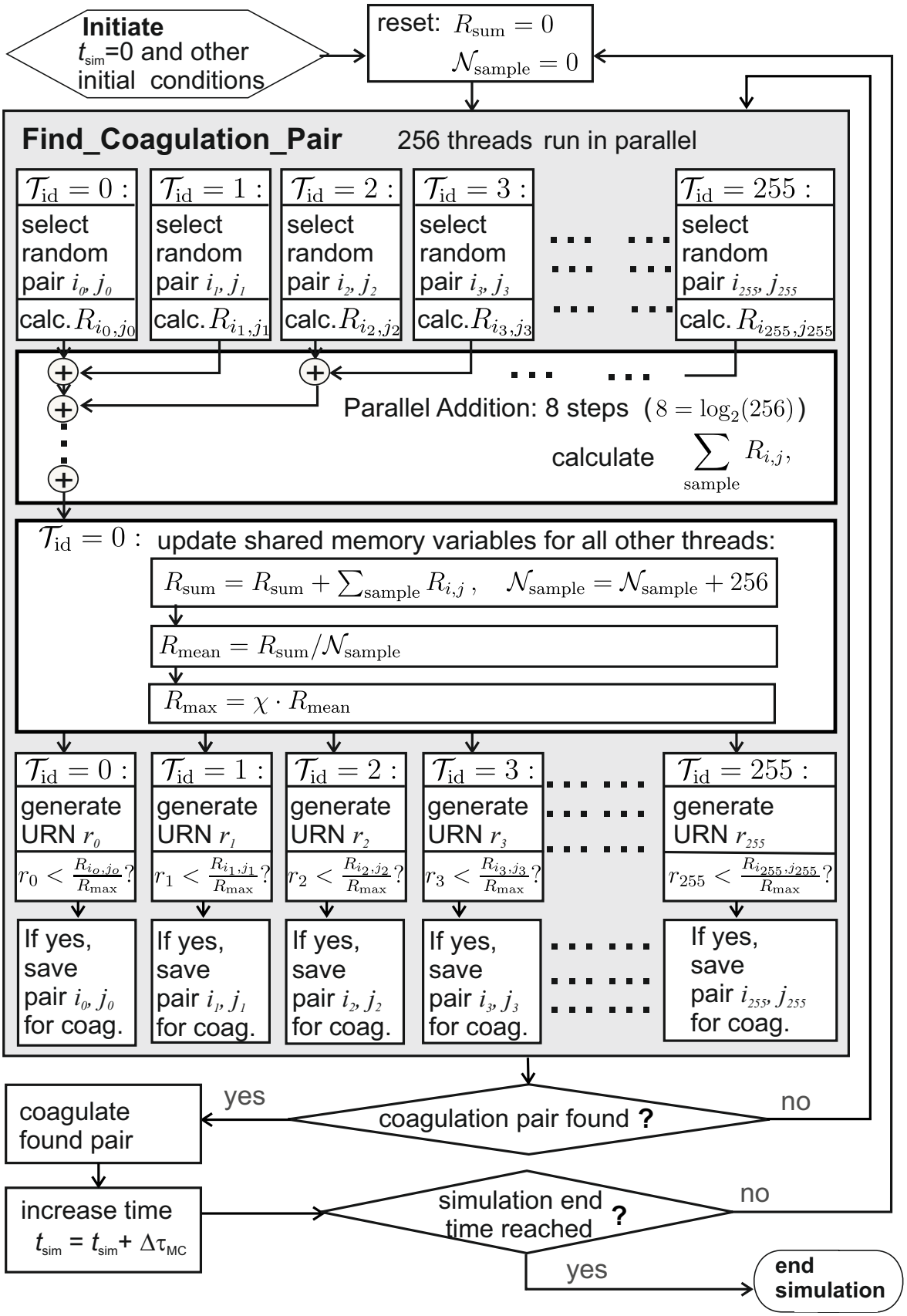

Figure 3.3: A GPU algorithm for the event-driven AR-based MC simulation as described in [204]. Uniformly distributed random numbers (URN) $r_i \in (0, 1)$ are used.

Chapter 4

Parallel Simulation Techniques for Weighted MC Particles

The main motivation for the usage of weighted MC particles is the ability to model simulation conditions in which two particle populations A and B interact and both populations differ in their particle number concentrations in several orders of magnitude. The populations A and B might also describe typical particles in different zones of a reactor or different apparatuses of a flowsheet simulation.

Let for example species A describe freshly nucleated particles of a size of around 3 nm with a total concentration of $10^{11}\,\mathrm{cm}^{-3}$ and species B represent a background particle population (intended to be coated with the newly nucleated particles A) with sizes of the magnitude of 100 nm and a total concentration of $10^{6}\,\mathrm{cm}^{-3}$. If each MC particle would represent the same number of real particles per m^3, W_{MC}, than W_{MC} would at least to be chosen to be $10^{4}\,\mathrm{cm}^{-3}$ (or $10^{5}\,\mathrm{cm}^{-3}$) in order to render at least 100 (or 1000) particles of the population B. One might argue that this low number of MC particles is insufficient to describe the behavior of the population B correctly, but even this very low number would entail 10^7 (or 10^8) MC particles representing the population A. Such a detailed representation of population A is 1) not necessary and 2) computationally extremely expensive. If, on the other hand, each MC particle i is assigned an individual statistical weight W_i, both populations A and B can be modeled with as many or as few MC particles, as it is deemed necessary. Such a modeling has already been briefly mentioned in section 2.2.3.1; the difference of the approximation of the PSDs by weighted and non-weighted MC particles is described by Eq. (2.23) and Eq. (2.24).

The assignment of a specific statistical weight to each MC particle combined with the application of parallel computing (by means of a GPU) allows the development of novel strategies for particulate processes. These techniques can be combined for the general solution of the PBE for a network of compartments (Eq. (2.10)). Where each compartment represents a unit of a flowsheet, like the one shown in Figure 1.1. Thereby, the single processes can be separated for short periods of time, Δt, leading to the following general algorithm:

1. Initiate initial $t_{\mathrm{sim}} = 0$, t_{end} and Δt.
2. As long as $t_{\mathrm{sim}} < t_{\mathrm{end}}$ do:
   (a) For each unit(or compartment) U:
      i. If coagulation has to be considered in unit U:
         - Perform one (or several, if $\Delta t > \Delta\tau_{\mathrm{MC}}^{U}$) coagulation step(s) for weighted simulation particles (section 4.1) in combination with parallel algorithm from section 3.2.
         - If a fractional time step is needed (e.g.: if $\Delta t < \Delta\tau_{\mathrm{MC}}^{U}$), use the fractional time steps from section 4.2.
         - Store intrinsic time step $\Delta\tau_{\mathrm{MC}}^{U}$.
      ii. If breakage of particles has to be considered in unit U:
         - Perform parallel breakage algorithm for time Δt from section 4.3.
         - Store intrinsic time step $\Delta\tau_{\mathrm{B}}^{U}$.
      iii. If nucleation without condensation/evaporation has to be considered in unit U:
         - Apply the method for nucleation in section 4.5 for a time step Δt, based on the merging of particles from section 4.4.

iv. If condensation/evaporation without nucleation has to be considered in unit U:
- Apply the method for growth and evaporation in section 4.7.1 for a time step Δt, detailed in section E.1.
- Store intrinsic time step $\Delta t_{\mathrm{RK}}^{\mathrm{ini},U}$.

v. If nucleation and condensation/evaporation have to be considered in unit U:
- Apply the algorithm for the growth, evaporation and nucleation from section 4.7.3 for a time step Δt, detailed in section E.2. This algorithm uses the method for nucleation in section 4.5, based on the merging of particles from section 4.4.
- Store intrinsic time step $\Delta t_{\mathrm{RK}}^{\mathrm{ini},U}$.

(b) Simulate particle transport for time Δt between compartments (or units) U, using methodology from section 4.6.1 based on merging of particles from section 4.4. Provide intrinsic transport time step $\Delta\tau_{\mathrm{Tr}}$.

(c) Increase time $t_{\mathrm{sim}} = t_{\mathrm{sim}} + \Delta t$.

(d) Estimate new time step Δt. For example: $\Delta t = \min_{\mathrm{all}\ U}(\Delta\tau_{\mathrm{MC}}^{U}, \Delta\tau_{\mathrm{B}}^{U}, \Delta t_{\mathrm{RK}}^{\mathrm{ini},U}, \Delta\tau_{\mathrm{Tr}})$.

3. Export results and end simulation.

The order of execution of the single algorithmic steps 2(a), 2(b) and 2(a)i - 2(a)v is rather arbitrary. The difference of the results between an algorithm performing step 2(b) first and then step 2(a) and the one which is shown (step 2(a) first and then 2(b)) could provide an approximation of the error introduced due to the operator splitting technique. It is expected to become smaller, the smaller Δt is chosen, at the cost of increasing computing times. Such complex simulations are, however beyond the scope of this thesis. The main topics are, however, the formulation and validation of each of the single components of this algorithm. Table 4.1 summarizes the mechanisms treated in the following sections in connection with the publications in which more detailed information can be found.

Table 4.1: Publications introducing the novel algorithms for mechanisms discussed in the following sections. The additional results can not be found in the listed papers.

Section	Mechanism	Publications	Additional results
4.1	Coagulation	[Paper I]	Method comparison (Figure 4.3)
			SWA derived from SR (appendix C)
4.2	Coagulation	[Paper II]	–
4.3	Breakage	[Paper III]	–
4.4	Merging	[Paper I]	–
4.5	Nucleation	[Paper I]	Random Merging (Figure 4.9)
4.6	Transport	[Paper V],[Paper VIII]	Stochastic outflow (Figure 4.11)
4.7	Growth/Evap.,	[Paper IV],[Paper V],	Validation (Figures 4.12–4.16)
	Nucleation,	[Paper VI],[Paper VII]	RK Implementation (appendix E)
	Coagulation		Pivot point method (appendix B.2)

4.1 Constant Number Schemes for Coagulation of Weighted MC Particles

The coagulation of weighted simulation particles (i and j) poses a fundamental problem, hence one has to devise a rule, of how a particle population represented by a concentration of e.g. $W_i = 10^8\,\mathrm{cm}^{-3}$ real particles (stored as MC particle i) interacts with another particle population represented by a concentration of e.g. $W_j = 10^{10}\,\mathrm{cm}^{-3}$ (stored as MC particle j). The more complicated mathematical concepts offer, on the other hand, the opportunity to formulate constant number schemes and avoid thus the necessity of continuous topping-up schemes or rescalings of the simulation volumes – as briefly discussed at the end of section 2.2.3.1.

4.1.1 Multi Monte Carlo (mMC) and Stochastic Weighted Algorithm (SWA)

Some approaches express the statistical weight as a function of the particle property. The mass flow algorithm (MFA) [214], for example, allows only statistical weights W_i for which the volume-concentration of each particle i (with volume v_i) remains constant throughout the simulation, i.e. $v_i \cdot W_i = const$. This approach might be useful for certain particle production processes, but might be less applicable for simulation scenarios in which different particle populations representing vastly different mass-concentrations are mixed.

One early formulation using individual weights W_i which are absolutely independent on the particle properties was the multi-Monte Carlo (mMC) formulation [215, 216]. This scheme provided a modified coagulation rate $R_{i,j}^{\mathrm{mMC}}$ and rules, how to adjust the statistical weights W_i and W_j of the particles with the volumes v_i and v_j, if selected for coagulation, Table 4.2 summarizes these values. Note, that the coagulation rates $R_{i,j}^{\mathrm{mMC}}$ (as well as the resulting novel particle properties) differ, dependent upon, whether the coagulation pair (i,j) or (j,i) has been selected for coagulation. The rates and new properties provided by Table 4.2, can be used in combination with the already described methods for the MC simulation for coagulation in sections 2.2.3.1 and 3.2 simply by using the expression R^{mMC} (resp. R^{SWA}) instead of R and changing the particle volumes and weights accordingly to Table 4.2.

Table 4.2: Coagulation rates for coagulation of weighted MC particles i and j (where $\beta_{i,j}$ is the coagulation kernel). The particle weights $W_i^{(\mathrm{new})}$, $W_j^{(\mathrm{new})}$ and volumes $v_i^{(\mathrm{new})}$, $v_j^{(\mathrm{new})}$ after coagulation of particles with weights W_i, W_j and volumes v_i, v_j before coagulation. $\alpha_{i,j}$ has to satisfy condition (4.1), suggested choices by [185] are shown in Table 4.3.

Method	Coagulation rate	$W_i^{(\mathrm{new})}$	$v_i^{(\mathrm{new})}$	$W_j^{(\mathrm{new})}$	$v_j^{(\mathrm{new})}$
mMC [215]	$R_{i,j}^{\mathrm{mMC}} = W_j \cdot \beta_{i,j}$	$W_i/2$	$v_i + v_j$	W_j	v_j
SWA [185]	$R_{i,j}^{\mathrm{SWA}} = W_j \cdot \beta_{i,j}$	$\alpha_{i,j} \cdot W_i$	$v_i + v_j$	W_j	v_j

A family of stochastic weighted algorithms (SWA) was introduced by [185] (also summarized in Table 4.2), the authors could show that the thus defined jump processes converge towards the expected solutions, if $\alpha_{i,j}$ is chosen in the following way:

$$\alpha_{i,j} + \alpha_{j,i} = 1\,. \tag{4.1}$$

The authors noted, that the specific choice of $\alpha_{i,j}$ could be also an arbitrary function $H(i)$ (resp. $H(j)$) dependent on the properties of the considered particle i (resp. j). Table 4.3 lists the explicit choices for $\alpha_{i,j}$ introduced by [185].

Table 4.3: Different settings for $\alpha_{i,j}$ as published in [185]. The function $H(i)$ may be any function depending on the properties of particle i, the formulation $H(i) = 1/W_i$ is used in the following – implying thus: SWA1 = SWA3.

	SWA1 / MFA [1]	SWA2 / mMC	SWA3 / SWA1 [2]	SWA4
$\alpha_{i,j}$	$\frac{W_j}{(W_i+W_j)}$	$\frac{1}{2}$	$\frac{H(i)}{H(i)+H(j)}$	$\frac{\sqrt{W_i}H(i)}{\sqrt{W_i}H(i)+\sqrt{W_j}H(j)}$

Despite a rigorous proof of the convergence of SWA2 [185], high noise levels remain an often lamented, inherent feature of this method [217]. Another disadvantage of all the methods presented in Table 4.2 is that the total volume concentration of all particles is not preserved exactly, but only in the statistical mean – except in the special case in which all particles satisfy $v_i \cdot W_i = const$ – SWA1 is equivalent to MFA then.

[1] The SWA1 is equivalent to MFA only, if all particles represent the same volume concentration at the beginning of the simulation i.e. $v_i \cdot W_i = V_0$ for all i. It is in this case: $\alpha_{i,j} = W_j/(W_i + W_j) = v_i/(v_i + v_j)$, one can see the volume conservation by inserting $\alpha_{i,j}$ into the expression for $W_i^{(\mathrm{new})}$ in Table 4.2, which results in $W_i^{(\mathrm{new})} \cdot v_i^{(\mathrm{new})} = v_i \cdot W_i$.

[2] If the function $H(i) = 1/W_i$ is used in combination with $v_i \cdot W_i = const.$, then SWA3 is equivalent to SWA1 and MFA.

4.1.2 Fictitious Particle (FP) Theory and Stochastic Resolution (SR)

The fictitious particle (FP) theory [190] represents an elegant, volume preserving, coagulation scheme, as it is presented in Figure 4.1, but poses a somewhat cumbersome derivation of the corresponding coagulation rates. Especially the resulting asymmetric coagulation rates for the same event (depending on, whether particle i coagulates with particle j or vice versa) is conceptually difficult to comprehend[3].

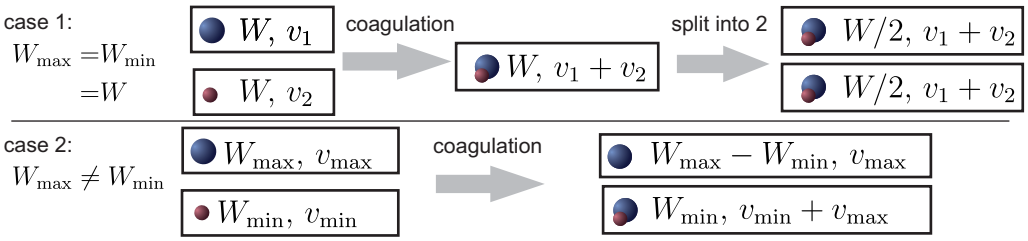

Figure 4.1: Coagulation scheme for weighted particles proposed by [190].

The scheme depicted in Figure 4.1 comprises two cases. If both particles are equally weighted (case 1), then a coagulation scheme as described for equally weighted particles can be applied, resulting in only one particle. This MC particle can be split up into two existing MC particles with half of the original weight, so that the same population is rendered by two simulation particles again. The second case shown in Figure 4.1 is more complicated: here only a part ($W_{\min}$) of all particles represented by the particle with $W_{\max}$ undergo the coagulation with the particle population represented by $W_{\min}$. Resulting in a particle population with the statistical weight of $W_{\min}$ and the properties after coagulation $v_{\min} + v_{\max}$. While the particles representing a statistical weight of $W_{\max} - W_{\min}$ do not participate in the coagulation at all. How can one formulate or derive the process rate for such a process?

The concept of stochastic resolution (SR) has been introduced in [Paper I], the idea is to consider a different system volume V_{sys} for each coagulation pair (i, j). The size of the chosen system volume can be considered as a stochastic resolution (called $1/s_{\text{F}}$ in [Paper I]): the larger the value for V_{sys}, the more details of the PSD can be captured.

The system volume V_{sys} is changed in such a way, that the concentration $W_{\min}$ translates to exactly one particle of the $W_{\min}$–species, and $W_{\min}/W_{\max}$ of the $W_{\max}$–species:

$$V_{\text{sys}} = 1/W_{\text{MC}} = 1/W_{\min}\,. \tag{4.2}$$

In this situation, the only one $W_{\min}$–species particle undergoes a coagulation with one of the other particles, while $W_{\min}/W_{\max} - 1$ of the $W_{\max}$–species remain unchanged. This situation is sketched in Figure 4.2.

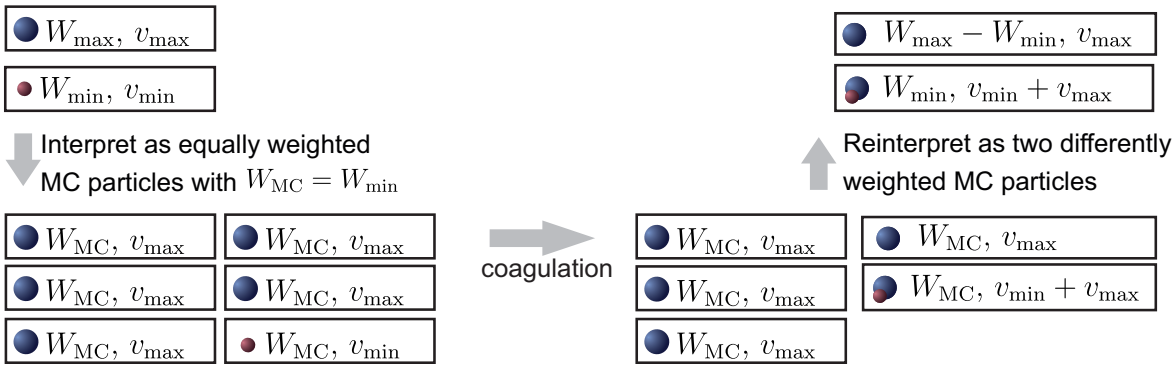

Figure 4.2: The reinterpretation of differently weighted MC particles as equally weighted particles helps to calculate the coagulation rates for a constant number scheme as suggested in [Paper I].

[3] The asymmetric rates described in Table 4.2 are on the other hand justified, hence the coagulation of the pair (i, j) leads to different $W_i^{(\text{new})}, W_j^{(\text{new})}, v_i^{(\text{new})}$ and $v_j^{(\text{new})}$ than the coagulation of the pair (j, i).

The derivation of the coagulation rate of this process is documented in section **2.2** in [Paper I] and written in comparison to the fictitious particle theory in Table 4.4. The SR theory formulates rates for each coagulation event - independent on whether particle i coagulates with j or vice versa, the summation of all coagulation rates is therefore only over all pairs (i, j) with $i > j$. In the scope of the FP, in contrast, the rate $R^{\mathrm{fp}}_{i,j}$ has to be interpreted as probability that particle i undergoes a coagulation with j, and the rate $R^{\mathrm{fp}}_{j,i}$ has to be interpreted as probability that particle j undergoes a coagulation with i, and the overall event-rate for the coagulation of the pair (i, j) is assumed to be the mean of both rates $(R^{\mathrm{fp}}_{i,j} + R^{\mathrm{fp}}_{j,i})/2$, which is the expression used for the time step calculation, where the summation is performed over all pairs (i, j) with $i \neq j$. Hence $(R^{\mathrm{fp}}_{i,j} + R^{\mathrm{fp}}_{j,i})/2 = R^{\mathrm{sr}}_{i,j}$, both methods lead to the same results. The description of the previously introduced SWA by SR can be found in appendix C.

Table 4.4: Coagulation rates and calculation of the time-steps $\Delta\tau_{\mathrm{MC}}$ for different weighted particle theories.

	Coagulation rate	Time step
Fictitious particle (FP) [190]	$R^{\mathrm{fp}}_{i,j} = 2\beta_{i,j} W_j \cdot \max(W_i, W_j)/(W_i + W_j)$	$2/\sum_{i\neq j} R^{\mathrm{fp}}_{i,j}$
Stochastic resolution (SR) [Paper I]	$R^{\mathrm{sr}}_{i,j} = \beta_{i,j} \cdot \max(W_i, W_j)$	$1/\sum_{i>j} R^{\mathrm{sr}}_{i,j}$

4.1.3 Comparison and Validation of Constant Number Schemes

The presented methods in Table 4.2 and Table 4.4 are compared with each other and Matsoukas' constant number scheme (CNMC, described on page 18) for equally weighted MC particles [180][4] in the following. The parallel algorithm presented in section 3.2 (the coagulation rates $\beta_{i,j}$ between particles i and j have to be replaced with $\beta^{\mathrm{sr}}_{i,j}$) is used for this purpose. As test case, the coagulation in the free-molecule regime of a monodisperse particle population is considered, as described in appendix A.3. The results are shown in dependency to the characteristic time τ_{fm} defined in Eq. (A.10).

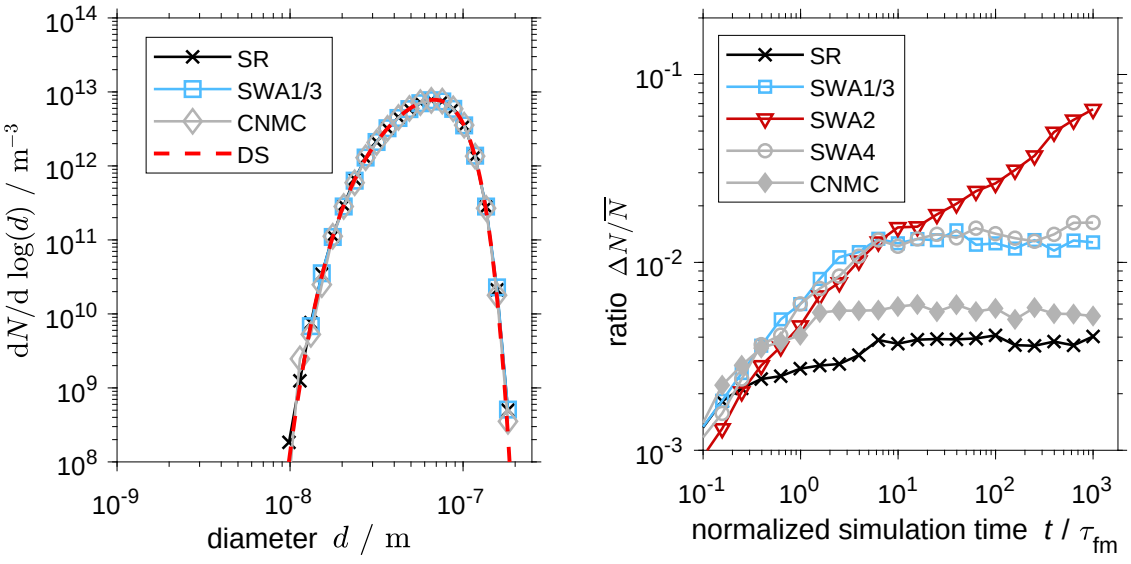

(a) PSDs after $t = 1000\,\tau_{\mathrm{fm}}$.

(b) Noise in number concentration.

Figure 4.3: Comparison of different methods for coagulation of $\mathcal{N}_{\mathrm{MC}} = 10^4$ weighted simulation particles under the conditions summarized in appendix A.3. $\overline{N}$ is defined in (D.3) and ΔN in (D.4).

Figure 4.3a shows that all simulation techniques are able to reproduce the PSD correctly by comparison to the discrete-sectional method (DS). The statistical noise resulting from different (quasi-)random

[4] The Markov jump technique [184] is similar to CNMC in the case of equally weighted simulation particles at the beginning of the simulation.

number sequences is, on the other hand, starkly dependent on the applied simulation technique. These noise levels can be quantified by the ratio of the arithmetical mean of all number concentrations $\overline{N}$ (defined in Eq. (D.3)) compared to the arithmetical standard deviation ΔN (defined in Eq. (D.4)) of 100 different quasi-random number sequences (and thus 100 different particle populations) for each simulation technique. Lower ratios $\Delta N/\overline{N}$ allow more precise estimations (i.e. smaller confidence intervals) of the number concentration, this is elaborated a little more further in appendix D.1. Figure 4.3b shows the values $\Delta N/\overline{N}$ for different simulation techniques, it can be seen that the SR based levels are even a little bit lower than the CNMC levels and much lower than those of the SWA techniques. Similar findings can be made for the values $\Delta d_\mathrm{g}/\overline{d_\mathrm{g}}$, $\Delta\sigma_\mathrm{g}/\overline{\sigma_\mathrm{g}}$ or for the ratio of the mean to the standard deviation of the concentration within single bins of a PSDs (only the mean values are shown in Figure 4.3a).

Table 4.5: Noise levels after $t = 1000\,\tau_\mathrm{fm}$, required computation times and number of MC steps for the simulation conditions summarized in appendix A.3.

	$\mathcal{N}_\mathrm{MC} = 10^3$ particles			$\mathcal{N}_\mathrm{MC} = 10^4$ particles		
Method	Accuracy $\Delta N/\overline{N}$	Number of MC steps / 1000	Computing time /sec	Accuracy $\Delta N/\overline{N}$	Number of MC steps / 1000	Computing time /sec
SR	0.011	13.1	7.46	0.0040	130.7	114.4
SWA1/3	0.039	21.4	13.26	0.0128	214.4	160.0
SWA2	0.187	21.4	13.48	0.0653	213.0	163.4
SWA4	0.043	21.4	13.26	0.0163	214.4	162.6
CNMC	0.016	9.7	5.78	0.0052	97.1	99.1

Table 4.5 compares the required computation times (an NVIDIA GTX 980 Ti has been used) and necessary number of MC steps with the gained accuracy for different simulation techniques and number of simulation particles. It can be seen, that the SR based simulation is able to assure levels of accuracy for 10^3 MC particles, which the SWA techniques are only able to attain if 10^4 particles are used – at the cost of much higher computation times, hence ten times more MC steps are required for this kind of simulation. The large difference in noise levels between SR and SWA algorithms is explained in appendix C.

4.2 Fractional MC Time Steps for Coagulation

Many application scenarios require a combination of the coagulation process with other mechanisms like nucleation, growth, breakage or transport as introduced in section 2.1. Approaches, which treat all of these processes in a stochastic way formulate for each particle probabilities for surface growth, breakage or transport (see e.g. [188]). Such formulations might prove computationally very costly and alternative approaches, which couple the stochastic simulation of coagulation with deterministically modeled surface processes (see e.g. [218, 219]) might not only prove to be computationally more effective, but also to produce less statistical noise – hence only one of many mechanisms is treated stochastically. In the scope of operator splitting techniques, the single mechanisms are decoupled for short periods of time, Δt. The method leads to errors if Δt is chosen to be too large and is less effective if Δt is too small. The stochastic simulation for coagulation should be therefore able, to simulate any desired time step Δt. This can be easily done by time-driven MC approaches which are, however, computationally less effective than event-driven methods as discussed in section 2.2.3.1 on page 17.

In order to be able to use the parallel algorithm discussed in section 3.2 in an operator-splitting approach, the algorithm has to be modified in such a way, that also time steps Δt which are smaller than the intrinsically approximated MC time step $\Delta\tau_\mathrm{MC}$ (Eq. (3.1)) are treated correctly. In the following section 4.2.1, the concept of 'fractional MC time steps' introduced in [Paper II] will be briefly sketched. It is also shown in section 4.2.2 that this methodology is necessary in order to simulate accurate results, which alternative approaches, like [198], are not able to reproduce.

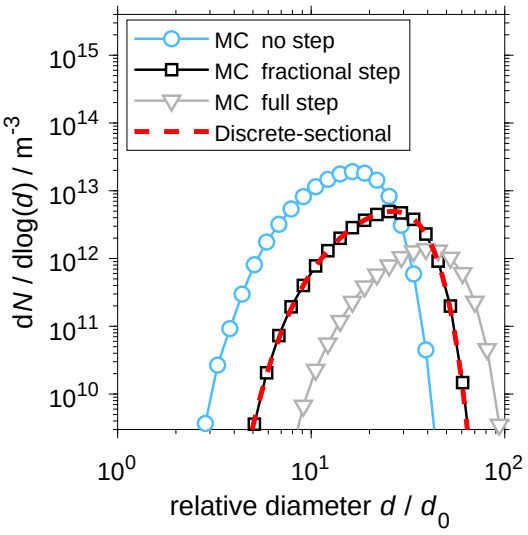

(a) PSDs after $t = 51.8\,\text{sec}$ for $\mathcal{N}_{\text{MC}} = 10^4$ and artificial stops every $t_{\text{stop}} = 10^{-3}$ s.

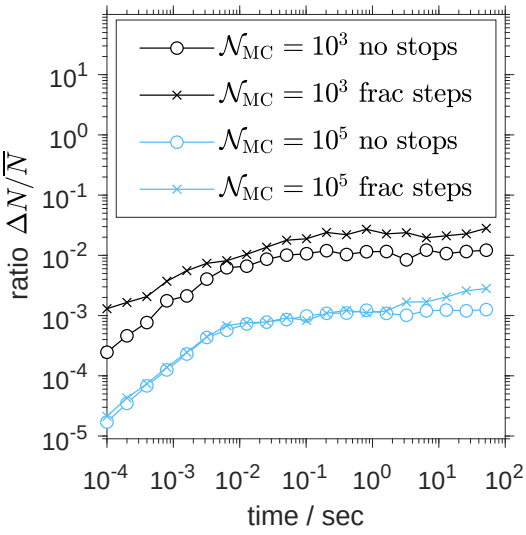

(b) Noise in number concentration for simulations with artificial stops every $t_{\text{stop}} = 10^{-5}$ s (frac step) and without artificial stops (no stop).

Figure 4.4: Simulation results of coagulation for conditions listed in section **3** in [Paper II]. $\overline{N}$ is defined in (D.3) and ΔN in (D.4).

4.2.1 Concept of Fractional MC Time Steps

The main idea of the concept of 'fractional MC time steps', is to consider the event-driven time step, $\Delta\tau_{\text{MC}}$, as a time frame during which the coagulation of the selected particle pair (i, j) would take place. If a smaller time step, $\Delta\tau_{\text{s}}$, has to be simulated, than there are only two possibilities: 1) the selected particle pair has already coagulated during $\Delta\tau_{\text{s}}$, or 2) no coagulation took place at all. This situation can be modeled with the conditional probability $P_{i,j}(\Delta\tau_{\text{s}}|\Delta\tau_{\text{MC}})$, which states the probability that the coagulation of the particles takes place within $\Delta\tau_{\text{s}}$, under the condition that the particles coagulate for sure within a larger time frame $\Delta\tau_{\text{MC}}$.

If $P_{i,j}(\Delta\tau_{\text{s}}|\Delta\tau_{\text{MC}})$ is known, a random number r can be used to decide, whether 1) the particles coagulate (if $r < P_{i,j}\,(\Delta\tau_{\text{s}}|\Delta\tau_{\text{MC}})$) or 2) no coagulation took place (if $r \geq P_{i,j}\,(\Delta\tau_{\text{s}}|\Delta\tau_{\text{MC}})$). The full algorithm is depicted in Figure **2** in [Paper II]. There, in section 2.1, the rule of Bayes is applied for the derivation of $P_{i,j}\,(\Delta\tau_{\text{s}}|\Delta\tau_{\text{MC}})$. The result is:

$$P_{i,j}(\Delta\tau_{\text{s}}|\Delta\tau_{\text{MC}}) \approx \Delta\tau_{\text{s}}/\Delta\tau_{\text{MC}}\,. \tag{4.3}$$

4.2.2 Validation of the Methodology and Stochastic Accuracy

In order to test the influence of the fractional time steps, the simulation of coagulation of a particle population was forced to stop each time the simulation time increased by an interval t_{stop}. For $t_{\text{stop}} = 10^{-3}\,\text{s}$, a total simulation time of 51.8 seconds translates to 51 800 artificial stops or necessary fractional MC steps. The PSDs resulting from such a simulation are shown in Figure 4.4a. It can be seen, that the application of fractional MC time steps marked as 'fractional steps' is able to reproduce the benchmark results gained by the discrete-sectional method [126] with grid settings as in [Paper II]. It can also be seen, that the following two approaches are not able to reproduce the simulation results:

1. **No step:** the chosen pair for coagulation is not coagulated, if the simulation time surpasses a time point for an artificial stop[5]. This corresponds to the setting $P_{i,j}(\Delta\tau_{\text{s}}|\Delta\tau_{\text{MC}}) = 0$ instead of Eq. (4.3).

[5]This approach has been applied in the context of a coupling to a CFD simulation [198], where the CFD simulation provided the external time frame.

2. **Full step:** the chosen pair for coagulation is coagulated, if the simulation time surpasses a time point for an artificial stop. This corresponds to the setting $P_{i,j}(\Delta\tau_s|\Delta\tau_{MC}) = 1$ instead of Eq. (4.3).

Increasing the number of forced stops (i.e. reducing t_{stop}) leads also to the same level of accurate reproduction of the PSDs for fractional time steps (see Figure 4 for $t_{stop} = 10^{-5}$ s), it leads, however, to deviations for other methods (see Figure 5 for the 'no step' scenario, τ_{TR} in the Paper corresponds to t_{stop}).

Hence random numbers are used to model the probability defined in Eq. (4.3), additional stochastic noise is introduced to the simulation by introduction of artificial stops. This is shown in Figure 4.4b, where a slight increase of noise levels (Eq. (D.3) and Eq. (D.4) define $\overline{N}$ and ΔN) for the simulations with artificial stops – compared to simulations without artificial stops (meaning simple simulation of coagulation with $t_{stop} = t_{end} = 51.8$ s) – can be seen. The noise levels are, however, controllable by the number of applied simulation particles, $\mathcal{N}_{MC}$. The increase is of the same magnitude as the difference between the Methods SWR and CNMC shown in Figure 4.3b.

4.3 Breakage of Weighted MC Particles

The main problem in the MC based description of particle breakage is the vast increase of particle numbers during the simulation. In a typical milling process, particles might be ground from 500 μm to 5 μm. This means that each initial particle of the size of 500 μm is replaced by ca. 10^6 particles with the sizes of around 5 μm at the end of the simulation – simply due to the conversation of mass. In order to be still able to simulate this process, early MC simulations resorted to the binning of particle sizes and counting the number of particles in each bin (or section) [220, 221, 222]. Such an approach has the main disadvantage of sectional methods, already discussed in section 2.2.2, namely the limitation to only 2-3 particle properties which can be tracked with discretization methods.

4.3.1 Constant Number Schemes for Particle Breakage

The application of weighted simulation particles allows new modeling techniques for the breakage process: the merging of the resulting fragments [216] has been suggested, this is shown in Figure 4.5: a weighted MC parent particle with the statistical weight W_P and volume v_P breaks into two equal fragments with the volumes v_F. Because both fragments are equal, they can be stored as one weighted MC particle with the statistical weight $W_F = 2 \cdot W_P$. As a consequence no novel particles have to be introduced into the simulation and the parent particle becomes the fragment.

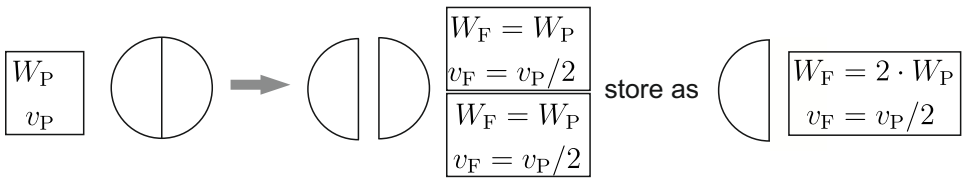

Figure 4.5: The breakage of a parent MC particle with the statistical weight W_P and volume v_P into two equal fragments (with W_F and v_F).

In the majority of realistic applications, however, the resulting fragments will have different volumes and more advanced merging strategies have to be applied for the resulting fragment distributions, one possible approach will be shown in section 4.6.1.3. Due to the computational intensity of such approaches, especially in cases where the breakage of one particle might result in e.g. 100 different fragment sizes, the stochastic determination of only one possible fragment volume has been suggested in the literature [79, 223].

4.3.1.1 Volume Based (VB) Selection Scheme

The MFA for coagulation has been extended by [223] to treat continuous breakage functions, $\gamma(v_F|v_P)$. The fragment properties, v_F, are thereby selected according to the probability density function (PDF) $f_{VB}(v_F|v_P)$ in Table 4.6, where the properties of the parent particle, v_P, are used. Once the new

Table 4.6: Definition of different methods for the selection of fragment sizes v_F after the breakage of a parent particle with the statistical weight W_P and volume v_P.

Selection method	PDF for selection of v_F	Statistical weight $W_F(v_F, v_P)$
Volume based (VB) [223]	$f_{VB} = \gamma(v_F\|v_P) \cdot v_F/v_P$	$W_P \cdot v_P/v_F$
Number based (NB) [79]	$f_{NB} = \gamma(v_F\|v_P)/B(v_P)$ (i)	$W_P \cdot B(v_P)$
General [Paper III]	$f_{Gen}(v_F\|v_P)$	$W_P \cdot \gamma(v_F\|v_P)/f_{Gen}(v_F\|v_P)$
Low volume (LV) [Paper III]	$f_{LV} = (\overline{C}\max(v_F, v_{lim}))^{-1}$ (ii)	$W_P \cdot \gamma(v_F\|v_P)\overline{C}\max(v_F, v_{lim})$

(i) The function $B(v_P)$ is defined in Eq. (4.4).
(ii) The constant 'cut-off volume' v_{lim} is needed for the normalization of f_{LV}. It is used in the following: $v_{lim} = 10^{-11} v_0$ (with the initial volume v_0). The constant $\overline{C}$ - written as $C(v_P)$ in [Paper III] - is defined in Eq. (**14**).

fragment volume v_F is estimated, the statistical weight, W_F, of the fragment is calculated using the statistical weight of the parent W_P, like listed for VB in Table 4.6. It can be seen that the volume-concentration rendered by one MC particle is conversed during breakage for this scheme, i.e. $v_P \cdot W_P = v_F \cdot W_F$.

4.3.1.2 Number Based (NB) Selection Scheme

The formalism of the MFA was extended by [79], the authors introduced a whole class of breakage schemes based on fragmentation weight transfer functions (FWTF) - one of these schemes is listed as NB in Table 4.6. The term $B(v_P)$ describes the number of all fragments[6] resulting from the breakage of one parent particle with the volume v_P:

$$B(v_P) = \int_0^{v_P} \gamma(v_F|v_P) \mathrm{d}v_F \,. \tag{4.4}$$

The NB scheme does not conserve the mass of the single particle during breakage (i.e. $v_P \cdot W_P \neq v_F \cdot W_F$), but it ascribes the correct increase $B(v_P)$ of the number concentration for each single breakage event – independently on the selected fragment volume v_F.

4.3.1.3 General Formulation for Selection Schemes

Both mentioned schemes VB and NB are not able to reproduce the smallest fractions of fragmented particles for continuous breakage functions – as shown in section 4.3.3. In order to be able to sketch even the smallest fragments resulting from breakage a novel approach has been introduced in [Paper III].

This approach is based on the consideration that the fragment properties, v_F, can be chosen independently of the breakage function, $\gamma(v_F|v_P)$, purely based on any possible PDF, $f_{Gen}(v_F|v_P)$[7] – as long as the statistical weights of the resulting fragments, W_F, are corrected accordingly. If a large number $\mathcal{N}_{mc}^{break}$ (e.g. 100) MC particles with identical volumes v_P and weights W_P and a total number concentration of $W_P^{tot} = W_P \cdot \mathcal{N}_{mc}^{break}$ would break, the resulting fragment volumes would be distributed – in the statistical mean – like the PSD n_{res}:

$$n_{res}(v_F) = \mathcal{N}_{mc}^{break} \cdot f_{Gen}(v_F|v_P) \cdot W_F(v_F|v_P) \,, \tag{4.5}$$

where $W_F(v_F|v_P)$ is a function describing which statistical weight needs to be set, depending on the selected fragment volume, v_F. The exact PSD n_{exact} of fragments is given by $\gamma(v_F|v_P)$, it is :

$$n_{exact}(v_F) = W_P^{tot} \cdot \gamma(v_F|v_P) \,. \tag{4.6}$$

[6] One can reinterpret the formalism which was introduced by [79] for binary breakage only ($B(v_P) = 2$), easily for a broader class of problems (i.e. $B(v_P) > 2$), as it is done here.

[7] The function $f_{Gen}(v_F|v_P)$ describes for each possible parent volume v_P a PDF for the selection of v_F, the only three constraints on the function are: 1.) $\int_0^{v_P} f_{Gen}(v_F|v_P) = 1$, 2.) $f_{Gen}(v_F|v_P) \geq 0$, and 3.) $f_{Gen}(v_F|v_P) > 0$ if $\gamma(v_F|v_P) > 0$.

Setting now Eq. (4.5) equal to Eq. (4.6) leads to an expression for $W_F(v_F|v_P)$ for any possible PDF $f_{Gen}(v_F|v_P)$ - this result is written as general formulation in Table 4.6. This selection method encompasses much more possible schemes as the suggested FWTF methodology by [79], as it is discussed in **Appendix A** of [Paper III]. The proposed low volume selection (LV) in Table 4.6 and the combined schemes further below can not be formulated with the FWTF formalism.

4.3.1.4 Low Volume (LV) Selection Scheme and Combination of Schemes

In order to capture the smallest fragments resulting from breakage, the PDF f_{LV} can be set proportional to $(v_F)^{-1}$ - at least for the interesting particle sizes, hence a 'cut-off' value v_{lim} is needed for the PDF normalization condition. This does not mean, that sizes $v_F < v_{lim}$ are excluded from consideration, but are selected independent on their size instead of proportionally to $(v_F)^{-1}$. It will be shown in the results section 4.3.3 that this approach is able to reproduce a much more detailed PSD at the beginning stages of the simulation, than the VB and NB methods.

4.3.1.5 Combination of Schemes NB-LV and VB-LV

The LV method, however, is not able to reproduce the correct results for longer simulation times (as shown in section 4.3.3). For this reason, the combination of schemes has been introduced in [Paper III], it is based on the idea that two different PDFs f_{VB} (resp. f_{NB}) and f_{LV} can be simply combined to a new PDF f_{VB-LV} (resp. f_{NB-LV}) with the help of a constant Υ:

$$\begin{aligned} & f_{VB-LV}(v_F|v_P) = \Upsilon \cdot f_{VB} + (1-\Upsilon)\cdot f_{LV}, \\ \text{resp.:}\quad & f_{NB-LV}(v_F|v_P) = \Upsilon \cdot f_{NB} + (1-\Upsilon)\cdot f_{LV}, \qquad \text{with: } 0<\Upsilon<1\,. \end{aligned} \tag{4.7}$$

The statistical weights W_F can be calculated for the selected fragment volume v_F using the general rule in Table 4.6:

$$\begin{aligned} & W_F(v_F, v_P) = W_P \cdot \gamma(v_F|v_P)/f_{VB-LV}(v_F|v_P) \\ \text{resp.:}\quad & W_F(v_F, v_P) = W_P \cdot \gamma(v_F|v_P)/f_{NB-LV}(v_F|v_P)\,. \end{aligned} \tag{4.8}$$

It will be shown in the results section 4.3.3, that such a modeling is indeed able to reproduce the whole PSD also for longer simulation times, but first a parallel implementation of these methodologies will be briefly sketched.

4.3.2 Time-Driven GPU-Implementation

In contrast to the coagulation of particles, time-driven algorithms are a suitable choice for the simulation of (pure) particle breakage. This is because all breakage events can be considered to happen independently from each other. Figure 4.6 shows an exemplary parallel algorithm, performing the following steps:

1. The maximal breakage rate is calculated using a parallel comparison algorithm, similar to the parallel sum algorithm discussed in Figure 3.3. For the calculation of the time step, $\Delta\tau_{MC}$, the tuning factor, α_T, is used. It is set to a value of 0.1 for the simulations shown in the following section.

2. For the decision, whether a particle breaks within $\Delta\tau_{MC}$, Eq. (2.20) is implemented, where the coagulation rates $\beta_{i,j}$ are replaced by the breakage rates of single particles, $b(v_i)$.

3. If the particle is selected for breakage, then

   (a) its new volume is selected according to the PDF $f_{Gen}(v_F, v_P)$. A simple AR algorithm[8] is used for this purpose marked as 'AR $v_{F,..}$ selection' in Figure 4.6.

   (b) The newly generated fragment volume v_F is used for the calculation of the new statistical weight of the particle, W_F, according to the formula in Table 4.6, resp in Eq. (4.8).

[8] The shown algorithm works very well for NB and VB schemes. However, the implementation of the LV scheme (or combinations of it) in this simple AR-scheme leads to extremely large computing times. The reason for this and the generation of non-uniformly distributed random numbers as a remedy are discussed in section **3.2.2** in [Paper III].

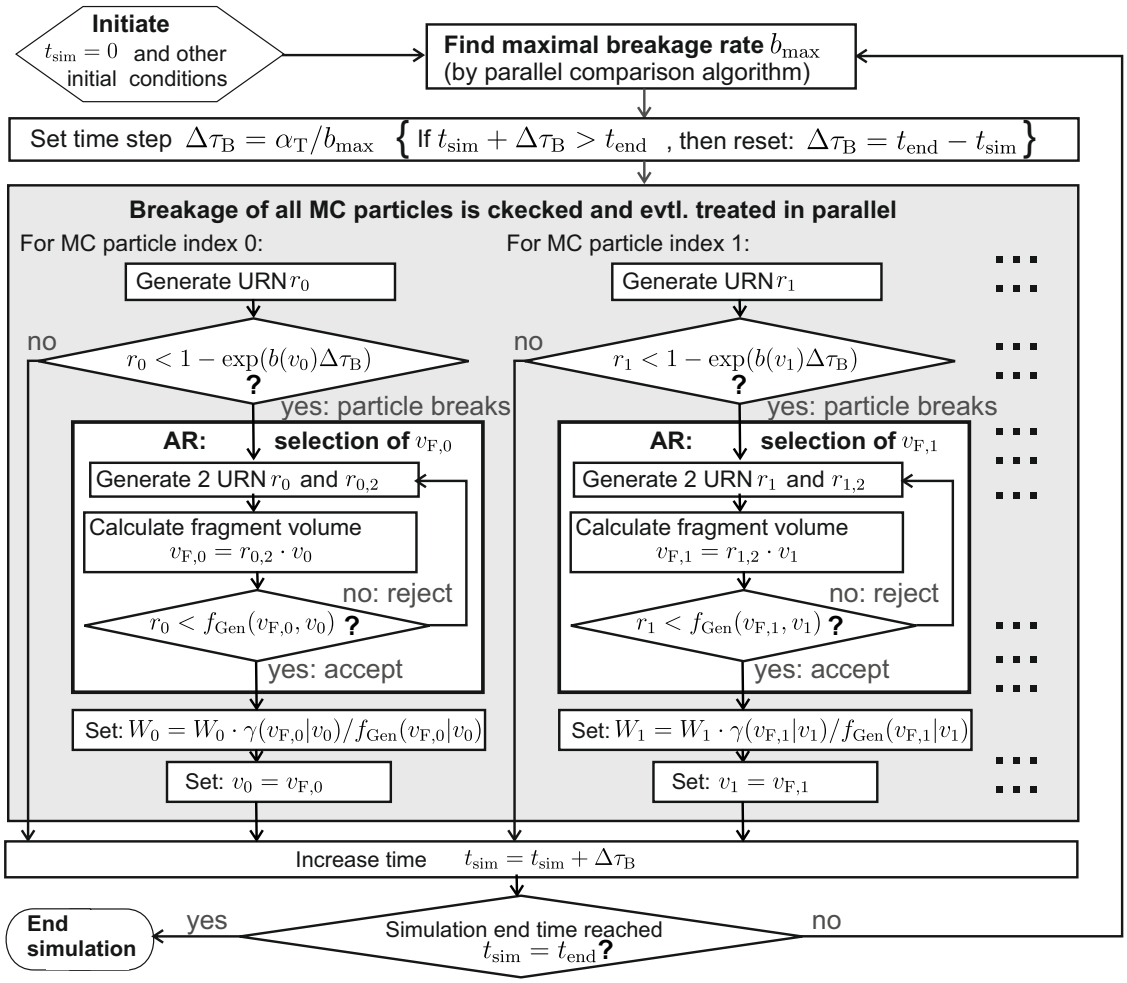

Figure 4.6: Parallel algorithm for MC simulation of particle breakage as described in [Paper III]. Uniformly distributed random numbers (URN) $\in (0, 1)$ are used.

4.3.3 Validation

It can be seen in Figure 4.7 that the LV scheme is able to render the full particle size spectrum at the beginning of the simulation, for longer simulation times, however the PSDs start to deviate from the analytic solutions. The introduced combination schemes, however, are able to reproduce the PSDs correctly, even for longer simulation times. It can also be seen, that the VB combinations are more accurate than the NB schemes. Higher fractions Υ of the VB (respectively NB) in the combination with the LV lead to a higher precision at the cost of less MC particles rendering smaller particle sizes. It could be shown recently that the errors are correlated to inaccuracies of the total volume concentration of the MC particles [CoPaper I] – the volume loss of the system could thus be used to devise an adaptive algorithm which adjusts the value for Υ automatically.

4.4 Merging of Weighted MC Particles

Both, the simulation of nucleation and of particulate transport lead to a situation, where novel particles have to be inserted into the simulation, on the one hand. On the other hand, only a finite number of MC particles can be stored in the memory. This problem is mostly solved by the removal of randomly selected particles – based on constant number schemes [180, 189, 188]. The simulation volume (resp. the statistical weights of all particles) is thereby adjusted in such a way, that the total mass (resp. volume) concentration of the MC particle population does not change due to the removal. In some cases, the subsequent removal of randomly selected particles increases the noise levels to such high values, that the produced results become unreliable - as it is shown for the nucleation in section 4.5 and

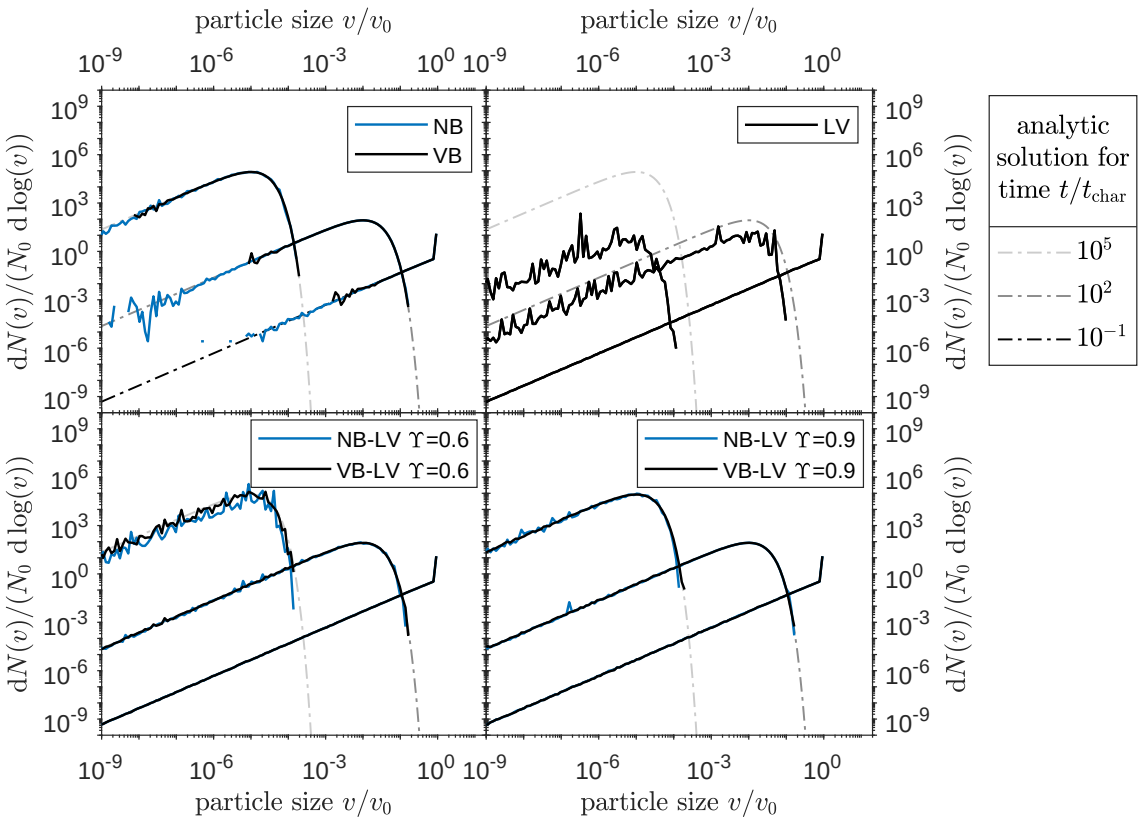

Figure 4.7: PSDs resulting from simulation conditions described as 'Case 1' (γ_B and b_l) in [Paper III], section **4**. The analytic solution from [47] is listed in Table **2**.

the transport in section 4.6. But first, an alternative to the random removal, the merging techniques, will be introduced in section 4.4.1.

The idea of merging has been introduced by [216] for particles with equal properties and is sketched in Figure 4.5: both resulting breakage fragments can be stored as one weighted MC particle, simply by adjusting its statistical weight – something, which is not possible for equally weighted MC particles. However, no guidance is given by [216] on:

1. How to find MC particles with equal (or almost equal) properties? In the simulated scenario [216], the breakage of one parent particle resulted in many identical fragments.

2. What to do, if no such equal particles can be found at all? Or, how to save two different particles as one. Or, how to merge them?

While the second problem 'how to merge particles?' is solved easily with the merging scheme described in section 4.4.1 further below, two merging algorithms will be introduced in sections 4.5 and 4.6 which address the fist problem 'how to find suitable particles for merging'.

4.4.1 Merging Scheme

A weighted addition is introduced in [Paper I] for the merging of the particles i (with weight W_i and several properties $p_i^{(k)}, k = 1, 2, \dots$) and j (with weight W_j and several properties $p_j^{(k)}$) into a new particle, with the following statistical weight W_new and properties $p_\mathrm{new}^{(k)}$ [9]:

$$W_\mathrm{new} = W_i + W_j, \quad \text{and} \quad p_\mathrm{new}^{(k)} = (W_i p_i^{(k)} + W_j p_j^{(k)})/(W_i + W_j), \quad \text{for all } k\,. \tag{4.9}$$

[9] This formula is applicable for properties which are simply added upon coagulation, like volumes or electrical charge. If the properties are not simply added (as for example the diameter), the rule of coagulation should give a good hint, on how to model the novel properties.

A merging error $E_{\mathrm{m}}(i,j)$ is introduced in [Paper I] in order to measure the deviation of particles i and j from each other: is introduced:

$$E_{\mathrm{m}}(i,j) = \sum_{\text{all properties } k} \omega_k \cdot \left[\left(p_i^{(k)} - p_j^{(k)} \right) / \min\left(p_i^{(k)}, p_j^{(k)} \right) \right]^2 . \tag{4.10}$$

The merging weights ω_i are constant values and express the relative severity of deviations of a property k_1 (i.e. $p_i^{(k_1)} - p_j^{(k_1)}$) compared to another property k_2 (i.e. $p_i^{(k_2)} - p_j^{(k_2)}$) . This formulation is rather arbitrary and should not be interpreted as a result of a rigorous mathematical derivation. There is especially no guarantee, that the merging of two different particle pairs with the same error E_{m} will have the same negative impact on the simulation. On the other hand, the specific tuning of the merging weights α_i as well as a good choice for E_{m} (hence a lot of alternatives to Eq. (4.10) are imaginable) might prove crucial for a correct and efficient merging algorithm[10]. Both points are also discussed in [Paper I].

4.5 Simulation of Nucleation

The combined simulation of coagulation and nucleation can be performed using a simple operator splitting technique resulting in the following two steps:

1. A parallel MC coagulation step is performed using the algorithm described in section 3.2 in combination with the SR-based coagulation rates defined in Table 4.4. The algorithm also provides a time step $\Delta\tau_{\mathrm{MC}}$, as defined in Eq. (3.1).

2. If a constant nucleation rate, J_{C} is used – the total concentration of newly nucleated particles within $\Delta\tau_{\mathrm{MC}}$ can be simply calculated to: $W_{\mathrm{nuc}} = J_{\mathrm{C}} \cdot \Delta\tau_{\mathrm{MC}}$, whereas the volume or diameter of the nucleating particles are assumed to be constant in this test case (and as presented in [Paper I]). The treatment of varying nucleation parameters as well as non-constant nucleation rates is discussed in section 4.7.3, in [Paper IV], [Paper V], [Paper VI] and [Paper VII].

It suffices to insert only one MC particle after each time step $\Delta\tau_{\mathrm{MC}}$ in order to simulate the nucleation[11] – so that the merging of two MC particles creates enough space for the insertion of the novel particle, i.e. only one suitable pair for merging has to be found.

For the simulation of transport, in contrast, the merging of a whole particle population might be necessary, as will be elaborated in section 4.6 in more detail.

4.5.1 Low Weight Merging Algorithm for Nucleation

The search of the pair (i,j), with the minimum merging error, $\min_{(i,j)}(E_{\mathrm{m}}(i,j))$ is simply too costly, because a huge number of comparison $((\mathcal{N}^{\,2}{}_{\mathrm{MC}} - \mathcal{N}_{\mathrm{MC}})/2)$ is necessary for this purpose – even if a parallel GPU algorithm is applied (this is discussed in the supplementary material of [Paper I] in more detail). This huge number of necessary comparisons can be reduced dramatically, if a particle k is chosen and then the minimal merging error is searched between all possible pairs with k, i.e.: $\min_{(i)}(E_{\mathrm{m}}(i,\ k))$ – this makes only $\mathcal{N}_{\mathrm{MC}} - 1$ comparisons necessary, and is shown in an exemplary implementation in Figure 4.8. The merging of a particle with itself is, of course, excluded from consideration by setting simply $E_{\mathrm{m}}(k,k) = \infty$.

The particle k could be selected completely by random – resulting in the random merging (RM) algorithm (which is not published in the papers). Or it could be selected as a MC particle with an especially low weight, leading to the low weight merging (LWM) algorithm as published in [Paper I] – the idea is to produce a list consisting of 100 MC particles with low statistical weights (i.e. whose weights are smaller than $\overline{W}/10$, where $\overline{W}$ is the mean statistical weight of all MC particles within one simulation[12], if less than 100 such particles are found, particles are selected by random). Each step, one MC particle of the list is selected as particle k for the merging and after 100 merge steps a new

[10] The shown simulation results use only one particle property, the volume v, α_1 can thus be set to any arbitrary constant value, $\alpha_1 = 1$ has been used explicitly.

[11] Extremely high nucleation rates might make smaller time steps necessary and extreme low nucleation rates might make larger time steps more computationally effective. An adjustment of the optimal time step for nucleation is strongly connected – and better expressed – by the definition of a nucleation threshold $\mathcal{V}_{\mathrm{T}}$ as it will be discussed in section 4.7.3.

[12] The explicit definition is $\overline{W} = \sum_{i=1}^{\mathcal{N}_{\mathrm{MC}}} W_i / \mathcal{N}_{\mathrm{MC}}$.

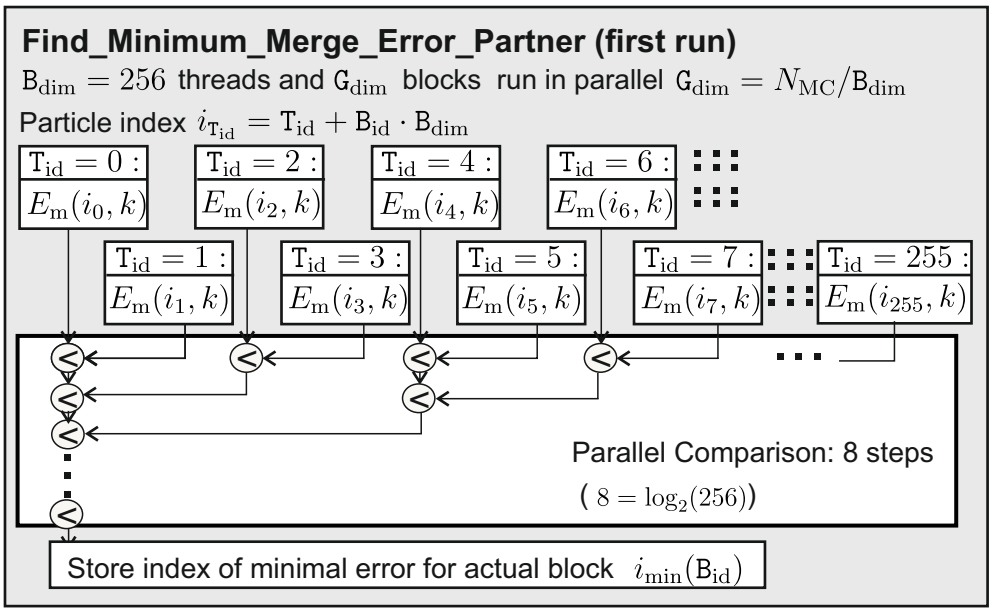

Figure 4.8: The algorithm stores the indices with the minimal merging error for each block $i_{\min}(\mathtt{B}_{\mathrm{id}})$. In a second run, these indices are used instead of the particle index, $i_{\mathtt{T}_{\mathrm{id}}}$. A third run is necessary if the used number of MC particles is larger than $256^2 = 65\,536$.

merge list is created. Hence the statistical weights of the merged particles are relatively small, the changes of the PSD due to merging are also to be expected to be small.

4.5.2 Validation

The same demanding test case as presented in [Paper I] has been chosen to demonstrate the validity of the proposed algorithm, by comparison with a solution resulting from the discrete-sectional method. The test case describes the coagulation in the free-molecule regime (β_{fm} in Table 2.1a) and a constant rate nucleation $J_{\mathrm{C}} = 10^{17}\,\mathrm{m}^{-3}\mathrm{s}^{-1}$, the explicit settings are the same as listed in Table **1** of [Paper I]. Figure 4.9 shows comparisons of results from the RM, the LWM and the random removal (RR) algorithm, as mentioned further above (the detailed implementation for weighted particles is described in [Paper I]). As already described in [Paper I], the LWM is able to reproduce the PSD even for these extreme simulation conditions, while the RR algorithm fails to reproduce the results accurately – this can be attributed to the higher noise levels which are connected to the random removal of the particles. Surprisingly, the RM algorithm also produces higher noise levels and is also not able to reproduce the PSD correctly. These errors can not be attributed to the merging (even smaller merging errors $E_{\mathrm{m}}(i,j)$ are found in total for the RM than for the LWM). It is rather probable, that the vast differences in the statistical weights of the MC particles due to the prolonged application of the RM (compared to the application of the LWM), lead to a situation, where the approximations of $\Delta\tau_{\mathrm{MC}}$ and R_{max} of the fast coagulation algorithm (section 3.2) cannot be assumed to be accurate enough.[13] This question could be further elucidated by the combined simulation of nucleation and coagulation, where the coagulation is treated by a method, like the smart book-keeping technique [179] or the majorant kernel technique [184, 185], where no approximations are made on $\Delta\tau_{\mathrm{MC}}$ and R_{max}, but such an investigation is out of the scope of this thesis.

The introduced LWM has been used in combination with non-constant nucleation rates for particle synthesis (resp. formation), as it is discussed in section 4.7.3 and in [Paper IV], [Paper V], [Paper VI] and [Paper VII]. The applicability of this approach has also been demonstrated in the scope of a dual PBE system describing the particle synthesis via flame spray pyrolysis [CoPaper II].

[13] Although the application of very high values of $\chi = 50\,000$ does not lead to an improvement of the shown results, it cannot be ruled out, that even higher values, e.g. $\chi = 1\,000\,000$, would lead to better agreement – such a simulation, on the other hand is computationally very costly. The simulation for $\chi = 50\,000$ required several days, it is expected that $\chi = 1\,000\,000$ would require 20 times that much.

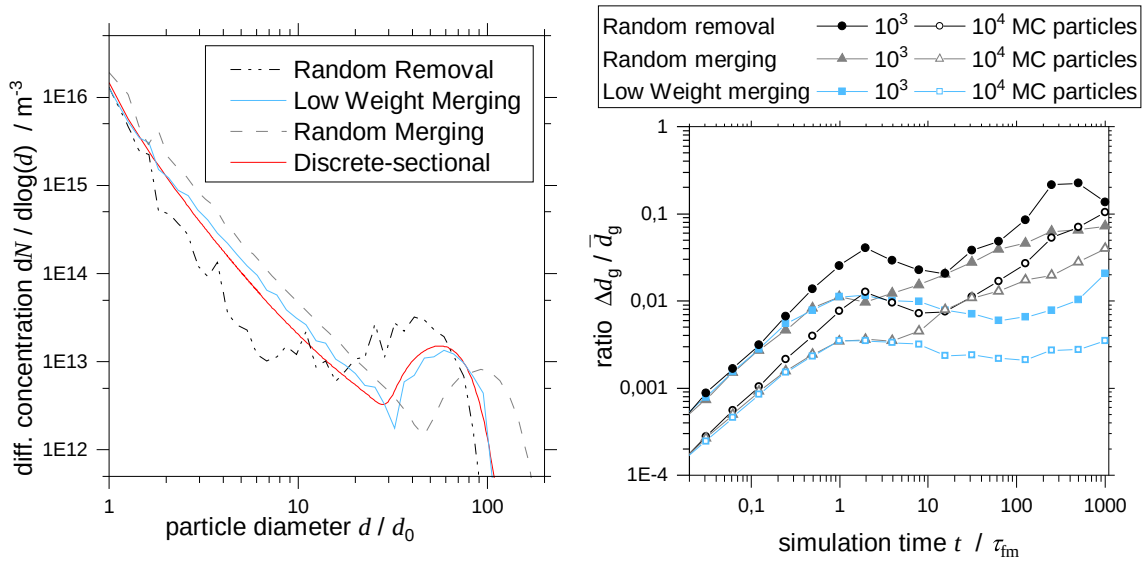

(a) PSDs for $t = 500\,\tau_{\mathrm{fm}}$ and 10^4 MC particles. **(b)** Stochastic noise in geometric mean diameter.

Figure 4.9: Results of combined simulation of coagulation in the free-molecule regime (β_{fm} in Table 2.1a) and a constant rate nucleation $J_{\mathrm{C}} = 10^{17}\ \mathrm{m^{-3}s^{-1}}$, the explicit settings are the same as listed in Table **1** of [Paper I] The characteristic time for coagulation $\Delta\tau_{\mathrm{fm}}$ is defined in (A.10), d_{g} and Δd_{g} are defined in Eq. (D.3) and (D.4).

4.6 Simulation of Transport

As an introduction to the problematic, the transport between two units, U_1 and U_2 is considered. Such a basic problem may be extended to more relevant applications, for example, the nucleation of particles and their subsequent growth due to condensation and coagulation in unit U_1 (the particles are modeled with a PSD n_{U_1}), and the collection of the produced particles with a filter or due to sedimentation in unit U_2 (the particles are modeled with a PSD n_{U_2}) .

If a simple linear flow rate $f_{U_1\to U_2}$ can be assumed, then the change of the PSDs due to transport is modeled as:

$$\frac{\mathrm{d}n_{U_1}}{\mathrm{d}t} = -f_{U_1\to U_2}\cdot n_{U_1}\,, \qquad \frac{\mathrm{d}n_{U_2}}{\mathrm{d}t} = +f_{U_1\to U_2}\cdot n_{U_1}\,. \tag{4.11}$$

4.6.1 Modeling of Transport with Weighted MC Particles

In the scope of a MC simulation, the PSDs are represented by MC particles. The corresponding number concentration of particles which is represented of each particle i in unit U_1 is given by the statistical weights W_{i,U_1}, so that the first part of Eq. (4.11) can be rewritten directly to represent the depletion of the statistical weight of particles in unit U_1:

$$\frac{\mathrm{d}W_{i,U_1}}{\mathrm{d}t} = -f_{U_1\to U_2}\cdot W_{i,U_1}\,. \tag{4.12}$$

The second part of Eq. (4.11) describing the inflow of novel particles into unit U_2, can be modeled by inclusion of novel particles with statistical weights W^{new}_{i,U_2} and with exactly the same volumes as the particles in unit U_1, i.e.:

$$\frac{\mathrm{d}W^{\mathrm{new}}_{i,U_2}}{\mathrm{d}t} = +f_{U_1\to U_2}\cdot W_{i,U_1}\,, \qquad v^{\mathrm{new}}_{i,U_2} = v_{i,U_1}\,. \tag{4.13}$$

The function $f_{U_1\to U_2}$ may be thereby dependent in time, or dependent on the specific properties of the particle i in unit U_1. If $f_{U_1\to U_2}$ has a constant value, one would obtain the solutions for a time $\Delta\tau_{\mathrm{Tr}}$:

$$W_{i,U_1}(\Delta\tau_{\mathrm{Tr}}) = W_{i,U_1}(0)\cdot\exp(-\Delta\tau_{\mathrm{Tr}}\cdot f_{U_1\to U_2}) \quad\text{and}\quad W^{\mathrm{new}}_{i,U_2}(\Delta\tau_{\mathrm{Tr}}) = W_{i,U_1}(0) - W_{i,U_1}(\Delta\tau_{\mathrm{Tr}})\,. \tag{4.14}$$

Alternatively Eq. (4.12) and (4.13), can be approximated for very small time steps $\Delta\tau_{\mathrm{Tr}}$ with the Euler formalism to:

$$W_{i,U_1}(\Delta\tau_{\mathrm{Tr}}) \approx W_{i,U_1}(0) - \Delta W_{i,U_1}\,, \qquad W^{\mathrm{new}}_{i,U_2}(\Delta\tau_{\mathrm{Tr}}) \approx +\Delta W_{i,U_1}\,, \tag{4.15}$$
$$\text{with:} \quad \Delta W_{i,U_1} = W_{i,U_1}(0)\cdot\Delta\tau_{\mathrm{Tr}}\cdot f_{U_1\to U_2}\,.$$

Independent on whether an exact solution (Eq. (4.14)) is available or an approximation (Eq. (4.15)) is used, changes to the MC particle population in unit 1 and unit 2 have to be performed. These changes encompass 1) the particle outflow from unit 1 and 2) the particle inflow into unit 2. In the following two methods to model the outflow (a deterministic and a stochastic one will be introduced) and two methods for the particle inflow (the merging and the random removal) are presented.

4.6.1.1 Deterministic Particle Outflow

The application of weighted particles offers the opportunity to adjust the statistical weights accordingly to the exact value W_{i,U_1} in unit 1 as provided by Eq. (4.14) (resp. (4.15)) and to create a particle population with the exact weights W^{new}_{i,U_2} for insertion into unit 2. However, a MC particle population might be already stored in unit 2 (e.g. 10 000 MC particles), so that the novel MC particles (e.g. 10 000 MC particles) have to be merged with the existing population, or the random removal of particles has to be implemented. It should be noted that the necessary adjustment of the statistical weights can be very efficiently done by a parallel algorithm.

4.6.1.2 Stochastic Particle Outflow

One can also translate the values given by Eq. (4.14) (or resp. (4.15)) as probabilities $P_{U_1\to U_2}(i)$ for a particle i of being transported from unit 1 to unit 2:

$$P_{U_1\to U_2}(i) = W^{\mathrm{new}}_{i,U_2}(\Delta\tau_{\mathrm{Tr}}) \,/\, W_{i,U_1}(0)\,. \tag{4.16}$$

For each particle i a URN $r_i \in (0,1]$ is used to determine whether the particle is removed from unit 1 and inserted into unit 2 (if $r_i < P_{U_1\to U_2}(i)$). As for the deterministic outflow, unit 2 might already store a particle population (e.g. 10 000 MC particles), but this time a smaller fraction (depending on $P_{U_1\to U_2}(i)$ and thus on $\Delta\tau_{\mathrm{Tr}}$, e.g. 100 MC particles) has to be merged with the existing population. It should be also noted that the empty places in unit 1 after the removal can be advantageous, if some novel particles (from another unit) have to be inserted into unit 1. They can be easily filled if weighted particles are used, simply by copying randomly selected particles and halving the corresponding statistical weights.[14]

4.6.1.3 Merging Algorithm for Particle Inflow

Independent on whether the particles have been selected by methods described as a deterministic outflow or a stochastic outflow, large particle populations (e.g. 10 000, resp. 100 MC particles) have to be inserted into unit 2, where already a large particle population (e.g. 10 000 MC particles) is stored.

The basic idea of the parallel merging algorithm is to define (arbitrarily) a m aximal allowable merging error, $\varepsilon_{\mathrm{merge}}$ (e.g. $\varepsilon_{\mathrm{merge}} = 10^{-4}$) and to merge all possible particle pairs i, j with $E_{\mathrm{m}}(i,j) < \varepsilon_{\mathrm{merge}}$. The application of a GPU enables to perform the necessary calculation, check $E_{\mathrm{m}}(i,j) < \varepsilon_{\mathrm{merge}}$ and possible subsequent merging (described by Eq.(4.9), in section 4.4.1) for a huge number of particle pairs in parallel. Figures **10**, **11** and **12** in [Paper V] depict the GPU implementation in more detail. This algorithm is forced to terminate by increment of the allowable merge error as the simulation progresses – this idea is also introduced in [Paper V] and [Paper VIII].

4.6.1.4 Random Removal for Particle Inflow

The constant number method [180] is applied. Thereby, the total volume concentration of all particles is preserved, i.e. a correction is applied to the statistical weights of all particles after the removal,

[14] If equally weighted MC particles are used, particles for copy can be selected by random and the simulation volume can be adjusted as in the random removal approach. This might lead, however, to the situation that particles in different units have different statistical weight.

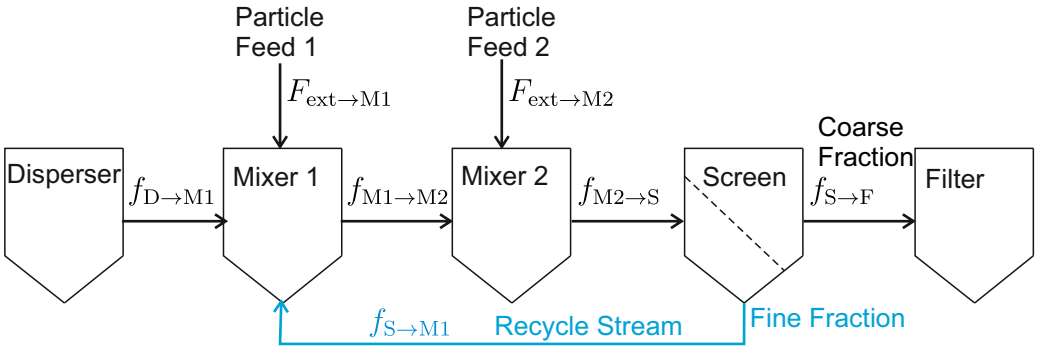

Figure 4.10: Exemplary flowsheet of the test case for validation. The explicit values for the flow rates $f_{A\to B}$ and the separation function for the screen unit are defined in [Paper VIII] .

so that the total volume concentration represented by the resulting MC particles is equal to the one prior to the removal. This approach leads to the correct description of the coagulation, whereas the conversation of the number concentration of all MC particles leads to wrong simulation results [180]. If applied in the here presented transport framework, no significant difference between a correction based on the volume concentration and a correction based on the number concentration could be seen[15]. The results for which the volume concentration is preserved during the removal is shown in the following.

In combination with the deterministic outflow (10 000 new MC particles have to be added to already existing 10 000 MC particles in the unit), a massively parallel implementation has been devised, deciding in parallel for each particle i whether to keep an existing particle in place or to replace it with a new particle. The probability for insertion of a new particle can be set to

1. 50% (MC particle number based), or
2. $W^{\text{new}}_{i,U_2}(\Delta\tau_{\text{Tr}})/(W^{\text{new}}_{i,U_2}(\Delta\tau_{\text{Tr}}) + W_{i,U_2})$ (number concentration based), or
3. $W^{\text{new}}_{i,U_2}(\Delta\tau_{\text{Tr}}) \cdot v^{\text{new}}_{i,U_2}/(W^{\text{new}}_{i,U_2}(\Delta\tau_{\text{Tr}}) \cdot v^{\text{new}}_{i,U_2} + W_{i,U_2} \cdot \cdot v_{i,U_2})$ (volume concentration based).

Hence no decisive difference has been seen between any of these three approaches, the results for the conventional first (MC particle number based) formulation are shown in the following - as in [Paper V] and [Paper VIII].

In combination with the stochastic outflow a much smaller number of novel particles has to be inserted into unit 2 (e.g. 100) - if particles were removed from unit 2 due to outflow to other units, than these places can be easily filled with a copy operation. The same parallel code as for the deterministic outflow is used on the remaining particles, but with a difference that a random offset index r_{off} (with $0 < r_{\text{off}} < \mathcal{N}_{\text{MC}} - 1$) is generated at each inflow step and the i-th novel particle particle is compared with the particle in unit 1 with the index $i + r_{\text{off}}$ (if this value equals or is larger than $\mathcal{N}_{\text{MC}}$, than $i + r_{\text{off}} - \mathcal{N}_{\text{MC}}$ is used for comparison). As for the combination with the deterministic outflow, no substantive differences between the three possible formulations for the removal probabilities have been found and the results for the first formulation (MC particle number based) are shown.

4.6.2 Validation

The proposed algorithms are validated by simulation of the exemplary flowsheet system depicted in Figure 4.10. It models the mixing of three different particle populations, which are distributed according to a log normal distribution (with the mean geometric diameters being 50 nm (disperser), 10 nm (feed to mixer 1) and 3 nm (feed to mixer 2)), the explicit flow rates and other simulation settings are defined in [Paper VIII]. The sieve unit is thereby separating the particles according to the function defined in Eq. (VIII.5), so that the flow rates are explicitly dependent on the particle size.

The results of the 4 possible combinations (2 outflow methods combined with 2 inflow methods) are shown in comparison with the results from the pivot point method in Figure 4.11. The PSDs

[15] Another possible approach would be to take the dynamics of the sieve unit – somehow – into account by approximating the correction with the separator function $S_{\text{sep}}(v_i)$, (Eq. (VIII.5)).

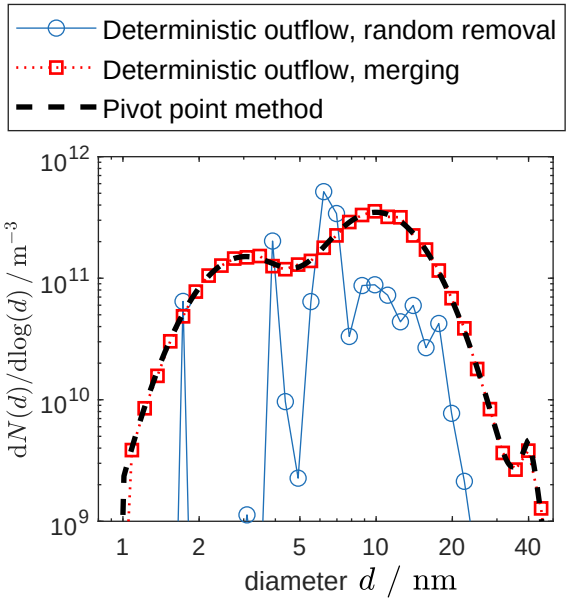

(a) PSDs after 28 s.

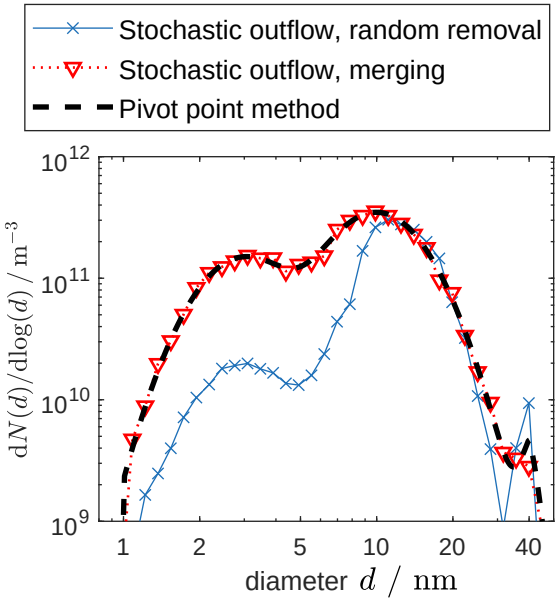

(b) PSDs after 28 s.

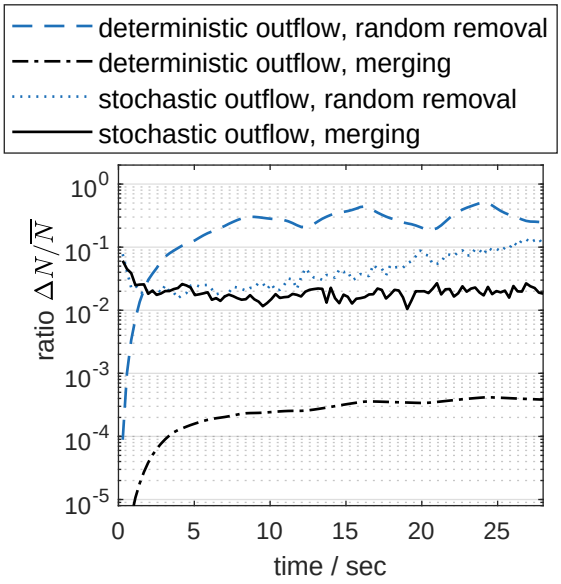

(c) Stochastic noise in number concentration.

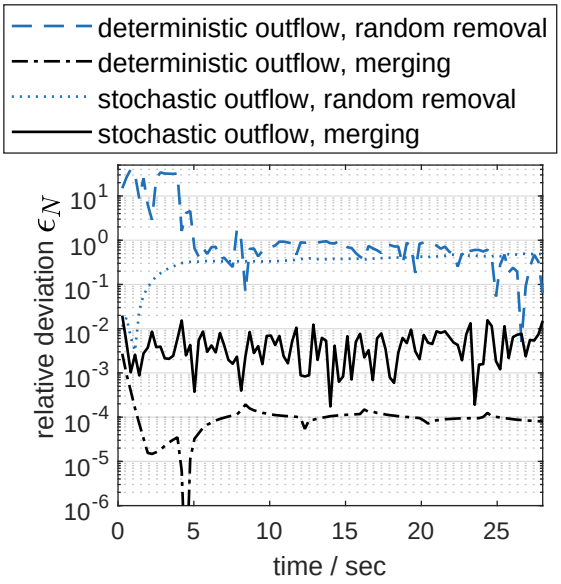

(d) Relative accuracy in number concentration.

Figure 4.11: Simulation results for the Mixer 2 unit shown in Figure 4.10 for flow rates defined in [Paper VIII] with 32 720 MC particles and $\Delta\tau_{Tr} = 0.001$. ϵ_N is defined in Eq. (D.10), $\overline{N}$ in (D.3) and ΔN in (D.4).

indicate that both, the deterministic outflow (Figure 4.11a) as well as the stochastic outflow (Figure 4.11b) have to be combined with the merging routines in order to produce correct simulation results, whereas the random merging leads to a wrong description. The deterministic transport in combination with the merging method is a deterministic algorithm, producing the same results for identical initial conditions – in the scope of numerical accuracy. However, if the memory places on which the particles are stored are changed by a permutation, different particle pairs are considered for merging and different particles are merged in comparison to the not permutated PSD. These differences can be considered as intrinsic stochastic noise and are measured by choosing a different permutation of MC particles for each simulation. The results are put into comparison with the internal stochastic noise produced by the application of random numbers by the other methods in Figure 4.11c. It can be seen, that the deterministic outflow combined with the merging produces far less statistical noise than the stochastic outflow due to the application of random numbers. This in turn, leads to a better approximation of the result from the pivot point method, as shown in Figure 4.11d.

Similar results (but for a different number of MC particles) are shown in [Paper VIII] for the deterministic outflow methods in the dependency of the setting $\Delta\,\tau_{\mathrm{Tr}}$. It is shown how the accuracy of the simulation can be increased – at the cost of increasing computing times – by lower $\Delta\tau_{\mathrm{Tr}}$ settings (in the frame-work of an Euler approximation of the flow equations - similar to Eq. (4.15)). The fine tuning of parameters for the parallel merging algorithm are discussed in [Paper V] (in section **3.2.2**). Although it is very probable, that the shown accuracy in Figure 4.11c and 4.11d is dependent on the choice of $\epsilon_{\mathrm{merge}}$ and the rules for its increment, a quantitative study of the impact of this and the other parameters mentioned in section **3.2.2** has not been presented to date. An important finding of [PaperV] is the identification of a minimal flowsheet system for which the random removal method is no longer applicable. It is found that the simplest flowsheet comprising of one recycle stream or one sieve unit are still described well with the combination of deterministic outflow and random removal – but the combination of a recycle stream and a sieve unit leads to severe deviations from the benchmark solution.

4.7 Growth and Evaporation of Weighted MC Particles

Coagulation, evaporation and growth are processes typically encountered during the production or processing of (nano) particles. The evaporation of particles smaller than the critical (Kelvin) diameter and the growth of particles which are larger than the Kelvin diameter is termed Ostwald-ripening and used to describe the formation of nanocrystals (resp. particles) in liquids [36, 224], the degradation of emulsions [225] or two-phase systems describing alloys [226]. It can also be used to model aerosol particle formation processes, as it is done in the following.

First (section 4.7.1) a parallel simulation scheme for evaporation and growth of MC simulation particles will be introduced, then (section 4.7.2) the coupling of this scheme with the already introduced simulation techniques for coagulation will be presented. And finally (section 4.7.3), this coupling will be combined with the nucleation and merging of MC particles.

4.7.1 Parallel Algorithm for Growth and Evaporation

The growth (resp. evaporation) rate G of particles with volume v describes the exact change of volume for each MC particle (Eq. (2.7) is formulated for each MC particle i):

$$\frac{\mathrm{d}v_i}{\mathrm{d}t} = G(v_i, N_{\mathrm{G}})\,. \tag{4.17}$$

A computational challenge is the coupling given by the mass balance equation for the depletion of monomers with volume v_{G} (Eq. (2.8)), which is reformulated in a discrete form:

$$\frac{\mathrm{d}N_{\mathrm{G}}}{\mathrm{d}t} = -\sum_{i=1}^{\mathcal{N}_{\mathrm{MC}}} W_i \cdot G(v_i, N_{\mathrm{G}})/v_{\mathrm{G}}\,. \tag{4.18}$$

The coupling makes the solution of this ODE system difficult.[16] The change of the volumes of all particles has to be taken into account for the correct calculation of the new concentration N_{G} of the

[16] The discetization schemes of the corresponding continuous PBE formulation (Eq. (2.6)) make the application of specialized numerical schemes necessary [227, 64].

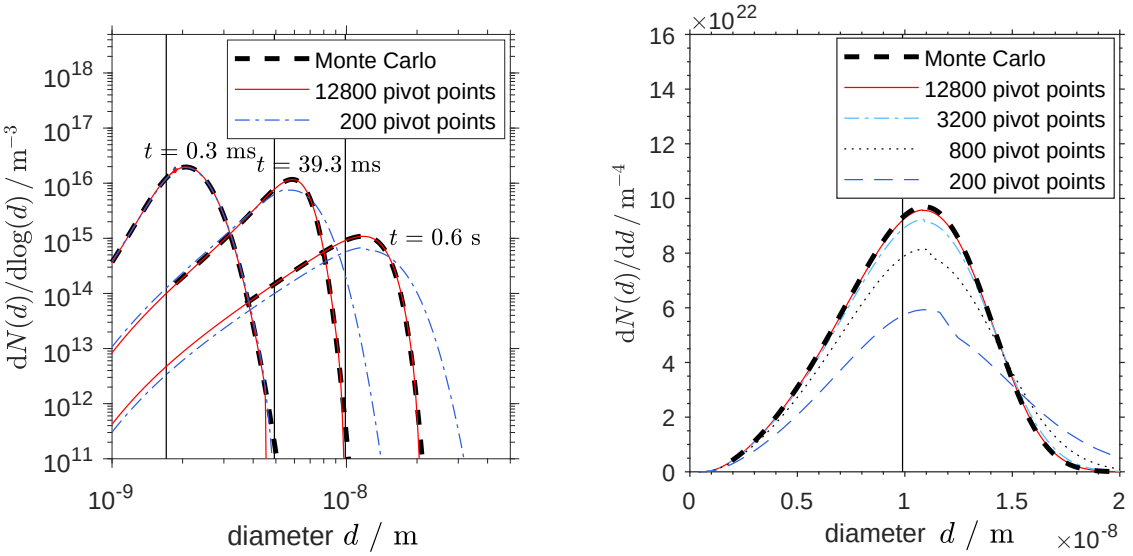

(a) Logarithmically scaled PSDs. **(b)** Linearly scaled PSDs at $t = 0.6\,\mathrm{s}$.

Figure 4.12: Simulation of condensation and evaporation for conditions listed in section A.4 with $S_0 = 10$. Horizontal lines mark the Kelvin diameter for respective time points.

gaseous material and thus the changed growth resp. evaporation rates G.

A large number of simulation particles makes it prohibitively costly to solve these differential equations numerically – if a CPU is applied. For this reason, growth is sometimes modeled as a stochastic event [215]. Another approach to reduce the computational toll of the necessary calculations is a deferred condensation [219] in a coagulation driven approach (i.e. if combined with the simulation of coagulation, the condensation of single particles is treated only, if these particles have been selected for coagulation). Such an approach is feasible if a more or less constant Kelvin diameter and supersaturation can be expected – leading thus to constant growth rates. This is not the case in Ostwald ripening scenarios, where the growth rate changes in time due to a fast evolving Kelvin diameter as well as changes of the particle diameters itself.

The application of a GPU makes the simultaneous handling of the large number of differential equations feasible. Not only the parallel evaluation of growth rates and update of particle volumes, but also the parallel summation of the condensated / evaporated volumes becomes possible, accelerating thus the calculation of the new gaseous monomer concentration via the mass balance equation (Eq. (4.18)). This idea is sketched in [Paper VII] in section VII.3 and figure VII.1. The shown algorithms are embedded in a framework already comprising coagulation and nucleation. Whereas figure VII.1 sketches an Euler step and the extension to the applied RK45 simulation scheme is left to the imagination of the reader, a more detailed description of the implementation can be found in the appendix E.1. The combination of discrete evaporation events with this continuous simulation of growth (resp. evaporation) can also be found in E.1.

4.7.1.1 Validation

In order to demonstrate the validity of this approach, a simple isothermic Fe system is considered. In this system, an initial aerosol Fe particle population is embedded in a mixture of carrier gas and supersaturated Fe vapor, as described in A.4. The changes of the PSD are shown in figure 4.12a, demonstrating not only the continuous growth of the PSD, but also the growth of the Kelvin diameter. The obtained results are benchmarked by comparison with the pivot point technique (the detailed implementation is described in A.4.2 and B.2.2). It can be seen, that higher number of used pivot points (i.e. detailed grids) lead to better approximations of the PSDs, the convergence in figure 4.12b resembles the discussion of the numerical diffusion in figure 2.3 - an inherent feature and main disadvantage of the pivot point method. However, the converging PSDs, as well as the convergence of the mean values of the geometric diameter, as shown in figure 4.13a, indicate the validity of the MC simulation technique.

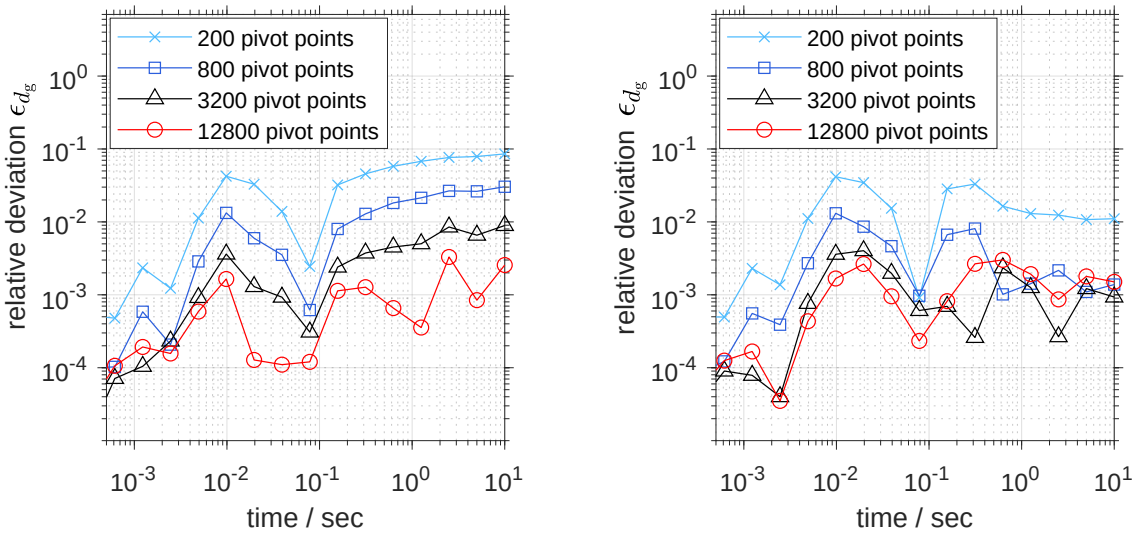

(a) Condensation and evaporation.

(b) Condensation, evaporation and coagulation.

Figure 4.13: Relative accuracy ϵ_{d_g} defined in Eq. (D.10) for simulation conditions listed in section A.4 with $S_0 = 10$.

4.7.2 Algorithm for Growth, Evaporation and Coagulation

The operator splitting technique is often used in order to separate the growth/evaporation process from the coagulation process for a short period of time. In this way, two different numerical techniques can be applied, one for the coagulation and the other one for the growth/evaporation, so that the best suited one is chosen for the solution of each of the two processes [228, 229].

In the scope of the here presented work, the event-driven time step, $\Delta\tau_{\mathrm{MC}}$ (defined in Eq. (2.20), in combination with SR coagulation rates $R^{\mathrm{sr}}_{i,j}$ from Table 4.4) is used to simulate a stochastic coagulation event. In a second step, the growth and evaporation of the resulting population is simulated for $\Delta\tau_{\mathrm{MC}}$, using the framework discussed above (section 4.7.1 and in more detail in E.1). Note, that the concept of fractional time steps, as described in section 4.2.1 would also allow the usage of smaller resp. bigger time steps, yielding possible gains in computational accuracy resp. efficacy. This makes another important parameter available for the control of the accuracy of the simulation.

4.7.2.1 Validation

A demonstration of the validity of this approach is shown using the same particle population as described above (section 4.7.1, or in detail in A.4) for the validation of the evaporation and condensation, but the stochastic mechanism of coagulation is also included into the simulation. This combined approach leads to an excellent agreement with the pivot point method, as shown for the PSDs in Figure 4.14 and the deviation of the mean geometric diameter in Figure 4.13b.

[Paper VI] shows, that the consideration of all mechanisms (i.e. coagulation, evaporation and coagulation) is necessary for the correct description of the PSD for a similar metallic system.

4.7.3 Algorithm for Growth, Evaporation, Coagulation and Nucleation

The operator-splitting technique as described above (section 4.7.2) with the MC time step $\Delta\tau_{\mathrm{MC}}$, is used to couple the stochastic simulation of coagulation with the combined simulation of evaporation, growth and nucleation. While the growth (resp. evaporation) of single particles is still described by Eq. (4.17), the change in the concentration N_{G} has to take the depletion due to nucleation into account, too. The mass balance in Eq. (4.18) is extended for this purpose to:

$$\frac{\mathrm{d}N_{\mathrm{G}}}{\mathrm{d}t} = -J \cdot (v^* + v_{\mathrm{G}})/v_{\mathrm{G}} - \sum_{i=1}^{\mathcal{N}_{\mathrm{MC}}} W_i \cdot G(v_i, N_{\mathrm{G}})/v_{\mathrm{G}}\,. \tag{4.19}$$

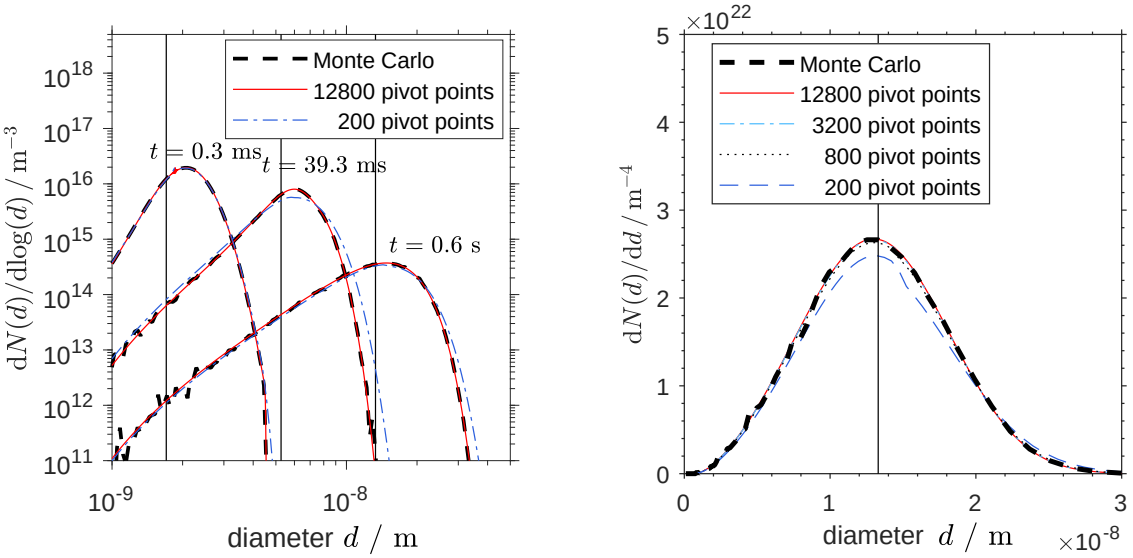

(a) Logarithmically scaled PSDs. **(b)** Linearly scaled PSDs at $t = 0.6\,\mathrm{s}$.

Figure 4.14: Simulation of condensation, evaporation and coagulation for conditions listed in section A.4 for $S_0 = 10$. Horizontal lines mark the Kelvin diameter for respective time points.

The continuous addition of nucleating particulate material (described by the nucleation rate J) is stored within a nucleation buffer, via the following ODE which is added to the coupled ODE system (Eq. (4.17) and Eq.(4.19)):

$$\frac{\mathrm{d}\mathcal{V}_\mathrm{B}}{\mathrm{d}t} = (v^* + v_\mathrm{G}) \cdot J\,. \tag{4.20}$$

The storage of the nucleated volume concentration ascertains a correct mass balance, even if the Kelvin volume v^*, changes in time. Once the nucleated volume concentration reaches a preset threshold value $\mathcal{V}_\mathrm{T}$, a MC particle with the volume $v^* + v_\mathrm{G}$ and statistical weight $\mathcal{V}_\mathrm{B}/(v^* + v_\mathrm{G})$ is inserted into the simulation, the low weight merging method discussed in section 4.5.1 is used in order to keep the number of used simulation particles constant, so that no additional memory has to be created to store the novel particle. Then, the nucleation buffer is reset to $\mathcal{V}_\mathrm{B} = 0$ and the next RK time step is simulated, the detailed algorithm is shown in section E.2, providing a little more details than in [Paper VII].

4.7.3.1 Validation

The algorithm is validated by the simulation of the same particle population as for the both benchmark cases above, the initial supersaturation, S, however has to be adjusted to $S = 10\,000$ (the detailed settings are listed in section A.4). This is because for $S = 10$ the nucleation rates J are negligibly small (as shown in Table A.4), leading to the same results as shown in Figures 4.14 and 4.13b.

The non negligible nucleation rates for $S = 10\,000$ lead to bimodal PSDs at the initial stages of the simulation. These bimodal PSDs consist of a particle population resulting from nucleation and the initial PSD. Hence the nucleation rates J differ in several orders of magnitude (the explicit values are listed in Table A.4), the resulting particle populations differ in several orders of magnitude, too, as can be seen in Figure 4.15a. The rendering of all three shown PSDs with a limited number of weighted MC particles shows the superiority of this approach compared to conventional MC techniques with non-weighted particles, it is hard to imagine, that these would be able to reproduce the shown PSDs. The application of weighted particles, on the other hand, allows to adjust the weight of the inserted particles to the desired order of magnitude simply by adjusting the critical threshold value $\mathcal{V}_\mathrm{T}$. This is one of the most important findings reported in [Paper IV], [Paper VI] and [Paper VII]. The specific settings for the simulations discussed in this section are listed in appendix A.4.1.

The comparison of the resulting PSDs with those originating from the pivot point method (details of the implementation can be found in the appendix A.4.2 and B.2) shown in Figures 4.15a and 4.15b displays an excellent agreement between both simulation techniques. A convergence (better results

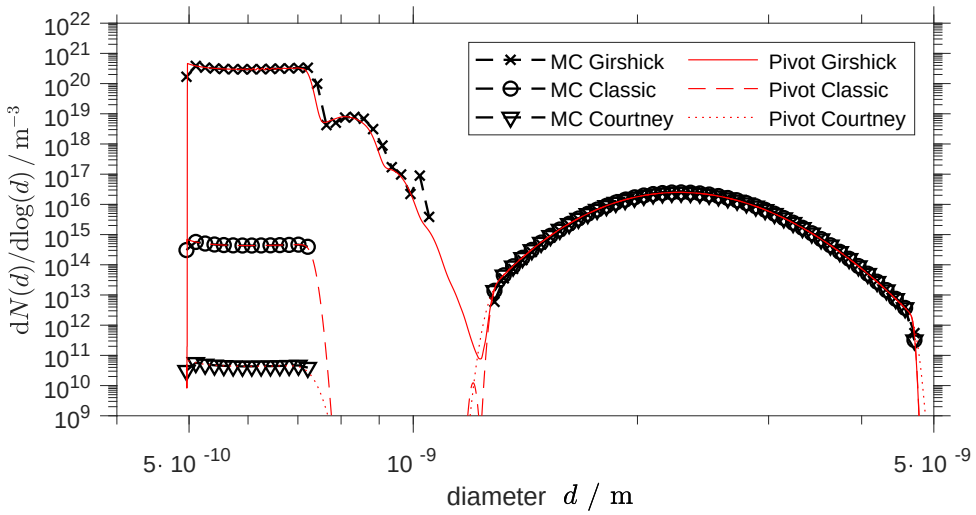

(a) PSDs for $t = 0.6\,\mu$s, 12 800 pivot points are used.

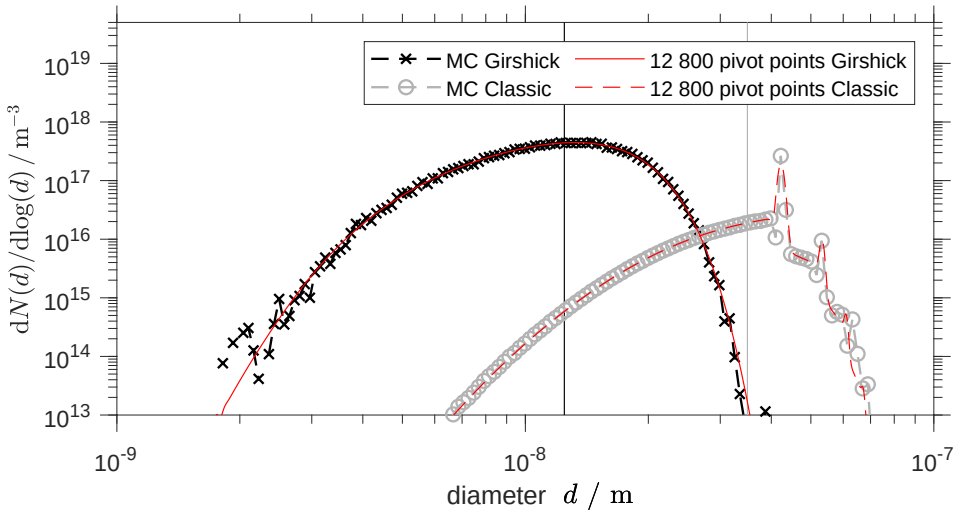

(b) PSDs for $t = 2.5\,$ms, 12 800 pivot points are used.

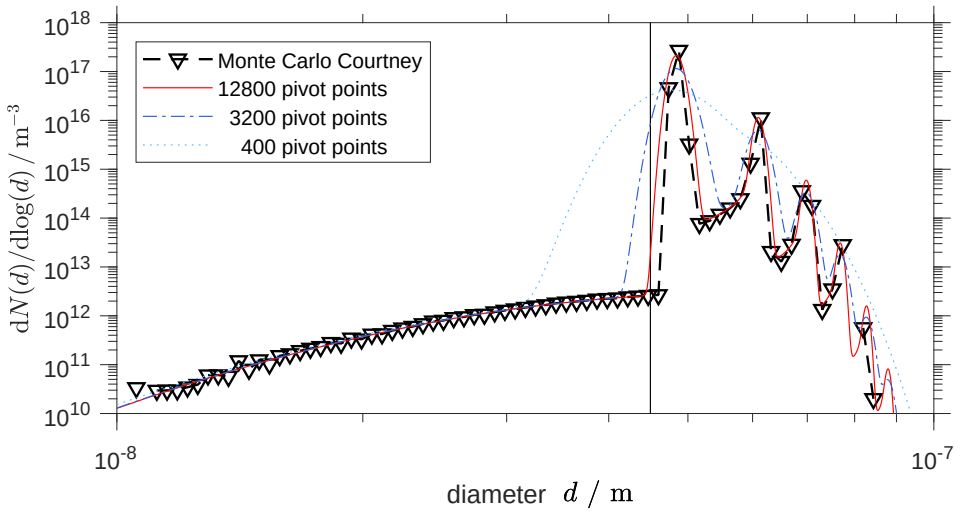

(c) PSDs for $t = 2.5\,$ms.

Figure 4.15: Simulation of combined nucleation, coagulation, condensation and evaporation for 10^5 MC particles and conditions listed in section A.4 with $S_0 = 10\,000$. The nucleation rates J_{cou} (Courtney), J_{cls} (Classic) and J_{gir} (Girshick) defined in Table 2.1c were used.

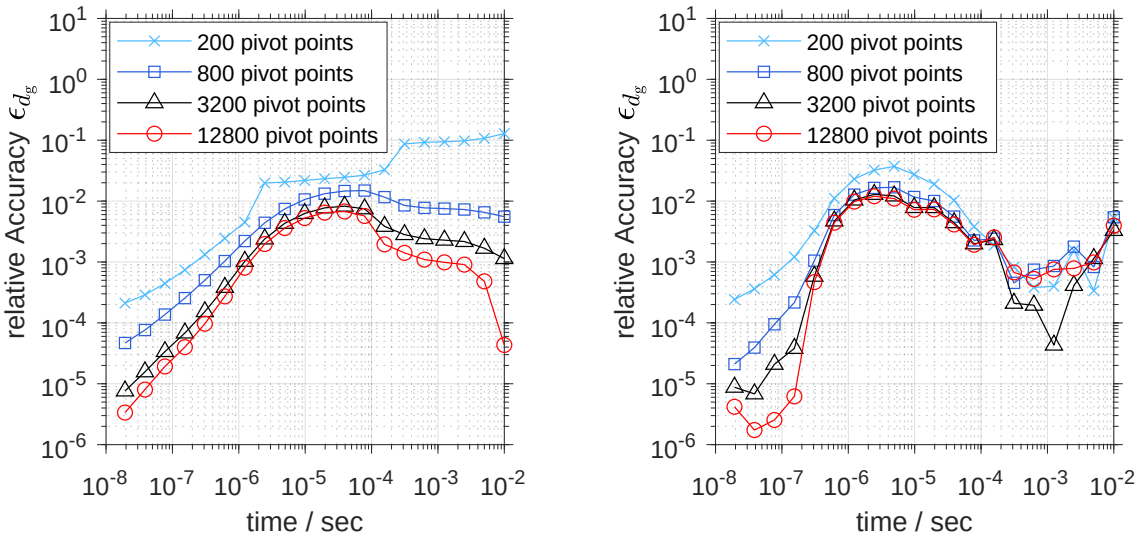

(a) Nucleation rate J_{cls} (Classic). **(b)** Nucleation rate J_{gir} (Girshick).

Figure 4.16: Relative accuracy ϵ_{d_g} defined in Eq. (D.10) for simulations of nucleation, coagulation, growth and evaporation for conditions listed in section A.4 with $S_0 = 10\,000$.

for higher number of used pivot points) can be seen in Figures 4.15c and 4.16.

4.7.3.2 Application Scenarios

Aerosol-based nucleation of particles can be subdivided in two different kinds of nucleation: 1) the nucleation via chemical decomposition of a precursor and 2) the physically induced nucleation.

1. The particle production through chemical decomposition of a precursor concentration in a gaseous phase is commonly modeled without the evaporation of the nucleated particles [9, 230, 151, 231]. This is due to the fact that typical Kelvin diameters encountered during the chemical precursor decomposition are assumed (following classical nucleation theories (see e.g. [50]) to be smaller than the size of a monomer (e.g. [232]). However, the surface growth has been identified as essential process [151], next to the exact chemistry of the decomposition process [233] for the description of this particle formation route.

2. The case of such a low Kelvin diameter (and thus the absence of evaporation) cannot be assumed for the modeling of particle formation by physically induced nucleation in an aerosol system, like it is encountered in condensation-evaporation reactors [234, 235], during laser ablation [236] or spark and arc discharges [237]. Although the evaporation is not included into the modeling of these works, it can be found in atmospheric aerosol modeling [228] (for phthalate at 300 - 400 K) or [238] (for typical atmospheric aerosols at 300 K).

The applicability of the presented simulation technique to the physically induced nucleation in the context of particle synthesis has been discussed for a metallic system, similar to Fe, but with a different vapor pressure, in [Paper VI] and [Paper VII], as well as for an Ag system in [Paper V], in section **2.3**. The identification of suitable experimental conditions for the investigation of nucleation rates (allowing thus to understand the nucleation mechanisms) during Ag particle synthesis is discussed in [Paper V]. The implications of different nucleation theories on the formation of new particles (and thus cloud condensation nuclei) have been discussed in [Paper IV].

Chapter 5

Conclusions

A general framework for the solution of the PBE for a network of compartments is introduced in this work. For its solution parallel stochastic and deterministic GPU algorithms are devised in combination with the decoupling of single mechanism for short periods of time (operator splitting). In this context, novel modeling techniques, or mathematical descriptions have been provided. These novel concepts are tested on relevant test cases, for which they show an excellent agreement with benchmark methods and also some superiority in comparison with alternative solution methods available to date, namely:

1. The concept of stochastic resolution (SR) offers a novel derivation of the coagulation rates for the coagulation process as it is described by the fictitious particle (FP) theory, leading to a somewhat simpler expression. It also allows to understand the description of alternative particle approaches, such as the stochastic weighted algorithm (SWA) and allows to understand the higher noise levels which are encountered in the application of the SWA simulation technique. Lower noise levels, and thus a higher precision can be seen in comparison to the conventionally used constant number MC (CNMC) technique.

2. The concept of fractional MC time steps allows the combination of artificially small time steps with an intrinsically event-driven MC algorithm. It is shown that the application of this novel algorithm is necessary for the reproduction of the correct PSD – in comparison to approaches in which no fractional time steps are applied.

3. A general rule for the probabilistic description of breakage of weighted simulation particles is introduced. This rule encompasses the existing, proposed schemes for the description for breakage (number based (NB), volume based (VB), as well as all other fragmented weight transfer function (FWTF) based formulations) of weighted MC particles. Novel descriptions, not covered by the FWTF, become possible, like the LV and the combinations LV-NB and LV-VB. This formulations allow to render all fragments and thus the full PSDs – in contrast to NB and NV, where only particles with a higher concentration are rendered.

4. Explicit rules for merging of unequal particles are formulated in combination with a functional expression for the merging error. This approach allows the formulation of parallel algorithms for the inclusion of novel particles in the context of nucleation and transport. The merging poses an attractive alternative to the otherwise used random removal (RR) method.

   (a) A parallel merging algorithm, low weight merging (LWM), for the inclusion of nucleated particles is introduced. It has been shown that the application of this algorithm is able to render a good approximation of the PSDs even for prolonged simulation times, in contrast to the method based on the RR of simulation particles.

   (b) Another parallel algorithm has been introduced for the merging of entire particle populations, one representing the particulate inflow into one unit (or compartment), the other representing the residing particle population within the unit (or compartment). It is shown, that the merging of the populations produces correct PSDs, even for complex flowsheet problems, involving screen units and tear streams. It is shown that for these systems, the RR technique cannot be applied.

The application of merging – and thus weighted simulation particles in general, hence the merging method cannot be formulated for equally weighted simulation particles – is necessary for the correct description of the presented test cases for transport and nucleation.

5. A parallel algorithm is presented for the simulation of growth and evaporation of weighted MC particles, avoiding the problem of numerical diffusion encountered in sectional methods.

   (a) It is demonstrated, that the application of a huge number of pivot points (3 200 – 12 800) is necessary, in order to reach the accuracy of the MC algorithm. Such a high number rules out the extension of the pivot technique to a 2D grid, rendering a second property.

   (b) The deterministic algorithm for growth and evaporation can be combined with the stochastic simulation of coagulation in an operator splitting technique, leading to excellent agreement with the pivot point technique.

   (c) The combined simulation of nucleation, coagulation, growth and evaporation shows also an excellent agreement with the pivot point technique. The definition of a nucleation threshold makes the explicit modeling of the statistical weight of the novel nucleating particles possible - allowing thus the adjustment of the simulation for a broad variety of simulation conditions, which could not be correctly described by the application of non-weighted simulation particles.

Outlook

The introduced algorithms constitute a promising starting point for further investigations. The first intriguing questions arise, of how to estimate optimal time steps for the operator splitting approach and whether the decoupling of the single simulation steps, poses a good approximation for the simulation of a complete flowsheet problem. The presented methods have all been formulated for particulate systems characterized by only one property (the particle size) – this happened out of the necessity to provide a benchmark case. The algorithms are, however, easily expandable to several properties. An initial testing of the coagulation algorithm presented in the third chapter indicated, that the computation of 2 or 8 properties lead to only slightly larger computing times. This is due to the fact, that most of the computing time was used for parallel summations and not for calculations in which the particle properties had to be considered. This raises the hope, that the other algorithms, which work in a similar fashion may show the same scaling behavior and make thus an efficient multivariate flowsheet simulation possible. Whether all of these algorithms can be combined in the present form – or if some further modifications (e.g. for the merging algorithm) are necessary for the simulation of such complex problems as introduced in the introduction remains an intriguing research question.

It is the hope of the author that the proposed methodology might in this or some modified and sophisticated form contribute to what Professor Jim Litster calls *"the joy of particulate products."*

Appendices

Appendix A Used Functions and Simulation Conditions

A.1 PSDs with Equal Moments in Figure 2.1

The PSDs are constructed from known PDFs $f(x)$, with $\int_0^\infty f(x)\mathrm{d}x = 1$. An arbitrary normalization constant C_U is introduced, so that $\int_0^\infty f(d/C_\mathrm{U})\mathrm{d}d = C_\mathrm{U}$. The PSD $n(d) = \frac{N_0}{C_\mathrm{U}} \cdot f(d/C_\mathrm{U})$ represents a total concentration of N_0[1]. The plot of the curves of $n(d)$ is identical to $f(x)$, where the x axis is replaced with the diameter d (unit C_U for 1) and y with $\mathrm{d}N/\mathrm{d}d$, where 1 is replaced with N_0/C_U.

1. The log normal distribution is defined by the following function:

$$n_\mathrm{LN}(d) = \frac{N_0}{C_\mathrm{U}\sqrt{2\cdot\pi}\cdot\breve{s}\cdot(d/C_\mathrm{U}))} \cdot \exp\left(\frac{-(\ln(d/C_\mathrm{U}) - \breve{m})^2}{2\cdot\breve{s}^2}\right), \qquad d \in (0,\infty),\ [d] = \mathrm{m} \quad \text{(A.1)}$$

   the plot is shown for the parameters:

$$\breve{m} = 3.22\ldots, \qquad \breve{s} = 0.2325\ldots, \qquad C_\mathrm{U} = 1\mu\mathrm{m} \quad \text{and} \quad N_0 = 10^5\,\mathrm{cm}^{-3}.$$

2. The Pareto distribution is defined by:

$$n_\mathrm{P}(d) = \frac{N_0}{C_\mathrm{U}} \cdot \frac{\breve{k}\cdot(\breve{x}_\mathrm{min})^{\breve{k}}}{(d/C_\mathrm{U})^{\breve{k}+1}}, \qquad d \in (\breve{x}_\mathrm{min}\cdot C_\mathrm{U}, \infty)\,, \quad \text{(A.2)}$$

   the following parameters are used for the plot:

$$\breve{k} = 5.359\ldots, \qquad \breve{x}_\mathrm{min} = 20.916\ldots, \qquad C_\mathrm{U} = 1\mu\mathrm{m} \quad \text{and} \quad N_0 = 10^5\,\mathrm{cm}^{-3}.$$

3. The arcsine distribution is defined by the following function:

$$n_\mathrm{AS}(d) = \frac{N_0}{C_\mathrm{U}\cdot\pi\cdot\sqrt{(d/C_\mathrm{U} - \breve{e})\cdot(\breve{f} - d/C_\mathrm{U})}}, \qquad d \in (\breve{e}\cdot C_\mathrm{U}, \breve{f}\cdot C_\mathrm{U})\,, \quad \text{(A.3)}$$

   the plot in the figure is shown for:

$$\breve{e} = 17.143\ldots, \qquad \breve{f} = 34.286\ldots, \qquad C_\mathrm{U} = 1\mu\mathrm{m} \quad \text{and} \quad N_0 = 10^5\,\mathrm{cm}^{-3}.$$

4. The triangular distribution is defined by:

$$n_\mathrm{T}(d) = \frac{2\cdot N_0}{C_\mathrm{U}} \cdot \begin{cases} (d/C_\mathrm{U} - \breve{a})/\left\{(\breve{b} - \breve{a})\cdot(\breve{c} - \breve{a})\right\} & \text{if } d \in [\breve{a}\cdot C_\mathrm{U}, \breve{c}\cdot C_\mathrm{U}]\,, \\ (\breve{b} - d/C_\mathrm{U})/\left\{(\breve{b} - \breve{a})\cdot(\breve{c} - \breve{a})\right\} & \text{if } d \in (\breve{c}\cdot C_\mathrm{U}, \breve{b}\cdot C_\mathrm{U}]\,, \\ 0 & \text{else}\,, \end{cases} \quad \text{(A.4)}$$

[1] While in the here presented example the dimensionless value z is replaced with d/C_U, it might be replaced with any other quantity, ψ/C_U, as long as the unit of C_U is chosen accordingly (i.e. $[C_\mathrm{U}] = [\psi]$).

the following parameters are used for the plot:

$$\breve{a} = 6.787\ldots, \qquad \breve{b} = 35.273\ldots, \qquad \breve{c} = 35.0823\ldots, \qquad C_{\mathrm{U}} = 1\mu\mathrm{m} \quad \text{and} \quad N_0 = 10^5\,\mathrm{cm}^{-3}\,.$$

Instead of the volume-based definition $\mu_i = \int v^i \cdot n(v)\,\mathrm{d}v$, the diameter based definition is used:

$$\mu_{\mathrm{d},i} = \int d^i \cdot n(d)\,\mathrm{d}d\,. \tag{A.5}$$

This leads to the following moments of all distributions 1.-4.:

$$\mu_{\mathrm{d},0} = N_0, \qquad \mu_{\mathrm{d},1} = N_0 \cdot C_{\mathrm{U}} \cdot 25.714\ldots, \qquad \mu_{\mathrm{d},2} = N_0 \cdot C_{\mathrm{U}}^2 \cdot 697.959\ldots\,.$$

A.2 Simulation Conditions for Constant Growth in Figure 2.3

A.2.1 Grid Settings and Initial Conditions

The used 1D-grid consists of equidistant diameter values, d_i, defining the volumes v_i of the pivot points with:

$$d_i = d_0 + \Delta d \cdot i\,, \qquad v_i = \pi \cdot d_i^3/6\,. \tag{A.6}$$

The initial condition shown in Figure 2.3 describes a constant PSD for all particle diameters d with $1\mu\mathrm{m} \leq d \leq 4\mu\mathrm{m}$. The constant value of $\frac{\mathrm{d}N}{\mathrm{d}d} = 10^{16}\,\mathrm{m}^{-4}$ corresponds to a total number concentration of $N_0 = 3 \cdot 10^{10}\mathrm{m}^{-3}$. The explicit values shown in Table A.1 ascertain that for all grid settings, the value $d_0 + \Delta d/2 = 1\mu\mathrm{m}$, which is the boundary between the first and second pivot point, as well as: $d_0 + \Delta d \cdot (\mathcal{N}_0^{\mathrm{PP}} + 0.5) = 4\mu\mathrm{m}$ - this is the boundary between the $(\mathcal{N}_0^{\mathrm{PP}} + 1)$-th and $(\mathcal{N}_0^{\mathrm{PP}} + 2)$-th pivot point.

Table A.1: Values used for 1D-grid described by Eq. (A.6) and computing times.

Number of pivot points	$d_0/\mu\mathrm{m}$	$\Delta d/\mu\mathrm{m}$	Number $\mathcal{N}_0^{\mathrm{PP}}$ of initial pivot points with $N_l \neq 0$	Computation time / sec
800	0.85	0.3	10	11
3 200	0.9625	0.075	40	253
12 800	0.990625	0.01875	160	14 857

A.2.2 Growth Rate and Analytical Solution

A diameter independent growth rate has been simulated with:

$$\frac{\mathrm{d}d}{\mathrm{d}t} = \tilde{C}_{\mathrm{d}}^{\mathrm{G}} = 10\mu\mathrm{m\,s}^{-1} \iff G(v) = \frac{\mathrm{d}v}{\mathrm{d}t} = v^{2/3} \cdot \underbrace{\frac{(36\pi)^{1/3}}{2} \cdot \tilde{C}_{\mathrm{d}}^{\mathrm{G}}}_{C_{\mathrm{d}}^{\mathrm{G}} \text{ in Table 2.1d}}\,. \tag{A.7}$$

The presented growth rate $G(v)$ is used in combination with Eq. (B.15)-(B.17) (resp. (2.15)). The growth rates $G(v_i)$ are independent on the monomer-concentration N_{G}, it is set $N_{\mathrm{G}} = 0$ and the monomer balance in Eq. (B.18) is not considered, $\frac{\mathrm{d}N_{\mathrm{G}}}{\mathrm{d}t} = 0$ is used instead.

The analytical solution for a constant growth rate can be written as (see e.g. [97] for a formulation for $n(v,t)$ and a volume independent growth rate):

$$n(d,t) = n(d - \tilde{C}_{\mathrm{d}}^{\mathrm{G}} \cdot t, 0)\,. \tag{A.8}$$

A.3 Conditions for Pure Coagulation in Figure 4.3 and Table 4.5 in Section 4.1.3

The simulated test-case describes the coagulation in the free-molecule regime as described by β_{fm} in Table 2.1a in combination with the physical parameters listed in Table A.2. The table also displays the safety factor which is used for the algorithm discussed in section 3.2 as well as the values for the monodisperse initial particle population. The statistical weight W_0 for each MC particle depends on the number of used simulation particles $\mathcal{N}_{\mathrm{MC}}$ and the initial total number concentration N_0:

$$W_0 = N_0/\mathcal{N}_{\mathrm{MC}}\,. \tag{A.9}$$

Table A.2: Simulation conditions for pure coagulation discussed in section 4.1.3.

Parameter type	Name	Symbol	Value	Unit
Physical parameter	Particle density	ρ_p	1000	kg/m^3
	Temperature	T	300	K
Computing parameter	Safety factor	χ	1000	–
Initial values	Particle diameter	d_0	3	nm
	Total number concentration	N_0	10^{13}	m^{-3}

The following characteristic time τ_fm is used for the presentation of the results:

$$\tau_\mathrm{fm} = \sqrt{\frac{1\cdot\rho_p}{3\cdot k_\mathrm{B}\cdot T\cdot d_0}}\cdot\frac{1}{N_0}. \tag{A.10}$$

This is the time in which a monodisperse model would predict the reduction of the initial particle number concentration by half [46]. Other physical parameters and initial values than those listed in Table A.2 lead to the same results[2] if the value for τ_fm is adjusted according to Eq. (A.10). The compared methods (SWA, SR, CNMC) are expected to produce the same noise levels and to require the same amount of MC steps (and thus computational times) as stated in Table 4.5 for the simulation of a time frame of $1000\,\tau_\mathrm{fm}$.

A.4 Conditions for Condensational Growth, Evaporation, Coagulation and Nucleation in Section 4.7

Table A.3 lists the physical parameters used for the simulation - these are used for the coagulation kernel β_fm and the growth rate G_fm in the free molecule regime, as well as for the nucleation rates J_cou, J_cls and J_gir in Table 2.1c.

Table A.3: Simulation conditions for MC simulations of growth and coagulation discussed in sections 4.7.1 and 4.7.2, the supersaturation of $S_0 = 10\,000$ is used if the simulations of nucleation is also included (section 4.7.3).

Parameter type	Name	Symbol	Value	Unit
Physical parameter	Particle density	ρ_p	7874	kg/m^3
	Temperature	T	1600	K
	Saturation pressure	p_s	0.1115	Pa
	Surface tension	σ	2.0038	J/m^2
	Atomic mass	m_G	$9.273\cdot10^{-26}$	kg
	Atomic volume	v_G	$1.177\cdot10^{-29}$	m^3
Computing parameter	Safety factor	χ	10 000	–
Initial values	Total number concentration	N_0	10^{16}	m^{-3}
	Supersaturation	S_0	10 or 10 000	–

The value for the surface tension for Fe is based on data from [239] and calculated with a linear interpolation for the temperature $T = 1600\,\mathrm{K}$. All other material parameters are chosen according to [240] – a formula for the interpolation of the partial pressure at the given temperature is provided there. The atomic volume has been calculated via: $v_\mathrm{G} = m_\mathrm{G}/\rho_\mathrm{p}$.

The initial PSD is a log normal distribution $n_\mathrm{LN}(d)$ defined in Eq. (A.1), with the parameters:

$$\breve{m} = \ln(2\cdot10^{-9}), \qquad \breve{s} = \ln(1.2), \qquad C_\mathrm{U} = 1\mathrm{m} \quad \text{and} \quad N_0 = 10^{16}\,\mathrm{m}^{-3}\,.$$

[2] The relative values d/d_0 and N/N_0 should be considered for the description of the PSDs in Figure 4.3a.

The total particle mass concentration, $M_{\mathrm{Fe,p}}$, of this distribution is calculated by $M_{\mathrm{Fe,p}} = \rho_{\mathrm{p}} \cdot \int_0^\infty \frac{\pi d^3}{6} n_{\mathrm{LN}}(d)\mathrm{d}d \approx 3.83 \cdot 10^{-7}\,\mathrm{kg\,m^{-3}}$. The application of the gas law yields the mass concentration of the Fe vapor ($M_{\mathrm{Fe,g}} = \rho_{\mathrm{p}} \cdot \frac{S p_{\mathrm{s}}}{k_{\mathrm{B}} T} \approx S \cdot 4.81 \cdot 10^{-7}\,\mathrm{kg\,m^{-3}}$), as well as the mass concentration of the carrier gas – N_2 at 1600 K and atmospheric pressure – $M_{\mathrm{N_2}} \approx 0.2113\,\mathrm{kg\,m^{-3}}$. This values are put into perspective as the mass load defined by $(M_{\mathrm{Fe,p}} + M_{\mathrm{Fe,g}})/M_{\mathrm{N_2}}$ tabulated next to the nucleation rates for the discussed simulation scenarios in Table A.4.

Table A.4: Initial nucleation rates and mass loads (ratio Fe mass concentration to carrier gas mass concentration) for $S_0 = 10$ and $S_0 = 10\,000$.

Supersaturation S_0	J_{cou} / $\mathrm{m^{-3}s^{-1}}$	J_{cls} / $\mathrm{m^{-3}s^{-1}}$	J_{gir} / $\mathrm{m^{-3}s^{-1}}$	$(M_{\mathrm{Fe,p}} + M_{\mathrm{Fe,g}})/M_{\mathrm{N_2}}$ / –
10	$2.61 \cdot 10^{-118}$	$2.61 \cdot 10^{-117}$	$1.90 \cdot 10^{-108}$	$2.43 \cdot 10^{-5}$
10 000	$7.97 \cdot 10^{+16}$	$7.97 \cdot 10^{+20}$	$5.80 \cdot 10^{+26}$	$2.25 \cdot 10^{-2}$

A.4.1 Implementation of Nucleation for MC method

The nucleation threshold $\mathcal{V}_{\mathrm{T}}$ is adjusted after each insertion of novel particles to a new value $\mathcal{V}_{\mathrm{T}}^{\mathrm{new}}$ by multiplication with a constant factor (1.005) until a maximum value, $\mathcal{V}^{\mathrm{max}}$, is reached:

$$\mathcal{V}_{\mathrm{T}}^{\mathrm{new}} = \min(\,\mathcal{V}_{\mathrm{T}}^{\mathrm{max}},\, 1.005 \cdot \mathcal{V}_{\mathrm{T}}^{\mathrm{old}}\,)\,. \tag{A.11}$$

The values $\mathcal{V}_{\mathrm{T}}^{\mathrm{max}}$ and $\mathcal{V}_{\mathrm{T}}^{\mathrm{ini}}$ are listed in table A.5.

Table A.5: Parameters for calculation of $\mathcal{V}_{\mathrm{T}}^{\mathrm{new}}$ in Eq. (A.11).

Nucleation Theory	Initial value $\mathcal{V}_{\mathrm{T}}^{\mathrm{ini}}$ / –	Maximal value $\mathcal{V}_{\mathrm{T}}^{\mathrm{max}}$ / –
Courtney (J_{cls})	10^{-26}	10^{-18}
Classic (J_{cou})	10^{-22}	10^{-14}
Girshick (J_{gir})	10^{-15}	10^{-10}

A.4.2 Implementation of the Pivot Point Method

According to the derivation presented in section B.2, the following set of coupled differential equations is solved:

- Growth/Evaporation Eq. (B.15) – (B.18):

$$\frac{\mathrm{d}N_j}{\mathrm{d}t} = \left(\frac{\mathrm{d}N_j}{\mathrm{d}t}\right)_{\mathrm{growth}} \quad \text{and} \quad \frac{\mathrm{d}N_{\mathrm{G}}}{\mathrm{d}t} = \left(\frac{\mathrm{d}N_{\mathrm{G}}}{\mathrm{d}t}\right)_{\mathrm{growth}}. \tag{A.12}$$

  The discrete-logarithmic grid is used as described by Eq. (A.16) and Eq. (A.17) with $v_{\mathrm{start}} = 2v_{\mathrm{G}}$.

- Growth/Evaporation and coagulation Eq. (B.15) – (B.18) and (2.14):

$$\frac{\mathrm{d}N_j}{\mathrm{d}t} = \left(\frac{\mathrm{d}N_j}{\mathrm{d}t}\right)_{\mathrm{growth}} + \left(\frac{\mathrm{d}N_j}{\mathrm{d}t}\right)_{\mathrm{coag}} \quad \text{and} \quad \frac{\mathrm{d}N_{\mathrm{G}}}{\mathrm{d}t} = \left(\frac{\mathrm{d}N_{\mathrm{G}}}{\mathrm{d}t}\right)_{\mathrm{growth}}. \tag{A.13}$$

- Growth/Evaporation, coagulation and nucleation Eq. (B.15) – (B.18), (2.14) and (B.22)–(B.23):

$$\frac{\mathrm{d}N_j}{\mathrm{d}t} = \left(\frac{\mathrm{d}N_j}{\mathrm{d}t}\right)_{\mathrm{growth}} + \left(\frac{\mathrm{d}N_j}{\mathrm{d}t}\right)_{\mathrm{coag}} + \left(\frac{\mathrm{d}N_j}{\mathrm{d}t}\right)_{\mathrm{nuc}} \quad \text{and} \quad \frac{\mathrm{d}N_{\mathrm{G}}}{\mathrm{d}t} = \left(\frac{\mathrm{d}N_{\mathrm{G}}}{\mathrm{d}t}\right)_{\mathrm{growth}} + \left(\frac{\mathrm{d}N_{\mathrm{G}}}{\mathrm{d}t}\right)_{\mathrm{nuc}}. \tag{A.14}$$

The presented solutions were obtained using MATLAB and the implicit ode15s solver. The rk45 solver was found to be not fast enough due to the stiffness of the problem. The discretized solution

using an Euler approach - as suggested by [134] was found to be - of course - worse than rk45. It requires a prohibitively small Euler time step - which has to be found via trial and error.

A.4.2.1 Grid Settings Growth/evaporation (with or without) coagulation

Combination of a linearly and logarithmic scaled grid - only allowing discrete multiples of v_G first and logarithmically increasing spacings ar at least as large as v_G.

$$v_i^\bullet = \begin{cases} v_{start} + v_G \cdot (i-1)\,, \text{ for } \quad i \leq \mathcal{N}_{dPP}\,, \\ [v_{start} + v_G \cdot (\mathcal{N}_{dPP} - 1)] \cdot q^{(i-\mathcal{N}_{dPP})}\,, \text{with: } q = 10^{\{9/(\mathcal{N}_{PP}-1)\}}\,, \text{ for } \quad \mathcal{N}_{dPP} < i\,. \end{cases} \tag{A.15}$$

The number of discrete points, $\mathcal{N}_{dPP}$, can be estimated by the condition, which ensures that the logarithmic spaced pivot points are at least separated by v_G. The real number $\mathcal{N}_{dPP}^{(R)}$ for which the logarithmic spacing would equal the discrete one is given by:

$$v_{start} + v_G \cdot (\mathcal{N}_{dPP}^{(R)}) = [v_{start} + v_G \cdot (\mathcal{N}_{dPP}^{(R)} - 1)] \cdot q \iff \mathcal{N}_{dPP}^{(R)} = \frac{q}{q-1} - \frac{v_{start}}{v_G}\,. \tag{A.16}$$

Hence $\mathcal{N}_{dPP}$ has to be an integer, the smallest integer bigger than $\mathcal{N}_{dPP}^{(R)}$ is used - with the ceiling function $\lceil x \rceil$ (designating the smallest integer i with $i > x$) one can write:

$$\mathcal{N}_{dPP} = \left\lceil \mathcal{N}_{dPP}^{(R)} \right\rceil = \left\lceil \frac{q}{q-1} - \frac{v_{start}}{v_G} \right\rceil\,. \tag{A.17}$$

Note that higher numbers of pivot points, $\mathcal{N}_{PP}$ lead to a lower value of q and thus to a higher number of discrete points $\mathcal{N}_{dPP}$.

This grid is used for the benchmark of the evaporation / condensation simulation with or without coagulation. (The results are shown in Figures 4.12 and 4.13).

Growth/evaporation, coagulation and nucleation

The logarithmically scaled grid used for the combined simulation of condensation/evaporation, coagulation and nucleation is defined as:

$$v_i^\bullet = 2 \cdot v_G \cdot q^{(i-1)}\,, \text{with: } q = 10^{\{8/(\mathcal{N}_{PP}-1)\}}\,. \tag{A.18}$$

This grid consists of pivot points, describing fractional atomic values (e.g. for $\mathcal{N}_{dPP} = 12\,800$: $v_1^\bullet = 2v_G$, $v_2^\bullet \approx 2.0029 \cdot v_G$, $v_3^\bullet \approx 2.0058 v_G$, etc.), it thus approximates a continuous growth process (i.e. Eq. (2.6) allows the particles to assume all possible fractional volumes v). While the grid defined by equations Eq. (A.15) models a more physically relevant system, in which lower particle volumes can only assume multiple atomic volumes (i.e.: $v_1^\bullet = 2v_G$, $v_2^\bullet = 3v_G$, $v_3^\bullet = 4v_G, \dots$). As can be seen in figure A.1a, these different grids lead to markedly different results in the initial stage of the simulation - which underlines that a different kind of MC simulation should be used if these very early simulation stages are in the center of interest.[3] It can also be seen, that for longer simulation times, the choice of the grid becomes irrelevant - as shown in figure A.1b. There seems to be no perceptible difference whether the continuous or discrete grid is used for the scenarios treating the evaporation/condensation with or without coagulation. This fact raises the hope that - if one is only interested in the (measurable) particle state for longer simulation times - the MC simulation corresponding to the logarithmic scaled grid is sufficient enough in order to investigate the possibility of formulating the complex dynamics of particle formation with the help of a single nucleation rate J, coupled to continuous growth/evaporation and coagulation.

[3] A small (i.e. 100) number of MC-particles with a constant volume of multiples of v_G could be used. The change of the statistical weights due to condensation/evaporation can be easily modeled by the solution of the corresponding equations already formulated for the pivot method (Eq. (B.15)). The coagulation could be treated as a discrete event, which decreases the concentration of the MC particle with the fixed volume by the concentration of the colliding particle (i.e. particle selected for coagulation).

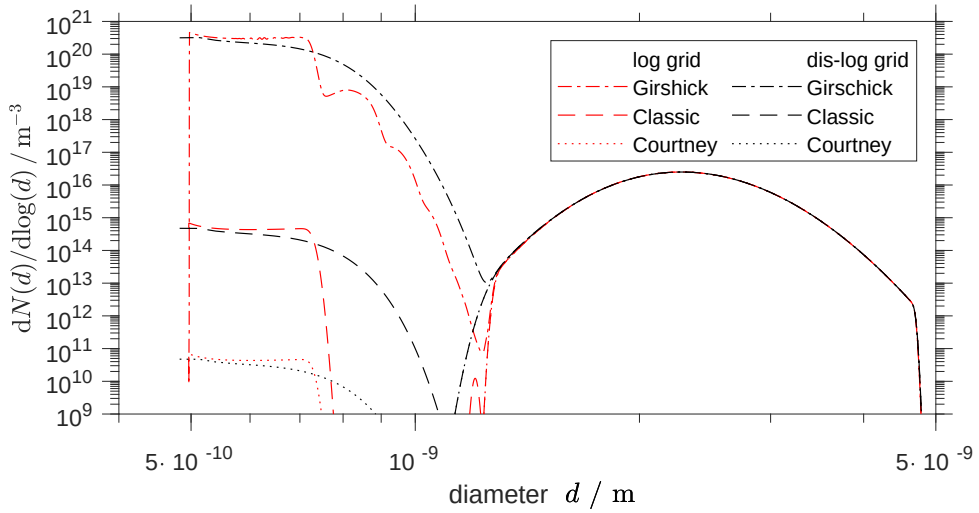

(a) PSDs for $t = 0.6\,\mu\mathrm{s}$

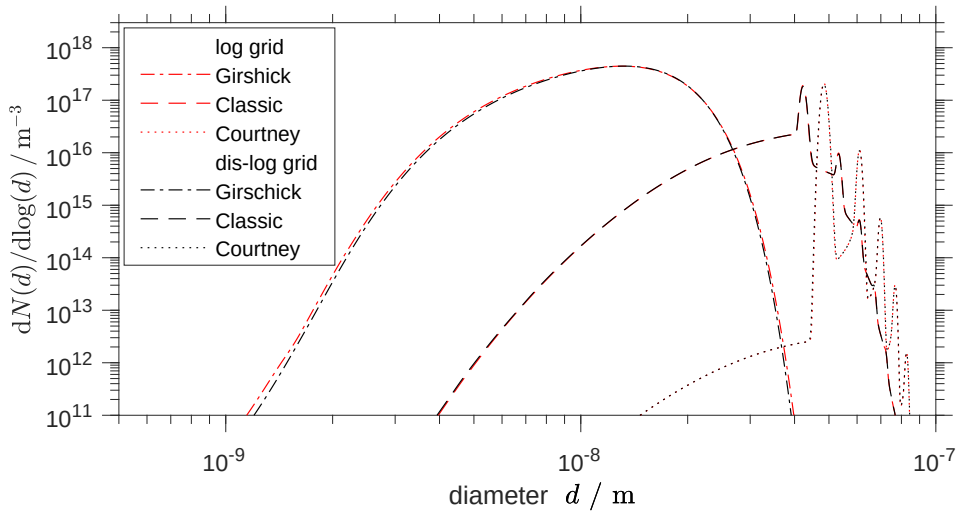

(b) PSDs for $t = 2.5\,\mathrm{ms}$

Figure A.1: Simulation of combined nucleation, coagulation, condensation and evaporation for conditions listed above (section A.4). Results for 12 800 Pivot points are shown using a discrete logarithmic grid (dis-log: pivot point values defined by Eq.(A.15)) and a logarithmic grid (log: pivot points defined by Eq. (A.18)).

Appendix B Explicit Formulas for Discretization Methods

B.1 Collision Integrals for the Sectional Method

The approximation

$$n(v,t) \approx N_l/(v_l^{\dashv} - v_{l-1}^{\dashv}) \qquad \text{for} \quad v_{l-1}^{\dashv} < v \leq v_l^{\dashv}\,, \tag{B.1}$$

is plugged into Eq. (2.2). The integration of the resulting expression with respect to dv over single sections l (i.e. $v = v_{l-1}^{\dashv} \dots v_l^{\dashv}$) leads to two expressions.

1. For the particle number concentration increase in section l due to coagulation of sections i and k:

$$\overline{\beta_{i,k\to l}} = \frac{1-\delta_{i,k}\cdot\delta_{k,l}\cdot\frac{1}{2}}{(v_i^{\dashv}-v_{i-1}^{\dashv})(v_k^{\dashv}-v_{k-1}^{\dashv})}\cdot\int_{v_{l-1}^{\dashv}}^{v_l^{\dashv}}\left[\int_{v_{i-1}^{\dashv}}^{v_i^{\dashv}}\tilde{\beta}(\hat{v}-v',v')\mathrm{d}v'\right]\mathrm{d}\hat{v}\,, \tag{B.2}$$

$$\text{whith: } \tilde{\beta}(\hat{v}-v',v') = \begin{cases}\beta(\hat{v}-v',v') & \text{, if } v_{k-1}^{\dashv} < \hat{v}-v' < v_k^{\dashv}\,,\\ 0 & \text{, else}\,.\end{cases}$$

$$\text{and: } \delta_i, j = \begin{cases}1 & \text{, if } i=j\,,\\ 0 & \text{, else}\,.\end{cases}$$

   The Factor $1/2$ is used in the cases $i = j = k$ to prevent a double-counting for the calculation of $\beta_{i,i\to i}$.

2. For the particle number concentration decrease due to coagulation of section l with another section k:

$$\overline{\beta_{l,k\to}} = \frac{1}{(v_l^{\dashv}-v_{l-1}^{\dashv})(v_k^{\dashv}-v_{k-1}^{\dashv})}\cdot\int_{v_{l-1}^{\dashv}}^{v_l^{\dashv}}\left[\int_{v_{k-1}^{\dashv}}^{v_k^{\dashv}}\beta(v',\hat{v})\mathrm{d}v'\right]\mathrm{d}\hat{v}\,. \tag{B.3}$$

B.1.1 Extension for DS Method

If the sectional method is used in combination with discrete points - as in the (DS) methods [126], additional integral expressions are used for

1. discrete point - section collision leading to increase in another section,
2. discrete point - discrete point collision leading to an increase in another section,
3. discrete point - discrete point collision leading to an increase in a discrete point.

The explicit values for these integrals can be found in [126].

B.2 Pivot Point Method

The in the following derived formulas recapitulate the formulation for coagulation ([127] in section B.2.1) in combination with the evaporation and condensation in section as stated in [134] – with a slightly more detailed description of the closures of the resulting equations. The real novelty is the interpretation of the resulting rate equations in the scope of the method of lines as a set of coupled ODEs as discussed in section A.4.2.

B.2.1 Coagulation

The coagulation of two particles with the volumes $v_i^{\bullet}$ and $v_j^{\bullet}$ leads to novel particles with the volume $v_{\text{new}} = v_i^{\bullet} + v_j^{\bullet}$. The splitting on both adjacent pivot points l and $l+1$ is done, so that the total increase of concentration in both nodes is equal to the increase of concentration of the novel particle, $\beta(v_i^{\bullet}, v_j^{\bullet})\cdot N_i \cdot N_j \cdot (1-\frac{1}{2}\delta_{i,j})$ (where the delta-Dirac function $\delta_{i,j}$ and the factor $\frac{1}{2}$ prevents from double counting of all possible coagulation pairs in the case $i = j$):

$$\overline{\beta_{i,j\to l}}\cdot N_i\cdot N_j + \overline{\beta_{i,j\to l+1}}\cdot N_i\cdot N_j = \beta(v_i^{\bullet},v_j^{\bullet})\cdot N_i\cdot N_j\ \cdot(1-\frac{1}{2}\delta_{i,j})\,. \tag{B.4}$$

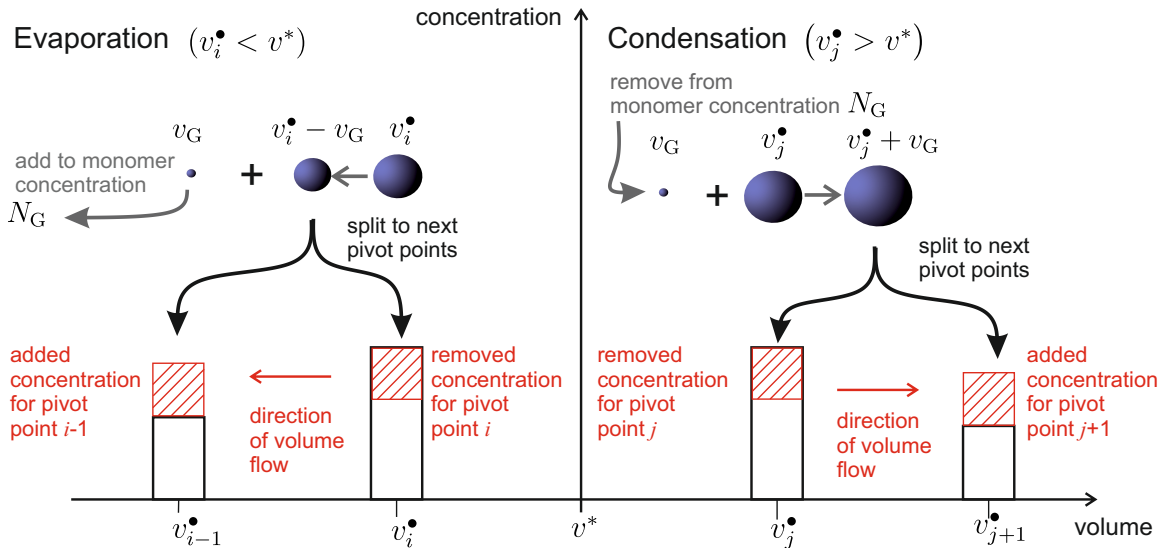

Figure B.1: The evaporation of pivot point i with volume $v_i^\bullet$ and condensational growth of j with $v_j^\bullet$ in the scope of the pivot point technique.

A similar equation can be postulated for the increase of the volume concentration due to coagulation ($(v_i^\bullet + v_j^\bullet) \cdot \beta(v_i^\bullet, v_j^\bullet) \cdot N_i \cdot N_j \cdot (1 - \frac{1}{2}\delta_{i,j})$):

$$v_l^\bullet \cdot \overline{\beta_{i,j\to l}} \cdot N_i \cdot N_j + v_{l+1}^\bullet \cdot \overline{\beta_{i,j\to l+1}} \cdot N_i \cdot N_j = (v_i^\bullet + v_j^\bullet) \cdot \beta(v_i^\bullet, v_j^\bullet) \cdot N_i \cdot N_j \cdot (1 - \frac{1}{2}\delta_{i,j})\,. \tag{B.5}$$

Plugging an expression for $\overline{\beta_{i,j\to l+1}}$ from Eq. (B.4) into Eq. (B.5) leads to:

$$\overline{\beta_{i,j\to l}} = \frac{v_{l+1}^\bullet - v_i^\bullet - v_j^\bullet}{v_{l+1}^\bullet - v_l^\bullet} \cdot \beta(v_i^\bullet, v_j^\bullet) \cdot (1 - \frac{1}{2}\delta_{i,j})\,, \qquad \overline{\beta_{i,j\to l+1}} = \frac{v_i^\bullet + v_j^\bullet - v_l^\bullet}{v_{l+1}^\bullet - v_l^\bullet} \cdot \beta(v_i^\bullet, v_j^\bullet) \cdot (1 - \frac{1}{2}\delta_{i,j})\,. \tag{B.6}$$

The second term results from plugging the first term above (i.e. left equation in (B.6)) into Eq. (B.4).

Eq. (B.6) can be rewritten to:

$$\overline{\beta_{i,j\to l}} = \begin{cases} \frac{v_{l+1}^\bullet - v_i^\bullet - v_j^\bullet}{v_{l+1}^\bullet - v_l^\bullet} \cdot \beta(v_i^\bullet, v_j^\bullet) \cdot (1 - \frac{1}{2}\delta_{i,j}), & \text{if: } v_{l+1}^\bullet > v_i^\bullet + v_j^\bullet \geq v_l^\bullet\,, \\ \frac{v_i^\bullet + v_j^\bullet - v_{l-1}^\bullet}{v_l^\bullet - v_{l-1}^\bullet} \cdot \beta(v_i^\bullet, v_j^\bullet) \cdot (1 - \frac{1}{2}\delta_{i,j}), & \text{if: } v_l^\bullet \geq v_i^\bullet + v_j^\bullet > v_{l-1}^\bullet\,, \\ 0 & \text{else}\,. \end{cases} \tag{B.7}$$

For the overall outflow kernel the coagulation kernel is used:

$$\overline{\beta_{i,j\to}} = \beta(v_i^\bullet, v_j^\bullet)\,. \tag{B.8}$$

The term $(1 - \frac{1}{2}\delta_{i,j})$ is dropped, because two particles have to be removed from the same pivot point i in the case of coagulation with each other.

B.2.2 Growth and Evaporation

A simple approach for the inclusion of condensational growth in the scope of fixed pivot simulation techniques has been suggested by [134] (the pivot points are termed 'nodes' in [134]). The authors proposed to treat condensational growth as coagulation of monomers (with volume v_G) with particles represented by single pivot points j (volume $v_j^\bullet$) and to split up the resulting particle (volume $v_G + v_j^\bullet$) on the originating pivot point j and the adjacent larger pivot point $j+1$ - just as it is done for the coagulation of single particles, like shown in Figure B.1. The growth rate G is thereby associated with the coagulation rate β via:

$$G(v_j^\bullet) = v_G \cdot \beta(v_G, v_j^\bullet) \cdot N_{sp}\,, \tag{B.9}$$

where N_{sp} is the monomer surplus concentration which is calculated with the monomer concentration, N_{G}, the monomer concentration at saturation pressure, N_{s}, and the Kelvin correction term, $K(d_j^\bullet)$, i.e.:

$$N_{\mathrm{sp}} = \left(N_{\mathrm{G}} - N_{\mathrm{s}} \cdot K(d_j^\bullet)\right), \quad N_{\mathrm{s}} = p_{\mathrm{s}}/(k_{\mathrm{B}} \cdot T) \quad \text{and} \quad K(d_j^\bullet) = \exp\left\{\frac{4 \cdot \sigma \cdot v_{\mathrm{G}}}{k_{\mathrm{B}} \cdot T \cdot d_j^\bullet}\right\}, \qquad \text{(B.10)}$$

$$\text{with: } v_j^\bullet = \pi \cdot \left(d_j^\bullet\right)^3/6\,.$$

The evaporation of particles is described analogously to the condensation: the pivot point i with the volume $v_i^\bullet$ is separated into 1) a smaller particle $v_i^\bullet - v_{\mathrm{G}}$ and 2) a monomer with the volume v_{G}. The smaller particle is split upon the originating pivot point i and the adjacent smaller pivot point $i-1$. The explicit rate of evaporation is also described by Eq. (B.9) (in this case $N_{\mathrm{G}} < N_{\mathrm{s}} \cdot K(d_j)$).

Analogously for the splitting of coagulation shown in the subsection above, the following formulas for growth (resp. evaporation) of the pivot point j can be formulated:

$$G(v_j^\bullet) > 0 \;\Rightarrow\; \text{Growth of } j\text{:} \qquad \text{decrease of } N_j: \qquad \left(\frac{\mathrm{d}N_j}{\mathrm{d}t}\right)_{j \overset{\text{growth}}{\to} j} = -\frac{G(v_j^\bullet)}{v_{j+1}^\bullet - v_j^\bullet} \cdot N_j\,, \qquad \text{(B.11)}$$

$$\text{increase of } N_{j+1}: \qquad \left(\frac{\mathrm{d}N_{j+1}}{\mathrm{d}t}\right)_{j \overset{\text{growth}}{\to} j+1} = +\frac{G(v_j^\bullet)}{v_{j+1}^\bullet - v_j^\bullet} \cdot N_j\,, \qquad \text{(B.12)}$$

$$G(v_j^\bullet) < 0 \;\Rightarrow\; \text{Evaporation of } j\text{:} \qquad \text{decrease of } N_j: \qquad \left(\frac{\mathrm{d}N_j}{\mathrm{d}t}\right)_{j \to j}^{\text{evap}} = +\frac{G(v_j^\bullet)}{v_j^\bullet - v_{j-1}^\bullet} \cdot N_j\,, \qquad \text{(B.13)}$$

$$\text{increase of } N_{j-1}: \qquad \left(\frac{\mathrm{d}N_{j-1}}{\mathrm{d}t}\right)_{j \overset{\text{evap}}{\to} j-1} = -\frac{G(v_j^\bullet)}{v_j^\bullet - v_{j-1}^\bullet} \cdot N_j\,. \qquad \text{(B.14)}$$

The first terms in Eq. (B.11) and Eq. (B.13) take thereby 1) the increase due to the particles resulting from the splitting and 2) the total depletion of the particles into account[4]. Assuming that the pivot points are sorted (i.e. $v_i^\bullet < v_i^\bullet + 1$) and that $K(v)$ is smaller for increasing particle diameters (i.e. $v_i^\bullet < v_j^\bullet \Rightarrow K(v_i^\bullet) > K(v_j^\bullet)$), leads for the following growth rates of all pivot points:

$$\left(\frac{\mathrm{d}N_j}{\mathrm{d}t}\right)_{\substack{\text{growth} \\ \{j \neq 1, \mathcal{N}_{\mathrm{PP}}\}}} = \begin{cases} -\frac{G(v_j^\bullet)}{v_{j+1}^\bullet - v_j^\bullet} \cdot N_j + \frac{G(v_{j-1}^\bullet)}{v_j^\bullet - v_{j-1}^\bullet} \cdot N_{j-1} & \text{, for: } v_j^\bullet > v_{j-1}^\bullet > v^*\,, \quad (G(v_j^\bullet) > 0)\,, \\ -\frac{G(v_j^\bullet)}{v_{j+1}^\bullet - v_j^\bullet} \cdot N_j & \text{, for: } v_j^\bullet > v^* \geq v_{j-1}^\bullet\,, \quad (G(v_j^\bullet) > 0)\,, \\ 0 & \text{, for: } v^* = v_j^\bullet\,, \quad (G(v_j^\bullet) = 0)\,, \\ +\frac{G(v_j^\bullet)}{v_j^\bullet - v_{j-1}^\bullet} \cdot N_j & \text{, for: } v_{j+1}^\bullet \geq v^* > v_j^\bullet\,, \quad (G(v_j^\bullet) < 0)\,, \\ +\frac{G(v_j^\bullet)}{v_j^\bullet - v_{j-1}^\bullet} \cdot N_j - \frac{G(v_{j+1}^\bullet)}{v_{j+1}^\bullet - v_j^\bullet} \cdot N_{j+1} & \text{, for: } v^* > v_{j+1}^\bullet > v_j^\bullet\,, \quad (G(v_j^\bullet) < 0)\,. \end{cases} \qquad \text{(B.15)}$$

For the last pivot point, $\mathcal{N}_{\mathrm{PP}}$ (with the largest volume $v_{\mathcal{N}_{\mathrm{PP}}}^\bullet$), no number concentration decrease

[4] The expressions for Eq. (B.11) and Eq. (B.12) result directly from the derived coagulation rates in Eq.(B.7):

$$\left(\frac{\mathrm{d}N_j}{\mathrm{d}t}\right)_{j \overset{\text{growth}}{\to} j} = \left(\overline{\beta_{\mathrm{G},j\to j}} - \overline{\beta_{\mathrm{G},j\to}}\right) N_{\mathrm{sp}} N_j = \frac{G(v_j^\bullet)}{v_{\mathrm{G}}} \left(\frac{v_{j+1}^\bullet - v_{\mathrm{G}} - v_j^\bullet}{v_{j+1}^\bullet - v_j^\bullet} - 1\right) N_j = -\frac{G(v_j^\bullet)}{v_{j+1}^\bullet - v_j^\bullet} N_j\,,$$

$$\left(\frac{\mathrm{d}N_{j+1}}{\mathrm{d}t}\right)_{j \overset{\text{growth}}{\to} j+1} = \overline{\beta_{\mathrm{G},j\to j+1}} N_{\mathrm{sp}} N_j = \frac{G(v_j^\bullet)}{v_{\mathrm{G}}} \cdot \frac{v_{\mathrm{G}} + v_j^\bullet - v_j^\bullet}{v_{j+1}^\bullet - v_j^\bullet} N_j = +\frac{G(v_j^\bullet)}{v_{j+1}^\bullet - v_j^\bullet} N_j\,,$$

and the mass balance: $\left(\frac{\mathrm{d}N_{\mathrm{G}}}{\mathrm{d}t}\right)_{j \overset{\text{growth}}{\to}} = -\overline{\beta_{\mathrm{G},j\to}} N_{\mathrm{sp}} N_j = -\frac{G(v_j^\bullet)}{v_{\mathrm{G}}} \cdot N_j\,.$

The evaporation is treated analogously by formulating equations similar to Eq. (B.4) and Eq. (B.5) for the split up of the resulting particles with mass $v_j^\bullet$ over the adjacent pivot points with the volumes $v_{j-1}^\bullet$ and $v_j^\bullet$ and a negative coagulation coefficient resulting from Eq. (B.9).

due to growth is modeled:

$$\left(\frac{\mathrm{d}N_{\mathcal{N}_{\mathrm{PP}}}}{\mathrm{d}t}\right)_{\mathrm{growth}} = \begin{cases} +\frac{G(v^\bullet_{\mathcal{N}_{\mathrm{PP}}-1})}{v^\bullet_{\mathcal{N}_{\mathrm{PP}}}-v^\bullet_{\mathcal{N}_{\mathrm{PP}}-1}} \cdot N_{\mathcal{N}_{\mathrm{PP}}-1} & \text{, for: } v^\bullet_{\mathcal{N}_{\mathrm{PP}}} > v^\bullet_{\mathcal{N}_{\mathrm{PP}}-1} > v^* \text{,} \quad (G(v^\bullet_{\mathcal{N}_{\mathrm{PP}}}) > 0)\text{,} \\ 0 & \text{, for: } v^\bullet_{\mathcal{N}_{\mathrm{PP}}} > v^* \geq v^\bullet_{\mathcal{N}_{\mathrm{PP}}-1} \text{,} \quad (G(v^\bullet_{\mathcal{N}_{\mathrm{PP}}}) > 0)\text{,} \\ \text{like (B.15)} & \text{, else.} \end{cases} \tag{B.16}$$

If the last pivot point, $\mathcal{N}_{\mathrm{PP}}$, assumes values > 0, the growth is no longer approximated correctly and a larger grid with points representing larger volumes should be chosen.

For the first pivot point $j = 1$, a coupling to the monomers can be modeled in the following way:

$$\left(\frac{\mathrm{d}N_1}{\mathrm{d}t}\right)_{\mathrm{growth}} = \begin{cases} -\frac{G(v^\bullet_1)}{v^\bullet_2-v^\bullet_1} \cdot N_1 + \frac{\beta(v_{\mathrm{G}},v_{\mathrm{G}})\cdot v_{\mathrm{G}}}{2\cdot(v^\bullet_1-v_{\mathrm{G}})} \cdot N_{\mathrm{G}}^2 & \text{, for: } v^\bullet_1 > v_{\mathrm{G}} \geq v^* \text{,} \quad (G(v^\bullet_1) > 0)\text{,} \\ -\frac{G(v^\bullet_1)}{v^\bullet_2-v^\bullet_1} \cdot N_1 & \text{, for: } v^\bullet_1 > v^* > v_{\mathrm{G}} \text{,} \quad (G(v^\bullet_1) > 0)\text{,} \\ 0 & \text{, for: } v^\bullet_1 = v^* \text{,} \quad (G(v^\bullet_1) = 0)\text{,} \\ +\frac{G(v^\bullet_1)}{v^\bullet_1-v_{\mathrm{G}}} \cdot N_1 & \text{, for: } v^\bullet_2 \geq v^* > v^\bullet_1 \text{,} \quad (G(v^\bullet_1) < 0)\text{,} \\ +\frac{G(v^\bullet_1)}{v^\bullet_1-v_{\mathrm{G}}} \cdot N_1 - \frac{G(v^\bullet_2)}{v^\bullet_2-v^\bullet_1} \cdot N_2 & \text{, for: } v^* > v^\bullet_2 > v^\bullet_1 \text{,} \quad (G(v^\bullet_1) < 0)\text{.} \end{cases} \tag{B.17}$$

The evaporation of the first pivot point is treated by splitting the resulting particle between the first pivot point and the monomers with volume v_{G} (the last two lines in Eq. (B.17). This depletion is also accounted for in the monomer balance equation (last line of second term in r.h.s. of Eq. (B.18)). In the case of growth, in which the coagulated monomers are stable ($v_{\mathrm{G}} > v^*$), an additional coagulation kernel might be added, describing the production of particles due to coagulation of the monomers. The depletion of the monomers undergoing the coagulation is also included in the monomer equation (as first line):

$$\left(\frac{\mathrm{d}N_{\mathrm{G}}}{\mathrm{d}t}\right)_{\mathrm{growth}} = -\left(\sum_{i=1,\ldots,\mathcal{N}_{\mathrm{PP}}} G(v_i^\bullet)\cdot N_i/v_{\mathrm{G}}\right) + \begin{cases} -\frac{\beta(v_{\mathrm{G}},v_{\mathrm{G}})\cdot v^\bullet_1}{2\cdot(v^\bullet_1-v_{\mathrm{G}})} \cdot N_{\mathrm{G}}^2 & \text{, for: } v_{\mathrm{G}} \geq v^* \text{,} \\ 0 & \text{, for: } v^\bullet_1 \geq v^* > v_{\mathrm{G}} \text{,} \\ -\frac{G(v^\bullet_1)}{v^\bullet_1-v_{\mathrm{G}}} \cdot N_1 & \text{, for: } v^* > v^\bullet_1 \text{,} \quad (G(v^\bullet_1) < 0)\text{.} \end{cases} \tag{B.18}$$

The first term on the r.h.s. of this equation accounts for the monomer increase (or decrease) due to evaporation (or condensation) over all nodes, like sketched in Figure B.1. Note that a change in N_{G} leads to different growth rates for each node, $G(v_i^\bullet)$, as described by Eq. (B.9) and Eq. (B.10). This leads to a set of differential equations, which proves to be very stiff, so that implicit solvers have to be applied for a quick solution.

B.2.3 Nucleation

The presented nucleation theories (which differ in the nucleation rates J_{cou}, J_{cls} and J_{gir} in Table 2.1c) all assume that particles become stable (i.e. do not evaporate) for sizes larger than the Kelvin diameter d^* resp. the Kelvin volume v^*, as described in Eq. (2.5):

$$d^* = 4\cdot\sigma\cdot v_{\mathrm{G}}/(k_{\mathrm{B}}\cdot T\cdot\ln(S))\,, \qquad \text{and } v^* = \pi\cdot(d^*)^3/6\,. \tag{B.19}$$

Thus, nucleating particles are assumed, to have the volume v_{nuc}, with:

$$v_{\mathrm{nuc}} = v^* + v_{\mathrm{G}}\,. \tag{B.20}$$

The supersaturation S – and v^* as well as v_{nuc} – changes in time and is calculated by the term (resulting from the definitions in Eq. (2.5)):

$$S = \frac{N_{\mathrm{G}} k_{\mathrm{B}} T}{p_{\mathrm{s}}}\,. \tag{B.21}$$

Because v_{nuc} changes in time, the adjacent pivot points l and $l+1$ with $v_l^\bullet < v_{\mathrm{nuc}} < v_{l+1}^\bullet$ change in time, too. They have to be found (i.e. calculated) again for each time point. Once these pivot points are found, the resulting concentration of nucleating particles is split upon these pivot points (similar

to the split up of the resulting particle for coagulation as described by Eq. (B.7)), so that:

$$\left(\frac{\mathrm{d}N_l}{\mathrm{d}t}\right)_{\mathrm{nuc}} = \begin{cases} \frac{v^\bullet_{l+1}-v_{\mathrm{nuc}}}{v^\bullet_{l+1}-v^\bullet_l} \cdot J, & \text{if: } v^\bullet_{l+1} > v_{\mathrm{nuc}} \geq v^\bullet_l\,, \\ \frac{v_{\mathrm{nuc}}-v^\bullet_{l-1}}{v^\bullet_l-v^\bullet_{l-1}} \cdot J, & \text{if: } v^\bullet_l \geq v_{\mathrm{nuc}} > v^\bullet_{l-1}\,, \\ 0 & \text{else}\,. \end{cases} \tag{B.22}$$

The mass balance is ensured by taking the depletion of the condensing vapor into account, each nucleating particle contains $v_{\mathrm{nuc}}/v_{\mathrm{G}}$ of atoms (resp. molecules) of the condensing material:

$$\left(\frac{\mathrm{d}N_{\mathrm{G}}}{\mathrm{d}t}\right)_{\mathrm{nuc}} = -J \cdot v_{\mathrm{nuc}}/v_{\mathrm{G}}\,. \tag{B.23}$$

Appendix C Description of SWA with SR Approach

The stochastic resolution theory does not only clarify the fictitious particle approach, it can also be used, to interpret the SWA methods described in Table 4.2, the statistical weights of the particles after the coagulation are compared for the SWA and the SR (for the specific setting $W_{\mathrm{MC}} = {}^{W_i \cdot W_j}/_{W_i+W_j}$) in Table C.1.

Table C.1: Resulting particles properties after coagulation of particle i (size v_i, weight W_i) and particle j (size v_j, weight W_j).

Theory / rate	After coagulation: statistical weights of particles with sizes		
	v_i	v_j	$v_j + v_i$
SR: $(W_i + W_j)\beta_{i,j}$	$W_i^2/(W_i + W_j)$	$W_j^2/(W_i + W_j)$	$W_j \cdot W_i/(W_i + W_j)$
SWA (i,j): $W_j\beta_{i,j}$	-	W_j	$\alpha_{i,j} \cdot W_i$
SWA (j,i): $W_i\beta_{j,i}$	W_i	-	$(1 - \alpha_{i,j}) \cdot W_j$

The SWA can be interpreted in such a way – summarizing the more elaborate discussion in the following two subsections: the exact statistical weights would be represented by the first line of Table C.1, a third (new) MC particle has to be introduced into the simulation for the correct description of the coagulation (as described by SR). Instead of introducing this third particle, the SWA sets the statistical weights in $P_{\mathrm{sel}}\big((i,j)\,\big|\,(i,j) \text{ or } (j,i)\big) = {}^{W_j}/_{W_i+W_j}$ of all cases to the second line and in $P_{\mathrm{sel}}\big((j,i)\,\big|\,(i,j) \text{ or } (j,i)\big) = {}^{W_i}/_{W_i+W_j}$ of all cases to the third line – resulting thus in the correct first line, but only in the statistical mean (i.e. if a lot of identical particle pairs (i,j) are selected for coagulation). This additional selection adds additional stochastic noise to the simulation, as it is shown in subsection 4.1.3.

C.1 Description by SR

A step on the way to the coagulation rate for the constant number scheme is Eq. (**6**) for the coagulation rate $R_{i,j}(W_{\mathrm{MC}})$ (named $\beta^{s_{\mathrm{F}}}_{\mathrm{SE}}(i,j)$ in [Paper I]) of equally weighted simulation particles with the weight W_{MC} (named s_{F} in [Paper I]):

$$R^{\mathrm{sr}}_{i,j}(W_{\mathrm{MC}}) = \frac{W_i \cdot W_j}{W_{\mathrm{MC}}} \cdot \beta(v_i, v_j)\,. \tag{C.1}$$

The coagulation rate depends on the stochastic resolution $1/W_{\mathrm{MC}}$, where $N_i = W_i/W_{\mathrm{MC}}$ is the number of equally weighted particles (with the weight W_{MC}) which are used for a weighted MC particle with the weight W_i. The value of W_{MC} can be adjusted freely and if it is set to $W_{\mathrm{MC}} = W_{\mathrm{min}}$, then the constant-number coagulation scheme in Figure 4.2 is described. The following setting leads to the description of the SWA:

$$W^{(\mathrm{swa})}_{\mathrm{MC}} = W_i \cdot W_j/(W_i + W_j) \;\Rightarrow\; R^{\mathrm{sr}}_{i,j}(W^{(\mathrm{swa})}_{\mathrm{MC}}) = W_i + W_j \cdot \beta(v_i, v_j)\,, \tag{C.2}$$

it is depicted in Figure C.1 [5].

The resulting statistical weights after coagulation are according to Figure C.1:

New statistical weights of MC particles with volume:

$$v_i: \quad W_i - W^{(\mathrm{swa})}_{\mathrm{MC}}, \qquad v_j: \quad W_j - W^{(\mathrm{swa})}_{\mathrm{MC}}, \qquad v_i + v_j: \quad W^{(\mathrm{swa})}_{\mathrm{MC}}\,. \tag{C.3}$$

Plugging of the expression for $W^{(\mathrm{swa})}_{\mathrm{MC}}$ in Eq. (C.2) into these resulting expressions leads to the first line of Table C.1.

[5] Because $W^{(\mathrm{swa})}_{\mathrm{MC}} = W_{\mathrm{min}} \cdot W_{\mathrm{max}}/(W_{\mathrm{max}} + W_{\mathrm{min}}) < W_{\mathrm{min}}$, there are always more than one equally weighted particles necessary to render the W_{min} particle species. The value $W^{(\mathrm{swa})}_{\mathrm{MC}} - W_{\mathrm{min}}$ can thereby also assume fractional values.

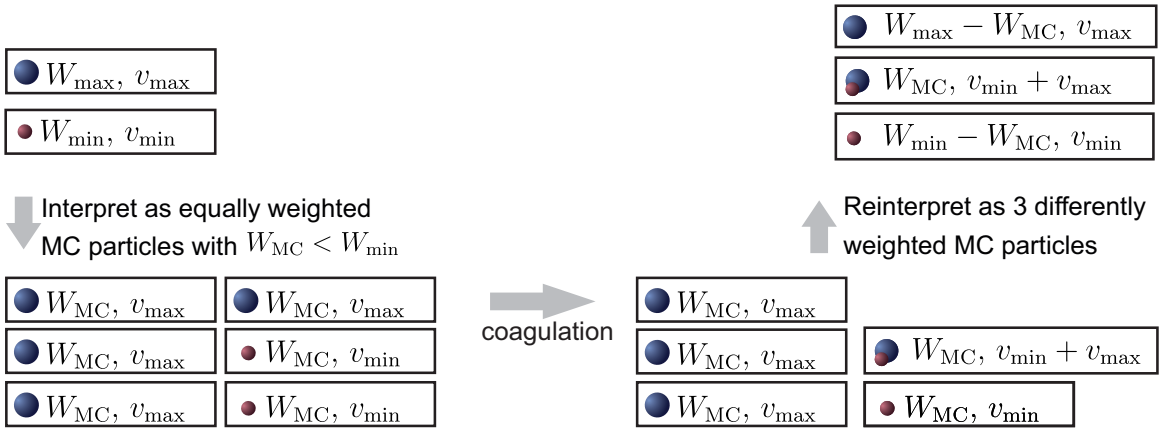

Figure C.1: The reinterpretation of the weighted MC particles as equally weighted MC particles with a stochastic resolution of $1/W_{\mathrm{MC}}$: if $W_{\mathrm{MC}} < W_{\min}$, 3 weighted MC particles are necessary to render all the resulting particles – like also summarized in Figure **1** in [Paper I].

C.2 Description by SWA

In the scope of the SWA, the coagulation (i,j) and (j,i) are two distinct events, if one is possible, the other has to be considered, too. So that the overall rate of any possible coagulation between the two particles i and j is:

$$R_{i,j}^{\mathrm{SWA}} + R_{j,i}^{\mathrm{SWA}} = W_j \beta_{i,j} + W_i \beta_{i,j} = R_{i,j}^{\mathrm{sr}}(W_{\mathrm{MC}}^{(\mathrm{swa})})\,, \tag{C.4}$$

this expression is equal to the rate used by the stochastic resolution with the weight $W_{\mathrm{MC}} = W_i \cdot W_j/(W_i + W_j)$.

The conditional probability $P_{\mathrm{sel}}\big((i,j)\,|\,(i,j) \text{ or } (j,i)\big)$ that the pair (i,j) has been selected for coagulation if one of the pairs (i,j) or (j,i) have been selected for sure can be calculated as:

$$P_{\mathrm{sel}}\big((i,j)\,|\,(i,j) \text{ or } (j,i)\big) = \frac{R_{i,j}^{\mathrm{SWA}}}{R_{i,j}^{\mathrm{SWA}} + R_{j,i}^{\mathrm{SWA}}} = \frac{W_j}{W_i + W_j}\,, \tag{C.5}$$

and analogously for the coagulation of the pair (j,i):

$$P_{\mathrm{sel}}\big((j,i)\,|\,(i,j) \text{ or } (j,i)\big) = \frac{R_{j,i}^{\mathrm{SWA}}}{R_{i,j}^{\mathrm{SWA}} + R_{j,i}^{\mathrm{SWA}}} = \frac{W_i}{W_i + W_j}\,. \tag{C.6}$$

If a large number N_{pair} of particle pairs(i_k, j_k), $(k = 1, \ldots, N_{\mathrm{pair}})$ with equal (k-independent) properties (v_i, W_i, v_j, W_j) have been selected for coagulation. Then, in the SR theory one would receive each time the three particles with the weights shown in the first line of Table C.1.

In the scope of the SWA the total of pairs (i,j) and the pairs (j,i) is selected with the same rate (as stated by Eq. (C.4)). But a fraction $P_{\mathrm{sel}}\big((i,j)\,|\,(i,j) \text{ or } (j,i)\big)$ of pairs would be a coagulation of the pair (i,j) and a fraction $P_{\mathrm{sel}}\big((j,i)\,|\,(i,j) \text{ or } (j,i)\big)$ would describe the coagulation of (j,i). In the *statistical mean* one would thus receive the following weights (by multiplying the second (resp. third) line of Table C.1 with the conditional probability $P_{\mathrm{sel}}\big((i,j)\,|\,(i,j) \text{ or } (j,i)\big)$ (resp. $P_{\mathrm{sel}}\big((j,i)\,|\,(i,j) \text{ or } (j,i)\big)$) and adding up both results):

Resulting statistical weights for particles with volume

$$\begin{aligned}
v_i: &\quad P_{\mathrm{sel}}\big((i,j)\,|\,(i,j) \text{ or } (j,i)\big)\cdot 0 &&+ P_{\mathrm{sel}}\big((j,i)\,|\,(i,j) \text{ or } (j,i)\big)\cdot W_i &&= \frac{W_i^2}{W_i + W_j}\,,\\
v_j: &\quad P_{\mathrm{sel}}\big((i,j)\,|\,(i,j) \text{ or } (j,i)\big)\cdot W_j &&+ P_{\mathrm{sel}}\big((j,i)\,|\,(i,j) \text{ or } (j,i)\big)\cdot 0 &&= \frac{W_j^2}{W_i + W_j}\,,\\
v_i + v_j: &\quad P_{\mathrm{sel}}\big((i,j)\,|\,(i,j) \text{ or } (j,i)\big)\cdot \alpha_{i,j} W_i &&+ P_{\mathrm{sel}}\big((j,i)\,|\,(i,j) \text{ or } (j,i)\big)\cdot (1-\alpha_{i,j}) W_j &&= \frac{W_i \cdot W_j}{W_i + W_j}\,.
\end{aligned}$$

This result is exactly the same as described by the SR – absolutely independent on the choice of $\alpha_{i,j}$ (as long as Eq. (4.1) holds, i.e. $\alpha_{i,j} + \alpha j, i = 1$) – but is only reached in the *statistical mean*.

Appendix D Characterization of Stochastic Results

D.1 Mean Values and Standard Deviations for MC Simulations

Each of the $\mathcal{N}_{\text{sim}}$ MC simulations uses different sequences of random numbers and produces therefore different PSDs described by the single weights and properties of the $\mathcal{N}_{\text{MC}}$ MC particles. The total number concentration $N^{(j)}$, the mean geometric diameter $d_{\text{g}}^{(j)}$ and the geometric standard deviation $\sigma_{\text{g}}^{(j)}$ for each simulation j is calculated using the statistical weight $W_i^{(j)}$ and the diameter $d_i^{(j)}$ of the i -th particle within the j-th simulation:

$$N^{(j)} = \sum_{i=1}^{\mathcal{N}_{\text{MC}}} W_i^{(j)}\,, \qquad \log\left(d_{\text{g}}^{(j)}\right) = \frac{1}{N^{(j)}} \sum_{i=1}^{\mathcal{N}_{\text{MC}}} W_i^{(j)} \cdot \log\left(d_i^{(j)}\right), \tag{D.1}$$

$$\left[\log\left(\sigma_{\text{g}}^{(j)}\right)\right]^2 = \frac{1}{N^{(j)}} \sum_{i=1}^{\mathcal{N}_{\text{MC}}} W_i^{(j)} \cdot \left[\log\left(d_i^{(j)}\right) - \log(d_{\text{g}}^{(j)})\right]^2 . \tag{D.2}$$

These results for single simulations are used for the calculation of the mean values:

$$\overline{N} = \frac{1}{\mathcal{N}_{\text{sim}}} \sum_{j=1}^{\mathcal{N}_{\text{sim}}} N^{(j)}\,, \qquad \overline{d_{\text{g}}} = \frac{1}{\mathcal{N}_{\text{sim}}} \sum_{j=1}^{\mathcal{N}_{\text{sim}}} d_{\text{g}}^{(j)}\,, \qquad \overline{\sigma_{\text{g}}} = \frac{1}{\mathcal{N}_{\text{sim}}} \sum_{j=1}^{\mathcal{N}_{\text{sim}}} \sigma_{\text{g}}^{(j)}\,, \tag{D.3}$$

as well as the (sample) standard deviations of these values:

$$\Delta N = \sqrt{\sum_{j=1}^{\mathcal{N}_{\text{sim}}} \frac{\left(N^{(j)} - \overline{N}\right)^2}{\mathcal{N}_{\text{sim}} - 1}}\,, \quad \Delta d_{\text{g}} = \sqrt{\sum_{j=1}^{\mathcal{N}_{\text{sim}}} \frac{\left(d_{\text{g}}^{(j)} - \overline{d_{\text{g}}}\right)^2}{\mathcal{N}_{\text{sim}} - 1}}\,, \quad \Delta\sigma_{\text{g}} = \sqrt{\sum_{j=1}^{\mathcal{N}_{\text{sim}}} \frac{\left(\sigma_{\text{g}}^{(j)} - \overline{\sigma_{\text{g}}}\right)^2}{\mathcal{N}_{\text{sim}} - 1}}\,. \tag{D.4}$$

D.2 Confidence Intervals for MC Simulations

The values obtained from Eq. (D.3) and (D.4) can be used in the framework of Student's t-test statistics to calculate the boundaries $\overline{N}^{b+}$ and $\overline{N}^{b-}$ of the confidence intervals for $\overline{N}$ (similar calculations can be done for $\overline{d_{\text{g}}}$ (resp. $\overline{\sigma_{\text{g}}}$) by replacing $\overline{N}$ and ΔN with $\overline{d_{\text{g}}}$ and Δd_{g} (resp. $\overline{\sigma_{\text{g}}}$ and $\Delta\sigma_{\text{g}}$)):

$$\overline{N}^{b+} = \overline{N} + z^*(P_{\text{stat}}, \mathcal{N}_{\text{sim}} - 1) \cdot \frac{\Delta N}{\sqrt{\mathcal{N}_{\text{sim}}}}\,, \quad \overline{N}^{b-} = \overline{N} - z^*(P_{\text{stat}}, \mathcal{N}_{\text{sim}} - 1) \cdot \frac{\Delta N}{\sqrt{\mathcal{N}_{\text{sim}}}}\,, \tag{D.5}$$

where $(\mathcal{N}_{\text{sim}} - 1)$ are the degrees of freedom for Student's t-distribution $f_{\text{sT}}^{(\mathcal{N}_{\text{sim}}-1)}(x)$, and P_{stat} is the statistical probability which the confidence interval has to ensure, defining thus $z^*(P_{\text{stat}}, \mathcal{N}_{\text{sim}} - 1)$:

$$P_{\text{stat}} = \int_{-z^*(P_{\text{stat}}, \mathcal{N}_{\text{sim}}-1)}^{z^*(P_{\text{stat}}, \mathcal{N}_{\text{sim}}-1)} f_{\text{sT}}^{(\mathcal{N}_{\text{sim}}-1)}(x)\ \mathrm{d}x\,. \tag{D.6}$$

Some exemplary values for z^* are listed in Table D.1.

Table D.1: Values for z^* for some $\mathcal{N}_{\mathrm{sim}}$ and P_{stat} calculated by the function `tinv` in Matlab [6].

P_{stat}	$\mathcal{N}_{\mathrm{sim}}$	$z^*(P_{\mathrm{stat}}, \mathcal{N}_{\mathrm{sim}}-1)$	$z^*(P_{\mathrm{stat}}, \mathcal{N}_{\mathrm{sim}}-1)/\sqrt{\mathcal{N}_{\mathrm{sim}}}$
0.90	10	1.83	0.580
0.90	50	1.67	0.237
0.90	100	1.66	0.166
0.95	100	1.98	0.198
0.99	100	2.62	0.262

A good measure for the statistical accuracy is the relative size of the confidence interval compared to the mean value. One can write for example for the number concentration:

$$(\overline{N}^{b+} - \overline{N}^{b-})/\overline{N} = \frac{2}{\sqrt{\mathcal{N}_{\mathrm{sim}}}} \cdot z^*(P_{\mathrm{stat}}, \mathcal{N}_{\mathrm{sim}}-1) \cdot \frac{\Delta N}{\overline{N}}\,. \tag{D.7}$$

Reducing thus the value $\frac{\Delta N}{\overline{N}}$ (for example by application of more MC particles or the choice of a method which produces simply smaller noise levels $\frac{\Delta N}{\overline{N}}$) leads to smaller confidence intervals for a given number of simulations $\mathcal{N}_{\mathrm{sim}}$ for the desired statistical accuracy P_{stat}.

D.3 Statistical Values for Pivot Point Method

The concentrations N_i for each pivot point i (with the diameter $d_i^{\bullet}$) are used for the calculation of the total concentration N^{PP}, the mean geometric diameter $d_{\mathrm{g}}^{\mathrm{PP}}$ and the standard deviation $\sigma_{\mathrm{g}}^{\mathrm{PP}}$:

$$N^{\mathrm{PP}} = \sum_{1}^{\mathcal{N}_{\mathrm{PP}}} N_i\,, \qquad \ln(d_{\mathrm{g}}^{\mathrm{PP}}) = \frac{1}{N^{\mathrm{PP}}} \sum_{1}^{\mathcal{N}_{\mathrm{PP}}} (N_i \cdot \ln(d_i^{\bullet}))\,, \tag{D.8}$$

$$\ln(\sigma_{\mathrm{g}}^{\mathrm{PP}}) = \sqrt{\frac{1}{N^{\mathrm{PP}}} \sum_{1}^{\mathcal{N}_{\mathrm{PP}}} N_i \cdot \left[\ln(d_i^{\bullet}) - \ln(d_{\mathrm{g}}^{\mathrm{PP}})\right]^2}\,. \tag{D.9}$$

D.4 Comparison of Pivot Point Values with MC Values

The deviations (ϵ_N) between the concentrations (resp. mean geometric diameters ($\epsilon_{d_{\mathrm{g}}}$) or geometric standard deviations ($\epsilon_{\sigma_{\mathrm{g}}}$)) resulting from the MC method to those resulting from the pivot point method are measured in relative values:

$$\epsilon_N = \frac{\left|N^{\mathrm{PP}} - \overline{N}\right|}{\overline{N}}\,, \qquad \epsilon_{d_{\mathrm{g}}} = \frac{\left|d_{\mathrm{g}}^{\mathrm{PP}} - \overline{d_{\mathrm{g}}}\right|}{\overline{d_{\mathrm{g}}}}\,, \qquad \epsilon_{\sigma_{\mathrm{g}}} = \frac{\left|\sigma_{\mathrm{g}}^{\mathrm{PP}} - \overline{\sigma_{\mathrm{g}}}\right|}{\overline{\sigma_{\mathrm{g}}}}\,. \tag{D.10}$$

The MC values $\overline{N}$, $\overline{d_{\mathrm{g}}}$ and $\overline{\sigma_{\mathrm{g}}}$ are defined in Eq. (D.3), their pivot point counterparts in Eq. (D.8) and (D.9).

[6] $P_{\mathrm{inv}} = 1 - (1 - P_{\mathrm{stat}})/2$ is used as input probability for the function `tinv`, which determines the value z^* for which $P_{\mathrm{inv}} = \int_{-\infty}^{z^*} f_{\mathrm{sT}}^{(\mathcal{N}_{\mathrm{sim}}-1)}(x)\,\mathrm{d}x$, which is used for one-tailed tests in contrast to the two-tailed test described with P_{stat} and Eq. (D.6).

Appendix E Algorithms for Condensation, Evaporation and Nucleation

"Every author of an ODE code wants to make it as easy as possible to use. At the same time the code must be able to solve typical problems. It is not easy to reconcile these goals."

Lawrence F. Shampine and Mark W. Reichelt introducing the Matlab ODE suite [241].

E.1 Growth and Evaporation

In the following a parallel implementation of the RK method for the solution of the system of ODEs given by Eq. (4.17) and Eq. (4.18) is shown. Sections E.1.1 and E.1.2 depict thereby the parallel implementation of the Runge Kutta (RK) 45 algorithm [242] as it is described for CPU application in [108].

If particle volumes become smaller than v_{G}, the corresponding particles are removed from the simulation. Section E.1.3 discusses a strategy for this removal which ensures the numerical stability of the RK algorithm. The explicit settings of the time step values for a simulation in combination of coagulation in the framework of operator splitting is discussed in section E.1.4.

E.1.1 Calculation of New Particle Volumes due to Growth and Evaporation

For each time step Δt_{RK} and particle i, the seven values $v_i^{\mathrm{RK},n}$ (with $n = 1 \dots 7$) are calculated (and stored in the main GPU memory for further computation) via:

$$v_i^{\mathrm{RK},n} = \Delta t_{\mathrm{RK}} \cdot G(v_i^{\mathrm{AP},n}, N_{\mathrm{G}}^{\mathrm{AP},n}, t + C_n^{\mathrm{T}} \cdot \Delta t_{\mathrm{RK}}) \,, \tag{E.1}$$

$$\text{with: } v_i^{\mathrm{AP},n} = v_i + \sum_{w=1}^{n-1} v_i^{\mathrm{RK},w} \cdot C_{n,w}^{\mathrm{RK}}, \quad \text{and} \quad N_{\mathrm{G}}^{\mathrm{AP},n} = N_{\mathrm{G}} + \sum_{w=1}^{n-1} N_{\mathrm{G}}^{\mathrm{RK},w} \cdot C_{n,w}^{\mathrm{RK}} \,.$$

The approximation values $v_i^{\mathrm{AP},n}$ and $N_{\mathrm{G}}^{\mathrm{AP},n}$ are discarded after the calculation of $v_i^{\mathrm{RK},n}$. For the calculation of $v_i^{\mathrm{RK},1}$ the initial volume is used ($v_i^{\mathrm{RK},1} = v_i$). Explicit values for $C_{n,w}^{\mathrm{RK}}$ are shown in Table E.1a.

The growth rate G is evaluated at the time $t + C_n^{\mathrm{T}} \cdot \Delta t$ the constants C_n^{T} are tabulated in Table E.1b.

The only change in the monomer results from growth (resp. evaporation), so that: $N_{\mathrm{G}}^{\mathrm{RK},n} = N_{\mathrm{G,growth}}^{\mathrm{RK},n}$, with:

$$N_{\mathrm{G,growth}}^{\mathrm{RK},n} = -\sum_{i=1}^{\mathcal{N}_{\mathrm{MC}}} W_i \cdot v_i^{\mathrm{RK},n} / v_{\mathrm{G}} \,. \tag{E.2}$$

The new resulting particle volume $v_i^{\mathrm{RK,new}}$ and the concentration in the gaseous phase $N_{\mathrm{G}}^{\mathrm{RK,new}}$ after Δt_{RK} is calculated by:

$$v_i^{\mathrm{RK,new}} = v_0 + \sum_{w=1}^{7} v_i^{\mathrm{RK},w} \cdot C_{7,w}^{\mathrm{RK}} \,, \quad N_{\mathrm{G}}^{\mathrm{RK,new}} = N_{\mathrm{G}} + \sum_{w=1}^{7} N_{\mathrm{G}}^{\mathrm{RK},w} \cdot C_{7,w}^{\mathrm{RK}} \,. \tag{E.3}$$

E.1.2 Calculation of the Next RK Time Step $\Delta t_{\mathrm{RK}}^{\mathrm{new}}$

The differences between the 4th order and the 5th order RK result $\Delta^{\mathrm{RK}} v_i$ for the particle volumes (and $\Delta^{\mathrm{RK}} N_{\mathrm{G}}$ for the concentration of gas molecules) are given by:

$$\Delta^{\mathrm{RK}} v_i = \left| \sum_{w=1}^{7} v_i^{\mathrm{RK},w} \cdot C_w^{\mathrm{E}} \right|, \qquad \Delta^{\mathrm{RK}} N_{\mathrm{G}} = \left| \sum_{w=1}^{7} N_{\mathrm{G}}^{\mathrm{RK},w} \cdot C_w^{\mathrm{E}} \right| . \tag{E.4}$$

These differences ($\Delta^{\mathrm{RK}} v_i$ and $\Delta^{\mathrm{RK}} N_{\mathrm{G}}$) are put into perspective by comparison with the tolerances $\varepsilon_i^{\mathrm{v}}$ and ε^{G} defined as:

Table E.1: Values of constants used for RK calculations.

(a) Constants $C^{\mathrm{RK}}_{n,w}$ used for the n-th RK step (Eq. (E.1), (E.3) and (E.11)) and constants C^{E}_{w} for the error calculation in Eq. (E.4). Values as in [108].

Index w	$C^{\mathrm{RK}}_{2,w}$	$C^{\mathrm{RK}}_{3,w}$	$C^{\mathrm{RK}}_{4,w}$	$C^{\mathrm{RK}}_{5,w}$	$C^{\mathrm{RK}}_{6,w}$	$C^{\mathrm{RK}}_{7,w}$	C^{E}_{w}
1	$\frac{1}{5}$	$\frac{3}{40}$	$\frac{44}{45}$	$\frac{19372}{6561}$	$\frac{9017}{3168}$	$\frac{35}{384}$	$\frac{35}{384} - \frac{5179}{57600}$
2	0	$\frac{9}{40}$	$-\frac{56}{15}$	$-\frac{25360}{2187}$	$-\frac{355}{33}$	0	0
3	0	0	$\frac{32}{9}$	$\frac{64448}{6561}$	$\frac{46732}{5247}$	$\frac{500}{1113}$	$\frac{500}{1113} - \frac{7571}{16695}$
4	0	0	0	$-\frac{212}{729}$	$\frac{49}{716}$	$\frac{125}{192}$	$\frac{125}{192} - \frac{393}{640}$
5	0	0	0	0	$-\frac{5103}{18656}$	$-\frac{2187}{6784}$	$-\frac{2187}{6784} + \frac{92097}{339200}$
6	0	0	0	0	0	$\frac{11}{84}$	$\frac{11}{84} - \frac{187}{2100}$
7	0	0	0	0	0	0	$-\frac{1}{4}$

,

(b) Constants C^{T}_{n} used for time calculation at n-th RK step. Values as in [108].

C^{T}_{1}	C^{T}_{2}	C^{T}_{3}	C^{T}_{4}	C^{T}_{5}	C^{T}_{6}	C^{T}_{7}
0	$\frac{1}{5}$	$\frac{3}{10}$	$\frac{4}{5}$	$\frac{8}{9}$	1	1

(c) Constants $C^{\mathrm{I}}_{n,k}$ used for interpolation (Eq. (E.13) and (E.14)). Values as seen in the Matlab implementation, based on [243, 108].

Index k	$C^{\mathrm{I}}_{1,k}$	$C^{\mathrm{I}}_{2,k}$	$C^{\mathrm{I}}_{3,k}$	$C^{\mathrm{I}}_{4,k}$	$C^{\mathrm{I}}_{5,k}$	$C^{\mathrm{I}}_{6,k}$	$C^{\mathrm{I}}_{7,k}$
1	1	0	0	0	0	0	0
2	$-\frac{183}{64}$	0	$\frac{1500}{371}$	$-\frac{125}{32}$	$\frac{9477}{3392}$	$-\frac{11}{7}$	$\frac{3}{2}$
3	$\frac{37}{12}$	0	$-\frac{1000}{159}$	$\frac{125}{12}$	$-\frac{729}{106}$	$\frac{11}{3}$	-4
4	$-\frac{145}{128}$	0	$\frac{1000}{371}$	$-\frac{375}{64}$	$\frac{25515}{6784}$	$-\frac{55}{28}$	$\frac{5}{2}$

$$\varepsilon^{\mathrm{v}}_i = \varepsilon_{\mathrm{v,abs}} + \varepsilon_{\mathrm{v,rel}} \cdot \max(v_i, v_i^{\mathrm{RK,new}}), \qquad \varepsilon^{\mathrm{G}} = \varepsilon_{\mathrm{g,abs}} + \varepsilon_{\mathrm{g,rel}} \cdot \max(N_{\mathrm{G}}, N_{\mathrm{G}}^{\mathrm{RK,new}}) \,. \tag{E.5}$$

Table E.2 summarizes the constants used for the calculation of the discussed cases in this work.

Table E.2: Constants used as tolerances for RK error calculations.

$\varepsilon_{\mathrm{v,abs}}$ / m^3	$\varepsilon_{\mathrm{v,rel}}$ / –	$\varepsilon_{\mathrm{g,abs}}$ / m^{-3}	$\varepsilon_{\mathrm{g,rel}}$ / –
0	10^{-4}	10^{+12}	10^{-7}

The following measure $\mathcal{R}_{\mathrm{A}}$ is used for the assessment of the given error:

$$\mathcal{R}_{\mathrm{A}} = \max\left((\max_{\text{all } i} \Delta^{\mathrm{RK}} v_i / \varepsilon^{\mathrm{v}}_i), \Delta^{\mathrm{RK}} N_{\mathrm{G}} / \varepsilon^{\mathrm{G}} \right) . \tag{E.6}$$

The time step is rejected, if $\mathcal{R}_{\mathrm{A}} > 1$. In this case the new time step $\Delta t^{\mathrm{new}}_{\mathrm{RK}}$ is calculated with the help of the value of the error done in the last RK step, $\mathcal{R}_{\mathrm{L}}$:

$$\Delta t^{\mathrm{new}}_{\mathrm{RK}} = \Delta t_{\mathrm{RK}} \cdot (\mathcal{R}_{\mathrm{A}})^{-0.7/5} \cdot (\mathcal{R}_{\mathrm{L}})^{0.4/5} \,. \tag{E.7}$$

In the case of an accepted time step, the same formula is used for the calculation of the time value for the next RK step. The actual value of $\mathcal{R}_{\mathrm{A}}$ is stored for the next run (i.e. it is set: $\mathcal{R}_{\mathrm{L}} = \mathcal{R}_{\mathrm{A}}$).

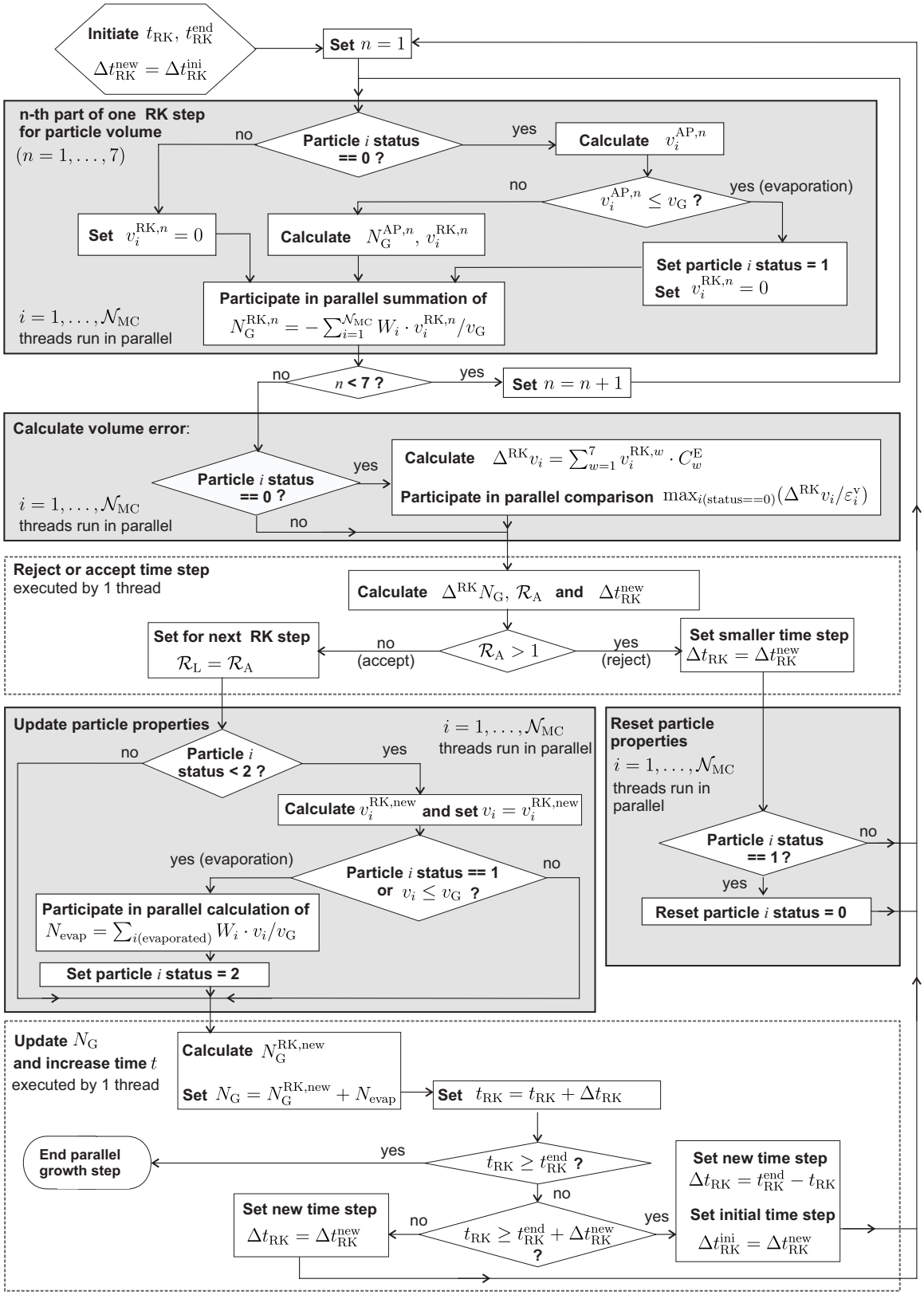

Figure E.1: Explicit formulas for the calculation of $v_i^{RK,n}$,$v_i^{AP,n}$ and $N_G^{AP,n}$ are shown in Eq. (E.1), $N_G^{RK,n}$ in Eq. (E.2), $v_i^{RK,new}$ and $N_G^{RK,new}$ in Eq. (E.3), $\Delta^{RK} v_i$ and $\Delta^{RK} N_G$ in Eq. (E.4), ε_i^Y in Eq. (E.5), $\mathcal{R}_A$ in Eq. (E.6) and t_{RK}^{new} in Eq. (E.7).

E.1.3 Treatment of Evaporation Events

For each particle, an additional variable stores the status of the particle. It can assume three different values:

- Particle status 0. The particle is active, its diameter larger than v_G, the growth equation for this particle is solved completely.
- Particle status 1. If during one of the n Rk steps, an intermediate value $v_i^{AP,n}$ with $v_i^{AP,n} < v_G$ is calculated, the particle status is 'marked' for evaporation. This ensures numerical stability - hence values smaller v_G are often negative and may have dramatic effects on the coupled growth terms - derailing the entire simulation.
    1. If the time step is rejected (i.e. the used value Δt_{RK} deemed to large), than the particle status is reset to 0.
    2. If the time step is accepted - the new resulting particle volume is calculated. And all the atoms (resp. molecules) forming the particle are moved to the gaseous phase - this is done by adding these via a parallel summation to the value N_{evap} and later to N_G and by marking the particle as evaporated (i.e. setting its status to 2).
- Particle status 2. The particle is evaporated and no coupling to the gaseous phase is simulated for this particle. A list is used to keep track of the indices of evaporated particles.
    1. Newly nucleated particles can be stored on the position of these evaporated particles without the application of merging routines. Simply by storing the particle properties at this position and setting the status back to 0.
    2. If there are particles with status 2 at the end of the entire RK step (i.e. if $t_{RK} = t_{RK}^{end}$, then particles with high concentration are selected and their properties copied onto the empty places (i.e. places with particle status =2) , the statistical weights are halved. This ensures that all $\mathcal{N}_{MC}$ particles are used for the (possible) following MC coagulation step.

The changing of the particle status allows thus the combination of discrete evaporation events with the application of the RK methodology for continuous growth and evaporation, as it is shown in Figure E.1.

E.1.4 Initialization of Simulation Times t_{RK}, t_{RK}^{end} and Time Step Δt_{RK}^{ini}

The situation in which the simulation time prior to the coagulation is t and the internal MC time step is $\Delta\tau_{MC}$ is considered. The initial settings for the RK time variable is: $t_{RK} = t$ and for the end time of the applied routine: $t_{RK}^{end} = t + \Delta\tau_{MC}$. The sketched RK-algorithm will perform several steps within one MC step, hence normally $\Delta\tau_{MC} \gg \Delta t_{RK}$. The last RK time step, $t_{RK}^{end} - t_{RK}$, is usually smaller than the RK time step according to the intrinsic RK error Δt_{RK}^{new}, defined in Eq. (E.7). Assuming, however, that the coagulation of one particle pair will lead to only slightly changes of the MC particle populations, the intrinsic error Δt_{RK}^{new} is far better suited as initial condition for the next RK time step, Δt_{RK}^{ini}, than the adjustment to reach the exact time value $t + \Delta\tau_{MC}$. The resetting of Δt_{RK}^{ini} during the last RK time step is also shown in Figure E.1. An appropriately small value for Δt_{RK}^{ini} has to be set for the first RK step. In the here presented test cases, $\Delta t_{RK}^{ini} = 10^{-12}$ s has been used.

E.2 Growth, Evaporation and Nucleation

The extension of the ODE system for growth and evaporation (in appendix E.1) to the coupled ODE system including nucleation (given by Eq. (4.17), Eq.(4.19) and (4.20)) in the framework of the RK 45 [242] algorithm is discussed in section E.2.1.

The introduction of a nucleation threshold $\mathcal{V}_T$ allows the control of the statistical weights of the MC particles which are inserted into the simulation and allows thus to simulate a variety of nucleation scenarios - as discussed in section 4.7.3.1. The numerical realization of this modeling makes the identification of the explicit nucleation time point t_{nuc} necessary. Hence (4.20) describes a monotonously growing function, the nucleation takes places if during one RK step, the following condition is registered:

$$\mathcal{V}_B(t) < \mathcal{V}_T \leq \mathcal{V}_B(t + \Delta t_{RK})\,. \tag{E.8}$$

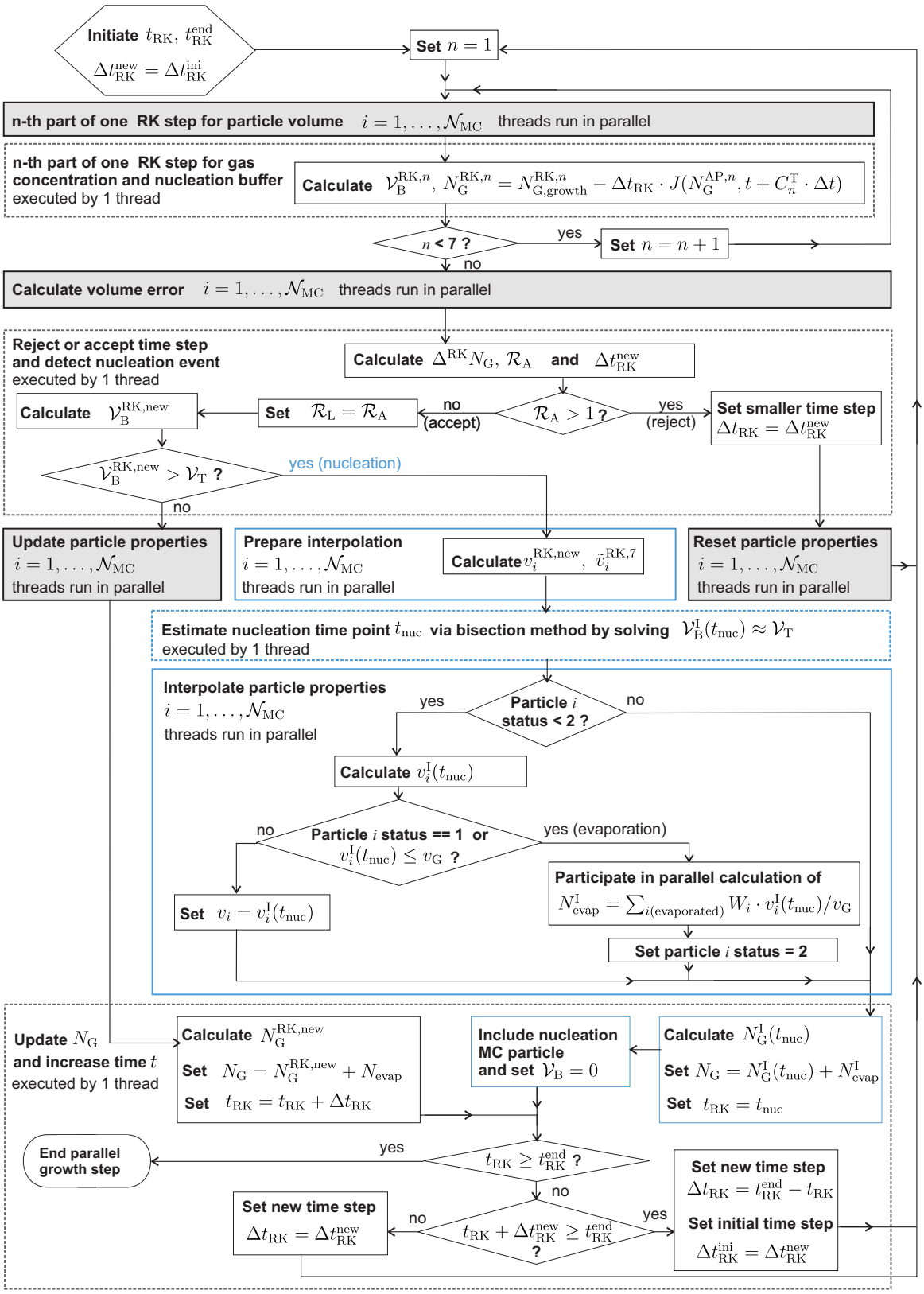

Figure E.2: Grey shaded parallel routines are the same as shown in more detail in Figure E.1. Explicit formulas for the calculation of $v_i^{\mathrm{RK},n}$,$v_i^{\mathrm{AP},n}$, $N_{\mathrm{G}}^{\mathrm{AP},n}$,$N_{\mathrm{G}}^{\mathrm{RK},n}$, $v_i^{\mathrm{RK,new}}$, $N_{\mathrm{G}}^{\mathrm{RK,new}}$, $\Delta^{\mathrm{RK}} v_i$, $\Delta^{\mathrm{RK}} N_{\mathrm{G}}$, $\mathcal{R}_{\mathrm{A}}$ and $t_{\mathrm{RK}}^{\mathrm{new}}$ are shown in Eq. (E.1) – (E.7).

In a naive approach, the MC particle with a statistical weight of $W_{\mathrm{nuc}} = \mathcal{V}_{\mathrm{B}}(t+\Delta t_{\mathrm{RK}})/(v^* + v_{\mathrm{G}})$ could be inserted into the simulation, without the search of the exact nucleation time point, t_{nuc}. Due to extremely high nucleation rates, this might result in values $\mathcal{V}_{\mathrm{B}}(t+\Delta t_{\mathrm{RK}})$ which are several orders of magnitude larger than $\mathcal{V}_{\mathrm{T}}$. In this scenario, the inserted particle weights, too, would differ in several orders of magnitude. W_{nuc} would then depend on factors, like the actual errors of the simulation defining the time step[7] in Eq. (E.7), or predefined time points (or simulation end times), for a result export to the CPU. Certain simulation conditions lead to the situation where resulting PSDs are more dependent on the preset simulation times for results export, and become independent on the values of $\mathcal{V}_{\mathrm{T}}$. This problem is avoided, if the exact nucleation time, t_{nuc} is used. The interpolation of the ODE system (given by Eq. (4.17), Eq.(4.19) and (4.20)) in the RK framework for a time t, with $t_{\mathrm{RK}} \leq t \leq t_{\mathrm{RK}} + \Delta t_{\mathrm{RK}}$, is termed dense output [108] and described in section E.2.2.

Figure E.2 shows the modifications (drawn in blue color) to the algorithm presented in section E.2.1 in order to incorporate the mechanism of nucleation. Novel particles are inserted into the simulation by means of the low weight merging technique es discussed in section 4.5.1.

E.2.1 Calculation of Gas Concentration N_{G} and Volume Concentration in Buffer $\mathcal{V}_{\mathrm{B}}$

The approximate values $v_i^{\mathrm{AP},n}$ and $N_{\mathrm{G}}^{\mathrm{AP},n}$ are used with the RK-coefficients for the volume approximation $v_i^{\mathrm{RK},n}$ as described in the section before in Eq. (E.1). The concentration depletion due to nucleation with a varying rate $J(N_{\mathrm{G}})$ is added to the growth equation (Eq. (E.2)):

$$N_{\mathrm{G}}^{\mathrm{RK},n} = -\sum_{i=1}^{\mathcal{N}_{\mathrm{MC}}} W_i \cdot v_i^{\mathrm{RK},n}/v_{\mathrm{G}} + \Delta t_{\mathrm{RK}} \cdot \left(\frac{\mathrm{d}N_{\mathrm{G}}}{\mathrm{d}t}\right)_{\mathrm{nuc}} (N_{\mathrm{G}}^{\mathrm{AP},n}, t + C_n^{\mathrm{T}} \cdot \Delta t) \tag{E.9}$$

$$= N_{\mathrm{G,growth}}^{\mathrm{RK},n} - \Delta t_{\mathrm{RK}} \cdot J(N_{\mathrm{G}}^{\mathrm{AP},n}, t + C_n^{\mathrm{T}} \cdot \Delta t)\,. \tag{E.10}$$

The volume concentration increase in the buffer for nucleating MC particles is calculated by:

$$\mathcal{V}_{\mathrm{B}}^{\mathrm{RK},n} = +\Delta t_{\mathrm{RK}} \cdot J(N_{\mathrm{G}}^{\mathrm{AP},n}, t + C_n^{\mathrm{T}} \cdot \Delta t) \cdot v_{\mathrm{nuc}}(N_{\mathrm{G}}^{\mathrm{AP},n}, t + C_n^{\mathrm{T}} \cdot \Delta t)\,,$$

$$\mathcal{V}_{\mathrm{B}}^{\mathrm{RK,new}} = \mathcal{V}_{\mathrm{B}} + \sum_{w=1}^{7} \mathcal{V}_{\mathrm{B}}^{\mathrm{RK},w} \cdot C_{7,w}^{\mathrm{RK}}\,. \tag{E.11}$$

E.2.2 Interpolation (Dense Output)

For the evaluation of the new particle volume, $v_i^{(\mathrm{new})}$, only the first six evaluated volumes ($v_i^{\mathrm{RK},1}, \ldots, v_i^{\mathrm{RK},6}$) are used, the value $v_i^{\mathrm{RK},7}$ is only necessary for the error estimation and the evaluation of the next RK time step value. Once, both values are estimated, the $v_i^{\mathrm{RK},7}$ can be overwritten by the values needed by the dense output routine for the evaluation of the exact event time point. (The $v_i^{\mathrm{RK},2}$ are also not used and could be overwritten at this stage of the simulation). The $v_i^{\mathrm{RK},7}$ are reset to $\tilde{v}_i^{\mathrm{RK},7}$ (in the prepare dense output routine):

$$\tilde{v}_i^{\mathrm{RK},7} = \Delta t_{\mathrm{RK}} \cdot G(v_i^{\mathrm{RK,new}}, N_{\mathrm{G}}^{\mathrm{RK,new}}, t + \Delta t_{\mathrm{RK}}), \quad \tilde{v}_i^{\mathrm{RK},n} = v_i^{\mathrm{RK},n}\,, \text{ if } n < 7\,. \tag{E.12}$$

For the calculation of the volume v_i of the particle i at the time t, with $t_{\mathrm{RK}} \leq t \leq t_{\mathrm{RK}} + \Delta t_{\mathrm{RK}}$, the following formula is used:

$$v_i^{\mathrm{I}}(t) = \sum_{n=1}^{7}\sum_{k=1}^{4} \tilde{v}_i^{\mathrm{RK},n} \cdot \theta^k \cdot C_{n,k}^{\mathrm{I}}, \qquad \text{with: } \theta = \frac{t - t_{\mathrm{RK}}}{\Delta t_{\mathrm{RK}}} \in [0,1]\,. \tag{E.13}$$

Analogously:

$$N_{\mathrm{G}}^{\mathrm{I}}(t) = \sum_{n=1}^{7}\sum_{k=1}^{4} \tilde{N}_{\mathrm{G}}^{\mathrm{RK},n} \cdot \theta^k \cdot C_{n,k}^{\mathrm{I}} \quad \text{and:} \quad \mathcal{V}_{\mathrm{B}}^{\mathrm{I}}(t) = \sum_{n=1}^{7}\sum_{k=1}^{4} \tilde{\mathcal{V}}_{\mathrm{B}}^{\mathrm{RK},n} \cdot \theta^k \cdot C_{n,k}^{\mathrm{I}}\,, \tag{E.14}$$

[7] Especially the simulation scenario without background particle populations allows for very large time steps.

with

$$\tilde{N}_{\mathrm{G}}^{\mathrm{RK},7} = -\sum_{i=1}^{\mathcal{N}_{\mathrm{MC}}} W_i \cdot \tilde{v}_i^{\mathrm{RK},7}/v_{\mathrm{G}} - \Delta t_{\mathrm{RK}} \cdot J(N_{\mathrm{G}}^{\mathrm{RK,new}}, t_{\mathrm{RK}} + \Delta t_{\mathrm{RK}})\,, \tag{E.15}$$

$$\tilde{\mathcal{V}}_{\mathrm{B}}^{\mathrm{RK},7} = \Delta t_{\mathrm{RK}} \cdot J(N_{\mathrm{G}}^{\mathrm{RK,new}}, t_{\mathrm{RK}} + \Delta t_{\mathrm{RK}}) \cdot v_{\mathrm{nuc}}(N_{\mathrm{G}}^{\mathrm{RK,new}}, t_{\mathrm{RK}} + \Delta t_{\mathrm{RK}})\,, \tag{E.16}$$

$$\tilde{N}_{\mathrm{G}}^{\mathrm{RK},n} = N_{\mathrm{G}}^{\mathrm{RK},n}, \quad \tilde{\mathcal{V}}_{\mathrm{B}}^{\mathrm{RK},n} = \mathcal{V}_{\mathrm{B}}^{\mathrm{RK},n}\,, \text{ for } n < 7\,. \tag{E.17}$$

Bibliography

Own Publications Included in this Thesis

[Paper I] G. Kotalczyk and F. E. Kruis. "A Monte Carlo method for the simulation of coagulation and nucleation based on weighted particles and the concepts of stochastic resolution and merging". *Journal of Computational Physics* 340 (2017), pp. 276–296. DOI: 10.1016/j.jcp.2017.03.041. See page 93.

[Paper II] G. Kotalczyk and F. E. Kruis. "Fractional Monte Carlo time steps for the simulation of coagulation for parallelized flowsheet simulations". *Chemical Engineering Research and Design* 136 (2018), pp. 71–82. DOI: 10.1016/j.cherd.2018.04.046. See page 115.

[Paper III] G. Kotalczyk, J. Devi, and F. E. Kruis. "A time-driven constant-number Monte Carlo method for the GPU-simulation of particle breakage based on weighted simulation particles". *Powder Technology* 317 (2017), pp. 417–429. DOI: 10.1016/j.powtec.2017.05.002. See page 129.

[Paper IV] G. Kotalczyk, I. Skenderović, and F. E. Kruis. "Monte Carlo simulations of homogeneous nucleation and particle growth in the presence of background particles". *Tellus, Series B: Chemical and Physical Meteorology* 71.1 (2019), pp. 1–10. DOI: 10.1080/16000889.2018.1554415. See page 143.

[Paper V] G. Kotalczyk and F. E. Kruis. "Compartmental Population Balances by Means of Monte Carlo Methods". In: *Dynamic Flowsheet Simulation of Solids Processes*. Ed. by S. Heinrich. Cham: Springer International Publishing, 2020, pp. 519–548. ISBN: 978-3-030-45168-4. See page 155.

[Paper VI] G. Kotalczyk, I. Skenderović, and F. E. Kruis. "Modeling of Particle Formation in Arc Discharges by Monte-Carlo Based Population Balance Modeling". *MRS Advances* 148 (2017), pp. 1–8. DOI: 10.1557/adv.2017.155. See page 187.

[Paper VII] G. Kotalczyk, I. Skenderović, and F. E. Kruis. "A GPU-based monte carlo technique for the simulation of simultaneous nucleation, coagulation and growth based on weighted simulation particles". In: *AIChE annual meeting (2016)*. ISBN: 978-151083444-6. See page 197.

[Paper VIII] G. Kotalczyk, K. Lambach, and F. E. Kruis. "Parallel GPU-based monte carlo techniques for the flow-sheet simulation of solid processes". In: *8th World Congress on Particle Technology (2018)*. ISBN: 978-151086969-1. See page 205.

Own Publications not Included in this Thesis

[CoPaper I] J. Devi, G. Kotalczyk, and F. E. Kruis. "Accuracy control in Monte Carlo simulations of particle breakage". *International Journal of Modelling, Identification and Control* 31.3 (2019), pp. 278–291. DOI: 10.1504/IJMIC.2019.098774

[CoPaper II] I. Skenderović, G. Kotalczyk, and F. E. Kruis. "Dual Population Balance Monte Carlo simulation of particle synthesis by flame spray pyrolysis". *Processes* 6.12 (2018). DOI: 10.3390/pr6120253

Other Publications

[1] Aspen Technology Inc. *Aspen Plus product webpage*. 2022. URL: https://www.aspentech.com/en/products/engineering/aspen-plus (visited on June 1, 2022).

[2] CAPE OPEN Laboratories Network. *The CAPE-OPEN Standard*. 2022. URL: http://www.colan.org/general-information-on-co-lan/ (visited on June 2, 2022).

[3] R. Schefflan. *Teach yourself the basics of Aspen plus*. Hoboken, N.J.: Wiley, 2011. ISBN: 978-1-119-27618-0.

[4] Chemstations Inc. *CHEMCAD product webpage*. 2022. URL: https://www.chemstations.com/CHEMCAD/ (visited on June 2, 2022).

[5] *Software architectures and tools for computer aided process engineering*. Vol. 11. Computer-aided chemical engineering. Amsterdam: Elsevier, 2002. ISBN: 9780080541365.

[6] I. T. Cameron et al. "Process systems modelling and applications in granulation: A review". *Chemical Engineering Science* 60.14 (2005), pp. 3723–3750. DOI: 10.1016/j.ces.2005.02.004.

[7] A. Braumann et al. "Modelling and validation of granulation with heterogeneous binder dispersion and chemical reaction". *Chemical Engineering Science* 62.17 (2007), pp. 4717–4728. DOI: 10.1016/j.ces.2007.05.028.

[8] H. Kruggel-Emden and F. Elskamp. "Modeling of screening processes with the discrete element method involving non-spherical particles". *Chemical Engineering and Technology* 37.5 (2014), pp. 847–856. DOI: 10.1002/ceat.201300649.

[9] M. Kraft. "Modelling of particulate processes". *KONA Powder and Particle Journal* 23 (2005), pp. 18–35. DOI: 10.14356/kona.2005007.

[10] M. L. Eggersdorfer and S. E. Pratsinis. "Agglomerates and aggregates of nanoparticles made in the gas phase". *Advanced Powder Technology* 25.1 (2014), pp. 71–90. DOI: 10.1016/j.apt.2013.10.010.

[11] V. Skorych et al. "Novel system for dynamic flowsheet simulation of solids processes". *Powder Technology* 314 (2017), pp. 665–679. DOI: 10.1016/j.powtec.2017.01.061.

[12] M. Dosta, J. D. Litster, and S. Heinrich. "Flowsheet simulation of solids processes: Current status and future trends". *Advanced Powder Technology* 31.3 (2020), pp. 947–953. DOI: 10.1016/j.apt.2019.12.015.

[13] J. Litster and I. D. L. Bogle. "Smart Process Manufacturing for Formulated Products". *Engineering* 5.6 (2019), pp. 1003–1009. DOI: 10.1016/j.eng.2019.02.014.

[14] J. Werther et al. "The ultimate goal of modeling - Simulation of system and plant performance". *Particuology* 9.4 (2011), pp. 320–329. DOI: 10.1016/j.partic.2011.03.006.

[15] W. L. McCabe, J. C. Smith, and P. Harriot. *Unit operations of chemical engineering*. 5. ed., internat. ed. McGraw-Hill chemical engineering series. New York: McGraw-Hill, 1993. ISBN: 978-0070448445.

[16] E. Ortega-Rivas. *Unit operations of particulate solids: Theory and practice*. Boca Raton, Fla: CRC Press, 2012. ISBN: 9781439849071.

[17] H. Rumpf. *Mechanische Verfahrenstechnik*. München: Hanser, 1975. ISBN: 3446119876.

[18] J. Litster. *Design and processing of particulate products*. Cambridge series in chemical engineering. Cambridge: Cambridge University Press, 2016. ISBN: 9781139017558.

[19] M. Dosta, S. Antonyuk, and S. Heinrich. "Multiscale simulation of agglomerate breakage in fluidized beds". *Industrial and Engineering Chemistry Research* 52.33 (2013), pp. 11275–11281. DOI: 10.1021/ie400244x.

[20] A. Khadilkar, P. L. Rozelle, and S. V. Pisupati. "Models of agglomerate growth in fluidized bed reactors: Critical review, status and applications". *Powder Technology* 264 (2014), pp. 216–228. DOI: 10.1016/j.powtec.2014.04.063.

[21] S. M. Iveson et al. "Nucleation, growth and breakage phenomena in agitated wet granulation processes: A review". *Powder Technology* 117.1-2 (2001), pp. 3–39. DOI: 10.1016/S0032-5910(01)00313-8.

[22] M. Sommer et al. "Agglomeration and breakage of nanoparticles in stirred media mills - A comparison of different methods and models". *Chemical Engineering Science* 61.1 (2006), pp. 135–148. DOI: 10.1016/j.ces.2004.12.057.

[23] J. Bałdyga and J. R. Bourne. *Turbulent mixing and chemical reactions*. Chichester and Weinheim: Wiley, 1999. ISBN: 9780471981718.

[24] L. Metzger. *Process simulation of technical precipitation processes (Dissertation)*. Karlsruhe: KIT Scientific Publishing, 2018. ISBN: 9783731507352.

[25] D. Ramkrishna and M. R. Singh. "Population balance modeling: Current status and future prospects". *Annual Review of Chemical and Biomolecular Engineering* 5 (2014), pp. 123–146. DOI: 10.1146/annurev-chembioeng-060713-040241.

[26] J. Makino et al. "On the mass distribution of planetesimals in the early runaway stage". *New Astronomy* 3.7 (1998), pp. 411–417. DOI: 10.1016/S1384-1076(98)00021-9.

[27] H. Tanaka, S. Inaba, and K. Nakazawa. "Steady-state size distribution for the self-similar collision cascade". *Icarus* 123.2 (1996), pp. 450–455. DOI: 10.1006/icar.1996.0170.

[28] E. Sherer et al. "Estimation of likely cancer cure using first- and second-order product densities of population balance models". *Annals of Biomedical Engineering* 35.6 (2007), pp. 903–915. DOI: 10.1007/s10439-007-9310-1.

[29] N. V. Mantzaris, P. Daoutidis, and F. Srienc. "Numerical solution of multi-variable cell population balance models: I. Finite difference methods". *Computers and Chemical Engineering* 25.11-12 (2001), pp. 1411–1440. DOI: 10.1016/S0098-1354(01)00709-8.

[30] M. Karl et al. "A study of new particle formation in the marine boundary layer over the central Arctic Ocean using a flexible multicomponent aerosol dynamic model". *Tellus, Series B: Chemical and Physical Meteorology* 64.1 (2012). DOI: 10.3402/tellusb.v64i0.17158.

[31] T. Olenius and I. Riipinen. "Molecular-resolution simulations of new particle formation: Evaluation of common assumptions made in describing nucleation in aerosol dynamics models". *Aerosol Science and Technology* 51.4 (2016), pp. 397–408. DOI: 10.1080/02786826.2016.1262530.

[32] B. J. Lee et al. "A two-class population balance equation yielding bimodal flocculation of marine or estuarine sediments". *Water research* 45.5 (2011), pp. 2131–2145. DOI: 10.1016/j.watres.2010.12.028.

[33] X. Shen et al. "A tri-modal flocculation model coupled with TELEMAC for estuarine muds both in the laboratory and in the field". *Water research* 145 (2018), pp. 473–486. DOI: 10.1016/j.watres.2018.08.062.

[34] M. Kuhn, C. Kirse, and H. Briesen. "Population balance modeling and opinion dynamics-A mutually beneficial liaison?" *Processes* 6.9 (2018). DOI: 10.3390/pr6090164.

[35] S. Hennart et al. "Characterization and modeling of a sub-micron milling process limited by agglomeration phenomena". *Chemical Engineering Science* 71 (2012), pp. 484–495. DOI: 10.1016/j.ces.2011.11.010.

[36] F. Wang et al. "Kinetics and mechanisms of aggregative nanocrystal growth". *Chemistry of Materials* 26.1 (2014), pp. 5–21. DOI: 10.1021/cm402139r.

[37] H.-C. Schwarzer et al. "Predictive simulation of nanoparticle precipitation based on the population balance equation". *Chemical Engineering Science* 61.1 (2006), pp. 167–181. DOI: 10.1016/j.ces.2004.11.064.

[38] A. Gerstlauer et al. "Development, analysis and validation of population models for continuous and batch crystallizers". *Chemical Engineering Science* 57.20 (2002), pp. 4311–4327. DOI: 10.1016/S0009-2509(02)00348-2.

[39] P. Seydel, J. Blömer, and J. Bertling. "Modeling Particle Formation at Spray Drying Using Population Balances". *Drying Technology* 24.2 (2006), pp. 137–146. DOI: 10.1080/07373930600558912.

[40] X. Hao et al. "Population balance-Monte Carlo simulation for gas-to-particle synthesis of nanoparticles". *Aerosol Science and Technology* 47.10 (2013), pp. 1125–1133. DOI: 10.1080/02786826.2013.823642.

[41] M. Peglow et al. "A generic population balance model for simultaneous agglomeration and drying in fluidized beds". *Chemical Engineering Science* 62.1-2 (2007), pp. 513–532. DOI: 10.1016/j.ces.2006.09.042.

[42] D. Ramkrishna. *Population balances: Theory and applications to particulate systems in engineering*. 1st ed. New York: Academic Press, 2000. ISBN: 9780125769709.

[43] A. Kumar et al. "Model-based analysis of high shear wet granulation from batch to continuous processes in pharmaceutical production–a critical review". *European journal of pharmaceutics and biopharmaceutics* 85.3 Part B (2013), pp. 814–832. DOI: 10.1016/j.ejpb.2013.09.013.

[44] S. K. Friedlander. *Smoke, dust, and haze: Fundamentals of aerosol dynamics*. 2. ed. Topics in chemical engineering. New York: Oxford Univ. Press, 2000. ISBN: 0195129997.

[45] J. H. Seinfeld and S. N. Pandis. *Atmospheric chemistry and physics: From air pollution to climate change*. 3. ed. Hoboken, NJ: Wiley, 2016. ISBN: 9781119221173.

[46] T. T. Kodas and M. J. Hampden-Smith. *Aerosol processing of materials*. New York, NY: Wiley-VCH, 1999. ISBN: 0471246697.

[47] R. M. Ziff and E. D. McGrady. "The kinetics of cluster fragmentation and depolymerisation". *Journal of Physics A: Mathematical and General* 18.15 (1985), pp. 3027–3037. DOI: 10.1088/0305-4470/18/15/026.

[48] W. G. Courtney. "Remarks on Homogeneous Nucleation". *The Journal of Chemical Physics* 35.6 (1961), pp. 2249–2250. DOI: 10.1063/1.1732252.

[49] R. Becker and W. Döring. "Kinetische Behandlung der Keimbildung in Übersättigten Dämpfen". *Annalen der Physik* 416.8 (1935), pp. 719–752. DOI: 10.1002/andp.19354160806.

[50] S. L. Girshick and C.-P. Chiu. "Kinetic nucleation theory: A new expression for the rate of homogeneous nucleation from an ideal supersaturated vapor". *The Journal of Chemical Physics* 93.2 (1990), pp. 1273–1277. DOI: 10.1063/1.459191.

[51] T. Nieminen, K. E. J. Lehtinen, and M. Kulmala. "Sub-10 nm particle growth by vapor condensation – effects of vapor molecule size and particle thermal speed". *Atmospheric Chemistry and Physics* 10.20 (2010), pp. 9773–9779. DOI: 10.5194/acp-10-9773-2010.

[52] M. Kostoglou, S. Dovas, and A. J. Karabelas. "On the steady-state size distribution of dispersions in breakage processes". *Chemical Engineering Science* 52.8 (1997), pp. 1285–1299. DOI: 10.1016/S0009-2509(96)00488-5.

[53] C. L. Prasher. *Crushing and grinding process handbook*. Chichester: Wiley, 1987. ISBN: 978-0-471105350.

[54] B. E. Wyslouzil and J. Wölk. "Overview: Homogeneous nucleation from the vapor phase - The experimental science". *Journal of Chemical Physics* 145.21 (2016). DOI: 10.1063/1.4962283.

[55] E. J. Davis. "A history and state-of-the-art of accommodation coefficients". *Atmospheric Research* 82.3-4 (2006), pp. 561–578. DOI: 10.1016/j.atmosres.2006.02.013.

[56] R. I. Jeldres, P. D. Fawell, and B. J. Florio. "Population balance modelling to describe the particle aggregation process: A review". *Powder Technology* 326 (2018), pp. 190–207. DOI: 10.1016/j.powtec.2017.12.033.

[57] M. J. Hounslow. "The population balance as a tool for understanding particle rate processes". *KONA Powder and Particle Journal* 16 (1998), pp. 179–193. DOI: 10.14356/kona.1998021.

[58] M. Kostoglou and A. J. Karabelas. "A contribution towards predicting the evolution of droplet size distribution in flowing dilute liquid/liquid dispersions". *Chemical Engineering Science* 56.14 (2001), pp. 4283–4292. DOI: 10.1016/S0009-2509(01)00108-7.

[59] A. W. Mahoney, F. J. Doyle III, and D. Ramkrishna. "Inverse problems in population balances: Growth and nucleation from dynamic data". *AIChE Journal* 48.5 (2002), pp. 981–990. DOI: 10.1002/aic.690480508.

[60] E. Goudeli, M. L. Eggersdorfer, and S. E. Pratsinis. "Coagulation-agglomeration of fractal-like particles: Structure and self-preserving size distribution". *Langmuir* 31.4 (2015), pp. 1320–1327. DOI: 10.1021/la504296z.

[61] E. Goudeli, M. L. Eggersdorfer, and S. E. Pratsinis. "Coagulation of Agglomerates Consisting of Polydisperse Primary Particles". *Langmuir* 32.36 (2016), pp. 9276–9285. DOI: 10.1021/acs.langmuir.6b02455.

[62] K. Terrazas-Velarde, M. Peglow, and E. Tsotsas. "Stochastic simulation of agglomerate formation in fluidized bed spray drying: A micro-scale approach: Chemical Engineering Science". 64.11 (2009), pp. 2631–2643. DOI: 10.1016/j.ces.2009.02.041.

[63] A. Braumann, P. L. W. Man, and M. Kraft. "Statistical Approximation of the Inverse Problem in Multivariate Population Balance Modeling". *Industrial and Engineering Chemistry Research* 49.1 (2010), pp. 428–438. DOI: 10.1021/ie901230u.

[64] M. Haderlein et al. "FIMOR: An efficient simulation for ZnO quantum dot ripening applied to the optimization of nanoparticle synthesis". *Chemical Engineering Journal* 260 (2015), pp. 706–715. DOI: 10.1016/j.cej.2014.09.040.

[65] C. Kiparissides. "Challenges in particulate polymerization reactor modeling and optimization: A population balance perspective". *Journal of Process Control* 16.3 (2006), pp. 205–224. DOI: 10.1016/j.jprocont.2005.06.004.

[66] F. Sporleder et al. "On the population balance equation". *Reviews in Chemical Engineering* 28.2-3 (2012), pp. 149–169. DOI: 10.1515/revce-2011-0013.

[67] S. Rjasanow, T. Schreiber, and W. Wagner. "Reduction of the Number of Particles in the Stochastic Weighted Particle Method for the Boltzmann Equation". *Journal of Computational Physics* 145.1 (1998), pp. 382–405. DOI: 10.1006/jcph.1998.6018.

[68] S. Rjasanow and W. Wagner. "A stochastic weighted particle method for the Boltzmann equation". *Journal of Computational Physics* 124.2 (1996), pp. 243–253. DOI: 10.1006/jcph.1996.0057.

[69] S. Rigopoulos. "Population balance modelling of polydispersed particles in reactive flows". *Progress in Energy and Combustion Science* 36.4 (2010), pp. 412–443. DOI: 10.1016/j.pecs.2009.12.001.

[70] H. Zhao and C. Zheng. "A population balance-Monte Carlo method for particle coagulation in spatially inhomogeneous systems". *Computers and Fluids* 71 (2013), pp. 196–207. DOI: 10.1016/j.compfluid.2012.09.025.

[71] J. Z. Wen et al. "An improved moving sectional aerosol model of soot formation in a plug flow reactor". *Combustion Science and Technology* 178.5 (2006), pp. 921–951. DOI: 10.1080/00102200500270007.

[72] M. Balthasar and M. Kraft. "A stochastic approach to calculate the particle size distribution function of soot particles in laminar premixed flames". *Combustion and Flame* 133.3 (2003), pp. 289–298. DOI: 10.1016/S0010-2180(03)00003-8.

[73] A. J. Pesthy, R. C. Flagan, and J. H. Seinfeld. "Theory of aerosol formation and growth in laminar flow". *Journal of Colloid and Interface Science* 91.2 (1983), pp. 525–545. DOI: 10.1016/0021-9797(83)90367-3.

[74] H. Rehage, S. Scherer, and M. Kind. "A steady-state precipitation model for flowsheet simulation and its application". *Computers and Chemical Engineering* 128 (2019), pp. 524–537. DOI: 10.1016/j.compchemeng.2019.06.030.

[75] J. Sanyal et al. "On the comparison between population balance models for CFD simulation of bubble columns". *Industrial and Engineering Chemistry Research* 44.14 (2005), pp. 5063–5072. DOI: 10.1021/ie049555j.

[76] J. Cheng et al. "Simulation of antisolvent crystallization in impinging jets with coupled multiphase flow-micromixing-PBE". *Chemical Engineering Science* 171 (2017), pp. 500–512. DOI: 10.1016/j.ces.2017.06.011.

[77] M. R. Bhole, J. B. Joshi, and D. Ramkrishna. "CFD simulation of bubble columns incorporating population balance modeling". *Chemical Engineering Science* 63.8 (2008), pp. 2267–2282. DOI: 10.1016/j.ces.2008.01.013.

[78] S. Schütz, G. Gorbach, and M. Piesche. "Modeling fluid behavior and droplet interactions during liquid–liquid separation in hydrocyclones". *Chemical Engineering Science* 64.18 (2009), pp. 3935–3952. DOI: 10.1016/j.ces.2009.04.046.

[79] K. F. Lee et al. “Stochastic weighted particle methods for population balance equations with coagulation, fragmentation and spatial inhomogeneity”. *Journal of Computational Physics* 303 (2015), pp. 1–18. DOI: 10.1016/j.jcp.2015.09.031.

[80] A. D. McGuire et al. “A high-dimensional, stochastic model for twin-screw granulation Part 2: Numerical methodology”. *Chemical Engineering Science* 188 (2018), pp. 18–33. DOI: 10.1016/j.ces.2018.04.077.

[81] A. H. Alexopoulos, D. Maggioris, and C. Kiparissides. “CFD analysis of turbulence non-homogeneity in mixing vessels a two-compartment model”. *Chemical Engineering Science* 57.10 (2002), pp. 1735–1752. DOI: 10.1016/S0009-2509(02)00053-2.

[82] F. Bezzo, S. Macchietto, and C. C. Pantelides. “General hybrid multizonal/CFD approach for bioreactor modeling”. *AIChE Journal* 49.8 (2003), pp. 2133–2148. DOI: 10.1002/aic.690490821.

[83] R. Irizarry. “Fast compartmental Monte Carlo simulation of population balance models: Application to nanoparticle formation in nonhomogeneous conditions”. *Industrial and Engineering Chemistry Research* 51.47 (2012), pp. 15484–15496. DOI: 10.1021/ie3011116.

[84] A. Boje et al. “Detailed population balance modelling of TiO2 synthesis in an industrial reactor”. *Chemical Engineering Science* 164 (2017), pp. 219–231. DOI: 10.1016/j.ces.2017.02.019.

[85] M. Dosta, S. Heinrich, and J. Werther. “Fluidized bed spray granulation: Analysis of the system behaviour by means of dynamic flowsheet simulation”. *Powder Technology* 204.1 (2010), pp. 71–82. DOI: 10.1016/j.powtec.2010.07.018.

[86] E.-U. Hartge et al. “Flowsheet Simulation of Solids Processes”. *KONA Powder and Particle Journal* 24 (2006), pp. 146–158. DOI: 10.14356/kona.2006017.

[87] B. Szilágyi and Z. K. Nagy. “Population Balance Modeling and Optimization of an Integrated Batch Crystallizer–Wet Mill System for Crystal Size Distribution Control”. *Crystal Growth & Design* 18.3 (2018), pp. 1415–1424. DOI: 10.1021/acs.cgd.7b01331.

[88] M. v. Smoluchowski. “Versuch einer mathematischen Theorie der Koagulationskinetik kolloider Lösungen”. *Zeitschrift fuer physikalische Chemie* 92 (1917), pp. 129–168.

[89] F. E. Kruis, A. Maisels, and H. Fissan. “Direct simulation Monte Carlo method for particle coagulation and aggregation”. *AIChE Journal* 46.9 (2000), pp. 1735–1742. DOI: 10.1002/aic.690460905.

[90] J. Kumar et al. “Improved accuracy and convergence of discretized population balance for aggregation: The cell average technique”. *Chemical Engineering Science* 61.10 (2006), pp. 3327–3342. DOI: 10.1016/j.ces.2005.12.014.

[91] Z. A. Melzak. “the effect of coalescence in certain collision processes”. *Quarterly of Applied Mathematics* 11.2 (1953), pp. 231–234.

[92] J. L. Spouge. “Solutions and critical times for the monodisperse coagulation equation when aij=A + B(i + j) + Cij”. *Journal of Physics A: General Physics* 16.4 (1983), pp. 767–773. DOI: 10.1088/0305-4470/16/4/014.

[93] D. P. Patil and J. Andrews. “An analytical solution to continuous population balance model describing floc coalescence and breakage — A special case”. *Chemical Engineering Science* 53.3 (1998), pp. 599–601. DOI: 10.1016/S0009-2509(97)00314-X.

[94] P. Lage. “Comments on the "An analytical solution to the population balance equation with coalescence and breakage-the special case with constant number of particles" by D.P. Patil and J.R.G. Andrews [Chemical Engineering Science 53(3) 599-601]”. *Chemical Engineering Science* 57.19 (2002), pp. 4253–4254. DOI: 10.1016/S0009-2509(02)00369-X.

[95] B. J. J. McCoy and G. Madras. “Analytical solution for a population balance equation with aggregation and fragmentation”. *Chemical Engineering Science* 58.13 (2003), pp. 3049–3051. DOI: 10.1016/S0009-2509(03)00159-3.

[96] E. D. McGrady and R. M. Ziff. “Analytical solutions to fragmentation equations with flow”. *AIChE Journal* 34.12 (1988), pp. 2073–2076. DOI: 10.1002/aic.690341218.

[97] S. Kumar and D. Ramkrishna. "On the solution of population balance equations by discretization - III. Nucleation, growth and aggregation of particles". *Chemical Engineering Science* 52.24 (1997), pp. 4659–4679. DOI: 10.1016/S0009-2509(97)00307-2.

[98] T. E. Ramabhadran, T. W. Peterson, and J. H. Seinfeld. "Dynamics of aerosol coagulation and condensation". *AIChE Journal* 22.5 (1976), pp. 840–851. DOI: 10.1002/aic.690220505.

[99] H. M. Hulburt and S. Katz. "Some problems in particle technology. A statistical mechanical formulation". *Chemical Engineering Science* 19.8 (1964), pp. 555–574. DOI: 10.1016/0009-2509(64)85047-8.

[100] A. D. Randolph. "A population balance for countable entities". *The Canadian Journal of Chemical Engineering* 42.6 (1964), pp. 280–281. DOI: 10.1002/cjce.5450420612.

[101] A. G. Fredrickson, D. Ramkrishna, and H. M. Tsuchiya. "Statistics and dynamics of procaryotic cell populations". *Mathematical Biosciences* 1.3 (1967), pp. 327–374. DOI: 10.1016/0025-5564(67)90008-9.

[102] K. W. Lee. "Change of particle size distribution during Brownian coagulation". *Journal of Colloid and Interface Science* 92.2 (1983), pp. 315–325. DOI: 10.1016/0021-9797(83)90153-4.

[103] L. Müller, A. Klar, and F. Schneider. "A numerical comparison of the method of moments for the population balance equation". *Mathematics and Computers in Simulation* 165 (2019), pp. 26–55. DOI: 10.1016/j.matcom.2019.02.020.

[104] S. E. Pratsinis. "Simultaneous nucleation, condensation, and coagulation in aerosol reactors". *Journal of Colloid and Interface Science* 124.2 (1988), pp. 416–427. DOI: 10.1016/0021-9797(88)90180-4.

[105] F. E. Kruis et al. "A Simple Model for the Evolution of the Characteristics of Aggregate Particles Undergoing Coagulation and Sintering". *Aerosol Science and Technology* 19.4 (1993), pp. 514–526. DOI: 10.1080/02786829308959656.

[106] R. McGraw. "Description of Aerosol Dynamics by the Quadrature Method of Moments". *Aerosol Science and Technology* 27.2 (1997), pp. 255–265. DOI: 10.1080/02786829708965471.

[107] D. L. Marchisio, R. D. Vigil, and R. O. Fox. "Quadrature method of moments for aggregation-breakage processes". *Journal of Colloid and Interface Science* 258.2 (2003), pp. 322–334. DOI: 10.1016/S0021-9797(02)00054-1.

[108] W. H. Press. *Numerical recipes: The art of scientific computing*. 3. ed. Cambridge: Cambridge University Press, 2007. ISBN: 9780521880688.

[109] D. L. Marchisio and R. O. Fox. "Solution of population balance equations using the direct quadrature method of moments". *Journal of Aerosol Science* 36.1 (2005), pp. 43–73. DOI: 10.1016/j.jaerosci.2004.07.009.

[110] A. Zucca et al. "Validation of bivariate DQMOM for nanoparticle processes simulation". *AIChE Journal* 53.4 (2007), pp. 918–931. DOI: 10.1002/aic.11125.

[111] R. O. Fox. "Optimal Moment Sets for Multivariate Direct Quadrature Method of Moments". *Industrial and Engineering Chemistry Research* 48.21 (2009), pp. 9686–9696. DOI: 10.1021/ie801316d.

[112] A. Buffo, M. Vanni, and D. L. Marchisio. "Multidimensional population balance model for the simulation of turbulent gas–liquid systems in stirred tank reactors". *Chemical Engineering Science* 70 (2012), pp. 31–44. DOI: 10.1016/j.ces.2011.04.042.

[113] E. Gavi, D. L. Marchisio, and A. A. Barresi. "CFD modelling and scale-up of Confined Impinging Jet Reactors". *Chemical Engineering Science* 62.8 (2007), pp. 2228–2241. DOI: 10.1016/j.ces.2006.12.077.

[114] B. Selma, R. Bannari, and P. Proulx. "Simulation of bubbly flows: Comparison between direct quadrature method of moments (DQMOM) and method of classes (CM)". *Chemical Engineering Science* 65.6 (2010), pp. 1925–1941. DOI: 10.1016/j.ces.2009.11.018.

[115] J. Akroyd et al. "Numerical investigation of DQMoM-IEM as a turbulent reaction closure". *Chemical Engineering Science* 65.6 (2010), pp. 1915–1924. DOI: 10.1016/j.ces.2009.11.010.

[116] D. Li, Z. Li, and Z. Gao. "Quadrature-based moment methods for the population balance equation: An algorithm review". *Chinese Journal of Chemical Engineering* 27.3 (2019), pp. 483–500. DOI: 10.1016/j.cjche.2018.11.028.

[117] L. Mazzei. "Limitations of quadrature-based moment methods for modeling inhomogeneous polydisperse fluidized powders". *Chemical Engineering Science* 66.16 (2011), pp. 3628–3640. DOI: 10.1016/j.ces.2011.04.038.

[118] C. Kirse and H. Briesen. "Numerical solution of mixed continuous-discrete population balance models for depolymerization of branched polymers". *Computers and Chemical Engineering* 73 (2015), pp. 154–171. DOI: 10.1016/j.compchemeng.2014.11.008.

[119] V. John et al. "Techniques for the reconstruction of a distribution from a finite number of its moments". *Chemical Engineering Science* 62.11 (2007), pp. 2890–2904. DOI: 10.1016/j.ces.2007.02.041.

[120] D. Meimaroglou, A. I. Roussos, and C. Kiparissides. "Part IV: Dynamic evolution of the particle size distribution in particulate processes. A comparative study between Monte Carlo and the generalized method of moments". *Chemical Engineering Science* 61.17 (2006), pp. 5620–5635. DOI: 10.1016/j.ces.2006.05.001.

[121] N. Lebaz et al. "Reconstruction of a distribution from a finite number of its moments: A comparative study in the case of depolymerization process". *Computers and Chemical Engineering* 84 (2016), pp. 326–337. DOI: 10.1016/j.compchemeng.2015.09.008.

[122] S. Mortier et al. "Comparison of techniques for reconstruction of a distribution from moments in the context of a pharmaceutical drying process". *Computers and Chemical Engineering* 65 (2014), pp. 1–8. DOI: 10.1016/j.compchemeng.2014.02.008.

[123] S. Salenbauch et al. "A numerically robust method of moments with number density function reconstruction and its application to soot formation, growth and oxidation". *Journal of Aerosol Science* 128 (2019), pp. 34–49. DOI: 10.1016/j.jaerosci.2018.11.009.

[124] L. Metzger and M. Kind. "The influence of mixing on fast precipitation processes – A coupled 3D CFD-PBE approach using the direct quadrature method of moments (DQMOM)". *Chemical Engineering Science* 169 (2017), pp. 284–298. DOI: 10.1016/j.ces.2016.07.006.

[125] F. Gelbard, Y. Tambour, and J. H. Seinfeld. "Sectional representations for simulating aerosol dynamics". *Journal of Colloid and Interface Science* 76.2 (1980), pp. 541–556. DOI: 10.1016/0021-9797(80)90394-X.

[126] J. D. Landgrebe and S. E. Pratsinis. "A discrete-sectional model for particulate production by gas-phase chemical reaction and aerosol coagulation in the free-molecular regime". *Journal of Colloid and Interface Science* 139.1 (1990), pp. 63–86. DOI: 10.1016/0021-9797(90)90445-T.

[127] S. Kumar and D. Ramkrishna. "On the solution of population balance equations by discretization - I. A fixed pivot technique". *Chemical Engineering Science* 51.8 (1996), pp. 1311–1332. DOI: 10.1016/0009-2509(96)88489-2.

[128] S. Kumar and D. Ramkrishna. "On the solution of population balance equations by discretization - II. A moving pivot technique". *Chemical Engineering Science* 51.8 (1996), pp. 1333–1342. DOI: 10.1016/0009-2509(95)00355-X.

[129] S.-Y. Lu. "Collision integrals of discrete-sectional model in simulating powder production". *AIChE Journal* 40.10 (1994), pp. 1761–1764. DOI: 10.1002/aic.690401016.

[130] M. J. Hounslow, R. L. Ryall, and V. R. Marshall. "Discretized population balance for nucleation, growth, and aggregation". *AIChE Journal* 34.11 (1988), pp. 1821–1832. DOI: 10.1002/aic.690341108.

[131] Litster J.D., Smit D.J., and Hounslow M.J. "Adjustable discretized population balance for growth and aggregation". *AIChE Journal* 41.3 (1995), pp. 591–603. DOI: 10.1002/aic.690410317.

[132] M. Vanni. "Approximate population balance equations for aggregation-breakage processes". *Journal of Colloid and Interface Science* 221.2 (2000), pp. 143–160. DOI: 10.1006/jcis.1999.6571.

[133] P. Marchal et al. "Crystallization and precipitation engineering-I. An efficient method for solving population balance in crystallization with agglomeration". *Chemical Engineering Science* 43.1 (1988), pp. 59–67. DOI: 10.1016/0009-2509(88)87126-4.

[134] A. Prakash, A. P. Bapat, and M. R. Zachariah. "A Simple Numerical Algorithm and Software for Solution of Nucleation, Surface Growth, and Coagulation Problems". *Aerosol Science and Technology* 37.11 (2003), pp. 892–898. DOI: 10.1080/02786820300933.

[135] J. Kumar. *Numerical approximations of population balance equations in particulate systems (Dissertation)*. 1. Aufl. Magdeburg: docupoint-Verl., 2006. ISBN: 9783939665137.

[136] N. V. Mantzaris et al. "Numerical solution of a mass structured cell population balance model in an environment of changing substrate concentration". *Journal of Biotechnology* 71.1-3 (1999), pp. 157–174. DOI: 10.1016/S0168-1656(99)00020-6.

[137] N. V. Mantzaris, P. Daoutidis, and F. Srienc. "Numerical solution of multi-variable cell population balance models. II. Spectral methods". *Computers and Chemical Engineering* 25.11-12 (2001), pp. 1441–1462. DOI: 10.1016/S0098-1354(01)00710-4.

[138] S. Motz, A. Mitrović, and E.-D. Gilles. "Comparison of numerical methods for the simulation of dispersed phase systems". *Chemical Engineering Science* 57.20 (2002), pp. 4329–4344. DOI: 10.1016/S0009-2509(02)00349-4.

[139] S. Qamar et al. "A comparative study of high resolution schemes for solving population balances in crystallization". *Computers and Chemical Engineering* 30.6-7 (2006), pp. 1119–1131. DOI: 10.1016/j.compchemeng.2006.02.012.

[140] C.-Y. Wu and P. Biswas. "Study of numerical diffusion in a discrete-sectional model and its application to aerosol dynamics simulation". *Aerosol Science and Technology* 29.5 (1998), pp. 359–378. DOI: 10.1080/02786829808965576.

[141] R. J. LeVeque. *Numerical Methods for Conservation Laws*. Second Edition. Lectures in Mathematics ETH Zürich, Department of Mathematics Research Institute of Mathematics. Basel: Birkhäuser Basel, 1992. ISBN: 9783034886291.

[142] D. L. Ma, D. K. Tafti, and R. D. Braatz. "High-Resolution Simulation of Multidimensional Crystal Growth". *Industrial and Engineering Chemistry Research* 41.25 (2002), pp. 6217–6223. DOI: 10.1021/ie010680u.

[143] C. B. Vreugdenhil, ed. *Numerical methods for advection-diffusion problems*. Vol. 45. Notes on numerical fluid mechanics. Braunschweig: Vieweg, 1993. ISBN: 3528076453.

[144] P. K. Sweby. "High Resolution Schemes Using Flux Limiters for Hyperbolic Conservation Laws". *SIAM Journal on Numerical Analysis* 21.5 (1984), pp. 995–1011. DOI: 10.1137/0721062.

[145] L. D. Erasmus, D. Eyre, and R. C. Everson. "Numerical treatment of the population balance equation using a Spline-Galerkin method". *Computers and Chemical Engineering* 18.9 (1994), pp. 775–783. DOI: 10.1016/0098-1354(94)E0007-A.

[146] M. Nicmanis and M. J. Hounslow. "Finite-element methods for steady-state population balance equations". *AIChE Journal* 44.10 (1998), pp. 2258–2272. DOI: 10.1002/aic.690441015.

[147] A. I. Roussos, A. H. Alexopoulos, and C. Kiparissides. "Part III: Dynamic evolution of the particle size distribution in batch and continuous particulate processes: A Galerkin on finite elements approach". *Chemical Engineering Science* 60.24 (2005), pp. 6998–7010. DOI: 10.1016/j.ces.2005.06.021.

[148] Y. P. Kim and J. H. Seinfeld. "Simulation of multicomponent aerosol condensation by the moving sectional method". *Journal of Colloid and Interface Science* 135.1 (1990), pp. 185–199. DOI: 10.1016/0021-9797(90)90299-4.

[149] F. Gelbard. "Modeling multicomponent aerosol particle growth by vapor condensation". *Aerosol Science and Technology* 12.2 (1990), pp. 399–412. DOI: 10.1080/02786829008959355.

[150] M. Kostoglou and A. J. Karabelas. "Evaluation of Numerical Methods for Simulating an Evolving Particle Size Distribution in Growth Processes". *Chemical Engineering Communications* 136.1 (1995), pp. 177–199. DOI: 10.1080/00986449508936360.

[151] P. T. Spicer et al. "Titania formation by TiCl4 gas phase oxidation, surface growth and coagulation". *Journal of Aerosol Science* 33.1 (2002), pp. 17–34. DOI: 10.1016/S0021-8502(01)00069-6.

[152] Y. Xiong and S. E. Pratsinis. "Formation of agglomerate particles by coagulation and sintering-Part I. A two-dimensional solution of the population balance equation". *Journal of Aerosol Science* 24.3 (1993), pp. 283–300. DOI: 10.1016/0021-8502(93)90003-R.

[153] S. Qamar et al. "Adaptive high-resolution schemes for multidimensional population balances in crystallization processes". *Computers and Chemical Engineering* 31.10 (2007), pp. 1296–1311. DOI: 10.1016/j.compchemeng.2006.10.014.

[154] N. V. Mantzaris, P. Daoutidis, and F. Srienc. "Numerical solution of multi-variable cell population balance models. III. Finite element methods". *Computers and Chemical Engineering* 25.11-12 (2001), pp. 1463–1481. DOI: 10.1016/S0098-1354(01)00711-6.

[155] A. H. Alexopoulos, A. Roussos, and C. Kiparissides. "Part V: Dynamic evolution of the multivariate particle size distribution undergoing combined particle growth and aggregation". *Chemical Engineering Science* 64.14 (2009), pp. 3260–3269. DOI: 10.1016/j.ces.2009.04.012.

[156] M. Wulkow, A. Gerstlauer, and U. Nieken. "Modeling and simulation of crystallization processes using parsival". *Chemical Engineering Science* 56.7 (2001), pp. 2575–2588. DOI: 10.1016/S0009-2509(00)00432-2.

[157] V. Kulikov et al. "Modular dynamic simulation for integrated particulate processes by means of tool integration". *Chemical Engineering Science* 60.7 (2005), pp. 2069–2083. DOI: 10.1016/j.ces.2004.11.037.

[158] C. Drumm, M. M. Attarakih, and H.-J. Bart. "Coupling of CFD with DPBM for an RDC extractor". *Chemical Engineering Science* 64.4 (2009), pp. 721–732. DOI: 10.1016/j.ces.2008.05.041.

[159] J. Loeffler, S. Das, and S. C. Garrick. "Large eddy simulation of titanium dioxide nanoparticle formation and growth in turbulent jets". *Aerosol Science and Technology* 45.5 (2011), pp. 616–628. DOI: 10.1080/02786826.2010.551147.

[160] W. L. Dunn and J. K. Shultis. *Exploring Monte Carlo methods*. Amsterdam: Elsevier/Academic Press, 2012. ISBN: 9780444515759.

[161] C. Graham and D. Talay. *Stochastic Simulation and Monte Carlo Methods*. Berlin, Heidelberg: Springer, 2013. ISBN: 9783642393631.

[162] N. Metropolis and S. Ulam. "The Monte Carlo Method". *Journal of the American Statistical Association* 44.247 (1949), pp. 335–341. DOI: 10.2307/2280232.

[163] N. G. Cooper, ed. *Special Issue on Stanislaw Ulam 1909 - 1984*. Los Alamos Science Number 15. 1987. DOI: 10.2172/1054744.

[164] L. Wang, S. L. Jacques, and L. Zheng. "MCML-Monte Carlo modeling of light transport in multi-layered tissues". *Computer Methods and Programs in Biomedicine* 47.2 (1995), pp. 131–146. DOI: 10.1016/0169-2607(95)01640-F.

[165] J. T. Kajiya. "The rendering equation". *Computer Graphics (ACM)* 20.4 (1986), pp. 143–150. DOI: 10.1145/15886.15902.

[166] R. L. Cook. "Stochastic sampling in computer graphics". *ACM Transactions on Graphics (TOG)* 5.1 (1986), pp. 51–72. DOI: 10.1145/7529.8927.

[167] M. V. Fischetti and S. E. Laux. "Monte carlo analysis of electron transport in small semiconductor devices including band-structure and space-charge effects". *Physical Review B* 38.14 (1988), pp. 9721–9745. DOI: 10.1103/PhysRevB.38.9721.

[168] G. Pennington and N. Goldsman. "Semiclassical transport and phonon scattering of electrons in semiconducting carbon nanotubes". *Physical Review B - Condensed Matter and Materials Physics* 68.4 (2003). DOI: 10.1103/PhysRevB.68.045426.

[169] D. P. Landau and K. Binder. *A Guide to Monte Carlo Simulations in Statistical Physics*. Cambridge: Cambridge University Press, 2014. ISBN: 9781139696463.

[170] W. Nolting. *Grundkurs Theoretische Physik 6: Statistische Physik*. 7. Aufl. 2014. Springer-Lehrbuch. Berlin: Springer Spektrum, 2014. ISBN: 9783642253928.

[171] W. C. Hinds. *Aerosol Technology: Properties, Behavior, and Measurement of Airborne Particles*. 2. Aufl. s.l.: Wiley-Interscience, 2012. ISBN: 9780471194101.

[172] G. A. Bird. *Molecular gas dynamics and the direct simulation of gas flows*. Vol. 42. The Oxford engineering science series. Oxford: Clarendon Pr, 1994. ISBN: 9780198561958.

[173] N. A. Fuchs. *The mechanics of aerosols*. New York: Pergamon Press, 1964. ISBN: 9780486660554.

[174] V. G. Mavrantzas and S. E. Pratsinis. "The impact of molecular simulations in gas-phase manufacture of nanomaterials". *Current Opinion in Chemical Engineering* 23 (2019), pp. 174–183. DOI: 10.1016/j.coche.2019.04.006.

[175] E. Goudeli. "Nanoparticle growth, coalescence, and phase change in the gas-phase by molecular dynamics". *Current Opinion in Chemical Engineering* 23 (2019), pp. 155–163. DOI: 10.1016/j.coche.2019.04.001.

[176] G. A. Kelesidis, E. Goudeli, and S. E. Pratsinis. "Flame synthesis of functional nanostructured materials and devices: Surface growth and aggregation". *Proceedings of the Combustion Institute* 36.1 (2017), pp. 29–50. DOI: 10.1016/j.proci.2016.08.078.

[177] K. Liffman. "A direct simulation Monte-Carlo method for cluster coagulation". *Journal of Computational Physics* 100.1 (1992), pp. 116–127. DOI: 10.1016/0021-9991(92)90314-O.

[178] H. Zhao et al. "Analysis of four Monte Carlo methods for the solution of population balances in dispersed systems". *Powder Technology* 173.1 (2007), pp. 38–50. DOI: 10.1016/j.powtec.2006.12.010.

[179] J. Wei. "A parallel Monte Carlo method for population balance modeling of particulate processes using bookkeeping strategy". *Physica A: Statistical Mechanics and its Applications* 402 (2014), pp. 186–197. DOI: 10.1016/j.physa.2013.12.047.

[180] M. Smith and T. Matsoukas. "Constant-number Monte Carlo simulation of population balances". *Chemical Engineering Science* 53.9 (1998), pp. 1777–1786. DOI: 10.1016/S0009-2509(98)00045-1.

[181] B. H. Shah, D. Ramkrishna, and J. D. Borwanker. "Simulation of particulate systems using the concept of the interval of quiescence". *AIChE Journal* 23.6 (1977), pp. 897–904. DOI: 10.1002/aic.690230617.

[182] A. L. Garcia et al. "A Monte Carlo simulation of coagulation". *Physica A: Statistical Mechanics and its Applications* 143.3 (1987), pp. 535–546. DOI: 10.1016/0378-4371(87)90164-6.

[183] J. Wei and F. E. Kruis. "GPU-accelerated Monte Carlo simulation of particle coagulation based on the inverse method". *Journal of Computational Physics* 249 (2013), pp. 67–79. DOI: 10.1016/j.jcp.2013.04.030.

[184] Z. Xu, H. Zhao, and C. Zheng. "Accelerating population balance-Monte Carlo simulation for coagulation dynamics from the Markov jump model, stochastic algorithm and GPU parallel computing". *Journal of Computational Physics* 281 (2015), pp. 844–863. DOI: 10.1016/j.jcp.2014.10.055.

[185] R. I. A. Patterson, W. Wagner, and M. Kraft. "Stochastic weighted particle methods for population balance equations". *Journal of Computational Physics* 230.19 (2011), pp. 7456–7472. DOI: 10.1016/j.jcp.2011.06.011.

[186] J. Wei. "A fast Monte Carlo method based on an acceptance-rejection scheme for particle coagulation". *Aerosol and Air Quality Research* 13.4 (2013), pp. 1273–1281. DOI: 10.4209/aaqr.2012.12.0369.

[187] K. Lee and T. Matsoukas. "Simultaneous coagulation and break-up using constant-N Monte Carlo". *Powder Technology* 110.1-2 (2000), pp. 82–89. DOI: 10.1016/S0032-5910(99)00270-3.

[188] S. Khalili et al. "Constant number Monte Carlo simulation of population balances with multiple growth mechanisms". *AIChE Journal* 56.12 (2010), pp. 3137–3145. DOI: 10.1002/aic.12233.

[189] Y. Lin, K. Lee, and T. Matsoukas. "Solution of the population balance equation using constant-number Monte Carlo". *Chemical Engineering Science* 57.12 (2002), pp. 2241–2252. DOI: 10.1016/S0009-2509(02)00114-8.

[190] H. Zhao, F. E. Kruis, and C. Zheng. "Reducing statistical noise and extending the size spectrum by applying weighted simulation particles in Monte Carlo simulation of coagulation". *Aerosol Science and Technology* 43.8 (2009), pp. 781–793. DOI: 10.1080/02786820902939708.

[191] T. Kovačević and H. Briesen. "Simulations of crystal aggregation and growth: Towards correct crystal area". *AIChE Journal* 65.5 (2019). DOI: 10.1002/aic.16525.

[192] C. S. Lindberg et al. "A two-step simulation methodology for modelling stagnation flame synthesised aggregate nanoparticles". *Combustion and Flame* 202 (2019), pp. 143–153. DOI: 10.1016/j.combustflame.2019.01.010.

[193] J.-G. Rosenboom et al. "Characterisation of lactose powder and granules for multivariate wet granulation modelling". *Chemical Engineering Science* 123 (2015), pp. 395–405. DOI: 10.1016/j.ces.2014.11.013.

[194] B. Weber et al. "CFD based compartment-model for a multiphase loop-reactor". *Chemical Engineering Science: X* 2 (2019), p. 100010. DOI: 10.1016/j.cesx.2019.100010.

[195] N. Yaghini and P. D. Iedema. "Predicting molecular weight distribution by deterministic modeling and Monte Carlo simulations of radical polymerization with branching and scission allowing for multiradicals and gelation in various reactor configurations". *Chemical Engineering Science* 130 (2015), pp. 310–318. DOI: 10.1016/j.ces.2015.03.003.

[196] J. Bouffard, F. Bertrand, and J. Chaouki. "A multiscale model for the simulation of granulation in rotor-based equipment". *Chemical Engineering Science* 81 (2012), pp. 106–117. DOI: 10.1016/j.ces.2012.06.025.

[197] W. J. Menz, J. Akroyd, and M. Kraft. "Stochastic solution of population balance equations for reactor networks". *Journal of Computational Physics* 256 (2014), pp. 615–629. DOI: 10.1016/j.jcp.2013.09.021.

[198] F. E. Kruis et al. "Computational fluid dynamics based stochastic aerosol modeling: Combination of a cell-based weighted random walk method and a constant-number Monte-Carlo method for aerosol dynamics". *Chemical Engineering Science* 70 (2012), pp. 109–120. DOI: 10.1016/j.ces.2011.10.040.

[199] Z. Xu, H. Zhao, and H. Zhao. "CFD-population balance Monte Carlo simulation and numerical optimization for flame synthesis of TiO2 nanoparticles". *Proceedings of the Combustion Institute* 36.1 (2017), pp. 1099–1108. DOI: 10.1016/j.proci.2016.07.008.

[200] S. Liu and T. L. Chan. "A coupled CFD-Monte Carlo method for simulating complex aerosol dynamics in turbulent flows". *Aerosol Science and Technology* 51.3 (2017), pp. 269–281. DOI: 10.1080/02786826.2016.1260087.

[201] NVIDIA Corporation. *NVIDIA Turing GPU Architecture*. 2018. URL: https://www.nvidia.com/content/dam/en-zz/Solutions/design-visualization/technologies/turing-architecture/NVIDIA-Turing-Architecture-Whitepaper.pdf (visited on June 6, 2022).

[202] F. P. Santos et al. "Solution of the population balance equation using parallel adaptive cubature on GPUs". *Computers and Chemical Engineering* 55 (2013), pp. 61–70. DOI: 10.1016/j.compchemeng.2013.04.012.

[203] A. V. Prakash, A. Chaudhury, and R. Ramachandran. "Parallel simulation of population balance model-based particulate processes using multicore CPUs and GPUs". *Modelling and Simulation in Engineering* 2013 (2013). DOI: 10.1155/2013/475478.

[204] J. Wei and F. E. Kruis. "A GPU-based parallelized Monte-Carlo method for particle coagulation using an acceptance–rejection strategy". *Chemical Engineering Science* 104 (2013), pp. 451–459. DOI: 10.1016/j.ces.2013.08.008.

[205] Khronos Group. *OpenCL. The open standard for parallel programming of heterogeneous systems*. 2022. URL: https://www.khronos.org/opencl/ (visited on June 6, 2022).

[206] The OpenACC Organization. *OpenACC Homepage*. 2022. URL: https://www.openacc.org/ (visited on June 6, 2022).

[207] NVIDIA Corporation. *CUDA Toolkit Documentation*. 2022. URL: https://docs.nvidia.com/cuda/ (visited on June 6, 2022).

[208] J. Sanders and E. Kandrot. *CUDA by example: An introduction to general-purpose GPU programming*. 3. printing. Upper Saddle River, NJ: Addison-Wesley, 2011. ISBN: 9780131387683.

[209] B. Stroustrup. *The C++ programming language*. 4. ed., Upper Saddle River, NJ: Addison-Wesley, 2015. ISBN: 0321563840.

[210] J. L. Hennessy and D. A. Patterson. *Computer architecture: A quantitative approach*. Fifth edition. Waltham, MA: Morgan Kaufmann, 2012. ISBN: 9780123838735.

[211] NVIDIA Corporation. *CUDA Compute Architecture Kepler GK 110/210*. 2014. URL: https://www.nvidia.com/content/dam/en-zz/Solutions/Data-Center/documents/NVIDIA-Kepler-GK110-GK210-Architecture-Whitepaper.pdf (visited on June 6, 2022).

[212] H. Nguyen. *GPU gems 3*. Safari Books Online. Upper Saddle River, N.J: Addison-Wesley, 2008. ISBN: 9780321515261.

[213] J. Wei. "Comparison of computational efficiency of inverse and acceptance–rejection scheme by Monte Carlo methods for particle coagulation on CPU and GPU". *Powder Technology* 268 (2014), pp. 420–423. DOI: 10.1016/j.powtec.2014.08.047.

[214] A. Eibeck and W. Wagner. "Stochastic particle approximations for Smoluchoski's coagulation equation". *Annals of Applied Probability* 11.4 (2001), pp. 1137–1165. DOI: 10.1214/aoap/1015345398.

[215] H. Zhao, C. Zheng, and M. Xu. "Multi-Monte Carlo method for coagulation and condensation/evaporation in dispersed systems". *Journal of Colloid and Interface Science* 286.1 (2005), pp. 195–208. DOI: 10.1016/j.jcis.2004.12.037.

[216] H. Zhao, C. Zheng, and M. Xu. "Multi-Monte Carlo approach for general dynamic equation considering simultaneous particle coagulation and breakage". *Powder Technology* 154.2–3 (2005), pp. 164–178. DOI: 10.1016/j.powtec.2005.04.042.

[217] H. Zhao and C. Zheng. "Correcting the multi-Monte Carlo method for particle coagulation". *Powder Technology* 193.1 (2009), pp. 120–123. DOI: 10.1016/j.powtec.2009.01.019.

[218] M. Celnik et al. "Coupling a stochastic soot population balance to gas-phase chemistry using operator splitting". *Combustion and Flame* 148.3 (2007), pp. 158–176. DOI: 10.1016/j.combustflame.2006.10.007.

[219] R. I. A. Patterson et al. "The linear process deferment algorithm: a new technique for solving population balance equations". *SIAM Journal on Scientific Computing* 28.1 (2006), pp. 303–320. DOI: 10.1137/040618953.

[220] V. Rod and T. Misek. "Stochastic modelling of dispersion formation in agitated liquid-liquid systems". *Transactions of the Institution of Chemical Engineers* 60.1 (1982), pp. 48–53.

[221] P. K. Das. "Monte Carlo simulation of drop breakage on the basis of drop volume". *Computers and Chemical Engineering* 20.3 (1996), pp. 307–313. DOI: 10.1016/0098-1354(95)00017-8.

[222] B. K. Mishra. "Monte Carlo simulation of particle breakage process during grinding". *Powder Technology* 110.3 (2000), pp. 246–252. DOI: 10.1016/S0032-5910(99)00281-8.

[223] M. Goodson and M. Kraft. "Simulation of coalescence and breakage: An assessment of two stochastic methods suitable for simulating liquid-liquid extraction". *Chemical Engineering Science* 59.18 (2004), pp. 3865–3881. DOI: 10.1016/j.ces.2004.05.029.

[224] J. Polte. "Fundamental growth principles of colloidal metal nanoparticles - a new perspective". *CrystEngComm* 17.36 (2015), pp. 6809–6830. DOI: 10.1039/c5ce01014d.

[225] P. Taylor. "Ostwald ripening in emulsions". *Advances in Colloid and Interface Science* 75.2 (1998), pp. 107–163. DOI: 10.1016/S0001-8686(98)00035-9.

[226] A. Baldan. "Progress in Ostwald ripening theories and their applications to nickel-base superalloys. Part I: Ostwald ripening theories". *Journal of Materials Science* 37.11 (2002), pp. 2171–2202. DOI: 10.1023/A:1015388912729.

[227] J. van Embden et al. "Evolution of colloidal nanocrystals: Theory and modeling of their nucleation and growth". *Journal of Physical Chemistry C* 113.37 (2009), pp. 16342–16355. DOI: 10.1021/jp9027673.

[228] T. H. Tsang and A. Rao. "Comparison of different numerical schemes for condensational growth of aerosols". *Aerosol Science and Technology* 9.3 (1988), pp. 271–277. DOI: 10.1080/02786828808959214.

[229] T. Goudon, F. Lagoutière, and L. M. Tine. "Simulations of the Lifshitz-Slyozov equations: The role of coagulation terms in the asymptotic behavior". *Mathematical Models and Methods in Applied Sciences* 23.7 (2013), pp. 1177–1215. DOI: 10.1142/S0218202513500061.

[230] R. Körmer et al. “Aerosol synthesis of silicon nanoparticles with narrow size distribution-Part 1: Experimental investigations”. *Journal of Aerosol Science* 41.11 (2010), pp. 998–1007. DOI: 10.1016/j.jaerosci.2010.05.007.

[231] W. J. Menz et al. “Synthesis of silicon nanoparticles with a narrow size distribution: A theoretical study”. *Journal of Aerosol Science* 44 (2012), pp. 46–61. DOI: 10.1016/j.jaerosci.2011.10.005.

[232] D. Lindackers et al. “Formation and growth of SiO2 particles in low pressure H2/O2/Ar flames doped with SiH4”. *Combustion Science and Technology* 123.1-6 (1997), pp. 287–315. DOI: 10.1080/00102209708935632.

[233] S. Tsantilis, H. K. Kammler, and S. E. Pratsinis. “Population balance modeling of flame synthesis of titania nanoparticles”. *Chemical Engineering Science* 57.12 (2002), pp. 2139–2156. DOI: 10.1016/S0009-2509(02)00107-0.

[234] S. Panda and S. E. Pratsinis. “Modeling the synthesis of aluminum particles by evaporation-condensation in an aerosol flow reactor”. *Nanostructured Materials* 5.7-8 (1995), pp. 755–767. DOI: 10.1016/0965-9773(95)00292-M.

[235] Y. Singh et al. “Approaches to increasing yield in evaporation/condensation nanoparticle generation”. *Journal of Aerosol Science* 33.9 (2002), pp. 1309–1325. DOI: 10.1016/S0021-8502(02)00072-1.

[236] J.-H. Jang and J. Lin. “An investigation of the synthesis of metallic nano-particles by laser ablation”. *Surface and Coatings Technology* 202.24 (2008), pp. 6136–6141. DOI: 10.1016/j.surfcoat.2008.07.022.

[237] A. Voloshko, J.-P. Colombier, and T. E. Itina. “Comparison of laser ablation with spark discharge techniques used for nanoparticle production”. *Applied Surface Science* 336 (2015), pp. 143–149. DOI: 10.1016/j.apsusc.2014.10.077.

[238] M. Z. Jacobson. “Analysis of aerosol interactions with numerical techniques for solving coagulation, nucleation, condensation, dissolution, and reversible chemistry among multiple size distributions”. *Journal of Geophysical Research Atmospheres* 107.19 (2002), pp. 1–23. DOI: 10.1029/2001JD002044.

[239] J. Brillo and I. Egry. “Surface tension of nickel, copper, iron and their binary alloys”. *Journal of Materials Science* 40.9-10 (2005), pp. 2213–2216. DOI: 10.1007/s10853-005-1935-6.

[240] D. R. Lide, ed. *CRC handbook of chemistry and physics: A ready-reference book of chemical and physical data*. 85. ed. Boca Raton: CRC Press, 2004. ISBN: 9780849304859.

[241] L. F. Shampine and M. W. Reichelt. “The MATLAB ODE Suite”. *SIAM Journal on Scientific Computing* 18.1 (1997), pp. 1–22. DOI: 10.1137/S1064827594276424.

[242] J. R. Dormand and P. J. Prince. “A family of embedded Runge-Kutta formulae”. *Journal of Computational and Applied Mathematics* 6.1 (1980), pp. 19–26. DOI: 10.1016/0771-050X(80)90013-3.

[243] L. F. Shampine. “Interpolation for Runge-Kutta Methods”. *SIAM Journal on Numerical Analysis* 22.5 (1985), pp. 1014–1027. DOI: 10.1137/0722060.

The Papers

Peer Reviewed Journal Publications

Book Chapters

Peer Reviewed Conference Proceedings

Conference Proceedings

The single authors contributed to the presented publications as follows:

Peer Reviewed Journal Publications

[Paper I] Stochastic Resolution and Merging – *Journal of Computational Physics*. See page 93.

- Gregor Kotalczyk developed the concepts of stochastic resolution and merging - both have been implemented as a parallel CUDA algorithm, based on a previous work from Einar Kruis.
- Gregor Kotalczyk interpreted and summarized the presented results and has embedded the findings in the context of the existing MC population balance literature.
- Einar Kruis has helped to chose appropriate test cases.

[Paper II] Fractional MC Time Steps – *Chemical Engineering, Research and Design*. See page 115.

- Einar Kruis provided the conceptual algorithmic idea for this paper.
- Gregor Kotalczyk developed a sound mathematical formulation for the additional probabilities of the MC time steps, implemented the algorithm, designed the test-cases and put the found results into the scientific context.

[Paper III] Time-Driven Particle Breakage – *Powder Technology*. See page 129.

- Einar Kruis provided the main idea for this paper (the parallel simulation of the mass-based breakage method), this was translated into a sound mathematical concept by Gregor Kotalczyk, this translation made the definition of other methods (such as the low weight merging) possible.
- Jherna Devi helped Gregor Kotalczyk to implement the algorithms.
- Gregor Kotalczyk provided suitable test-cases (analytical solutions) from literature review and put the findings into the context of existing literature.
- Jherna Devi provided the analysis of the computational accuracy of the method.

[Paper IV] Homogeneous Nucleation and Particle Growth – *Tellus B*. See page 143.

- Gregor Kotalczyk provided the idea to test different nucleation theories under atmospheric conditions, analyzed and summarized the simulation results.
- Einar Kruis helped to identify suitable simulation conditions and with the literature review.
- Ivan Skenderović helped to test the algorithm under the new simulation conditions.

Book Chapters

[Paper V] Compartmental Population Balances by Means of MC Methods. See page 155.

- Gregor Kotalczyk performed the necessary novel simulations, provided the simulation results and wrote the text.
- Einar Kruis edited and selected the topics for publication.

Peer Reviewed Conference Proceedings

[Paper VI] Modeling of Particle Formation in Arc Discharges – *MRS Advances*. See page 187.

- Gregor Kotalczyk provided the main algorithmic idea of how to couple the different processes i.e. physical algorithms together.
- Ivan Skenderović helped to identify suitable simulation conditions and to test and debug the algorithms in the framework of his master thesis.
- Einar Kruis provided guidance on the overall form of the publication.

Conference Proceedings

[Paper VII] Simultaneous Nucleation, Coagulation and Growth – *2016 AIChE*. See page 197.

- Einar Kruis pointed out the importance of the simulated system and the lack of alternative methods for its simulation.
- Ivan Skenderović helped to design, test and debug the algorithm for the evaporation, growth and nucleation as well as to find suitable simulation conditions in the framework of his master thesis, which was supervised by Gregor Kotalczyk and Einar Kruis.
- Gregor Kotalczyk designed interfaces for the coupling with the coagulation algorithm, analyzed the results and wrote the vast majority of the text.

[Paper VIII] Flowsheet Simulation of Solid Processes – *2018 WCPT*. See page 205.

- Einar Kruis helped to formulate a flow-sheet system which is relevant in a chemical engineering context.
- Krishan Lambach designed (in the framework of his bachelor thesis) a C++ based compartmental network and helped to implement under the supervision of Gregor Kotalczyk the main algorithms of particulate transport in the CUDA framework.
- Gregor Kotalczyk formulated the mathematical framework, designed the algorithms and wrote the publication.

Coauthored Publications not Included in this Thesis

[CoPaper I] J. Devi, G. Kotalczyk, and F. E. Kruis. "Accuracy control in Monte Carlo simulations of particle breakage". *International Journal of Modelling, Identification and Control* 31.3 (2019), pp. 278–291. DOI: 10.1504/IJMIC.2019.098774

- Ivan Skenderović designed the test-cases and identified suitable simulation conditions from literature review of experimental set-ups.
- Gregor Kotalczyk helped to apply the existing coagulation and nucleation code to the given scenario and to develop a benchmark method.
- Einar Kruis contributed by conceptual design of the paper and by developing the computational efficacy chapter with Ivan Skenderović.

[CoPaper II] I. Skenderović, G. Kotalczyk, and F. E. Kruis. "Dual Population Balance Monte Carlo simulation of particle synthesis by flame spray pyrolysis". *Processes* 6.12 (2018). DOI: 10.3390/pr6120253

- Einar Kruis provided the main idea and line of inquiry which lead to this paper.
- Jherna Devi implemented the simulation scenario, analyzed the data and summarized the numerical accuracy and efficacy of the method.
- Gregor Kotalczyk helped in describing the used simulation techniques and embedding the findings in the context of the existing literature.

Paper I

Version of record published in:
Journal of Computational Physics 340 (2017), pp. 276–296.
Available online at: https://doi.org/10.1016/j.jcp.2017.03.041

A Monte Carlo Method for the Simulation of Coagulation and Nucleation Based on Weighted Particles and the Concepts of Stochastic Resolution and Merging

G. Kotalczyk and F.E. Kruis

Journal of Computational Physics 340 (2017) 276–296

Contents lists available at ScienceDirect

Journal of Computational Physics

www.elsevier.com/locate/jcp

A Monte Carlo method for the simulation of coagulation and nucleation based on weighted particles and the concepts of stochastic resolution and merging

G. Kotalczyk *, F.E. Kruis

Institute of Technology for Nanostructures (NST) and Center for Nanointegration Duisburg–Essen (CENIDE), University Duisburg–Essen, Duisburg, D-47057, Germany

ARTICLE INFO

Article history:
Received 20 October 2016
Received in revised form 20 March 2017
Accepted 21 March 2017
Available online 24 March 2017

Keywords:
Simulation
Population balance
Coagulation
Nucleation
Monte Carlo
GPU computing

ABSTRACT

Monte Carlo simulations based on weighted simulation particles can solve a variety of population balance problems and allow thus to formulate a solution-framework for many chemical engineering processes. This study presents a novel concept for the calculation of coagulation rates of weighted Monte Carlo particles by introducing a family of transformations to non-weighted Monte Carlo particles. The tuning of the accuracy (named 'stochastic resolution' in this paper) of those transformations allows the construction of a constant-number coagulation scheme. Furthermore, a parallel algorithm for the inclusion of newly formed Monte Carlo particles due to nucleation is presented in the scope of a constant-number scheme: the low-weight merging. This technique is found to create significantly less statistical simulation noise than the conventional technique (named 'random removal' in this paper). Both concepts are combined into a single GPU-based simulation method which is validated by comparison with the discrete-sectional simulation technique. Two test models describing a constant-rate nucleation coupled to a simultaneous coagulation in 1) the free-molecular regime or 2) the continuum regime are simulated for this purpose.

1. Introduction

The processes occurring during particle production are usually modeled with the help of the population balance equation (PBE) which is described in detail by [1]. This modeling approach plays a crucial role for the analysis of aerosol reactors [2], fluidized beds [3,4], crystallizers [5,6] and many other processes used in the field of chemical engineering [7].

A variety of methods exists allowing to solve the PBE numerically. However, the correct description of simultaneous processes like nucleation, coagulation, growth, breakage, mixing, sintering and other processing mechanisms poses a major problem, which has not been solved to a satisfactory extent, yet.

The classical moment methods [8,9] and the newer direct quadrature method of moments (DQMOM) [10] are only able to render the time-dependency of certain values for the moments of the particle size distribution (PSD), and not the full PSD. Sectional methods [11] face problems when combined with growth processes in the form of numerical diffusion [12] and make the extension to multiple dimensions complicated [13]. Finite element methods avoid the problem of numerical

* Corresponding author.
E-mail address: Gregor.Kotalczyk@uni-due.de (G. Kotalczyk).

http://dx.doi.org/10.1016/j.jcp.2017.03.041
0021-9991/

diffusion [14], but they are computationally demanding for time-depending coagulation kernels [15] and necessitate special treatment of discontinuities, which are typically encountered in nucleation processes [16].

The Monte Carlo (MC) simulation [17] avoids per se the problem of numerical diffusion for the growth process [18] and is easily extensible to multiple particle properties – making it thus a most promising approach in order to describe all of the processes mentioned above. The disadvantages of the MC simulation are long simulation times and the inherent stochastic noise of the method.

The description of the nucleation process poses a fundamental problem for the MC simulation, hence the continuous incorporation of newly nucleated particles has to be reconciled with limited computational capacities. The here presented work focuses on the simulation of coagulation and nucleation, only, in order to investigate the extent of the amount of the statistical noise stemming from different particle insertion techniques.

The traditional two solutions for the problem of including new simulation particles into the simulation are 1) the resizing approaches also called 'topping-up' [19] or 2) the so called constant-number approaches, introduced to coagulation first [20] and extended to the joined simulation of coagulation and nucleation later [21], this approach will be called 'random removal' in the following. An alternative approach is the rarely applied merging of simulation particles, which is used by [22].

A novel merging strategy, the low-weight merging, for the inclusion of newly formed particles is proposed in this paper which is able to preserve all particle properties in contrast to the merging technique by [22], which preserves the properties only, if two simulation particles with equal properties can be found. It is shown that simulations using the low-weight merging technique produce far less statistical noise than the ones using the traditional random removal method [21].

The presented low-weight merging technique resorts to the use of weighted MC particles. The use of differentially weighted simulation particles (a particle i with statistical weight W_i represents a concentration W_i of real particles) has several advantages: it allows to describe the interaction between simulation particles having different concentrations coming from different cells or compartments and it can also be used as a tool to control the number of simulation particles (e.g. to gain numeric accuracy). The combination of stochastically formulated coagulation events with an ordinary differential equation(ODE)-based growth and nucleation processes [18,23], based on the operator splitting technique, or [2] with less formal framework, is facilitated, because no restrictions are posed upon the statistical weight of the particles included into the simulation due to nucleation.

The difficulty associated with weighted MC particles is the correct description of the coagulation rates and schemes. The mathematically complex stochastic weighted algorithm developed by [24] and further refined by [25] has been suggested in this context. The recently proposed Markov jump models [26] describe the coagulation by resorting to constant-number methods introduced by the Matsoukas group [20]. An alternative approach has been elaborated by [27] leading to the concept of 'fictitious particles', the attribution of two distinct rates or probabilities for the same coagulation event are conceptually difficult to understand.

We introduce an alternative approach for the derivation of the coagulation rates for various coagulation schemes by elaborating the theory of 'stochastic resolution'.

2. Theoretic concepts for weighted simulation entries

In order to provide more clarity, the differentially weighted MC particles (also named 'stochastic particles' [25], or 'fictitious particles' [27] in other publications) will be called simulation entries (SE) for which the statistical weight (a concentration in units m^{-3}) and the properties of the SEs are stored on the computer.

2.1. Operator splitting technique

The simultaneous nucleation and coagulation processes are described by the following PBE:

$$\frac{\mathrm{d}n(v)}{\mathrm{d}t} = \frac{1}{2}\int_0^v \beta(v-v', v')n(v-v')n(v')dv' - n(v)\int_0^\infty \beta(v, v')n(v')dv' + \delta(v_{\mathrm{nuc}} - v)R_{\mathrm{N}}(t)\,. \tag{1}$$

The first two terms on the r.h.s. of the equation describe the coagulation process. $n(v)$ is the number density of particles with the property v and $\beta(v, v')$ is the coagulation kernel, describing the rate of coagulation between particles of types v and v' (the newly formed particle has the type $v + v'$). The particle properties are defined by the type space considered in the problem and this can be univariate or multivariate. The last term of Eq. (1) describes the insertion of particles with the property v_{nuc} with the nucleation rate $R_{\mathrm{N}}(t)$. For a given time-step τ_{mc}, the concentration of the nucleated particles can be written as:

$$W_{\mathrm{nuc}} = \int_{t_{\mathrm{start}}}^{t_{\mathrm{start}}+\tau_{\mathrm{mc}}} R_{\mathrm{N}}(t)\mathrm{d}t\,. \tag{2}$$

The nucleation rate R_{N} as well as the volume (or multivariate properties) of the nucleated particles, v_{nuc}, can be time-dependent, especially in the context of a physically induced homogeneous nucleation (e.g. [28,29]) due to the dependence

on the supersaturation. A constant nucleation rate R_N and a constant (one-dimensional) volume v_nuc are used in this work. This simplifies Eq. (2) to:

$$W_\mathrm{nuc} = \int_{t_\mathrm{start}}^{t_\mathrm{start}+\tau_\mathrm{mc}} R_\mathrm{N}\,\mathrm{d}t = \tau_\mathrm{mc}\cdot R_\mathrm{N}\,. \tag{3}$$

Instead of treating the nucleation as a competitive MC event (e.g. [30]) to the coagulation process, both processes can be simulated independently for small intervals of time [31]. This technique is called operator splitting [32]. The application of this algorithm in combination with weighted SEs has already been investigated and used (e.g. [23]). This work makes use of a simple implementation of this method:

1. An event-driven MC coagulation-step is performed (introduced in section 2.2.2, the explicit algorithm is in Appendix A). A specific value for the time-step τ_mc is gained by this algorithm.
2. Following Eq. (3), the statistical weight, W_nuc, of the SE representing the nucleated particles is calculated. Then a SE with this weight and the property v_nuc is inserted by one of the insertion techniques introduced in section 2.3.

Both steps are repeated until the time t reaches or surpasses the simulation time t_tot (i.e. $t \geq t_\mathrm{tot}$). Algorithm 1 in Appendix A summarizes this simulation procedure.

2.2. Coagulation

Section 2.2.1 treats the coagulation of weighted SEs. The concept of 'stochastic resolution' is introduced, which defines specific coagulation events and states the corresponding rates at which these events occur. The implementation of the gained results in the framework of a GPU-based fast simulation technique is shown in section 2.2.2.

2.2.1. Rendering of coagulation events by weighted SEs

The PSD rendered by all SEs can be rendered by equally weighted simulation entries (EWSE). Each EWSE represents the same concentration s_F of real particles (in the units m^{-3}) in the scope of a 'classic' MC simulation. The more EWSEs are used (the lower the value s_F) to render one specific PSD, the higher is the accuracy of the MC simulation: the coagulation events can be rendered at a higher resolution. The stochastic resolution of this transformation can conveniently be defined to $1/s_\mathrm{F}$. Fig. 1 shows how one coagulation event between the particle populations represented by two SEs i and j is rendered in the scope of three arbitrarily chosen stochastic resolutions: First the SEs are converted to EWSEs. Second, two of the EWSEs coagulate with each other and form one new EWSE. This process takes place with the coagulation rate $\beta_\mathrm{SE}^{s_\mathrm{F}}$. Finally, all the EWSEs are converted back to weighted SEs.

The chosen stochastic resolution $1/s_\mathrm{F}$ determines the number of EWSEs N_i (resp. N_j) which are used to render the SE i (resp. j) with the weight W_i (resp. W_j) via:

$$N_i = \frac{W_i}{s_\mathrm{F}} \quad \text{and} \quad N_j = \frac{W_j}{s_\mathrm{F}}\,. \tag{4}$$

The continuous PSD, $n(v)$, of the real particle population is approximated by all N_EWSE EWSEs with the help of the Dirac delta function δ to:

$$n(v) \approx s_\mathrm{F} \sum_k^{N_\mathrm{EWSE}} \delta(v - v_k)\,. \tag{5}$$

The PBE for coagulation for continuous PSDs $n(v)$ can be translated into a discrete form for single EWSEs. This procedure is outlined in Appendix B. The resulting coagulation rate $\beta_\mathrm{SE}^{s_\mathrm{F}}(i,j)$ for two SEs i and j in Eq. (B.11) combined with the actual number of EWSEs defined via Eq. (4) yields:

$$\beta_\mathrm{SE}^{s_\mathrm{F}}(i,j) = N_i N_j \cdot s_\mathrm{F} \cdot \beta(v_i, v_j) \overset{(4)}{=} \frac{W_i W_j}{s_\mathrm{F}} \cdot \beta(v_i, v_j)\,. \tag{6}$$

The coagulation event with the rate $\beta_\mathrm{SE}^{s_\mathrm{F}}$ renders the coagulation of two EWSE into one new EWSE which represents a real particle concentration of s_F. The SE representing the newly coagulated EWSE has therefore the statistical weight of $W_\mathrm{coag}^\mathrm{new} = s_\mathrm{F}$. The statistical weights W_i and W_j of the coagulating SEs i and j have to be adjusted to W_i^new and W_j^new, reflecting the loss of real particles with a concentration of s_F due to the coagulation event (like summarized in Fig. 1):

$$W_i^\mathrm{new} = W_i - s_\mathrm{F}, \quad W_j^\mathrm{new} = W_j - s_\mathrm{F}, \quad W_\mathrm{coag}^\mathrm{new} = s_\mathrm{F}\,. \tag{7}$$

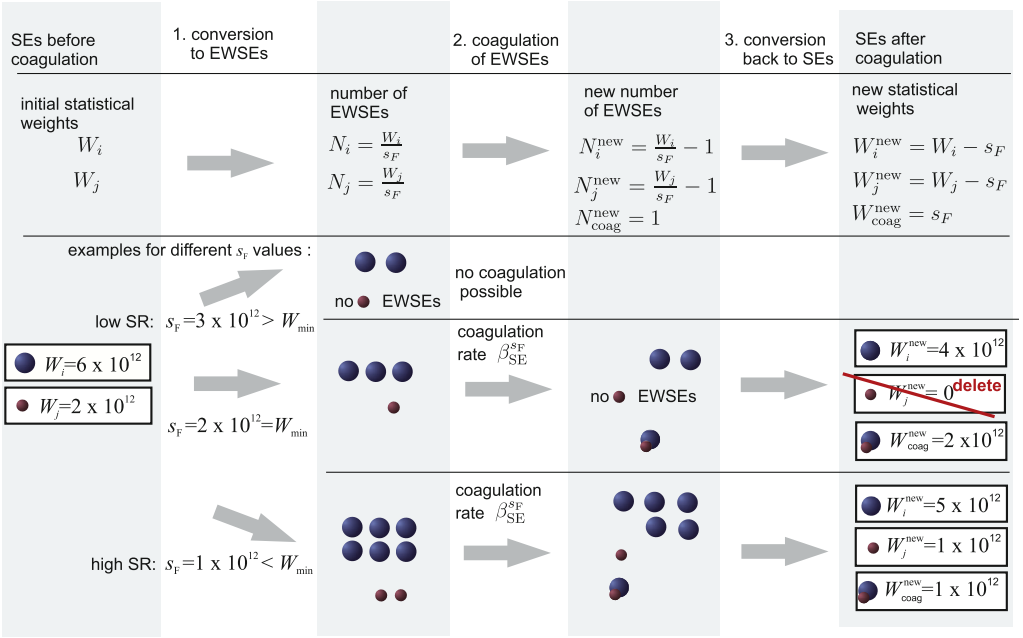

Fig. 1. The hypothetical three-step process for the description of the coagulation of weighted SEs in the framework of EWSEs. The creation of an additional SE is necessary, if s_F is set to a value lower than W_{min}. If s_F is set to a value higher than W_{min}, the coagulation event cannot be rendered at all.

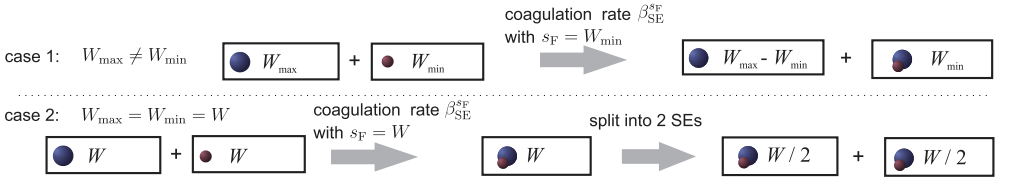

Fig. 2. The setting of $s_F = W_{min}$ leads to a coagulation scheme, which preserves the number of SEs.

The properties v are modified via the following equation:

$$v_i^{new} = v_i, \quad v_j^{new} = v_j, \quad v_{coag}^{new} = v_i + v_j . \tag{8}$$

These general expressions (Eqs. (6), (7) and (8)) are valid for all chosen values for s_F, with $s_F \leq \min(W_i, W_j)$.

Constant-number scheme. In order to avoid the problem of creating at each coagulation step new memory space for new SEs resulting from the coagulation, the value of s_F can be set for each coagulation pair to[1]:

$$s_F = W_{min} = \min(W_i, W_j) . \tag{9}$$

The coagulation rate of the pair (i, j) is calculated in a different stochastic resolution than the coagulation rate of the pair (k, l), if $\min(W_i, W_j) \neq \min(W_k, W_l)$. In this case, the coagulation of particles represented by the SEs i and j is described with a different accuracy (or resolution) than the coagulation of particles represented by the SEs k and l.

The corresponding coagulation rates $\beta_{i,j}^{(SR)}$ result from Eq. (6) in combination with Eq. (9), with $W_{max} = \max(W_i, W_j)$:

$$\beta_{i,j}^{(SR)} = W_{max} \cdot \beta(v_i, v_j) . \tag{10}$$

In the case $W_i = W_j$, the resulting SE can be split into two with the weight: $W = W_{min}/2$, like shown in Fig. 2. The detailed algorithm is presented as Algorithm 2 in Appendix A.

Comparison to other methods. The thus gained coagulation scheme (Fig. 2) is different from the Markov jump model [26], but it is the same as the fictitious particle-based scheme introduced by [27]. However, the authors [27] state a different coagulation kernel $\beta^{(FP)}$ resulting from the fictitious particle-theory:

[1] We consider s_F as a function, which is dependent on the specific properties of the SEs i and j considered for coagulation, the specific setting in Eq. (9), is one out of many possibilities. Different settings lead to different non-constant-number schemes (see Fig. 1), a plethora of methods can be constructed in this way. Other properties, like e.g. the volume of the SEs can be taken into account in order chose the value of s_F.

$$\beta_{i,j}^{(\mathrm{FP})} = \frac{2W_j \cdot W_{\max}}{W_i + W_j} \cdot \beta(v_i, v_j)\,. \tag{11}$$

This coagulation rate is asymmetric, making a distinction necessary, whether SE i coagulates with j or vice versa. The coagulation event between i and j is the same as between j and i, as can be seen in Fig. 2. It is difficult to understand conceptually, how the same event can be described with two different rates, and thus probabilities. A more detailed discussion of the differences between the fictitious particle based coagulation kernel and the stochastic resolution based one is given in Appendix C.

2.2.2. Fast simulation technique for coagulation

For the selection of one coagulation event, the calculation of the exact maximal coagulation rate $\beta_{\max}$ and the mean coagulation rate β_{mean} is necessary in the framework of the acceptance–rejection (AR) method. Several methods exist in order to accelerate the computationally demanding calculation of these values. Book-keeping strategies [33] can be used in order to update the at the beginning of the simulation exactly calculated values $\beta_{\max}$ and β_{mean} after each discrete event.[2] This method becomes less applicable if the coagulation and nucleation processes are combined with growth or evaporation processes which are rendered in a hybrid continuous implementation.

Majorant kernel techniques ([25,26]) use simpler mathematical formulations $\widehat{\beta}(v_i, v_j)$, which satisfy: $\widehat{\beta}(v_i, v_j) \geq \beta^{(\mathrm{SR})}(v_i, v_j)$ and allow thus a simple and computationally efficient approximation of $\beta_{\max}$. Although such a formulation can be easily formulated for many physical systems like the here used free-molecular regime, a general expression $\widehat{\beta}(v_i, v_j)$ for all sorts of coagulation kernels (possibly rendering multidimensional particle properties) might prove difficult to formulate or prove computationally very demanding.

A GPU-based acceptance–rejection technique introduced by [34] reduced the computation time for the MC simulation by the usage of a representative sample of pairs of SEs (256 pairs are used in this work, $N_{\mathrm{sample}} = 256$). The mean value of the coagulation rates of this sample β_{mean} is multiplied with a constant factor $\gamma \geq 1$ in order to provide a coarse approximation of the maximal coagulation rate: $\beta_{\max}^{(\mathrm{app})} \geq \gamma \cdot \beta_{\mathrm{mean}}$.

This leads to the following algorithm for the fast selection of a coagulation pair:

1. Execute N_{sample} GPU-threads in parallel, each one repeats:
   (a) Select a pair of weighted SEs (i, j) randomly.
   (b) Participate in the Calculation of β_{mean} (via Eq. (10))

$$\beta_{\mathrm{mean}} = \frac{1}{N_{\mathrm{sample}}} \sum_{\text{all sample SE-pairs } (i,j)} \beta_{i,j}^{(\mathrm{SR})}\,. \tag{12}$$

   (c) Generate a random number $r_{i,j} \in (0, 1)$ and select the pair (i, j) for coagulation, if

$$r_{i,j} \leq \frac{\beta_{i,j}}{\gamma \cdot \beta_{\mathrm{mean}}} = \frac{\beta_{i,j}}{\beta_{\max}^{(\mathrm{app})}} \tag{13}$$

   until at least one pair has been found for coagulation (by at least one GPU-thread).[3]
2. Coagulate the coagulation pair according to Fig. 2.
3. Set the MC time step to

$$\tau_{\mathrm{mc}}^{(\mathrm{app})} = \frac{2}{N_{\mathrm{SE}}(N_{\mathrm{SE}} - 1)\beta_{\mathrm{mean}}}\,. \tag{14}$$

A detailed description of this algorithm can be found as Algorithm 2 in combination with Algorithm 3 in Appendix A.

This approach leads to a mathematical correct description, if $\beta_{\max}^{(\mathrm{app})} \geq \beta_{\max}$. The results are therefore exact in the scope of the MC simulation, if γ is set high enough. Systematic errors are introduced into the simulation, if $\beta_{\max}^{(\mathrm{app})} < \beta_{\max}$. The condition $\beta_{\max}^{(\mathrm{app})} \geq \beta_{\max}$ ensures the correct description of the probabilities for the single events via Eq. (13), like in the scope of a majorant kernel technique, e.g. [25]. The majorant kernel technique ensures the correct time steps by the concept of 'fictitious time steps', which are selected coagulation pairs, which lead to a time increment, but to no coagulation of the selected SEs. Therefore, many successfully selected particles might be necessary in order to make one coagulation step. This is not the case for the γ-based method introduced by [34], where the time step for one coagulation attempt is approximated by Eq. (14), thus only one selected particle pair is sufficient to perform a full coagulation step.

[2] If the SEs i and j have coagulated, the sum β_{sum} of the rates is updated via: $\beta_{\mathrm{sum}} = \beta_{\mathrm{sum}} - \sum_k \beta_{k,i(\mathrm{old})} - \sum_k \beta_{k,j(\mathrm{old})} + \sum_k \beta_{k,i(\mathrm{new})} + \sum_k \beta_{k,j(\mathrm{new})}$, leading to $\beta_{\mathrm{mean}} = \beta_{\mathrm{sum}}/N_{\mathrm{SE}} \cdot (N_{\mathrm{SE}} - 1)$. Similarly, it is checked, whether a new maximal coagulation rate, $\beta_{\max}$, has to be used, if any k exists, with $\beta_{\max} < \beta_{k,i(\mathrm{new})}$ or $\beta_{\max} < \beta_{k,j(\mathrm{new})}$. The notation $i(\mathrm{old})$ (resp. $i(\mathrm{new})$) designates the properties and statistical weight of the SE i before (resp. after) the coagulation. These updates require only a multiple of N_{SE} computational steps, reducing vastly the cost of the exact calculation, which makes $N_{\mathrm{SE}} \cdot (N_{\mathrm{SE}} - 1)$ additions necessary.

[3] Hence all (parallel) threads store the hypothetically found coagulation pair in the same place, only one selected pair is used for the following coagulation code. This specific point is discussed in Appendix A (Algorithm 3) in more detail.

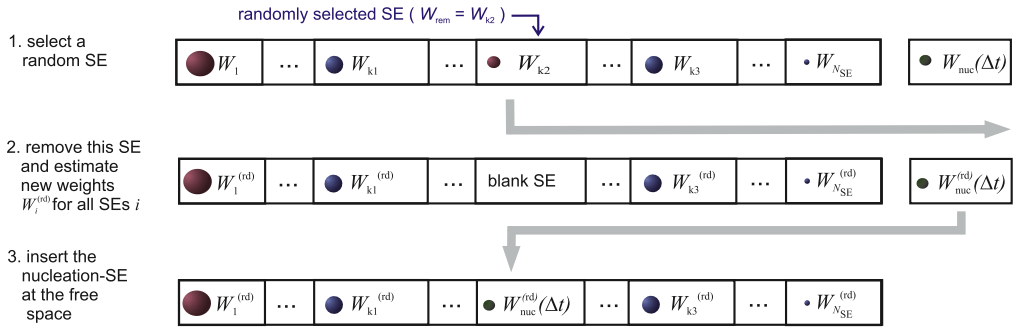

Fig. 3. Alteration of the N_{SE} SEs during one random removal step.

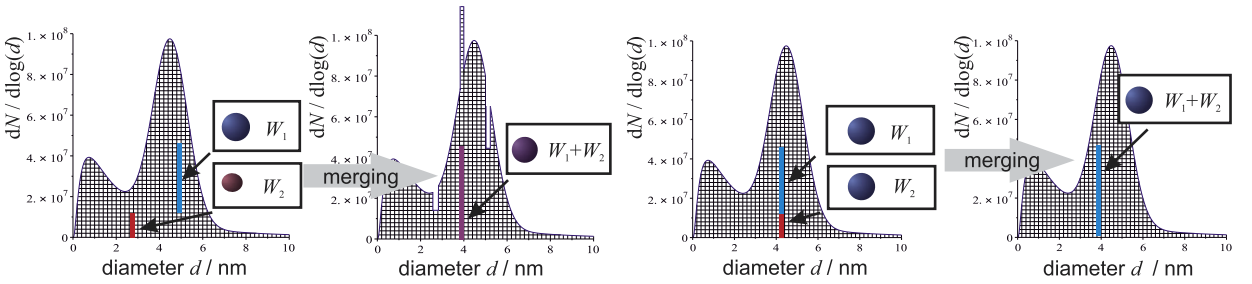

(a) Merging of SEs with distinct properties.

(b) Merging of SEs with equal properties.

Fig. 4. The concept of merging of SEs. The merging alters the PSD and introduces systematic errors as shown in (a). These errors can be limited by the selection of SEs whose properties are nearly similar (b).

2.3. Techniques for the insertion of new SEs

Constant-number algorithms can be used to model the inclusion of nucleated particles or particles included by other processes: like breakage or transport. First the conventionally used method, the random removal will be presented in section 2.3.1. Section 2.3.2 introduces the newly developed low-weight merging technique.

2.3.1. Random removal

The modeling of the nucleation of new particles using a constant-number method was realized by the removal of randomly chosen EWSEs [21]. In the scope of this approach it has been found, that the mass of the removed EWSE has to be redistributed over the remaining population.

This technique can be easily extended to weighted SEs, and is summarized in Fig. 3. If a SE (with the weight W_{rem} and mass m_{rem}) is removed from the simulation, the weights W_i of all other SEs (with the mass m_i) have to be adjusted to new weights $W_i^{(\mathrm{rd})}$ via the following formula:

$$W_i^{(\mathrm{rd})} = W_i \cdot \frac{M_{\mathrm{T}}}{M_{\mathrm{T}} - m_{\mathrm{rem}} \cdot W_{\mathrm{rem}}}, \qquad \text{with: } M_{\mathrm{T}} = \sum_{k=1}^{N_{\mathrm{SE}}^{\mathrm{old}}} W_k \cdot m_k, \tag{15}$$

where $\sum_{k=1}^{N_{\mathrm{SE}}^{\mathrm{old}}}$ refers to the summation over all SEs including the removed SE, but without the freshly nucleated SE. A detailed implementation of this algorithm using smart bookkeeping is shown as Algorithm 4 in Appendix A.3.

This method conserves the total mass of the system exactly but not the total number-concentration of the simulated particles, if the volume (or mass) is the single property of the system. This approach has been successfully applied on weighted SEs, making it the conventionally used technique for the inclusion of new SEs [35,23,2].

2.3.2. Merging techniques

The following concept of merging of SEs is proposed here: if two SEs with exactly the same properties are merged, the resulting representation of the PSD will not change and all the physical processes will be described in the same way. If the SEs differ slightly in their properties, a small error will be introduced. The idea is summarized in Fig. 4.

Merging scheme. The here proposed merging scheme preserves 1) the statistical weight and 2) the properties of the SEs throughout the merge step.

The merging of two SEs i (with the weight W_i) and j (with the weight W_j) into a new SE at the position i (with the new weight $W_i^{(\mathrm{mrg})}$) conserves the number-concentration rendered by those SEs. This defines the value of $W_i^{(\mathrm{mrg})}$ by:

- Calculation of statistical weight:

$$W_i^{(\mathrm{mrg})} = W_i + W_j \,. \tag{16}$$

Furthermore, each SE i contains the values of the other properties $v_i = \left(v_i^{(1)}, v_i^{(2)}, v_i^{(3)}, \dots\right)^{\mathrm{T}}$ of the rendered part of the particle population (where $v_i^{(A)}$ is a property of the SE such as the volume, composition, electric charge, etc. for $A = 1, 2, 3, \dots$). In a general situation, conserved extensive properties[4] $v_i^{(A)}$ are most suitable for the here presented merging scheme, because the total amount of the property (per system volume) $v_{\mathrm{tot}(i,j)}^{(A)}$ rendered by the two SEs i and j can be rendered by a weighted addition:

$$v_{\mathrm{tot}(i,j)}^{(A)} = W_i \cdot v_i^{(A)} + W_j \cdot v_j^{(A)} \,. \tag{17}$$

This total amount (per system volume) can also be rendered by the merged particle at the position i with the new properties $v_i^{(A,\mathrm{mrg})}$, $A = 1, 2, 3 \dots$:

$$W_i^{(\mathrm{mrg})} \cdot v_i^{(A,\mathrm{mrg})} = v_{\mathrm{tot}(i,j)}^{(A)} = W_i \cdot v_i^{(A)} + W_j \cdot v_j^{(A)} \,. \tag{18}$$

This equation defines the new property values $v_i^{(A,\mathrm{mrg})}$, for all A, because the value for the new statistical weight $W_i^{(\mathrm{mrg})}$ has already been defined in Eq. (16). The combination of these two equations leads to an explicit formula for the value of the new property $v_i^{(A,\mathrm{mrg})}$ after the merge step:

- Calculation of each particle property value for $A = 1, 2, 3 \dots$:

$$v_i^{(A,\mathrm{mrg})} = \frac{W_i \cdot v_i^{(A)} + W_j \cdot v_j^{(A)}}{W_i + W_j} \,. \tag{19}$$

By using Eq. (16) and Eq. (19), the total mass and the particle concentration of the simulated system can be preserved exactly, if the volume (or mass) is the single property of the SE. This stands in contrast to the merging method presented by [22], which does preserve the total mass only if two SEs with $v_i \approx v_j$ can be found.

Merging error. The error introduced into the simulation by the merging of the SEs i and j can be estimated by the following formula:

$$E_{(i,j)} = \sum_{\substack{\text{all properties} \\ A=1,2,\dots}} \alpha_A \cdot \left(\frac{\left(v_i^{(A)} - v_j^{(A)}\right)}{\min\left(v_i^{(A)}, v_j^{(A)}\right)} \right)^2 \,, \tag{20}$$

where α_A are *merging weights*, which can be set arbitrarily (depending on the simulated physical system) they can be interpreted as a measure of the severity, which the deviation of the property $v_i^{(A_1)}$ from $v_j^{(A_1)}$ would have – compared to the deviation of other properties $v_i^{(A_2)}$ from $v_j^{(A_2)}$. In the case of a single simulated particle property, any setting for the parameter $\alpha_1 > 0$ would lead to the same result of the low-weight merging algorithm further below. The specific value $\alpha_1 = 1$ has been used in this work.

Low-weight merging. The random selection of two SEs i and j would result in a random merging error $E_{(i,j)}$ which may be excessively high. The smallest possible merging error can be estimated by the comparison of all possible pairs of SEs. The determination of this pair would prove very costly: $N_{\mathrm{SE}} \cdot (N_{\mathrm{SE}} - 1)$ comparisons are necessary, if N_{SE} SEs are used. A sound compromise between both scenarios is the sampling of a representation of the SEs and the estimation of the minimum error of this representation.

The low-weight merging is a technique for finding a SE-pair (i, j) with a minimal merging error. For one SE i_{LW} with a low (statistical) weight the merging error, $E_{i_{LW},j}$, which would arise from the merging with one of the other SEs j is calculated. A parallel algorithm, easily adaptable for GPU computing can be applied in order to calculate all $N_{\mathrm{SE}} - 1$ possible

[4] Conserved extensive properties, are properties whose total amount (per system volume) $v_{\mathrm{tot}(i)}^{(A)}$ rendered by a SE i can be written as: $v_{\mathrm{tot}(i)}^{(A)} = W_i \cdot v_i^{(A)}$. Examples for such properties are: the mass, volume, electric charge, etc.

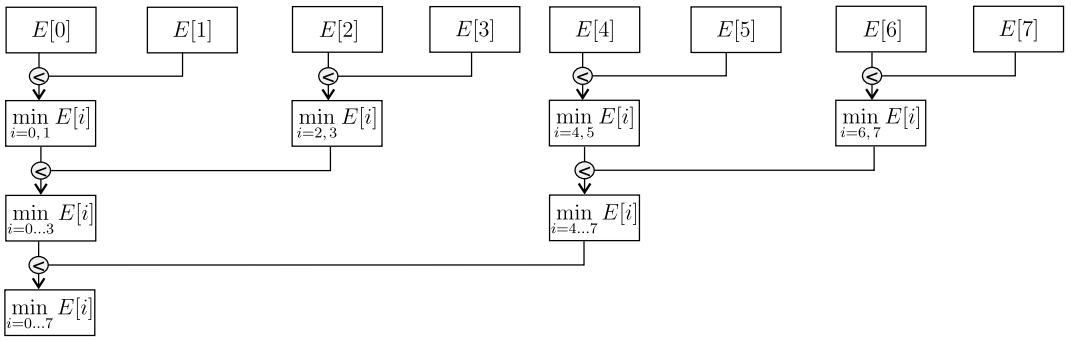

Fig. 5. One example for the parallel comparison algorithm, only $\log_2(N)$ parallel steps are necessary in order to find the minimum value of N elements.

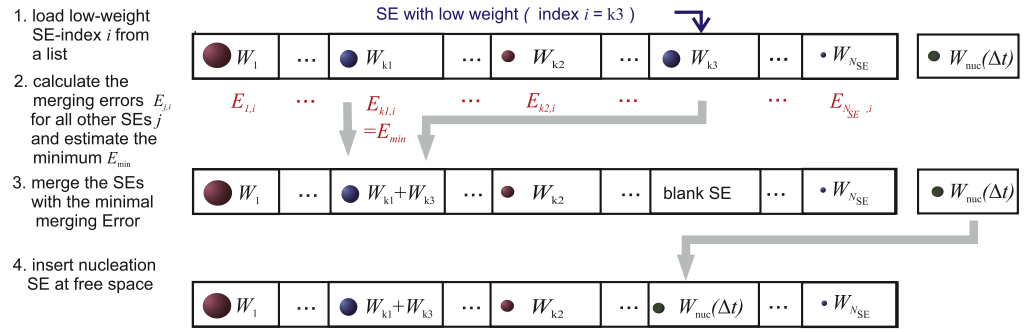

Fig. 6. Alteration of the N_{SE} SEs during one low-weight merging step.

combinations and find the pair with the minimal value. Only $\log_2 N_{\mathrm{SE}}$ computational steps are necessary if the algorithm in Fig. 5 is used. We discuss in the provided supplementary material, that the required resources for the exact computation of all $N_{\mathrm{SE}} \cdot (N_{\mathrm{SE}} - 1)$ merging pairs in order to find the exact merging error is not feasible with standard GPUs available to date, because the architecture of the GPU prohibits using Fig. 5 to compute the exact error with $O(2\log_2 N_{\mathrm{SE}})$ cost.

The algorithm in Fig. 5 is similar to the calculation of the mean coagulation rate presented by [34]. Fig. 6 summarizes the steps of the low-weight merging algorithm, which is shown in full detail as Algorithm 5 in Appendix A.4.

A new list with the indices of 100 SEs with low weights is created after every 100 merge steps. The necessary search of SEs with low weights is replaced in this way by a simple load operation of the indices of the SEs. If no SEs with a low weight can be found (e.g. at the beginning of the simulation, if all SEs have equal weights), the index of a randomly selected SE is stored in the list.

The preference for SEs with low weights has two reasons: first, the alterations of the PSD are smaller than due to the merging of SEs with higher weights. Second, the replacement of SEs with the lowest statistical weights with SEs with higher weights allows the coagulation steps to be performed within a lower stochastic resolution and makes thus less simulation steps necessary.

3. Validation

3.1. Simulated system

Only one particle property, the volume v is used to characterize the SEs. The coagulation kernel for the free-molecular regime, β_{fm} is chosen as one option for the description of the coagulation process (i.e. the kernel β).

$$\beta_{\mathrm{fm}} = \left(\frac{3}{4\pi}\right)^{\frac{1}{6}} \sqrt{\frac{6k_{\mathrm{B}}T}{\rho_p}} \cdot \sqrt{\frac{1}{v_1} + \frac{1}{v_2}} \cdot \left(v_1^{\frac{1}{3}} + v_2^{\frac{1}{3}}\right)^2 . \tag{21}$$

This coagulation kernel describes the rate of coagulation of two aerosol particles with the volumes v_1 and v_2, where the particle size is much smaller than the mean free path of the gas. The chosen variables and their settings are listed in Table 1, k_{B} is the Boltzmann constant.

The coagulation kernel in the continuum regime, β_{co}, has been investigated as well:

$$\beta_{\mathrm{co}} = \frac{2k_{\mathrm{B}} \cdot T}{3\eta} \cdot \left(v_1^{\frac{1}{3}} + v_2^{\frac{1}{3}}\right) \cdot \left(v_1^{-\frac{1}{3}} + v_2^{-\frac{1}{3}}\right) . \tag{22}$$

Table 1
The parameters used for the simulation of combined nucleation and coagulation.

	Free-molecular system ($\beta = \beta_{\mathrm{fm}}$)	Continuum system ($\beta = \beta_{\mathrm{co}}$)
Temperature	$T = 300\,\mathrm{K}$	$T = 300\,\mathrm{K}$
Particle density	$\rho_p = 1\,\frac{\mathrm{g}}{\mathrm{cm}^3}$	–
Viscosity	–	$\eta = 1.865 \cdot 10^{-5}\,\mathrm{Pa\,s}$
Initial concentration	$N_0 = 10^{17}\,\mathrm{m}^{-3}$	$N_0 = 10^{17}\,\mathrm{m}^{-3}$
Initial/nuclei diameter	$d_0 = 3 \cdot 10^{-9}\,\mathrm{m}$	$d_0 = 3 \cdot 10^{-9}\,\mathrm{m}$
Nucleation rates	$R_{\mathrm{N}} = 10^{14}, 10^{15}, 10^{16}, 10^{17}\,\mathrm{m}^{-3}\mathrm{s}^{-1}$	$R_{\mathrm{N}} = 10^{17}\,\mathrm{m}^{-3}\mathrm{s}^{-1}$
Inserted nucleation mass during $t_{\mathrm{tot}}^{(\mathrm{fm})}$ or $t_{\mathrm{tot}}^{(\mathrm{co})}$	ca. 5%, 50%, 500% and 5000% fraction (%) of the initial mass	ca. 3000%
Simulation time	$t_{\mathrm{tot}}^{(\mathrm{fm})} = 1000 \cdot \tau_{\mathrm{fm}} \approx 51.8\,\mathrm{s}$	$t_{\mathrm{tot}}^{(\mathrm{co})} = 1000 \cdot \tau_{\mathrm{co}} \approx 33.8\,\mathrm{s}$

This kernel describes the coagulation of aerosol particles whose particle size is much bigger than the mean free path of the gas. It is also valid for particles in liquids, such as encountered in crystallization processes. The value for the used viscosity η is also listed in Table 1.

The particles are modeled as spheres and the usage of Eq. (21) (resp. Eq. (22)) in combination with the PBEs (Eq. (1)) implicitly states that particles formed due to coagulation are spheres as well.[5] The diameter d of those particles will be used in order to describe the initial conditions and simulation results.

For both coagulation kernels, a monodisperse particle population with a concentration N_0 and diameter d_0 (both listed in Table 1) is used as initial condition. The concentration is distributed uniformly over the N_{SE} SEs, so that each SE i has a statistical weight of $W_i = N_0/N_{\mathrm{SE}}$ at the beginning of the simulation.

The typical time scale for the coagulation of such a monodisperse initial population is τ_{fm} for the free-molecular regime and τ_{co} for the continuum regime, with:

$$\tau_{\mathrm{fm}} \approx \sqrt{\frac{1 \cdot \rho_p}{3 \cdot k_{\mathrm{B}} \cdot T \cdot d_0}} \cdot \frac{1}{N_0} \quad \text{and} \quad \tau_{\mathrm{co}} \approx \frac{3}{4} \cdot \frac{\eta}{k_{\mathrm{B}} \cdot T} \cdot \frac{1}{N_0}. \tag{23}$$

This is the time in which the initial concentration N_0 would reduce to $N_0/2$ due to the coagulation in a monodisperse model in absence of any other physical process [36]. A total simulation time of $t_{\mathrm{tot}}^{(\mathrm{fm})} = 1000 \cdot \tau_{\mathrm{fm}}$ is simulated for the free-molecular regime and $t_{\mathrm{tot}}^{(\mathrm{co})} = 1000 \cdot \tau_{\mathrm{co}}$ for the continuum regime.

Constant nucleation rates listed in Table 1 have been investigated. The particles were included with a diameter $d_0 = 3\,\mathrm{nm}$, which is the diameter of the monodisperse initial population. Although the diameters of the included SEs can easily be altered in the scope of the MC simulation, a constant diameter facilitates an accurate benchmark simulation with the help of the discrete-sectional method.

3.2. Validation method

For validation, a volume-based discrete-sectional model was applied, based on the work by [37] which is an extension of the sectional method introduced by [38] by discrete points in order to render the first monomer values more correctly. The simplification by [39] has been used, too. The discrete-sectional method solves the PBE (1) by a discretization of the continuous variable v into discrete points and sections, a one-dimensional grid (referred to as 'grid' in the following) is applied for the discretization. The partial differential equation (1) is transformed in this way to a set of coupled ordinary differential equations (ODE), which can be solved by application of available ODE solvers. The Gear method is used for this purpose in this work. The discrete-sectional-model is considered to produce a very exact numerical solution of the coagulation equation when a very fine discretization grid is chosen [11]. In this work, 250 discrete points designating integer multiples of the initial volume, and 400 sections, whose width increase with the factor $2^{\frac{1}{12}} \approx 1.059$, have been used in combination with the discrete volume-based model from [37].

Simulations with finer grid settings have been performed in order to measure, whether further refinement of the grid has a significant impact on the PSD. The results for the free-molecular regime with a nucleation rate of $R_{\mathrm{N}} = 10^{17}\,\mathrm{m}^{-3}$ for the time $t_{\mathrm{tot}}^{\mathrm{fm}}$ are shown in the following, because they exhibited the strongest dependency on the grid settings. Table 2 summarizes the used grid settings and the estimated values for the mean geometric diameter d_{DS} and the geometric standard deviation σ_{DS}, the precise calculation of these values for discrete-sectional grids is described in [37]. The subscript 'DS' is used (instead of d_g and σ_g) in order to underline that the calculated values are estimated by means of the discrete-sectional method. We expect the 'finest' grid (with 1000 discrete points, and 1600 sections) to produce the most accurate results $\sigma_{\mathrm{DS}}^{\mathrm{acc}}$, $d_{\mathrm{DS}}^{\mathrm{acc}}$. In order to quantify the relative error in reference to these accurate results, the relative values $\Delta\sigma_{\mathrm{DS}}$ and Δd_{DS} are used, which are defined by:

[5] This models an instantaneous coalescence of the newly formed particles. The behavior of droplets can be described with the same kernel and PBEs as well.

Table 2
Characteristic values of the PSD (for the free-molecular regime, $R_N = 10^{17}\,\mathrm{m}^{-3}$ and $t_{tot}^{(fm)}$) resulting from different grid settings for the discrete-sectional method.

Grid settings[a]			Geometric mean diameter		Geo. standard deviation		Computing
Points/sections	Q	$2^{1/Q}$	d_{DS}/nm	$\Delta d_{DS}/10^{-3}$	σ_{DS}	$\Delta\sigma_{DS}/10^{-3}$	time/10^3 sec
63/100 (42)	3	1.260	3.4458	1.36	1.3455	2.01	0.01
125/200 (78)	6	1.122	3.4434	0.58	1.3440	0.89	0.18
250/400 (144)	12	1.059	3.4423	0.26	1.3433	0.37	1.82
500/800 (263)	24	1.029	3.4417	0.09	1.3429	0.07	18.7
1000/1600 (478)	48	1.015	3.4414	–	1.3428	–	240

[a] The number of used discrete points N_{dp}, the total number of used sections N_{sec} and (in brackets) the number of sections, which are smaller than $100\,d_0$ are shown. The factor Q is used to calculate the value $2^{1/Q}$, with which the width of the sections increases. The specific values for boundaries of the sections are: $B_k = d_0 \cdot (N_{dp} + 0.5)^{1/3} \cdot 2^{k/3\cdot Q}$. The 2 boundaries B_{k-1} and B_k define the section k with $k = 1 \ldots N_{sec}$.

$$\Delta\sigma_{DS} = \frac{|\sigma_{DS}^{acc} - \sigma_{DS}|}{\sigma_{DS}^{acc}}\,, \qquad \Delta d_{DS} = \frac{|d_{DS}^{acc} - d_{DS}|}{d_{DS}^{acc}}\,. \tag{24}$$

This values are dependent on the used grid and listed in Table 2. For the setting of 250 discrete points and 400 sections, a value of ca. $\Delta\sigma_{DS} = 2 \cdot 10^{-4}$ is reached. This systematical error is lower than the inherent statistical noise of the MC simulations discussed in the results section below, and can be therefore neglected for the benchmarking process.

4. Results and discussion

In order to determine which particle insertion technique leads to the highest precision, the MC simulations were performed for a very high γ-setting ($\gamma = 2 \cdot 10^4$) with a coagulation kernel resulting from the stochastic resolution theory.

This high γ-values are necessary, in order to avoid systematic errors caused by the approximation of β_{max} by the fast simulation technique. Lower γ values than 20 000 lead to systematic errors, higher γ values lead to no palpable alteration of the simulation results. This stands in contrast to earlier findings of a relatively small γ-value for the simulation of coagulation (based on the fictitious particle theory) of broad, bimodal PSDs in the free-molecular regime ($\gamma = 40$) [34] or the continuum regime ($\gamma = 40$–200) [40]. Both cited studies used results of the integration of log-normal PSDs as statistical weights for the SEs. It can be assumed, that the statistical scatter of those weights is much smaller than the one resulting from the simulation algorithms (low-weight merging and random removal) presented in this study. The lower statistical scatter of those weights leads in turn to lower necessary γ-values. This would explain the discrepancy of the cited studies to the presented results.

4.1. Nucleation and coagulation in the free-molecular regime

In this section, the results of the nucleation combined with the coagulation in the free-molecular regime is discussed.

Fig. 7 shows exemplary PSDs for the nucleation rate $R_N = 10^{14}\,\mathrm{m}^{-3}\,\mathrm{s}^{-1}$ gained from MC simulation in comparison with the benchmark solution based on the discrete-sectional method. The inserted mass due to the nucleation process comprises only a small fraction of the initial mass (5% during $t_{tot}^{(fm)}$). The mass-based PSD assumes therefore a form which would be attained for the coagulation process (without nucleation) with a single 'coagulation peak'. The number-based PSD is marked by the coagulation peak and a second 'nucleation peak' for larger simulation times t.

It can be seen, that both techniques (random removal and low-weight merging) reproduce PSDs in reasonable agreement with the benchmark solution. Higher nucleation rates lead to higher particle concentrations and thus higher coagulation rates and smaller MC time steps, τ_{mc}. Thus more MC time steps are needed for the simulation of the time $t_{tot}^{(fm)}$ and more SEs are inserted into the simulation. This leads to an augmentation of the systematic and stochastic errors.

For a high nucleation rate $\left(R_N = 10^{17}\,\mathrm{m}^{-3}\,\mathrm{s}^{-1}\right)$ and a long simulation time ($t = 1000\tau_{fm}$), only the low-weight merging using 10^4 SEs is still able to produce a good approximation of the results, while using 1000 SEs or the random removal technique (with 10^3 or 10^4 SEs) lead to clear deviations from the benchmark solution, as shown in Fig. 8.

The mean geometric diameter d_g is used to calculate the geometric standard deviation (GSD) σ_g by the summation over all SEs i with the diameter d_i and the statistical weight W_i:

$$\ln(d_g) = \frac{\sum_i \ln(d_i) W_i}{\sum_i W_i}\,, \quad \left(\ln(\sigma_g)\right)^2 = \frac{\sum_i \left(\ln(d_i) - \ln(d_g)\right)^2 W_i}{\sum_i W_i}\,. \tag{25}$$

The values of σ_g of the PSDs resulting from MC simulation results can be used as a measure of the statistical noise and the systematic errors. The statistical noise is measured by comparison of the arithmetic mean, $\overline{\sigma}_{MC}$, for 100 values of σ_g gained by MC simulations (with 100 different random numbers), to the arithmetic standard deviation $\Delta\sigma_{MC}$ of those values. Fig. 9 shows the ratio $\Delta\sigma_{MC}/\overline{\sigma}_{MC}$. The much higher precision of the low-weight merging technique compared to

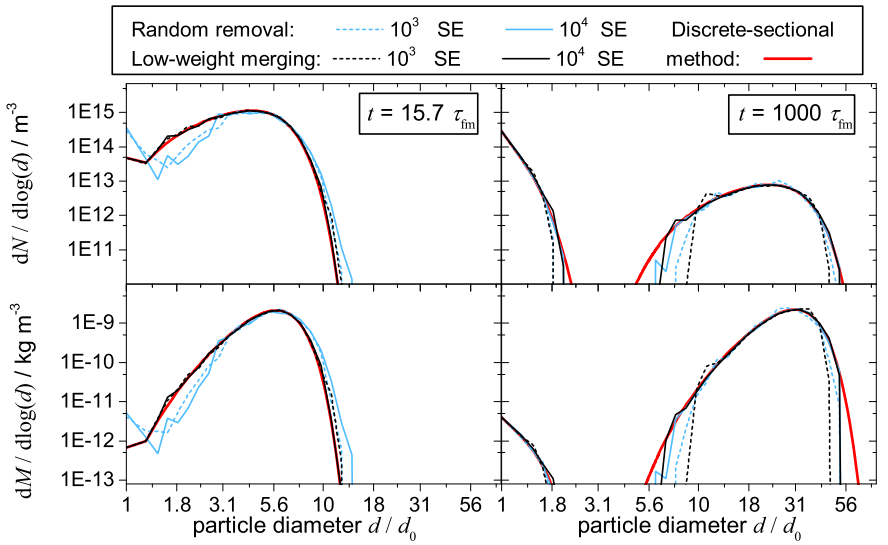

Fig. 7. Number- ($\mathrm{d}N/\mathrm{dlog}(d)$) and mass-based ($\mathrm{d}M/\mathrm{dlog}(d)$) PSDs resulting for the nucleation rate $R_\mathrm{N} = 10^{14}\ \mathrm{m}^{-3}\,\mathrm{s}^{-1}$ and coagulation in the free-molecular regime.

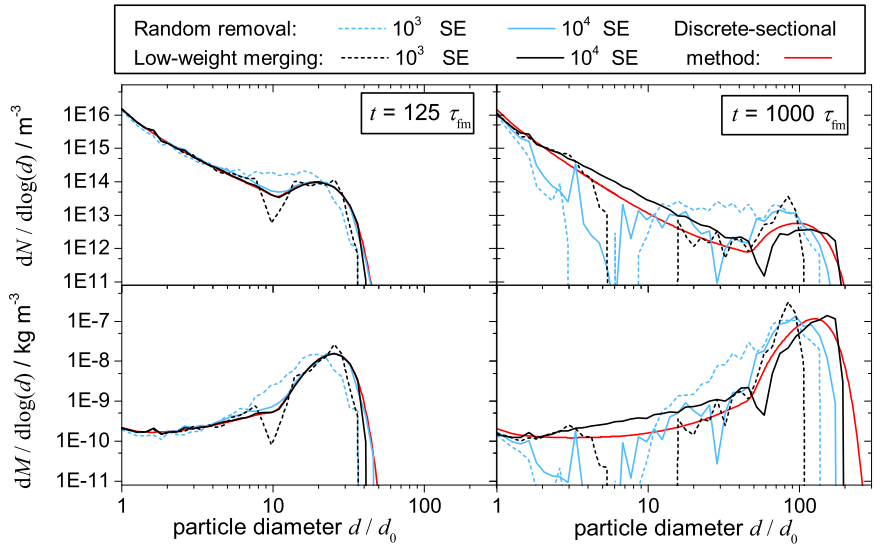

Fig. 8. Number- ($\mathrm{d}N/\mathrm{dlog}(d)$) and mass-based ($\mathrm{d}M/\mathrm{dlog}(d)$) PSDs for the nucleation rate $R_\mathrm{N} = 10^{17}\ \mathrm{m}^{-3}\,\mathrm{s}^{-1}$ and coagulation in the free-molecular regime.

the random removal method can be clearly seen. For longer simulation times, the simulations using the random removal technique with 10 000 SEs cannot attain the level of accuracy of the low-weight merging technique with 1000 SEs which applies only one tenth of the computational resources.

The increase of the statistical errors in the course of the simulation can be explained by the broadening of the PSD, for the random removal method. Hence the randomly selected particle can represent any part of the PSD, so that a broader PSD is more susceptible to the noise introduced by the random selection of the removed particle.

The systematic errors introduced into the MC simulations are measured by the comparison of $\overline{\sigma}_\mathrm{MC}$ to the benchmark value σ_DS, which is the value for σ_g resulting from the discrete-sectional simulations. Fig. 10 shows the values $|(\overline{\sigma}_\mathrm{MC}/\sigma_\mathrm{DS}) - 1|$.

The systematic errors introduced into the simulation due to the low-weight merging technique are increasing for higher nucleation rates $\left(10^{17}\,\mathrm{m}^{-3}\,\mathrm{s}^{-1}\right)$ and longer simulation times t. This increase can be explained by the broadening of the corresponding PSDs, which diminishes the chances of finding a pair of SEs with a low merging error. However, the low-weight merging technique can clearly ascertain a higher accuracy than the random removal method, whose accuracy is limited by the much higher statistical errors shown in Fig. 9.

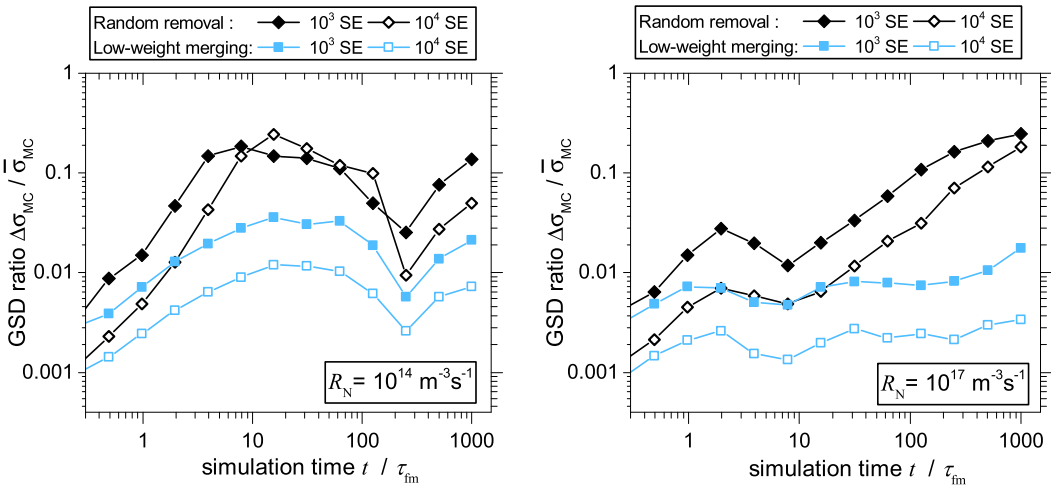

Fig. 9. The ratio $\Delta\sigma_{MC}/\overline{\sigma}_{MC}$ for different nucleation rates R_N and coagulation in the free-molecular regime. This ratio is used as a measure for the statistical errors.

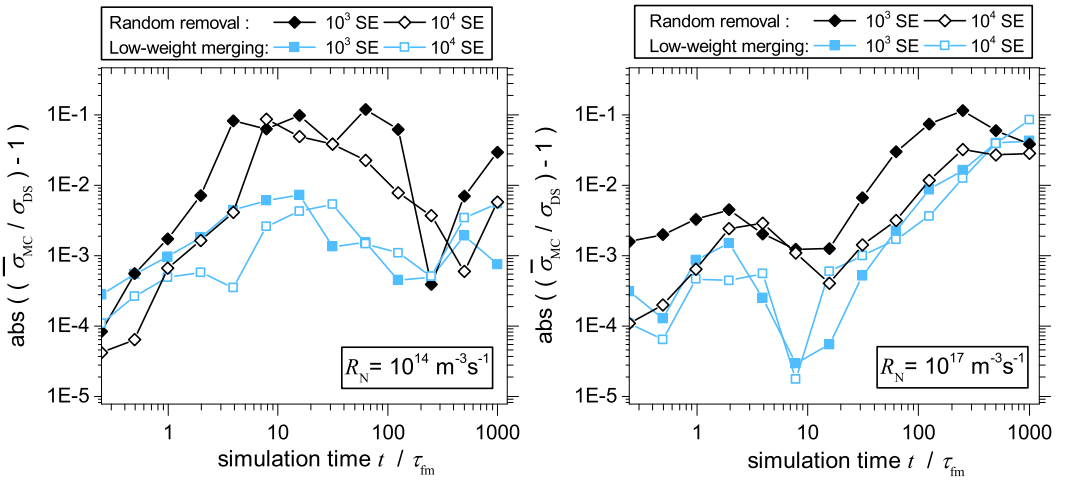

Fig. 10. The value $|(\overline{\sigma}_{MC}/\sigma_{DS}) - 1|$ for different nucleation rates R_N and coagulation in the free-molecular regime. This value is used as a measure for the systematic errors of the MC simulations.

The simulation becomes less reliable for longer simulation times (for $N_R = 10^{17}$ m^{-3} s^{-1}), casting a doubt on the applicability of the simulation for particle sizes up to the micrometer scale (i.e. until $d \approx 10^3 d_0$–$10^4 d_0$). For practical industrial applications, however, the assumption of a constant nucleation rate is not realistic for particle synthesis from the gaseous phase, i.e. [23,2], where particle sizes up to hundreds of nanometers are simulated. For particle growth to micron-sized particles, the supersaturation would be greatly reduced due to the monomer consumption and the nucleation rate would become very small.

A more challenging modeling task would be the application of coating of micron sized particles in fluidized beds [41], where continuously nanoparticles are fed into the reactor. The question whether the developed techniques are applicable to the simulation of such a bivariate system is out of the scope of this paper.

4.2. Nucleation and coagulation in the continuum regime

The results for the simulation of nucleation and coagulation in the continuum regime show the same characteristics as the simulations with the free-molecular regime, i.e. higher accuracy if the low-weight merging technique is used than the random removal method, given the same number of N_{SE}. Higher numbers of SE, $N_{SE} = 10^5$, have been used for the simulation in order to show that the accuracy can be increased further by the application of more SEs, as can be seen in the PSDs shown in Fig. 11.

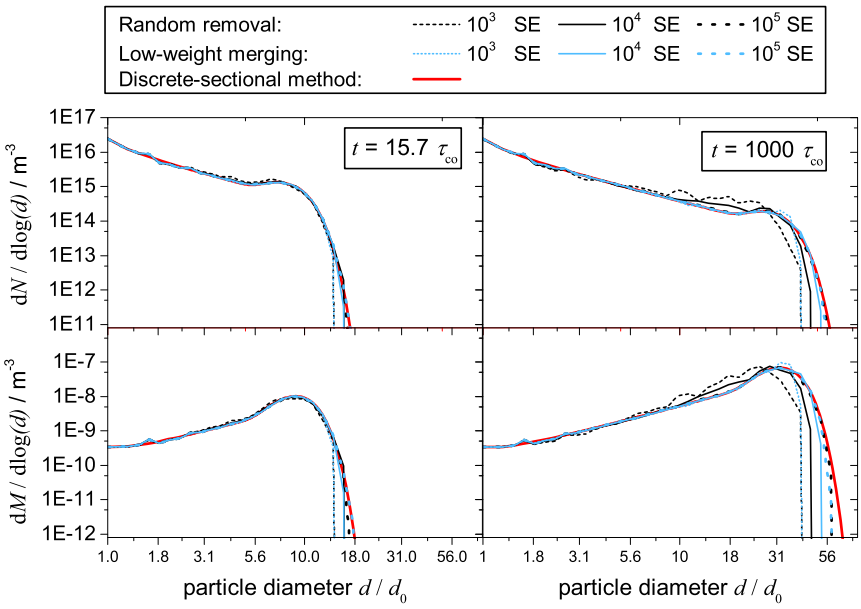

Fig. 11. Number- ($\mathrm{d}N/\mathrm{dlog}(d)$) and mass-based ($\mathrm{d}M/\mathrm{dlog}(d)$) PSDs for the nucleation rate $R_\mathrm{N} = 10^{17}$ m^{-3} s^{-1} and coagulation in the continuum regime.

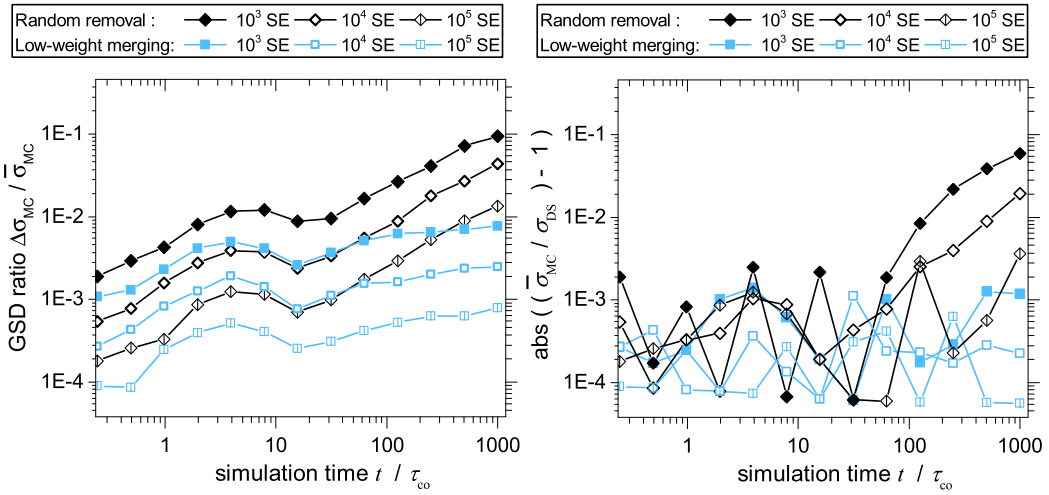

Fig. 12. The values $\Delta\sigma_\mathrm{MC}/\overline{\sigma}_\mathrm{MC}$ (statistical errors) and $|(\overline{\sigma}_\mathrm{MC}/\sigma_\mathrm{DS}) - 1|$ (systematic errors) for the nucleation rate $R_\mathrm{N} = 10^{17}$ m^{-3} s^{-1} and coagulation in the continuum regime.

Fig. 12 shows the increase of the statistical and systematic errors in the course of the simulation. These results are similar to the findings for the free-molecule regime presented in Fig. 9 and Fig. 10. As expected for MC simulations, the factor $\Delta\sigma_\mathrm{MC}/\overline{\sigma}_\mathrm{MC}$ is proportional to $\frac{1}{\sqrt{N_\mathrm{SE}}}$.

4.3. Computational efficiency

The required computational times are shown in Fig. 13. All MC simulations were carried out on a GPU, Nvidia's GeForce GTX Titan X. The implementation on the GPU allows for the parallel calculation of 100 or more simulations,[6] the computing times shown in Fig. 13 refer to these parallel calculations. The simulations for the discrete-sectional method were carried out on the CPU (Intel i7-4790K, quad-core 4.00 GHz and 32 GB RAM) and the CPU time for one simulation is shown in Fig. 13a. The computing times in dependency of the grid setting for the discrete-sectional method are discussed in

[6] This can at least be programmed, how many simulations are actually performed in parallel, depends on the complexity of the single computing step and the used GPU, a more detailed discussion of this topic can be found in the supplementary material (section 1.2).

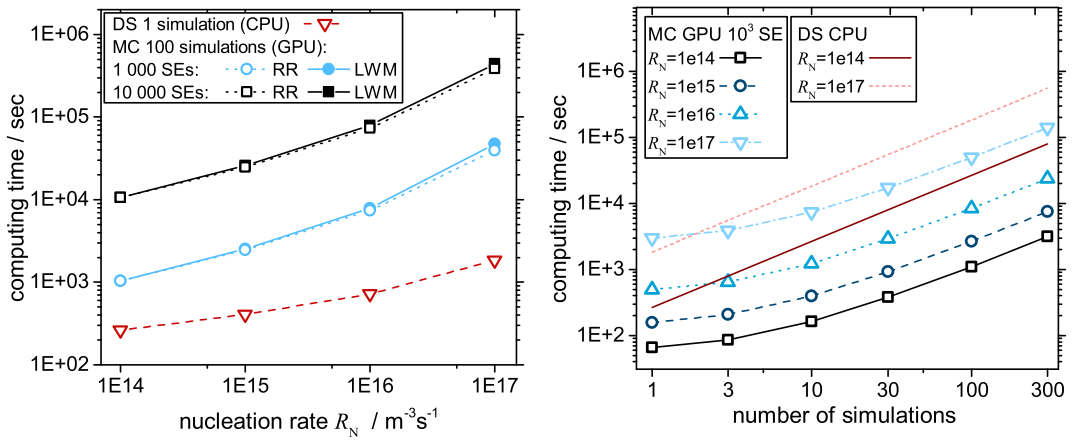

(a) Computational times for 100 MC simulations. (b) Computational times for LWM-based MC simulations.

Fig. 13. The computational times for the simulation of the time $t_{\mathrm{tot}}^{(fm)}$ required for simulations using the low-weight merging (LWM) or the random removal (RR) techniques for different nucleation rates $R_{\mathrm{N}}/\mathrm{s}^{-1}\,\mathrm{m}^{-3}$ and the free-molecule regime. The results of the discrete-sectional method (DS) are shown for 250 discrete points and 400 sections.

Table 2. In order to make the computational times more comparable with each other, the CPU times for more than one simulation are shown for the discrete-sectional method in Fig. 13b, these values are linear projections (i.e. X times the measured value for one simulation is the CPU time for X simulations). It can be seen in Fig. 13b, that a certain level of parallelism can be attained for the MC simulations and that the simulation times become proportional to the number of simulations for larger numbers of simulations. The computational time which is required for 100 simulations is only 10 times larger than the computational time required for one simulation. It can be seen in Fig. 13a, that the low-weight merging technique (marked as LWM) requires nearly the same simulation time as the random removal technique (marked as RR). The increment of the SEs by a factor of 10 leads to computational times, which are a factor 10 higher. However, even if the random removal technique is performed for 10 000 and not 1000 SEs, the statistical accuracy of the low-weight merging technique with just 1000 SEs cannot be reached at least for longer simulation times, as can be seen in Fig. 9. The discrete-sectional method, is an excellent benchmark for this specific problem, as can be seen in Table 2 by the high levels of accuracy which are gained by the different grid settings. Even a rather modest grid (consisting of 250 discrete points and 400 sections), whose CPU times are shown in Fig. 13, can provide a much higher level of accuracy (the shown value $\Delta^{(\mathrm{DS})}\sigma_g = 3.7 \cdot 10^{-4}$ in Table 2 is the maximal value attained at the end of the simulation) than MC simulations with 10^4 SE.

5. Conclusions

The MC-based simulation of coagulation and nucleation is very challenging as the continuous inclusion of freshly nucleated particles has to be incorporated into the simulation. A simple test system simulating coagulation in the free-molecular regime and a constant rate nucleation has been proposed as a benchmark because very accurate simulation results can be gained by the application of the discrete-sectional method to this problem. The simulation of this system by MC methods poses a challenging task: The conventionally used random removal technique infers a large amount of statistical noise into the simulation, like shown in this work. An alternative approach has been presented for weighted simulation entries: the low-weight merging, which produces clearly less statistical noise and is able to render the simulation results correctly, for conditions for which the random removal method fails. The computational times which are required for the low-weight merging are only slightly higher than for the random-removal method.

The coagulation of differentially weighted simulation entries is a relatively novel concept and several methods have been proposed [25,27,26] for the correct description of the coagulation rates, resulting in different coagulation schemes. A novel approach in order to estimate the coagulation rates has been presented in this paper: virtual transformation of the simulation entries to equally weighted simulation entries are proposed in order to calculate the coagulation rates for distinct coagulation events. The setting of the accuracy of this transformation, the stochastic resolution, can be tuned in such a way, that only those coagulation events are considered, which keep the number of the simulation entries constant-describing a constant-number scheme in this way. This constant-number scheme is similar to the one proposed by [27] in the context of the fictitious particle theory. The corresponding coagulation rates are however different, depending on whether the stochastic resolution or the fictitious particle theory is used.

Notation

Latin letters

d	diameter
d_0	diameter of initial condition and nuclei diameter (Table 1)
d_{DS}	geometric mean diameter from discrete-sectional method
$d_{\mathrm{DS}}^{\mathrm{acc}}$	d_{DS} for most points/sections in Table 2
$\mathrm{d}N/\mathrm{d}\log(d)$	number-based PSD
$\mathrm{d}M/\mathrm{d}\log(d)$	mass-based PSD
$E_{i,j}$	merging error for 2 SEs i, j (Eq. (20))
$n(v)$	PSD
$N(\tilde{v}_\xi)$	number of EWSEs with $\tilde{v}_\xi$ (Eq. (B.1))
N_i	number of EWSEs for SE i (Eq. (4))
N_0	initial particle concentration (Table 1)
N_{SE}	total number of used SEs
R_{N}	nucleation rate/$\mathrm{m}^{-3}\,\mathrm{s}^{-1}$ (Table 1)
s_{F}	concentration of real particles per EWSE/m^{-3} (Eq. (4))
$t_{\mathrm{tot}}^{(\mathrm{fm})}$, $t_{\mathrm{tot}}^{(\mathrm{co})}$	total simulation time (Table 1)
v_i	property of EWSE i or SE i if $\dim(v) > 1$: $v_i = (v_i^{(1)}, v_i^{(2)}, v_i^{(3)}, \dots)^{\mathrm{T}}$
$v_i^{(A)}$	component A of vector v_i
$v_i^{(A,\mathrm{mrg})}$	$v_i^{(A)}$ after one merge step (Eq. (19))
$\tilde{v}_\xi$	property which any EWSE has prior to or can attain due to coagulation (Eq. (B.1))
W_i	statistical weight of SE i/m^{-3} (Eq. (4))
W_i^{new}	W_i after one coagulation event (Eq. (7))
$W_i^{(\mathrm{mrg})}$	W_i after one merge step (Eq. (16))
$W_i^{(\mathrm{rd})}$	W_i after one random removal step (Eq. (15))
W_{min}	$\min(W_i, W_j)$ for 2 SEs i, j
W_{max}	$\max(W_i, W_j)$ for 2 SEs i, j
W_{nuc}	W_i of freshly nucleated SE (Eq. (3))

Greek letters

β	physical coagulation rate (Eq. (21) or Eq. (22))
$\beta_{i,j}$	coagulation rate for 2 SEs or EWMCs i, j
$\beta^{(\mathrm{FP})}$	fictitious particle based $\beta_{i,j}$ for 2 SEs (Eq. (11))
$\beta^{(\mathrm{SR})}$	stochastic resolution based $\beta_{i,j}$ for 2 SEs for the constant-number scheme (Eq. (10))
$\beta_{\mathrm{EWSE}}^{s_{\mathrm{F}}}$	coagulation rate for 2 EWSEs i, j (Eq. (B.10))
$\beta_{\mathrm{SE}}^{s_{\mathrm{F}}}$	coagulation rate for 2 SEs i, j (Eq. (6))
Δd_{DS}	relative deviation of d_{DS} from $d_{\mathrm{DS}}^{\mathrm{acc}}$ (Eq. (24))
$\Delta\sigma_{\mathrm{DS}}$	relative deviation of σ_{DS} from $\sigma_{\mathrm{DS}}^{\mathrm{acc}}$ (Eq. (24))
$\Delta\sigma_{\mathrm{MC}}$	arithmetic standard deviation of σ_g for 100 MC simulations
γ	parameter (fast simulation technique, sec. 2.2.2)
σ_g	number-based geometric standard deviation (Eq. (25))
$\overline{\sigma}_{\mathrm{MC}}$	mean σ_g from 100 MC simulations
σ_{DS}	σ_g from discrete-sectional simulation
τ_{fm}, τ_{co}	time scale for coagulation (Eq. (23))
$\sigma_{\mathrm{DS}}^{\mathrm{acc}}$	σ_{DS} for most points/sections in Table 2

Acknowledgements

This work has been supported by the Deutsche Forschungsgemeinschaft (DFG) in the scope of the priority program SPP 1679 (KR 1723/15-2). G. Kotalczyk wishes to thank prof. Heiko Briesen (TU München) for an inspiring discussion on transformations of the PBE.

Appendix A. Algorithms

A.1. Main algorithm

Algorithm 1 Main algorithm for 1 CPU-thread.

$t \leftarrow 0$
repeat
  MC_Coag_step (Algorithm 2) ▷ calculates τ_{mc}
  $t \leftarrow t + \tau_{mc}$
  $W_{nuc} \leftarrow \tau_{mc} \cdot R_N$
  $v_{nuc} \leftarrow v_0$
  include_nuc_SE (Algorithm 5 low-weight-merging)
until $t \geq t_{tot}$

A.2. Fast Algorithm for one MC coagulation step

Algorithm 2 MC_coag_step algorithm for 1 CPU-thread.

repeat ▷ calculates β_{mean}
  find_coag_pair (i, j) (Algorithm 3)
until a coagulation pair (i, j) is found
▷ coagulation like in Fig. 2
if $W_i == W_j$ **then**
  $W_i \leftarrow W_i/2$
  $W_j \leftarrow W_j/2$
  $v_i \leftarrow v_i + v_j$
  $v_j \leftarrow v_i$
else
  if $W_i > W_j$ **then** ▷ $W_{max} = W_i$
    $W_i \leftarrow W_i - W_j$
    $v_j \leftarrow v_i + v_j$
  else ▷ $W_{max} = W_j$
    $W_j \leftarrow W_j - W_i$
    $v_i \leftarrow v_i + v_j$
  end if
end if
▷ time step
$\tau_{mc} \leftarrow ((N_{SE} - 1) \cdot N_{SE} \cdot \beta_{mean}/2)^{-1}$

The following calculation of β_{mean} follows the algorithm presented by [34] and is also depicted in Fig. 5 (the comparison operations have to be replaced with additions).

Algorithm 3 find_coag_pair algorithm for N_{sample} GPU-threads which execute the code in parallel, the command 'synchronize threads' forces the threads to stop and wait until all other threads have reached this point of execution.

▷ two SEs are drawn randomly (different values for each thread)
repeat
  $SE_1 \leftarrow$ uniform random integer $\in [0, (N_{SE} - 1)]$
  $SE_2 \leftarrow$ uniform random integer $\in [0, (N_{SE} - 1)]$
until $SE_1 \neq SE_2$
▷ calculation of β_{mean}
$\beta_{local} \leftarrow \beta^{(SR)}(SE_1, SE_2)$ via Eq. (10)
$\beta_{sum}[N_{sample}]$ declared as array with N_{sample} elements shared by all threads
$T_{idx} \leftarrow$ current thread index $(T_{idx} \in [0, (N_{sample} - 1)])$
$\beta_{sum}[T_{idx}] \leftarrow \beta_{local}$
synchronize threads
for $i = 1$; $i \leq \log_2(N_T)$; $i \leftarrow i + 1$ **do**
  DivBy $\leftarrow 2^i$
  Dist $\leftarrow 2^{i-1}$
  if $\mathrm{mod}(T_{idx}, \mathrm{DivBy}) == 0$ **then**
    $\beta_{sum}[T_{idx}] \leftarrow \beta_{sum}[T_{idx}] + \beta_{sum}[T_{idx} + \mathrm{Dist}]$
  end if
  synchronize threads
end for
$\beta_{mean} \leftarrow \beta_{sum}[0]/N_{sample}$ (stored as global variable)
▷ AR selection of coagulation pair
$U_3 \leftarrow$ uniform random floating point $\in (0, 1)$
if $U_3 < \beta_{local} \cdot (\beta_{mean} \cdot \gamma)^{-1}$ **then**
  CoagPair $(i, j) \leftarrow (SE_1, SE_2)$ (stored as global variable)
▷ The value is overwritten, if more than one pair is found.
end if

If there are more than one selected pairs, the selection of the last pair is equivalent to the random selection of one pair out of the selected pairs. The probability to select a pair (i, j) is equal for any thread. If two specific pairs (i_1, j_1) and (i_2, j_2) have been selected by two threads t_1 and t_2, without knowing which specific thread t has selected which pair (i, j), the probability to find the pair (i_1, j_1) by t_1 is equal to the probability to find (i_1, j_1) by $t2$. This is the fact for truly independent random numbers. We tested, that the XORWOW quasi-random number generator [42] used in this work ensures a sufficient independence of the generated random numbers.

A.3. Random removal algorithm

The smart bookkeeping method doesn't change the weights of the SEs during one random removal step, but adjusts a factor f, so that the explicit weight $W_i^{(\mathrm{real})}$ of the SE is $W_i^{(\mathrm{real})} = f \cdot W_i^{(\mathrm{stored})}$. The weights $W_i^{(\mathrm{stored})}$ are used for each coagulation step, because the probabilities are the same, independent on whether $W_{\max}^{(\mathrm{real})} = \max(W_i^{(\mathrm{real})}, W_j^{(\mathrm{real})})$ or $W_{\max}^{(\mathrm{stored})} = \max(W_i^{(\mathrm{stored})}, W_j^{(\mathrm{stored})}) = W_{\max}^{(\mathrm{real})}/f$ is used:

$$P_{i,j} = \frac{\beta^{(\mathrm{SR})}}{\gamma \cdot \beta_{\mathrm{mean}}^{(\mathrm{SR})}} = \frac{f \cdot W_{\max}^{(\mathrm{stored})} \cdot \beta(i,j)}{\gamma \cdot f \cdot \sum W_{\max}^{(\mathrm{stored})} \cdot \beta(i,j)}. \tag{A.1}$$

The time step has to be adjusted, because the stored values of $W_i^{(\mathrm{stored})}$ are used to calculate a value $\beta_{\mathrm{mean}}^{(\mathrm{stored})}$, so that the value $\tau_{\mathrm{mc}}^{(\mathrm{stored})}$ is returned by Algorithm 2 instead of the real value $\tau_{\mathrm{mc}}^{(\mathrm{real})}$:

$$\tau_{\mathrm{mc}}^{(\mathrm{stored})} = \frac{2}{(N_{\mathrm{SE}}-1)\cdot N_{\mathrm{SE}} \cdot \beta_{\mathrm{mean}}^{(\mathrm{stored})}}, \qquad \tau_{\mathrm{mc}}^{(\mathrm{real})} = \frac{2}{(N_{\mathrm{SE}}-1)\cdot N_{\mathrm{SE}} \cdot \beta_{\mathrm{mean}}^{(\mathrm{real})}}. \tag{A.2}$$

Hence $\beta_{\mathrm{mean}}^{(\mathrm{real})} = \beta_{\mathrm{mean}}^{(\mathrm{stored})} \cdot f$, the returned time step needs to be adjusted to the correct value by: $\tau_{\mathrm{mc}}^{(\mathrm{real})} = \tau_{\mathrm{mc}}^{(\mathrm{stored})}/f$.

This leads to the following Algorithm 4 for the MC simulation of coagulation and nucleation implemented for the random removal algorithm:

Algorithm 4 Main algorithm for 1 CPU-thread replaces Algorithm 1.

$t \leftarrow 0$
$f \leftarrow 1$
$M_{\mathrm{T}} \leftarrow \sum_{i=0}^{(N_{\mathrm{SE}}-1)} W_i \cdot v_i$
repeat
  MC_Coag_step (Algorithm 2) ▷ calculates $\tau_{\mathrm{mc}}^{(\mathrm{stored})}$
  $W_{\mathrm{nuc}} \leftarrow \tau_{\mathrm{mc}}^{(\mathrm{stored})} \cdot R_{\mathrm{N}}/f$
  $v_{\mathrm{nuc}} \leftarrow v_0$
  $t \leftarrow t + \tau_{\mathrm{mc}}^{(\mathrm{stored})}/f$
  $R \leftarrow$ uniform random integer $\in [0, N_{\mathrm{SE}}-1]$ ▷ estimate SE index R for removal
  $f \leftarrow f \cdot M_{\mathrm{T}}/(M_{\mathrm{T}} - v_R \cdot W_R)$ ▷ set values for next removal steps, Eq. (15)
  $M_{\mathrm{T}} \leftarrow M_{\mathrm{T}} + \tau_{\mathrm{mc}} \cdot R_{\mathrm{N}}$
  $v_R \leftarrow v_{\mathrm{nuc}}$ ▷ insert new SE
  $W_R \leftarrow W_{\mathrm{nuc}}$
until $t \geq t_{\mathrm{tot}}$

For the nucleation entry, the value $W_{\mathrm{nuc}}^{\mathrm{stored}} = \tau_{\mathrm{mc}} \cdot R_{\mathrm{N}}/f$ is stored, so that the real value $W_{\mathrm{nuc}}^{\mathrm{real}} = f \cdot W_{\mathrm{nuc}}^{\mathrm{stored}}$ is rendered correctly.

A.4. Parallel implementation of low-weight merging scheme

Algorithm 5 low_weight_merging algorithm for N_{SE} GPU-threads which execute the code in parallel leading to a free SE_1. The command 'synchronize threads' forces the threads to stop and wait until all other threads have reached this point of execution.

▷ select two SEs for the merging

$SE_1 \leftarrow$ low_weight_list[list_idx]
$T_{idx} \leftarrow$ current thread index ($T_{idx} \in [0, (N_{\mathrm{sample}} - 1)]$)
if $T_{idx} == 0$ **then**
  list_idx $\leftarrow$ list_idx $- 1$
end if
$SE_2 \leftarrow \mathrm{mod}(SE_1 + T_{idx}, N_{\mathrm{T}})$

▷ calculation of E_{min}

$E_{\mathrm{local}} \leftarrow E_{(i,j)}(SE_1, SE_2)$ via Eq. (20)
$E_{\mathrm{m}}[N_{\mathrm{T}}]$ declared as array with N_{T} elements visible for all threads
$\mathrm{m_{id}}[N_{\mathrm{T}}]$ declared as array visible for all threads
$E_{\mathrm{m}}[T_{idx}] \leftarrow E_{\mathrm{local}}$
$\mathrm{m_{id}}[T_{idx}] \leftarrow T_{idx}$
synchronize threads
for $i = 1\ ;\ i \leq \log_2(N_{\mathrm{T}})\ ;\ i \leftarrow i + 1$ **do**
  Div $\leftarrow 2^i$
  Dist $\leftarrow 2^{i-1}$
  if $\mathrm{mod}(T_{idx}, \mathrm{Div}) == 0$ **and** $(T_{idx} + \mathrm{Dist} \leq N_{\mathrm{SE}})$ **then**
    if $E_{\mathrm{m}}[\mathrm{m_{id}}[T_{idx}]] > E_{\mathrm{m}}[\mathrm{m_{id}}[T_{idx} + \mathrm{Dist}]]$ **then**
      $\mathrm{m_{id}}[T_{idx}] \leftarrow \mathrm{m_{id}}[T_{idx} + \mathrm{Dist}]$
    end if
  end if
  synchronize threads
end for

▷ merge and include new SE

if $T_{idx} == 0$ **then**

▷ merge step Eqs. (16) and (19) with global variables v and W

  $SE_2 \leftarrow SE_1 + \mathrm{m_{id}}[0]$
  $v_{SE_2} \leftarrow \left(v_{SE_1} \cdot W_{SE_1} + v_{SE_2} \cdot W_{SE2}\right) / \left(W_{SE_1} + W_{SE_2}\right)$
  $W_{SE_2} \leftarrow W_{SE_1} + W_{SE_2}$

▷ include new SE with global variables v and W

  $v_{SE_1} \leftarrow v_{\mathrm{nuc}}$
  $W_{SE_1} \leftarrow W_{\mathrm{nuc}}$
end if

Appendix B. Transformation of the PBE to the discrete EWSE-form

A finite set of EWSEs implies a finite set (consisting of N_{prop} elements) of all possible property-values $\tilde{v}_\xi$ ($\xi = 1, 2, \ldots, N_{\mathrm{prop}}$) which any EWSE has prior to – or could hypothetically attain after one coagulation step. Instead of summing over all EWSEs for the rendition of the PSD, one can also sum over all property values $\tilde{v}_\xi$:

$$n(v) = s_F \sum_i \delta(v - v_i) = s_{\mathrm{F}} \sum_\xi N(\tilde{v}_\xi)\delta(v - \tilde{v}_\xi)\,. \tag{B.1}$$

$N(\tilde{v}_\xi)$ denotes the number of all EWSEs, whose property v is exactly equal to $\tilde{v}_\xi$.
This expression (Eq. B.1) is inserted into the PBE for coagulation[7]:

$$\frac{\mathrm{d}n(v)}{\mathrm{d}t} = \frac{1}{2}\int_0^v \beta(v - v', v')n(v - v')n(v')dv' - n(v)\int_0^\infty \beta(v, v')n(v')dv'\,. \tag{B.2}$$

This yields the equation (B.3) = (B.4) + (B.5), with:

$$\frac{\mathrm{d}}{\mathrm{d}t}\left(s_{\mathrm{F}} \sum_\xi N(\tilde{v}_\xi)\delta(\tilde{v}_\xi - v)\right) \tag{B.3}$$

$$= \frac{s_{\mathrm{F}}^2}{2}\int_0^v \beta(v - v', v') \sum_\xi N(\tilde{v_\xi})\delta(\tilde{v}_\xi - (v - v')) \quad \times \sum_\chi N(\tilde{v_\chi})\delta(\tilde{v}_\chi - v')\mathrm{d}v' \tag{B.4}$$

[7] The term $v'' = v - v'$ has to be interpreted in such a way, that the coagulation of two particles with the (possibly multi-dimensional) properties v' and v'' leads to a particle with the property v.

$$-s_F^2 \sum_{\xi} N(\tilde{v}_\xi)\delta(\tilde{v}_\xi - v) \quad \times \int_0^\infty \beta(v, v') \sum_{\chi} N(\tilde{v_\chi})\delta(\tilde{v}_\chi - v')\mathrm{d}v' \,. \tag{B.5}$$

The integrations can be evaluated with the following rule:

$$\int_C \sum_{\xi} N(\tilde{v}_\xi)\delta(\tilde{v}_\xi - v)\mathrm{d}v = \sum_{\xi,\ \tilde{v}_\xi \in C} N(\tilde{v}_\xi) \,, \tag{B.6}$$

this leads to an expression for Eq. (B.4):

$$\text{(B.4)} = \frac{s_F^2}{2} \sum_{\tilde{v}_\chi < v} \beta(v - \tilde{v}_\chi, \tilde{v}_\chi) \sum_{\xi} N(\tilde{v_\xi})\delta(\tilde{v}_\xi - (v - \tilde{v}_\chi))N(\tilde{v_\chi}) \,. \tag{B.7}$$

The short notation $\sum_{\xi,\ \tilde{v}_\xi < v}$ denotes the summation over all properties $\tilde{v}_\xi$ which are smaller[8] than v. The integration of Eq. (B.5) yields:

$$\text{(B.5)} = -s_F^2 \sum_{\xi} N(\tilde{v}_\xi)\delta(\tilde{v}_\xi - v) \sum_{\chi} \beta(v, \tilde{v}_\chi)N(\tilde{v}_\chi) \,. \tag{B.8}$$

For each of all possible property values, $\tilde{v}_\phi$, there exists a region, C_ϕ, so that $\tilde{v}_\phi \in C_\phi$ and all other $\tilde{v}_\psi$ with $\psi \neq \phi$ are not within C_ϕ: $\tilde{v}_\psi \notin C_\phi$. The integration of (B.3)–(B.5) over the so defined[9] domain C_ϕ leads to:

$$\int_{C_\phi} \text{Eq. (B.3)} = s_F \frac{\mathrm{d}}{\mathrm{d}t} \int_{C_\phi} \sum_{\xi} \delta(\tilde{v}_\xi - v)N(\tilde{v}_\xi) = s_F \frac{\mathrm{d}}{\mathrm{d}t} N(\tilde{v}_\phi) \,.$$

With Eq. (B.4) = Eq. (B.7) one receives:

$$\int_{C_\phi} \text{Eq. (B.4)} = \frac{s_F^2}{2} \sum_{\substack{\xi,\chi \\ \tilde{v}_\xi + \tilde{v}_\chi = \tilde{v}_\phi}} N(\tilde{v}_\xi) \cdot N(\tilde{v}_\chi) \cdot \beta(\tilde{v}_\chi, \tilde{v}_\xi) \,.$$

The short notation $\sum_{\xi,\chi:\ \tilde{v}_\xi + \tilde{v}_\chi = \tilde{v}_\phi}$ denotes the summation over all possible property pairs $(\tilde{v}_\xi, \tilde{v}_\chi)$, for which a coagulation of two EWSEs with the properties $\tilde{v}_\xi$ and $\tilde{v}_\chi$ would lead to one EWSE with the property $\tilde{v}_\phi$.

$$\int_{C_\phi} \text{Eq. (B.5)} \overset{\text{(B.5)}=\text{(B.8)}}{=} -s_F^2 \cdot N(\tilde{v}_\phi) \sum_{\chi} \beta(\tilde{v}_\phi, \tilde{v}_\chi) \cdot N(\tilde{v}_\chi) \,.$$

The division of the expression $\int_{C_\phi}$ Eq. (B.3) $= \int_{C_\phi}$ Eq. (B.4) $+ \int_{C_\phi}$ Eq. (B.5) by the factor s_F leads finally to the PBE in its discrete form for each property $\tilde{v}_\phi$. The PBEs describe the evolution of the total number $N(\tilde{v}_\phi)$ of all EWSEs with the property $\tilde{v}_\phi$ in time:

$$\frac{\mathrm{d}N(\tilde{v}_\phi)}{\mathrm{d}t} = \frac{1}{2} \sum_{\substack{\text{all properties } \tilde{v}_\xi, \tilde{v}_\chi \\ \text{with } \tilde{v}_\xi + \tilde{v}_\chi = \tilde{v}_\phi}} N(\tilde{v}_\xi)N(\tilde{v}_\chi)s_F\beta(\tilde{v}_\chi, \tilde{v}_\xi) - N(\tilde{v}_\phi) \sum_{\text{all properties } \tilde{v}_\xi} s_F\beta(\tilde{v}_\phi, \tilde{v}_\xi) \cdot N(\tilde{v}_\xi) \,. \tag{B.9}$$

The coagulation rate $\beta_{\mathrm{EWSE}}^{s_F}(v_i, v_j)$ between one EWSE with the property v_i and one with a property v_j can therefore be identified as the coagulation kernel of the PBE above (Eq. (B.9)):

$$\beta_{\mathrm{EWSE}}^{s_F}(v_i, v_j) = s_F \cdot \beta(v_i, v_j) \,. \tag{B.10}$$

Hence the weighted SE i (resp. j) is converted to N_i (resp. N_j) EWSEs (according to Fig. 1), the overall rate for the coagulation $\beta_{\mathrm{SE}}^{s_F}$ of two weighted SEs i and j (with the properties v_i and v_j) is equal to the total coagulation rate of all EWSEs (N_i and N_j) which represent those SEs:

$$\beta_{\mathrm{SE}}^{s_F}(i, j) = \beta_{\mathrm{EWSE}}^{s_F}(v_i, v_j) \cdot N_i \cdot N_j = s_F \cdot \beta(v_i, v_j) \cdot N_i \cdot N_j \,. \tag{B.11}$$

[8] For multidimensional properties, each component $\tilde{v}_\xi^{(A)}$ of the vector $\tilde{v}_\xi$ has to be smaller than the component $v^{(A)}$ of the vector v. Hence $\int_0^v$ is interpreted as $\int_0^{v^{(1)}} \int_0^{v^{(2)}} \dots$.

[9] In a one dimensional property space, it suffices to chose an ϵ with $\epsilon \in \mathbb{R} > 0$ small enough: $C_\phi = [\tilde{v}_\phi - \epsilon, \tilde{v}_\phi + \epsilon]$. In a multidimensional space, ϵ can be considered as a radius of a multidimensional sphere C_ϕ, whose center is the point $\tilde{v}_\phi$.

Appendix C. Detailed comparison between the fictitious particle theory and the stochastic resolution

Coagulation probabilities and rates for the inverse method.

In the framework of a MC simulation, the probability $P_{i,j}$, that two MC particles i and j coagulate within the MC time step τ_{mc} is defined via [17]:

$$P_{i,j} = \frac{\beta_{i,j}}{\sum_{i \neq j} \beta_{i,j}}, \qquad \tau_{\mathrm{mc}} = \frac{2}{\sum_{i \neq j} \beta_{i,j}}. \tag{C.1}$$

Thereby denotes $\beta_{i,j}$ the coagulation rate between the MC particles i and j. The particles might be EWSEs ([17] then: $\beta_{i,j} = \beta_{\mathrm{EWSE}}(v_i, v_j)$) or weighted SEs, the coagulation rate might be based on the FP-theory, like defined by ([27] then: $\beta_{i,j} = \beta_{i,j}^{(\mathrm{FP})}$), or on the stochastic resolution-theory (then: $\beta_{i,j} = \beta_{i,j}^{(\mathrm{SR})}$).

The overall probability $P^{(\mathrm{tot})} = P_{i,j} + P_{j,i}$, that one SE i coagulates with another SE j is the same within the theories of stochastic resolution and fictitious particle, because:

$$\begin{aligned} &\beta_{i,j}^{(\mathrm{FP})} + \beta_{j,i}^{(\mathrm{FP})} = \frac{2W_j + 2W_i}{W_j + W_i} \max\left(W_i, W_j\right) \cdot \beta(v_i, v_j) \\ &= \beta_{i,j}^{(\mathrm{SR})} + \beta_{i,j}^{(SR)} = 2 \cdot \max\left(W_i, W_j\right) \cdot \beta(v_i, v_j). \end{aligned}$$

The MC time step, τ_{mc}, defined in equation (C.1) is equal as well.[10]

Therefore, the usage of both coagulation kernels (stochastic resolution or fictitious particle) will produce the same results, if those values are estimated exactly. The symmetric formulation of the stochastic resolution-based coagulation kernel makes, however, only half of the calculation effort necessary.

Appendix D. Supplementary material

Supplementary material related to this article can be found online at http://dx.doi.org/10.1016/j.jcp.2017.03.041.

References

[1] D. Ramkrishna, Population Balances: Theory and Applications to Particulate Systems in Engineering, Acad. Press, New York, 2000.
[2] X. Hao, H. Zhao, Z. Xu, C. Zheng, Population balance-Monte Carlo simulation for gas-to-particle synthesis of nanoparticles, Aerosol Sci. Technol. 47 (2013) 1125–1133.
[3] A. Khadilkar, P.L. Rozelle, S.V. Pisupati, Models of agglomerate growth in fluidized bed reactors: critical review, status and applications, Powder Technol. 264 (2014) 216–228.
[4] M. Peglow, J. Kumar, S. Heinrich, G. Warnecke, E. Tsotsas, L. Mörl, B. Wolf, A generic population balance model for simultaneous agglomeration and drying in fluidized beds, Chem. Eng. Sci. 62 (2007) 513–532.
[5] A. Gerstlauer, S. Motz, A. Mitrović, E.-D. Gilles, Development, analysis and validation of population models for continuous and batch crystallizers, Chem. Eng. Sci. 57 (2002) 4311–4327.
[6] R. Irizarry, Fast compartmental Monte Carlo simulation of population balance models: application to nanoparticle formation in nonhomogeneous conditions, Ind. Eng. Chem. Res. 51 (2012) 15484–15496.
[7] D. Ramkrishna, M.R. Singh, Population balance modeling: current status and future prospects, Annu. Rev. Chem. Biomol. Eng. 5 (2014) 123–146.
[8] H.M. Hulburt, S. Katz, Some problems in particle technology. A statistical mechanical formulation, Chem. Eng. Sci. 19 (1964) 555–574.
[9] G. Madras, B.J. McCoy, Time evolution to similarity solutions for polymer degradation, AIChE J. 44 (1998) 647–655.
[10] D.L. Marchisio, R.O. Fox, Solution of population balance equations using the direct quadrature method of moments, J. Aerosol Sci. 36 (2005) 43–73.
[11] M. Vanni, Approximate population balance equations for aggregation-breakage processes, J. Colloid Interface Sci. 221 (2000) 143–160.
[12] T.H. Tsang, A. Rao, Comparison of different numerical schemes for condensational growth of aerosols, Aerosol Sci. Technol. 9 (1988) 271–277.
[13] Y. Xiong, M. Kamal Akhtar, S.E. Pratsinis, Formation of agglomerate particles by coagulation and sintering – Part II. The evolution of the morphology of aerosol-made titania, silica and silica-doped titania powders, J. Aerosol Sci. 24 (1993) 301–313.
[14] A.I. Roussos, A.H. Alexopoulos, C. Kiparissides, Part III: dynamic evolution of the particle size distribution in batch and continuous particulate processes: a Galerkin on finite elements approach, Chem. Eng. Sci. 60 (2005) 6998–7010.
[15] N.V. Mantzaris, P. Daoutidis, F. Srienc, Numerical solution of multi-variable cell population balance models: I. Finite difference methods, Comput. Chem. Eng. 25 (2001) 1411–1440.
[16] A.W. Mahoney, D. Ramkrishna, Efficient solution of population balance equations with discontinuities by finite elements, Chem. Eng. Sci. 57 (2002) 1107–1119.
[17] A.L. Garcia, C. van den Broeck, M. Aertsens, R. Serneels, A Monte Carlo simulation of coagulation, Phys. A, Stat. Mech. Appl. 143 (1987) 535–546.
[18] M. Celnik, R.I.A. Patterson, M. Kraft, W. Wagner, Coupling a stochastic soot population balance to gas-phase chemistry using operator splitting, Combust. Flame 148 (2007) 158–176.
[19] K. Liffman, A direct simulation Monte-Carlo method for cluster coagulation, J. Comput. Phys. 100 (1992) 116–127.
[20] M. Smith, T. Matsoukas, Constant-number Monte Carlo simulation of population balances, Chem. Eng. Sci. 53 (1998) 1777–1786.
[21] Y. Lin, K. Lee, T. Matsoukas, Solution of the population balance equation using constant-number Monte Carlo, Chem. Eng. Sci. 57 (2002) 2241–2252.

[10] It should be noted that the formulation $2/\sum_{i \neq j}$ replaces formally the reciprocal of the sum of all possible coagulation events: $1/\sum_{i>j}$, because it is usually assumed, that $\beta_{i,j} = \beta_{j,i}$. The usage of formula (C.1) for the fictitious particle-theory implicitly postulates a 'mean' coagulation rate $\overline{\beta}_{i,j}$ for the coagulation of two SEs i and j: $\overline{\beta}_{i,j} = \frac{1}{2} \cdot (\beta_{i,j}^{(\mathrm{FP})} + \beta_{j,i}^{(\mathrm{FP})})$.

[22] H. Zhao, C. Zheng, M. Xu, Multi-Monte Carlo approach for general dynamic equation considering simultaneous particle coagulation and breakage, Powder Technol. 154 (2005) 164–178.
[23] W.J. Menz, J. Akroyd, M. Kraft, Stochastic solution of population balance equations for reactor networks, J. Comput. Phys. 256 (2014) 615–629.
[24] A. Eibeck, W. Wagner, Stochastic particle approximations for Smoluchoski's coagulation equation, Ann. Appl. Probab. 11 (2001) 1137–1165.
[25] R.I.A. Patterson, W. Wagner, M. Kraft, Stochastic weighted particle methods for population balance equations, J. Comput. Phys. 230 (2011) 7456–7472.
[26] Z. Xu, H. Zhao, C. Zheng, Accelerating population balance-Monte Carlo simulation for coagulation dynamics from the Markov jump model, stochastic algorithm and GPU parallel computing, J. Comput. Phys. 281 (2015) 844–863.
[27] H. Zhao, C. Zheng, A new event-driven constant-volume method for solution of the time evolution of particle size distribution, J. Comput. Phys. 228 (2009) 1412–1428.
[28] D.W. Oxtoby, Homogeneous nucleation: theory and experiment, J. Phys. Condens. Matter 4 (1992) 7627–7650.
[29] J.H. Seinfeld, S.N. Pandis, Atmospheric Chemistry and Physics: From Air Pollution to Climate Change, 2nd ed., Wiley, Hoboken, NJ, 2006, http://www.loc.gov/catdir/enhancements/fy0826/2005058370-b.html.
[30] S. Khalili, Y. Lin, A. Armaou, T. Matsoukas, Constant number Monte Carlo simulation of population balances with multiple growth mechanisms, AIChE J. 56 (2010) 3137–3145.
[31] D.T. Gillespie, Exact method for numerically simulating the stochastic coalescence process in a cloud, J. Atmos. Sci. 32 (1975) 1977–1989.
[32] D.A.H. Jacobs (Ed.), The State of the Art in Numerical Analysis: Proceedings of the Conference on The state of the Art in Numerical Analysis, Held at the University of York, April 12th–15th, 1976, Organized by The Institute of Mathematics and Its Applications, Academic Press, London, 1977.
[33] J. Wei, F.E. Kruis, A GPU-based parallelized Monte-Carlo method for particle coagulation using an acceptance–rejection strategy, Chem. Eng. Sci. 104 (2013) 451–459.
[34] J. Wei, A fast Monte Carlo method based on an acceptance–rejection scheme for particle coagulation, Aerosol Air Qual. Res. 13 (2013) 1273–1281.
[35] S. Shekar, W.J. Menz, A.J. Smith, M. Kraft, W. Wagner, On a multivariate population balance model to describe the structure and composition of silica nanoparticles, Comput. Chem. Eng. 43 (2012) 130–147.
[36] T.T. Kodas, M.J. Hampden-Smith, Aerosol Processing of Materials, Wiley–VCH, New York, NY, 1999, http://www.loc.gov/catdir/description/wiley034/98003623.html.
[37] J.D. Landgrebe, S.E. Pratsinis, A discrete-sectional model for particulate production by gas-phase chemical reaction and aerosol coagulation in the free-molecular regime, J. Colloid Interface Sci. 139 (1990) 63–86.
[38] F. Gelbard, J.H. Seinfeld, Simulation of multicomponent aerosol dynamics, J. Colloid Interface Sci. 78 (1980) 485–501.
[39] S.-Y. Lu, Collision integrals of discrete-sectional model in simulating powder production, AIChE J. 40 (1994) 1761–1764.
[40] J. Wei, F.E. Kruis, GPU-accelerated Monte Carlo simulation of particle coagulation based on the inverse method, J. Comput. Phys. 249 (2013) 67–79.
[41] J.R. Wank, S.M. George, A.W. Weimer, Nanocoating individual cohesive boron nitride particles in a fluidized bed by ALD, Powder Technol. 142 (2004) 59–69.
[42] G. Marsaglia, Xorshift RNGs, J. Stat. Softw. 8 (2003) 1–6.

Paper II

Version of record published in:
Chemical Engineering Research and Design 136 (2018), pp. 71–82.
Available online at: https://doi.org/10.1016/j.cherd.2018.04.046

Fractional Monte Carlo Time Steps for the Simulation of Coagulation for Parallelized Flowsheet Simulations

G. Kotalczyk and F.E. Kruis

Contents lists available at ScienceDirect

Chemical Engineering Research and Design

journal homepage: www.elsevier.com/locate/cherd

Fractional Monte Carlo time steps for the simulation of coagulation for parallelized flowsheet simulations

G. Kotalczyk*, F.E. Kruis

Institute of Technology for Nanostructures (NST) and Center for Nanointegration Duisburg-Essen (CENIDE), University Duisburg-Essen, Duisburg, D-47057, Germany

ARTICLE INFO

Article history:
Received 29 January 2018
Received in revised form 25 April 2018
Accepted 29 April 2018
Available online 7 May 2018

Keywords:
Monte Carlo simulation
Coagulation
Flowsheet simulation
GPU computing
Population balance
Time step

ABSTRACT

The event-driven acceptance rejection (AR) method is a computationally very advantageous Monte Carlo (MC) simulation technique for the solution of population balance equations (PBE) of coagulating systems. In the scope of the event-driven simulation approach, the simulation time is stepwise increased by a simulation time step τ, which is given be the simulated particle properties. Within this time step τ, exactly one coagulation event takes place. The method is therefore not applicable in situations, for which specific time points have to be reached by the simulation, or the time step has to be reset to a smaller value. We propose a methodology termed 'fractional MC step' which allows to reset the simulation time step of the AR method to any arbitrary smaller value than the one initially proposed. The proposed method is validated by simulations of coagulation for different initial conditions and comparison with results gained from the discrete sectional method. The potential increase of the stochastic noise is investigated by comparisons with the results from conventional MC simulation techniques. The advantages of a parallel implementation are briefly discussed.

1. Introduction

The solution of the population balance equation (PBE) (Ramkrishna, 2000; Ramkrishna and Singh, 2014) is of importance for the description of the behaviour of many apparatuses used in the field of chemical engineering. Unit operations like granulation (Cameron et al., 2005), crystallization (Wang et al., 2014), milling (Sommer et al., 2006) or particle production in aerosol reactors (Kraft, 2005) are typical examples, in which the coagulation of particulate material has to be considered — next to other processes like nucleation, growth, evaporation, breakage etc.

The modelling of the PBE as a set of many connected compartments is often used in order to describe single unit operations, like inhomogeneities of a single particle reactor (Hao et al., 2013; Irizarry, 2012), or different spray zones within a granulator (Lee et al., 2015) or in order to simulate entire flowsheet simulations (Skorych et al., 2017). In all these cases a PBE is solved for each compartment. The PBEs include additional terms describing particulate transport between the compartments.

In an equation oriented approach, all the concerning equations have to be solved simultaneously. The additional coupling of the PBEs complicates the already difficult solution of one uncoupled PBE even more.[1] The mostly applied solution techniques for a simple PBE can be classified into 3 classes: (1) moment methods, (2) sectional methods and (3) stochastic methods.

1) The classical method of moments (Hulburt and Katz, 1964), or newer 'direct quadrature of moments' approaches (Marchisio and Fox, 2005) are only able to track some moments of the particle size distribution (PSD). The reconstruction of the PSD from these moments is not unequivocally possible.

[1] A sequential modular approach (Skorych et al., 2017) may simplify the solution by reducing the complexity of the equations — at the cost of additional computational times due to complex convergence schemes, like the waveform relaxation technique.

* *Corresponding author.*
E-mail address: gregor.kotalczyk@uni-due.de (G. Kotalczyk).

https://doi.org/10.1016/j.cherd.2018.04.046

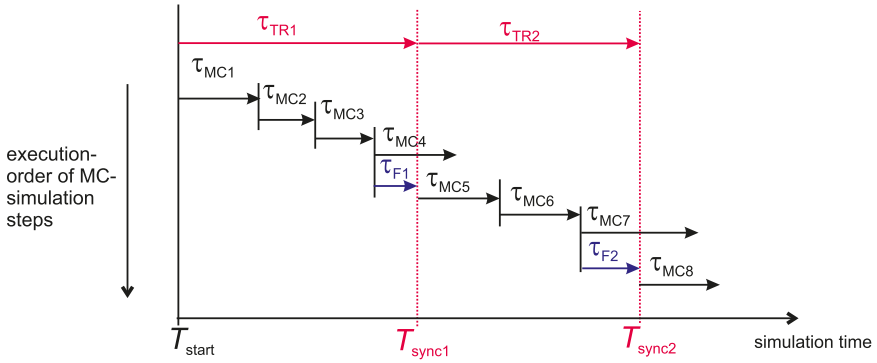

Fig. 1 – The transport time steps τ_{TR1} and τ_{TR2} define the synchronization time points T_{sync1} and T_{sync2}. The MC time steps τ_{MC4} and τ_{MC7} have to be reset to the fractional time steps τ_{F1} and τ_{F2} so that the synchronization time points T_{sync1} and T_{sync2} can be reached exactly.

2) Simple sectional (Kumar and Ramkrishna, 1996; Landgrebe and Pratsinis, 1990; Vanni, 2000) or more complicated finite element (resp. volume) methods (Mantzaris et al., 2001; Qamar et al., 2006) require a discretization of the particle properties into a grid. These methods are only applicable to a limited number of particle properties (ca. 2–3) because the computational cost becomes too expensive for many properties. The application of moving grids (Kumar and Ramkrishna, 1996) becomes also more complicated if the transport between simple compartments has to be included into the simulation.
3) Stochastic simulation techniques or Monte Carlo (MC) methods (Kruis et al., 2000; Maisels et al., 2004; Morgan et al., 2006; Smith and Matsoukas, 1998) translate the continuous PBE into discrete events with certain probabilities for each event. Because MC simulations are generally computationally demanding, if all processes are modelled as discrete events (see e.g. Khalili et al., 2010), hybrid methods based on the operator splitting technique are used. These describe the coagulation in a stochastic way and other processes like particulate growth in a deterministic way (Patterson et al., 2006). The application of graphic processing units (GPU) in combination with parallelized simulation techniques (Wei, 2014a; Wei and Kruis, 2013a) prove to further reduce the computational times significantly (Wei, 2014b). The application of weighted simulation particles leads to the reduction of the statistical noise (Zhao et al., 2009).

This work investigates the applicability of a parallelized MC simulation technique for flowsheet simulations using an operator splitting technique. Applying an operator splitting technique means to decouple the single compartments for a small time step $\Delta\tau_{TR}$ and solve the corresponding PBE within each compartment independently of the other compartments — and then to perform the exchange of particles between each compartment.

Between the transport steps, the coagulation of particles has to be simulated for the time interval τ_{TR}. This can be easily done, if a time-driven MC technique is applied (see e.g. Liffman, 1992; Zhao et al., 2007). In the scope of this technique, a small time step τ_{MC} can be set freely[2] and it is checked for each possible coagulation event, whether it happened within the time step. Fig. 1 shows how some optimal MC time steps τ_{MC} for the time-driven method (not too large and not too short) have to be reset to shorter 'fractional' time steps τ_F in order to reach the synchronization time points given by the transport time steps. This adjustment is especially necessary in the case in which the small MC time step τ_{MC} is much larger than the transport time step $\Delta\tau_{TR}$.

[2] Although $\Delta\tau_{MC}$ can be chosen freely, it has to be kept relatively small, so that not too many coagulation events happen within one time step. Because each coagulation event alters the coagulation rates between the simulation particles and it is assumed that the coagulation rates between the particles calculated before the time step are somehow constant throughout the time step and only negligibly small changes occur.

Although the shorter fractional time steps can be easily simulated by the time-driven approach (simply by replacing the 'optimal' time step τ_{MC}), its application is computationally very demanding. Because all possible coagulation events may happen within the time step τ_{MC} (resp. τ_F), all of these events have to be considered (meaning the probability of their occurrence has to be compared to a random number) during one MC time step. A much more effective approach is the acceptance–rejection (AR) technique (Garcia et al., 1987; Wei and Kruis, 2013b). In the scope of this technique the coagulation pairs are selected randomly and the very low probability to select a specific pair is incorporated into the coagulation probability — which would be otherwise very low (Garcia et al., 1987). So that only few selection attempts are necessary to find a coagulation pair. It is assumed that exactly one coagulation event takes place during the specific time step τ_{MC}. This time step cannot be set freely and is given by the properties of the simulated particle population (i.e. the reciprocal of the sum of all possible coagulation rates, as it is elaborated further below) at the given time point of the simulation. This makes the incorporation of the AR based MC simulation into a flowsheet simulation, like it is sketched in Fig. 1 not possible.

This problem is addressed in this work by the introduction of 'fractional MC time steps', which allow to make a smaller stochastic simulation step τ_F than the intrinsic AR-based MC time step τ_{MC}.

First, the notion of the 'fractional MC' step is introduced in the theoretic section of this paper. The derived methodology is tested on simple coagulation problems for which accurate numerical solutions are easily obtainable by application of the known discrete sectional method (Gelbard et al., 1980; Landgrebe and Pratsinis, 1990). It is shown in the results section that the introduced fractional MC time steps – although stochastic in its nature – only marginally increase the inherent statistical noise of the simulation (by comparison with MC simulations without the fractional time steps). The computational advantages of the parallel solution of PBEs describing particle populations whose concentrations vary with several orders of magnitude (which translates to intrinsic MC steps which vary in several orders of magnitude) is addressed as well.

2. Theory: fractional MC time steps for the acceptance–rejection (AR) scheme

The AR methodology allows the solution of the PBE for coagulation given by:

$$\frac{dn(v,t)}{dt} = +\frac{1}{2}\int_0^v \beta(v-v',v')\cdot n(v-v',t)\cdot n(v',t)dv' - n(v,t)\int_0^\infty \beta(v,v')\cdot n(v',t)dv', \quad (1)$$

where $n(v,t)$ describes the PSD (i.e. the term $N = \int n(v,t)dv$ is a number-concentration in units m^{-3}) and $\beta(v, v')$ describes the rate of coagulation between the particles of the sizes v and v'.

In the context of MC simulations, the PSD is rendered by discrete MC simulation particles, which are selected for coagulation by stochastic means and alter their properties, if selected for coagulation. In the scope of the AR method (Garcia et al., 1987), exactly one coagulation pair (i, j) is selected within one time step τ_{MC}, defined by:

$$\tau_{MC} = 1 / \sum_{i>j} \beta_{i,j} \ . \tag{2}$$

The summation accounts all possible coagulation pairs (i, j) with their respective coagulation rates $\beta_{i,j}$ (these rates are derived from the continuous expression $\beta(v,v')$). A randomly selected pair (i, j) is chosen for coagulation with the probability $P_{i,j}^{(AR)}$, which is derived (Garcia et al., 1987) as:

$$P_{i,j}^{(AR)} = \beta_{i,j} / \max_{i \neq j} \beta_{i,j} \ . \tag{3}$$

For the application of this AR technique for flowsheet simulations, the situation in Fig. 1 has to be accounted for, in which a shorter time step τ_F than the suggested one by Eq. (2) has to be performed in order to reach a synchronization time point. We assume that a particle pair (i, j) that is selected accordingly to Eq. (3) is the 'correct' coagulation pair for the time interval τ_{MC}. Within the shorter time step τ_F, only two possibilities can happen: (1) the selected pair (i, j) coagulates, or (2) no pair coagulates at all. The decision whether the pair coagulates or not can be done stochastically, if the probability $P_{i,j}(\tau_F \mid \tau_{MC})$, which describes the probability that the pair (i, j) coagulates within the time interval τ_F under the condition, that the pair is coagulating for sure within the time interval τ_{MC}, is known. A uniformly distributed random number r can then be compared with the probability $P_{i,j}(\tau_F \mid \tau_{MC})$. The selected particles coagulate if r is smaller than $P_{i,j}(\tau_F \mid \tau_{MC})$ or not, if it is larger. The full algorithm is displayed in Fig. 2. A detailed description of the parallel AR algorithm for the selection of a coagulation pair accordingly to Eq. (3) can be found in Wei and Kruis (2013a) or

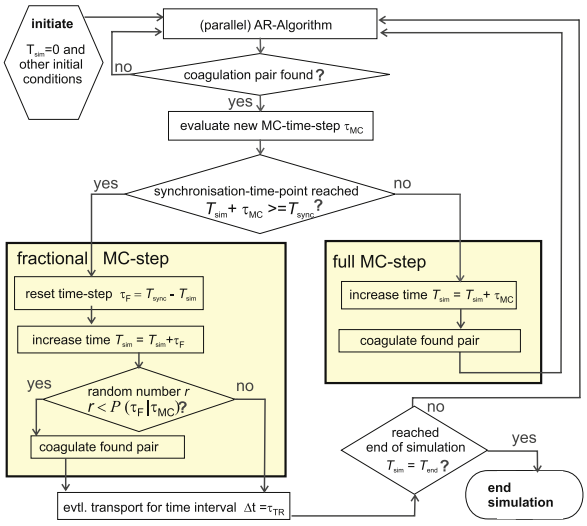

Fig. 2 – Flowchart of the MC simulation of coagulation and possibly other processes combined by the operator splitting technique. The simulation time T_{sim} is increased by the conventional MC time step τ_{MC} or a fractional time step τ_F until the last synchronization time point T_{end} is reached.

Kotalczyk and Kruis (2017). In the results section, this implementation will be compared with two other algorithms: both increase the simulation time only by τ_F if the synchronization time point is reached, but no fractional time step is applied. The first algorithm performs a normal (or 'full') MC time step, the second algorithm performs no coagulation at all. This second approach is similar to the methodology proposed by Kruis et al. (2012).

2.1. *Calculation of the conditional probability $P_{i,j}(\tau_F \mid \tau_{MC})$*

The conditional probability $P_{i,j}(\tau_F \mid \tau_{MC})$ can be described by Bayes' theorem as:

$$P_{i,j}(\tau_F|\tau_{MC}) = P_{i,j}(\tau_{MC} \mid \tau_F) \cdot P_{i,j}(\tau_F)/P_{i,j}(\tau_{MC}) \ . \tag{4}$$

The term $P_{i,j}(\tau_F)$ describes thereby the (non-conditional) probability for the coagulation of the particles i and j within the time interval τ_F. $P_{i,j}(\tau_{MC})$ gives the coagulation probability within the time interval τ_{MC}. The expression $P_{i,j}(\tau_{MC} \mid \tau_F)$ describes the probability that the particles i and j coagulate within the time interval τ_{MC} under the condition that they coagulate within the time interval τ_F. Hence $\tau_F < \tau_{MC}$, it follows that $P_{i,j}(\tau_{MC} \mid \tau_F) = 1$. This simplifies Eq. (4) to:

$$P_{i,j}(\tau_F \mid \tau_{MC}) = P_{i,j}(\tau_F)/P_{i,j}(\tau_{MC}) \ . \tag{5}$$

The coagulation of two particles (i, j) is generally considered as a Poisson process, meaning that a given coagulation rate $\beta_{i,j}$ is associated with a density distribution $f_{i,j}$ in respect to the time point t at which the coagulation occurs with:

$$f_{i,j} = \beta_{i,j} \exp(-\beta_{i,j} \cdot t) \ . \tag{6}$$

The probability $P_{i,j}(\tau)$ for the coagulation between the particles i and j within the time interval τ can be calculated via (i.e. (Garcia et al., 1987; Liffman, 1992), without the application of the term 'Poisson process', sometimes the term 'interval of quiescence' is used, if probabilities for all possible events are considered (Shah et al., 1977; Song and Qiu, 1999)):

$$P_{i,j}(\tau) = \int_0^{\tau} f_{i,j} dt = 1 - \exp(-\beta_{i,j} \cdot \tau) \, . \tag{7}$$

Especially for $\tau = \tau_{MC}$ follows:

$$P_{i,j}(\tau_{MC}) = 1 - \exp(-\beta_{i,j} \cdot \tau_{MC}) \Leftrightarrow \beta_{i,j} = -\ln(1 - P_{i,j}(\tau_{MC}))/\tau_{MC} \ . \tag{8}$$

The resulting expression for $\beta_{i,j}$ in Eq. (8) can be inserted into Eq. (7) for $\tau = \tau_F$, which yields:

$$P_{i,j}(\tau_F) = 1 - (1 - P_{i,j}(\tau_{MC}))^{(\tau_F/\tau_{MC})} \ . \tag{9}$$

The expression $(1-x)^{\alpha}$ can be rewritten as the first two terms of a Taylor series for small values of x, to: $(1-x)^{\alpha} \approx 1 - \alpha \cdot x$. This simplifies Eq. (9) to:

$$P_{i,j}(\tau_F) = \ P_{i,j}(\tau_{MC}) \cdot \tau_F/\tau_{MC} \ . \tag{10}$$

Table 1 – Physical parameters used for the simulation describing typical aerosol properties.

Symbol	Designated property	Value
T	Temperature	644 K
ρ_p	Particle density	1000 kg m^{-3}

The substitution of Eq. (10) into the description of the conditional probability (Eq. (5)) leads to a simple expression for the conditional probability:

$$P_{i,j}(\tau_F \mid \tau_{MC}) = \tau_F/\tau_{MC} \ . \tag{11}$$

The approximation leading to Eq. (10) is valid, because the term $P_{i,j}(\tau_{MC})$ is usually small. This is because exactly one event happens within τ_{MC}, which is equivalent to: $\sum_{i>j} P_{i,j}(\tau_{MC}) = 1$. If a small number of 1000 simulation particles is used, the sum consists of $(1000^2 - 1000)/2 = 499{,}500$ elements. In the improbable case, in which $P_{i,j}(\tau_{MC})$ becomes too large for the approximation leading to Eq. (10), the exact expression for $P_{i,j}(\tau_{MC})$ defined via Eq. (7) can be inserted into the exact formula defined by Eq. (9). Both expressions are inserted into Eq. (5), leading to the correct expression: $P_{i,j}(\tau_F \mid \tau_{MC}) = (1 - \exp(-\beta_{i,j}\cdot\tau_F))/(1 - \exp(-\beta_{i,j}\cdot\tau_{MC}))$. This approach, however is computationally more expensive than the application of the simple resulting formula (11).

3. Validation method

3.1. System for validation

In order to discuss the influence of the application of fractional time steps, compartments containing an initial particle population are considered and the process of coagulation is simulated only (without any transport steps between compartments). The kernel for coagulation in the free molecule regime (i.e. the particle size is much smaller than the mean free path of the carrier gas (Friedlander, 2000; Hinds, 2012)) is used. It describes the rate of coagulation of two spherically shaped particles with the volumes v and v' by:

$$\beta_{fm}(v, v') = \left(\frac{3}{4\pi}\right)^{\frac{1}{6}} \sqrt{\frac{6k_B T}{\rho_p}} \cdot \sqrt{\frac{1}{v} + \frac{1}{v'}} \cdot \left(v^{\frac{1}{3}} + v'^{\frac{1}{3}}\right)^2 . \tag{12}$$

The parameters used for the simulation are summarized in Table 1, k_B designates the Boltzmann constant. It is assumed that two coagulating spheres with the volumes v and v' form a new sphere with the volume $v + v'$.

Monodisperse initial conditions are simulated, with an initial particle diameter of $d_0 = 3$ nm. Five different scenarios are used in this context, these describe different initial concentrations N_0 spanning values which differ four orders of magnitude: $N_0 = 10^{13}$ m^{-3},...,10^{17} m^{-3}. The chosen MC time step τ_{MC} depends vastly on the chosen initial concentration and correlates to the characteristic time for coagulation τ_{coag}, which is defined as the time in which the monodisperse initial number-concentration reduces by half due to coagulation in a monodisperse model (Kodas and Hampden-Smith, 1999):

$$\tau_{coag} \approx \sqrt{\rho_p/(3 \cdot k_B \cdot T \cdot d_0)} \,/\, N_0 \ . \tag{13}$$

The different settings for the initial concentration N_0 result in vastly different characteristic times for coagulation τ_{coag}. All scenarios are simulated for the same time span T_{end} which can be also expressed as a multiple value of τ_{coag} (i.e. $T_{end} = \alpha \cdot \tau_{coag}$). The higher the multiplication factor α, the more coagulation events are expected to happen within the simulated time span T_{end}. Table 2 summarizes the different simulated scenarios, the shown initial MC time steps $\tau_{MC}^{(0)}$ are defined for the weighted particle methodology described further below.

In the absence of other processes besides the coagulation, no artificial synchronization of the simulations is necessary. However, for the validation of the proposed methodology and the measurement of the potential increase of the intrinsic stochastic noise of the MC simulations, artificial synchronization points are included into the simulation. The simulations are forced to stop after constant time spans τ_{TR}, which range from $\tau_{TR} = 0.1$ s,...,0.1 ms. The used settings and the total number of synchronization points are summarized in Table 3. The dependency of the simulation time and the added stochastic noise for all scenarios (described in Table 2) is discussed in dependency of the applied time span τ_{TR} (summarized in Table 3) in the results section.

3.2. Parallel MC simulations based on weighted simulation particles

The methodology for the MC time steps introduced in the theoretic section of the paper, culminating in the algorithm presented in Fig. 2 is applicable to conventional AR methods based on equally weighted MC particles (Garcia et al., 1987; Maisels et al., 2004). The derived methodology can also be applied for algorithms based on weighted simulation particles, for which different theoretic descriptions of the coagulation have been formulated recently (Kotalczyk and Kruis, 2017; Patterson et al., 2011; Xu et al., 2015; Zhao et al., 2009).

In contrast to conventional methods, weighted simulation particles are characterized by an additional property, the statistical weight W (which is a number concentration with units m^{-3}) of the rendered simulation particles. This additional property is stored with all other particle properties. In this work, only the particle size v is used as other particle property.

The application of weighted particles is advantageous, especially in the context of flowsheet simulations, which describe compartments with vastly different particle number-concentrations. If, for example, two compartments with total number-concentrations of 10^{13} m^{-3} and 10^{17} m^{-3} are simulated and at least 1000 simulation particles are needed for a certain computational accuracy. The application of equally weighted particles would lead to an equal weight of 10^{13} m$^{-3}/1000 = 10^{10}$ m^{-3}, which would entail a necessary number of 10^{17} m$^{-3}/10^{10}$ m$^{-3} = 10^7$ simulation particles for the compartment with the higher concentration of 10^{17} m^{-3}. The application of weighted simulation particles allows the simple modelling of these different compartments by adjusting the initial statistical weight W_0 of the simulation particles accordingly to the initial number-concentration N_0 (and the number of the used simulation particles N_{SP}) via:

$$W_0 = N_0/N_{SP} \ . \tag{14}$$

3.2.1. Initialization of weighted simulation particles

The weighted simulation particles in this work are initiated with the initial volume which corresponds to the initial diameter $d_0 = 3$ nm. For each initial number-concentration summarized in Table 2, the values W_0 are calculated via Eq. (14) taking into account the used number of simulation particles, N_{SP}.

Table 2 – Summary of the used scenarios defined by the initial concentrations N_0, resulting in different characteristic times for coagulation τ_{coag}, defined in Eq. (13) and initial MC time steps, defined in Eq. (16) for 10,000 simulation particles.

Scenario	Initial concentration N_0	Initial MC time step $\tau_{MC}^{(0)}$	Characteristic time τ_{coag}	Total simulation time T_{end}
1	10^{13} m^{-3}	12.5 ms	517 s	51.7 s = 0.1·τ_{coag}
2	10^{14} m^{-3}	1.25 ms	51.7 s	51.7 s = 1·τ_{coag}
3	10^{15} m^{-3}	125 μs	5.17 s	51.7 s = 10·τ_{coag}
4	10^{16} m^{-3}	12.5 μs	517 s	51.7 s = 100·τ_{coag}
5	10^{17} m^{-3}	1.25 μs	51.7 s	51.7 s = 1000·τ_{coag}

Table 3 – The different values used for the time spans τ_{TR} between different synchronization points.

Time span τ_{TR}	Number of fractional time steps within T_{end}
None	None
100 ms	517
10 ms	5170
1 ms	51,700
0.1 ms	517,000
0.01 ms	5,170,000

3.2.2. *Coagulation of weighted simulation particles*

In this work, the coagulation scheme based on the concept of stochastic resolution (Kotalczyk and Kruis, 2017) is used. The coagulation between two differentially weighted MC particles is described according to the scheme presented in Fig. 3 (which is equivalent to the scheme introduced by Zhao et al. (2009) in the context of the 'fictitious particle' theory).

The rate of both coagulation schemes shown in Fig. 3 has been derived by a transformation of the PBE (Eq. (1)) to a discrete form for equally weighted particles (see Kotalczyk and Kruis, 2017 for details):

$$\beta_{i,j} = \max(W_i, W_j) \cdot \beta_{fm}(v_i, v_j) \ , \tag{15}$$

where $\beta_{fm}(v_i, v_j)$ denotes the coagulation rate between particles with the size v_i and v_j, given by the continuous PBE (Eq. (1)). In this work, the coagulation rate in the free-molecule regime (Eq. (12)) is considered.

The rate $\beta_{i,j}$ in Eq. (15) is used for the methodology described in the theoretic part describing the fractional MC time steps. If the particles are selected for coagulation, the scheme sketched in Fig. 3 is applied upon the selected particles.

The calculation of the initial (full) MC time step $\tau_{MC}^{(0)}$ at the beginning of the simulation is performed by the insertion of Eq. (15) into Eq. (2). The consideration of the initial condition defined by Eq. (14) leads to:

$$\begin{aligned} \tau_{MC}^{(0)} &= 1/\left[\sum_{i>j} \max(W_i, W_j)\beta_{fm}(v_i, v_j)\right] \\ &= 2/\left[N_0\,(N_{SP}-1)\,\beta_{fm}(v_0, v_0)\right]. \end{aligned} \tag{16}$$

Typical values for $\tau_{MC}^{(0)}$ are listed in Table 2 (for 10,000 simulation particles).

3.2.3. *Fast simulation technique*

The calculation of the exact values for the maximum coagulation rate ($\max_{i\neq j}\beta_{i,j}$, used in Eq. (3) for the selection probability $P_{i,j}^{(AR)}$) as well as the exact sum of all coagulation rates ($\sum_{i>j}\beta_{i,j}$, used in Eq. (2) for the calculation of the time step τ_{MC}) are computationally very expensive, hence all possible coagulation pairs have to be considered for the exact calculation. Alternatively to the widely used majorant kernel techniques in combination with fictitious jumps (Patterson et al., 2011; Xu et al., 2015), the exact sum ($\sum_{i>j}\beta_{i,j}$) can be approximated by the calculation of the mean value β_{mean} of a representative sample (Wei and Kruis, 2013a). This mean value can also be used in order to approximate the maximum coagulation rate by $\beta_{max} = \gamma\cdot\beta_{mean}$, with a constant 'safety' factor γ, which assures that the so calculated value β_{max} is larger than the exact value, i.e.: $\beta_{max} > \max_{i\neq j}\beta_{i,j}$. This safety factor is necessary in order to ensure that all calculated selection probabilities are smaller than 1. The implementational details of this simulation technique can be found in Kotalczyk and Kruis (2017). The calculation of the coagulation rates of the randomly selected coagulation pairs can in this way not only be used for the determination, whether the particles coagulate (via Eq. (3)), but also for the quick approximation of β_{max} and β_{mean}. The other advantage of the scheme is, that it is applicable for all sorts of coagulation kernels, especially for those, for which a majorant kernel is not applicable — or at least not computationally efficient applicable. A value of $\gamma = 10{,}000$ is used for the discussed scenario in this work, which has proven to be sufficient for more demanding simulation scenarios (Kotalczyk and Kruis, 2017).

3.2.4. *Parallel implementation of heterogeneous flowsheet conditions*

The main advantage of the fast simulation technique used in this work (Wei and Kruis, 2013a) is the parallel check of randomly selected coagulation pairs. Hence the coagulation probability is usually relatively low (even in an AR approach), a large amount of comparisons might be necessary in order to find a coagulation pair. In a serial implementation, most of the selection attempts (marked as '(parallel) AR-algorithm in Fig. 2) would fail and be called again (the decision marked as "coagulation pair found?" would branch to the 'no' scenario). A parallel implementation compares 256 coagulation pairs in parallel (in our implementation) and reduces thus the number of repetitions (the detailed implementation of this code can be found in Kotalczyk and Kruis (2017)).

The mean number N_{sel} of selection attempts using the here presented fast simulation technique can be approximated to be the inverse of the mean probabilities $P_{i,j}^{(AR)}$ (defined in Eq. (3)) to select the pair (i, j):

$$\begin{aligned} N_{sel} &= (N_{SP}(N_{SP}-1))/2\sum_{i>j} P_{i,j}^{(AR)} \\ &= \beta_{max}N_{SP}(N_{SP}-1)/2\sum_{i>j}\beta_{i,j} = \beta_{max}/\beta_{mean} = \gamma. \end{aligned} \tag{17}$$

The approximation of β_{max} via: $\beta_{max} = \gamma\cdot\beta_{mean}$ (as discussed in the previous 'fast simulation technique' paragraph) has been used. The GPU architecture forbids the efficient processing of a large amount of data by one multi streaming processor

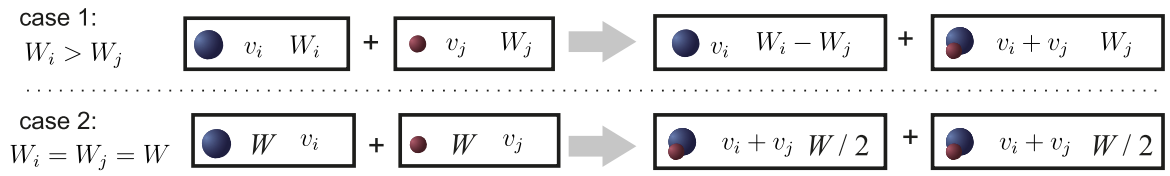

Fig. 3 – The coagulation of weighted MC particles is described by a change of the statistical weight W and the volume v of the particles participating in the coagulation event. In the case of unequal statistical weights (case 1), only a fraction of the particle population represented by W_i, participates in the coagulation, the rest $W_i - W_j$ remains unchanged.

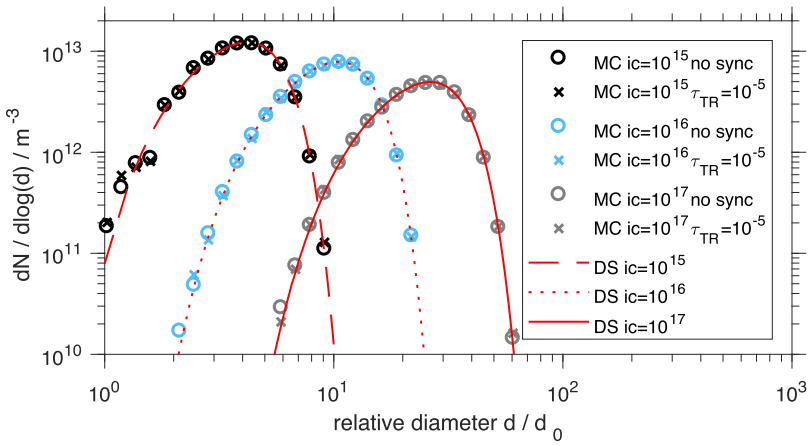

Fig. 4 – PSDs resulting from Monte Carlo (MC) simulation using 1000 simulation particles compared with the discrete sectional (DS) method for a simulation time of T_{end} = 51.8 s for different initial number-concentrations ((ic), units: m^{-3}). The initial diameter d_0 = 3 nm has been used for all simulations.

— for this reason, a large data set consisting of 10,000 data points is divided in smaller blocks of 256 elements (alternatively, 128, 512 or 1024 elements are commonly used). For the here used value of γ = 10,000, 40 parallel blocks (each processing 256 coagulation pairs) are launched for each simulation. If all 50 simulations are run in parallel — 50 × 40 = 2000 data blocks are initiated to be launched in parallel via the CUDA programming language, each one processing 256 particle pairs in parallel. Due to the physical limitations of the used GPU, a NVIDIA GTX 980 Ti, only up to 200 data blocks (which process 256 data points in parallel) can be executed in parallel, so that ca. 10 sequential processing steps of 200 parallel blocks are executed. The advantage of executing all 5 simulation scenarios in parallel (i.e. scheduling the launch of the computation of 5 × 2000 = 10,000 parallel data blocks) in contrast to the sequential computation of the 5 different scenarios is discussed in Section 4.2.

3.3. *Discrete sectional method*

In order to ensure that the MC simulation techniques describe the solutions correctly, the results are also compared with the discrete sectional method (Landgrebe and Pratsinis, 1990), which extends the sectional method proposed by Gelbard et al. (1980) by discrete points. This makes the method very accurate for the investigation of simulation scenarios with monodisperse initial conditions. The initial particles can be approximated by the first discrete point. In this work, a one dimensional grid, consisting of 250 discrete points and 400 sections is used. It has been shown, that these settings are able to reproduce the results with an accuracy much larger than that of the MC method (Kotalczyk and Kruis, 2017).

4. Results and discussion

4.1. *Validation and statistical accuracy*

Fig. 4 shows the excellent agreement of the resulting MC simulations with the DS benchmark. It can be seen that the PSDs resulting from simulations using forced synchronizations (marked as '$\tau_{TR} = 10^{-5}$' in Fig. 4, this setting corresponds to a synchronization every $\tau_{TR} = 10^{-5}$ s) lead to similar PSDs as the ones without synchronization points (marked as 'no sync' in Fig. 4).

The PSDs shown in Fig. 4 comprise simulation results for the largest number of synchronization points (every $\tau_{TR} = 10^{-5}$ s one synchronization point is included) and smallest number of used simulation particles (1000). These results cannot be reproduced, if instead of fractional time steps full time steps or no time steps (following the algorithm in Kruis et al., 2012) are used. Fig. 5 underlines this finding. It can also be seen, that the algorithm with no MC time steps underestimates (resp. the algorithm with full MC time steps overestimates) the coagulation process leading to smaller particle sizes at higher particle concentrations (resp. larger particle sizes at lower particle concentrations). The smaller the synchronization time intervals τ_{TR} are set, the larger are the deviations from the benchmark results. It should also be pointed out, that if the synchronization intervals τ_{TR} are set to lower values than the initial MC time steps $\tau_{MC}^{(0)}$ (defined in Eq. (16) and tabulated in Table 2), the algorithm using no coagulation step (Kruis et al., 2012) would not simulate the coagulation at all. The initial monodisperse PSD would be reproduced for all simulation times in this scenario.

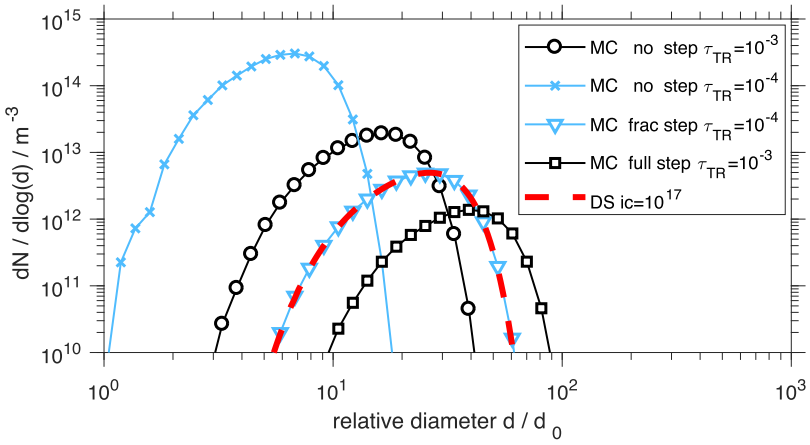

Fig. 5 – PSDs resulting from MC simulations using fractional MC time steps (marked as 'frac step') compared with simulations without additional time step (marked as 'no step') and normal MC time steps ('full step').

In order to quantify the influence of the applied simulation particles and synchronization intervals τ_{TR}, the total number concentration and the geometric mean diameter of the resulting simulations are compared with each other for different simulation settings and values for the synchronization intervals τ_{TR}.

The total number-concentration N_i and the geometric standard deviation $d_g^{(i)}$ are calculated for one MC simulation i via:

$$N_i = \sum_{n=1..N_{SP}} W_n^{(i)}, \tag{18}$$

$$\ln(d_g^{(i)}) = \sum_{n=1..N_{SP}} W_n^{(i)} \cdot \ln(d_n^{(i)})/N_i \ , \tag{19}$$

where $W_n^{(i)}$ is the statistical weight and $d_n^{(i)}$ the diameter of the n-th simulation particle of the i-th MC simulation. The mean values $\bar{N}$ and $\overline{d_g}$ for 50 MC simulations used for the investigations of this work are calculated by:

$$\bar{N} = \sum_{i=1..50} N_i/50\,, \quad \bar{d}_g = \sum_{i=1..50} d_g{}^{(i)}/50\ . \tag{20}$$

These values are used in the following for the comparison with the results originating from the DS method, N_{DS} and $d_{g,DS}$. The calculation method for these values by means of the DS method can be found in Landgrebe and Pratsinis (1990), the specific grid employed within this work (250 discrete points and 400 continuous sections) is specified in more detail in Kotalczyk and Kruis (2017).

The following formulas are applied for the measurement of the systematic deviations N_{Err} and $d_{g,Err}$ from the DS results:

$$N_{Err} = |N_{DS} - \bar{N}|/N_{DS}, \quad d_{g,Err} = |d_{g,DS} - \overline{d_g}|/d_{g,DS}\,. \tag{21}$$

The assumed values of these systematic errors during the simulation are displayed in Figs. 6 and 7. It can be seen, that independent of the case, whether no synchronization points are included (marked with 'no sync' in the figures) or the most demanding setting is applied (marked with '$\tau_{TR} = 10^{-5}$' and corresponding to scenario 5 in Table 2) nearly the same deviations are reached. Smaller numbers of simulation particles ($N_{SP} = 10^3$) lead to higher deviations, which are connected to higher noise levels of the simulations.

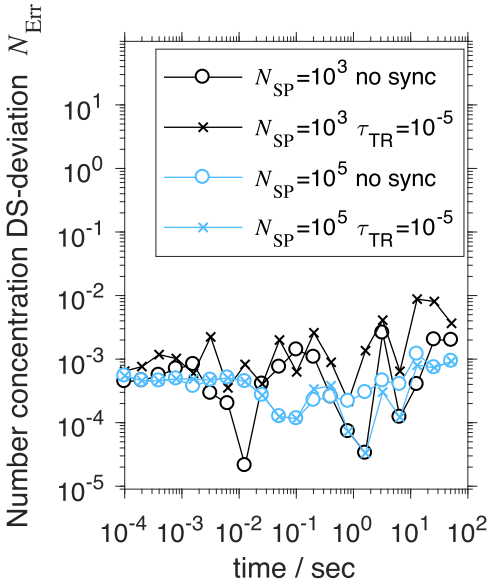

Fig. 6 – The deviations N_{Err} defined in Eq. (21) of the mean values for the MC-based total number-concentration from the values from the discrete sectional (DS) method, for an initial condition of $N_0 = 10^{17}$ m^{-3} for different values of simulation particles N_{SP}.

The statistical noise of the MC simulations is quantified by comparison of the arithmetic standard deviation ΔN (resp. Δd_g) to the mean values $\bar{N}$ (resp. $\overline{d_g}$) defined in Eq. (20), the explicit formulas for the calculation of the arithmetic standard deviation applied in this work are:

$$\Delta N = \sqrt{\sum_{i=1..50} \left(N_i - \bar{N}\right)^2/49}, \qquad \Delta d_g = \sqrt{\sum_{i=1..50} \left(d_g^{(i)} - \overline{d_g}\right)^2/49}\ . \tag{22}$$

The stochastic noise for the mean concentration and the geometric diameter is depicted in Figs. 8 and 9. It can be seen that these values depend strongly on the number of used simulation particles N_{SP}. As expected, an increase of simulation particles by a factor of 100 leads to an increase of the stochastic accuracy by a factor of 10 (the stochastic noise level of MC simulations is expected to scale proportional to $1/\sqrt{N_{SP}}$). It can also be seen in Figs. 8 and 9 that the noise levels of simulations with the most synchronization points (marked with '$\tau_{TR} = 10^{-5}$') lead to nearly the same noise levels as the simulations without any synchronization (marked with 'no sync').

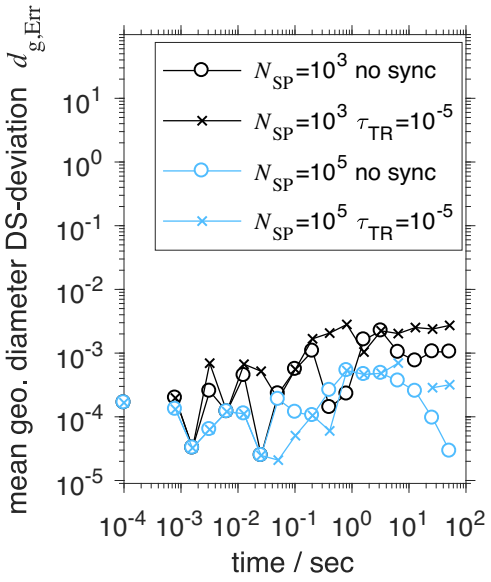

Fig. 7 – The deviations $d_{g,Err}$ defined in Eq. (21) of the mean values for the MC-based mean geometric diameter from the values from the discrete sectional (DS) method, for an initial condition of $N_0 = 10^{17}$ m^{-3} for different values of simulation particles N_{SP}.

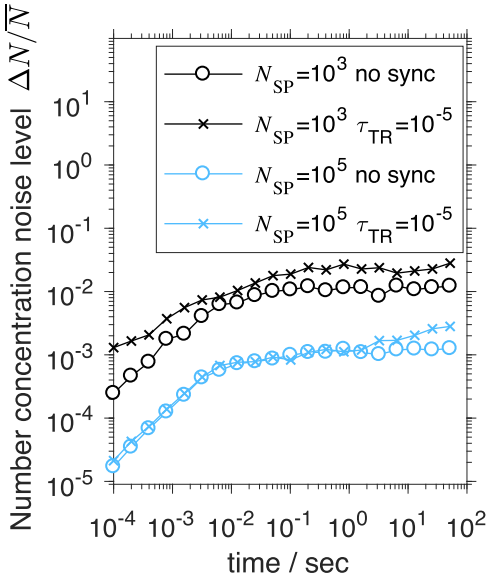

Fig. 8 – The stochastic noise for the values of the mean concentration for MC simulations with an initial concentration of $N_0 = 10^{17}$ m^{-3} for different values of simulation particles N_{SP}. Eqs. (22) and (20) define ΔN and $\bar{N}$.

Similar findings concerning the systematic and statistical accuracy of the simulation can be made for simulations with different initial concentrations. Fig. 10 compares the evolution of the noise levels for different values of initial conditions, N_0. The simulations with forced synchronizations (marked with '$\tau_{TR} = 10^{-5}$') and lower initial concentrations ($N_0 = 10^{13}$, 10^{15} m^{-3}) exhibit much higher noise levels (up to a factor of 10) than the simulations without synchronization points (marked with 'no sync'), at the initial stages of the simulations. At these initial stages of the simulation, the noise levels are found to be much lower than in the scenarios with the large initial concentration ($N_0 = 10^{17}$ m^{-3}).

This increase of the noise levels during the early stages of the simulation can be explained by the transition of the

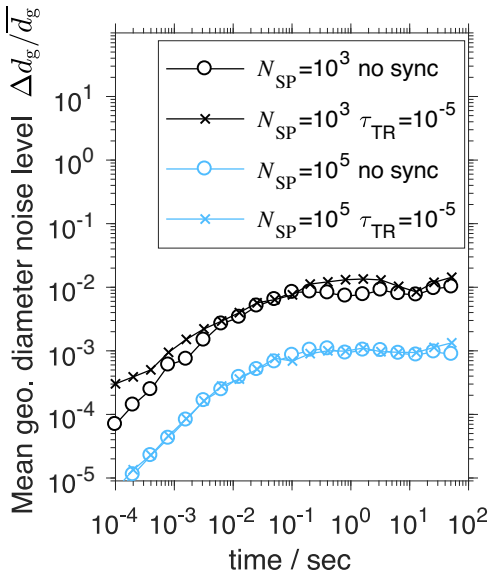

Fig. 9 – The stochastic noise for the values of the geometric mean diameter for simulations with an initial concentration of $N_0 = 10^{17}$ m^{-3} for different numbers of simulation particles N_{SP}. Eqs. (22) and (20) define Δd_g and $\overline{d_g}$.

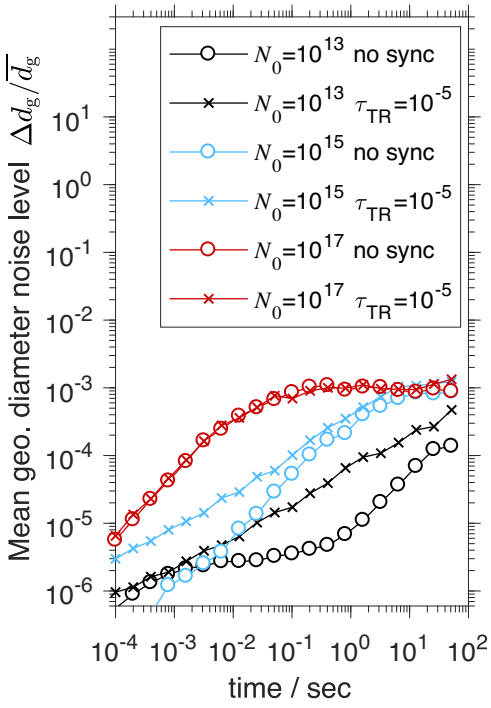

Fig. 10 – The stochastic noise for the values of the geometric mean diameters for MC simulations with $N_{SP} = 10^5$ simulation particles and different initial concentrations N_0 (shown values are in units of m^{-3}). Eqs. (22) and (20) define Δd_g and $\overline{d_g}$.

PSD from a monodisperse initial condition (which is exact, so no noise at all is related to the initial condition) to a self-preserving PSD (Friedlander and Wang, 1966), which is marked by a constant noise level. The self-preserving PSD is attained more quickly if higher initial concentrations N_0 are used. An indicator for the attainment of the self-preserving PSD is the geometric standard deviation of the simulations ($\sigma_g^{(i)}$ for the i-th simulation and $\overline{\sigma_g}$ as mean value for all MC simulations), which can be calculated by:

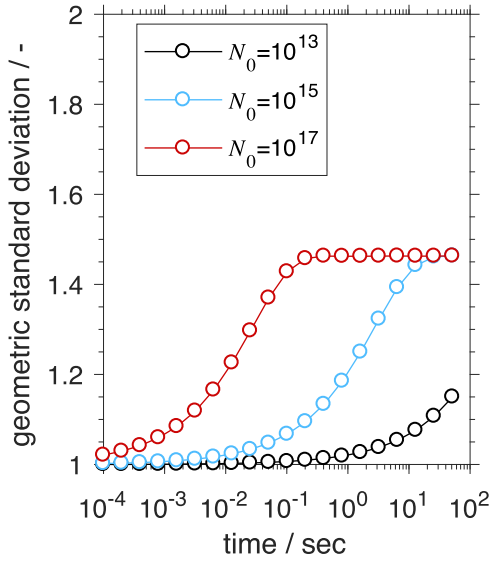

Fig. 11 – The geometric standard deviation $\overline{\sigma_g}$ for some values of the initial concentration N_0 (in units m^{-3}) for simulations without synchronization points and $N_{SP} = 10^5$ simulation particles.

$$\left[\ln(\sigma_g^{(i)})\right]^2 = \sum_{n=1..N_{SP}} W_n^{(i)} \left(\ln(d_n^{(i)}) - \ln(d_g^{(i)})\right)^2 / N_i, \qquad \overline{\sigma_g} = \sum_{i=1..50} \sigma_g^{(i)} / 50, \tag{23}$$

where N_i is the total concentration of the i-th simulation and $d_g^{(i)}$ is the geometric mean value of the simulation, defined in Eqs. (18) and (19). $W_n^{(i)}$ is the statistical weight and $d_n^{(i)}$ the diameter of the n-th simulation particle of the i-th MC simulation.

The corresponding values are shown in Fig. 11. The plateau of $\overline{\sigma_g} \approx 1.46$ has been found in earlier studies to correspond to the onset of the self-preserving PSD (Vemury et al., 1994), with a time-lag to reach this value of ca. $5 \cdot \tau_{coag}$ (see Eq. (13) for the definition of τ_{coag} for the free-molecule regime discussed in this work). Both findings are consistent with Fig. 11 and the different values τ_{coag} defined for each N_0 in Table 2.

It can be thus concluded that the statistical noise increases as the PSD are converging towards the self-preserving PSD and that the forced synchronization leads to much higher noise levels due to the synchronization during this simulation stage. Once the self-preserving PSD is reached, the simulations with and without synchronization exhibit nearly the same noise levels. Hence the noise levels are relatively low, before the self-preserving PSD is reached, the additional stochastic noise due to the forced synchronizations has only small effects on the accuracy of the simulation. This can be seen in Fig. 12: the deviations from the DS method are of the same magnitude for the simulations without synchronizations (marked as 'no sync') as those with the maximal number of synchronization points (marked with '$\tau_{TR} = 10^{-5}$').

4.2. *Computational efficacy*

The inclusion of artificial synchronization points leads to an increase of the computational times (all simulations have been performed on the NVIDIA GTX 980 Ti), as can be seen in Table 4. The smaller the synchronization intervals, the more synchronization points are included (as already mentioned in Table 3) and the longer are the simulation times. Although this

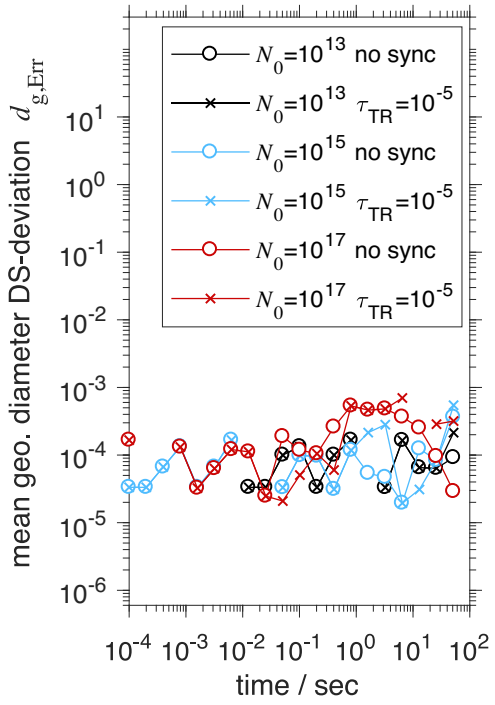

Fig. 12 – The deviations $d_{g,Err}$ defined in Eq. (21) of the mean values for the MC-based mean geometric diameter from the values from the discrete sectional (DS) method. Different initial conditions N_0 (in units m^{-3}) are shown for $N_{SP} = 10^5$ simulation particles.

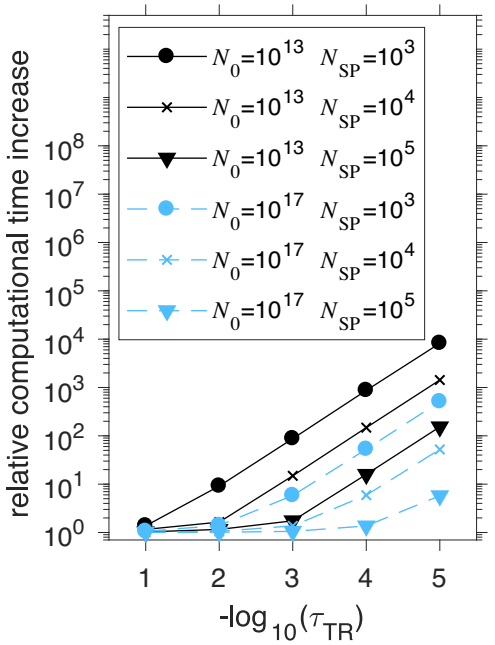

Fig. 13 – The vertical axis shows the ratio of the computation time for the given synchronization interval τ_{TR} to the computational time without synchronization. The values of the computational times are summarized in Table 4.

increase is negligible at first, it scales linearly at the end — this is the situation, in which the number of synchronization time points surpasses the genuine number of performed MC time steps in the scenario without the synchronization time points. Fig. 13 shows this typical scaling scenario.

In the context of flowsheet simulation, the 5 different scenarios representing different initial concentration N_0 may

Table 4 – The computational times are shown for different values of simulation particles N_{SP}, initial concentrations N_0 and different synchronization intervals described by τ_{TR}, 'no sync' designates simulations without synchronization points.

Number of simulation particles	Initial number concentration	Computation times/seconds					
		No sync	$\tau_{TR} = 10^{-1}$ s	$\tau_{TR} = 10^{-2}$ s	$\tau_{TR} = 10^{-3}$ s	$\tau_{TR} = 10^{-4}$ s	$\tau_{TR} = 10^{-5}$ s
1000	10^{13} m^{-3}	2.6	3.5	23.3	223.4	2221.4	20,968.2
	10^{14} m^{-3}	8.2	10.3	23.3	225.4	2225.1	21,040.0
	10^{15} m^{-3}	18.8	21.0	34.3	218.4	2222.3	21,072.9
	10^{16} m^{-3}	29.9	32.7	46.4	229.2	2180.6	21,085.7
	10^{17} m^{-3}	41.4	43.8	57.9	241.0	2186.6	21,085.7
10,000	10^{13} m^{-3}	14.8	17.2	24.3	220.5	2187.8	21,156.6
	10^{14} m^{-3}	73.6	76.8	91.7	221.5	2195.3	21,221.0
	10^{15} m^{-3}	181.1	184.6	201.2	329.8	2198.6	21,259.8
	10^{16} m^{-3}	293.6	298.9	315.7	445.3	2307.2	21,270.1
	10^{17} m^{-3}	408.9	414.5	431.3	560.6	2421.4	21,378.8
100,000	10^{13} m^{-3}	137.8	141.6	159.5	240.5	2195.5	21,122.2
	10^{14} m^{-3}	732.2	741.8	762.5	926.4	2204.5	21,199.8
	10^{15} m^{-3}	1804.1	1818.4	1847.1	2065.7	3283.1	21,304.5
	10^{16} m^{-3}	2943.8	2965.5	2995.1	3175.6	4437.3	22,403.0
	10^{17} m^{-3}	4092.4	4117.8	4146.4	4317.6	5586.4	23,565.3

Table 5 – The computational times and speed up of the parallelized simulations. The speed-up factor is the ratio of the parallelized simulation set up to the sequential simulation set up.

Number of simulation particles	Simulation mode	Computation times (seconds) or speed up (–)					
		No sync	$\tau_{TR} = 10^{-1}$ s	$\tau_{TR} = 10^{-2}$ s	$\tau_{TR} = 10^{-3}$ s	$\tau_{TR} = 10^{-4}$ s	$\tau_{TR} = 10^{-5}$ s
1000	Sequential	100.8	111.2	185.4	1137.4	11,036.0	105,252.4
	Parallel	55.4	102.0	153.5	880.2	8493.0	82,011.9
	Speed-up	**0.549**	**0.918**	**0.828**	**0.774**	**0.770**	**0.779**
10,000	Sequential	972.1	992.0	1064.2	1777.8	11,310.2	106,286.4
	Parallel	514.6	913.5	974.3	1493.9	8804.9	82,048.2
	Speed-up	**0.529**	**0.921**	**0.916**	**0.840**	**0.778**	**0.772**
100,000	Sequential	9710.4	9785.0	9910.5	10,725.8	17,706.7	109,594.9
	Parallel	5094.0	8988.9	9125.4	9745.2	15,030.1	86,048.3
	Speed-up	**0.525**	**0.919**	**0.921**	**0.909**	**0.849**	**0.785**

represent 5 different simulation compartments. The 50 MC simulations may be performed for each of these compartments in a sequential order or all 250 simulations may be performed in parallel at once. Table 5 shows that even the already highly parallelized 50 simultaneous MC simulations can be parallelized further and that the parallel simulation of these heterogeneous simulation settings leads to further advantages. (It should be noted that a decrease of the computational time from 105,000 s to 82,000 s corresponds to a decrease of the simulation time from 29.2 h to 22.7 h).

Hence only one (on the used random numbers dependent) fraction of all 50 (resp. 250) simulations finds a coagulation pair (in Fig. 2, the decision marked as 'coagulation pair found?' would branch to the 'yes' scenario), only this fraction of simulations performs a full or fractional coagulation step τ_{MC} or τ_F and increases the time. The increase is also dependent on the used random numbers. This is the reason, why some simulations reach a synchronization time point earlier than other simulations. The status of these simulations is switched to 'inactive' as they reach a synchronization time point, reducing thus the number of active simulations $N_{\text{active Simulations}}$. The number of necessary parallel comparisons (in order to find a coagulation pair) reduces as well to $N_{\text{active Simulations}} \cdot 256 \cdot 40$. This may lead to the disadvantageous situation, that only a few or even one simulation is active, so that the full parallel architecture of the GPU is not used and many computational resources lie idle. This situation becomes more dominant in the simulation scenarios using fractional time steps, which in turn leads to lower speed-up factors than the ones reported for the non-synchronized simulations, as it is shown in Table 5 and Fig. 13.

5. Conclusions

The applicability of event-driven MC simulations of coagulation in the context of flowsheet simulations is investigated. Event-driven MC methods define a time-step τ_{MC} within which one MC event happens — the specific event is selected stochastically and the simulation time is increased by τ_{MC}. We find, that this approach becomes not applicable if smaller simulation time steps τ_F have to be simulated (i.e. $\tau_F < \tau_{MC}$), in order to synchronize the simulation with other processes or simulation compartments (or units within a flow sheet simulation).

In order to allow such a synchronization, a novel methodology – the concept of 'fractional Monte Carlo time steps' – for the simulation of coagulation based on the acceptance rejection method is proposed. The fractional MC time steps allow to force an event driven MC simulation to stop at arbitrarily defined synchronization time points.

An exemplary simulation of five compartments with distinct simulation conditions is set up. The particle population and thus the intrinsic event-driven time steps vary by the

order of 10^4 between the largest and lowest initial number-concentrations.

Although the simulation of intercompartmental transport is not included in the presented work, the compartments are forcefully synchronized for a 'hypothetic' transport step in order to highlight the computational efficacy of the application due to the parallelized simulation.

It is shown that the application of fractional MC time steps leads to the same results as those gained by conventional event-driven MC methods and the discrete sectional method. The comparison with the conventional event-driven MC method shows that the stochastic nature of the fractional MC steps does not increase the statistical noise of the simulation significantly and that specific benchmark values are reproduced with the same accuracy as by simulations without the artificially added synchronizations.

The computational costs of the forced synchronizations and the advantages of the parallel implementation are briefly mentioned and the advantages of a parallel implementation of a heterogeneous simulation are shown.

Acknowledgement

This work has been financially supported by the Deutsche Forschungsgemeinschaft in the frame of the priority program SPP 1679.

References

Cameron, I.T., Wang, F.Y., Immanuel, C.D., Stepanek, F., 2005. Process systems modelling and applications in granulation: a review. Chem. Eng. Sci. 60 (14), 3723–3750, http://dx.doi.org/10.1016/j.ces.2005.02.004.

Friedlander, S.K., 2000. Smoke, Dust, and Haze: Fundamentals of Aerosol Dynamics, 2nd ed. Oxford Univ. Press, New York, 407 pp.

Friedlander, S.K., Wang, C.S., 1966. The self-preserving particle size distribution for coagulation by Brownian motion. J. Colloid Interface Sci. 22 (2), 126–132.

Garcia, A.L., van den Broeck, C., Aertsens, M., Serneels, R., 1987. A Monte Carlo simulation of coagulation. Physica A 143 (3), 535–546.

Gelbard, F., Tambour, Y., Seinfeld, J.H., 1980. Sectional representations for simulating aerosol dynamics. J. Colloid Interface Sci. 76 (2), 541–556, http://dx.doi.org/10.1016/0021-9797(80)90394-X.

Hao, X., Zhao, H., Xu, Z., Zheng, C., 2013. Population balance-Monte Carlo simulation for gas-to-particle synthesis of nanoparticles. Aerosol Sci. Technol. 47 (10), 1125–1133, http://dx.doi.org/10.1080/02786826.2013.823642.

Hinds, W.C., 2012. Aerosol Technology: Properties, Behavior, and Measurement of Airborne Particles, 2nd ed. Wiley-Interscience, 464 pp.

Hulburt, H.M., Katz, S., 1964. Some problems in particle technology. A statistical mechanical formulation. Chem. Eng. Sci. 19 (8), 555–574.

Irizarry, R., 2012. Fast compartmental Monte Carlo simulation of population balance models: application to nanoparticle formation in nonhomogeneous conditions. Ind. Eng. Chem. Res. 51 (47), 15484–15496.

Khalili, S., Lin, Y., Armaou, A., Matsoukas, T., 2010. Constant number Monte Carlo simulation of population balances with multiple growth mechanisms. AIChE J. 56 (12), 3137–3145, http://dx.doi.org/10.1002/aic.12233.

Kodas, T.T., Hampden-Smith, M.J., 1999. Aerosol Processing of Materials. Wiley-VCH, New York, NY, 680 pp.

Kotalczyk, G., Kruis, F.E., 2017. A Monte Carlo method for the simulation of coagulation and nucleation based on weighted particles and the concepts of stochastic resolution and merging. J. Comput. Phys. 340, 276–296, http://dx.doi.org/10.1016/j.jcp.2017.03.041.

Kraft, M., 2005. Modelling of particulate processes. KONA Powder Part. J. 23 (March), 18–35, http://dx.doi.org/10.14356/kona.2005007.

Kruis, F.E., Maisels, A., Fissan, H., 2000. Direct simulation Monte Carlo method for particle coagulation and aggregation. AIChE J. 46 (9), 1735–1742.

Kruis, F.E., Wei, J., van der Zwaag, T., Haep, S., 2012. Computational fluid dynamics based stochastic aerosol modeling: combination of a cell-based weighted random walk method and a constant-number Monte-Carlo method for aerosol dynamics. Chem. Eng. Sci. 70, 109–120, http://dx.doi.org/10.1016/j.ces.2011.10.040.

Kumar, S., Ramkrishna, D., 1996. On the solution of population balance equations by discretization — II. A moving pivot technique. Chem. Eng. Sci. 51 (8), 1333–1342.

Landgrebe, J.D., Pratsinis, S.E., 1990. A discrete-sectional model for particulate production by gas-phase chemical reaction and aerosol coagulation in the free-molecular regime. J. Colloid Interface Sci. 139 (1), 63–86.

Lee, K.F., Patterson, R.I.A., Wagner, W., Kraft, M., 2015. Stochastic weighted particle methods for population balance equations with coagulation, fragmentation and spatial inhomogeneity. J. Comput. Phys. 303, 1–18, http://dx.doi.org/10.1016/j.jcp.2015.09.031.

Liffman, K., 1992. A direct simulation Monte-Carlo method for cluster coagulation. J. Comput. Phys. 100 (1), 116–127, http://dx.doi.org/10.1016/0021-9991(92)90314-O.

Maisels, A., Kruis, F.E., Fissan, H., 2004. Direct simulation Monte Carlo for simultaneous nucleation, coagulation, and surface growth in dispersed systems. Chem. Eng. Sci. 59 (11), 2231–2239, http://dx.doi.org/10.1016/j.ces.2004.02.015.

Mantzaris, N.V., Daoutidis, P., Srienc, F., 2001. Numerical solution of multi-variable cell population balance models. III. Finite element methods. Comput. Chem. Eng. 25 (11–12), 1463–1481, http://dx.doi.org/10.1016/S0098-1354(01)00711-6.

Marchisio, D.L., Fox, R.O., 2005. Solution of population balance equations using the direct quadrature method of moments. J. Aerosol Sci. 36 (1), 43–73, http://dx.doi.org/10.1016/j.jaerosci.2004.07.009.

Morgan, N.M., Wells, C.G., Goodson, M.J., Kraft, M., Wagner, W., 2006. A new numerical approach for the simulation of the growth of inorganic nanoparticles. J. Comput. Phys. 211 (2), 638–658, http://dx.doi.org/10.1016/j.jcp.2005.04.027.

Patterson, R.I.A., Singh, J., Balthasar, M., Kraft, M., Norris, J.R., 2006. The linear process deferment algorithm: a new technique for solving population balance equations. SIAM J. Sci. Comput. 28 (1), 303–320.

Patterson, R.I.A., Wagner, W., Kraft, M., 2011. Stochastic weighted particle methods for population balance equations. J. Comput. Phys. 230 (19), 7456–7472, http://dx.doi.org/10.1016/j.jcp.2011.06.011.

Qamar, S., Elsner, M.P., Angelov, I.A., Warnecke, G., Seidel-Morgenstern, A., 2006. A comparative study of high resolution schemes for solving population balances in crystallization. Comput. Chem. Eng. 30 (6–7), 1119–1131, http://dx.doi.org/10.1016/j.compchemeng.2006.02.012.

Ramkrishna, D., 2000. Population Balances: Theory and Applications to Particulate Systems in Engineering. Acad. Press, New York, 355 pp.

Ramkrishna, D., Singh, M.R., 2014. Population balance modeling: current status and future prospects. Annu. Rev. Chem. Biomol. Eng. 5, 123–146, http://dx.doi.org/10.1146/annurev-chembioeng-060713-040241.

Shah, B.H., Ramkrishna, D., Borwanker, J.D., 1977. Simulation of particulate systems using the concept of the interval of quiescence. AIChE J. 23 (6), 897–904, http://dx.doi.org/10.1002/aic.690230617.

Skorych, V., Dosta, M., Hartge, E.-U., Heinrich, S., 2017. Novel system for dynamic flowsheet simulation of solids processes.

Powder Technol. 314, 665–679, http://dx.doi.org/10.1016/j.powtec.2017.01.061.
Smith, M., Matsoukas, T., 1998. Constant-number Monte Carlo simulation of population balances. Chem. Eng. Sci. 53 (9), 1777–1786, http://dx.doi.org/10.1016/S0009-2509(98)00045-1.
Sommer, M., Stenger, F., Peukert, W., Wagner, N.J., 2006. Agglomeration and breakage of nanoparticles in stirred media mills — a comparison of different methods and models. Chem. Eng. Sci. 61 (1), 135–148, http://dx.doi.org/10.1016/j.ces.2004.12.057.
Song, M., Qiu, X.-J., 1999. An alternative to the concept of the interval of quiescence (IQ) in the Monte Carlo simulation of population balances. Chem. Eng. Sci. 54 (23), 5711–5715.
Vanni, M., 2000. Approximate population balance equations for aggregation-breakage processes. J. Colloid Interface Sci. 221 (2), 143–160, http://dx.doi.org/10.1006/jcis.1999.6571.
Vemury, S., Kusters, K.A., Pratsinis, S.E., 1994. Time-lag for attainment of the self-preserving particle size distribution by coagulation. J. Colloid Interface Sci. 165 (1), 53–59, http://dx.doi.org/10.1006/jcis.1994.1204.
Wang, F., Richards, V.N., Shields, S.P., Buhro, W.E., 2014. Kinetics and mechanisms of aggregative nanocrystal growth. Chem. Mater. 26 (1), 5–21, http://dx.doi.org/10.1021/cm402139r.
Wei, J., 2014a. A parallel Monte Carlo method for population balance modeling of particulate processes using bookkeeping strategy. Physica A: Stat Mech Appl 402, 186–197, http://dx.doi.org/10.1016/j.physa.2013.12.047.
Wei, J., 2014b. Comparison of computational efficiency of inverse and acceptance–rejection scheme by Monte Carlo methods for particle coagulation on CPU and GPU. Powder Technol. 268, 420–423, http://dx.doi.org/10.1016/j.powtec.2014.08.047.
Wei, J., Kruis, F.E., 2013a. A GPU-based parallelized Monte-Carlo method for particle coagulation using an acceptance–rejection strategy. Chem. Eng. Sci. 104, 451–459, http://dx.doi.org/10.1016/j.ces.2013.08.008.
Wei, J., Kruis, F.E., 2013b. GPU-accelerated Monte Carlo simulation of particle coagulation based on the inverse method. J. Comput. Phys. 249, 67–79, http://dx.doi.org/10.1016/j.jcp.2013.04.030.
Xu, Z., Zhao, H., Zheng, C., 2015. Accelerating population balance-Monte Carlo simulation for coagulation dynamics from the Markov jump model, stochastic algorithm and GPU parallel computing. J. Comput. Phys. 281, 844–863, http://dx.doi.org/10.1016/j.jcp.2014.10.055.
Zhao, H., Kruis, F.E., Zheng, C., 2009. Reducing statistical noise and extending the size spectrum by applying weighted simulation particles in Monte Carlo simulation of coagulation. Aerosol Sci. Technol. 43 (8), 781–793, http://dx.doi.org/10.1080/02786820902939708.
Zhao, H., Maisels, A., Matsoukas, T., Zheng, C., 2007. Analysis of four Monte Carlo methods for the solution of population balances in dispersed systems. Powder Technol. 173 (1), 38–50, http://dx.doi.org/10.1016/j.powtec.2006.12.010.

Paper III

Version of record published in:
Powder Technology 317 (2017), pp. 417–429.
Available online at: https://doi.org/10.1016/j.powtec.2017.05.002

A Time-Driven Constant-Number Monte Carlo Method for the GPU-Simulation of Particle Breakage Based on Weighted Simulation Particles

G. Kotalczyk, J. Devi and F.E. Kruis

Powder Technology 317 (2017) 417–429

Contents lists available at ScienceDirect

Powder Technology

journal homepage: www.elsevier.com/locate/powtec

A time-driven constant-number Monte Carlo method for the GPU-simulation of particle breakage based on weighted simulation particles

Gregor Kotalczyk[a,*], Jherna Devi[a,b], Frank Einar Kruis[a]

[a] Institute of Technology for Nanostructures (NST) and Center for Nanointegration Duisburg-Essen (CENIDE), University Duisburg-Essen, Duisburg D-47057, Germany
[b] Department of Information Technology, Quaid-e-Awam University of Engineering Science & Technology, Nawabshah, Sindh 67480, Pakistan

ARTICLE INFO

Article history:
Received 12 September 2016
Received in revised form 12 April 2017
Accepted 5 May 2017
Available online 10 May 2017

Keywords:
Monte Carlo
Population balances
Breakage
Weighted simulation particles
GPU computing

ABSTRACT

Monte Carlo (MC) simulations based on weighted particles offer novel and more precise techniques for the solution of the population balance equation for particulate systems. A recent constant-number approach named stochastic weighted algorithm (SWA) (Lee et al. (2015), J. Comput. Phys. (303) 1–18) has been developed, which renders the breakage of a simulation particle by an alteration of its properties, without the creation of novel simulation particles. The theoretic justification of the general formulation for all possible SWAs is limited to binary breakage kernels. We present a novel approach for the derivation of the properties of the MC particles representing fragments, which is applicable for all sorts of breakage kernels. This general scheme encompasses the already introduced SWA schemes, especially a number-based (SWA1, named NBS in this paper) and volume-based (SWA2, named VBS in this paper) breakage scheme, and it makes novel formulations possible: the low volume scheme (LVS), which renders preferably lower fragment sizes, and the combination of LVS with the NBS (LVS-NBS) or VBS (LVS-VBS). The implementation of these breakage schemes in the context of a GPU-based time-driven method is presented and the gained results are validated by comparison with results of the analytic solutions of a homogeneous binary breakage kernel. It is found, that the SWA methods (NBS and VBS) are only able to render large particle sizes, and that LVS, NBS-LVS and VBS-LVS are able to render the whole spectrum of particle sizes. Smaller noise levels are found for VBS and specific VBS-LVS schemes, making both more suitable for prolonged simulations than the other presented methods.

1. Introduction

The solution of the Population Balance Equation (PBE) rendering the breakage of particles is not only interesting for the description of crushing and grinding processes, it is also used to understand liquid-liquid dispersions, polymer degradation and formulation of products through granulation. The most common approaches for the solution of the PBE are the methods of moments, discretization methods and Monte Carlo (MC) methods.

Sectional simulation methods encompass the discretization of the particle property space, which can be combined with deterministic formulations of the particle concentration in single sections [1,2], or with the mass-conserving form of the PBE for a finite volume scheme [3,4]. Those approaches require the specific a priori designation of the interesting particle size domain, which can become problematic in a multidimensional property space. Additional processes like condensation and evaporation can only be incorporated with a great computational effort (via moving grids [5] or by a reformulation of the problem with the help of finite elements [6]) hence simpler implementations of growth processes lead to numerical diffusion [7].

Monte Carlo (MC) simulations render particle populations with the help of simulation particles, each simulation particle represents thereby a certain concentration (in m^{-3}) of real particles and avoid therefore the numerical diffusion characteristic for sectional approaches. The rendering of the large number of particles which are produced during the continuous breakage process poses a major problem for MC simulations, because large computational resources have to be provided for this purpose. In a typical milling process, for example, reductions of the particle diameters from 500 μm to 0.5 μm are encountered, the same amount of volume, which is

* Corresponding author.
E-mail address: Gregor.Kotalczyk@uni-due.de (G. Kotalczyk).

http://dx.doi.org/10.1016/j.powtec.2017.05.002
0032-5910/

rendered by one simulation particle with a size of 500 μm has to be rendered by 10^9 simulation particles with a diameter of 0.5 μm, if all particles represent the same number concentration of real particles.

Early MC simulations solved this problem by a discretization of the particle property into bins and counting, how many MC particles [8] or the corresponding volume [9] or mass[1] [10] can be found within a specific bin. These approaches bear the same disadvantages as the sectional methods mentioned above.

An alternative concept in order to avoid large numbers of simulation particles is the constant-number MC approach developed by the Matsoukas group for the agglomeration [11], and extended to the simulation of breakage [12]. In the scope of this approach, the loss of simulation particles due to coagulation events could be compensated by a copy of randomly selected simulation particles - and the memory space for new simulation particles resulting from the breakage event could be created by the removal of randomly selected simulation particles. This method is known to produce a high level of statistical simulation noise [13,14].

The MC-simulation based on weighted particles allows the technique of merging two simulation particles into one ([15], introduced for the Multi-Monte Carlo approach). Although it was found that the Multi-Monte Carlo method led to systematic errors of the simulation [16], the merging methods can be combined with other simulation techniques based on weighted particles [14,17,18] or [13]. However, the resulting estimation of two suited simulation particles for a merge step has to be performed for each additional particle resulting from the breakage, leading to large computing times especially for particle systems describing the breakage of one particle into a large number of fragments - assuming that two particles suitable for the merging step can be found at all.

This problem is avoided by the mass-flow algorithm (MFA) which was introduced for the coagulation process [19] and extended to the breakage process [20] as well. In the scope of this approach, the resulting fragments are represented by only one MC-particle which replaces the original particle, selected for breakage, leading thus to a constant-number scheme. The simulation particles used by the MFA are differentially weighted (i.e. each simulation particle represents a different concentration of real particles) but renders the same amount of mass concentration, so that the statistical weight is defined by the property (mass) of the simulation particle. This causes the incorporation of growth processes to be difficult, hence specifically defined statistical weights as a second particle property are needed [21]. This problem has been solved by the formulation of stochastic weighted algorithms (SWA) [18] for the coagulation, which could be extended to the breakage process [13].

A general breakage scheme is presented in the scope of the SWA for breakage [13], consisting of two parts. The first part describes the probability distribution function (PDF) with which the new volume of the simulation particle is selected. The second part describes how to calculate the statistical weight of the simulation particle depending on the selected volume. This derivation was performed for a binary breakage kernel and is founded on symmetry arguments. In this paper, we present an alternative approach for the derivation of the breakage scheme in Section 2 by resorting to the argument, that the breakage of many MC-particles with equal properties and weights has to lead to a particle size distribution (PSD) of fragments, which is described by the corresponding breakage kernel. The implementation of the gained results on the GPU in the scope of a time-driven MC simulation will be discussed in Section 3.

[1] The mass-based formulation is equivalent to the volume-based one, if the same density ρ is assigned to the simulated particles. The assignment of different densities for different particles is easily done in the scope of a MC simulation, but not investigated in this paper or the cited works. The terms 'mass' and 'volume' are therefore used synonymously in this paper.

2. Theory

In order to provide a higher level of clarity, it will be distinguished between particles and differentially weighted simulation entries (SE) in the following. The particles refer to existing physical objects, whose behavior is described by kinetic equations. The SE are representations of the PSDs of the particles stored on the computer. A SE i contains the properties of the particles (in the here presented case the volume v_i) and an additional property: the statistical weight W_i, which is a concentration (in units m^{-3}).

The existing number-based and volume-based formulations for (real) particles of the breakage process are summarized in Section 2.1. Section 2.2 presents different selection schemes for the properties of the fragment SEs in order to render the breakage process.

The formulation of the population balance equation (PBE) used in this work is based on one particle property, the volume v (the term 'size' is used synonymously).

2.1. Formulations of the PBE for breakage

2.1.1. Number-based formulation

The number-based PBE [2], for breakage describes the temporal change of the number-based PSD[2] $n(v)$ of the particle population:

$$\frac{\mathrm{d}n(v)}{\mathrm{d}t} = -S(v)\cdot n(v) + \int_v^\infty n(v')\cdot S(v')\cdot b_\mathrm{n}(v,v')\mathrm{d}v'. \tag{1}$$

The breakage rate of a particle with the volume v_P is denoted by $S(v_\mathrm{P})$. The number-based distribution of the resulting fragments is described by the breakage function $b_\mathrm{n}(v_\mathrm{F}, v_\mathrm{P})$ which states, that $b_\mathrm{n}(v_\mathrm{F}, v_\mathrm{P})\mathrm{d}v_\mathrm{F}$ fragments with the volume between v_F and $v_\mathrm{F} + \mathrm{d}v$ are created due to the breakage of a parent particle with the volume v_P. The mean total number of fragments resulting from the breakage of one parent particle is:

$$B(v_\mathrm{P}) = \int_0^{v_\mathrm{P}} b_\mathrm{n}\,(v_\mathrm{F}, v_\mathrm{P})\,\mathrm{d}v_\mathrm{F}. \tag{2}$$

In the special case of a binary breakage, there are exactly two fragments, so that: $B(v_\mathrm{P}) = 2$ for all v_P.

The conservation of the volume during the breakage poses a restriction on all possible formulations for $b_\mathrm{n}(v_\mathrm{F}, v_\mathrm{P})$ by the following formula:

$$v_\mathrm{P} = \int_0^{v_\mathrm{P}} b_\mathrm{n}\,(v_\mathrm{F}, v_\mathrm{P})\cdot v_\mathrm{F}\mathrm{d}v_\mathrm{F}. \tag{3}$$

2.1.2. Volume-based formulation

The volume-based formulation of the PBE [1] can be gained by setting the volume-based PSD $M(v)$ to $M(v) = v\cdot n(v)$:

$$\frac{\mathrm{d}M(v)}{\mathrm{d}t} = -S(v)\cdot M(v) + \int_v^\infty M(v')\cdot S(v')\cdot b_\mathrm{m}(v,v')\,\mathrm{d}v'. \tag{4}$$

The thus resulting volume-based breakage kernel b_m is written in accordance to [1] as:

$$b_\mathrm{m}\,(v_\mathrm{F}, v_\mathrm{P}) = \frac{v_\mathrm{F}}{v_\mathrm{P}}\cdot b_\mathrm{n}\,(v_\mathrm{F}, v_\mathrm{P})\,.$$

[2] This means, that the value $N = \int_{v_\mathrm{start}}^{v_\mathrm{end}} n(v)\mathrm{d}v$ gives a number-concentration (units m^{-3}) of particles which can be found with $v_\mathrm{start} \le v \le v_\mathrm{end}$.

2.2. Selection schemes for volumes of the fragment SEs

The breakage of a SE i in the framework of a constant-number scheme is rendered by the change of its volume v and statistical weight W due to the breakage event. The properties of the SE representing the parent particle $(v_P(i), W_P(i))$ before the breakage are stored in the same place on the computer as those of the fragment SE $(v_F(i), W_F(i))$ after the breakage. The values of the volume $v_F(i)$ of the fragment SEs are thereby distributed according to a probability density function (PDF), $f_{mc}(v_F, v_P)$.

Although the probability to find fragments of the size v_F is defined by $\frac{b_n(v_F,v_P)}{B(v_P)}\mathrm{d}v_F$, the function f_{mc} can be set independently of $b_n(v_F, v_P)$ and $B(v_P)$. This is because the used SE i contains the statistical weight W_i as additional information, which can be set in such a way, that the resulting fragment PSD (of the breakage of many SEs with v_P) is equal to the distribution $b_n(v_F, v_P)$. This notion is elaborated in Section 2.2.1 in more detail.

Table 1 summarizes the selection methods used in this work. Each selection method is defined by the PDFs f_{mc} for the selection of the volume v_F of the fragment SEs and the corresponding values for the statistical weights W_F. Table 1 can also be used as a look-up reference for the abbreviations used in this work. The single methods are explained in Sections 2.2.2–2.2.5.

In Section 2.2.6, an example is presented which shows how the application of different functions f_{mc} leads to the expected fragment distributions by the adjustment of the statistical weights of the fragment SEs according to Table 1.

2.2.1. General breakage scheme

It is assumed in the following, that a statistically large number of SEs is used for the MC simulation, so that a statistically large number N_p of parent SEs have been selected for breakage and attain (nearly) the same property (or at least cluster in the vicinity of) (v_P, W_P), so that $(v_P(i), W_P(i)) \approx (v_P, W_P)$ for $i = 1, 2, \ldots, N_p$. The total statistical weight W_{Tot} before the breakage event rendered by this population is then:

$$W_{Tot} = \sum_{i=1}^{N_p} W_P(i) = N_p \cdot W_P. \tag{5}$$

The number-based PSD $n_F^{(exact)}(v)$ which results from the breakage of all these SEs (i.e. all $(v_F(i), W_F(i))$ values with $i = 1, 2 \ldots, N_P$) should be equal to the number-based breakage function $b_n(v_F, v_P)$ times the total concentration W_{Tot} rendered by the SEs before the breakage:

$$n_F^{(exact)}(v_F) = W_{Tot} \cdot b_n(v_F, v_P). \tag{6}$$

The probability $P_{mc}(v_F, v_P)$ that the fragment SE is assigned a volume $v \in [v_F, v_F + \mathrm{d}v]$ is given by $P_{mc}(v_F, v_P) = f_{mc}(v_F, v_P)\mathrm{d}v_F$. If N_p SEs with the volume v_P are selected for breakage, the number $N_f(v_F)$ of fragment SEs with $v \in [v_F, v_F + \mathrm{d}v]$ is therefore described by:

$$N_f(v_F) = P_{mc}(v_F, v_P) N_p = f_{mc}(v_F, v_P)\,\mathrm{d}v \cdot N_p. \tag{7}$$

The total number-concentration rendered by those SEs can be written as:

$$\begin{aligned} n_F^{(mc)}(v_F)\,\mathrm{d}v &= W_F(v_F) \cdot N_f(v_F)\,\mathrm{d}v \\ &= W_F(v_F) \cdot f_{mc}(v_F, v_P) \cdot N_p \mathrm{d}v. \end{aligned} \tag{8}$$

This value should be equal to the exact number-based PSD (i.e.: $n_F^{(exact)}(v_F)\,\mathrm{d}v = n_F^{(mc)}(v_F)\,\mathrm{d}v$). One obtains therefore with Eqs. (6) and (8):

$$W_F(v_F) = \frac{W_{Tot}}{N_p} \cdot \frac{b_n(v_F, v_P)}{f_{mc}(v_F, v_P)} \overset{(5)}{=} W_P \cdot \frac{b_n(v_F, v_P)}{f_{mc}(v_F, v_P)}. \tag{9}$$

In addition to the non-negative requirement for a PDF, $f_{mc}(v_F, v_P) \geq 0, \forall 0 \leq v_F \leq v_P$, the function $f_{mc}(v_F, v_P)$ has to be non-zero if the corresponding breakage function $b_n(v_F, v_P)$ is non-zero:

$$f_{mc}(v_F, v_P) > 0, \quad \text{if: } b_n(v_F, v_P) > 0. \tag{10}$$

This is necessary in order to guarantee Eq. (6) = Eq. (8).[3] In addition to these requirements, f_{mc} satisfies the normalization condition:

$$\int_0^{v_P} f_{mc}(v_F, v_P)\,\mathrm{d}v_F = 1, \quad \forall v_P. \tag{11}$$

It is shown in Appendix A that this general description encompasses all of the breakage schemes introduced by [13] (named SWA). The method proposed here is even more general, because the restrictions posed by Eqs. (10) and (11) are much weaker than the restriction posed by Eq. (A.1) in the context of the SWA. In the following, the specific choices for f_{mc} will be discussed.

2.2.2. Number-based selection (NBS)

The simplest specific choice for f_{mc} is to set it proportional to the number-based breakage function: $f_{mc}^N \propto b_n(v_F, v_P)$. The normalization condition (Eq. (11)) defines the PDF for the NBS, f_{mc}^N, via:

$$f_{mc}^N = \frac{b_n(v_F, v_P)}{\int_0^{v_P} b_n(v_F, v_P)\,\mathrm{d}v_F} = \frac{b_n(v_F, v_P)}{B(v_P)}.$$

This specific choice leads to the following weights of the fragment SEs - according to Eq. (9):

$$W_F(v_F) = B(v_P) \cdot W_P.$$

So that the assigned statistical weight is independent on the specifically chosen size of the fragment SE, v_F. This scheme is introduced by [13] as well, named SWA1.

Note, that the resulting number-concentration of the breakage of particles with the total concentration W_{Tot} is always $B(v_P) \cdot W_{Tot}$, which is the correct value, although the specific realization of $n_F^{(mc)}(v_F)$ depends upon the random variates for v_F.

2.2.3. Volume-based selection (VBS)

The total volume (per system volume $\mathrm{m}^3/\mathrm{m}^3$) rendered by the SE is conserved during the breakage event, if and only if:

$$v_P \cdot W_P = v_F \cdot W_F \Longleftrightarrow W_F = W_P \cdot \frac{v_P}{v_F}. \tag{12}$$

This setting defines the PDF for the fragment selection of the VBS, f_{mc}^V, via Eq. (9):

$$f_{mc}^V = \frac{W_P}{W_F} \cdot b_n(v_F, v_P) \overset{(12)}{=} \frac{v_F}{v_P} \cdot b_n(v_F, v_P).$$

The value $f_{mc}^V(v_F, v_P)$ is indeed a probability density: the volume conservation stated in Eq. (3) leads to: $\int_0^{v_F} f_{mc}^V(v_F, v_P)\,\mathrm{d}v_F = 1$.

[3] The division by zero in Eq. (9) is per se avoided for $f_{mc}(v_F, v_P) = 0$, hence no fragment SE with v_F is selected and Eq. (9) is not applied for the calculation of $W(v_F)$.

Table 1
The shown methods are defined by the PDF for the selection of the volume v_F of the fragment SE and the assignment of its statistical weight W_F.

Method	Probability density function (PDF) $f_{mc}(v_F, v_P)$ or probability $\hat{p}_{mc}(v_F, v_P)$ for selection of v_F	Statistical weight W_F of fragment simulation entry (SE)	Remarks or alternative nomenclature in literature
General form	$f_{mc}\left(v_F, v_P\right)$	$W_P \cdot b_n(v_F, v_P) / f_{mc}(v_F, v_P)$	Normalization condition: $\int_0^{v_P} f_{mc}(v_F, v_P) dv_F = 1$
Number-based selection (NBS)	$f_{mc}^N = b_n(v_F, v_P) / B(v_P)$	$W_P \cdot B(v_P)$	stochastic weighted algorithm (SWA) 1 in [13]
volume-based selection (VBS)	$f_{mc}^V = b_n(v_F, v_P) \cdot v_F / v_P$	$W_P \cdot \frac{v_P}{v_F}$	Mass flow algorithm (MFA) in [20], SWA 2 in [13], equivalent to [10]
Low volume selection (LVS)	$f_{mc}^L = 1/\ (C(v_P)\, v_{max})$	$W_P \cdot b_n(v_F, v_P) C(v_P) v_{max}$	with $v_{max} = \max(v_F, v_{lim})$ Eq. (14) defines $C(v_P)$
Combined schemes VBS-LVS; NBS-LVS	$f_{mc}^{C(R)} = R f_{mc}^A + (R-1) f_{mc}^B$	$W_P \cdot \frac{b_n(v_F, v_P)}{R \cdot f_{mc}^A + (R-1) \cdot f_{mc}^B}$	for all R with $0 < R < 1$; A=VBS (resp. NBS) B=LVS
for discrete kernels $\hat{b}$	$\hat{p}_{mc}(v_F, v_P)$	$W_P \cdot \hat{b}_n(v_F, v_P) / \hat{p}_{mc}(v_F, v_P)$	Normalization condition: $\sum_{\text{all } v_F} \hat{p}_{mc}(v_F, v_P) = 1$

The so derived scheme is equal to the SWA2 algorithm introduced by [13]. In the absence of other processes (like growth), the volume concentration rendered by one SE (m^3/m^3) remains constant throughout the entire simulation, so that the resulting scheme is equivalent to the MFA presented by [20]. The grouping of the fragment volume-concentration not as a specific SE but to a discretized bin has been modeled by [10] with the same probabilities, hence the PDF for VBS is equal to the volume-based breakage kernel: $f_{mc}^V = b_m$, one can therefore speak of a certain equivalence of the methods.

2.2.4. Low volume selection (LVS)

The question arises, how a specific part of the PSD can be rendered with more detail by the tuning of $f_{mc}(v_F, v_P)$. Hence initial testing showed, that smaller particle size fractions couldn't be rendered by the resulting fragment SEs (this will be discussed in the results Section 5), a scheme has been developed in order to render specifically those smaller particle sizes. This can be done by setting $f_{mc}(v_F, v_P) \propto \frac{1}{v_F}$, leading to higher probabilities for smaller v_F.

Some limitation has to be set, in order to ensure the normalization condition stated in Eq. (11). This can be done, by setting f_{mc} to a constant maximal value for all particle sizes smaller than v_{lim}, leading to $f_{mc}^L(v_F, v_P) \propto (\max(v_F, v_{lim}))^{-1}$. If the parent SE has a volume smaller than v_{lim}, then the volumes of the fragment SE will be selected according to a uniform distribution. The explicit form of f_{mc}^L can be calculated with the help of a constant $C(v_P)$:

$$f_{mc}^L(v_F, v_P) = (C(v_P) \cdot \max(v_F, v_{lim}))^{-1}\ . \tag{13}$$

The value for $C(v_P)$ is given by the normalizing condition (Eq. (11)):

$$C(v_P) = \begin{cases} 1 + \ln\left(\frac{v_P}{v_{lim}}\right) & , v_P > v_{lim} \\ \frac{v_P}{v_{lim}} & , v_P < v_{lim}\ . \end{cases} \tag{14}$$

The weights of the fragment SE result from Eq. (9):

$$W(v_F) = (C(v_P) \cdot \max(v_F, v_{lim})) \cdot b_n(v_F, v_P) \cdot W_P.$$

This breakage scheme cannot be formulated in the scope of the SWA-theory (even if a binary and thus symmetric breakage kernel b_n is postulated), because the corresponding function γ (which results from inserting f_{mc}^L defined in Eq. (13) as f_{mc}^γ into Eq. (A.2)) does not meet the requirement defined in Eq. (A.1). The following combination schemes cannot be formulated by the SWA for the same reason.

2.2.5. Combination of breakage schemes

In the scope of the NBS or the VBS scheme, the formation of smaller particles is not possible, even if a large number of SEs are used as will be shown later in the results Section 5. These small particles can be described by the LVS scheme correctly, but larger particles, which represent the main part of the simulated volume to a specific time point, are not rendered with sufficient precision by this method leading to systematic errors for longer simulation times (this is discussed in the results section, too).

In order to render the whole particle size spectrum of the resulting particle population correctly, the LVS breakage scheme can be used in combination with VBS (or NBS) by splitting up the rendering of single breakage events between those two methods. If N_p parent particles have been selected for breakage, then $R \cdot N_p$ breakage events are rendered with VBS (or NBS) and $(R-1) \cdot N_p$ with LVS, R is a constant factor with $0 < R < 1$. This scheme is not only easy to implement (this is shown in Section 3.2.2 and Appendix B.2), it is also easy to formulate the PDF of this scheme $f_{mc}^{C(R)}$ by a combination of f_{mc}^V (or f_{mc}^N) and f_{mc}^L via:

$$f_{mc}^{C(R)} = R \cdot f_{mc}^V + (R-1) \cdot f_{mc}^L. \tag{15}$$

The statistical weight, which has to be attributed to the fragment SE can be gained via the general Eq. (9):

$$W_F = W_P \frac{b_n(v_F, v_P)}{R \cdot f_{mc}^V(v_F, v_P) + (R-1) \cdot f_{mc}^L(v_F, v_P)}. \tag{16}$$

Several different combination methods can be constructed, depending upon the selected value of R. The explicit equations for the combination VBS-LVS are gained by replacing f_{mc}^V by f_{mc}^N in Eqs. (15) and (16).

2.2.6. Example system

In order to illustrate the differences between the methods, a simple example describing the polymer breakage of a 3-polymer (volume $v_P = 3v_0$) into a 2-polymer (volume $v_F = 2v_0$) and a 1-polymer (volume $v_F = v_0$) is discussed. This break-up event is modeled by a discrete breakage function $\hat{b}_n(v_F, v_P)$ which assumes the following two values:

$$\hat{b}_n(v_0, 3v_0) = \hat{b}_n(2v_0, 3v_0) = 1\ . \tag{17}$$

The total amount of particles which are produced by the breakage of one particle is $B(v_P) = 2$. If a concentration of W_0 3-polymers breaks, one expects to find exactly W_0 2-polymers and W_0 1-polymers.

One can write in general [22]:

$$b_n = \sum_{v_{F,i}} \delta(v - v_{F,i}) \cdot \hat{b}_n \Rightarrow \quad f_{mc} = \sum_{v_{F,i}} \delta(v - v_{F,i}) \cdot \hat{p}_{mc}.$$

The continuous PDFs f_{mc} (summarized in Table 1) are thus easily reformulated as discrete probabilities $\hat{p}_{mc}$, via $\hat{p}_{mc}^N = \frac{\hat{b}}{B}$ and Eq. (17) for NBS:

$$\hat{p}_{mc}^N(v_0, 3v_0) = \frac{1}{2}, \quad \hat{p}_{mc}^N(2v_0, 3v_0) = \frac{1}{2}. \tag{18}$$

The probability $\hat{p}^{\mathrm{V}}_{\mathrm{mc}} = \frac{\hat{b}}{B} \cdot \frac{v_{\mathrm{F}}}{v_{\mathrm{P}}}$ is used with Eq. (17) for VBS:

$$\hat{p}^{\mathrm{V}}_{\mathrm{mc}}(v_0, 3v_0) = \frac{1}{3}, \quad \hat{p}^{\mathrm{V}}_{\mathrm{mc}}(2v_0, 3v_0) = \frac{2}{3}. \tag{19}$$

For the LVS, no limit value v_{lim} is needed for the normalization:

$$\hat{p}^{\mathrm{L}}_{\mathrm{mc}} = \left(v_{\mathrm{F}} \cdot \widehat{C}\right)^{-1}. \tag{20}$$

The value of the constant $\widehat{C}$ is for the here presented example:

$$1 = \frac{1}{\hat{C} v_0} + \frac{1}{\hat{C} 2v_0} \Longleftrightarrow \hat{C} = \frac{3}{2v_0}. \tag{21}$$

This leads to $\hat{p}^{\mathrm{L}}_{\mathrm{mc}} = \frac{2\hat{v}_0}{3v_{\mathrm{F}}}$ for LVS:

$$\hat{p}^{\mathrm{L}}_{\mathrm{mc}}(v_0, 3v_0) = \frac{2}{3}, \quad \hat{p}^{\mathrm{L}}_{\mathrm{mc}}(2v_0, 3v_0) = \frac{1}{3}. \tag{22}$$

The statistical weights of the SEs are calculated analogously to Eq. (9) by:

$$W_{\mathrm{F}}(v_{\mathrm{F}}) = W_{\mathrm{P}} \cdot \frac{\hat{b}\,(v_{\mathrm{F}}, v_{\mathrm{P}})}{\hat{p}_{\mathrm{mc}}\,(v_{\mathrm{F}}, v_{\mathrm{P}})}. \tag{23}$$

This value is dependent on the used probability (i.e. whether $\hat{p}_{\mathrm{mc}}$ is set to $\hat{p}^{\mathrm{N}}_{\mathrm{mc}}, \hat{p}^{\mathrm{V}}_{\mathrm{mc}}$ or $\hat{p}^{\mathrm{L}}_{\mathrm{mc}}$). Fig. 1 shows the modeling of the initial population by 6 SEs (in this case $N_{\mathrm{p}} = 6$) with the concentrations W, so that $W_0 = 6W$. It can be seen, how the number $N_{\mathrm{f}}(v_0)$ (resp. $N_{\mathrm{f}}(2v_0)$) of the resulting fragment SEs with specific volume v_0 (resp. $2v_0$) depends upon which discrete probability ($\hat{p}^{\mathrm{N}}_{\mathrm{mc}}, \hat{p}^{\mathrm{V}}_{\mathrm{mc}}$ or $\hat{p}^{\mathrm{L}}_{\mathrm{mc}}$) is used and how the corresponding setting of the statistical weights, W_{F} leads to the correct PSD, $n^{(\mathrm{mc})}_{\mathrm{F}}(v_{\mathrm{F}})$.

Fig. 2 shows an exemplary combined NBS-LVS scheme with $R = \frac{2}{3}$, the initial population is modeled by 9 SEs (in this case $N_{\mathrm{p}} = 9$) with the concentrations W, so that $W_0 = 9W$.

3. Parallel time-driven GPU-implementation

3.1. Time-driven MC-simulation method

The derived breakage schemes in Table 1 can be implemented in an event-driven (e.g. [23]) or time-driven MC-simulation (e.g. [24]). Both methods can be explained with the concept of the interval of quiescence [25]. The probability $P_i(t_{\mathrm{ev}} < \Delta t)$, that any event i happens to a time t_{ev}, which is earlier than a time Δt, is modeled in the scope of the interval of quiescence approach by a Poisson distribution defined by the rate K_i of this event:

$$P_i\,(t_{\mathrm{ev}} < \Delta t) = 1 - \exp\,(-\Delta t \cdot K_i)\,. \tag{24}$$

3.1.1. Event-driven method

In the scope of the event-driven method, single events are modeled, which occur with the total rate $K_{\mathrm{tot}} = \sum K_i$. This leads to an inter-event time of $\frac{1}{K_{\mathrm{tot}}}$, which has to be re-evaluated after each single event. For each time step only one event is selected, the probability $P_{\mathrm{s}}(i)$ to select the event is proportional to the event rate: $P_{\mathrm{s}}(i) = \frac{K_i}{K_{\mathrm{tot}}}$.

3.1.2. Time-driven method

In the framework of the time-driven method, multiple events can be rendered within a time step Δt. The probability that an event i happens within the time Δt is given by Eq. (24) and has to be checked for every event in order to describe one time step.

The rates are assumed to be constant throughout the time step Δt. In order to avoid errors due to changes of the rates of the events, a

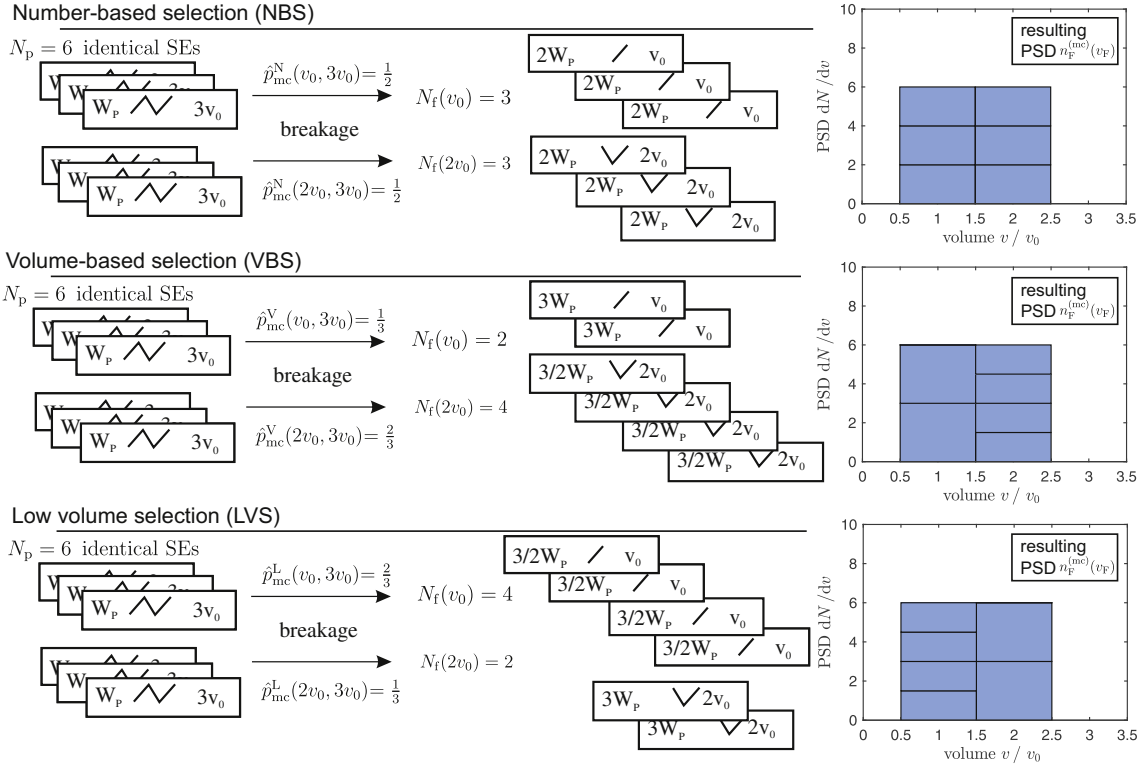

Fig. 1. The changes of the properties of the SEs due to a breakage step are shown. Each of the fragment SEs represents one rectangle in the resulting PSD $n^{(\mathrm{mc})}_{\mathrm{F}}(v_{\mathrm{F}})$ - these are mean values which would be attained, if this specific breakage event would be repeated multiple times. The total volume rendered by each SE is preserved by the VBS scheme only.

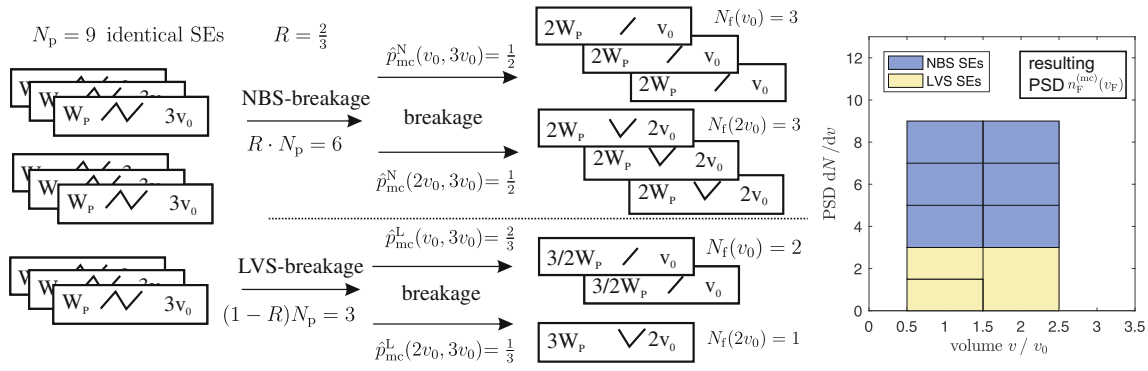

Fig. 2. The changes of the properties of the SEs within a combined breakage step are shown, the factor R determines how many SEs are simulated by the schemes NBS and LVS presented in Fig. 1 and defined in Table 1.

setting of $\Delta t = [\max_{\text{all rates } i}(K_i)]^{-1} \cdot \alpha_T$ is suggested, with the tuning factor α_T, which is set to $\alpha_T = 0.1$ [24] (resp. $\alpha_T = 0.01$ in another study [26]). The value $K_{max} = \max_{\text{all rates } i}(K_i)$ has to be evaluated for each time step.

For the specific simulation of breakage based on SEs, the event i describes the breakage of the SE i within Δt, the subsequent breakage of the resulting particle population (rendered by the fragment SE) within Δt is not modeled in this approach.[4] A low setting of the tuning factor α_T is therefore necessary, in order to avoid the situation, in which the (real) particle population rendered by the SE undergoes two breakage events within Δt.

3.2. Parallel GPU-algorithm

In the here presented parallel GPU-approach, each breakage event of a single SE is treated as a specific process K_i, so that: $K_i = S(v_i)$ and $K_{max} = \max_{\text{all } i} S(v_i)$. If 10^5 SEs are used for the simulation, then 10^5 breakage events (each $S(v_i)$) have to be checked (via Eq. (24)) in each time step Δt. This might sound very ineffective first, but we point out, that the 10^5 comparisons are executed in parallel.

The thus gained parallel algorithm consist of the following simple steps:

1. Initiate $t = 0$
2. Repeat
   (a) Calculate the maximal breakage rate $S_{max} = \max_{\text{all SEs } i}(S(v_i))$. The parallel implementation of this step is shown in Section 3.2.1.
   (b) Set the time step:

$$\Delta t = \min\left(\alpha_T \cdot S_{max}^{-1} \ , \ t_{end} - t\right). \tag{25}$$

   (c) Perform for each SE in parallel:
      i. Check, whether the SE breaks in the given time step. This is done by a uniformly distributed random number $U \in (0, 1)$. The particle breaks according to Eq. (24), if $U < 1 - \exp(-\Delta t \cdot S(v_i))$.
      ii. If the particle breaks, estimate the new fragment-SE properties:
         A. Select the fragment size v_F by the rejection algorithm using the probability density $f_{mc}(v_F, v_P)$ summarized in Table 1. The procedure is explained in more detail in Section 3.2.2, and comprised as Algorithm 1 (resp. Algorithm 2 for combined methods) in Appendix B.2.
         B. Calculate the new statistical weight $W_F(v_F)$ summarized in Table 1.
   (d) Increase the simulation time to $t + \Delta t$.

Until $t \geq t_{end}$

The end time of the simulation, t_{end}, is set by the user.

3.2.1. Parallel calculation of the maximal breakage rate

Fig. 3 shows an exemplary algorithm for the calculation of the maximal breakage rate S_{max}. Only $\log_2(N_{SE})$ computational steps are necessary, if N_{SE} SEs are used. This algorithm is similar to the algorithms for a parallel sum (the sum has to be replaced with the compare operation) calculation, used by [29,30] in the scope of the parallel solution of the PBE for the coagulation process - a detailed discussion of the computational efficacy of this algorithm can be found in [14].

3.2.2. Selection of the fragment-size v_F

The inverse method and the rejection method are the mostly used methods for the generation of random variates v_F for a given PDF f_{mc}. Both methods are discussed in Appendix B in more detail.

For the rejection method, a specific sampling is required for the proposal of a random variate, two sampling methods, a uniform sampling (U) and an inverse sampling (I) are investigated in Appendix B.2. The following findings are gained for the necessary number of iterations Y_U (for uniform sampling) and Y_I (for inverse sampling) in dependency of the applied selection schemes defined in

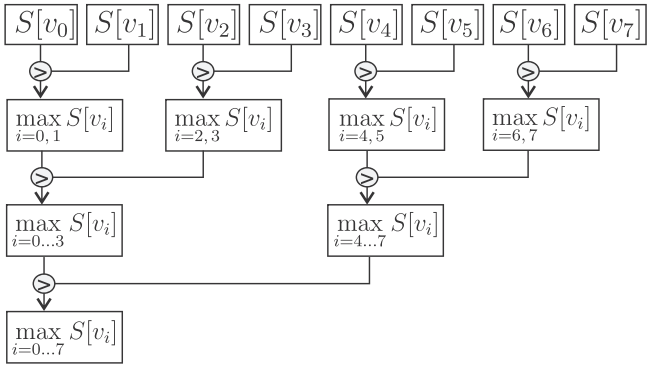

Fig. 3. An exemplary parallel algorithm for the estimation of the maximal breakage rate S_{max} is shown. Each thread calculates the breakage rate $S(v_i)$ of one SE i.

[4] The τ-leap technique [27,28] could be used for the modeling of multiple breakage events of one SE during Δt. In this approach, the properties of the hypothetical fragments have to be used for the calculation of the probability of a second breakage event during the time step Δt.

Table 2
The cases used for validation describe the homogeneous binary breakage of a monodisperse initial population with the volume v_0.

	$b_n(v_F, v_P)$	$S(v)$	$F(v_{F,1}, v_{F,2})$ in [31]	Solution $n(v,t)$ for $n(v,0) = \delta(v - v_0), t_{char} = S(v_0)^{-1}$
Case 1	$2/v_P$	v	1	$[2t + t^2(v_0 - v)]\exp(-v \cdot t) + \delta(v_0 - v)\exp(-t \cdot v_0), v \le v_0$
Case 2	$2/v_P$	v^2	$v_{F,1} + v_{F,2}$	$2t \cdot v_0 \exp(-t \cdot v^2) + \delta(v_0 - v)\exp(-t \cdot v_0^2) \quad , v \le v_0$

Table 1 for the test cases introduced in Section 4 (i.e. specifically for $b_n(v_F, v_P) = \frac{2}{v_P}$):

- For the NBS and VBS (see Table 1 for definitions), the uniform sampling is more suited for application, hence it leads to a generation of a random number within only $Y_U = 1 - 2$ iterations (in comparison with more than 20 iterations for the inverse sampling ($Y_I > 20$)).
- For the LVS scheme (see Table 1 for definition), the number of necessary iterations is found to be dependent on the volume v_P of the parent SE selected for breakage. More than $Y_U = 10^9$ iterations are necessary (for the initial volume of the test cases, $v_P = v_0$) if the uniform sampling is used, leading to very long computational times, while the application of the inverse sampling leads to a relatively low number of necessary iterations (i.e. $Y_I < 10$) for a large spectrum of particle sizes (i.e. ca. $v_P > 10^{-10} v_0$).

In order to provide a computational efficient selection method for the combined methods NBS-LVS and VBS-LVS (see Table 1 for definition), an alteration of the classic acceptance-rejection algorithm is presented in Appendix B.2, which uses the uniform sampling for the fraction R of SEs described by the NBS (or VBS) and the inverse sampling for the fraction $(1 - R)$ of SEs described by LVS.

4. Validation

A system describing a homogeneous monomer-break-up (i.e. $b_n(v_F, v_P) = \frac{2}{v_P} \Rightarrow B(v_P) = 2$) has been chosen for the validation of the proposed methods and the measurement of the resulting MC-noise. Analytical solutions of this system could be derived for the breakage rate $S(v) = v^{\zeta}$ and some values for the parameter ζ [31]. The used cases and the analytic solutions $n(v,t)$ are summarized in Table 4.

The authors [31] applied a specific form of the PBE, suited for analytic derivations of the solution:

$$\frac{dn(v,t)}{dt} = -n(v,t)\int_0^v F(v_F, v - v_F)dv_F + 2\int_v^\infty n(v_P,t) \cdot F(v, v_P - v)dv_P \; . \tag{26}$$

The expression $F(v_{F,1}, v_{F,2})$ denotes the rate of the break-up of a parent particle with $v_P = v_{F,1} + v_{F,2}$ into 2 fragments with the volumes $v_{F,1}$ and $v_{F,2}$, the same rate can also be written as $S(v_{F,1} + v_{F,2}) \cdot \frac{1}{2} b_n(v_{F,1}, v_{F,1} + v_{F,2})$. The equivalence of Eqs. (26) to (1) can be therefore shown via:

$$F(v_{F,1}, v_{F,2}) = S(v_{F,1} + v_{F,2})\frac{1}{2} b_n(v_{F,1}, v_{F,1} + v_{F,2}) \; .$$

Table 3
The values for minimal and maximal sizes of the fragment SE, $v_F^{(min)}$ and $v_F^{(max)}$ (Eqs. (28) and (29)) are shown.

	NBS	VBS	LVS
$v_F^{(min)}$	v_P/N_{SE}	$v_P/\sqrt{N_{SE}}$	$\left(1 + \ln(\frac{v_P}{v_{lim}})\right) \cdot \frac{v_{lim}}{N_{SE}}$
$v_F^{(max)}$	$\left(1 - \frac{1}{N_{SE}}\right) \cdot v_P$	$\sqrt{1 - \frac{1}{N_{SE}}} \cdot v_P$	$\exp(\frac{-1}{N_{SE}}) \cdot \left(\frac{v_P}{v_{lim}}\right)^{\frac{1}{N_{SE}}} \cdot v_P$

The mean time of the breakage of the initial population has been used as characteristic time t_{char}, i.e. $t_{char} = S(v_0)^{-1}$ and simulation times up to $t_{end} = 10^8 \cdot t_{char}$ have been investigated. The discussed system exhibits a self-similar behavior for longer simulation times ($t \gg t_{char}$) which are discussed by [22,32] and can be seen in the PSDs in Figs. 4 and 5 in the result section.

Note, that a logarithmically normed representation is used in this paper, i.e. the function $\frac{dN}{d\log v}$ representing the PSD in Figs. 4 and 5 is defined by:

$$n(v)dv = \frac{dN}{d\log(v)} d\log(v) \Longleftrightarrow \frac{dN}{d\log(v)} = v \cdot n(v) \; . \tag{27}$$

5. Results and discussion

5.1. Limitations of the rendered PSD

The resulting PSDs are shown in Figs. 4 and 5. It can be seen, that smaller particle sizes are not rendered by the number-based (NBS) and volume-based (VBS) methods defined in Table 1.

The limitation of the particle sizes stems from the discrete representation of the PSD by a finite number of SEs. The more SEs are used, the larger is the rendered particle size spectrum. One can define maximal and minimal particle sizes, $v_F^{(max)}$ and $v_F^{(min)}$, which define the boundaries of the PSD resulting from the breakage of N_{SE} SEs with the volume v_P. It can be approximated, that (nearly) all SEs representing the PSDs for $t = t_{char} \cdot 10^{-1}$ result from one breakage event of the initial particle population.

A simple approximation for $v_F^{(min)}$ can be made by considering, that the number of used SEs, N_{SE}, defines the probability to select this minimal size via:

$$\frac{1}{N_{SE}} = P(v_F \le v_F^{(min)}) = \int_0^{v_F^{(min)}} f_{mc}(v_F, v_P)dv_F \; . \tag{28}$$

A similar approximation can be made for $v_F^{(max)}$:

$$\frac{1}{N_{SE}} = P(v_F \ge v_F^{(max)}) = \int_{v_F^{(max)}}^{v_P} f_{mc}(v_F, v_P)dv_F \; . \tag{29}$$

Table 5 shows the values of $v^{(min)}$ and $v^{(max)}$ in dependency of the number of used SEs, the value for $v_F^{(min)}$ is also limited due to the applied rejection scheme - which allows only values larger than $v_{lim\_AR} = 10^{-12} v_P$ for the low volume scheme (LVS) defined in Table 1. For 10^5 SEs, one receives $v_F^{(min)} = 10^{-5} \cdot v_P$ (for NBS), $v_F^{(min)} \approx 3.2 \cdot 10^{-3} \cdot v_P$ (for VBS) and $v_F^{(min)} \approx 2.6 \cdot 10^{-15} \cdot v_P$ (for LVS and the initial condition $v_P = v_0$, in this case the v_F is also limited by

Table 4
Summary of the different sampling techniques for the rejection method used in this work.

Method	Uniform sampling (U)	Inverse sampling (I)
PDF $g(v_F, v_P)$	$g_U(v_F) = 1/v_P$	$g_I(v_F) = \left[v_F \ln\left(\frac{v_P}{v_{lim\_AR}}\right)\right]^{-1}$
$v_F = G^{-1}(U_1)$	$G_U^{-1}(U_1) = U_1 \cdot v_P$	$G_I^{-1}(U_1) = v_P \cdot 10^{-12 \cdot U_1}$
limitations for v_F	$0 < v_F < v_P$	$v_{lim\_AR} = 10^{-12} v_P < v_F < v_P$

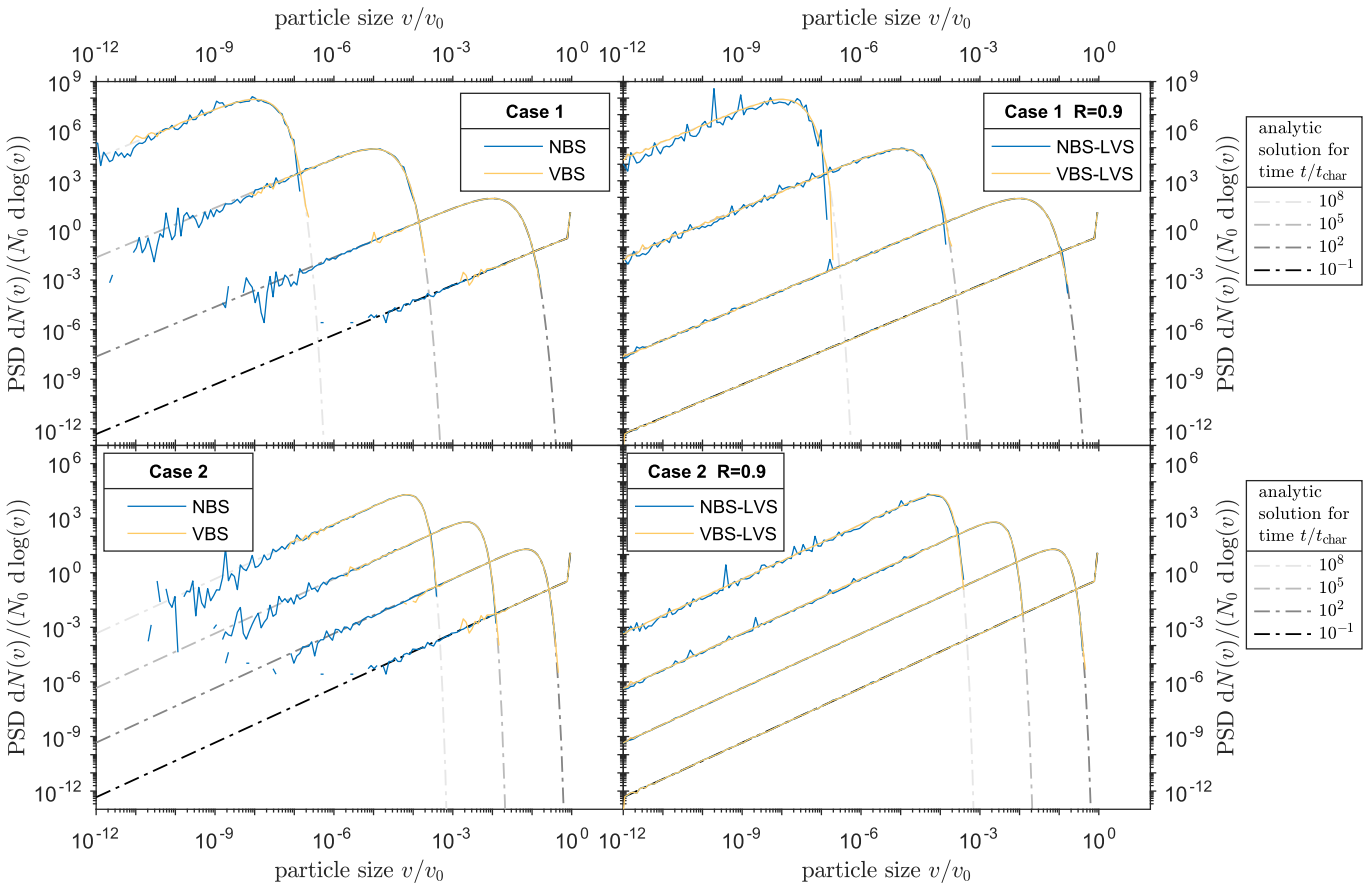

Fig. 4. The number-based PSDs are shown for various simulation time points, which are marked by a gray scale for the analytical results. The simulation results are shown for $\alpha_{\mathrm{T}} = 0.1$ and 10^5 SEs. The used abbreviations (methods) are defined in Table 1.

$v_{\mathrm{lim\_AR}}$). This is in good agreement with the shown PSDs in the Figs. 4 and 5 rendering the PSDs (for $t = t_{\mathrm{char}} \cdot 10^{-1}$).[5]

Fig. 4 shows that the methods VBS, NBS and the combinations NBS-LVS and VBS-LBS (all defined in Table 1) both with $R = 0.9$ are able to approximate the results correctly even for long simulation times. It can be seen that the NBS is able to render smaller particle sizes than the VBS method - at the expense of more statistical noise of the simulation. Both, the NBS-LVS($R = 0.9$) and the VBS-LVS($R = 0.9$) methods are able to render even the smallest particle sizes at the initial stages of the simulation, the much higher level of statistical noise is produced by the NBS-LVS combination.

Fig. 5 shows that the NBS-LVS schemes produce much more statistical noise than the VBS-LVS schemes - for all different settings of R, i.e. $R = 0.5, 0.7$ and 0.8. It can also be seen, that the accuracy of the simulation decreases with decreasing R-values and that accuracies as high as in Fig. 4 (for $R = 0.9$) cannot be reached. It can also be seen that the LVS method leads to severe systematic errors in the course of the simulation, although it is able to render the PSD correctly for early initial stages of the simulation (i.e. $t/t_{\mathrm{char}} = 10^{-1}$).

[5] Standard MC methods would include 2 MC particles due to each breakage event, so that Eq. (28) has to be modified to $\frac{1}{2N_{\mathrm{SE}}} = \int_0^{v_{\mathrm{F}}^{(\min)}} f_{\mathrm{mc}}(v_{\mathrm{F}}, v_{\mathrm{P}})\mathrm{d}v_{\mathrm{F}}$. The properties of the fragments would be selected with NBS (resp. VBS) if each classical MC particle represents the same concentration (resp. mass concentration) of real particles. This would lead to the following formula: $v_{\mathrm{F}}^{(\min)} = \frac{v_0}{2N_{\mathrm{SE}}}$ (resp. $v_{\mathrm{F}}^{(\min)} = \frac{v_0}{2\sqrt{N_{\mathrm{SE}}}}$). So that $N_{\mathrm{SE}} = 5 \cdot 10^{11}$ (resp. $N_{\mathrm{SE}} = 5 \cdot 10^{23}$) MC particles would be necessary to render particles of the size $10^{-12} v_0$ at the simulation time $t = t_{\mathrm{char}} \cdot 10^{-1}$.

It can be thus seen, that if a small particle fraction (10% $\Longleftrightarrow R = 0.9$) of the SE is used for the rendering of smaller particle sizes (i.e. in combination with LVS), a more detailed rendering of the PSD can be gained at the expense of a reasonable increase of the statistical noise. The combination VBS-LVS tends thereby to produce less statistical noise than NBS-LVS. The usage of higher fractions of the SEs for the LVS-method (i.e. $R < 0.9$) leads to an increase of the statistical noise and renders the results not usable for $R \leq 0.7$.

5.2. Quantification of the statistical noise

In order to measure the statistical noise more quantitatively, the total concentration N rendered by all SEs resulting from the MC simulation has been used. For 100 MC-simulations, the mean number $\overline{N}$ and the arithmetic standard deviation of this value, ΔN, has been calculated and the values $\frac{\Delta N}{\overline{N}}$ have been plotted in Figs. 6 and 7.

Fig. 6 shows the dependency of the statistical noise on the used number of SEs. Lower noise values are attained for higher number of SEs, N_{SE}, as expected for MC-simulations (where values are usually distributed according to $\propto \frac{1}{\sqrt{N_{\mathrm{SE}}}}$). It can also be seen, that the VBS method attains a constant value of statistical noise, while the NBS method leads to a steady increase in the course of the simulation. This is in agreement to earlier findings [13]. It can also be seen, that the VBS-LVS($R = 0.9$) scheme produces less statistical noise than the NBS scheme, although it also increases throughout the simulation.

Higher levels of the statistical noise for lower R−settings can be seen in Fig. 7. The NBS-LVS schemes produce more statistical noise than the VBS-LVS scheme underscoring the results already shown in the PSD-Figs. 4 and 5.

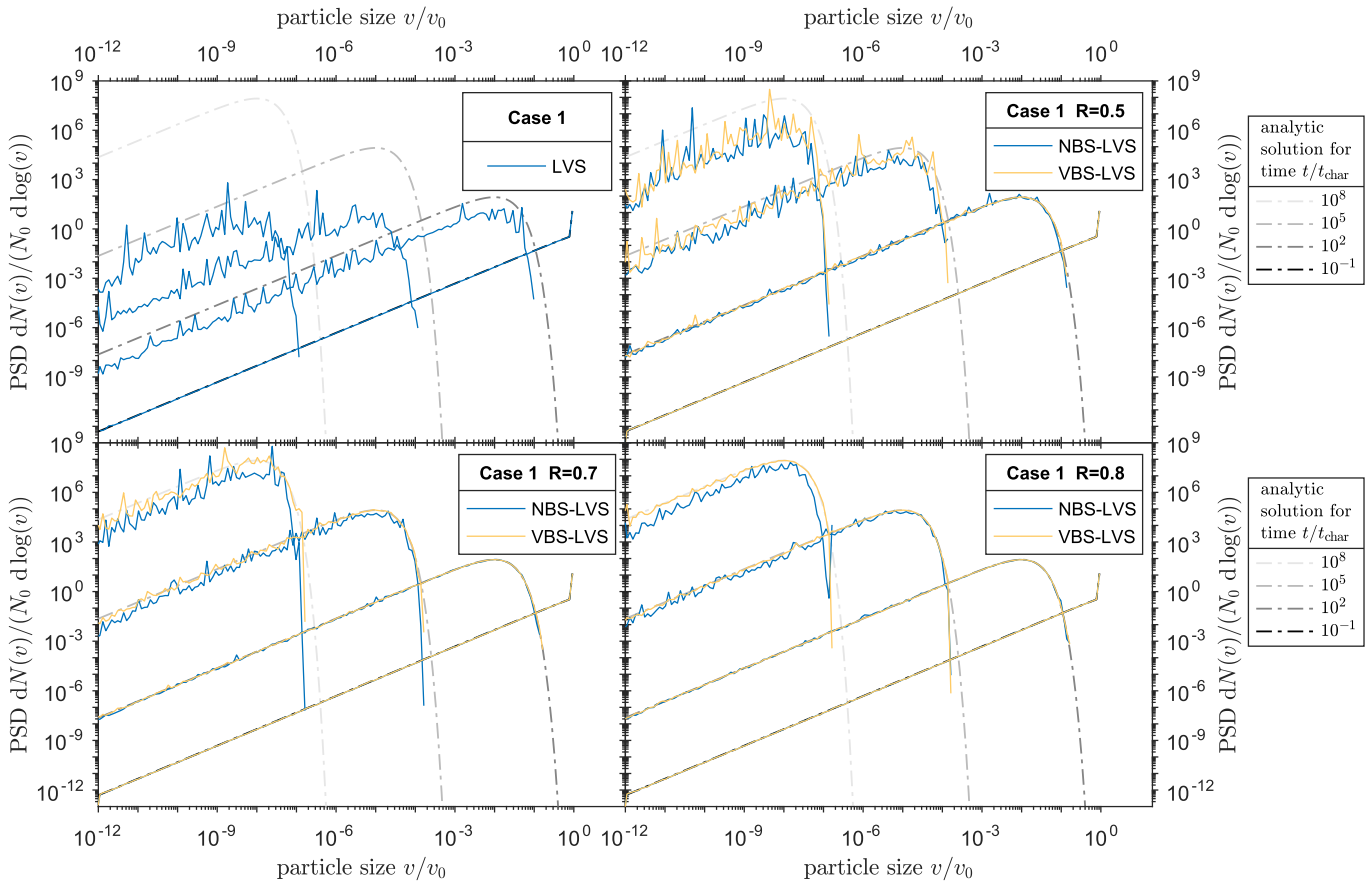

Fig. 5. The number-based PSDs are shown for various simulation time points, which are marked by a gray scale for the analytical results. The simulation results are shown for $\alpha_{\mathrm{T}} = 0.1, N_{\mathrm{SE}} = 10^5$ SEs and case 1. The used abbreviations (methods) are defined in Table 1.

5.3. Systematic errors and computational efficacy

In order to measure the systematic errors introduced into the simulation, the mean number $\overline{N}$ attained for all 100 MC-simulations has been compared to the values N_{BM} resulting from the analytical solution summarized in Table 4, with:

$$N_{\mathrm{BM}} = \int_0^{v_0} n(v)\mathrm{d}v\ . \tag{30}$$

The results are shown in Fig. 8 in dependency of the used tuning factor α_{T}.

The systematic error caused by the tuning factor dominates for lower simulation times, for longer simulation times, the systematic error is caused mainly by the statistical scatter of the simulation, the level of this scatter can be seen in Fig. 6.

Lower values of α_{T} lead to lower systematic errors, as expected. It can be seen, that a setting of $\alpha = 0.1$ leads to a reasonable systematic error, that is in the same order of magnitude, as the statistical MC-noise presented in Figs. 6 and 7.

The tuning factor has to be set to $\alpha_{\mathrm{T}} \leq 0.1$ in order to ensure a certain level of stochastic accuracy, lower values of α_{T} lead on the other hand to larger computing times, as can be seen in Fig. 9. The figure shows the simulation times which are needed in order to simulate 100 MC simulations and depicts the efficiency of a GPU implementation of the presented algorithms: only 100 s are required for the calculation of 100 simulations, each containing 10^5 SEs. For this specific setting, 10^7 evaluations of Eq. (24) are performed in parallel with the optional subsequent while-loops (the specific algorithms are presented in Appendix B2) for each MC time step. (for $\alpha_{\mathrm{T}} = 0.1$ ca. 2800 steps are needed to simulate a time frame of $t_{\mathrm{end}} = 10^8 t_{\mathrm{char}}$, for $\alpha_{\mathrm{T}} = 0.01$, the number of steps is ca. 28, 000).

6. Conclusions

The application of weighted MC simulation entries for the solution of the population balance equation for breakage is investigated.

Table 5
The mean number of iterations Y and the selection condition H (used in Algorithms 1 and 2) for the uniform (U) and inverse (I) sampling methods (Table 2) are shown in combination with the PDFs f_{mc} (presented in Table 1). Y_{I} is calculated ($\approx$) for $v_{AR\_\mathrm{lim}} = 10^{-12} v_{\mathrm{P}}$.

Scheme	f_{mc} for $b_{\mathrm{n}} = \frac{2}{v_{\mathrm{P}}}$	$H_{\mathrm{U}} = \frac{f_{mc}(v_{\mathrm{F}})}{Y_{\mathrm{U}} g_{\mathrm{U}}(v_{\mathrm{F}})}$	$H_{\mathrm{I}} = \frac{f_{\mathrm{mc}}(v_{\mathrm{F}})}{Y_{\mathrm{I}} g_{\mathrm{I}}(v_{\mathrm{F}})}$	Mean number of iterations Y_{U}	Mean number of iterations Y_{I}
NBS	$1/v_{\mathrm{P}}$	1	$v_{\mathrm{F}}/v_{\mathrm{P}}$	1	$\ln\left(\frac{v_{\mathrm{P}}}{v_{\mathrm{lim\_AR}}}\right) \approx 27.63$
VBS	$2v_{\mathrm{F}}/v_{\mathrm{P}}^2$	$v_{\mathrm{F}}/v_{\mathrm{P}}$	$v_{\mathrm{F}}^2/v_{\mathrm{P}}^2$	2	$2\ln\left(\frac{v_{\mathrm{P}}}{v_{\mathrm{lim\_AR}}}\right) \approx 56.26$
LVS ($v_{\mathrm{P}} > v_{\mathrm{lim}}$) $v_{\mathrm{lim}} = 10^{-11} v_0$	$\frac{1}{v_{\mathrm{max}}\left(1+\ln\left(\frac{v_{\mathrm{P}}}{v_{\mathrm{lim}}}\right)\right)}$ $v_{\mathrm{max}} = \max(v_{\mathrm{F}}, v_{\mathrm{lim}})$	$v_{\mathrm{lim}}/v_{\mathrm{max}}$	v_{F}/v_{max}	$\frac{v_{\mathrm{P}}}{v_{\mathrm{lim}}\left(1+\ln\left(\frac{v_{\mathrm{P}}}{v_{\mathrm{lim}}}\right)\right)}$	$\frac{\ln\left(\frac{v_{\mathrm{P}}}{v_{\mathrm{lim\_AR}}}\right)}{\left(1+\ln\left(\frac{v_{\mathrm{P}}}{v_{\mathrm{lim}}}\right)\right)}$

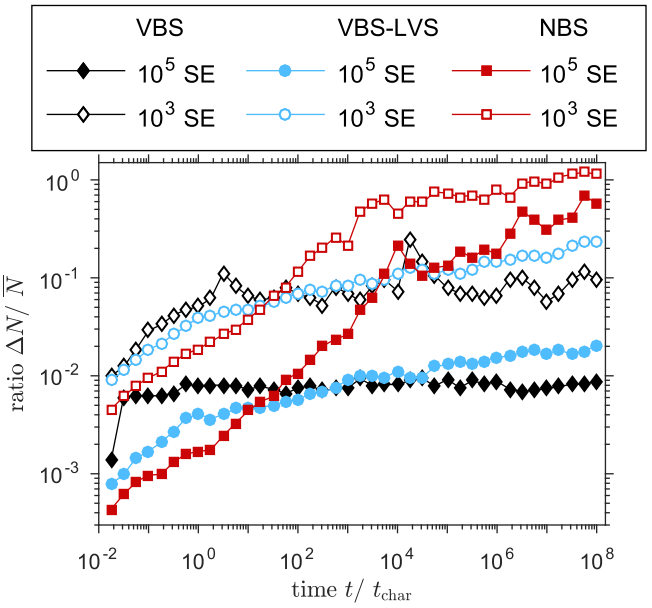

Fig. 6. The statistical errors of the simulation schemes compared with each other. The used abbreviations (methods) are defined in Table 1. The VBS-LVS method is shown for $R = 0.9$. The results are shown for case 1 and $\alpha_T = 0.1$.

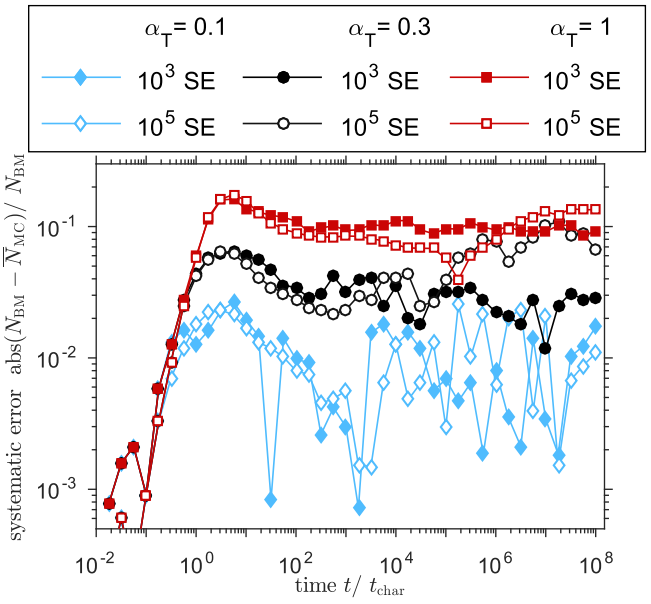

Fig. 8. The systematic errors in dependency of the tuning factor, α_T, are shown for case 1 and the volume-based selection (VBS) scheme. The used abbreviations (methods) are defined in Table 1.

We present a theoretical derivation of several possible constant-number breakage schemes, which describe the breakage of one simulation entry by a modification of its weight and property (here: volume). The thus gained results are applicable to all sorts of breakage kernels and encompass the special results gained for a binary breakage by [13].

The number-based breakage scheme (NBS - named SWA 1 in [13]) and a volume-based scheme (VBS - named SWA 2 in [13]) already introduced in the literature could be further validated by comparisons with analytic results for two test cases.

The resulting PSDs (form NBS or VBS) are only able to cover the particle size spectrum which corresponds to large particle concentrations. Parts of the PSD representing low particle concentrations could not be rendered - in analogy to traditional MC methods (where e.g. 10^{10} particles are necessary in order to render PSDs which describe differences in particle concentrations ranging from $10^8 m^{-3}$ to $10^{18} m^{-3}$). We introduced a novel scheme (which cannot be described with the SWA theory [13]) based on the selection of low volume particles (LVS), which is able to render the full resulting PSDs, which describe even extremely low particle concentrations correctly - at least for the beginning of the simulation. For longer simulation times, it is found that the LVS scheme leads to serious deviations from the analytical solution.

These deviations can be curtailed to a minimal level by the combination of the introduced LVS scheme with the already defined NBS (or VBS) schemes. The theoretical concept of combination of

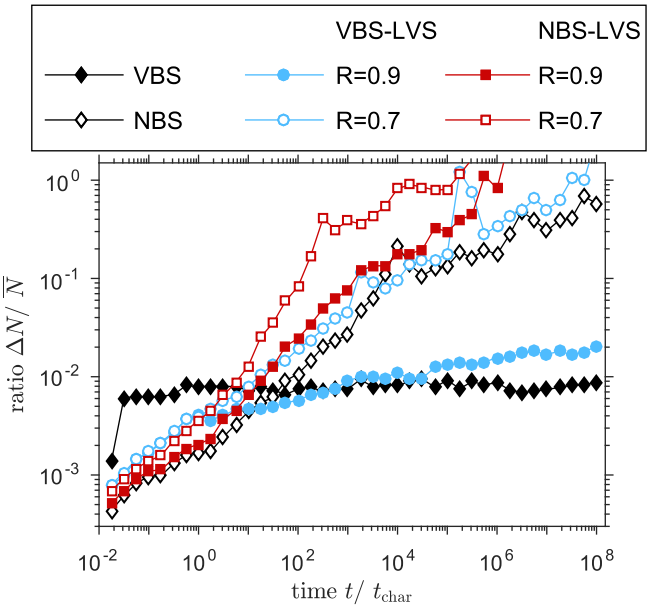

Fig. 7. The statistical simulation noise resulting from different R settings is shown for case 1, $\alpha_T = 0.1$ and 10^5 SEs. The used abbreviations (methods) are defined in Table 1.

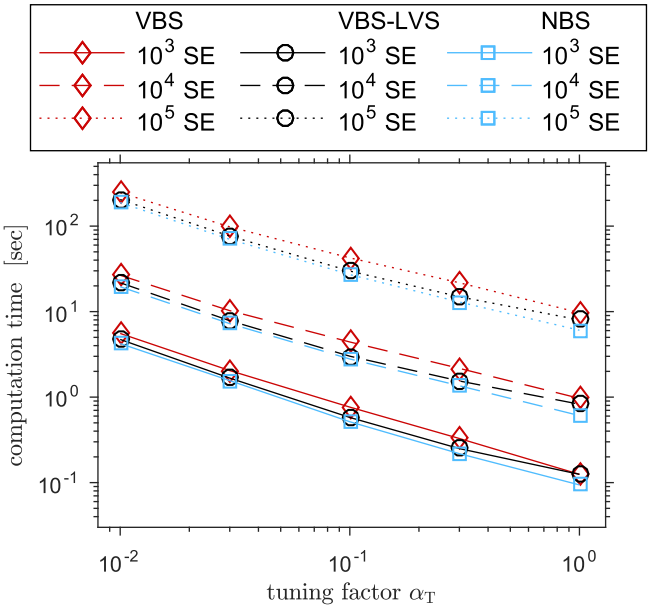

Fig. 9. The computational times are shown for different numbers of SE indicated in the legend of the figure. The computational times refer to 100 simulations executed in parallel for $t_{end} = 10^8 t_{char}$. The used abbreviations (methods) are defined in Table 1. The results for the VBS-LVS combination are shown for $R = 0.9$.

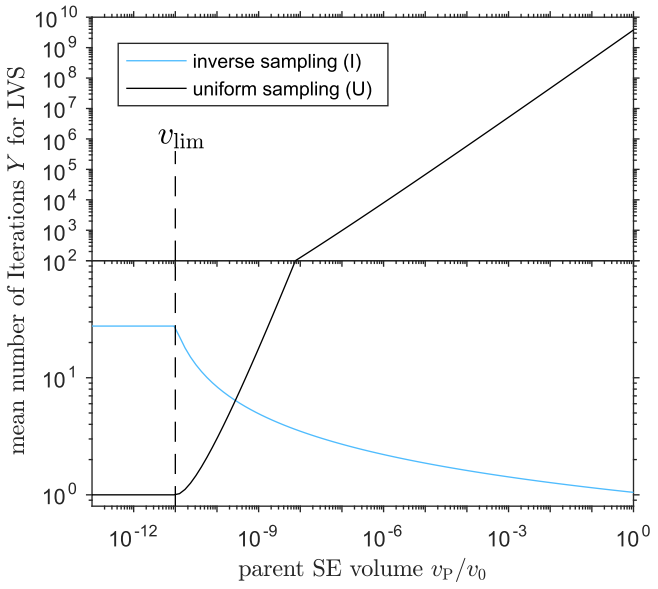

Fig. 10. The mean number of selection attempts Y_I and Y_U (in Table 3) for the LVS scheme are shown in dependency of the volume v_P of the SE selected for breakage. The calculations are based on the specific values used in this work: $v_{\mathrm{AR\_lim}} = 10^{-12} v_\mathrm{P}$ and $v_\mathrm{lim} = 10^{-11} v_0$.

breakage schemes is introduced for this purpose and an efficient implementation in the scope of the acceptance-rejection approach is documented. It is found, that these combinations (named NBS-LVS and VBS-LVS) can describe the full particle size spectrum, even for long simulation times.

A simple time-driven GPU implementation of the introduced schemes is sketched. It is shown that the computing times of the VBS-LVS scheme are within the same magnitude than those of the NBS and VBS schemes.

Notation

b_n	number-based breakage kernel, Eq. (1)
$\hat{b}_\mathrm{n}$	number-based discrete breakage kernel
b_m	volume-based breakage kernel, Eq. (4)
$B(v_\mathrm{P})$	mean number of fragments, Eq. (2)
$C(v_\mathrm{P})$	constant for the LVS, Eq. (14)
f_mc	PDF for selection of v_F, Table 1
F_mc	Cumulative distribution function for f_mc, Appendix B
g	PDF for selection of v_F for rejection method, Appendix B
G	Cumulative distribution function for g for rejection method, Appendix B
H	abbreviation used in Algorithms 1 and 2, Table 3
K_i	process rates defined in Section 3.1
$M(v)$	volume-based PSD, Eq. (4)
$n(v)$	number-based PSD, Eq. (1)
$n_\mathrm{F}^{(\mathrm{exact})}(v)$	expected $n(v)$ formed by particle fragments, Eq. (6)
$n_\mathrm{F}^{(\mathrm{mc})}(v)$	$n(v)$ formed by fragment SEs, Eq. (8)
$N_\mathrm{f}(v_\mathrm{F})$	number of fragment SEs with v_F
N_p	number of SEs selected for breakage, Section 2.2.1
N_SE	number of SEs used for simulation
N_BM	analytic value of total concentration, Eq. (30)
$\hat{p}_\mathrm{mc}$	probability to select v_F for discrete kernels, Table 1
P_mc	probability to select $v \in [v_\mathrm{F}, v_\mathrm{F} + \mathrm{d}v]$, Table 1
$P_i(t_\mathrm{ev} < \Delta t)$	probability that an event takes place within $t_\mathrm{ev} < \Delta t$, Section 3.1
R	combination factor, Eq. (15), Eq. (16)
S_i	rate of a process in a general MC-formulation, Section 3.1
S_max	maximal breakage rate of all SEs, Section 3.1
$S(v)$	breakage rate, Eq. (1)
t_char	characteristic time
U	uniformly distributed random number
v	volume of a particle or SE
v_0	initial volume of the particle or SE
v_F	volume of a fragment or fragment SE
$v_\mathrm{F}^{(\mathrm{max})}$	approx for maximal fragment volume, Eq. (29)
$v_\mathrm{F}^{(\mathrm{min})}$	approx for minimal fragment volume, Eq. (28)
v_P	volume of a parent particle or SE
v_lim	cut-off value for LVS, Eq. (13)
$v_{\mathrm{lim\_AR}}$	inverse-sampling cut-off value, Table 2
W_F	statistical weight of a fragment SE
W_P	statistical weight of a parent SE
W_Tot	total statistical weight SEs selected for breakage
Y	mean number of loops for rejection method, Appendix B
α_T	tuning factor for MC time step, Section 3.1
γ	fragmentation weight transfer function in [13], Eq. (A.1)
Δt	MC time step value, Section 3.1
ζ	parameter defining $S(v) = v^\zeta$ in [31]

Acknowledgments

The support of the Deutsche Forschungsgemeinschaft DFG in the scope of the priority program SPP 1679 (KR 1723/15-2) is greatly acknowledged. J. Devi has been supported by the Quaid-E-Awam university, Nawabshah (Pakistan) by a scholarship under the Faculty Development Programme (FDP). We also thank Dennis Kiesler for his help during the development of the inverse sampling.

Appendix A. Comparison of the general form in Table1 with SWA

In [13], a general formulation for breakage schemes (named SWA) is presented based on the fragmentation weight transfer function $\gamma(v_\mathrm{F}, v_\mathrm{P})$ with the following restriction:

$$\frac{1}{\gamma(v_\mathrm{F}, v_\mathrm{P})} + \frac{1}{\gamma(v_\mathrm{P} - v_\mathrm{F}, v_\mathrm{P})} = 1\,. \tag{A.1}$$

The PDF f_mc^γ for the selection of the volume v_F of a fragment SE is stated as:

$$f_\mathrm{mc}^\gamma = \frac{b_\mathrm{n}(v_\mathrm{F}, v_\mathrm{P})}{\gamma(v_\mathrm{F}, v_\mathrm{P})}\,. \tag{A.2}$$

The statistical weight of the fragment, W_F, is set to:

$$W_\mathrm{F} = \gamma(v_\mathrm{F}, v_\mathrm{P}) \cdot W_\mathrm{P}\,. \tag{A.3}$$

The values v_P and W_P are the volume and statistical weight of the selected SE for breakage.

This formulation is obviously equivalent to the presented Eq. (9), hence $W_\mathrm{F} = \frac{b_\mathrm{n}(v_\mathrm{F}, v_\mathrm{P})}{f_\mathrm{mc}^\gamma(v_\mathrm{F}, v_\mathrm{P})} \cdot W_\mathrm{P}$. For a full equivalence, it is still necessary to show that f_mc^γ is a PDF.

The function γ has been postulated for the symmetric binary-breakage only, so having the following restrictions:

$$b_\mathrm{n}(v_\mathrm{F}, v_\mathrm{P}) = b_\mathrm{n}(v_\mathrm{P} - v_\mathrm{F}, v_\mathrm{P}) \tag{A.4}$$

and $\int_0^{v_P} b_n(v_F, v_P)\mathrm{d}v_F = 2$. (A.5)

We show, that all these conditions lead in combination to the normalization condition (Eq. (11)), i.e.: $\int_0^{v_P} \frac{b_n(v_F,v_P)}{\gamma(v_F,v_P)}\mathrm{d}v_F = 1$. It is:

$$\int_0^{v_P} \frac{b_n(v_F, v_P)}{\gamma(v_F, v_P)}\mathrm{d}v_F \tag{A.6}$$

$$\overset{(A.1)}{=} \int_0^{v_P} b_n(v_F, v_P)\mathrm{d}v_F - \int_0^{v_P} \frac{b_n(v_F, v_P)}{\gamma(v_P - v_F, v_P)}\mathrm{d}v_F$$
$$\overset{(A.4),(A.5)}{=} 2 - \int_0^{v_P} \frac{b_n(v_P - v_F, v_P)}{\gamma(v_P - v_F, v_P)}\mathrm{d}v_F .$$

The substitution $\xi = v_P - v_F$ leads to: $\int_0^{v_P} \frac{b_n(v_P-v_F,v_P)}{\gamma(v_P-v_F,v_P)}\mathrm{d}v_F = \int_0^{v_F} \frac{b_n(\xi,v_P)}{\gamma(\xi,v_P)}\mathrm{d}\xi$, so that:

$$\text{Eq. (A.6)} \Longleftrightarrow 2\int_0^{v_P} \frac{b_n(v_F, v_P)}{\gamma(v_F, v_P)}\mathrm{d}v_F = 2 ,$$

which is equivalent to the normalization condition: $\int_0^{v_P} \frac{b_n(v_F,v_P)}{\gamma(v_F,v_P)}\mathrm{d}v_F = 1$, or $\int_0^{v_P} f_{mc}(v_F, v_P)\mathrm{d}v_F = 1$.

Appendix B. Algorithms for the selection of the fragment size v_F

B.1. Inverse method

In order to apply the inverse method (see e.g. [33]), the cumulative probability distribution $F_{mc}(v_F) = \int_0^{v_F} f_{mc}(v'_F, v_P)\mathrm{d}v'_F$ has to be inverted, yielding the function $F_{mc}^{-1}(U)$ which maps from $U \in (0,1)$ to $v_F \in (0, v_P)$. Uniformly distributed random numbers $U \in (0,1)$ inserted into $F_{mc}^{-1}(U)$ produce therefore values v_F which are distributed according to f_{mc}.

This method is more efficient than the rejection method, but it can be applied only, if an analytical expression F_{mc}^{-1} exists. This cannot be guaranteed for all f_{mc}^N or f_{mc}^V, because these depend on the specifically used breakage kernels b_n (see Table 1). Although F_{mc}^{-1} can be easily calculated for the case $b_n = \frac{2}{v_P}$ which is discussed in the results section of this paper, we present the implementation in the scope of the rejection method, so that the presented algorithm is applicable to all general cases.

B.2. Rejection method

For the rejection method (see e.g. [33]), a random variate v_F is generated, which is distributed like a freely chosen PDF $g(v_F)$. The function $g(v_F)$ can be chosen freely, but it should be chosen in such a way, that it is easy to calculate $G(v_F) = \int_0^{v_F} g(y_F)\mathrm{d}y_F$ and its inverse function G^{-1}, hence a uniformly distributed random number U_1 can be used to generate v_F via the inverse method: $v_F = G^{-1}(U_1)$.

The so generated random variate v_F is accepted, if a second uniformly distributed random number $U_2 \in (0,1)$ is smaller than the expression $f_{mc}(v_F, v_P)\cdot[g(v_F)\cdot Y]^{-1}$. If v_F is rejected, new random numbers U_1 and U_2 are generated, leading to a new variate v_F for which the condition above is checked again, leading to Algorithm 1 which generates values v_F that are distributed according to f_{mc}.

The constant factor Y has to be set in such a way, that $\frac{f_{mc}(v_F,v_P)}{Y\cdot g(v_F)} \leq 1$ for all v_F (i.e. $Y = \max\left(\frac{f_{mc}(v_F,v_P)}{g(v_F)}\right)$). The specific value of Y is the mean number of selection attempts (i.e. loop iterations), which are needed in order to generate one fragment-volume v_F. (This is only true, if $\int_0^{v_P} f(v_F, v_P)\mathrm{d}v_F = 1$ and $\int_0^{v_P} g(v_F)\mathrm{d}v_F = 1$.)

Algorithm 1. Rejection method for v_F selection, see Table 2 for the exact values of G^{-1} and g.

repeat
  $U_1 \leftarrow$ uniform random number $\in (0,1)$
  $U_2 \leftarrow$ uniform random number $\in (0,1)$
  $v_F \leftarrow G^{-1}(U_1)$
until $U_2 \leq f_{mc}(v_F, v_P)/\left(g(v_F)\cdot Y\right)$ $\quad (= H \text{ in table 3})$

In this work, two sampling methods described by g_U and g_I were used. $g_U(v_F) = \frac{1}{v_P}$ leading to $G_U^{-1}(U_2) = U_2\cdot v_P$ describes a uniform sampling. An inverse sampling is described by: $g_I(v_F) \propto \frac{v_P}{v_F}$. In order to norm this function, fragment-sizes smaller than the value $v_{lim\_AR} = 10^{-12}v_P$ are excluded from consideration[6] allowing thus only fragment values v_F with $v_{lim\_AR} \leq v_F \leq v_P$. This leads to the following explicit form: $g_I = \frac{1}{v_F}\cdot\left[\ln\left(\frac{v_P}{v_{lim\_AR}}\right)\right]^{-1}$ and to $G_I^{-1}(U_2) = v_{lim\_AR}^{U_2} = v_P\cdot 10^{-12\cdot U_2}$, the detailed derivation is shown in Appendix B.2.1.

Table 2 summarizes the used sampling methods and Table 3 shows how many iterations Y are necessary for each fragment particle selection scheme (i.e. NBS, VBS and LVS defined in Table 1). It can be clearly seen, that the NBS and VBS require ca. 26 (resp. 56) less iterations, if they are combined with the uniform sampling instead of the inverse sampling. The corresponding values for the LVS scheme are dependent on the volume, v_P, of the SE selected for breakage and are shown in Fig. 10. It can be seen that the LVS method cannot be reasonably used in combination with the uniform sampling (because of the computational time required for 10^9 iterations) but is well suited for the inverse sampling (because of the relatively low computational time required for less than 10 iterations). For smaller particle volumes, $v_P < v_{lim}$, the LVS scheme attains constant values which are equal to the ones for the NBS scheme shown in Table 3. This is due to the definition of the LVS scheme, which is equal to the NBS scheme for $v_P < v_{lim}$ for the here discussed breakage function $b_n = \frac{2}{v_P}$. (I.e. $f_{mc}^N = f_{mc}^L$, if $v_P < v_{lim}$.)

The combination of the NBS (resp. VBS) scheme with the LVS scheme can be easily performed with an additional random number, U_3. A comparison of U_3 with R determines which of the schemes is used for the selection of v_F, Algorithm 2 depicts this technique.

Algorithm 2. Rejection method for v_F selection with the combined NBS-LVS scheme. Table 2 summarizes the expressions for G_I^{-1}, G_U^{-1} and g_U, g_I. The VBS-LVS scheme results by replacing f_{mc}^N with f_{mc}^V. The values H_U and H_I are shown in Table 3 for the simulated cases.

$U_3 \leftarrow$ uniform random number $\in (0,1)$
if $U_3 \leq R$ **then** ▷ uniform sampling for NBS
  repeat
    $U_1 \leftarrow$ uniform random number $\in (0,1)$
    $U_2 \leftarrow$ uniform random number $\in (0,1)$
    $v_F \leftarrow G_U^{-1}(U_1)$
  until $U_2 \leq f_{mc}^N(v_F, v_P)/\left(g_U(v_F)Y_U\right)$ $\quad (= H_U)$
else ▷ inverse sampling for LVS
  repeat
    $U_1 \leftarrow$ uniform random number $\in (0,1)$
    $U_2 \leftarrow$ uniform random number $\in (0,1)$
    $v_F \leftarrow G_I^{-1}(U_1)$
  until $U_2 \leq f_{mc}^L(v_F, v_P)/\left(g_I(v_F)\cdot Y_I\right)$ $\quad (= H_I)$
end if

[6] Note that this exclusion is different from the setting v_{lim} for the VLS scheme (all particle sizes can be selected by LVS, but for sizes $v < v_{lim}$ the PDF is at a constant maximum and not increasing). The value v_{lim} is set to $10^{-11}v_0$ and only dependent on the initial volume. The value $v_{lim\_AR} = 10^{-12}\cdot v_P$ is dependent on the size v_P of the SE selected for breakage.

B.2.1. Derivation of $G_I^{-1}(U_2)$

The distribution g_I can be normed with a constant C, so that $g_I = \frac{1}{C}\cdot\frac{v_P}{v_F}$ hence $v_{lim} \le v_F \le v_P$, it is:

$$\frac{1}{C}\cdot\int_{v_{lim\_AR}}^{v_P}\frac{v_P}{v_F}dv_F = 1 \Rightarrow C = v_P\ln\left(\frac{v_P}{v_{lim\_AR}}\right).$$

This allows the calculation of $G(v_F)$:

$$G(v_F) = \frac{1}{\ln\left(\frac{v_P}{v_{lim\_AR}}\right)}\int_{v_{lim\_AR}}^{v_F}\frac{1}{v_F} = \frac{\ln\left(\frac{v_F}{v_{lim\_AR}}\right)}{\ln\left(\frac{v_P}{v_{lim\_AR}}\right)}.$$

The inverse function is calculated by setting $G(v_F) = U$ which is equivalent to:

$$\ln\left(\frac{v_F}{v_{lim\_AR}}\right) = \ln\left(\frac{v_P}{v_{lim\_AR}}\right)^U$$
$$\Longleftrightarrow v_F = v_{lim\_AR}\cdot\left(\frac{v_P}{v_{lim\_AR}}\right)^U\cdot\frac{v_P}{v_P}$$
$$\Rightarrow G^{-1}(U) = v_F = v_P\cdot\left(\frac{v_{lim\_AR}}{v_P}\right)^{1-U}.$$

Hence the values for U are evenly distributed between 0 and 1, one can replace the expression $A^{(1-U)}$ with A^U This is equivalent to changing the direction of the integration in the calculation of $G(v_F)$ from $\int_{v_{lim\_AR}}^{v_F} g(v)dv$ to $\int_{v_P}^{v_F} g(v)dv$.

References

[1] P.J. Hill, K.M. Ng, New discretization procedure for the breakage equation, AIChE J. 41 (5) (1995) 1204–1216. http://dx.doi.org/10.1002/aic.690410516.

[2] M. Vanni, Approximate population balance equations for aggregation-breakage processes, J. Colloid Interface Sci. 221 (2) (2000) 143–160. http://dx.doi.org/10.1006/jcis.1999.6571.

[3] R. Kumar, J. Kumar, Numerical simulation and convergence analysis of a finite volume scheme for solving general breakage population balance equations, Appl. Math. Comput. 219 (10) (2013) 5140–5151. http://dx.doi.org/10.1016/j.amc.2012.10.098.

[4] J. Kumar, J. Saha, E. Tsotsas, Development and convergence analysis of a finite volume scheme for solving breakage equation, SIAM J. Numer. Anal. 53 (4) (2015) 1672–1689. http://dx.doi.org/10.1137/140980247.

[5] S. Kumar, D. Ramkrishna, On the solution of population balance equations by discretization - III. Nucleation, growth and aggregation of particles, Chem. Eng. Sci. 52 (24) (1997) 4659–4679.

[6] A.I. Roussos, A.H. Alexopoulos, C. Kiparissides, Part III: Dynamic evolution of the particle size distribution in batch and continuous particulate processes: a Galerkin on finite elements approach, Chem. Eng. Sci. 60 (24) (2005) 6998–7010. http://dx.doi.org/10.1016/j.ces.2005.06.021.

[7] T.H. Tsang, A. Rao, Comparison of different numerical schemes for condensational growth of aerosols, Aerosol Sci. Technol. 9 (3) (1988) 271–277.

[8] V. Rod, T. Misek, Stochastic modelling of dispersion formation in agitated liquid-liquid systems, Trans. Inst. Chem. Eng. 60 (1) (1982) 48–53.

[9] P.K. Das, Monte Carlo simulation of drop breakage on the basis of drop volume, Comput. Chem. Eng. 20 (3) (1996) 307–313.

[10] B.K. Mishra, Monte Carlo simulation of particle breakage process during grinding, Powder Technol., 110 (3) (2000) 246–252. http://dx.doi.org/10.1016/S0032-5910(99)00281-8.

[11] M. Smith, T. Matsoukas, Constant-number Monte Carlo simulation of population balances, Chem. Eng. Sci. 53 (9) (1998) 1777–1786. http://dx.doi.org/10.1016/S0009-2509(98)00045-1.

[12] K. Lee, T. Matsoukas, Simultaneous coagulation and break-up using constant-N Monte Carlo, Powder Technol. 110 (1-2) (2000) 82–89. http://dx.doi.org/10.1016/S0032-5910(99)00270-3.

[13] K.F. Lee, R.I.A. Patterson, W. Wagner, M. Kraft, Stochastic weighted particle methods for population balance equations with coagulation, fragmentation and spatial inhomogeneity, J. Comput. Phys. 303 (2015) 1–18. http://dx.doi.org/10.1016/j.jcp.2015.09.031.

[14] G. Kotalczyk, F.E. Kruis, A Monte Carlo method for the simulation of coagulation and nucleation based on weighted particles and the concepts of stochastic resolution and merging, J. Comput. Phys. 340 (2017) 276–296. http://dx.doi.org/10.1016/j.jcp.2017.03.041.

[15] H. Zhao, C. Zheng, M. Xu, Multi-Monte Carlo approach for general dynamic equation considering simultaneous particle coagulation and breakage, Powder Technol. 154 (2-3) (2005) 164–178. http://dx.doi.org/10.1016/j.powtec.2005.04.042.

[16] H. Zhao, C. Zheng, Correcting the multi-Monte Carlo method for particle coagulation, Powder Technol. 193 (1) (2009) 120–123. http://dx.doi.org/10.1016/j.powtec.2009.01.019.

[17] H. Zhao, F.E. Kruis, C. Zheng, Reducing statistical noise and extending the size spectrum by applying weighted simulation particles in Monte Carlo simulation of coagulation, Aerosol Sci. Technol. 43 (8) (2009) 781–793. http://dx.doi.org/10.1080/02786820902939708.

[18] R.I.A. Patterson, W. Wagner, M. Kraft, Stochastic weighted particle methods for population balance equations, J. Comput. Phys. 230 (19) (2011) 7456–7472. http://dx.doi.org/10.1016/j.jcp.2011.06.011.

[19] A. Eibeck, W. Wagner, Stochastic particle approximations for Smoluchoski's coagulation equation, Ann. Appl. Probab. 11 (4) (2001) 1137–1165. http://dx.doi.org/10.1214/aoap/1015345398.

[20] M. Goodson, M. Kraft, Simulation of coalescence and breakage: an assessment of two stochastic methods suitable for simulating liquid-liquid extraction, Chem. Eng. Sci. 59 (18) (2004) 3865–3881. http://dx.doi.org/10.1016/j.ces.2004.05.029.

[21] E. Debry, B. Sportisse, B. Jourdain, A stochastic approach for the numerical simulation of the general dynamics equation for aerosols, J. Comp. Phys. 184 (2) (2003) 649–669. http://dx.doi.org/10.1016/S0021-9991(02)00041-4.

[22] N.V. Mantzaris, Transient and asymptotic behaviour of the binary breakage problem, J. Phys. A: Math. Gen. 38 (23) (2005) 5111–5132. http://dx.doi.org/10.1088/0305-4470/38/23/004.

[23] S. Khalili, Y. Lin, A. Armaou, T. Matsoukas, Constant number Monte Carlo simulation of population balances with multiple growth mechanisms, AIChE J. 56 (12) (2010) 3137–3145. http://dx.doi.org/10.1002/aic.12233.

[24] K. Liffman, A direct simulation Monte-Carlo method for cluster coagulation, J. Comput. Phys. 100 (1) (1992) 116–127. http://dx.doi.org/10.1016/0021-9991(92)90314-O.

[25] B.H. Shah, D. Ramkrishna, J.D. Borwanker, Simulation of particulate systems using the concept of the interval of quiescence, AIChE J. 23 (6) (1977) 897–904. http://dx.doi.org/10.1002/aic.690230617.

[26] H. Zhao, A. Maisels, T. Matsoukas, C. Zheng, Analysis of four Monte Carlo methods for the solution of population balances in dispersed systems, Powder Technol. 173 (1) (2007) 38–50. http://dx.doi.org/10.1016/j.powtec.2006.12.010.

[27] R. Irizarry, Fast Monte Carlo methodology for multivariate particulate systems-II: τ-PEMC, Chem. Eng. Sci. 63 (1) (2008) 111–121. http://dx.doi.org/10.1016/j.ces.2007.09.006.

[28] D.T. Gillespie, Approximate accelerated stochastic simulation of chemically reacting systems, J. Chem. Phys. 115 (4) (2001) 1716–1733. http://dx.doi.org/10.1063/1.1378322.

[29] J. Wei, F.E. Kruis, A GPU-based parallelized Monte-Carlo method for particle coagulation using an acceptance-rejection strategy, Chem. Eng. Sci. 104 (2013) 451–459. http://dx.doi.org/10.1016/j.ces.2013.08.008.

[30] Z. Xu, H. Zhao, C. Zheng, Accelerating population balance-Monte Carlo simulation for coagulation dynamics from the Markov jump model, stochastic algorithm and GPU parallel computing, J. Comput. Phys. 281 (2015) 844–863. http://dx.doi.org/10.1016/j.jcp.2014.10.055.

[31] R.M. Ziff, E.D. McGrady, The kinetics of cluster fragmentation and depolymerisation, J. Phys. A Math. Gen. 18 (15) (1985) 3027–3037. http://dx.doi.org/10.1088/0305-4470/18/15/026.

[32] Z. Cheng, S. Redner, Scaling theory of fragmentation, Phys. Rev. Lett. 60 (24) (1988) 2450–2453. http://dx.doi.org/10.1103/PhysRevLett.60.2450.

[33] L. Devroye, Chapter 4 Nonuniform random variate generation, Simulation, Vol. 13 of Handbooks in Operations Research and Management Science, Elsevier. 2006, pp. 83–121. http://dx.doi.org/10.1016/S0927-0507(06)13004-2.

Paper IV

Version of record published in:
Tellus B: Chemical and Physical Meteorology 71, Issue 1 (2019), pp. 1-8.
Available online at: https://doi.org/10.1080/16000889.2018.1554415

Monte Carlo Simulations of Homogeneous Nucleation and Particle Growth in the Presence of Background Particles

G. Kotalczyk, I. Skenderović and F.E. Kruis

Tellus SERIES B CHEMICAL AND PHYSICAL METEOROLOGY
PUBLISHED BY THE INTERNATIONAL METEOROLOGICAL INSTITUTE IN STOCKHOLM

Monte Carlo simulations of homogeneous nucleation and particle growth in the presence of background particles

By GREGOR KOTALCZYK*, IVAN SKENDEROVIĆ AND FRANK EINAR KRUIS

Institute of Technology for Nanostructures and Center for Nanointegration Duisburg-Essen (CENIDE), University of Duisburg-Essen, Duisburg, Germany

(Manuscript received 14 September 2017; in final form 23 November 2018)

ABSTRACT

The application of the Monte Carlo (MC) simulation technique for the modelling of nucleation processes with an existing background particle concentration is presented in this paper. Next to the nucleation of novel particles, the coagulation of an existing particle population as well as the condensational growth and evaporation of unstable particles (whose diameter is smaller than the critical Kelvin diameter) are included into the simulation. The usage of statistically weighted MC particles allows the description of particle size distribution (PSD), whose concentrations differ in several orders of magnitude. It is shown, that this approach allows to model the complex interplay between freshly nucleated particles and an existing background particle population. In this work, the nucleation of novel particles is modelled by three different nucleation theories discussed by [Girshick, S. L. and C.-P. Chiu (1990), *The Journal of Chemical Physics* 93], which comprise of (1) the classical nucleation theory, (2) a mathematical correction to (1) and (3) a self-consistency correction of (2). For the chosen simulation conditions, the resulting PSDs are independent of the used nucleation theory for longer simulation times, in which the simulations are described by the coagulation mechanism only. The time-frame is identified for which relevant discrepancies of the PSDs have to be taken into account.

Keywords: Monte Carlo, population balances, nucleation, coagulation, condensational growth, evaporation, weighted simulation particles

1. Introduction

The description of particle formation processes plays an important role in the context of atmospheric sciences describing the planetary boundary layer (e.g. Svenningsson et al., 2008; Karl et al., 2012; Kulmala et al., 2013) and the free troposphere (Bianchi et al., 2016).

Atmospheric particulate matter is a product of a multi-component mixture of vapours, such as sulphuric acid, volatile organic compounds, ammonia, amines, ozone, sulphur dioxide and nitrogen oxides, which undergoes a complex nucleation mechanism (Kulmala et al., 2013). CLOUD experiments investigate the role of single components and their interactions on the particle nucleation rates (Kirkby et al., 2011).

Traditional aerosol dynamic population balance methods recourse to sectional or moment models (Zhang et al., 1999) or do not describe the composition of the formed particles at all, resorting to a one component/quasi-unary system (Olenius and Riipinen, 2017). The internal composition is an important property of the particulate matter in the atmosphere and in the focus of interest of atmospheric air quality, as well for the description of climatological systems. Therefore, there is a need for the correct description of the composition of the particle population.

Multicomponent sectional models are theoretically known (Gelbard, 1990), but their practical application is limited to a relatively low number of components (i.e. 2–3). In order to avoid such a multidimensional discretisation (leading to huge numbers of necessary

*Corresponding author. e-mail: gregor.kotalczyk@uni-due.de

Citation: Tellus B: 2019, **71**, 1445379, https://doi.org/10.1080/16000889.2018.1554415

computational resources and times), the Monte Carlo (MC) method can be applied; hence, the increment of the necessary computational resources depends only linearly on the number of used components.

It has already been shown that MC methods are well suited to describe multicomponent coagulation of aerosols (Efendiev and Zachariah, 2003; Zhao and Kruis, 2014). The inclusion of the homogeneous nucleation into a MC simulation is much more challenging, due to the fact, that continuous nucleation leads to the increase of the number of MC simulation particles. It was already shown, that the application of weighted MC particles makes this problem accessible. The designation of different statistical weights to each simulation particle makes the development of the concept of 'particle merging' possible (Kotalczyk and Kruis, 2017). We have also already shown, that this method can be applied to nucleation and growth in aerosol reactors (Kotalczyk et al., 2016, 2017). In atmospheric systems, however, a population of earlier formed background particles has to be taken into account (e.g. Olenius and Riipinen, 2017). The simultaneous description of (1) the background particle population and (2) the freshly nucleating particles poses a numerical challenge; hence, the number-concentrations of those two populations can differ several orders of magnitude. If the number-concentration of the background particles is 10^{10} m^{-3} and the freshly nucleated particle are described by a large number-concentration, like 10^{14} m^{-3}, the application of non-weighted MC particles becomes nearly impossible: a huge number of 1,000,000 simulation particles would be needed, if the background particle population is to be modelled by a modest number of 100 particles. We show in the following, that such systems can be simulated by means of weighted MC simulation particles, but we refrain the simulated system to one component, only.

The theoretical description of the nucleation poses a difficult task, as described by the reviews (Oxtoby, 1992; Ford, 2004; Bennett and Barrett, 2012; Zhang et al., 2012). The great difficulty in the investigation of the nucleation phenomena lies in the fact, that several reasonable theories can be formulated, leading to nucleation rates, which differ in several orders of magnitude. Most theories resort to cluster–cluster interactions of unstable molecules which grow to a critical size and become stable, assumptions about interaction potentials (in case of molecular dynamics simulations, e.g. Tanaka et al., 2014) or about the kinetic collision rates (in case of kinetic formulations, e.g. Oxtoby, 1992; Laaksonen et al., 1995) have to be made. These assumptions cannot be verified by experiments (yet), because an experimental technique, which measures the concentration of the smallest (unstable) clusters would be necessary for this purpose (Wyslouzil and Wölk, 2016).

In this work, we focus on one component nucleation as a result of rapidly changing atmospheric conditions, e.g. a rapid temperature drop leading to a strong increase of the supersaturation. This is numerically a more challenging system than the otherwise applied supersaturation profiles used in atmospheric modelling, which describe a slow increase of the supersaturation at lower supersaturation levels. This system is tested by comparing three well-known expressions for the nucleation rate with each other. The decrease of the supersaturation, the total number concentration and the particle size distributions (PSD) are compared for this purpose. We show, that early stages of the simulation lead to strongly different results, while for longer simulation times the results of different nucleation models become undistinguishable from each other.

2. Methods

In the first subsection, a general parallel simulation algorithm for the solution of the PBE by means of weighted simulation particles is sketched. In the following, second section, the simulated system, consisting of the initial conditions and the used nucleation theories, is discussed in detail.

2.1. MC simulation algorithm

The use of statistically weighted MC simulation particles (Zhao et al., 2009; Lee et al., 2015) allows new modelling approaches, hence no limitations have to be set on the statistical weight of the newly included simulation particles (Menz et al., 2012; Hao et al., 2013). We combine a stochastic coagulation process of weighted MC particles with a deterministically described growth and evaporation process, which can be combined with the nucleation of novel particles, too.

The discrete coagulation events are separated from the continuous growth processes in a simple operator splitting approach (also used to describe the chemical decomposition of a precursor concentration during particle synthesis) (Celnik et al., 2007), so that the simulation of a time step consists of two steps: the MC-driven coagulation step and a growth (resp. evaporation) step which is solved by the solution of the corresponding ODEs. During the nucleation time step many particles could be inserted into the simulation as described further below. Treating the condensation as a continuous process instead of formulating single events for events describing monomer attachments or detachments leads to remarkable speed-ups of the simulations (Patterson et al., 2006). These approximations are valid for the description of larger particle sizes (i.e. >1 nm), discretization errors

might be found for lower particle sizes and a different approach might become necessary, if the here presented approach is coupled to a kinetic MC simulation describing the nucleation (like e.g. in Filipponi and Giammatteo, 2016 or Davari and Mukherjee, 2018).

2.1.1. MC coagulation step. First, the coagulation time step τ_{mc} is estimated from the given PSD, which is defined by the reciprocal of the sum of all possible event rates: $\tau_{mc} = 1/\sum_{i,j<i} \beta_{i,j}^{(SR)}$, where $\beta_{i,j}^{(SR)} = \max(W_i, W_j) \cdot \beta(v_i, v_j)$, is the coagulation rate within the concept of 'stochastic resolution', according to (Kotalczyk and Kruis, 2017), where v_i (resp. v_j) are the volumes and W_i (resp. W_j) the statistical weights of simulated MC particles with the indices i and j. The coagulation kernel β describes the rate of coagulation between two real particles.

The particles are selected for coagulation by selecting the particle indices i and j by random and selecting this random pair for coagulation, if an additional random number r is smaller than $\beta_{i,j}^{SR}/\beta_{max}^{SR}$. The maximal coagulation rate β_{max}^{SR} can thereby be quickly approximated by a fast parallel algorithm introduced by (Wei and Kruis, 2013). The parallel implementation of this algorithm can be found in (Wei and Kruis, 2013) or (Kotalczyk and Kruis, 2017). We point out, that the applied coagulation time step $\tau_{mc} = 1/\sum_{i>j} \max(W_i, W_j) \cdot \beta_{i,j}$ is also dependent on the number of used simulation particles, and that higher numbers of simulation particles lead to lower values for the applied time step (the values of $\max(W_i, W_j)$ decrease linearly with the increase of the simulation particles, while the number of summands increases quadratically). So that the tuning of shorter separation times of the coagulation and the other processes becomes possible.

2.1.2. Continuous growth step. Second, in order to describe the condensational growth (or evaporation) of the particles, the corresponding growth equation is solved for each particle:

$$\frac{dv_i}{dt} = G(v_i, n_G) \tag{1}$$

The monomer concentration in the gaseous phase n_G determines thereby the Kelvin diameter d^*. It is thus determined whether the particle grows ($G>0$, if $d>d^*$) or evaporates ($G<0$, if $d<d^*$) and the exact rate of this process. The depletion (resp. increase) of the monomers is taken into account by the following mass balance (i.e. the first term on the r.h.s. of Equation (2)):

$$\frac{dn_G}{dt} = -\sum_i W_i \cdot G(v_i, n_G)/v_M - N_R \cdot i^* \tag{2}$$

The second term on the r.h.s. of Equation (2) describes the monomer depletion of the monomer concentration due to the nucleation of novel particles; each nucleated particle consists thereby of i^* monomers (where $i^* = \pi \cdot d^{*3}/(6 \cdot v_M)$).

The coupled set of ordinary differential equations, consisting of Equation (2) and as many equations of the form of Equation (1), as there are MC particles (in the here presented simulations, 10,000) is solved by the Runga-Kutta technique for the time step τ_{mc}, which is set by the coagulation process discussed above.

The total mass of the nucleated material is stored as a special buffer variable M_B, so that the set above is extended by one simple equation:

$$\frac{dM_B}{dt} = +N_R \cdot i^* \cdot v_M \tag{3}$$

If the value M_B surpasses a pre-set limit M_{TR} (in the simulated scenario presented in this paper: $M_{TR} = 10^{-20}\mathrm{kgm}^{-3}$), a novel MC particle with the statistical weight of $W_{nuc} = M_B/(v_M \cdot i^*)$ is inserted into the simulation by the procedure described in the following subsection. It should be noted, that many nucleation events are possible during one coagulation step, dependent on the set threshold M_{TR} and on the number of performed Runge Kutta (RK) time steps. These steps are set by comparison of the RK result of the 4th order technique to the 5th order technique. The difference between both techniques is compared to a predefined acceptable error in order to adjust the next time step or repeat the actual RK step for a much smaller interval of time (like described in Press et al., 2007).

2.1.3. Inclusion of newly nucleated particles: Low weight merging. Hence, the continuous inclusion of novel particles would lead to large numbers of simulation particles and thus higher computational times, the 'low weight merging' of particles is applied. This technique selects two 'nearly similar' MC particles (i,j) and it stores their properties as one particle in the memory space of the former particle j, so that the newly nucleated particle can be stored in the memory space of the former particle i. The statistical weight W_{new} of the novel particle and its new volume v_{new} are calculated by:

$$W_{new} = W_i + W_j \quad \text{and} \quad v_{new} = (W_i \cdot v_i + W_j \cdot v_j)/W_{new} \tag{4}$$

This applied scheme preserves the total mass of the involved particles exactly; hence, $v_{new} \cdot W_{new} = (W_i \cdot v_i + W_j \cdot v_j)$. As a measure for the magnitude of the introduced error, the value E_{mer} is introduced:

$$E_{mer} = (v_i - v_j)^2/\min(v_i, v_j) \tag{5}$$

An algorithm is applied, which merges particles with low statistical weights (in order to introduce the lowest alternations to the PSD). The particles with low statistical

weights are compared to all other particles, and the pair with the lowest merging error, E_{mer} is merged. The exact computational procedure for the selection of two 'nearly similar' particles is presented in (Kotalczyk and Kruis, 2017) in more detail.

2.2. Simulated system

The system consists of a background particle population and a condensable monomer concentration n_G (describing thus the supersaturation S of the system). It is assumed that the background particles and the gaseous monomers are one compound, with the properties summarized in Table 1. These values could designate a quasi-unary atmospheric aerosol consisting of sulphuric acid and organic compounds in a scenario describing sulphuric acid induced nucleation of the organic molecules (Olenius and Riipinen, 2017). The system is simulated for isothermal conditions (280 K) and 24 hr.

The background particle population is modelled as a lognormal distribution with a geometric mean of 50 nm and a geometric standard deviation of 1.46, which corresponds to the geometric standard deviation of the self-preserving PSD for the coagulation process (Vemury et al., 1994). These initial particles encompass a total number concentration of $N_0 = 10^{10}\mathrm{m}^{-3}$, this might describe a polluted environment.

The initial supersaturation is set to the value of $S_0 = 10^5$ at the beginning, which also corresponds to a polluted environment—but is also tested for lower values ($S_0 = 10^4$, 10^3 and 10^2). This modelling does not take into account a slowly increase and decrease of the monomer concentration, which is sometimes modelled in a sinusoidal way reflecting the diurnal cycle (Olenius and Riipinen, 2017). It is assumed that these conditions are reached (due to drastic cooling or convection) at the beginning of the simulation and that the condensational growth or evaporation of the existing particles as well as the nucleation are the only reasons for changes of the supersaturation. This assumption is a rather artificial modelling of the complex interplay of an existing background particle population with condensable material in the form monomers in the gaseous phase, whose saturation is slowly increased by cooling or monomer convection. It poses, however, a much more challenging system for the here discussed MC methodology, hence a slow increase would lead to less nucleation and thus less new particles which have to be included into the simulation. The kernel for coagulation in the free molecule regime is used. It describes the rate of coagulation of two particles with the sizes v and v' by:

$$\beta(v,v') = \left(\frac{3}{4\pi}\right)^{\frac{1}{6}} \sqrt{\frac{6k_B T}{\rho_p}} \cdot \sqrt{\frac{1}{v}+\frac{1}{v'}} \cdot \left(v^{\frac{1}{3}} + v'^{\frac{1}{3}}\right)^2 \tag{6}$$

The used symbols are summarized in Table 1 and k_B is the Boltzmann's constant:

The condensational growth is described by the formula for the free-molecule regime as well and depends on the volume v_i (resp. the diameter d_i, with $v_i = \pi d_i^3/6$) of the particle and the monomer concentration n_G in the gaseous phase:

$$G(v_i, n_G) = \frac{\mathrm{d}v_i}{\mathrm{d}t} = \frac{v_M \cdot \pi \cdot d_i^2}{\sqrt{2\pi \cdot m_1 \cdot k_B \cdot T}} \cdot \left(k_B \cdot T \cdot n_G - p_s \cdot \exp\left\{4 \cdot \gamma \cdot v_M/(k_B \cdot T \cdot d_i)\right\}\right) \tag{7}$$

The used symbols and its values are described in Table 1. It is assumed, that the nucleated particles and the background particle population consist of the same material and that all simulated particles grow (resp. evaporate) like described by Equation (7). The exponential term describes thereby the Kelvin correction, this leads to an evaporation of all particles whose diameter d_i is smaller than the Kelvin diameter d^*, with:

$$d^* = 4 \cdot \gamma \cdot v_M/(k_B \cdot T \cdot \ln(S)) \tag{8}$$

This diameter is also the diameter of the inserted particles due to nucleation.

Three different expressions are investigated for the nucleation rate N_R. First the classic nucleation theory by (Becker and Döring, 1935) has been investigated, denoting it as 'classic' in this work, or as $N_R^{(cls)}$ in Equation (10). A correction to this expression in the framework of a kinetic formulation has been proposed by (Courtney, 1961) and its mathematical necessity is stressed by many works (e.g. Girshick and Chiu, 1990; Oxtoby, 1992), it will be marked as $N_R^{(cou)}$ in Equation (9). A self-consistent correction to this kinetic nucleation theory (called 'Courtney' in the following) has been proposed by (Girshick and Chiu, 1990) and is denoted as $N_R^{(gir)}$ in Equation (10).

$$N_R^{(cou)}(n_G) = n_G \cdot \sqrt{\frac{2\gamma}{\pi \cdot m_1}} \frac{p_s}{k_B \cdot T} \cdot v_1 \cdot \exp\left(-\frac{16 \cdot \pi \cdot \gamma^3 \cdot v_m^2}{3 \cdot k_B^3 \cdot T^3 \cdot \ln(S)^2}\right), \quad \text{with} \quad S = \frac{n_G k_B T}{p_s} \tag{9}$$

$$N_R^{(gir)}(n_G) = N_R^{(cou)} \cdot \exp\left((36 \cdot \pi)^{\frac{1}{3}} \cdot \frac{\gamma \cdot v_1^{\frac{2}{3}}}{k_B \cdot T}\right);$$

$$N_R^{(cls)}(n_G) = N_R^{(cou)} \cdot S \tag{10}$$

3. Results

The compared nucleation theories influence directly the characteristics of the simulated particle population. Due to different nucleation rates, a different depletion of the

Table 1. Values used for the simulation describing typical aerosol properties of a quasi-unary model, described by (Olenius and Riipinen, 2017).

Symbol	Designated property	Value
m_1	Molecular mass	1.62×10^{-25} kg
p_s	Vapor pressure	5×10^{-11} Pa
T	Temperature	280 K
v_M	Molecular volume	1.085×10^{-28} m^{-3}
γ	Surface tension	0.05 N m^{-1}
ρ_p	Particle density	1500 kg m^{-3}

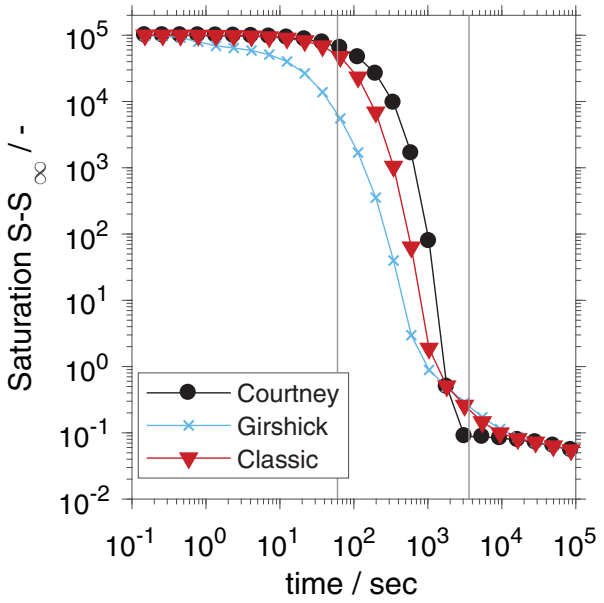

Fig. 1. The supersaturation surplus $S-S_\infty$ for an initial supersaturation of $S_0 = 10^5$ and $S_\infty = 1$. The vertical lines designate the simulation times of 1 min and 1 hr, a total simulation time of 24 hr is presented.

monomer concentration takes place, as can be seen in Fig. 1. These variations of the saturation in time affect directly the nucleation rates, shown in Fig. 2. One can coarsely distinct the simulation time into three regions: (1) an initial time span (simulation times smaller than 1 min), for which nearly constant nucleation rates can be observed, which correspond to constant monomer concentration values—meaning that the depletion of the monomer concentration due to condensational growth and nucleation can be neglected during this time-span; (2) a transition time span (simulation times between 1 min and 1 hr), in which a depletion of the monomer concentration can be seen (caused by the condensational growth on the existing particle population and the nucleation of novel particles); (3) a steady state region (simulation times larger than 1 hr), which is described by the continuous growth/evaporation and coagulation and marked by

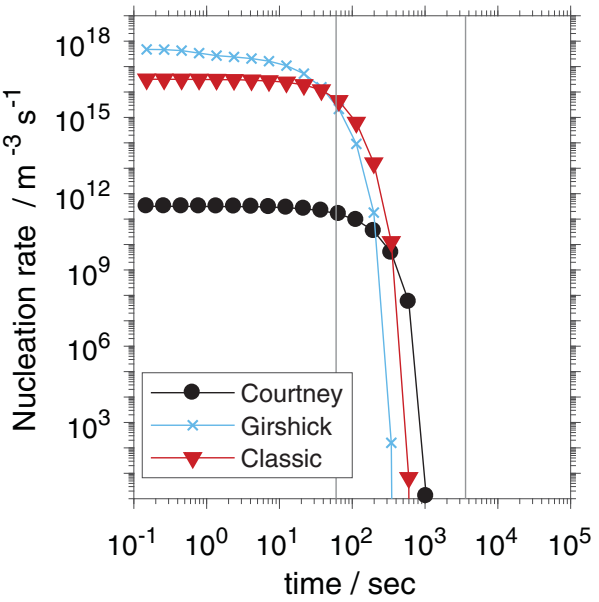

Fig. 2. The nucleation rates for the three discussed nucleation theories for an initial supersaturation of $S_0 = 10^5$. The vertical lines represent the simulation times of 1 min and 1 hr, a total simulation time of 24 hr is presented.

a slow decrease of the surplus supersaturation. In the here presented simulation conditions, the contributions of the growth/evaporation term are nearly negligible for longer simulation times and the supersaturation seems to reach a steady state. Therefore, one can consider the coagulation to be the only one driving force for particulate growth—in contrast to the system describing industrial Fe production conditions (Kotalczyk et al., 2016), for which the complex interplay of coagulation and growth/evaporation has to be taken into account for the correct description of the PSD (Kotalczyk et al., 2017).

The different nucleation rates have, of course a direct impact on the overall number concentration of the particles, as can be seen in Fig. 3. A steep increase in the particle concentration is found in the initial stage of the simulation for the classic and Girshick nucleation theory. The Courtney theory is not describing such high nucleation rates as the other two theories (as can be seen in Fig. 2), which leads to no drastic increase of the particle concentration. The transition time span is marked by a decline of the particle concentration, which can be explained by the onset of the coagulation of the particles.

These findings can also be drawn from the PSDs shown in Figs. 4–6 describing the particle populations after a total simulation time of 1 min, 1 hr and 24 hr. The 10,000 particles are sorted into 80 logarithmically spaced bins and mean values for 100 simulations are shown. Figure 4 shows that after 1 min the differences of the particle concentrations presented in Fig. 3 can be attributed

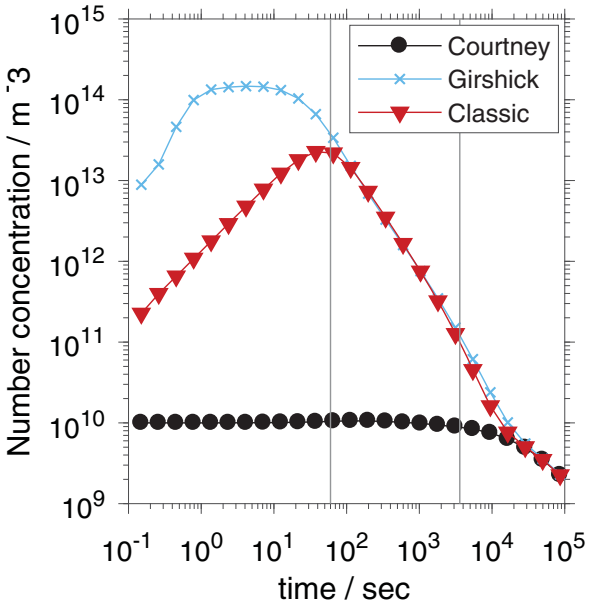

Fig. 3. The number concentration in dependency of the used nucleation theories are shown. The vertical lines represent the simulation times of 1 min and 1 hr, a total simulation time of 24 hr is presented.

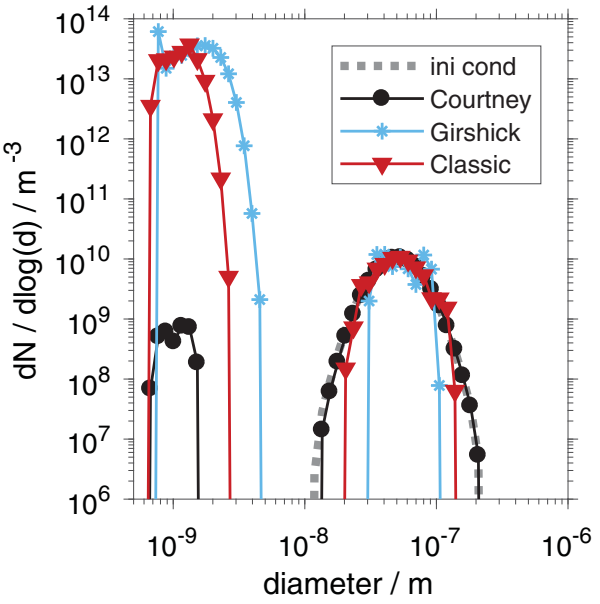

Fig. 4. The PSDs resulting from the three different nucleation theories after a simulation time of 1 min for $S_0 = 10^5$.

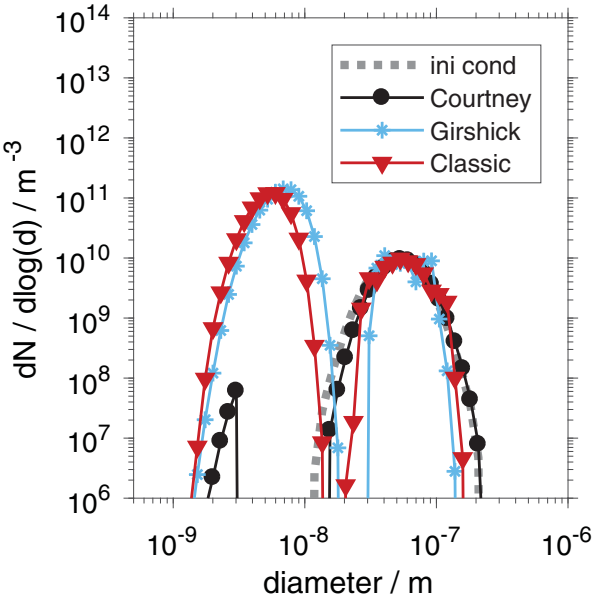

Fig. 5. The PSDs resulting from the three different nucleation theories after a simulation time of 1 hr for $S_0 = 10^5$.

to the nucleated particles, which represent the smaller sizes of the particle size spectrum. The PSD based on the Girshick nucleation theory exhibits not only higher concentrations of the nucleated particles as the other nucleation theories, but the sizes of the particles are larger as well. This indicates that the newly nucleated particles have coagulated with each other. This explains the number concentration plateau for the initial stage of the simulation shown in Fig. 3 for the Girshick nucleation theory: the increase of the particle number concentration is limited by the onset of the coagulation, which decreases the particle number concentration.

The part of the PSD representing mainly the background particle population changes its shape slightly. It can be seen that the parts representing smaller concentrations of the PSD are not rendered in the results based on the Girshick and the Classic theory. This can be attributed to the 'low weight merging', necessary for the novel inclusion of a nucleated particle. The higher the nucleation rate and the more new particles have to be included into the simulation, the less accurate becomes the rendering of the fringes of the background particle population. It should be noted, that the regions, in which these inaccuracies are observed constitute a small part of the PSD (note the logarithmic plot). This small part (especially the larger particles), could describe the part of the PSD, which is responsible for the light-scattering behaviour of the aerosol or act as cloud condensation nuclei (CCN). The 'removal' of these particles due to the merging technique might therefore introduce serious errors in the context of the simulation of an atmospheric system. These errors could be prevented by the following 2 approaches: (1) the particles which are large enough to act as CCNs could be locked against merging, simply by not comparing and merging them with other particles; (2) the light-scattering cross-section (resp. power) σ_i of each particle i

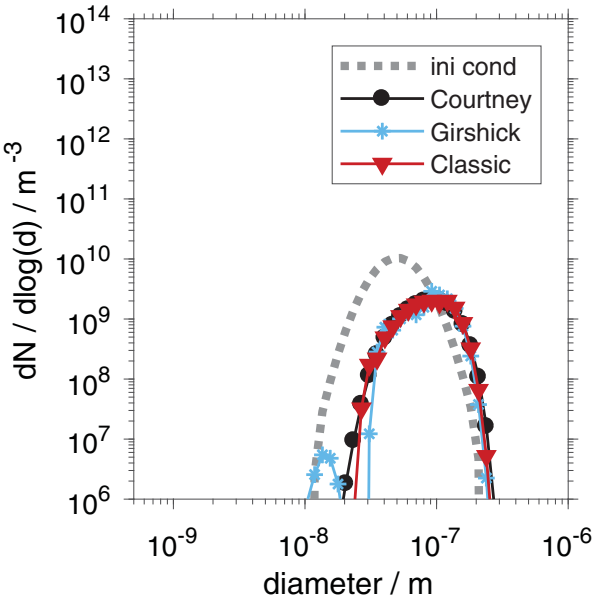

Fig. 6. The PSDs resulting from the three different nucleation theories after a simulation time of 24 hr for $S_0 = 10^5$.

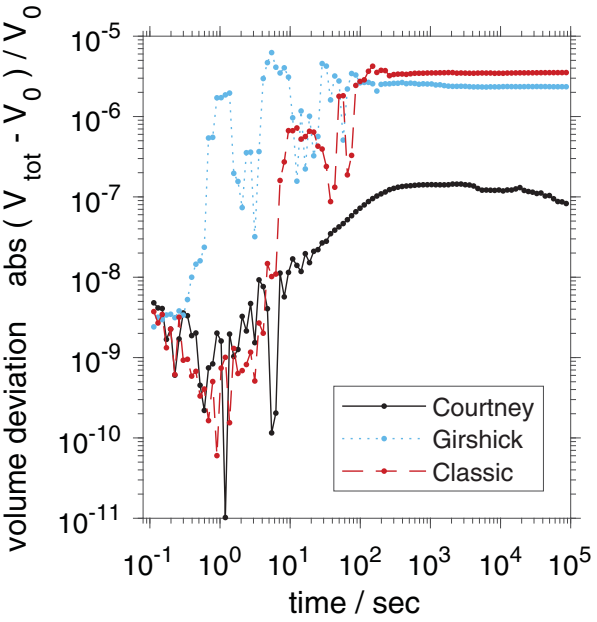

Fig. 7. The relative deviation of the total volume V_{tot} [defined in Equation (11)] from the initial total volume V_0.

could be considered for the calculation of the merging error, in this approach, the expression in Equation (5) could be replaced by: $E_{\text{mer}} = (v_i - v_j)^2/\min(v_i, v_j) + (\sigma_i - \sigma_j)^2/\sigma_{\text{gauche}}$, where σ_{gauche} is some pre-set light-scattering cross-section. This second approach would penalize the merging of particles with different light-scattering cross-sections, if one of them is higher than σ_{gauche}.

Although the fringes of the PSDs change due to the here applied merging techniques, the total volume V_{tot} is conserved in the course of the simulation, where:

$$V_{\text{tot}} = \sum_i W_i \cdot v_i + n_{\text{G}} \cdot v_{\text{m}} \tag{11}$$

The mean value for V_{tot} (for all 100 simulations) is compared with the initial value V_0 at the beginning of the simulation in Fig. 7. It can be seen that it changes only slightly. The relative deviation of 10^{-7} corresponds to the magnitude of the floating point precision applied for the calculations. This value accumulates to levels of 10^{-6} for simulations of high nucleation scenarios. These levels are still acceptable.

We also observed, that the application of a higher number of simulation particles leads to less deviations within the background PSDs, so that the number of simulation particles can be applied as a control parameter for these deviations. The same values for the moments of the PSDs (such as mean geometric diameter or total number-concentration) could be reproduced, independent on the number of the applied simulation particles.

The PSD based on the Courtney theory expresses the background condition with the same accuracy as the initial condition, hence little to none particles have to be inserted into the simulation in this scenario. In turn, much higher differences between the concentrations of the nucleated particles and the concentrations of background particles are described by the PSD based on the Girshick theory as the one based on the Courtney theory.

In the time span, between 1 min and 1 hr (the transition time span), the nucleation of novel particles ceases completely (see Fig. 2). The evolution of the PSD in this time span is mainly described by the coagulation of the particles, the condensational growth of the particle population might be considered to be very small, hence the corresponding driving force $S - S_\infty$ decreases several orders of magnitude, as can be seen in Fig. 1. The result is a PSD, which consists of two peaks, which can be attributed to the nucleated population and the initial background particle population. Figure 5 shows that the growth of the background particle population due to condensation and due to coagulation with the nucleated particles is relatively small. The part of the PSD, which represents the background particles (around 50 nm), is nearly of the same shape as the initial condition (disregarding the shape changes due to the merging on the edges of this distribution).

The part of the PSD, which can be attributed to the nucleated particles (covering the whole range between 1 and 20 nm) exhibits the form of the self-preserving form for coagulation. The differences between the PSDs are clearly visible, making a distinction between each other

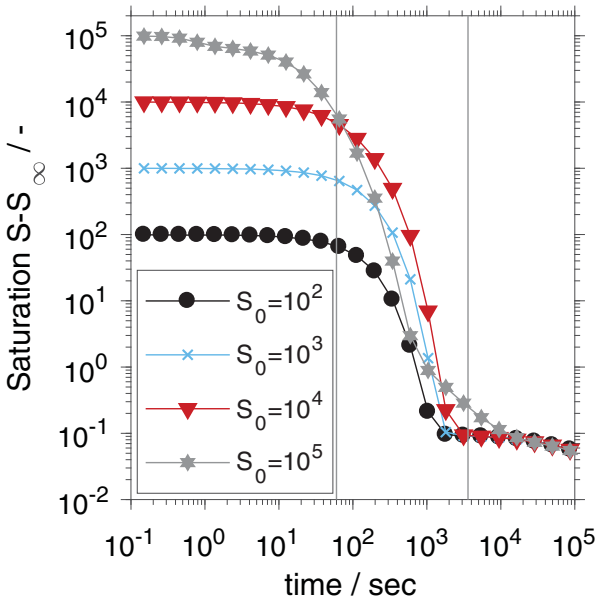

Fig. 8. The supersaturation in dependency of its initial value S_0 for the Girshick nucleation theory. The vertical lines represent the simulation times of 1 min and 1 hr, a total simulation time of 24 hr is presented.

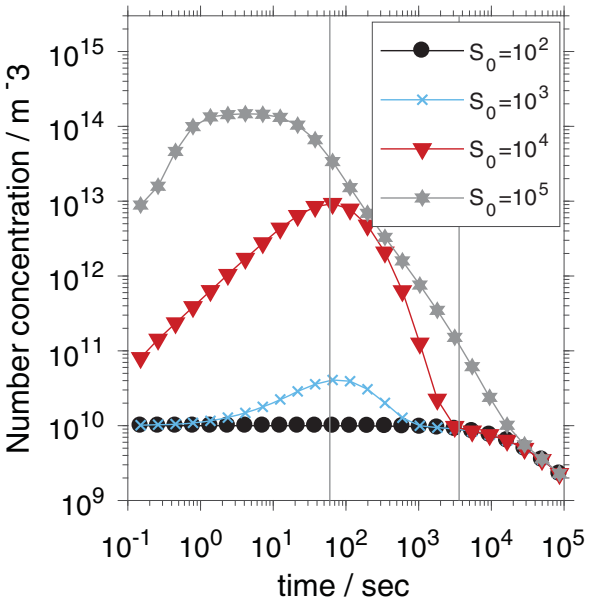

Fig. 9. The number concentration in dependency of the initial supersaturation value S_0 for the Girshick nucleation theory. The vertical lines represent the simulation times of 1 min and 1 hr, a total simulation time of 24 hr is presented.

possible. The attribution of the corresponding nucleation theory based on the size of the PSD in this size spectrum would be therefore possible, while the form of the background particles (all particles with the size 20 nm or higher) would not allow to draw conclusions on the nucleation mechanisms

These distinctions vanish, however in the further course of the simulation and the resulting PSDs attain a self-preserving form for the coagulation, making no more distinctions between each other possible, as can be seen in Fig. 6. The depicted results describe the PSDs after 24 hr. A clear difference between the PSDs for 24 hr and the initial PSD can be seen, which can be attributed to the coagulation within this long 'steady state time span'. Each PSD is rendered with the same accuracy. This indicates that the differences of the rendering of the background particle population in Figs. 4 and 5, which originate from the 'low weight merging' technique did not propagate into the simulation and were in fact not critical for the correct description of the general behaviour of the PSD. However, the negligence of the larger particles might lead to a wrong description of the light scattering behaviour of the aerosol—or its ability to act as CCNs—both points could be addressed by modifying the merging technique as discussed above.

Similar findings can be made for different values for the initial concentration S_0, exemplary plots of the supersaturation in Fig. 8 and the number concentration in Fig. 9 show, that the nucleation takes place mostly during the first minute of the simulation and that the depletion of the supersaturation takes place between the first minute and hour of the simulation. This time frame may also be identified as the one, which allows to pose assumptions on the nucleation mechanisms from the shapes of the PSDs.

Higher nucleation rates can be—obviously—observed for higher initial supersaturations S_0 as can be seen in Fig. 8, for the lowest supersaturation, $S_0 = 100$, no nucleation can be observed at all and the total monomer concentration is depleted due to condensational growth of the background particles. This means, that high supersaturations are necessary for the nucleation of novel particles in the presence of a background particle population.

The decrease of the supersaturation is much faster for $S_0 = 10^5$ than for $S_0 = 10^4$ or $S_0 = 10^3$. This can be attributed to the much higher concentration of nucleated particles of this system, which in turn act as a source for monomer depletion through condensational growth—an effect, which would not become apparent, if the growth (resp. evaporation) of the particle population would not be included into the simulation.

4. Conclusions

We investigate the homogeneous nucleation of an aerosol under isothermal conditions and in the presence of a background particle population. Three different nucleation theories are simulated. We show that each of these

theories results in different rates of nucleation and thus different particle concentrations at the beginning of the simulation. For longer simulation times (>1 hr), the resulting PSD become undistinguishable from each other, as can be expected from different systems with the same total particulate mass, which are driven by the coagulation only. In this way, the identification of a time frame relevant for measurements can be established.

The applied MC simulation algorithm makes use of weighted simulation particles. It is shown, that this simulation technique is able to describe PSDs, which are characterized by huge differences in the number-concentrations of the freshly nucleated particles and the already existing background particles. This shows that the presented MC technique could also be used for the description of a multicomponent atmospheric aerosol system. An investigation of the influence of more complex, kinetic MC simulation based nucleation theories (like Davari and Mukherjee, 2018) could also be simulated in a future work.

Disclosure Statement

No potential conflict of interest was reported by the authors.

Funding

This work has been financially supported by the Deutsche Forschungsgemeinschaft in the frame of the priority programs SPP 1679 [grant number KR 1723/15-2] and SPP 1980 [grant number KR 1723/18-1].

ORCID

Gregor Kotalczyk http://orcid.org/0000-0003-0157-6047
Ivan SkenderoviĆ http://orcid.org/0000-0002-7815-6414
Frank Einar Kruis http://orcid.org/0000-0001-5008-8133

References

Becker, R. and Döring, W. 1935. Kinetische Behandlung der Keimbildung in Übersättigten Dämpfen. *Ann. Phys.* **416**, 719–752. doi:10.1002/andp.19354160806.

Bennett, T. P. and Barrett, J. C. 2012. Water nucleation. A comparison between some phenomenological theories and experiment. *J. Chem. Phys.* **137**(12), 124702. doi:10.1063/1.4754662.

Bianchi, F., Tröstl, J., Junninen, H., Frege, C., Henne, S. and co-authors. 2016. New particle formation in the free troposphere. A question of chemistry and timing. *Science* **352**, 1109–1112. doi:10.1126/science.aad5456.

Celnik, M., Patterson, R. I. A., Kraft, M. and Wagner, W. 2007. Coupling a stochastic soot population balance to gas-phase chemistry using operator splitting. *Combust. Flame* **148**, 158–176. Online at: http://www.scopus.com/inward/record.url?eid=2-s2.0-33846040006&partnerID=40&md5=fcab22044588d3b277a83007-d4085ea1

Courtney, W. G. 1961. Remarks on homogeneous nucleation. *J. Chem. Phys.* **35**, 2249–2250. doi:10.1063/1.1732252.

Davari, S. A. and Mukherjee, D. 2018. Kinetic Monte Carlo simulation for homogeneous nucleation of metal nanoparticles during vapor phase synthesis. *AIChE J.* **64**, 18–28. doi:10.1002/aic.15887.

Efendiev, Y. and Zachariah, M. R. 2003. Hierarchical hybrid Monte-Carlo method for simulation of two-component aerosol nucleation, coagulation and phase segregation. *J. Aerosol Sci.* **34**, 169–188. doi:10.1016/S0021-8502(02)00156-8.

Filipponi, A. and Giammatteo, P. 2016. Kinetic Monte Carlo simulation of the classical nucleation process. *J. Chem. Phys.* **145**(21), 211913. doi:10.1063/1.4962757.

Ford, I. J. 2004. Statistical mechanics of nucleation. A review. *Proc. Inst. Mech. Eng. C J. Mech. Eng. Sci.* **218**, 883–899. doi:10.1243/0954406041474183.

Gelbard, F. 1990. Modeling multicomponent aerosol particle growth by vapor condensation. *Aerosol Sci. Technol.* **12**, 399–412. doi:10.1080/02786829008959355.

Girshick, S. L. and Chiu, C.-P. 1990. Kinetic nucleation theory. A new expression for the rate of homogeneous nucleation from an ideal supersaturated vapor. *J. Chem. Phys.* **93**, 1273–1277. doi:10.1063/1.459191.

Hao, X., Zhao, H., Xu, Z. and Zheng, C. 2013. Population balance-Monte Carlo simulation for gas-to-particle synthesis of nanoparticles. *Aerosol Sci. Technol.* **47**, 1125–1133. doi:10.1080/02786826.2013.823642.

Karl, M., Leck, C., Gross, A. and Pirjola, L. 2012. A study of new particle formation in the marine boundary layer over the central Arctic Ocean using a flexible multicomponent aerosol dynamic model. *Tellus B Chem. Phys. Meteorol.* **64**. Online at: https://www.tandfonline.com/doi/full/10.3402/tellusb.v64i0.17158

Kirkby, J., Curtius, J., Almeida, J., Dunne, E., Duplissy, J. and co-authors. 2011. Role of sulphuric acid, ammonia and galactic cosmic rays in atmospheric aerosol nucleation. *Nature* **476**, 429–433. doi:10.1038/nature10343.

Kotalczyk, G. and Kruis, F. E. 2017. A Monte Carlo method for the simulation of coagulation and nucleation based on weighted particles and the concepts of stochastic resolution and merging. *J. Comput. Phys.* **340**, 276–296. doi:10.1016/j.jcp.2017.03.041.

Kotalczyk, G., Skenderovic, I. and Kruis, F. E. 2016. A GPU-based Monte Carlo technique for the simulation of simultaneous nucleation, coagulation and growth based on weighted simulation particles. In: 2016 AIChE Annual Meeting, San Francisco, AIChE, 490–497.

Kotalczyk, G., Skenderovic, I. and Kruis, F. E. 2017. Modeling of particle formation in arc discharges by Monte-Carlo based population balance modeling. *MRS Adv.* **148**, 1–8. doi:10.1557/adv.2017.155.

Kulmala, M., Kontkanen, J., Junninen, H., Lehtipalo, K., Manninen, H. E. and co-authors. 2013. Direct observations of atmospheric aerosol nucleation. *Science* **339**, 943–946. doi: 10.1126/science.1227385.

Laaksonen, A., Talanquer, V. and Oxtoby, D. W. 1995. Nucleation: Measurements, theory, and atmospheric applications. *Annu. Rev. Phys. Chem.* **46**, 489–524. Online at: http://www.scopus.com/inward/record.url?eid=2-s2.0-0000848866&partnerID=40&md5=ed1189d650578ad48509e6760-b0e7986 doi:10.1146/annurev.pc.46.100195.002421

Lee, K. F., Patterson, R. I. A., Wagner, W. and Kraft, M. 2015. Stochastic weighted particle methods for population balance equations with coagulation, fragmentation and spatial inhomogeneity. *J. Comput. Phys.* **303**, 1–18. doi:10.1016/j.jcp.2015.09.031.

Menz, W. J., Shekar, S., Brownbridge, G. P. E., Mosbach, S., Körmer, R. and co-authors. 2012. Synthesis of silicon nanoparticles with a narrow size distribution: A theoretical study. *J. Aerosol Sci.* **44**, 46–61. doi:10.1016/j.jaerosci.2011.10.005.

Olenius, T. and Riipinen, I. 2017. Molecular-resolution simulations of new particle formation. Evaluation of common assumptions made in describing nucleation in aerosol dynamics models. *Aerosol Sci. Technol.* **51**, 397–408. doi: 10.1080/02786826.2016.1262530.

Oxtoby, D. W. 1992. Homogeneous nucleation: Theory and experiment. *J. Phys. Condens. Matter* **4**, 7627–7650. Online at: http://www.scopus.com/inward/record.url?eid=2-s2.0-0013306867&partnerID=40&md5=09ca343f82ab68294d285a20e33e88b5

Patterson, R. I. A., Singh, J., Balthasar, M., Kraft, M. and Norris, J. R. 2006. The linear process deferment algorithm: A new technique for solving population balance equations. *SIAM J. Sci. Comput.* **28**, 303–320. Online at: http://www.scopus.com/inward/record.url?eid=2-s2.0-33846113883&partnerID=40&md5=7bdc70864d1e911f579ca0e81cfe24f0

Press, W. H., Teukolsky, S. A., Vetterling, W. T. and Flannery, B. P. 2007. *Numerical Recipes. The Art of Scientific Computing*. 3rd ed. Cambridge University Press, Cambridge.

Svenningsson, B., Arneth, A., Hayward, S., Holst, T., Massling, A. and co-authors. 2008. Aerosol particle formation events and analysis of high growth rates observed above a subarctic wetland-forest mosaic. *Tellus B Chem. Phys. Meteorol.* **60**, 353–364. doi:10.1111/j.1600-0889.2008.00351.x.

Tanaka, K. K., Kawano, A. and Tanaka, H. 2014. Molecular dynamics simulations of the nucleation of water: Determining the sticking probability and formation energy of a cluster. *J. Chem. Phys.* **140**, 114302. doi:10.1063/1.4867909.

Vemury, S., Kusters, K. A. and Pratsinis, S. E. 1994. Time-lag for attainment of the self-preserving particle size distribution by coagulation. *J. Colloid Interface Sci.* **165**, 53–59. doi: 10.1006/jcis.1994.1204.

Wei, J. and Kruis, F. E. 2013. A GPU-based parallelized Monte-Carlo method for particle coagulation using an acceptance–rejection strategy. *Chem. Eng. Sci.* **104**, 451–459. doi:10.1016/j.ces.2013.08.008.

Wyslouzil, B. E. and Wölk, J. 2016. Overview. Homogeneous nucleation from the vapor phase – The experimental science. *J. Chem. Phys.* **145**(21), 211702. doi:10.1063/1.4962283.

Zhang, R., Khalizov, A., Wang, L., Hu, M. and Xu, W. 2012. Nucleation and growth of nanoparticles in the atmosphere. *Chem. Rev.* **112**, 1957–2011. Online at: http://www.scopus.com/inward/record.url?eid=2-s2.0-84863338057&partnerID=40&md5=a4a3f5128beb39fd0902abd134fba850

Zhang, Y., Seigneur, C., Seinfeld, J. H., Jacobson, M. Z. and Binkowski, F. S. 1999. Simulation of aerosol dynamics. A comparative review of algorithms used in air quality models. *Aerosol Sci. Technol.* **31**, 487–514. doi:10.1080/027868299304039.

Zhao, H. and Kruis, F. E. 2014. Dependence of steady-state compositional mixing degree on feeding conditions in two-component aggregation. *Ind. Eng. Chem. Res.* **53**, 6047–6055. doi:10.1021/ie500316g.

Zhao, H., Kruis, F. E. and Zheng, C. 2009. Reducing statistical noise and extending the size spectrum by applying weighted simulation particles in Monte Carlo simulation of coagulation. *Aerosol Sci. Technol.* **43**, 781–793. doi:10.1080/02786820902939708.

Paper V

Reproduced with permission from Springer Nature. Version of record published in:
Dynamic Flowsheet Simulation of Solids Processes (2020), ISBN 978-3-030-45168-4
Chapter 15, pp 519-548.
Available online at: https://doi.org/10.1007/978-3-030-45168-4_15

Compartmental Population Balances by Means of Monte Carlo Methods

G. Kotalczyk and F.E. Kruis

Chapter 15
Compartmental Population Balances by Means of Monte Carlo Methods

Gregor Kotalczyk and Frank Einar Kruis

Abstract Stochastic simulation techniques for the solution of a network of population balance equations (PBE) are discussed in this chapter. The application of weighted Monte Carlo (MC) particles for the solution of compartmental PBE systems is summarized and its computational efficacy in form of a parallel GPU implementation is pointed out. Solution strategies for coagulation, nucleation, breakage, growth and evaporation are thereby presented. An application example treats the simultaneous coagulation, nucleation, evaporation and growth encountered during particle production through the aerosol route. Furthermore, the simulation of a compartmental network is discussed and parallel simulation techniques for the transport of weighted MC particles are presented. The proposed methodology is benchmarked by comparison with a pivot method for a variety of test cases with an increasing degree of complexity. Simulation conditions are identified, for which conventional, non-weighted MC simulation techniques are not applicable. It is found, that the specific combination of a screen unit with tear-streams cannot be simulated by conventional methods, termed 'random removal', and make thus other techniques—like the here introduced merging techniques necessary.

Nomenclature

b	Breakage rate [s^{-1}]
d_g	Geometric mean diameter [m]
C_{dist}	Compare distance on GPU memory (integer) [–]
d^*	Kelvin diameter [m]
d	Diameter of particle [m]
$E_{i,j}$	Merging error of particles i and j [–]

G. Kotalczyk · F. E. Kruis (✉)
Institute of Technology for Nanostructures (NST),
University of Duisburg-Essen, Duisburg, Germany
e-mail: einar.kruis@uni-due.de

G. Kotalczyk
e-mail: gregor.kotalczyk@uni-due.de

S. Heinrich (ed.), *Dynamic Flowsheet Simulation of Solids Processes*,
https://doi.org/10.1007/978-3-030-45168-4_15

$f_{A\to B}$	Relative particle exchange flow rate from compartment A to B [s^{-1}]
$F_{A\to B}$	Absolute particle exchange flow rate from compartment A to B [s^{-1}]
G	Growth rate [m s^{-1}]
k_B	Boltzmann constant [J K^{-1}]
m_1	Atomic (resp, molecule) mass [kg]
N_MC	Number of MC simulation particles [–]
N_G	Concentration of gas atoms (or molecules) [m^{-3}]
$n_C(v)$	PSD in compartment C [m^{-6}]
o_idx	Destination index on GPU memory (integer) [–]
i^*	Number of atoms (resp. molecules) in critical cluster [–]
$p_A^{(i)}$	i-th property of particle A [unit of i-th property]
p_s	Saturation pressure [Pa]
$Q_{A\to B}$	Volumetric flow rate of carrier gas/liquid from compartment A to B [m^3 s^{-1}]
R	Mixing ratio for breakage scheme [–]
R_N	Nucleation rate [m^{-3} s^{-1}]
S	Supersaturation [–]
S_sep	Separation function for screen [–]
s_f	Reciprocal of stochastic resolution [m^{-3}]
T	Temperature [K]
t	(simulation) time [s]
t_char	Characteristic time [s]
v	Particle volume [m^3]
v^*	Kelvin volume [m^3]
v_M	Atomic (resp. molecular) volume [m^3]
V_C	Volume within compartment C filled with carrier liquid (or gas) [m^3]
W_i	Statistical weight of MC particle i [m^{-3}]
α_i	Merging weight for property i
β	Coagulation kernel [m^3 s^{-1}]
γ	Breakage function [–]
ε	Maximal admittable merging error [–]
τ	Time step [s]
σ	Surface tension [N m^{-2}]

Indices

0	Initial values

1 Introduction

The solution of the population balance equation (PBE) [1] plays an important role in a wide area of applications ranging from natural sciences to many fields of engineering [2]. Especially the modelling of chemical engineering problems such as crystallization [3], milling [4], granulation [5] or particle production in aerosol reactors [6] resort to PBE based process modelling.

The modelling of single apparatuses can be seldomly done with the assumption of spatial uniformity (as in e.g. [7]) and the application of Computational Fluid Dynamics (CFD) simulations and/or compartmental modelling becomes necessary in order to describe different zones of single apparatuses correctly.

CFD modelling allows a very high spatial resolution of the investigated system: 30,000 [8]−1,000,000 [9] cells are sometimes applied. The drawback of a CFD-PBE modelling is its enormous computational cost, hence a PBE has to be solved for each of these cells. Due to the high computational cost, only a rough approximation of the particle size distribution (PSD) is encountered in such simulations which typically resort to sectional methods with a low resolution (of ca. 12–30 discrete points or sections [10, 11]) or to the method of moments [12, 13], limiting the particle modelling mostly to one property—the size.

To overcome this problem, compartmental modelling is often applied, simplifying the spatial complexity to a low number of compartments (examples are 3 compartments or 10 compartments [14]). This allows, on the other hand, a more complex particle modelling with a more detailed sectional grid (e.g. 1000 discrete sections for 3 compartments [15]) or even with a Monte Carlo (MC) simulation, where more than one particle property allow to model a more complex morphology of the particles [14].

The PBE for a network of compartments, like presented in Fig. 1. can be described by the following formula:

$$
\begin{aligned}
\frac{\mathrm{d}n_C(v,t)}{\mathrm{d}t} = &+ \underbrace{\frac{1}{2}\int_0^v \beta_C(v', v-v')n_C(v',t)n_C(v-v',t)\mathrm{d}v'}_{\text{coagulation birth term}} \\
&- \underbrace{n_C(v,t)\int_0^\infty \beta_C(v,v')n_C(v',t)\mathrm{d}v'}_{\text{coagulation death term}} \\
&+ \underbrace{R_{\mathrm{N},C}(t)\cdot\delta(v-v_C^*(t))}_{\text{nucleation}} \underbrace{-\nabla_v(G_C(v,t)n_C(v,t))}_{\text{growth(G>0)/evaporation(G<0)}} \\
&\underbrace{-b_C(v)\cdot n_C(v,t)}_{\text{breakage death term}} + \underbrace{\int_v^\infty b_C(v')\cdot n_C(v',t)\cdot\gamma_C(v|v')\mathrm{d}v}_{\text{breakage birth term}} \\
&+ \sum_{\text{inflow from all compartments } i} f_{i\to C}\cdot n_i(v,t) \\
&- \sum_{\text{outflow to all compartments } i} f_{C\to i}\cdot n_C(v,t)
\end{aligned}
\tag{1}
$$

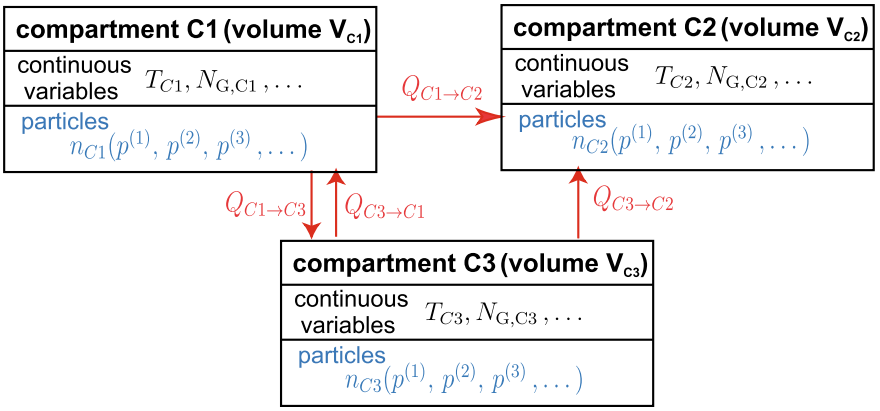

Fig. 1 A network of compartments. Each compartment C_i models parts of a reactor (or equipment) volume, which is filled with the carrier gas (or liquid) with a volume V_C. The compartment contains a PSD, n_C, and is described by other continuous variables, like temperature T_C, a gas concentration $N_{\mathrm{G},C}$, etc

where the coagulation kernels β_C, growth rates G_C, nucleation rates $R_{\mathrm{N},C}$ and sizes of the nucleating particles v_C^*, breakage rates $b_C(v)$ and breakage functions $\gamma_C(v|v')$ can be defined differently for each compartment C . The shown particle exchange flowrates $f_{i\to C}$ and $f_{C\to i}$ may assume constant values, or reflect more complex—nonlinear—and particle size or time dependent forms. The given volumetric flow rates $Q_{A\to B}$ (shown in Fig. 1) of the carrier gas (or liquid) and the volumes of the carrier gas (or liquid) of the outflow compartments, V_A, are thereby used in order to determine the particle exchange flowrates via:

$$f_{A\to B} = Q_{A\to B}/V_A \tag{2}$$

In this way, a complex reactor structure can be modelled in more detail [16, 17] or the interconnection of single processing units in a flowsheet simulation can be analyzed [15, 18, 19].

Although Eq. (1) describes only one particle property, the volume v, one could interpret v as a vector describing multiple properties of the particle, such as volume ($p^{(1)}$), surface area ($p^{(2)}$), wet content ($p^{(3)}$), and so on, as suggested in Fig. 1. Only a stochastic modelling is able to solve Eq. (1) for a high number of properties and render the complete particle morphology.

In the following, stochastic solution strategies for Eq. (1) will be discussed in the frame-work of an operator splitting approach meaning that the single processes coagulation, nucleation, growth/evaporation, breakage and transport of particles are decoupled for short periods of time τ. The approximation error introduced by this decoupling can be minimized by a choice of a low enough separation time step τ. For this reason, the solution strategies for single processes, like coagulation, nucleation, growth/evaporation and breakage are discussed for one compartment first. The

implementation of the coagulation in the framework of a compartmental network, as well as the transport between single compartments is discussed in the section afterwards, where the modelling of multiple compartments is applied.

2 Weighted Monte Carlo Particles for the Solution of the Population Balance Equation

The use of weighted simulation particles (a particle with weight w represents w real particles within a given reactor volume) has several advantages: it allows to describe the interaction between simulation particles having different concentrations coming from different cells or compartments [14, 20, 21]. It can also be used as a tool to control the number of simulation particles (e.g. to gain numerical accuracy). In the following, some techniques will be introduced to solve the single mechanisms presented in Eq. (1) by the application of weighted MC particles.

2.1 Coagulation

The correct description of the coagulation rates for the weighted particles, especially for a complex coagulation scheme, like the one introduced Zhao et al. [22] shown in Fig. 2, poses a great difficulty.

The authors [22] presented the 'ficticious particle theory' which leads to the following modified coagulation kernel:

$$\beta^{(fp)} = \frac{2W_j \max\left(W_i, W_j\right)}{W_i + W_j}\beta \tag{3}$$

The weights of the particles are denoted by W_i and W_j. The coagulation kernel β describes the coagulation of the original (non-weighted) system—which might be the Brownian kernel for the free molecular regime, etc. The resulting coagulation rate is asymmetric, making a distinction necessary, whether particle i coagulates with j or vice versa. This definition is 1) difficult to understand conceptually and 2) difficult to extend on other process—like nucleation or transport of fictitious particles.

We developed in [23] the concept of the stochastic resolution which describes each coagulation in the frame-work of equally weighted MC-particles, where each MC-particle describes s_f real particles. The value for the parameter s_f can be set arbitrarily. Figure 2 shows that the setting $s_f = W_{\min} = \min\left(\mathrm{W_i}, \mathrm{W_j}\right)$ leads to the correct description of the coagulation-scheme. The scaling factor s_f depends on the chosen coagulation pair, so that different coagulation-events are described in different stochastic resolutions.

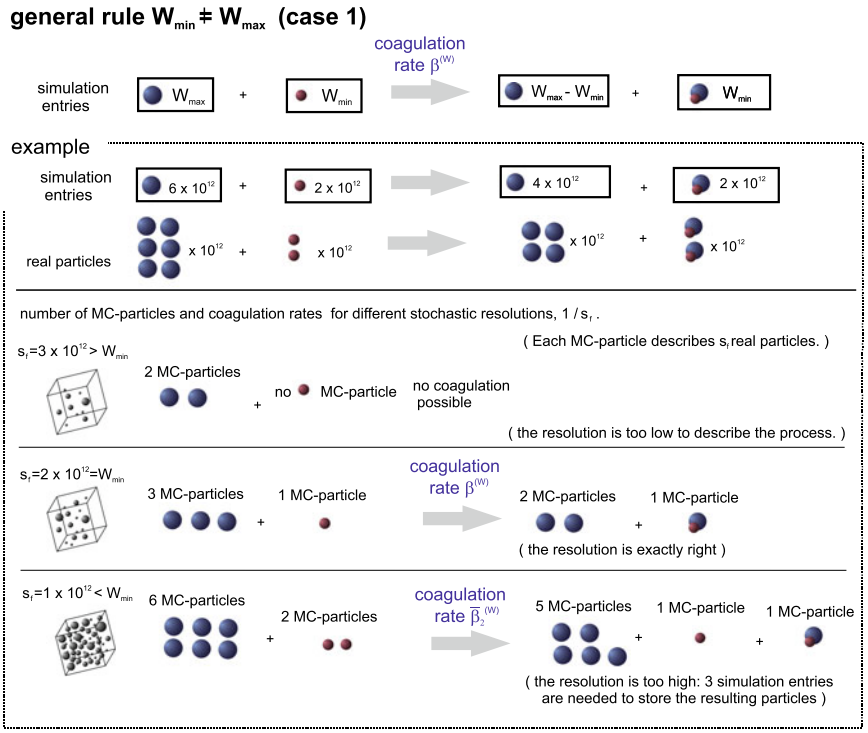

Fig. 2 The concept of 'stochastic resolution' can be used to describe the coagulation-scheme developed Zhao et al. [22]. Only the choice for $\mathbf{s_f} = \mathbf{W_{min}}$ leads to the correct description of the general rule presented in the 'simulation entries' line

The coagulation rate $\beta^{(w)}$ for this coagulation-scheme can be derived from the population balance equation:

$$\frac{\mathrm{d}n(v)}{\mathrm{d}t} = \frac{1}{2}\int_0^v \beta\left(v-v', v'\right)n\left(v-v'\right)n\left(v'\right)\mathrm{d}v' - n(v)\int_0^\infty \beta\left(v, v'\right)n\left(v'\right)\mathrm{d}v' \tag{4}$$

Instead of the 'original' concentrations $n(v)$, the concentrations of the MC-systems $n^{(MC)}(v) = \frac{n(v)}{s_f}$ are being considered. The multiplication of the PBE with the factor $\frac{1}{s_f} = \frac{1}{W_{\min}}$ leads to the following modified coagulation rate of the MC-particles: $\beta^{(MC)} = W_{\min} \cdot \beta$. Hence there is one MC-particle of the $W_{\min}$-species and $\frac{W_{\max}}{W_{\min}}$ MC-particles of the $W_{\max}$-species, the overall rate for the coagulation between one $W_{\min}$-MC-particle and one of the $W_{\max}$-MC-particles is:

$$\beta^{(w)} = \frac{W_{\max}}{W_{\min}} \cdot \beta^{(MC)} = W_{\max} \cdot \beta \tag{5}$$

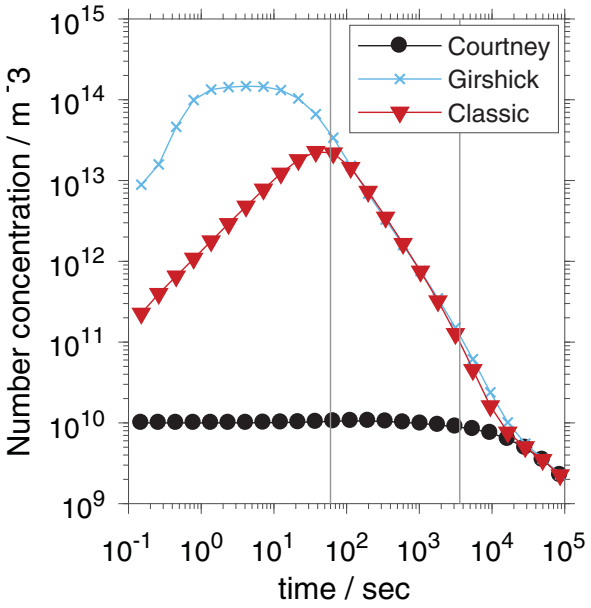

Fig. 3. The number concentration in dependency of the used nucleation theories are shown. The vertical lines represent the simulation times of 1 min and 1 hr, a total simulation time of 24 hr is presented.

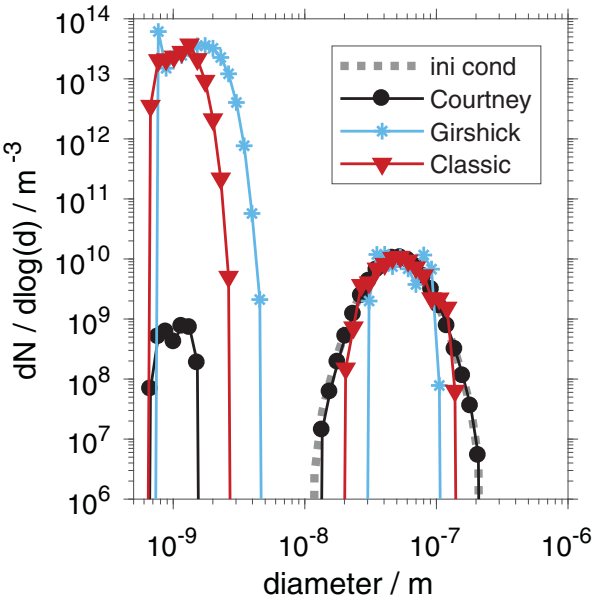

Fig. 4. The PSDs resulting from the three different nucleation theories after a simulation time of 1 min for $S_0 = 10^5$.

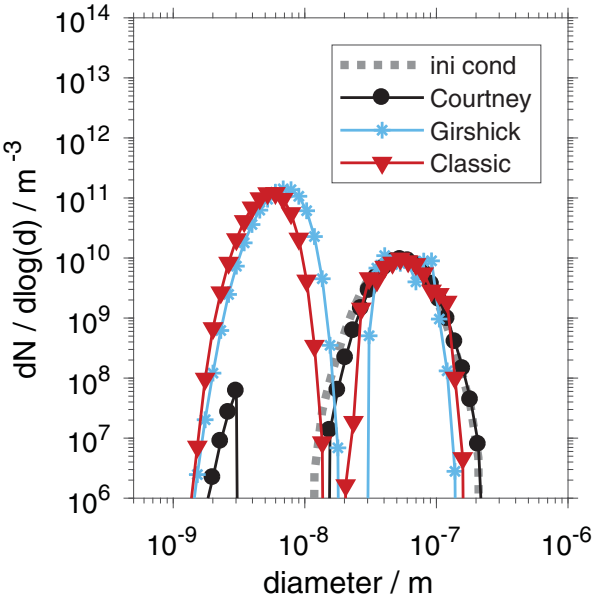

Fig. 5. The PSDs resulting from the three different nucleation theories after a simulation time of 1 hr for $S_0 = 10^5$.

to the nucleated particles, which represent the smaller sizes of the particle size spectrum. The PSD based on the Girshick nucleation theory exhibits not only higher concentrations of the nucleated particles as the other nucleation theories, but the sizes of the particles are larger as well. This indicates that the newly nucleated particles have coagulated with each other. This explains the number concentration plateau for the initial stage of the simulation shown in Fig. 3 for the Girshick nucleation theory: the increase of the particle number concentration is limited by the onset of the coagulation, which decreases the particle number concentration.

The part of the PSD representing mainly the background particle population changes its shape slightly. It can be seen that the parts representing smaller concentrations of the PSD are not rendered in the results based on the Girshick and the Classic theory. This can be attributed to the 'low weight merging', necessary for the novel inclusion of a nucleated particle. The higher the nucleation rate and the more new particles have to be included into the simulation, the less accurate becomes the rendering of the fringes of the background particle population. It should be noted, that the regions, in which these inaccuracies are observed constitute a small part of the PSD (note the logarithmic plot). This small part (especially the larger particles), could describe the part of the PSD, which is responsible for the light-scattering behaviour of the aerosol or act as cloud condensation nuclei (CCN). The 'removal' of these particles due to the merging technique might therefore introduce serious errors in the context of the simulation of an atmospheric system. These errors could be prevented by the following 2 approaches: (1) the particles which are large enough to act as CCNs could be locked against merging, simply by not comparing and merging them with other particles; (2) the light-scattering cross-section (resp. power) σ_i of each particle i

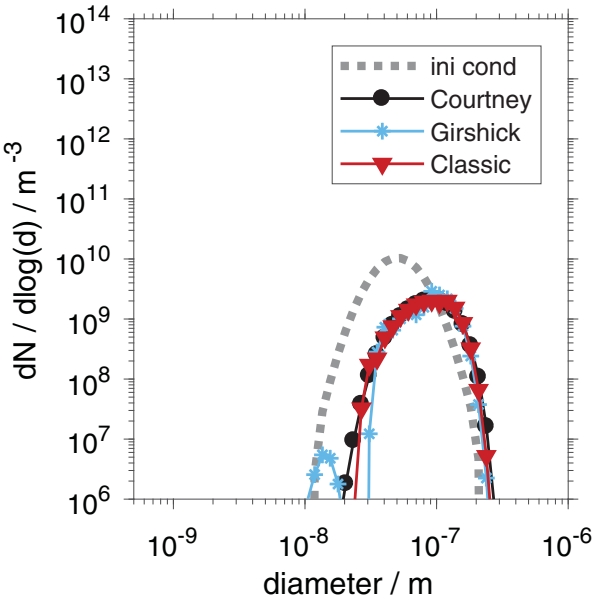

Fig. 6. The PSDs resulting from the three different nucleation theories after a simulation time of 24 hr for $S_0 = 10^5$.

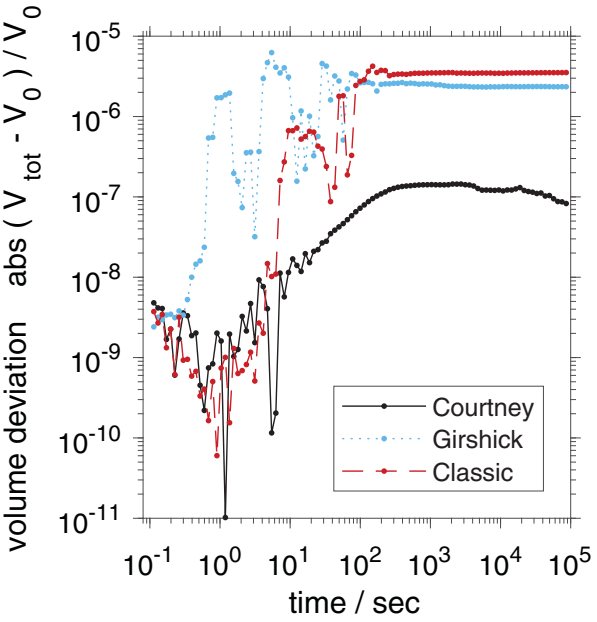

Fig. 7. The relative deviation of the total volume V_{tot} [defined in Equation (11)] from the initial total volume V_0.

could be considered for the calculation of the merging error, in this approach, the expression in Equation (5) could be replaced by: $E_{\text{mer}} = (v_i - v_j)^2/\min(v_i, v_j) + (\sigma_i - \sigma_j)^2/\sigma_{\text{gauche}}$, where σ_{gauche} is some pre-set light-scattering cross-section. This second approach would penalize the merging of particles with different light-scattering cross-sections, if one of them is higher than σ_{gauche}.

Although the fringes of the PSDs change due to the here applied merging techniques, the total volume V_{tot} is conserved in the course of the simulation, where:

$$V_{\text{tot}} = \sum_i W_i \cdot v_i + n_{\text{G}} \cdot v_{\text{m}} \tag{11}$$

The mean value for V_{tot} (for all 100 simulations) is compared with the initial value V_0 at the beginning of the simulation in Fig. 7. It can be seen that it changes only slightly. The relative deviation of 10^{-7} corresponds to the magnitude of the floating point precision applied for the calculations. This value accumulates to levels of 10^{-6} for simulations of high nucleation scenarios. These levels are still acceptable.

We also observed, that the application of a higher number of simulation particles leads to less deviations within the background PSDs, so that the number of simulation particles can be applied as a control parameter for these deviations. The same values for the moments of the PSDs (such as mean geometric diameter or total number-concentration) could be reproduced, independent on the number of the applied simulation particles.

The PSD based on the Courtney theory expresses the background condition with the same accuracy as the initial condition, hence little to none particles have to be inserted into the simulation in this scenario. In turn, much higher differences between the concentrations of the nucleated particles and the concentrations of background particles are described by the PSD based on the Girshick theory as the one based on the Courtney theory.

In the time span, between 1 min and 1 hr (the transition time span), the nucleation of novel particles ceases completely (see Fig. 2). The evolution of the PSD in this time span is mainly described by the coagulation of the particles, the condensational growth of the particle population might be considered to be very small, hence the corresponding driving force $S - S_\infty$ decreases several orders of magnitude, as can be seen in Fig. 1. The result is a PSD, which consists of two peaks, which can be attributed to the nucleated population and the initial background particle population. Figure 5 shows that the growth of the background particle population due to condensation and due to coagulation with the nucleated particles is relatively small. The part of the PSD, which represents the background particles (around 50 nm), is nearly of the same shape as the initial condition (disregarding the shape changes due to the merging on the edges of this distribution).

The part of the PSD, which can be attributed to the nucleated particles (covering the whole range between 1 and 20 nm) exhibits the form of the self-preserving form for coagulation. The differences between the PSDs are clearly visible, making a distinction between each other

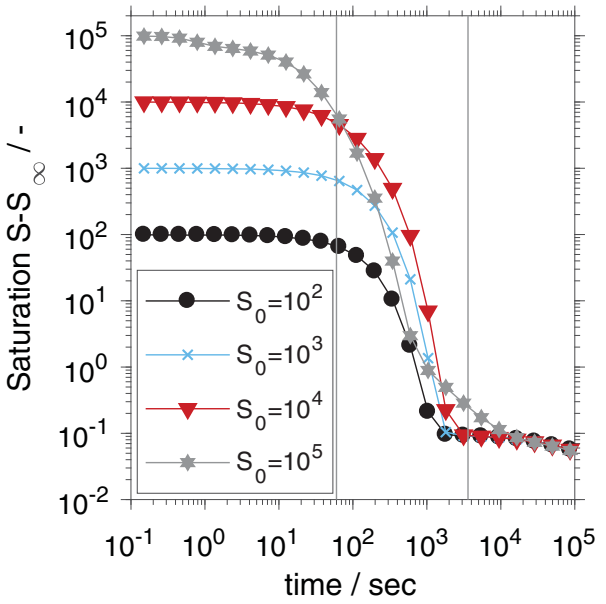

Fig. 8. The supersaturation in dependency of its initial value S_0 for the Girshick nucleation theory. The vertical lines represent the simulation times of 1 min and 1 hr, a total simulation time of 24 hr is presented.

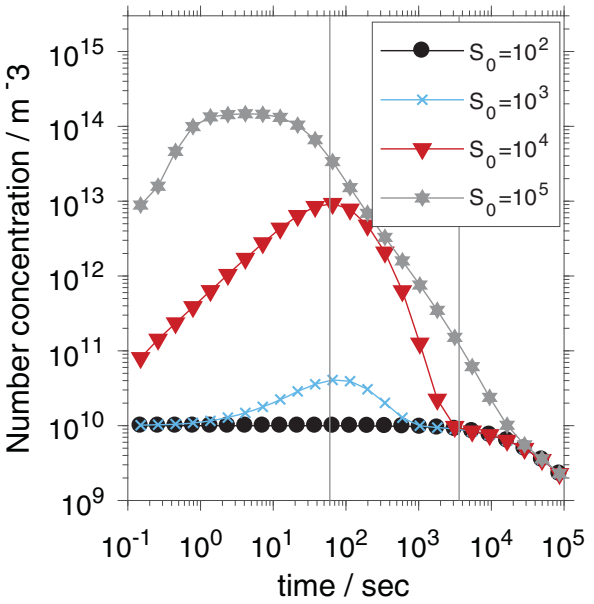

Fig. 9. The number concentration in dependency of the initial supersaturation value S_0 for the Girshick nucleation theory. The vertical lines represent the simulation times of 1 min and 1 hr, a total simulation time of 24 hr is presented.

possible. The attribution of the corresponding nucleation theory based on the size of the PSD in this size spectrum would be therefore possible, while the form of the background particles (all particles with the size 20 nm or higher) would not allow to draw conclusions on the nucleation mechanisms

These distinctions vanish, however in the further course of the simulation and the resulting PSDs attain a self-preserving form for the coagulation, making no more distinctions between each other possible, as can be seen in Fig. 6. The depicted results describe the PSDs after 24 hr. A clear difference between the PSDs for 24 hr and the initial PSD can be seen, which can be attributed to the coagulation within this long 'steady state time span'. Each PSD is rendered with the same accuracy. This indicates that the differences of the rendering of the background particle population in Figs. 4 and 5, which originate from the 'low weight merging' technique did not propagate into the simulation and were in fact not critical for the correct description of the general behaviour of the PSD. However, the negligence of the larger particles might lead to a wrong description of the light scattering behaviour of the aerosol—or its ability to act as CCNs—both points could be addressed by modifying the merging technique as discussed above.

Similar findings can be made for different values for the initial concentration S_0, exemplary plots of the supersaturation in Fig. 8 and the number concentration in Fig. 9 show, that the nucleation takes place mostly during the first minute of the simulation and that the depletion of the supersaturation takes place between the first minute and hour of the simulation. This time frame may also be identified as the one, which allows to pose assumptions on the nucleation mechanisms from the shapes of the PSDs.

Higher nucleation rates can be—obviously—observed for higher initial supersaturations S_0 as can be seen in Fig. 8, for the lowest supersaturation, $S_0 = 100$, no nucleation can be observed at all and the total monomer concentration is depleted due to condensational growth of the background particles. This means, that high supersaturations are necessary for the nucleation of novel particles in the presence of a background particle population.

The decrease of the supersaturation is much faster for $S_0 = 10^5$ than for $S_0 = 10^4$ or $S_0 = 10^3$. This can be attributed to the much higher concentration of nucleated particles of this system, which in turn act as a source for monomer depletion through condensational growth—an effect, which would not become apparent, if the growth (resp. evaporation) of the particle population would not be included into the simulation.

4. Conclusions

We investigate the homogeneous nucleation of an aerosol under isothermal conditions and in the presence of a background particle population. Three different nucleation theories are simulated. We show that each of these

theories results in different rates of nucleation and thus different particle concentrations at the beginning of the simulation. For longer simulation times (>1 hr), the resulting PSD become undistinguishable from each other, as can be expected from different systems with the same total particulate mass, which are driven by the coagulation only. In this way, the identification of a time frame relevant for measurements can be established.

The applied MC simulation algorithm makes use of weighted simulation particles. It is shown, that this simulation technique is able to describe PSDs, which are characterized by huge differences in the number-concentrations of the freshly nucleated particles and the already existing background particles. This shows that the presented MC technique could also be used for the description of a multicomponent atmospheric aerosol system. An investigation of the influence of more complex, kinetic MC simulation based nucleation theories (like Davari and Mukherjee, 2018) could also be simulated in a future work.

Disclosure Statement

No potential conflict of interest was reported by the authors.

Funding

This work has been financially supported by the Deutsche Forschungsgemeinschaft in the frame of the priority programs SPP 1679 [grant number KR 1723/15-2] and SPP 1980 [grant number KR 1723/18-1].

ORCID

Gregor Kotalczyk http://orcid.org/0000-0003-0157-6047
Ivan SkenderoviĆ http://orcid.org/0000-0002-7815-6414
Frank Einar Kruis http://orcid.org/0000-0001-5008-8133

References

Becker, R. and Döring, W. 1935. Kinetische Behandlung der Keimbildung in Übersättigten Dämpfen. *Ann. Phys.* **416**, 719–752. doi:10.1002/andp.19354160806.

Bennett, T. P. and Barrett, J. C. 2012. Water nucleation. A comparison between some phenomenological theories and experiment. *J. Chem. Phys.* **137**(12), 124702. doi:10.1063/1.4754662.

Bianchi, F., Tröstl, J., Junninen, H., Frege, C., Henne, S. and co-authors. 2016. New particle formation in the free troposphere. A question of chemistry and timing. *Science* **352**, 1109–1112. doi:10.1126/science.aad5456.

Celnik, M., Patterson, R. I. A., Kraft, M. and Wagner, W. 2007. Coupling a stochastic soot population balance to gas-phase chemistry using operator splitting. *Combust. Flame* **148**, 158–176. Online at: http://www.scopus.com/inward/record.url?eid=2-s2.0-33846040006&partnerID=40&md5=fcab22044588d3b277a83007-d4085ea1

Courtney, W. G. 1961. Remarks on homogeneous nucleation. *J. Chem. Phys.* **35**, 2249–2250. doi:10.1063/1.1732252.

Davari, S. A. and Mukherjee, D. 2018. Kinetic Monte Carlo simulation for homogeneous nucleation of metal nanoparticles during vapor phase synthesis. *AIChE J.* **64**, 18–28. doi:10.1002/aic.15887.

Efendiev, Y. and Zachariah, M. R. 2003. Hierarchical hybrid Monte-Carlo method for simulation of two-component aerosol nucleation, coagulation and phase segregation. *J. Aerosol Sci.* **34**, 169–188. doi:10.1016/S0021-8502(02)00156-8.

Filipponi, A. and Giammatteo, P. 2016. Kinetic Monte Carlo simulation of the classical nucleation process. *J. Chem. Phys.* **145**(21), 211913. doi:10.1063/1.4962757.

Ford, I. J. 2004. Statistical mechanics of nucleation. A review. *Proc. Inst. Mech. Eng. C J. Mech. Eng. Sci.* **218**, 883–899. doi:10.1243/0954406041474183.

Gelbard, F. 1990. Modeling multicomponent aerosol particle growth by vapor condensation. *Aerosol Sci. Technol.* **12**, 399–412. doi:10.1080/02786829008959355.

Girshick, S. L. and Chiu, C.-P. 1990. Kinetic nucleation theory. A new expression for the rate of homogeneous nucleation from an ideal supersaturated vapor. *J. Chem. Phys.* **93**, 1273–1277. doi:10.1063/1.459191.

Hao, X., Zhao, H., Xu, Z. and Zheng, C. 2013. Population balance-Monte Carlo simulation for gas-to-particle synthesis of nanoparticles. *Aerosol Sci. Technol.* **47**, 1125–1133. doi:10.1080/02786826.2013.823642.

Karl, M., Leck, C., Gross, A. and Pirjola, L. 2012. A study of new particle formation in the marine boundary layer over the central Arctic Ocean using a flexible multicomponent aerosol dynamic model. *Tellus B Chem. Phys. Meteorol.* **64**. Online at: https://www.tandfonline.com/doi/full/10.3402/tellusb.v64i0.17158

Kirkby, J., Curtius, J., Almeida, J., Dunne, E., Duplissy, J. and co-authors. 2011. Role of sulphuric acid, ammonia and galactic cosmic rays in atmospheric aerosol nucleation. *Nature* **476**, 429–433. doi:10.1038/nature10343.

Kotalczyk, G. and Kruis, F. E. 2017. A Monte Carlo method for the simulation of coagulation and nucleation based on weighted particles and the concepts of stochastic resolution and merging. *J. Comput. Phys.* **340**, 276–296. doi:10.1016/j.jcp.2017.03.041.

Kotalczyk, G., Skenderovic, I. and Kruis, F. E. 2016. A GPU-based Monte Carlo technique for the simulation of simultaneous nucleation, coagulation and growth based on weighted simulation particles. In: 2016 AIChE Annual Meeting, San Francisco, AIChE, 490–497.

Kotalczyk, G., Skenderovic, I. and Kruis, F. E. 2017. Modeling of particle formation in arc discharges by Monte-Carlo based population balance modeling. *MRS Adv.* **148**, 1–8. doi:10.1557/adv.2017.155.

Kulmala, M., Kontkanen, J., Junninen, H., Lehtipalo, K., Manninen, H. E. and co-authors. 2013. Direct observations of atmospheric aerosol nucleation. *Science* **339**, 943–946. doi: 10.1126/science.1227385.

Laaksonen, A., Talanquer, V. and Oxtoby, D. W. 1995. Nucleation: Measurements, theory, and atmospheric applications. *Annu. Rev. Phys. Chem.* **46**, 489–524. Online at: http://www.scopus.com/inward/record.url?eid=2-s2.0-0000848866&partnerID=40&md5=ed1189d650578ad48509e6760-b0e7986 doi:10.1146/annurev.pc.46.100195.002421

Lee, K. F., Patterson, R. I. A., Wagner, W. and Kraft, M. 2015. Stochastic weighted particle methods for population balance equations with coagulation, fragmentation and spatial inhomogeneity. *J. Comput. Phys.* **303**, 1–18. doi:10.1016/j.jcp.2015.09.031.

Menz, W. J., Shekar, S., Brownbridge, G. P. E., Mosbach, S., Körmer, R. and co-authors. 2012. Synthesis of silicon nanoparticles with a narrow size distribution: A theoretical study. *J. Aerosol Sci.* **44**, 46–61. doi:10.1016/j.jaerosci.2011.10.005.

Olenius, T. and Riipinen, I. 2017. Molecular-resolution simulations of new particle formation. Evaluation of common assumptions made in describing nucleation in aerosol dynamics models. *Aerosol Sci. Technol.* **51**, 397–408. doi: 10.1080/02786826.2016.1262530.

Oxtoby, D. W. 1992. Homogeneous nucleation: Theory and experiment. *J. Phys. Condens. Matter* **4**, 7627–7650. Online at: http://www.scopus.com/inward/record.url?eid=2-s2.0-0013306867&partnerID=40&md5=09ca343f82ab68294d285a20e33e88b5

Patterson, R. I. A., Singh, J., Balthasar, M., Kraft, M. and Norris, J. R. 2006. The linear process deferment algorithm: A new technique for solving population balance equations. *SIAM J. Sci. Comput.* **28**, 303–320. Online at: http://www.scopus.com/inward/record.url?eid=2-s2.0-33846113883&partnerID=40&md5=7bdc70864d1e911f579ca0e81cfe24f0

Press, W. H., Teukolsky, S. A., Vetterling, W. T. and Flannery, B. P. 2007. *Numerical Recipes. The Art of Scientific Computing*. 3rd ed. Cambridge University Press, Cambridge.

Svenningsson, B., Arneth, A., Hayward, S., Holst, T., Massling, A. and co-authors. 2008. Aerosol particle formation events and analysis of high growth rates observed above a subarctic wetland-forest mosaic. *Tellus B Chem. Phys. Meteorol.* **60**, 353–364. doi:10.1111/j.1600-0889.2008.00351.x.

Tanaka, K. K., Kawano, A. and Tanaka, H. 2014. Molecular dynamics simulations of the nucleation of water: Determining the sticking probability and formation energy of a cluster. *J. Chem. Phys.* **140**, 114302. doi:10.1063/1.4867909.

Vemury, S., Kusters, K. A. and Pratsinis, S. E. 1994. Time-lag for attainment of the self-preserving particle size distribution by coagulation. *J. Colloid Interface Sci.* **165**, 53–59. doi: 10.1006/jcis.1994.1204.

Wei, J. and Kruis, F. E. 2013. A GPU-based parallelized Monte-Carlo method for particle coagulation using an acceptance–rejection strategy. *Chem. Eng. Sci.* **104**, 451–459. doi:10.1016/j.ces.2013.08.008.

Wyslouzil, B. E. and Wölk, J. 2016. Overview. Homogeneous nucleation from the vapor phase – The experimental science. *J. Chem. Phys.* **145**(21), 211702. doi:10.1063/1.4962283.

Zhang, R., Khalizov, A., Wang, L., Hu, M. and Xu, W. 2012. Nucleation and growth of nanoparticles in the atmosphere. *Chem. Rev.* **112**, 1957–2011. Online at: http://www.scopus.com/inward/record.url?eid=2-s2.0-84863338057&partnerID=40&md5=a4a3f5128beb39fd0902abd134fba850

Zhang, Y., Seigneur, C., Seinfeld, J. H., Jacobson, M. Z. and Binkowski, F. S. 1999. Simulation of aerosol dynamics. A comparative review of algorithms used in air quality models. *Aerosol Sci. Technol.* **31**, 487–514. doi:10.1080/027868299304039.

Zhao, H. and Kruis, F. E. 2014. Dependence of steady-state compositional mixing degree on feeding conditions in two-component aggregation. *Ind. Eng. Chem. Res.* **53**, 6047–6055. doi:10.1021/ie500316g.

Zhao, H., Kruis, F. E. and Zheng, C. 2009. Reducing statistical noise and extending the size spectrum by applying weighted simulation particles in Monte Carlo simulation of coagulation. *Aerosol Sci. Technol.* **43**, 781–793. doi:10.1080/02786820902939708.

Paper V

Reproduced with permission from Springer Nature. Version of record published in:
Dynamic Flowsheet Simulation of Solids Processes (2020), ISBN 978-3-030-45168-4
Chapter 15, pp 519-548.
Available online at: https://doi.org/10.1007/978-3-030-45168-4_15

Compartmental Population Balances by Means of Monte Carlo Methods

G. Kotalczyk and F.E. Kruis

Chapter 15
Compartmental Population Balances by Means of Monte Carlo Methods

Gregor Kotalczyk and Frank Einar Kruis

Abstract Stochastic simulation techniques for the solution of a network of population balance equations (PBE) are discussed in this chapter. The application of weighted Monte Carlo (MC) particles for the solution of compartmental PBE systems is summarized and its computational efficacy in form of a parallel GPU implementation is pointed out. Solution strategies for coagulation, nucleation, breakage, growth and evaporation are thereby presented. An application example treats the simultaneous coagulation, nucleation, evaporation and growth encountered during particle production through the aerosol route. Furthermore, the simulation of a compartmental network is discussed and parallel simulation techniques for the transport of weighted MC particles are presented. The proposed methodology is benchmarked by comparison with a pivot method for a variety of test cases with an increasing degree of complexity. Simulation conditions are identified, for which conventional, non-weighted MC simulation techniques are not applicable. It is found, that the specific combination of a screen unit with tear-streams cannot be simulated by conventional methods, termed 'random removal', and make thus other techniques—like the here introduced merging techniques necessary.

Nomenclature

b	Breakage rate [s^{-1}]
d_g	Geometric mean diameter [m]
C_{dist}	Compare distance on GPU memory (integer) [–]
d^*	Kelvin diameter [m]
d	Diameter of particle [m]
$E_{i,j}$	Merging error of particles i and j [–]

G. Kotalczyk · F. E. Kruis (✉)
Institute of Technology for Nanostructures (NST),
University of Duisburg-Essen, Duisburg, Germany
e-mail: einar.kruis@uni-due.de

G. Kotalczyk
e-mail: gregor.kotalczyk@uni-due.de

S. Heinrich (ed.), *Dynamic Flowsheet Simulation of Solids Processes*,
https://doi.org/10.1007/978-3-030-45168-4_15

$f_{A\to B}$	Relative particle exchange flow rate from compartment A to B [s^{-1}]
$F_{A\to B}$	Absolute particle exchange flow rate from compartment A to B [s^{-1}]
G	Growth rate [m s^{-1}]
k_B	Boltzmann constant [J K^{-1}]
m_1	Atomic (resp, molecule) mass [kg]
N_MC	Number of MC simulation particles [–]
N_G	Concentration of gas atoms (or molecules) [m^{-3}]
$n_C(v)$	PSD in compartment C [m^{-6}]
o_idx	Destination index on GPU memory (integer) [–]
i^*	Number of atoms (resp. molecules) in critical cluster [–]
$p_A^{(i)}$	i-th property of particle A [unit of i-th property]
p_s	Saturation pressure [Pa]
$Q_{A\to B}$	Volumetric flow rate of carrier gas/liquid from compartment A to B [m^3 s^{-1}]
R	Mixing ratio for breakage scheme [–]
R_N	Nucleation rate [m^{-3} s^{-1}]
S	Supersaturation [–]
S_sep	Separation function for screen [–]
s_f	Reciprocal of stochastic resolution [m^{-3}]
T	Temperature [K]
t	(simulation) time [s]
t_char	Characteristic time [s]
v	Particle volume [m^3]
v^*	Kelvin volume [m^3]
v_M	Atomic (resp. molecular) volume [m^3]
V_C	Volume within compartment C filled with carrier liquid (or gas) [m^3]
W_i	Statistical weight of MC particle i [m^{-3}]
α_i	Merging weight for property i
β	Coagulation kernel [m^3 s^{-1}]
γ	Breakage function [–]
ε	Maximal admittable merging error [–]
τ	Time step [s]
σ	Surface tension [N m^{-2}]

Indices

0	Initial values

1 Introduction

The solution of the population balance equation (PBE) [1] plays an important role in a wide area of applications ranging from natural sciences to many fields of engineering [2]. Especially the modelling of chemical engineering problems such as crystallization [3], milling [4], granulation [5] or particle production in aerosol reactors [6] resort to PBE based process modelling.

The modelling of single apparatuses can be seldomly done with the assumption of spatial uniformity (as in e.g. [7]) and the application of Computational Fluid Dynamics (CFD) simulations and/or compartmental modelling becomes necessary in order to describe different zones of single apparatuses correctly.

CFD modelling allows a very high spatial resolution of the investigated system: 30,000 [8]−1,000,000 [9] cells are sometimes applied. The drawback of a CFD-PBE modelling is its enormous computational cost, hence a PBE has to be solved for each of these cells. Due to the high computational cost, only a rough approximation of the particle size distribution (PSD) is encountered in such simulations which typically resort to sectional methods with a low resolution (of ca. 12–30 discrete points or sections [10, 11]) or to the method of moments [12, 13], limiting the particle modelling mostly to one property—the size.

To overcome this problem, compartmental modelling is often applied, simplifying the spatial complexity to a low number of compartments (examples are 3 compartments or 10 compartments [14]). This allows, on the other hand, a more complex particle modelling with a more detailed sectional grid (e.g. 1000 discrete sections for 3 compartments [15]) or even with a Monte Carlo (MC) simulation, where more than one particle property allow to model a more complex morphology of the particles [14].

The PBE for a network of compartments, like presented in Fig. 1. can be described by the following formula:

$$
\begin{aligned}
\frac{\mathrm{d}n_C(v,t)}{\mathrm{d}t} = &+ \underbrace{\frac{1}{2}\int_0^v \beta_C(v', v-v')n_C(v',t)n_C(v-v',t)\mathrm{d}v'}_{\text{coagulation birth term}} \\
&- \underbrace{n_C(v,t)\int_0^\infty \beta_C(v,v')n_C(v',t)\mathrm{d}v'}_{\text{coagulation death term}} \\
&+ \underbrace{R_{\mathrm{N},C}(t)\cdot\delta(v-v_C^*(t))}_{\text{nucleation}} \underbrace{-\nabla_v(G_C(v,t)n_C(v,t))}_{\text{growth(G>0)/evaporation(G<0)}} \\
&\underbrace{-b_C(v)\cdot n_C(v,t)}_{\text{breakage death term}} + \underbrace{\int_v^\infty b_C(v')\cdot n_C(v',t)\cdot\gamma_C(v|v')\mathrm{d}v}_{\text{breakage birth term}} \\
&+ \sum_{\text{inflow from all compartments } i} f_{i\to C}\cdot n_i(v,t) \\
&- \sum_{\text{outflow to all compartments } i} f_{C\to i}\cdot n_C(v,t)
\end{aligned}
\tag{1}
$$

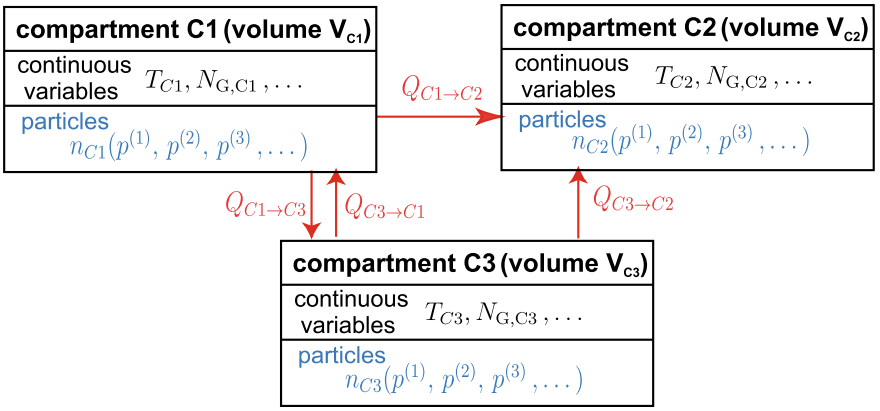

Fig. 1 A network of compartments. Each compartment C_i models parts of a reactor (or equipment) volume, which is filled with the carrier gas (or liquid) with a volume V_C. The compartment contains a PSD, n_C, and is described by other continuous variables, like temperature T_C, a gas concentration $N_{\mathrm{G},C}$, etc

where the coagulation kernels β_C, growth rates G_C, nucleation rates $R_{\mathrm{N},C}$ and sizes of the nucleating particles v_C^*, breakage rates $b_C(v)$ and breakage functions $\gamma_C(v|v')$ can be defined differently for each compartment C . The shown particle exchange flowrates $f_{i\to C}$ and $f_{C\to i}$ may assume constant values, or reflect more complex—nonlinear—and particle size or time dependent forms. The given volumetric flow rates $Q_{A\to B}$ (shown in Fig. 1) of the carrier gas (or liquid) and the volumes of the carrier gas (or liquid) of the outflow compartments, V_A, are thereby used in order to determine the particle exchange flowrates via:

$$f_{A\to B} = Q_{A\to B}/V_A \tag{2}$$

In this way, a complex reactor structure can be modelled in more detail [16, 17] or the interconnection of single processing units in a flowsheet simulation can be analyzed [15, 18, 19].

Although Eq. (1) describes only one particle property, the volume v, one could interpret v as a vector describing multiple properties of the particle, such as volume ($p^{(1)}$), surface area ($p^{(2)}$), wet content ($p^{(3)}$), and so on, as suggested in Fig. 1. Only a stochastic modelling is able to solve Eq. (1) for a high number of properties and render the complete particle morphology.

In the following, stochastic solution strategies for Eq. (1) will be discussed in the frame-work of an operator splitting approach meaning that the single processes coagulation, nucleation, growth/evaporation, breakage and transport of particles are decoupled for short periods of time τ. The approximation error introduced by this decoupling can be minimized by a choice of a low enough separation time step τ. For this reason, the solution strategies for single processes, like coagulation, nucleation, growth/evaporation and breakage are discussed for one compartment first. The

implementation of the coagulation in the framework of a compartmental network, as well as the transport between single compartments is discussed in the section afterwards, where the modelling of multiple compartments is applied.

2 Weighted Monte Carlo Particles for the Solution of the Population Balance Equation

The use of weighted simulation particles (a particle with weight w represents w real particles within a given reactor volume) has several advantages: it allows to describe the interaction between simulation particles having different concentrations coming from different cells or compartments [14, 20, 21]. It can also be used as a tool to control the number of simulation particles (e.g. to gain numerical accuracy). In the following, some techniques will be introduced to solve the single mechanisms presented in Eq. (1) by the application of weighted MC particles.

2.1 Coagulation

The correct description of the coagulation rates for the weighted particles, especially for a complex coagulation scheme, like the one introduced Zhao et al. [22] shown in Fig. 2, poses a great difficulty.

The authors [22] presented the 'ficticious particle theory' which leads to the following modified coagulation kernel:

$$\beta^{(fp)} = \frac{2W_j \max\left(W_i, W_j\right)}{W_i + W_j}\beta \tag{3}$$

The weights of the particles are denoted by W_i and W_j. The coagulation kernel β describes the coagulation of the original (non-weighted) system—which might be the Brownian kernel for the free molecular regime, etc. The resulting coagulation rate is asymmetric, making a distinction necessary, whether particle i coagulates with j or vice versa. This definition is 1) difficult to understand conceptually and 2) difficult to extend on other process—like nucleation or transport of fictitious particles.

We developed in [23] the concept of the stochastic resolution which describes each coagulation in the frame-work of equally weighted MC-particles, where each MC-particle describes s_f real particles. The value for the parameter s_f can be set arbitrarily. Figure 2 shows that the setting $s_f = W_{\min} = \min\left(\mathrm{W_i}, \mathrm{W_j}\right)$ leads to the correct description of the coagulation-scheme. The scaling factor s_f depends on the chosen coagulation pair, so that different coagulation-events are described in different stochastic resolutions.

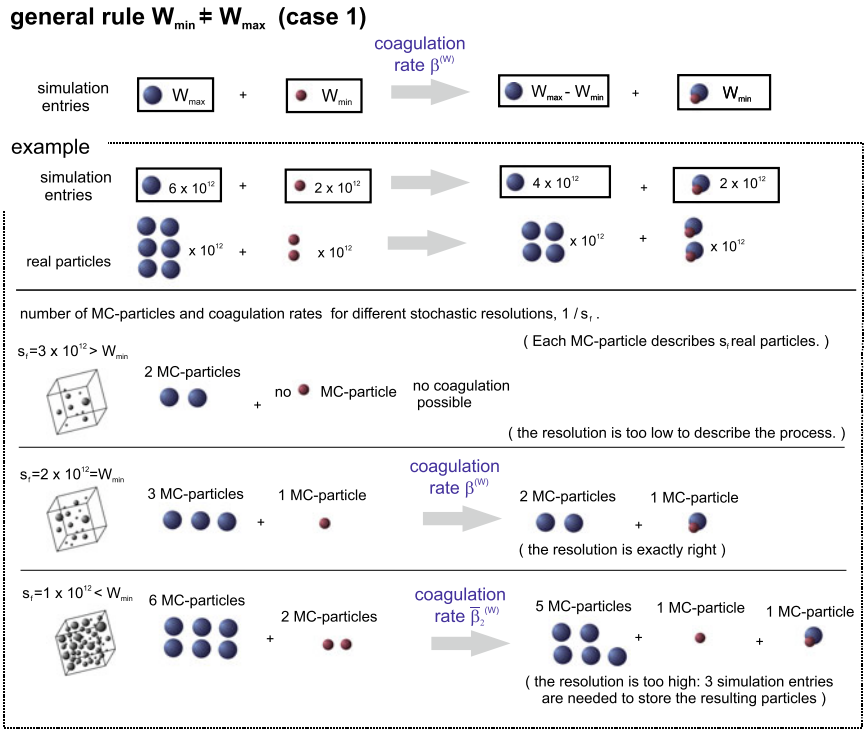

Fig. 2 The concept of 'stochastic resolution' can be used to describe the coagulation-scheme developed Zhao et al. [22]. Only the choice for $\mathbf{s_f} = \mathbf{W_{min}}$ leads to the correct description of the general rule presented in the 'simulation entries' line

The coagulation rate $\beta^{(w)}$ for this coagulation-scheme can be derived from the population balance equation:

$$\frac{\mathrm{d}n(v)}{\mathrm{d}t} = \frac{1}{2}\int_0^v \beta\left(v-v', v'\right)n\left(v-v'\right)n\left(v'\right)\mathrm{d}v' - n(v)\int_0^\infty \beta\left(v, v'\right)n\left(v'\right)\mathrm{d}v' \tag{4}$$

Instead of the 'original' concentrations $n(v)$, the concentrations of the MC-systems $n^{(MC)}(v) = \frac{n(v)}{s_f}$ are being considered. The multiplication of the PBE with the factor $\frac{1}{s_f} = \frac{1}{W_{\min}}$ leads to the following modified coagulation rate of the MC-particles: $\beta^{(MC)} = W_{\min} \cdot \beta$. Hence there is one MC-particle of the $W_{\min}$-species and $\frac{W_{\max}}{W_{\min}}$ MC-particles of the $W_{\max}$-species, the overall rate for the coagulation between one $W_{\min}$-MC-particle and one of the $W_{\max}$-MC-particles is:

$$\beta^{(w)} = \frac{W_{\max}}{W_{\min}} \cdot \beta^{(MC)} = W_{\max} \cdot \beta \tag{5}$$

The second case $W_{max} = W_{min}$, which is not shown in Fig. 2, is also described with the resolution $s_f = W_{min}$. Both particle species are described by only one MC-particle, so that only one MC-particle can be found after the coagulation. In order to apply the constant number scheme, the weight of the simulation entry representing this particle is divided by two and the particle properties are stored in both positions.

The thus derived coagulation kernel $\beta^{(w)}$ is easier to calculate than the originally introduced $\beta^{(fp)}$ —a speed up of the simulation up to 10% could be noticed. Due to its symmetric form, computational advantages for the implementation of the inverse method can be expected, as only half of the computations of the $\beta^{(w)}$ kernel are necessary. The simulation results of particle coagulation for the newly estimated coagulation kernel $\beta^{(w)}$ could be found to be as accurate as the $\beta^{(fp)}$-kernel results (which show excellent agreement with the solution produced by means of the Discrete-sectional-method in the first place) within the MC-stochastic noise [23].

2.2 Nucleation

Homogeneous nucleation is a mechanism that leads to the formation of new particles, which have to be included among the simulation entries. Constant number simulation-schemes sum up all possible algorithms, which update—somehow—the simulation properties, but keep the number of the used simulation entries constant. Keeping the number of simulation entries constant ensures a constant level of stochastic accuracy and makes a simple prediction of needed computational resources possible. Figure 3 shows possible constant-number nucleation algorithms. They can be used to model the inclusion of the nucleation particles or particles included by other processes: like breakage or transport.

The random removal algorithm has been introduced Lin et al. [24] in the framework of the concept of a 'constant number Monte Carlo simulation' which is based on the not-weighted particle scheme. The algorithms applying the merging step are based on the weighted-particles scheme and the concept of the merging error. They cannot be used for non-weighted MC simulations. The merge-List is created each 100 merge-steps and contains 100 simulation entries with low-weights.

2.2.1 Merging

The concept of 'merging' of simulation entries is proposed in [23]: if two simulation entries with exactly the same properties are merged, the resulting representation of the particle size distribution will not change and all the physical processes will be described in the same way. If the simulation entries differ slightly in their properties, a small error will be introduced.

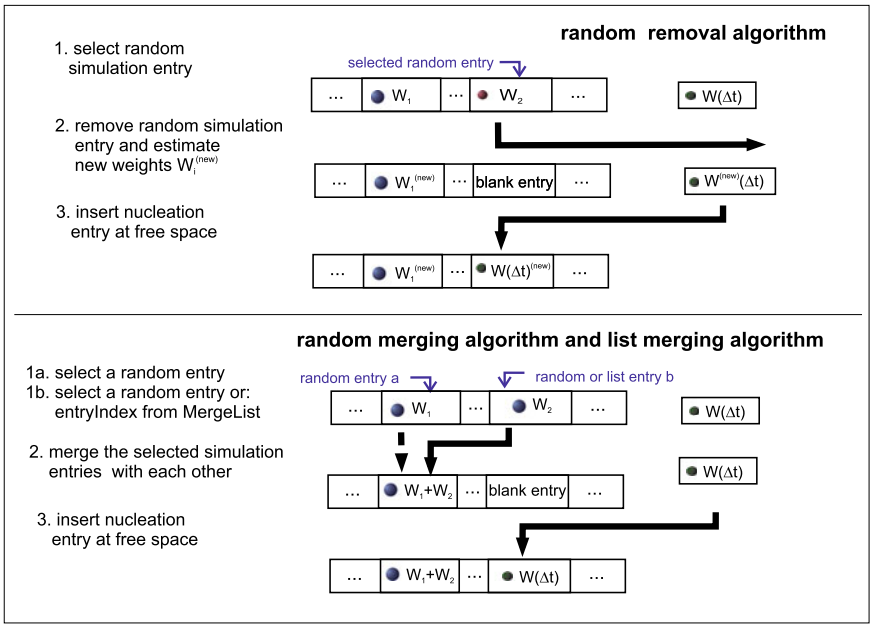

Fig. 3 Different simulation algorithms which combine the MC constant-number simulations based on weighted particles with the nucleation process

The merging scheme:
Each simulation entry contains the weight W, and other properties $p^{(1)}, p^{(2)}, p^{(3)}, \ldots$ of the rendered part of the particle population (where $p^{(i)}$ could be the volume, porosity, electric charge, etc.). If the simulation entry A (weight W_A) and B (weight W_B) are merged into the new simulation entry C (weight W_C and several properties $p_C^{(i)}$), the following two rules should apply:

(i) The total weight of the simulation-entries before and after the merge-step should be preserved:

$$W_C = W_A + W_B \tag{6}$$

(ii) If the total amount of the particle-properties is preserved one can write:

$$W_C \cdot p_C^{(i)} = W_A \cdot p_A^{(i)} + W_B \cdot p_B^{(i)} \Leftrightarrow p_C^{(i)} = \frac{W_A \cdot p_A^{(i)} + W_B \cdot p_B^{(i)}}{W_A + W_B} \tag{7}$$

This is the most simple assumption which should hold true for most of the physical applications, but other definitions—which make a more complex calculation necessary can be used. E.g., if the described property is the diameter d but the volume v is preserved, one can write (assuming sphere-like particles):

$$W_C \cdot \frac{\pi}{6}(d_C)^3 = W_A \cdot \frac{\pi}{6}(d_A)^3 + W_B \cdot \frac{\pi}{6}(d_B)^3$$
$$\Leftrightarrow d_C = \left(\frac{W_A \cdot (d_A)^3 + W_B \cdot (d_B)^3}{W_A + W_B}\right)^{1/3} \tag{8}$$

The merging error:
The error introduced into the simulation by the merging of the simulation entries can be estimated by the following formula:

$$E_{(A,B)} = \sum_{\text{all roperties } i} \alpha_i \cdot \left(\frac{p_A^{(i)} - p_B^{(i)}}{\min\left(p_A^{(i)}, \cdot p_B^{(i)}\right)}\right)^2 \tag{9}$$

where α_i are merging-weights, which can be set arbitrarily—depending on the physical process—they can be interpreted as a measure of the severity, which the deviation of the property $p_A^{(i)}$ from $p_B^{(i)}$ would have—compared to the deviation of other properties $p_A^{(j)}$ from $p_B^{(j)}$.

2.2.2 Parallel Merging Algorithm

The merging-algorithms presented in Fig. 3. use the selection of random simulation entries, resulting therefore in a random merging error $E_{(A,B)}$—which may be excessively high. The smallest possible merging error can be estimated by the comparison of all simulation-entry-pairs—which would prove very costly: $N_{\text{MC}} \cdot (N_{\text{MC}} - 1)/2$ comparisons are necessary, if N_{MC} simulation-entries are used. A sound compromise between both scenarios is the sampling of a 'representation of the simulation entries' and the estimation of the minimum merging error of this representation. A parallel algorithm can be applied for this purpose, easily adaptable for GPU computing: the merging errors for $(N_{\text{MC}} - 1)$ pairs of simulation-entries can be computed in parallel and the comparison of the calculated merging errors is done within only $\log_2 N$ computational steps, like shown in Fig. 4.

2.2.3 Validation of Coupled Coagulation and Nucleation

The nucleation is combined with the simulation of coagulation in two steps: First, a classical event-driven MC coagulation step is performed, this includes the selection of the coagulation pair via the fast parallel A/R-method introduced Wei [25] with the

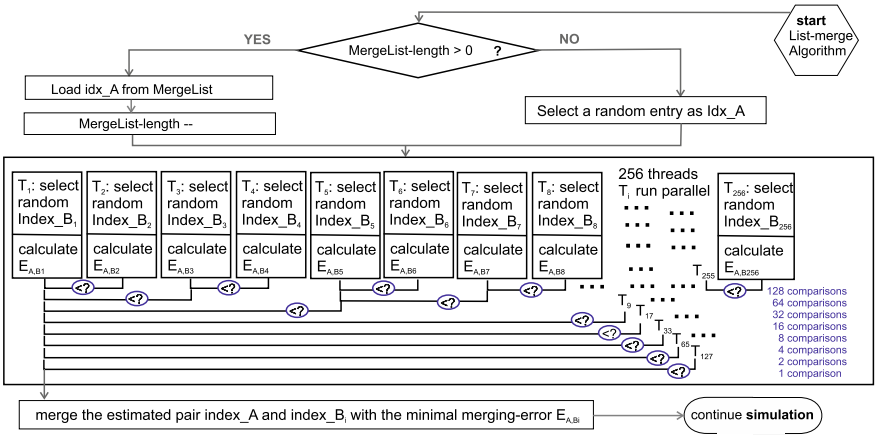

Fig. 4 The parallel low weight merging algorithm [23]: only 8 parallel thread-executions are necessary in order to estimate the pair (1 out of 256) of simulation-entries with the minimal merging error

weighting scheme based on the stochastic resolution—the actual time-step $\Delta\tau_{MC}$ is evaluated in this step, too. In a second step, the number of the nucleating particles is estimated, for this purpose the solution of the differential equation (which describes the nucleation) can be approximated by the Euler-method (more complicated Runge-Kutta methods or other ODE-solvers can be used for the modeling of the interaction with the continuous phase [26, 27]). The newly created simulation entry is then included by means of the merging algorithms from Fig. 4.

A typical benchmark test case[1] shows the advantage of the merging of particles compared to the random removal method, as sketched in Fig. 3. A part of the simulation results already discussed in [23] are summarized in Table 1, where the mean values d_g and standard deviations Δd_g of the geometric mean diameter are shown. Hence each MC simulation is executed with a different sequence of random numbers, the resulting geometric mean diameter $d_g^{(i)}$ is different for each simulation i. The arithmetic mean values (d_g) and standard deviations Δd_g of 100 $d_g^{(i)}$ values resulting from of 100 MC simulations are shown. (Similar findings could also be presented for the number concentration of the particles or the geometric standard deviations of the resulting PSDs.) It can be clearly seen that the application of merging techniques leads to significantly lower noise levels. For example, 10,000 simulation particles in combination with the random removal method cannot reach the same precision levels as the application of 1000 simulation particles in combination with the low

[1] A constant nucleation rate R_N is assumed, so that newly introduced simulation entries have the weight $W_0 = R_N \cdot \Delta\tau_{MC}$ and a predefined diameter d_0. For the simulation has been set: $R_N = 10^{14}\,\frac{1}{\mathrm{m^3\,s}}$, $d_0 = 3$ nm. A monodisperse population with an initial concentration of $10^{17}\,\frac{1}{\mathrm{m^3}}$ has been used as start condition, the initial MC particles are equally weighted. The temperature was set to 300 K and the particle density to $1\,\frac{\mathrm{g}}{\mathrm{cm^3}}$. The simulated time was ca. 25.8 s, which is 500 times the characteristic time needed to reach the self-preserving distribution [28] due to coagulation.

Table 1 Values of the geometric mean diameter and simulation times (CPU time) for the discrete sectional (DS) method and MC simulations using Random removal (RR) and Low weight Merging (LWM) with 1000 and 10,000 MC particles

Method	Mean value d_g [nm]	Standard deviation Δd_g (absolute) [nm]	$100\Delta d_g/d_g$ (percent) [–]	CPU time [s]
DS (20 100)	4.736	–	–	8.4
DS (250 380)	4.740	–	–	332.1
RR 1000	4.820	0.544	11.29	330.3
RR 10,000	4.736	0.180	3.79	3964.2
LWM 1000	4.733	0.100	2.11	300.4
LWM 10,000	4.742	0.033	0.70	3643.2

The number of used sections and discrete points for DS are indicated by the values in the brackets (discrete points, sections). The exact 1D grid specifications are described in [23]

weight merging. It should also be noted that the computation of 10,000 MC particles requires ca. 10 times larger computing times than of 1000 particles. The computing times shown in Table 1 refer to the simulation of 100 MC simulations run in parallel on the GPU and one discrete-sectional run sequentially on the CPU.

2.3 *Coupled Condensational Growth and Evaporation, Coagulation and Nucleation*

A varying nucleation rate, R_N, as well as a changing critical nucleus size, d^*, is often encountered when a metallic vapor is created and then cools down, leading to the nucleation rate increasing over tens of orders of magnitude and then going down when the free atoms have been largely consumed. The size of the critical nucleus, d^*, on the other hand, decreases from very large values to atomic sizes, and rises again when the nucleation rate is increasing. This presents a severe test for the numerical solution, as the source term is moving rapidly through the size spectrum, leading to a dramatic change of the growth and evaporation rates of the simulated particles, as well. Hence particles larger than the nucleating particle (i.e. with volumes $v_i > v^*$) will grow, while those which are smaller (i.e. with volumes $v_i < v^*$) will evaporate. This is described by the equation of the growth-rate $G(v_i, N_G)$ of particles with the volumes v_i in the free-molecule regime [29]:

$$G(v_i, N_G) = \frac{\mathrm{d}v_i}{\mathrm{d}t} = \frac{v_M \cdot \pi \cdot d_i^2}{\sqrt{2\pi \cdot m_1 \cdot k_B \cdot T}} \cdot (k_B \cdot T \cdot N_G - p_s \cdot \exp\{4 \cdot \sigma \cdot v_M/(k_B \cdot T \cdot d_i)\}) \quad (10)$$

The value of the critical diameter is given by:

$$d^* = 4 \cdot \sigma \cdot \upsilon_\mathrm{M}/(k_\mathrm{B} \cdot T \cdot \ln(S)) \quad \text{with} \quad S = \frac{N_\mathrm{G} k_\mathrm{B} T}{p_\mathrm{S}} \tag{11}$$

So that $G(v_i, N_\mathrm{G}) = 0$ for $v_i = v^*$ and $G(v_i, N_\mathrm{G}) > 0$ for $v_i > v^*$. The growth rate of the particles is also dependent on the number of atoms (or molecules) of the condensable material in the gaseous phase, N_G. The depletion (resp. increase) of the monomers due to condensation on (resp. evaporation of) the particles is described by a mass balance:

$$\frac{\mathrm{d}N_\mathrm{G}}{\mathrm{d}t} = -\sum_i W_i \cdot G(v_i, N_\mathrm{G})/\upsilon_\mathrm{M} - R_\mathrm{N} \cdot i^* \tag{12}$$

Thereby, the nucleation of particles is also taken into account by the nucleation rate R_N and the number of atoms (resp. molecules) i^* in a particle of the critical size d^*.

We proposed an operator-splitting based approach for the parallel solution of this system [26, 27, 30], by decoupling the growth-evaporation and nucleation mechanism from the coagulation mechanisms for short periods of time, like in the presented coupled simulation of coagulation and nucleation in Sect. 2.2.3. The condensational growth (resp. evaporation) of the simulated particles is solved in parallel by application of time-step adaptive Runge-Kutta techniques (see e.g. [31]). A parallel addition algorithm, similar to the presented parallel comparison algorithm in Fig. 4, is used for the fast calculation of the term $\sum_i W_i \cdot G(v_i, N_\mathrm{G})$ in Eq. (12). A more detailed description of this approach can be found in [30]. This modelling of the continuous PSD with discrete MC particles avoids the effect of numerical diffusion [32, 33], encountered in models describing particle growth, in analogy to moving grid techniques for sectional methods [34].

It has be shown, that all of the mentioned mechanisms (i.e. evaporation, condensation, nucleation and coagulation) have to be considered and that the omission of one of these mechanisms leads to severe deviations from the 'complete' system [26].

The thus introduced methodology can be used to determine the influence of different formulations of nucleation rates and allows to identify experimental conditions for the experimental investigation of those. There exist several approaches for the description of nucleation theories [35]. We consider in the following these three expressions for the nucleation rate R_N, as discussed in [36]:

$$R_\mathrm{N}^{(\mathrm{cou})}(N_\mathrm{G}) = N_\mathrm{G} \cdot \sqrt{\frac{2\sigma}{\pi \cdot m_1} \frac{p_\mathrm{s}}{k_\mathrm{B} \cdot T}} \cdot v_1 \cdot \exp\left(-\frac{16 \cdot \pi \cdot \sigma^3 \cdot v_\mathrm{M}^2}{3 \cdot k_B^3 \cdot T^3 \cdot \ln(S)^2}\right),$$

Table 2 Material constants for Ag at a temperature of 1300 K

Symbol	Description	Value	Source
m_1	Atomic mass	1.792×10^{-25} kg	[37]
v_M	Atomic volume	1.922×10^{-29} m^3	[37]
p_s	Vapor pressure	1.324 pa	[37]
σ	Surface tension	0.9024 J/m^2	[38]

$$\text{with} \quad S = \frac{N_G k_B T}{p_s} \tag{13}$$

$$R_N^{(gir)}(N_G) = R_N^{(cou)} \cdot \exp\left((36 \cdot \pi)^{\frac{1}{3}} \cdot \frac{\sigma \cdot v_1^{\frac{2}{3}}}{k_B \cdot T} \right); \quad R_N^{(cls)}(N_G) = R_N^{(cou)} \cdot S \tag{14}$$

The influence of these different nucleation theories has been discussed for atmospheric simulation scenarios [27] and are briefly sketched for a metallic system describing the nucleation of Ag vapor in the following. The material parameters in Eqs. (10–14) assume values summarized in Table 2 at a temperature of $T = 1300$ K.

The simulation of a isothermal nucleation induced due to an initial supersaturation of $S_0 = 100$ of Ag vapor and the presence of an initial (background) PSD with a mean geometric diameter of 2 nm and a geometric standard deviation of 1.2 rendering a total number-concentration of 10^{16} m^{-3} is used as an initial condition. The temperature is kept constant to 1300 K during the course of the simulation.

The monomer concentration exhibits the fastest depletion rate for the Girshick-based nucleation rate, as is shown in Fig. 5a. This is due the highest nucleation rate which is plotted in comparison with other nucleation theories in Fig. 5b. This leads in turn to the highest particle concentrations for the Girshick-based nucleation theory (see figure Fig. 5c). The nucleation theories show the most striking differences at the early stages of the simulation, for longer simulation times, (i.e. t > 0.01 s), similar

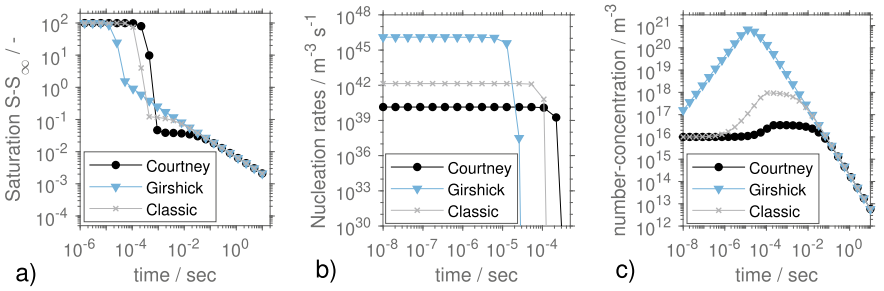

Fig. 5 Isothermal Ag particle synthesis with initial PSD and supersaturation $S_0 = 100$. The saturation surplus $S - 1$ (**a**), the corresponding nucleation rates (**b**) and the total particle number-concentrations (**c**) are shown. The nucleation rates $R_N^{(cou)}$ (Courtney) $R_N^{(gir)}$ (Girshick) and $R_N^{(cls)}$ (Classic) are defined in Eqs. (13) and (14)

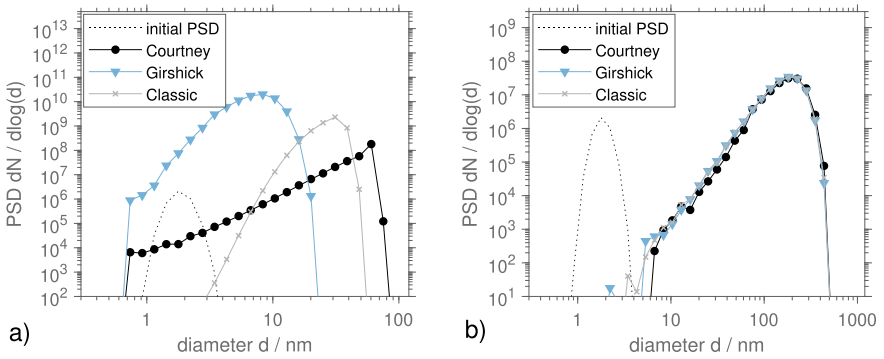

Fig. 6 Isothermal Ag particle synthesis with initial PSD and supersaturation $S_0 = 100$. Resulting PSDs after $2.2 \cdot 10^{-4}$s (**a**) and $1.4 \cdot 10^{-1}$s (**b**) for the nucleation rates $R_N^{(kin)}$ (Kinetic) $R_N^{(gir)}$ (Girshick) and $R_N^{(cou)}$ (Courtney) defined in Eqs. (13) and (14)

supersaturations and concentrations can be observed (in Fig. 5 a-c). This is a signature of the similar PSDs resulting from the simulation, as they are shown in Fig. 6.

The PSDs at the initial stages of the simulation (see Fig. 6a) show tremendous differences and allow to attribute each of the different shapes to a specific nucleation theory. For longer simulation times, on the other hand, a self-preserving PSD is reached and all of the presented nucleation theories can be attributed to the shown PSDs. The shown self-preserving PSD is the result of the complex coupling of the mechanisms of coagulation and evaporation. This PSD deviates from the self-preserving PSD for the coagulation only as reported Vemury and Pratsinis [28]. Similar self-preserving PSDs deviating from the self-preserving PSD for coagulation only have been already reported for similar metallic systems [26] and [30]. This approach allows thus to roughly approximate a time window, for which specific differences between the different nucleation rates can be expected. Allowing thus to give hints for measurements set-ups investigating the specific forms of the nucleation rate R_N.

2.4 Breakage

Breakage of particles is relevant for the modeling of particle mills, but also for granulation, emulsions, sprays and even for aerosols when agglomerates break up by collisions or turbulences. The rendering of the large number of particles which are produced during the continuous breakage process poses a major problem for MC simulations, because large computational resources have to be provided for this purpose. In a typical milling process, for example, reductions of the particle diameters from 500 to 0.5 μm are encountered, the same amount of volume, which is rendered by one simulation particle with a size of 500 μm has to be rendered by

10^9 simulation particles with a diameter of 0.5 μm, if all particles represent the same number concentration of real particles.

Traditional solutions of this problem encompass the discretization of the particle property into bins [39], which would render the combination with the developed growth/evaporation algorithm impossible, and constant-number approaches [40], which are known to produce a high level of statistical noise [41].The application of merging schemes [42] (i.e. the approximation of the properties of several simulation particles by one simulation particle) would pose an attractive alternative. However, the vast amount of newly resulting particles makes a lot of merging steps necessary, leading to large computing times. A recent constant-number method has been presented [41], which renders the breakage event of one particle into many fragments by a single particle. The size of the fragment is selected stochastically, the use of many simulation particles leads to the correct distribution of fragment sizes. This scheme is only able to render the parts of the particle size distribution which represent high number concentrations of the particles. Furthermore, only binary breakage can be described.

We developed an alternative approach [43] for the derivation of the breakage scheme by resorting to the argument that the breakage of many MC-particles with equal properties and weights has to lead to a particle size distribution (PSD) of fragments, which is described by the corresponding breakage kernel. It allows to formulate any probability distribution function (PDF) with which the new volume of the simulation particle is selected by adjusting the statistical weight of the resulting fragments depending on 1) the selected particle properties, 2) the used PDF and 3) the given breakage density function. This newly proposed scheme encompasses the already introduced SWA schemes, especially a number-based (NB, named SWA1 in [41]) and volume-based (VB, named SWA2 in [41]) breakage scheme, and it makes novel formulations possible: the low volume scheme (LV), which renders preferably fragment particle sizes at the lower end of the size spectrum, and the combination of LV with the NB (NB-LV) or VB (VB-LV). Exemplary simulation results are shown in Fig. 7. It can be seen that the SWA methods (NB and VB) are only able to render large particle sizes, and that LV, NB-LV and VB-LV are able to render the whole spectrum of particle sizes. Smaller noise levels are found for VB and specific VB-LV schemes, making both more suitable for prolonged simulations than the other presented methods. The LV based simulation method fails to predict the correct PSDs for longer simulation times. For this reason, the combinations of LV with VB or NB are needed, in order to ensure the correct shapes of the PSDs for longer simulation times. The combination ratio $R \in (0, 1)$ between the LV and NB leads to different schemes, while lower ratios R lead to a higher representation of low-volume MC particles, they also lead to higher noise levels: the setting $R = 0.6$ leads to more statistical noise than $R = 0.9$, as it can be seen in Fig. 7. The adaptive resetting of the factor R in order to avoid the systematical errors, as it is shown in Fig. 7 for the LV scheme is briefly discussed in [44].

The required simulation times are listed in Table 3, 10^5 simulation particles are required in order to ascertain a computational accuracy of less than 1%. (I.e. the

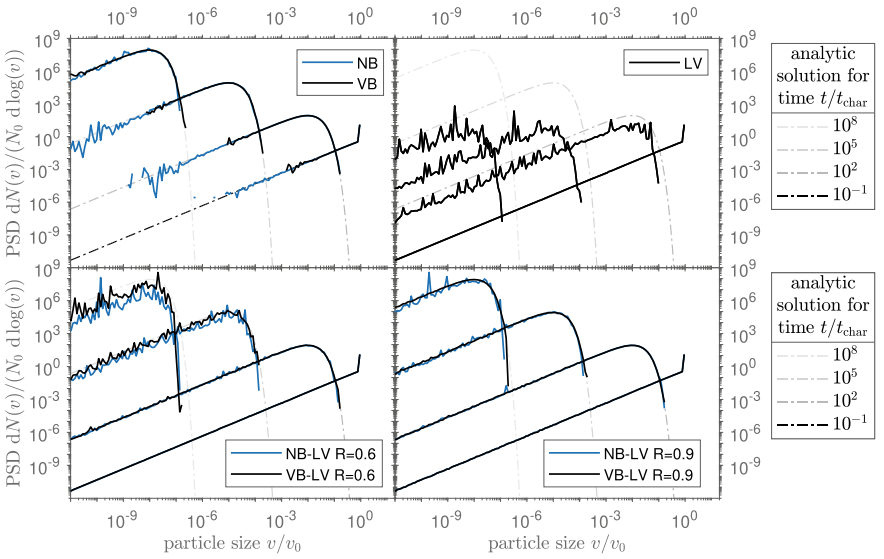

Fig. 7 Resulting PSDs from the simulation of a test cases describing a binary, homogeneous particle breakage function $\gamma(v_{\mathrm{F}}, v_{\mathrm{P}}) = 2/v_{\mathrm{P}}$ and a breakage rate $b(v) = v$ (test case 1 in [43]) for a monodisperse initial condition v_0 and the thus defined characteristic time $t_{\mathrm{char}} = b(v_0)^{-1}$. The MC-simulations are compared with analytic solutions found in [46]

Table 3 Computational times required for the simulation of $t = t_{\mathrm{char}} \times 10^8$ in dependency on the used number of simulation particles

Simulation particles	NB	VB	VB-LV
1000	0.5 s	0.8 s	0.6 s
10,000	2.8 s	4.4 s	3.0 s
100,000	27.1 s	42.5 s	29.8 s

arithmetic standard deviation of the moments of the distributions performed for 100 different sets of random numbers is smaller than 1% of the mean value.)

3 Compartmental Population Balance Modelling

The modelling of flow-sheet simulations in the scope of an operator-splitting approach (see e.g. [47]) requires a specific time step management, so that ongoing simulations processes can be forced to stop at specific simulation time points. This issue is addressed first, in a second, longer paragraph, the implementation of particle transport between single compartments by means of weighted MC particles is introduced and some typical simulation scenarios are presented.

3.1 Time Step Control for Compartmental PBE Networks

The combination of simultaneous processes rendered by the PBE solver poses a challenging task, hence the characteristic time-scales for the corresponding processes may differ in several orders of magnitude and change vastly during the simulation. Although the developed algorithms for the breakage, coagulation and growth (resp. evaporation) already adapt to the optimal time-step for each single process (in the absence of other processes), the simulation of the combined coagulation, nucleation and growth is driven by the discrete coagulation processes providing an inherent MC time step τ_{MC}. This is a computationally advantageous setting, if the inherent growth step τ_{G} is smaller than the coagulation step τ_{MC}. The opposite case, in which τ_{G} is bigger than τ_{MC}, forces the simulation to use much smaller time steps τ'_{G} and thus to use much more computationally demanding growth steps. The incorporation of the breakage as a third process with an inherent time step τ_{B} may force the simulation to reset this step to a lower value τ'_{B} in a coagulation driven implementation, as well.

This situation becomes even more complicated, if the PBE is solved for different compartments and a particulate flow between the compartments is simulated. Consider, for example two compartments, in which coagulation takes place, so that compartment 1 has an intrinsic MC coagulation time step $\tau_{\mathrm{MC}}^{(C1)}$, while the second compartment has the inherent coagulation time step $\tau_{\mathrm{MC}}^{(C2)}$, the additional particulate flowrate between compartment 1 and compartment 2 might make the update of the particle populations due to the transport of particles each time interval τ_{Tr} necessary. It depends on the specific modelled application, whether the minimum of these three time steps has to be used, or some other minimal time step τ_{min} can be applied. In all cases, there exists the need, to perform, at least in one of the two compartments, a smaller time step than the one intrinsically provided ($\tau_{\mathrm{MC}}^{(C1)}$ and/or $\tau_{\mathrm{MC}}^{(C2)}$).

The application of time-driven MC methods [48] allows the setting of a variable time step, but this time step has to be set proportional to the intrinsic step in order to avoid systematical errors [49], although smaller values are allowed. The main disadvantage of this approach is, however, its computational costs, hence all possible coagulation pairs have to be checked for coagulation during the suggested time step—special book-keeping methods [50] might help to address this problem for the single simulation of coagulation but their usage is not possible[2] in the context of a PBE network modelling multiple simultaneous processes.

We have developed the concept of 'fractional MC time steps' [51], in order to address this problem. In the scope of this approach, we modified the fast GPU acceptance-rejection algorithm [25] in such a way, that an additional stochastic probability is formulated, whether the particles coagulate or not if a smaller time step than the intrinsic MC AR-time step is needed. We compared our methodology (marked

[2]Special modeling is necessary in order to capture the changes of the 'book kept' entries due to other non-coagulation processes—this might or might not be possible, depending on the specific process being modelled. Additionally, the tracking of the changes might prove more expensive than the application of the time-driven MC methods without book-keeping.

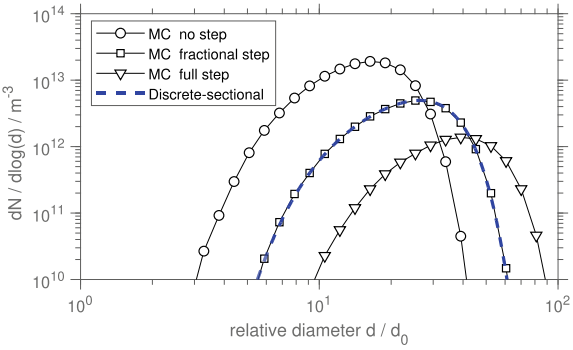

Fig. 8 PSDs resulting from simulation conditions as described in [51]

as 'MC full step') with (1) another approach from the literature [21], where no coagulation of the particles takes place in such an event (marked as 'no step') and (2) with the self-proposed approach, where the particles simply coagulate—even if the simulated time step is smaller than the intrinsic time step (marked as 'full step'). A typical isothermal coagulation scenario describing Brownian motion of particles in the free-molecule regime (full details can be found in [51]), leads to the following simulation results shown in Fig. 8, if the simulated system is forced to perform not the intrinsic MC time steps but an artificial time step of 1 ms. It can be clearly seen, that only the application of the fractional MC time steps leads to the correct description of the PSDs, which is in excellent agreement with the reference result gained by the application of the discrete-sectional method, as described in [52, 53].

3.2 Compartmental Monte Carlo Simulation

Modelling of MC particle transport as a stochastic process with discrete events is sometimes suggested [54]. Such a modelling, could—however— entail a large number of stochastic events for small simulation times and slow down the simulation considerably. The other disadvantage of such an approach is the potential increase of the stochastic noise of the simulation.

The description of weighted simulation particles makes novel simulation strategies for the transport possible, the adjustment of the statistical weight of each MC particle makes the exact description of the depletion of particles due to particle outflow possible—as is discussed in [20] (termed 'rescale outflow') and shown in the following. First, the description of a two-step (inflow and outflow) method is suggested and the merging and random removal techniques are briefly described, then the methodologies are validated and compared by simulations of exemplary flowsheets.

3.2.1 Transport of Weighted MC Particles

In the following, the transport of MC particles from one compartment to other compartments will be described. It consists of two steps: (1) the particle outflow and (2) the particle inflow. This is being realized by the computational implementation of 'streams' which are able to store a population of MC particles, as large as the population stored for each compartment.

In the first outflow step, particles are inserted into the streams. This can be easily done by copying all particles from the hold-up into the stream and adjusting the statistical weights accordingly, in the stream and in the hold-up. If, for example, the particles from compartment 1 stream into compartment 2 with the size v dependent relative rate $f_{1\to2}(v)$, then one can describe for each particle i the change of its statistical weight W_i for a small interval of time Δt as:

$$W_i(t+\Delta t) = W_i(t) - \Delta t \cdot f_{1\to2}(v_i) \cdot W_i(t) \tag{15}$$

This is shown as particle outflow step in Fig. 9. The new weights W_i^{s1} and $\overline{W}_i^{c1}$ are set to $W_i^{s1} = \Delta t \cdot f_{1\to2}(v_i) \cdot W_i^{c1}$ and $\overline{W}_i^{c1} = W_i^{c1} - W_i^{s1}$.

In the inflow step in Fig. 9, the particles from the streams are inserted into the compartments. Analogously to the already discussed nucleation of particles, one encounters at this step the problem of the limited CPU memory: each connecting stream contains as many particles as the destination compartment, so that only a fraction of all MC particles can be stored in the destination compartments. This problem has been solved in two ways in the here presented work: (1) randomly selected particles are removed from the simulation—adjusting the statistical weights in such a way, that the mass of the system remains constant as in the conventionally used constant number algorithms [55, 56] and (2) the particles are merged together using a parallel merge algorithm as it is briefly discussed in [57].

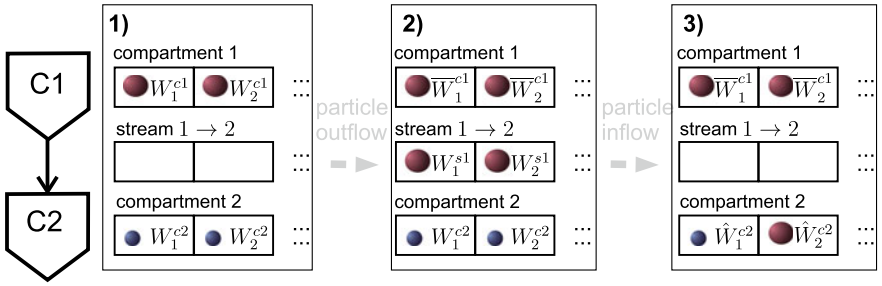

Fig. 9 MC particles stored in the memory assigned for compartment 1 and 2, as well as in the stream connecting both compartments. The stages (1) before the particle outflow (2) between outflow and inflow and (3) after the inflow during the simulation of a single time step are shown

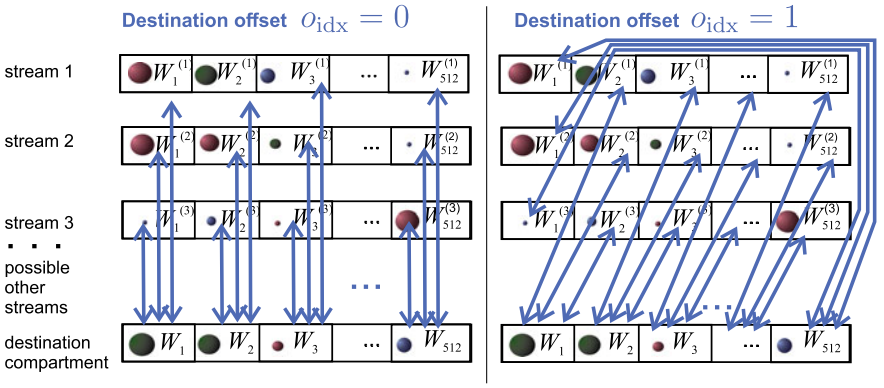

Fig. 10 Compartment-Stream merge pattern. Each double arrow represents one merge attempt. All merge attempts which are executed in parallel with the destination offset $o_{\mathrm{idx}} = 0$ are shown in comparison with all parallel merge attempts made for the offset $o_{\mathrm{idx}} = 1$

3.2.2 Parallel Merge Algorithm

The merging algorithm described in Fig. 4 could be used for the merging of MC particles within stream and the destination compartment. However, such an approach would be computationally not efficient due to the large number of MC particles ranging in typical applications between 1000 and 10000. This would imply 1000 or 10000 sequential or parallel invocations of the algorithm presented in Fig. 4. In order to accelerate the merging process, a novel parallel algorithm has been briefly sketched in [57] and is discussed here in more detail. The GPU's capability to process a large amount of data in parallel can be exploited in a more efficient way, if not only one (as in Fig. 4) but a large number of MC particles has to be merged together (as in Fig. 9).

The merging scheme described by Eq. (6) and (7) can be thereby used in combination with the merging error described by Eq. (9). A maximal admittable merging error ε can be formulated and all particle pairs (i, j) with a merging error $E_{i,j}$ (Eq. (9)) smaller than ε are merged together. A large number of parallel comparisons can thereby be performed, forming potential pairs for the merging by calculation of the merging errors of the pairs consisting of one particle in the destination compartment and one particle in one of the streams, as shown as 'Compartment-stream merge pattern' in Fig. 10. The destination offset, o_{idx}, is thereby increased by one after each comparison attempt, so that different pairs are formed for the calculation of the merging error. After 512 steps, all possible pairs between each of the compartment particle and another stream MC particle would have been checked in this way.[3] An internal check between particles stored in the compartment (resp. streams) is also

[3] In order to use the GPU efficiently, larger particle numbers (like e.g. 10000) have to be divided into data blocks consisting of e.g. 512 particle numbers. In the here presented implementation, particle numbers that are multiples of 512 are considered.

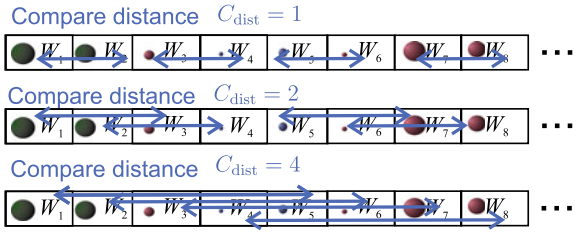

Fig. 11 Intern merge pattern. All merge attempts which are executed in parallel within one stream or compartment with different compare distances C_{dist}

performed, in order to address situations, in which the populations in the streams are so different from the population in the compartment, that a merging is only possible with very high merging errors. These 'internal merges' are shown in Fig. 11. The multiplication of the compared distance C_{dist} with the factor of 2, ensures the treatment of different pairs after each invocation of the routine.

The complete algorithm for the parallel merging is shown in Fig. 12, the following settings are set arbitrarily:

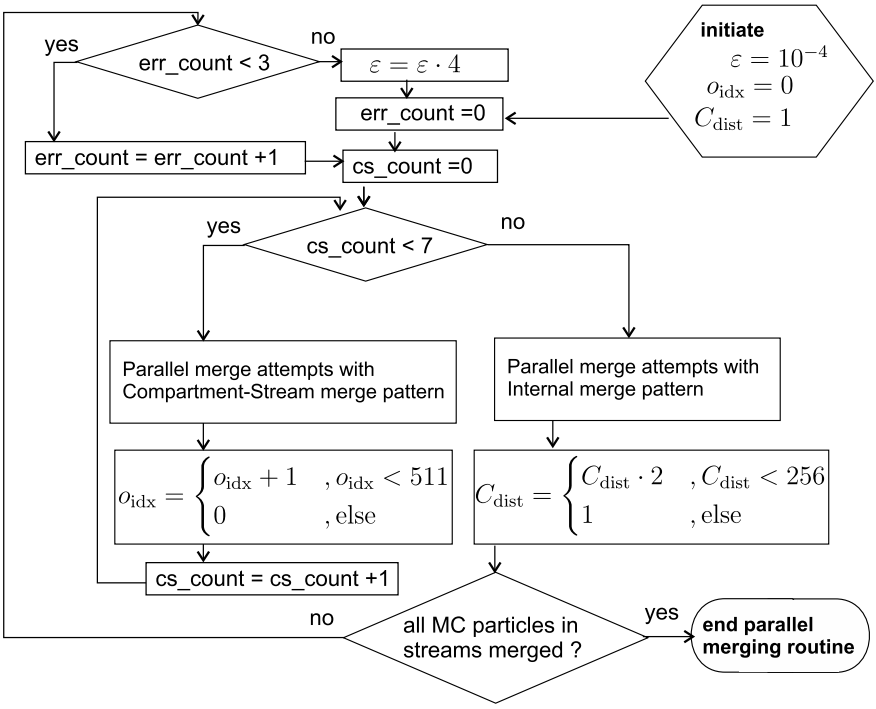

Fig. 12 Sketch of the merge algorithm for MC particle insertion. The Compartment-Stream merge pattern is shown in Fig. 10 and the internal merge pattern is shown in Fig. 11

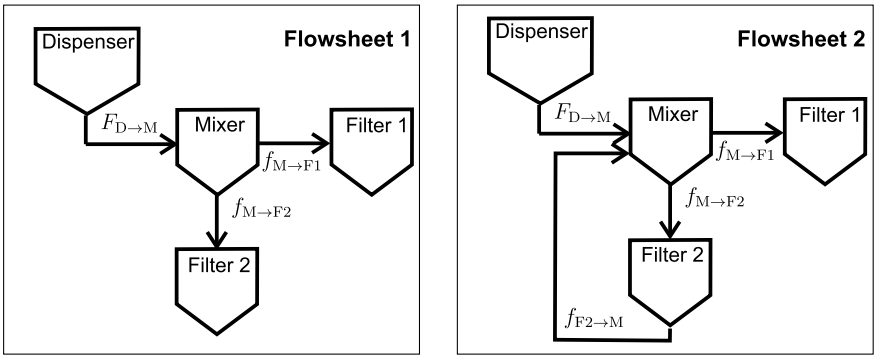

Fig. 13 Exemplary flow-sheets with and without a feedback stream

- 8 Compartment-Stream merge patterns are performed for each invoked intern merge-pattern ('cs_count < 7' in Fig. 12). This combination is invoked each time before the (rather costly) check if all particles have been merged is initiated.
- After each 4 unsuccessful checks if all particles have merged, the maximal admittable merging error is increased ('err_count < 3' in Fig. 12).
- The maximal admittable merging error is increased by a factor of 4 ('$\varepsilon = \varepsilon \cdot 4$').

These settings prove to work efficiently for the presented test cases in the validation section. Other settings might be more appropriate for other application scenarios and the dynamic adaptation of these values to given simulation conditions might pose an interesting research topic for future investigations.

3.2.3 Validation

The proposed simulation techniques are validated on several test-cases, which reflect simple engineering problems and are shown in the figures Figs. 13 and 14. The shown flowsheets increase in complexity, hence the implementation of a tear stream (Flowsheet 2, Fig. 13) or a sieve unit (Flowsheet 3, Fig. 14) or both in combination (Flowsheet 4, Fig. 14) poses a greater challenge for the numerical solution than the simple flowsheet 1 in Fig. 13. This methodology allows to identify the specific simulation scenario, for which conventional MC strategies are not suitable and the here presented methodology based on weighted MC particles has to be applied in order to obtain correct results.

For each of the presented units in Fig. 13, the evolution of the PSDs n_{M} (mixer), n_{F1} (filter 1) and n_{F2} (filter 2) can be modelled by the explicit set of differential equations:

$$\begin{aligned}\frac{\mathrm{d}n_{\mathrm{M}}(v,t)}{\mathrm{d}t} &= + f_{\mathrm{F2}\to\mathrm{M}} \cdot n_{\mathrm{F2}}(v,t) - f_{\mathrm{M}\to\mathrm{F1}} \cdot n_{\mathrm{M}}(v,t) - f_{\mathrm{M}\to\mathrm{F2}} \cdot n_{\mathrm{M}}(v,t) \\ &\quad + F_{\mathrm{D}\to\mathrm{M}} \cdot n_{\mathrm{D}}(v,t)\end{aligned}$$

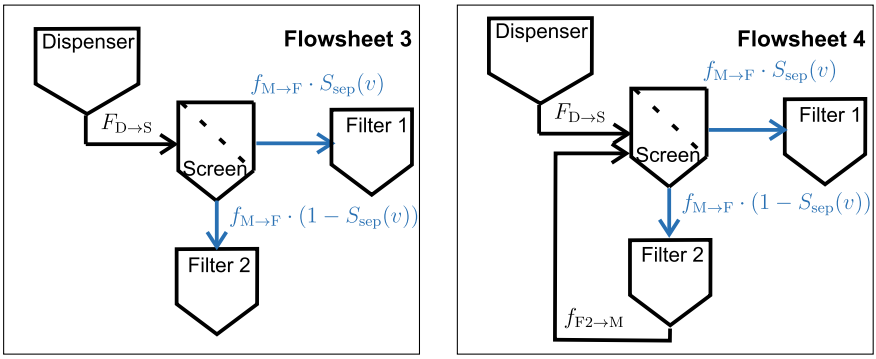

Fig. 14 Exemplary flow-sheets with and without feedback including a feedback stream

$$\begin{aligned} \frac{\mathrm{d}n_{F1}(v,t)}{\mathrm{d}t} &= + f_{M\to F1} \cdot n_M(v,t) \\ \frac{\mathrm{d}n_{F2}(v,t)}{\mathrm{d}t} &= + f_{M\to F2} \cdot n_M(v,t) - f_{F2\to M} \cdot n_{F2}(v,t) \end{aligned} \tag{16}$$

The relative particle exchange rates $f_{A\to B}$ from unit A to unit B are multiplied with the particle PSDs in A, n_A, which change over time. The external particle exchange rate $F_{D\to M}$ is multiplied with a PSD, n_D, which does not change in time, realizing thus in a constant in-flow into the mixer unit. The explicit values for the exchange rates used for these benchmarking test cases are summarized in Table 4.

The system in Fig. 13 described by Eq. (16) does not take specific particle sizes v into account, so that the same particle exchange rates apply for all sizes v. The application of a screen unit changes this situation, so that the total particle exchange rate from the screen to both filters, $f_{S\to F}$, is multiplied with the separator function, $S_{sep}(v)$. This leads to the following set of equations for the flowsheets shown in Fig. 14:

Table 4 Particle exchange rates for Eqs. (16) and (17)

	Flowsheet 1 in Fig. 13	Flowsheet 2 in Fig. 13	Flowsheet 3 in Fig. 14	Flowsheet 4 in Fig. 14
$F_{D\to M}$ or $F_{D\to S}$ [1/s]	3	3	3	3
$f_{M\to F1}$ [1/s]	1	1	–	–
$f_{M\to F2}$ [1/s]	2	2	–	–
$f_{M\to F}$ [1/s]	–	–	3	3
$f_{F2\to M}$ or $f_{F2\to S}$ [1/s]	0	2	0	2

$$\begin{aligned}
\frac{\mathrm{d}n_{\mathrm{S}}(v,t)}{\mathrm{d}t} &= +f_{\mathrm{F2}\to S}\cdot n_{\mathrm{F2}}(v,t) - f_{\mathrm{S}\to\mathrm{F}}\cdot n_{\mathrm{M}}(v,t) + F_{\mathrm{D}\to\mathrm{S}}\cdot n_{\mathrm{D}}(v,t)\\
\frac{\mathrm{d}n_{\mathrm{F1}}(v,t)}{\mathrm{d}t} &= +f_{\mathrm{S}\to\mathrm{F}}\cdot n_{\mathrm{S}}(v,t)\cdot S_{\mathrm{sep}}(v)\\
\frac{\mathrm{d}n_{\mathrm{F2}}(v,t)}{\mathrm{d}t} &= +f_{\mathrm{S}\to\mathrm{F}}\cdot n_{\mathrm{S}}(v,t)\cdot(1-S_{\mathrm{sep}}(v)) - f_{\mathrm{F2}\to S}\cdot n_{\mathrm{F2}}(v,t)
\end{aligned} \tag{17}$$

The explicit particle exchange rates for these equations are summarized in Table 4. The following form of the separation function $S_{\mathrm{sep}}(v)$ has been used for the screen:

$$S_{\mathrm{sep}}(v) = \begin{cases} 1, & v > v_{\mathrm{max}}^{\mathrm{sep}} \\ (v - v_{\mathrm{min}}^{\mathrm{sep}})/(v_{\mathrm{max}}^{\mathrm{sep}} - v_{\mathrm{min}}^{\mathrm{sep}}), & v_{\mathrm{max}}^{\mathrm{sep}} > v > v_{\mathrm{min}}^{\mathrm{sep}} \\ 0, & v_{\mathrm{min}}^{\mathrm{sep}} > v \end{cases} \tag{18}$$

The separation cut-off values $v_{\mathrm{max}}^{\mathrm{sep}} = \pi(d_{\mathrm{max}}^{\mathrm{sep}})^3/6$ and $v_{\mathrm{min}}^{\mathrm{sep}} = \pi(d_{\mathrm{max}}^{\mathrm{sep}})^3/6$ correspond to the diameters $d_{\mathrm{max}}^{\mathrm{sep}} = 57$ nm and $d_{\mathrm{min}}^{\mathrm{sep}} = 40$ nm.

As initial conditions for the PSDs in the mixer $n_{\mathrm{M}}^0(v)$ (resp. screen $n_{\mathrm{S}}^0(v)$), two identic log-normal distributions with a geometric mean diameter of 50 nm, a geometric standard deviation of 1.2 and a total number-concentration of $10^{10}\mathrm{m}^{-3}$ have been used. The same distribution has been used as feed PSD, i.e. $n_{\mathrm{D}}(v)$. Both filters are empty at the beginning of the simulation ($n_{\mathrm{F1}}^0(v) = n_{\mathrm{F2}}^0(v) = 0$).

A fixed pivot method [58] has been used as benchmark. The continuous initial PSDs are thereby discretized with the help of a geometric grid of 1000 pivot points, covering a particle size range from 1 nm to 10 µm. In the scope of this approach, the set of Eqs. (16) or (17) is interpreted as the rate of change for each single pivot point with its respective volume v.

The resulting PSDs after a simulation time of 10 s are shown in Figs. 15, 16, 17, 18. It can be seen, that flowsheet 1 (without tear streams and a screen) is very well

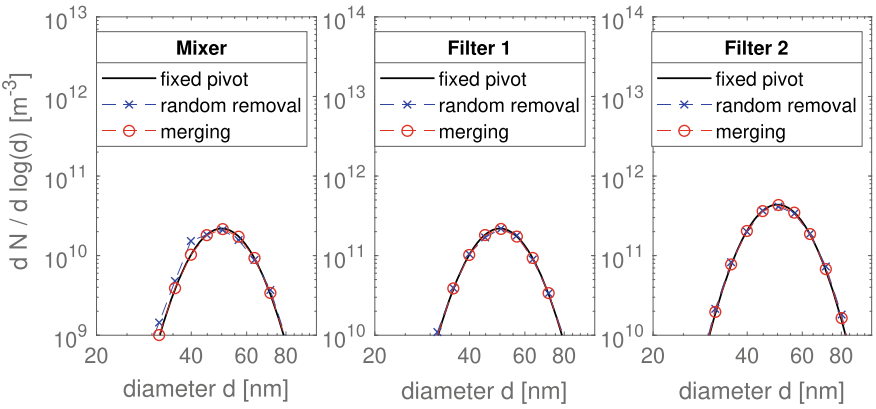

Fig. 15 PSDs in compartments as described in Flowsheet 1 in Fig. 13 and Eq. (16)

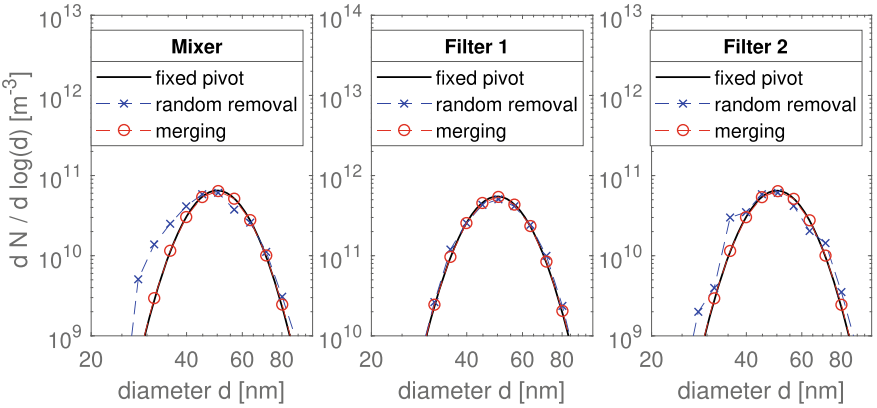

Fig. 16 PSDs in compartments as described in Flowsheet 2 in Fig. 13 and Eq. (16)

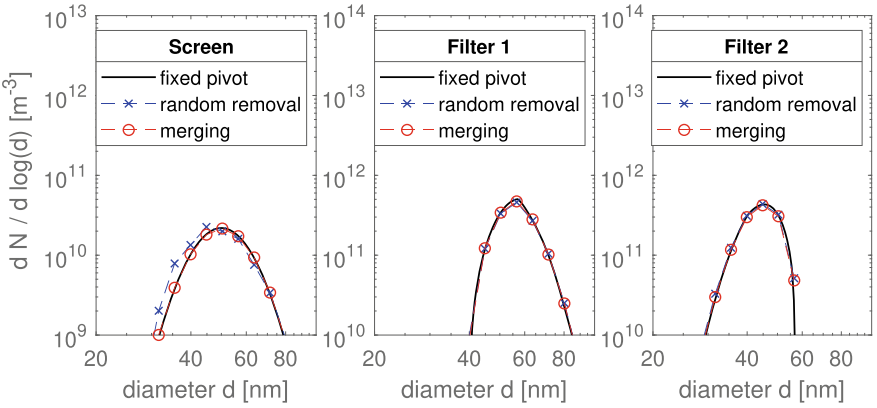

Fig. 17 PSDs in compartments as described in Flowsheet 3 in Fig. 14 and Eq. (17)

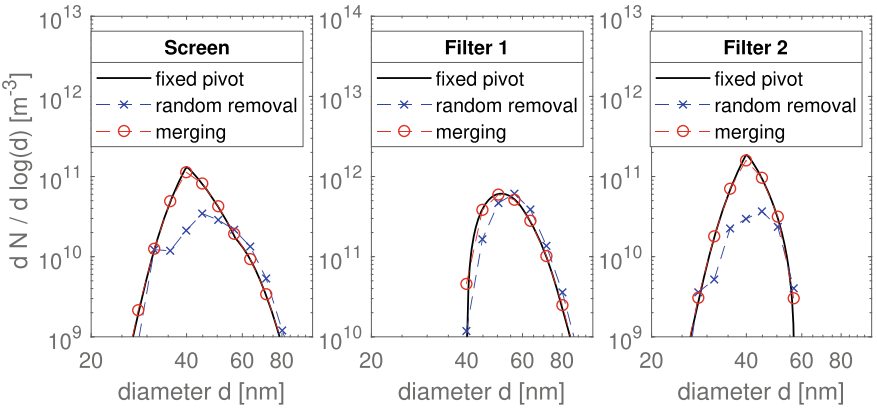

Fig. 18 PSDs in compartments as described in Flowsheet 4 in Fig. 14 and Eq. (17)

reproduced by the merging as well as the random removal approach. The random removal approach leads to larger noise levels, which can be seen in slight deviations of the PSD in the mixer unit in Fig. 15. The addition of a tear stream leads to an increase of these noise levels, as can be seen Fig. 16—the approximations based on the random removal technique become less accurate but can be still considered to be in accordance with the results obtained by the fixed pivot method.

The replacement of the mixer with a sieve unit (or replacing flowsheet 1 with flowsheet 3) leads also to a system, which can be well simulated by the random removal technique (see Fig. 17). The addition of a tear stream to flowsheet 3 (resulting in flowsheet 4) leads—however—to such a complex system, that the random removal method is not applicable. Figure 18 shows the striking deviations of the PSDs obtained with the random removal method—which predict a wrong particle-number concentration in the screen and filter 2 by a factor of nearly 10. The suggested merging techniques—on the other hand—are able to reproduce the benchmark results with a very high accuracy. This allows to say, that the specific combination of tear-stream and screen leads to a simulation scenario, which cannot be addressed with conventional MC simulation techniques—as the random removal technique. This finding also explains the failure of the random removal techniques to describe an even more complex simulation scenario, reported in [57].

4 Conclusions

The application of weighted MC particles for the solution of a compartmental network in the framework of an operator splitting approach (the single processes like coagulation and nucleation are separated for short periods of time) has been discussed.

First, the solution of a one-compartmental system has been discussed, it has been found that:

- the application of the stochastic resolution allows to describe the coagulation between weighted simulation particles (like already discussed in [23]).
- merging techniques allow to simulate the combined nucleation and coagulation with a lower amount of statistical noise than conventional MC simulation techniques (like already discussed in [23]).
- the parallel simulation of evaporation and condensational growth allows to simulate particles formation processes and investigate the role of different nucleation theories (this has been already discussed for metallic [26] and atmospheric systems [27], but the here presented case-study of Ag-particle synthesis has not been published prior to this work).
- novel selection and weighting techniques of the MC fragment population resulting from particle breakage lead to simulation techniques which are able to render the full particle size spectrum completely (these simulation techniques and findings have already been presented in [43]).

As a second step, the combination of the findings above in an operator splitting approach for the full simulation of a compartmental network has been sketched. It has been found that:

- the computationally advantageous event-driven simulation technique can be also used for the simulation of smaller time steps than the intrinsic MC time step—making this method applicable for a network of PBE compartments (like already discussed in [51]).
- the merging techniques introduced in [23] can be used for the simulation of particle transport between single compartments. (These findings have already been presented on a more complicated system in [57], the here presented description of the simulation algorithm is, however, far more detailed.)
- out of 4 case studies of a flow-sheet with increasing degree of complexity,[4] conventional MC methods can simulate the 3 simplest cases while merging techniques are needed for the simulation of the most complex case (this finding has not been published prior to this work).

Acknowledgements This work is supported by the DFG (Deutsche Forschungsgemeinschaft) within the priority program SPP 1679 "Dynamic flowsheet simulation of interconnected solids processes" [KR 1723/15–1,2&3].

References

1. Ramkrishna, D.: In: Population Balances: Theory and Applications to Particulate Systems in Engineering, 1st edn., Academic (2000). ISBN 978–0-12-576970-9
2. Ramkrishna, D., Singh, M.R.: Population balance modeling: current status and future prospects. Ann. Rev. Chem. Biomol. Eng. **5**, 123–146 (2014)
3. Schwarzer, H.-C., Peukert, W.: Combined experimental/numerical study on the precipitation of nanoparticles. AIChE J. **50**(12), 3234–3247 (2004)
4. Sommer, M., Stenger, F., Peukert, W., Wagner, N.J.: Agglomeration and breakage of nanoparticles in stirred media mills—a comparison of different methods and models. Chem. Eng. Sci. **61**(1), 135–148 (2006)
5. Peglow, M., Kumar, J., Heinrich, S., Warnecke, G., Tsotsas, E., Mörl, L., et al.: A generic population balance model for simultaneous agglomeration and drying in fluidized beds. Chem. Eng. Sci. **62**(1–2), 513–532 (2007)
6. Kraft, M.: Modelling of particulate processes. KONA Powder Particle J. **23**, 18–35 (2005)
7. Kiparissides, C.: Challenges in particulate polymerization reactor modeling and optimization: a population balance perspective. J. Process. Control. **16**(3), 205–224 (2006)
8. Bhole, M.R., Joshi, J.B., Ramkrishna, D.: CFD simulation of bubble columns incorporating population balance modeling. Chem. Eng. Sci. **63**(8), 2267–2282 (2008)
9. Schütz, S., Gorbach, G., Piesche, M.: Modeling fluid behavior and droplet interactions during liquid–liquid separation in hydrocyclones. Chem. Eng. Sci. **64**(18), 3935–3952 (2009)

[4]The four case studies comprise: (1) a flowsheet without recycle stream and screen units, (2) a flowsheet with one recycle stream and without sieve unit, (3) a flowsheet with one sieve unit and without recycle stream and (4) a flowsheet with a recycle stream and a sieve unit.

10. Sanyal, J., Marchisio, D.L., Fox, R.O., Dhanasekharan, K.: On the comparison between population balance models for CFD simulation of bubble columns. Ind. Eng. Chem. Res. **44**(14), 5063–5072 (2005)
11. Cheng, J., Yang, C., Jiang, M., Li, Q., Mao, Z.-S.: Simulation of antisolvent crystallization in impinging jets with coupled multiphase flow-micromixing-PBE. Chem. Eng. Sci. **171**, 500–512 (2017)
12. Marchisio, D.L., Fox, R.O.: Solution of population balance equations using the direct quadrature method of moments. J. Aerosol Sci. **36**(1), 43–73 (2005)
13. Gavi, E., Marchisio, D.L., Barresi, A.A.: CFD modelling and scale-up of Confined Impinging Jet Reactors. Chem. Eng. Sci. **62**(8), 2228–2241 (2007)
14. Boje, A., Akroyd, J., Sutcliffe, S., Edwards, J., Kraft, M.: Detailed population balance modelling of TiO_2 synthesis in an industrial reactor. Chem. Eng. Sci. **164**, 219–231 (2017)
15. Szilágyi, B., Nagy, Z.K.: Population balance modeling and optimization of an integrated batch crystallizer-wet mill system for crystal size distribution control. Cryst. Growth Des. **18**(3), 1415–1424 (2018)
16. Hao, X., Zhao, H., Xu, Z., Zheng, C.: Population balance-Monte Carlo simulation for gas-to-particle synthesis of nanoparticles. Aerosol Sci. Technol. **47**(10), 1125–1133 (2013)
17. Irizarry, R.: Stochastic simulation of population balance models with disparate time scales: hybrid strategies. Chem. Eng. Sci. **66**(18), 4059–4069 (2011)
18. Dosta, M., Heinrich, S., Werther, J.: Fluidized bed spray granulation: analysis of the system behaviour by means of dynamic flowsheet simulation. Powder Technol. **204**(1), 71–82 (2010)
19. Skorych, V., Dosta, M., Hartge, E.-U., Heinrich, S.: Novel system for dynamic flowsheet simulation of solids processes. Powder Technol. **314**, 665–679 (2017)
20. Menz, W.J., Akroyd, J., Kraft, M.: Stochastic solution of population balance equations for reactor networks. J. Comput. Phys. **256**, 615–629 (2014)
21. Kruis, F.E., Wei, J., van der Zwaag, T., Haep, S.: Computational fluid dynamics based stochastic aerosol modeling: combination of a cell-based weighted random walk method and a constant-number Monte-Carlo method for aerosol dynamics. Chem. Eng. Sci. **70**, 109–120 (2012)
22. Zhao, H., Kruis, F.E., Zheng, C.: Reducing statistical noise and extending the size spectrum by applying weighted simulation particles in Monte Carlo simulation of coagulation. Aerosol Sci. Technol. **43**(8), 781–793 (2009)
23. Kotalczyk, G., Kruis, F.E.: A Monte Carlo method for the simulation of coagulation and nucleation based on weighted particles and the concepts of stochastic resolution and merging. J. Comput. Phys. **340**, 276–296 (2017)
24. Lin, Y., Lee, K., Matsoukas, T.: Solution of the population balance equation using constant-number Monte Carlo. Chem. Eng. Sci. **57**(12), 2241–2252 (2002)
25. Wei, J.: A fast Monte Carlo method based on an acceptance-rejection scheme for particle coagulation. Aerosol Air Quality Research **13**(4), 1273–1281 (2013)
26. Kotalczyk, G., Skenderovic, I., Kruis, F.E.: Modeling of particle formation in arc discharges by Monte-Carlo based population balance modeling. MRS. Adv. **148**, 1–8 (2017)
27. Kotalczyk, G., Skenderovic, I., Kruis, F.E.: Monte Carlo simulations of homogeneous nucleation and particle growth in the presence of background particles. Tellus, Ser. B. Chem. Phys. Meteorol. **71**(1), 1–10 (2019)
28. Vemury, S., Pratsinis, S.E.: Self-preserving size distributions of agglomerates. J. Aerosol Sci. **26**(2), 175–185 (1995)
29. Kodas, T.T., Hampden-Smith, M.J.: Aerosol Processing of Materials, Wiley-VCH (1999). ISBN 0471246697
30. Kotalczyk, G., Skenderovic, I., Kruis, F.E.: A GPU-based Monte Carlo technique for the simulation of simultaneous nucleation, coagulation and growth based on weighted simulation particles. In: AIChE Annual Meeting, pp. 490–497 (2016)
31. Press, W.H.: In: Numerical recipes: The Art of Scientific Computing, 3rd edn. Cambridge University Press (2007). ISBN 978-0521880688
32. Tsang, T.H., Rao, A.: Comparison of different numerical schemes for condensational growth of aerosols. Aerosol Sci. Technol. **9**(3), 271–277 (1988)

33. Wu, C.-Y., Biswas, P.: Study of numerical diffusion in a discrete-sectional model and its application to aerosol dynamics simulation. Aerosol Sci. Technol. **29**(5), 359–378 (1998)
34. Kumar, S., Ramkrishna, D.: On the solution of population balance equations by discretization – III. Nucleation, growth and aggregation of particles. Chem. Eng. Sci. **52**(24), 4659–4679 (1997)
35. Wyslouzil, B.E., Wölk, J.: Overview: homogeneous nucleation from the vapor phase−the experimental science. J. Chem. Phys. **145**(21) (2016)
36. Girshick, S.L., Chiu, C.-P.: Kinetic nucleation theory: a new expression for the rate of homogeneous nucleation from an ideal supersaturated vapor. J. Chem. Phys. **93**(2), 1273–1277 (1990)
37. Lide, D.R. (ed.): CRC Handbook of Chemistry and Physics: A Ready-Reference Book of Chemical and Physical Data, 85th edn. CRC Press, Boca Raton (2004)
38. Egry, I., Ricci, E., Novakovic, R., Ozawa, S.: Surface tension of liquid metals and alloys-recent developments. Adv. Coll. Interface. Sci. **159**(2), 198–212 (2010)
39. Mishra, B.K.: Monte Carlo simulation of particle breakage process during grinding. Powder Technol. **110**(3), 246–252 (2000)
40. Lee, K., Matsoukas, T.: Simultaneous coagulation and break-up using constant-N Monte Carlo. Powder Technol. **110**(1–2), 82–89 (2000)
41. Lee, K.F., Patterson, R.I.A., Wagner, W., Kraft, M.: Stochastic weighted particle methods for population balance equations with coagulation, fragmentation and spatial inhomogeneity. J. Comput. Phys. **303**, 1–18 (2015)
42. Zhao, H., Zheng, C., Xu, M.: Multi-Monte Carlo approach for general dynamic equation considering simultaneous particle coagulation and breakage. Powder Technol. **154**(2–3), 164–178 (2005)
43. Kotalczyk, G., Devi, J., Kruis, F.E.: A time-driven constant-number Monte Carlo method for the GPU-simulation of particle breakage based on weighted simulation particles. Powder Technol. **317**, 417–429 (2017)
44. Devi, J., Kotalczyk, G., Kruis, F.E.: Accuracy control in Monte Carlo simulations of particle breakage. Int. J. Model. Ident. Control **31**(3), 278–291 (2019)
45. Muscato, O., Di Stefano, V., Wagner, W.: A variance-reduced electrothermal Monte Carlo method for semiconductor device simulation. Comput. Math Appl. **65**(3), 520–527 (2013)
46. Ziff, R.M., McGrady, E.D.: The kinetics of cluster fragmentation and depolymerisation. J. Phys. A: Math. Gen. **18**(15), 3027–3037 (1985)
47. Celnik, M., Patterson, R.I.A., Kraft, M., Wagner, W.: Coupling a stochastic soot population balance to gas-phase chemistry using operator splitting. Combust. Flame **148**(3), 158–176 (2007)
48. Liffman, K.: A direct simulation Monte-Carlo method for cluster coagulation. J. Comput. Phys. **100**(1), 116–127 (1992)
49. Zhao, H., Maisels, A., Matsoukas, T., Zheng, C.: Analysis of four Monte Carlo methods for the solution of population balances in dispersed systems. Powder Technol. **173**(1), 38–50 (2007)
50. Wei, J.: A parallel Monte Carlo method for population balance modeling of particulate processes using bookkeeping strategy. Physica A **402**, 186–197 (2014)
51. Kotalczyk, G., Kruis, F.E.: Fractional Monte Carlo time steps for the simulation of coagulation for parallelized flowsheet simulations. Chem. Eng. Res. Des. **136**, 71–82 (2018)
52. Gelbard, F., Tambour, Y., Seinfeld, J.H.: Sectional representations for simulating aerosol dynamics. J. Colloid Interface Sci. **76**(2), 541–556 (1980)
53. Landgrebe, J.D., Pratsinis, S.E.: A discrete-sectional model for particulate production by gas-phase chemical reaction and aerosol coagulation in the free-molecular regime. J. Colloid Interface Sci. **139**(1), 63–86 (1990)
54. Marshall, C.L., Rajniak, P., Matsoukas, T.: Multi-component population balance modeling of granulation with continuous addition of binder. Powder. Technol. **236**, 211–220 (2013)
55. Khalili, S., Lin, Y., Armaou, A., Matsoukas, T.: Constant number Monte Carlo simulation of population balances with multiple growth mechanisms. AIChE J. **56**(12), 3137–3145 (2010)

56. Smith, M., Matsoukas, T.: Constant-number Monte Carlo simulation of population balances. Chem. Eng. Sci. **53**(9), 1777–1786 (1998)
57. Kotalczyk, G., Lambach, K., Kruis, F.E.: Parallel GPU-based monte carlo techniques for the flow-sheet simulation of solid processes. In: 8th World Congress on Particle Technology (2018)−Applications of Solids Processing Unit Operations, pp. 64–71
58. Kumar, S., Ramkrishna, D.: On the solution of population balance equations by discretization –I. A fixed pivot technique. Chem. Eng. Sci. **51**(8), 1311–1332 (1996)

Paper VI

Reproduced with permission from Springer Nature. Version of record published in:
MRS Advances 2, Issue 28 (2017), pp. 1511–1518.
Available online at: https://doi.org/10.1557/adv.2017.155

Modeling of Particle Formation in Arc Discharges by Monte-Carlo Based Population Balance Modeling

G. Kotalczyk, I. Skenderović and F.E. Kruis

MRS Advances © 2017 Materials Research Society
DOI: 10.1557/adv.2017.155

Modeling of Particle Formation in Arc Discharges by Monte-Carlo Based Population Balance Modeling

Gregor Kotalczyk, Ivan Skenderovic and Frank Einar Kruis
Institute of Technology for Nanostructures (NST) and Center for Nanointegration Duisburg-Essen (CENIDE), University Duisburg-Essen, Duisburg, D-47057, Germany

ABSTRACT

A simulation method is presented which encompasses all relevant mechanisms, which are necessary for the description of the early stages of particle formation in arc discharges. Next to discrete coagulation and nucleation events, a continuous surface growth process is included into the simulation, making thus the description of the evaporation of thermodynamic unstable particles possible. The driving force for the nucleation and growth/evaporation is coupled to the monomer concentration in the gaseous phase and thus subject to change in the further course of the simulation. It is shown, that the simulation results gained by the incorporation of all three of these processes cannot be reproduced, if one of those processes is not simulated.

INTRODUCTION

The scale-up of the production of metallic nanoparticles can be done efficiently by means of arc discharge in an inert carrier gas. The use of many single production units in parallel, which can be thoroughly optimized and tested on a lab scale for a given material, ensures that a highly effective scale-up of the synthesis process in terms of cost and energy consumption is possible. We demonstrated the integration of this technology in the aerotaxy production line for solar cells, direct deposition of nanoparticles on textiles, nanocomposites, deposition of nanoparticles within periodic arrays for photonics, higher heat transfer with nanoparticle dispersions and direct deposition of catalytic nanoparticles on membrane structures. [1]

This work addresses the problems which appear when modeling the particle formation from an atomic vapor, formed by plasma evaporation from a melt as in the case of arc discharge. The modeling of particle formation initiated by a physically induced nucleation controlled by the local temperature, is especially challenging due to a strong variation of the Kelvin diameter which makes it almost impossible to apply conventional discrete-sectional population balances.

Inclusion of nucleation in a Monte-Carlo approach is challenging as the number of simulation particles which can be used is limited. The application of weighted simulation particles offers here a practical solution. Keeping the number of simulation particles constant requires strategies to discard other simulation particles while keeping the loss of information to a minimum, merging techniques show here the best performance. Another challenge is the modeling of condensational growth, here the continuous variation of the Kelvin diameter, induced by e.g. temperature variation or monomer depletion, has to be taken into account. Care has to be taken that particles smaller than the Kelvin diameter effectively evaporate while large ones grow. Although many recent works deal with the same problem [2,3], these approaches are applied to particulate systems with a surface growth mechanism modelled by chemical reactions, making a consideration of the evaporation of the simulated particles unnecessary.

We present the implementation of a test system, which describes the simultaneous mechanisms of coagulation, nucleation and growth, including a physical growth mechanism resulting from the saturation of the gaseous phase, which leads to the evaporation of particles whose diameter is below the Kelvin diameter. It is shown, that the simulation of all three mechanisms leads to results, which cannot be reproduced, if one of these mechanisms is not simulated.

THEORY

Simulated physical system

The physical particle synthesis is usually described by the onset of the nucleation of novel particles due to a rapid increase of the saturation *S* of the gaseous phase. This is usually done by a quick cooling of a saturated vapor (*S*=1). The cooling leads to decrease of the saturation pressure p_s which in turn leads to changes of the nucleation rates over several orders of magnitude. The classical nucleation theory [4] describes the nucleation rate N_R with the following formula (1):

$$N_R(n_G) = n_G \cdot \sqrt{\frac{2\gamma}{\pi \cdot m_1}} \frac{p_s}{k_B \cdot T} \cdot \exp\left(-\frac{16 \cdot \pi \cdot \gamma^3 \cdot v_m^2}{3 \cdot k_B^3 \cdot T^3 \cdot \ln(S)^2} \right) \text{ , with } S = \frac{n_G k_B T}{p_s} \qquad (1)$$

n_G is the monomer concentration in the gaseous phase and its decrease due to condensation or nucleation is taken into account in this work, as well as an increase due to the evaporation of other particles.
The other physical parameters used for the simulation model typical metallic properties (density $\rho_p = 7.874 \text{ g cm}^{-3}$, atomic volume $v_M = 1.178 \cdot 10^{-29} \text{ m}^3$, atomic weight $m_1 = 9.27 \cdot 10^{-26} \text{ kg}$, surface tension $\gamma = 0.29 \text{ J m}^{-2}$ and vapor pressure $p_s = 0.805 \text{ Pa}$), a temperature T of 1380 K has been simulated.

The nucleated particles form growth centers for further condensational growth, which, if coupled to the continuous phase, lead to a further decrease of the monomer concentration. The free-molecular description of the growth process is adequate in the initial stages of the particle formation, given by the following formula (2):

$$G(v, n_G) = \frac{v_M \cdot \pi \cdot d^2}{\sqrt{2\pi \cdot m_1 \cdot k_B \cdot T}} \cdot \left(k_B \cdot T \cdot n_G - p_s \cdot \exp\left\{ 4 \cdot \gamma \cdot v_M / (k_B \cdot T \cdot d) \right\} \right) \qquad (2)$$

The growth due to condensation of new monomers on the particle surface is described by positives values for *G* in (2), which are equivalent to a particle diameter *d* which is bigger than the Kelvin diameter d^*. The evaporation of particles smaller than d^* is described by negative values for *G* in (2). In order to discuss the specific effect of the evaporation, simulation growth-rates G_{ALT}, which do not depend on the particle size *d* have been added to the simulation. A positive growth rate and no evaporation is expected for all saturations $S > 1$, if the following equation for the growth rate is used:

$$G_{ALT}(v,n_G)=\frac{v_M\cdot\pi\cdot d^2}{\sqrt{2\pi\cdot m_1\cdot k_B\cdot T}}\cdot\left(k_B\cdot T\cdot n_G-p_s\right) \tag{3}$$

Coagulation is an additional growth mechanism, especially important, if high particle concentrations are encountered at the early stages of the simulation. In the following, the free-molecular regime will be used for the simulation, given by formula (4):

$$\beta(v,v')=\left(\frac{3}{4\pi}\right)^{\frac{1}{6}}\sqrt{\frac{6k_BT}{\rho_p}}\cdot\sqrt{\frac{1}{v}+\frac{1}{v'}}\cdot\left(v^{\frac{1}{3}}+v'^{\frac{1}{3}}\right)^2 \tag{4}$$

Hybrid Monte Carlo simulation method based on weighted particles

To account for the difficulties of the simulation of all these simultaneous processes, a Hybrid Monte Carlo simulation has been applied. The usage of weighted simulation particles introduced by [5] allows to describe multimodal particle populations, the single modes might represent particle concentrations, which differ in several orders of magnitude from each other. The authors described the coagulation rate of differentially weighted particles with each other by introducing the concept of 'ficticious particles' which constitutes a constant number simulation scheme. Figure 1 demonstrates the applied coagulation scheme, the value W_{max} (resp. W_{min}) denotes the maximum (resp. minimum) of the statistical weights of the two particles selected for coagulation.

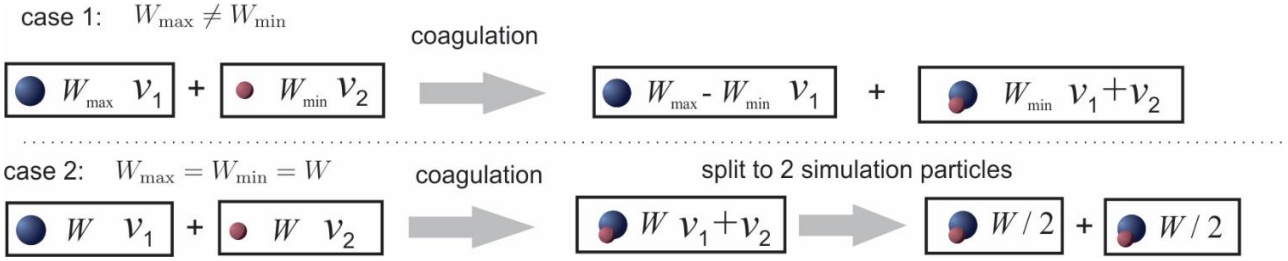

Figure 1. The statistical weights *W* and the particle volumes *v* are altered during one coagulation process, but the number of simulation particles remains constant.

A speed-up of the computationally demanding Monte Carlo simulation could be recently gained by the application of a GPU algorithm, which uses a representative sample of coagulation pairs, in order to determine quickly the maximal coagulation rate, which is needed for the correct description of the coagulation probability in the scope of the acceptance-rejection algorithm [6]. This formulation allows not only a faster simulation, it is also applicable to all sorts of coagulation kernels, and not only limited to certain forms, for which a majorant formulation (see e.g. [7]) can be found.

We extended this coagulation algorithm by the addition of a condensation and nucleation process., resorting to an operation splitting technique. Such approaches were already applied to simulations based on weighted simulated particles [8], but these application are mostly limited to surface growth resulting from chemical reactions and do not encompass the evaporation of

particles whose diameter are smaller than the Kelvin diameter. In the simplest form of this approach, a time-driven Monte Carlo step is used to estimate a time-step which describes the coagulation event, which is an inherent property of the simulated particles. Then, a growth step is performed, which consists of the solution of the corresponding differential equations. No numerical diffusion [9] is encountered, if the growth process is modelled by discrete MC particles. This growth simulation corresponds in some way, to the simulation of a moving pivot technique [10], where no diffusion is encountered. In contrast to the pivot technique, the coagulation is treated stochastically and new particles are created for each nucleation event.

The differential equations describing the growth (resp. evaporation) of the existing particles as well as the formation of novel particles due to nucleation can be solved in an efficient, parallel way on the GPU. The continuous nucleation process, which is described as a steady inflow of particles, is discretized here by the use of a nucleation threshold. The total amount of particle volume resulting from the nucleation is stored to a specific buffer. If the value of this buffer surpasses a certain threshold, the volume stored on the buffer is included into the simulation as one simulation particle, containing all the volume in the buffer and the buffer is cleared for the further simulation. In order to preserve a constant number of simulation particles, two already existing particles are merged into a new one, leading to a free storage space, at which the novel particle is included. (this technique is briefly mentioned by [11]).

DISCUSSION

The combined processes of nucleation, coagulation and growth (called 'complete system') have been simulated for an initial particulate system described by a lognormal distribution with the geometric mean value d_g =2 nm and the geometric standard deviation σ_g =1.2, comprising a total number-concentration of 10^{16} m^{-3}. This initial particle population has been combined with initial monomer saturations of S_0= 4.5. The gained simulation results are compared with results of the simulation of two reduced systems, which are traditionally used in order to decrease the level of complexity. The reduced systems investigated here are: 1) simulations of the coagulation and nucleation only (neglecting the growth/evaporation process), for which the condensable material is included at the very beginning of the simulation, modelling thus a 'nucleation burst (called 'reduced system 1' in the following) and 2) the single combination of nucleation and growth (resp. evaporation), neglecting the coagulation process (called 'reduced system 2' in the following).

In order to address the effect of the evaporation, the complete system and the system 2 are simulated with the full growth term G (marked with an additional (E) in the figures) and with the growth term G_{ALT} neglecting the Kelvin effect (marked with an additional (NE) in the figures).

1. Coagulation and nucleation only (reduced system 1)

For the reduced system 1, an additional particle population with a number-concentration of 3 10^{19} m^{-3} and a diameter of 0.47 nm is inserted into the simulation, so that a 2nd initial condition is used for this case. This sudden inclusion can be interpreted as a 'nucleation burst'. Although clear higher particle number-concentrations can be found in the initial stages of the simulation for the reduced system 1 compared to the complete system (see figure 2a), the results are predicted more accurately for the later stages of the simulation (figure 2b), the characteristic

shape is – of course – the self-preserving size distribution for coagulation [12], which differs from the shape which is obtained for the combined processes of coagulation and growth. This self-preserving distribution for combined coagulation and growth/evaporation has been discussed recently by [13]. It can be seen, that the self-preserving PSD for coagulation is reached for the reduced system and the complete system without the size-dependent evaporation term.

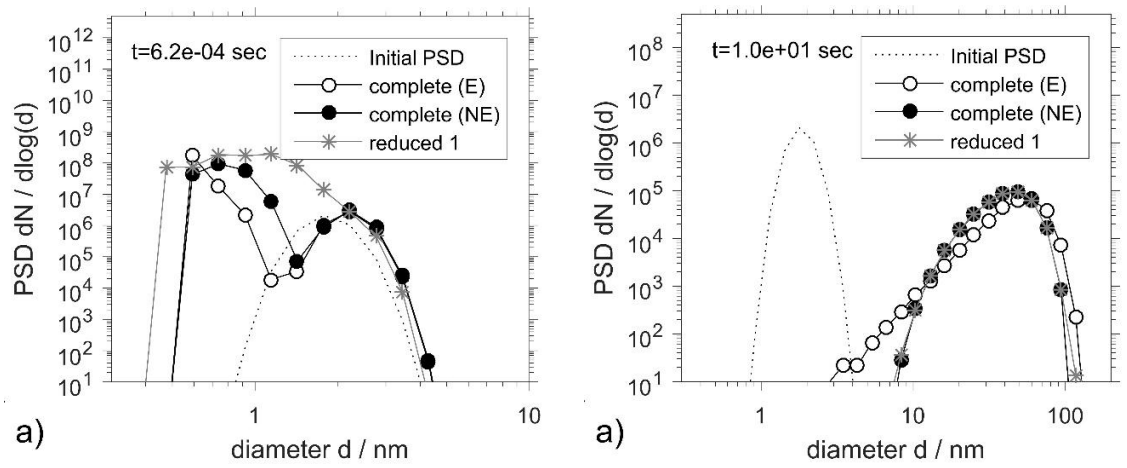

Figure 2. The PSDs resulting from the reduced system 1 compared to the complete system with evaporation (E) and without (NE) for S_0=4.5 at the initial stage of the simulation (a) and for longer simulation times (b).

2. Nucleation and growth (reduced system 2)

Typical PSDs reached by the reduced system 2 are shown in figure 3 for an initial saturation of S_0=4.5, which leads to significant deviations from the complete system, even after a short simulation time (figure 3a). Both simulation techniques lead to self-preserving size distributions. The self-preserving size distribution for systems comprising the system 2 (E) due to coupling to the continuous phase is described in the context of the LWS theory for liquid systems and reflects a broadening of the PSD [14,15]. Most theories used for aerosol systems do not describe the broadening of the PSD, because the evaporation can be neglected for the discussed cases [16,17]. Although the shape of the reduced system 2 approximates much better the shape of the complete system than the self-preserving distribution for the coagulation (reduced system 1), the values of the mean diameters of both systems deviate significantly from each other, as can be seen in figure 3b.

Figure 4a shows the driving force of the growth process, $S - S_\infty$, with $S_\infty = 1$. It can be seen, that the value $S = S_\infty$ is reached very quickly, if the evaporation is neglected. The reduced system 2 (NE) attains therefore a constant state after a short time, which can be seen by the constant value for σ_g in figure 4b. The reduced system 2 (E) is described by two linear growth phases of the particles which are connected to the drop of σ_g , the self-preserving state reached at the end of the simulation is marked with a high simulation noise, which is a consequence of the rendering of the PSD with discrete particles. For the same reason, the self-preserving PSD for coagulation is reached very quickly for the complete system (NE) with G_{ALT}, while the complete system with

G is marked by much broader distribution, which were found to have a self-preserving character in [13].

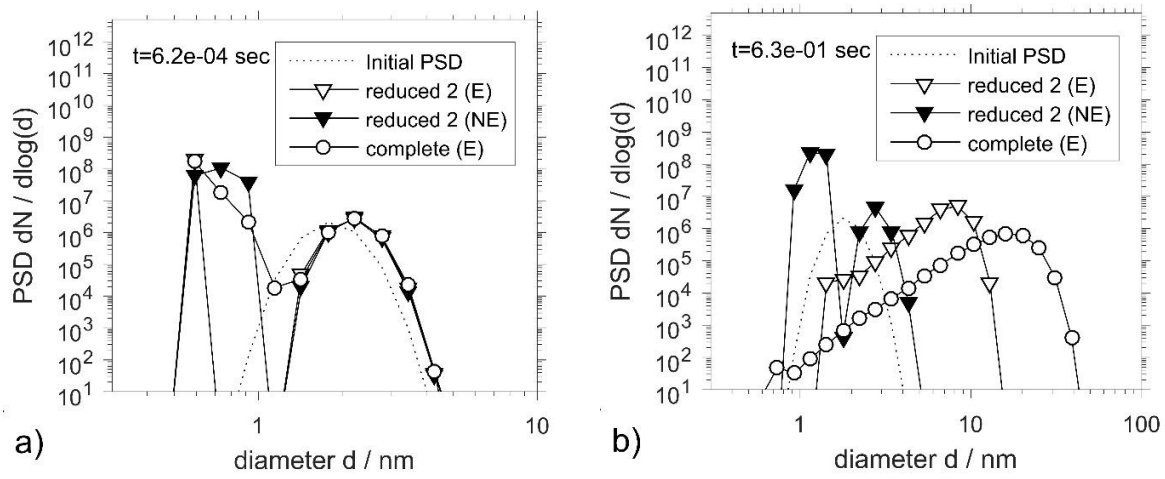

Figure 3. The PSDs resulting from the reduced system 2 compared to the complete system are shown for systems comprising evaporation (E) and without (NE) at the initial stage of the simulation (a) and for longer simulation times (b).

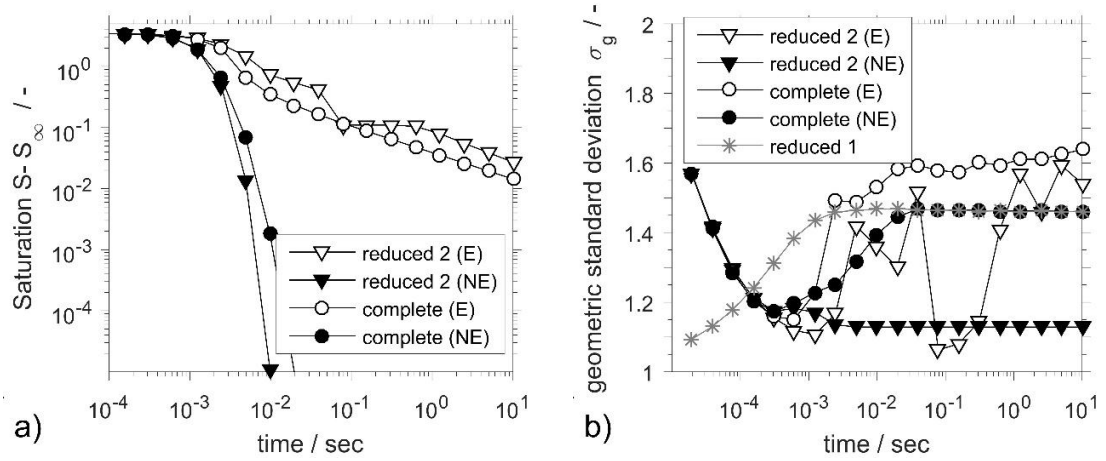

Figure 4. The saturation surplus $S - S_\infty$ (with $S_\infty = 1$) and the geometric standard deviation σ_g of the complete system compared to the reduced systems. No saturation is simulated for the reduced system 1.

4. Computational times

The computational times which are required for the simulation of the real time of 10 seconds of the considered system are shown in table 1. The results were gained by parallel computations of 100 simulations (with identical initial conditions but different random numbers), using a NVIDIA GTX 980 graphic processor unit (GPU). The simulations used 1000 weighted MC simulation particles. This setting allowed a computational accuracy of ca. 2-4% (arithmetic

standard deviations of the moments of the PSDs) throughout the simulation for all simulation with included also the coagulation process. The reduced system 2, was limited by the numerical accuracy, which is given by the accuracy of the used floating point numbers, i.e. 10^{-14}.

Table 1. The computational times (in seconds) required for the simulation of the discussed system compared with the complete system. The 'X' marks whether the single processes are simulated by the systems.

Simulated system	Coagulation	Growth	Nucleation	E (sec)	NE (sec)
Complete system	X	X	X	235.7	216.2
Reduced system 1	X	-	Burst	-	97.2
Reduced system 2	-	X	X	6.4	2.5

Table 1 makes obvious, that the coagulation process is the most demanding simulation process. The computational times required for the complete system are in the same order of magnitude than the approximation of the nucleation burst (reduced system 1). This approximation leads therefore to only modest increases of the computational efficiency for higher initial saturations.

CONCLUSIONS

We discussed systems describing the combined processes of coagulation, nucleation and growth (resp. evaporation) and their suitability for the modelling of early stages of particle synthesis due to physical nucleation and surface growth. It is shown, that all three processes have to be considered in order to describe the particle size distribution at all stages of the simulation. If the process of coagulation is not included into the simulation, severe deviations to the complete system (comprising the –simulation of all three processes) can be seen. If the process rendering the particle growth is neglected and only the nucleation is included (which is rendered as an instantaneous nucleation burst at the beginning of the simulation), the particle concentrations are clearly overestimated at the beginning of the simulation, however a coarse approximation of the complete system is given for longer simulation times. Hence only the coagulation is rendered by this simulation technique, the resulting self-preserving PSD, is only a coarse approximation of the self-preserving PSD resulting from the combined simulation of coagulation and growth / resp. evaporation.

ACKNOWLEDGMENTS

This work has been financially supported by the Deutsche Forschungsgemeinschaft in the frame of the priority program SPP 1679.

REFERENCES

1. BUONAPART-E Project (2016). Available at: http://www.buonapart-e.eu/ (accessed 13 December 2016).
2. S. Khalili, Y. Lin, A. Armaou, T. Matsoukas, AIChE J. **56,** 12 (2010).

3. W.J. Menz, J. Akroyd, M. Kraft, J. Comput. Phys. **256** (2014).
4. D.W. Oxtoby, J. Phys. Condens. Matter **4,** 38 (1992).
5. H. Zhao, F.E. Kruis, C. Zheng, Aerosol Sci. Technol. **43,** 8 (2009).
6. J. Wei and F.E. Kruis, J. Comput. Phys. **249** (2013).
7. R.I.A. Patterson, W. Wagner, M. Kraft, J. Comput. Phys. **230,** 19 (2011).
8. M. Celnik, R.I.A. Patterson, M. Kraft, W. Wagner, Combust. Flame **148,** 3 (2007).
9. T.H. Tsang and A. Rao, Aerosol Sci. Technol. **9,** 3 (1988).
10. S. Kumar and D. Ramkrishna, Chem. Eng. Sci. **51,** 8 (1996).
11. H. Zhao, C. Zheng, M. Xu, Powder Technol. **154,** 2–3 (2005).
12. S.K. Friedlander and C.S. Wang, J. Colloid Interface Sci. **22,** 2 (1966).
13. G. Kotalczyk, I. Skenderovic, F.E. Kruis, in: AIChE annual meeting, 2016. San Francisco. 978-0-8169-1097-7.
14. I.M. Lifshitz and V.V. Slyozov, Journal of Physics and Chemistry of Solids **19,** 1 (1961).
15. C. Wagner, Zeitschrift für Elektrochemie, Berichte der Bunsengesellschaft für physikalische Chemie **65,** 7-8 (1961).
16. S. Park, K. Lee, M. Shimada, K. Okuyama, Journal of Aerosol Science **32,** 2 (2001).
17. S. Tsantilis and S.E. Pratsinis, Journal of Aerosol Science **35,** 3 (2004).

Paper VII

Preprint submitted for publication in:
AIChE Annual Meeting, San Francisco, 2016, Proceedings ISBN: 978-0-8169-1097-7
Available online at:
https://www.aiche.org/conferences/aiche-annual-meeting/2016/proceeding/paper/658b-gpu-based-monte-carlo-technique-simulation-simultaneous-nucleation-coagulation-and-growth-based

A GPU-Based Monte Carlo Technique for the Simulation of Simultaneous Nucleation, Coagulation and Growth Based on Weighted Simulation Particles

G. Kotalczyk, I. Skenderović and F.E. Kruis

Abstract

A hybrid Monte Carlo method is investigated, which combines discrete coagulation and nucleation events with the continuous growth or evaporation of particles. An efficient parallel implementation of this hybrid method on the GPU is discussed, taking into account the coupling of the growth mechanisms to a continuous monomer concentration in the gaseous (or liquid) phase. Exemplary simulations of the gas-phase synthesis of particles are presented, which lead to multimodal initial particle size distributions which evolve into a self-preserving form for longer simulation times. This self-preserving form is described by the competing mechanisms of coagulation and evaporation.

VII.1 Introduction

The synthesis and production of particles is usually modelled with the population balance equation (PBE) [VII.1]. The Monte Carlo (MC) simulation is one method among others to solve this equation numerically. It has the advantage that it can be easily adapted to particle populations described by several particle properties. It can render single particle events and track thus the history of single particles. The usage of weighted particles in the scope of the MC-simulation allows a higher accuracy [VII.2] and the simple incorporation of nucleation processes into the simulation in the scope of a hybrid approach [VII.3, VII.4] constituting thus an attractive alternative to the usually used constant-number schemes [VII.5].

The MC-simulations require in general large computational times which arise due to the demanding coagulation process. MC simulations are therefore not well suited for the coupling to CFD- or compartmental models. Several techniques have been proposed to overcome this problem. One of those recent approaches made use of a GPU and a fast approximation of the mean coagulation rate [VII.6]. Speed-ups of a factor of 200 were reported by the mere use of the GPU for the coagulation process [VII.7].

We present in the following an extension of the constant-number algorithm for the simulation of coagulation [VII.6]. The operator splitting technique [VII.8] is used to simulate in a hybrid approach the growth of particles and nucleation of new ones during one MC time step. The implementation of the nucleation algorithm is based on a parallel merging algorithm, which keeps the number of the simulation-particles constant. The growth of single simulation particles is simulated by the parallel solution of the corresponding differential equations describing the growth rates. This makes the simulation of condensation and evaporation processes possible. We present in this context the fast parallel summation technique in order to account for the mass-balance (i.e. the coupling to the gaseous phase). This coupling influences in turn the nucleation and condensation (or evaporation) rates of the simulated particles, so that Ostwald-ripening (typical for crystallization processes) can be simulated by the algorithm as well.

We present the application of this algorithm to the simulation of particles in a hot wall reactor and discuss the dependency of the particle properties on the initial saturation of the system.

VII.2 Population Balance Equation

The PBE describes the temporal change of the particle size distribution (PSD) $n(v)$ for particles with the volume v. The simultaneous process of coagulation, nucleation and growth are described by the following equation:

$$\begin{aligned}\frac{\mathrm{d}n(v,t)}{\mathrm{d}t} =& \frac{1}{2}\int_0^v \beta(v', v-v')n(v',t)n(v-v',t)\mathrm{d}v' - n(v,t)\int_0^\infty \beta(v,v')n(v',t)\mathrm{d}v \\ & - \nabla_v(G(v,n_\mathrm{G})n(v,t)) + N_R(n_\mathrm{G})\cdot\delta(v-v_\mathrm{nuc}(n_\mathrm{G}))\,.\end{aligned} \tag{VII.1}$$

The first two terms on the r.h.s. in equation (VII.1) describe the coagulation process for a given coagulation kernel $\beta(v, v')$, which is the collision frequency between two particles with the volumes v and v'. The third term on the r.h.s. describes the growth (if $G(v, n_\mathrm{G}) > 0$) or evaporation (if $G(v, n_\mathrm{G}) < 0$) of a particle with the size v with the corresponding rate $G(v, n_\mathrm{G})$. The last term describes the nucleation of new particles with the volume $v_\mathrm{nuc}(n_\mathrm{G})$ which are introduced with a nucleation rate of $N_\mathrm{R}(n_\mathrm{G})$ into the simulated system. The growth and nucleation rates $G(v, n_\mathrm{G})$ and $N_\mathrm{R}(n_\mathrm{G})$ (as well as the volume of the nucleated particles, $v_\mathrm{nuc}(n_\mathrm{G})$) depend on the concentration n_G of the monomers in the continuous gaseous (or liquid, if precipitation processes are described) phase. A general mass-balance equation has to be added in order to account for the conservation of the total mass (neglecting optional terms, which describe an additional in or out flow of n_G into the simulated system):

$$\frac{\mathrm{d}n_\mathrm{G}}{\mathrm{d}t} = -N_\mathrm{R}(n_\mathrm{G})\frac{v_\mathrm{nuc}}{v_\mathrm{M}} - \frac{1}{v_\mathrm{M}}\int_0^\infty n(v')G(v', n_\mathrm{G})dv'\,. \tag{VII.2}$$

The atomic (resp. molecular) volume of the material is denoted by v_M.

VII.3 Parallel, Hybrid Monte Carlo Algorithm

Instead of treating all simulated processes as competitive Monte Carlo events (see. [VII.5] for example), the coagulation is combined in a hybrid manner with the growth and nucleation processes based on the operator splitting technique. This technique decouples the coagulation and the nucleation and growth for small intervals of time. These intervals are chosen in this work to be equal to the event-driven MC time steps t_MC. The following simulation algorithm describes this notion:

- Initiate the time $t = 0$ and the nucleation volume buffer $V_\mathrm{B} = 0$.
- Repeat:
  1. Perform a parallel MC-event-driven step (one coagulation event) and estimate the time step value t_MC. This procedure is described in [VII.6] in detail.
  2. Simulate the growth (or evaporation) of all particles in parallel for the interval of time t_MC by the repetition of small steps $\Delta t \leq t_{MC}$:
     - Initiate the time $t_\mathrm{Growth} = 0$.
     - Repeat:

(a) For each MC-particle i (which has a statistical weight W_i and a volume v_i) the following equation is solved:

$$\frac{\mathrm{d}v_i}{\mathrm{d}t} = G(v_i, n_\mathrm{G}) \Rightarrow v_i^{(new)} = v_i + \Delta t \cdot G(v_i, n_\mathrm{G})\,. \tag{VII.3}$$

(b) Remove particles r from the simulation, if $v_r^{(new)} < v_\mathrm{M}$.

(c) Take the coupling to the continuous phase into account (Eq. (VII.2)):

$$n_\mathrm{G}^{(new)} = n_\mathrm{G} - \Delta t \cdot N_\mathrm{R}(n_\mathrm{G}) \frac{v_\mathrm{nuc}(n_\mathrm{G})}{v_\mathrm{M}} - \frac{\Delta t}{v_\mathrm{M}} \sum_{\substack{\text{not} \\ \text{evaporated} \\ \text{particles}}} W_i G(v_i, n_\mathrm{G}) + \sum_{\substack{\text{evaporated} \\ \text{particles}}} \frac{v_r}{v_\mathrm{M}} W_r\,. \tag{VII.4}$$

(d) Add the volume-concentration of newly nucleated particles to the buffer V_B:

$$V_\mathrm{B} = V_\mathrm{B} + \Delta t \cdot N_\mathrm{R}(n_\mathrm{G}) v_\mathrm{nuc}(n_\mathrm{G})\,. \tag{VII.5}$$

(e) If V_B is greater than a specific threshold value V_T, then:

i. include a new simulation particle into the simulation with the volume v_nuc and the statistical weight $W_\mathrm{nuc} = V_\mathrm{B}/v_\mathrm{nuc}$.

ii. Reset the buffer which stores the nucleated volume: $V_\mathrm{B} = 0$.

(f) Increase the time $t_\mathrm{Growth} = t_\mathrm{Growth} + \Delta t$.

– Until the time t_MC is reached: $t_\mathrm{Growth} = t_\mathrm{MC}$.

3. Increase the time $t = t + t_\mathrm{MC}$.

- Until the simulation end time t_end is reached: $t \geq t_\mathrm{end}$.

The parallel implementation of step 2a and 2c of the algorithm is depicted in Figure VII.1, first the updates of the volumes of each simulation particle are calculated, and then a parallel adding technique is used in order to estimate the new value of the concentration n_G. Only 14 parallel computational steps are necessary for the summation of 10 000 simulation particles.

Figure VII.1 and the described algorithm depict a Euler-implementation of the solution of the differential equation, in the here presented work a 4-5 Runge-Kutta-method has been used. This method comprises of the calculation of 7 consecutive v values, the algorithm in Figure VII.1 is thus repeated 7 times for one Runge-Kutta time step Δt.

VII.4 Simulated Test Cases

Small particle sizes are encountered in early stages of the gas-phase synthesis. The coagulation kernel describing the free-molecular regime can be used in order to describe the corresponding coagulation process:

$$\beta(v, v') = \left(\frac{3}{4\pi}\right)^{\frac{1}{6}} \sqrt{\frac{6 k_B T}{\rho_p}} \cdot \sqrt{\frac{1}{v} + \frac{1}{v'}} \cdot \left(v^{\frac{1}{3}} + v'^{\frac{1}{3}}\right)^2 \tag{VII.6}$$

Table VII.1 summarizes the parameter values and constants used for the simulation, k_B is the Boltzmann constant.

Table VII.1: Constants and parameters used for the simulation.

Name	Value
Temperature	$T = 1380\,\mathrm{K}$
Density (Fe)	$\rho_p = 7.874\,\mathrm{g\,cm^{-3}}$
Atomic volume (Fe)	$v_\mathrm{M} = 1.178 \cdot 10^{-29}\,\mathrm{m^{-3}}$
Atomic weight (Fe)	$m_1 = 9.27 \cdot 10^{-26}\,\mathrm{kg}$
Surface tension (Fe, 1380 K)	$\gamma = 0.29\mathrm{J\,m^{-2}}$
Vapor pressure (Fe, 1380 K)	$p_\mathrm{s} = 0.805\,\mathrm{Pa}$

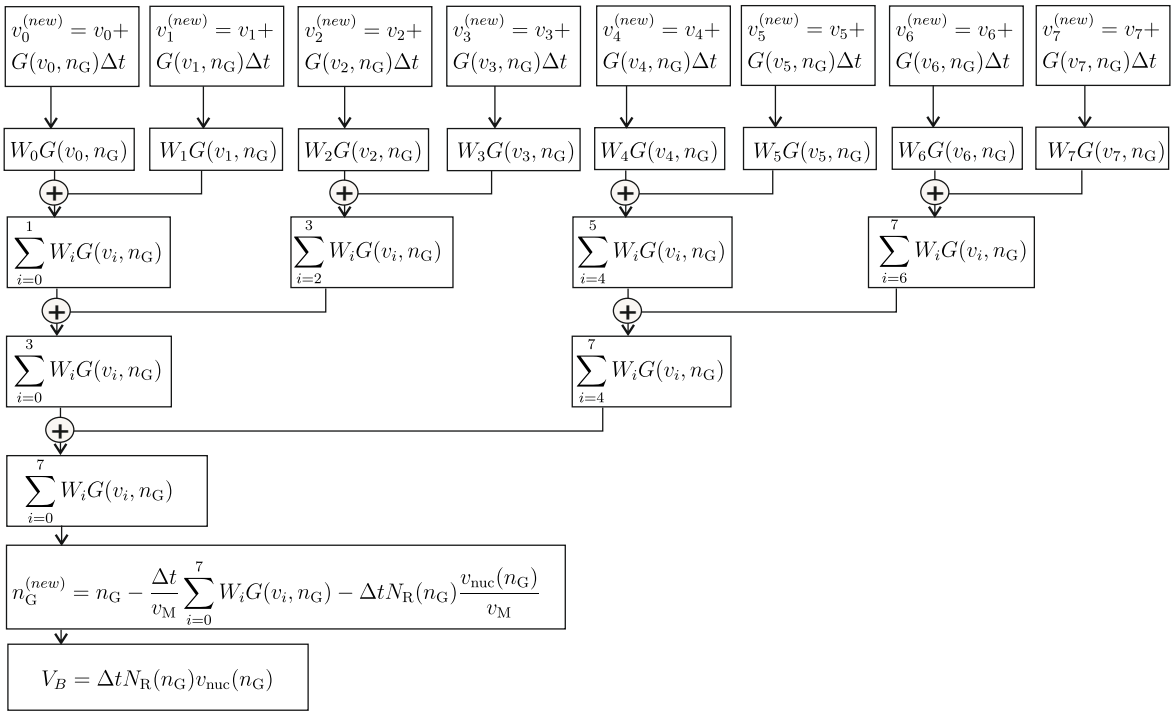

Figure VII.1: The parallel algorithm calculates the new volumes $v_i^{(new)}$ of the simulation particles i in the first row. The evaluated values $\Delta t \cdot G(v_i, n_G) \cdot W_i$ (resp. v_i / v_M in the case of evaporation) are reused in the consecutive computational steps for the parallel calculation of $n_G^{(new)}$.

The growth rate in the free-molecular regime is described by:

$$G(v, n_G) = \frac{v_M \cdot \pi \cdot \left(\frac{6v}{\pi}\right)^{\frac{2}{3}}}{\sqrt{2\pi \cdot m_1 \cdot k_B \cdot T}} \cdot \left(k_B \cdot T \cdot n_G - p_s \cdot \exp\left\{ \frac{4 \cdot \gamma \cdot v_M}{k_B \cdot T \cdot \left(\frac{6v}{\pi}\right)^{\frac{1}{3}}} \right\} \right) . \tag{VII.7}$$

The nucleation term is described by the classical kinetic theory:

$$N_R(n_G) = n_G \cdot \sqrt{\frac{2\gamma}{\pi \cdot m_1}} \frac{p_s}{k_B \cdot T} \cdot \exp\left(- \frac{16 \cdot \pi \cdot \gamma^3 \cdot v_m^2}{3 \cdot k_B^3 \cdot T^3 \cdot \ln(S)^2} \right) \quad , \text{ with } S = \frac{n_G k_B T}{p_s} . \tag{VII.8}$$

The volume of the nucleated particles is given by the Kelvin diameter d^*, with

$$v_{nuc}(n_G) = \frac{\pi (d^*)^3}{6} = \frac{64 \cdot \pi^4 \cdot v_M^3}{6 \cdot k_B^3 \cdot T^3 \cdot (\ln(S))^3} \quad , \text{ with } S = \frac{n_G k_B T}{p_s} . \tag{VII.9}$$

The initial conditions for the simulated system consist of a lognormal PSD, with the geometric mean value d_g=2 nm and the geometric standard deviation σ_g=1.2, rendering a total number-concentration of 1016 m-3. The change of the PSD depending on the initial saturations of S_0=1.5, 2.5 and 4.5 are discussed in the results section.

VII.5 Simulation Results

The nucleation rates depend strongly on the saturation of the system, as shown in Figure VII.2a and VII.2b, a slight drop of the saturation from 2.5 to 1.5 leads to a drop off which comprises nearly 20 orders of magnitude. This leads in turn to dramatic changes of the number-concentration, as can be seen in Figure VII.2c.

Exemplary PSDs are shown in Figure VII.3 for the time points marked by the horizontal lines in Figure VII.2. A growth of the initial PSD is accompanied with the nucleation of novel particles in both presented cases leading to a multimodal PSD. The higher nucleation rates for S_0=4.5 (Figure VII.3b) lead to a nucleation peak which describes particle concentrations, which are 3 orders of magnitude

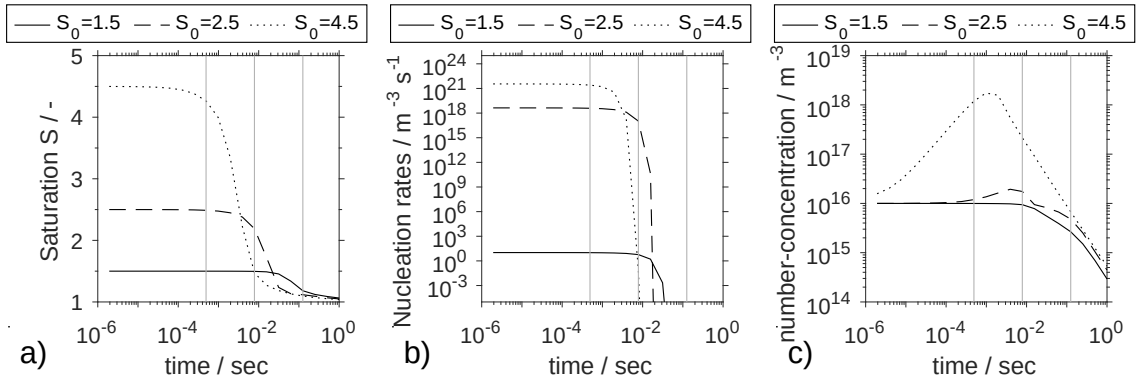

Figure VII.2: The saturation S (a), nucleation rates $N_{\mathrm{R}}(n_{\mathrm{G}})$ (b) and the number-concentration of all simulation particles (c) are shown in dependency of the initial saturation S_0.

higher than the particles rendered by the initial PSD concentration. It can be seen, that the usage of weighted particles allows to render even such extreme PSDs, which are only reproducible if a very large number of equally weighted simulation particles is used.

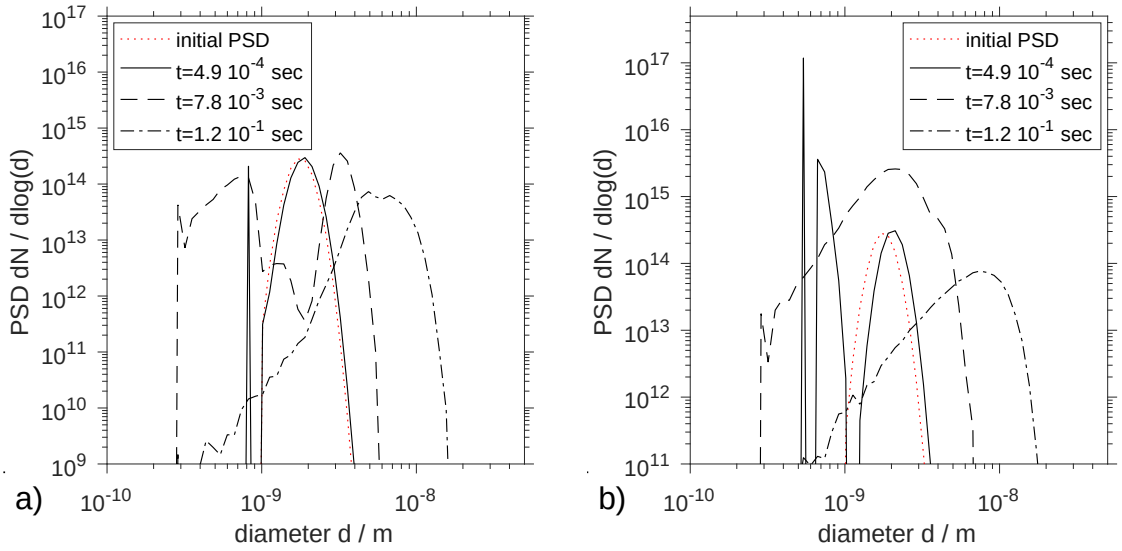

Figure VII.3: The PSDs for the initial saturation S_0=2.5 (a) and S_0=4.5 (b) are shown.

The moments of the PSDs are shown Figure VII.4 it can be seen, that for longer simulation times the geometric standard deviation reaches a constant value (large noise levels are found for this value due to the rendition of evaporation by discrete particles, the left side of the PSD in Figure VII.5b), while the mean geometric diameter increases linearly, this marks the characteristics of a self-preserving particle size distribution (SPD), whose form is the same for all simulated initial saturations S_0 and is discussed for the case S_0=1.5 in more detail.

Low initial saturation values S_0 lead to negligible nucleation rates, so that the development of the given initial PSD is described by the coagulation and growth only. Exemplary simulation results for this scenario are shown in Figure VII.5 for S_0=1.5. It can be seen, that the PSDs attain a self-preserving distribution (SPD), which is slightly different from the SPD which is attained for the coagulation only. It can also be seen, that the major part of the SPD is smaller than the corresponding Kelvin diameter and should therefore evaporate in the absence of the coagulation process. The simulation particles have therefore to be simulated as long as they are bigger than the monomer (atomic) size of the simulated material – instead of removing them already from the simulation when they reach sizes which are smaller than the Kelvin diameter.

The computational times are summarized in Table VII.2, the results show the required simulation times for 100 simulations which are executed in parallel, each simulation consists of 1000 simulation

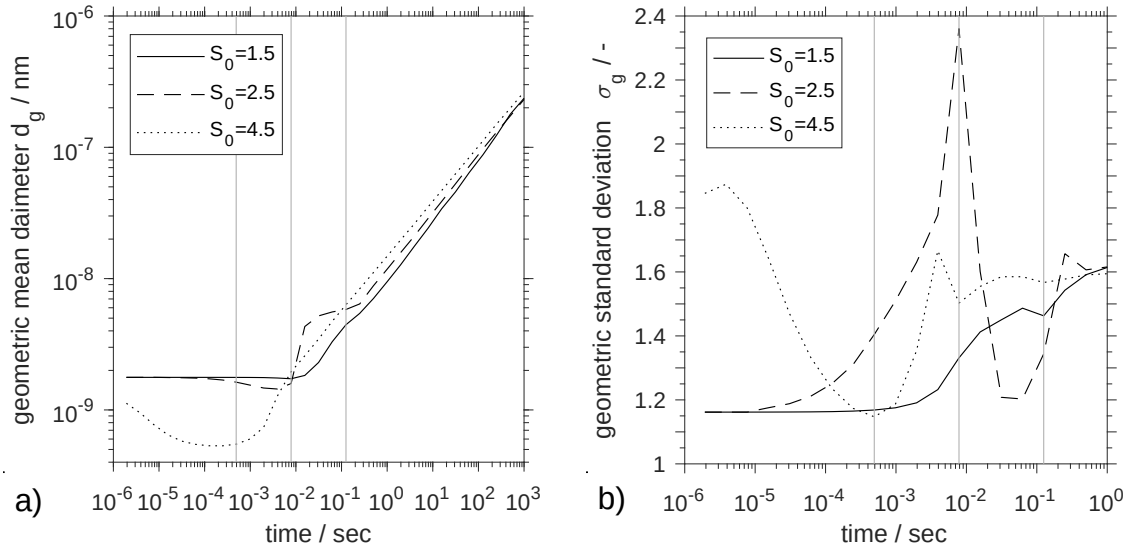

Figure VII.4: The geometric mean diameter (a) and standard deviation (b) are shown.

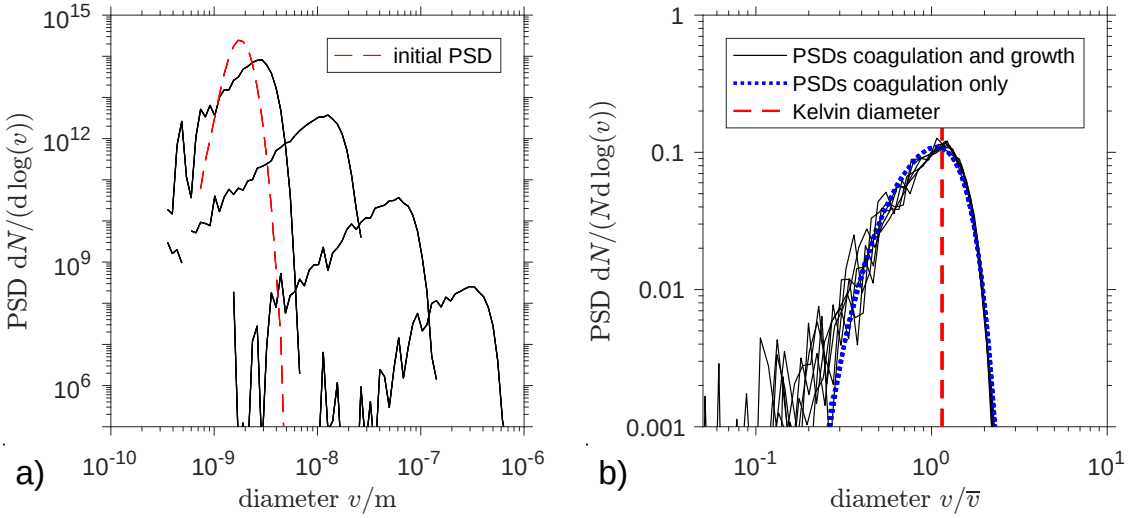

Figure VII.5: The PSDs for the simulation of combined coagulation and growth are shown in (a) for an initial saturation of S_0=1.5. The PSDs are normed to the mean diameter $\overline{v}$ and the particle number-concentration N in (b) in order to highlight the self-preserving character of the PSDs.

particles. This means, that 10^5 coupled differential equations have been solved in total (combined with the event driven Monte Carlo code). This finding underscores the computational efficiency of the presented algorithm. The simulations were performed on a NVIDIA GTX 980 graphics processing unit.

VII.6 Conclusions

A hybrid GPU-based simulation technique for the simultaneous simulation of coagulation, nucleation and growth (resp. evaporation) with a coupling to the continuous phase is presented. The combination of a parallel, event-driven Monte Carlo simulation with a Runge-Kutta based parallel solution of differential equations is discussed for this purpose. The resulting Algorithm can be used to describe the gas-phase synthesis of particles. The usage of weighted simulation particles allows to render multimodal PSDs, for which each mode represents different particle concentration which vary several orders of magnitude and are typically encountered at the initial stages of the simulation. The detailed rendering of the evaporation process of the particles allows the description of a self-preserving size

Table VII.2: Computational times required for the simulation of t= 1000 seconds.

	S_0=1.5	S_0=2.5	S_0=4.5
Computing time	45 sec	74 sec	145 sec

distribution which results from the competing process of evaporation and coagulation and is encountered at the later stages of the simulation. Although the explicit calculations of several thousands of coupled differential equations poses a severe computational task, we show, that an efficient GPU implementation of this problem is able to produce relevant results which describe the simulated process completely within just a few minutes. The algorithm is therefore applicable in the framework of compartmental models or flow-sheet simulations.

Acknowledgments

The financial support of DFG (Deutsche Forschungsgemeinschaft) within the priority program SPP 1679 "Dynamic flowsheet simulation of interconnected solids processes" is gratefully acknowledged.

References

[VII.1] D. Ramkrishna. *Population balances: Theory and applications to particulate systems in engineering*. 1st ed. New York: Academic Press, 2000. ISBN: 9780125769709.

[VII.2] H. Zhao, F. E. Kruis, and C. Zheng. "Reducing statistical noise and extending the size spectrum by applying weighted simulation particles in Monte Carlo simulation of coagulation". *Aerosol Science and Technology* 43.8 (2009), pp. 781–793. DOI: 10.1080/02786820902939708.

[VII.3] W. J. Menz, J. Akroyd, and M. Kraft. "Stochastic solution of population balance equations for reactor networks". *Journal of Computational Physics* 256 (2014), pp. 615–629. DOI: 10.1016/j.jcp.2013.09.021.

[VII.4] X. Hao et al. "Population balance-Monte Carlo simulation for gas-to-particle synthesis of nanoparticles". *Aerosol Science and Technology* 47.10 (2013), pp. 1125–1133. DOI: 10.1080/02786826.2013.823642.

[VII.5] S. Khalili et al. "Constant number Monte Carlo simulation of population balances with multiple growth mechanisms". *AIChE Journal* 56.12 (2010), pp. 3137–3145. DOI: 10.1002/aic.12233.

[VII.6] J. Wei and F. E. Kruis. "A GPU-based parallelized Monte-Carlo method for particle coagulation using an acceptance–rejection strategy". *Chemical Engineering Science* 104 (2013), pp. 451–459. DOI: 10.1016/j.ces.2013.08.008.

[VII.7] J. Wei. "Comparison of computational efficiency of inverse and acceptance–rejection scheme by Monte Carlo methods for particle coagulation on CPU and GPU". *Powder Technology* 268 (2014), pp. 420–423. DOI: 10.1016/j.powtec.2014.08.047.

[VII.8] M. Celnik et al. "Coupling a stochastic soot population balance to gas-phase chemistry using operator splitting". *Combustion and Flame* 148.3 (2007), pp. 158–176. DOI: 10.1016/j.combustflame.2006.10.007.

Paper VIII

Preprint submitted for publication in:
8th World Congress on Particle Technology (WCPT), Orlando, 2018
Proceedings ISBN: 978-0-8169-1105-9
Available online at:
https://www.aiche.org/conferences/world-congress-on-particle-technology/2018/proceeding/paper/49d-parallel-gpu-based-monte-carlo-techniques-flowsheet-simulation-solid-processes

Parallel GPU-Based Monte Carlo Techniques for the Flowsheet Simulation of Solid Processes

G. Kotalczyk, K. Lambach and F.E. Kruis

Abstract

We describe two parallel algorithms (the deterministic 'merging' algorithm and the stochastic 'random removal' method) for the simulation of particulate flow between single units in the context of flow-sheet simulations. These algorithms are tested on an exemplary flow-sheet system modelling typical particle production processes. The mixing of several particulate instreams into single units as well as the separation of particles in screen units according to their size are included into this test system. The proposed methods are validated by comparison with numerical solutions of the corresponding sets of differential equations. Although the 'random removal' technique can be used in the context of coagulation or nucleation, we find that it leads to very high levels of statistical noise in the here presented transport implementation. These high noise levels make the method nearly inapplicable for problems of the same complexity as the here presented one. The presented introduced parallel merging algorithm shows less statistical noise and a very good reproduction of the benchmark results at the cost of greater computational complexity and thus computing times.

VIII.1 Introduction

The description of particle production processes by means of a flow-sheet simulation allows a simple framework for performance analysis and optimization. The modularization of a whole process into single unit operations allows the investigation of specific settings of single units and consequences of these settings for the overall process. The solution of the corresponding equations, however, poses a subject of great difficulty, hence mostly several particle properties have to be taken into account for the complete characterization of the particulate material. The corresponding particle dynamics may exhibit strong non-linear dependencies on these multi-variate properties and are mostly described by the population balance equation (PBE) (see e.g. [VIII.1, VIII.2]). The Monte Carlo (MC) technique poses a solution method for the PBE, which allows to take several particle properties into account. Such multivariate modelling requires normally a large amount of computational resources, if a sectional method is used for the solution of the PBE (see e.g. [VIII.3]).

The modelled particle size distributions (PSD) can describe differences in particle concentrations which can span several orders of magnitudes. The computational efficient description of such large differences of particle concentrations becomes possible by the application of weighted MC simulation particles [VIII.4, VIII.5]. Recent algorithms for the nucleation, coagulation [VIII.6], condensational growth/evaporation [VIII.7] and breakage [VIII.8] of particles by means of weighted MC simulation particles have been formulated specifically for graphic processing units (GPU). It has been shown that the parallel computation of the GPU architecture could be exploited for the accelerated solution of the PBE, making thus the incorporation of this stochastic technique for the simulation of flow-sheet processes suitable.

Production processes on plant scale can be mostly formulated as a sequence of coupled unit operations (with possible tear-streams), which in turn can be described by the PBEs. There exist several approaches, to solve such a system, next to the sequential modular approach, a (simultaneous) equation-oriented approach can be chosen to describe such a coupled system (see e.g. [VIII.9, VIII.10]). The parallel formulation of the solution of the PBEs by means of the MC method is best suited for the equation-oriented approach.

We present in the following a parallel simulation algorithm for particulate transport, which allows the incorporation of these several mechanisms in an operator splitting technique (see e.g. [VIII.11]), this in turn allows the analysis and optimization of a complex manufacturing process, like it is described in the next section further below.

VIII.2 Simulated System

We describe a transport algorithm for a particle production process as it is shown in Figure VIII.1. The initial particulate material represented by large particles of the size of ca. 50 nm is dispersed into a carrier gas. These initial particles are mixed in two subsequent units with pulsed aerosol feeds carrying particles of different materials, representing size ranges of around 3nm and 10 nm, the exact properties of the simulated particles can be found in Table VIII.1. In a real application, the particles would grow due to agglomeration and the screen would separate large agglomerated product particles (these are collected by the following filter) from smaller particles (these are directed to a mixer unit for further agglomeration). Hence the agglomeration process is not considered in this work, the screen is operating in a different size range (defined further below) than the one presented in Figure VIII.1.

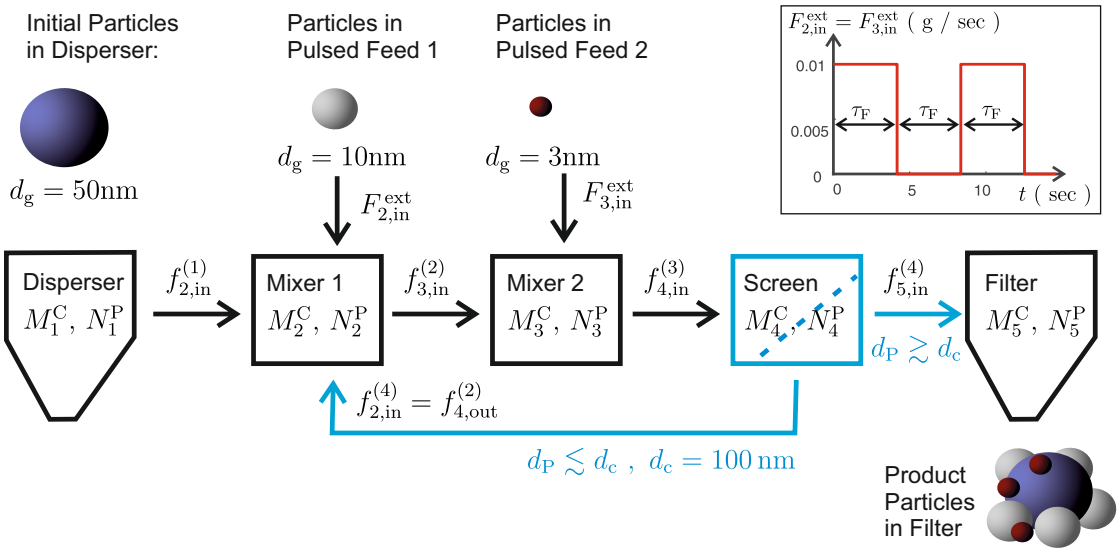

Figure VIII.1: Flowsheet of the simulated system.

Table VIII.1: Properties of the initial particle populations and the particles within the feeds.

Location of particle population with unit number () or Feed symbol	Initial population in disperser (1)	In Feed 1 $F_{2,\mathrm{in}}^{(\mathrm{ext})}$	In Feed 2 $F_{3,\mathrm{in}}^{(\mathrm{ext})}$
Particle concentration $n_{\mathrm{F},i}$ / kg (carrier gas)	-	$5 \cdot 10^{15}$	$2 \cdot 10^{15}$
Initial number of particles in disperser / resp. total number of particles inserted by feeds in 28 s	10^{10}	$8 \cdot 10^{11}$	$3.2 \cdot 10^{11}$
Initial particle mass in disperser / resp. particle mass inserted by feeds in 28 s / ng	5.98	6.28	0.07
Mean geometric diameter d_{g} /nm	50	10	3
Geometric standard deviation	1.2	1.46	1.46.

VIII.2.1 Transport Equations for the Carrier Gas

The net amount of carrier mass $M_i^{(\mathrm{C})}$ (units kg) changes over time for each unit i and is modeled by the following set of equations:

$$\frac{\mathrm{d}M_i^{\mathrm{C}}}{\mathrm{d}t} = \sum_{j \neq i} \left(f_{i,\mathrm{in}}^{(j)} \cdot M_j - f_{i,\mathrm{out}}^{(j)} \cdot M_i \right) + F_{i,\mathrm{in}}^{(\mathrm{ext})} \,, \qquad \text{with: } f_{i,\mathrm{in}}^{(j)} = f_{j,\mathrm{out}}^{(i)} \forall i \neq j \,, \tag{VIII.1}$$

where $f_{i,\mathrm{in}}^{(j)}$ denotes the relative inflow rate (units 1/s) into unit i from unit j and $f_{i,\mathrm{in}}^{(j)}$ the outflow from unit i to unit j. The exact values are listed in Table VIII.2. The pulsed feeds $F_{2,\mathrm{in}}^{(\mathrm{ext})}$ and $F_{3,\mathrm{in}}^{(\mathrm{ext})}$ are described by the following formula:

$$F_{2,\mathrm{in}}^{(\mathrm{ext})}(t) = F_{3,\mathrm{in}}^{(\mathrm{ext})}(t) = \begin{cases} F_{\mathrm{in}}^{(\max)} = 0.01\mathrm{g/sec} = & \text{, if } \lfloor t/\tau_{\mathrm{F}} \rfloor = 0, 2, 4, 6, \ldots \\ 0 & \text{, if } \lfloor t/\tau_{\mathrm{F}} \rfloor = 1, 3, 5, 7, \ldots \end{cases} \,, \quad \text{with: } \tau_{\mathrm{F}} = 4 \text{ sec} \,. \tag{VIII.2}$$

The floor function $\lfloor x \rfloor$ denotes thereby the largest integer number smaller than the rational number x.

Table VIII.2: Initial Conditions and flow rates for each unit in Figure VIII.1. The properties of the particle populations are listed in Table VIII.1.

	Disperser	Mixer 1	Mixer 2	Screen	Filter
Unit number in Eqs. (VIII.1) and (VIII.3)	(1)	(2)	(3)	(4)	(5)
Initial particle populations	Yes	No	No	No	No
Initial carrier gas masses $M_i^{\mathrm{C},(0)}$ /mg	100	0.1	0.1	0.1	0
Outflow rates / s^{-1}	$f_{1,\mathrm{out}}^{(2)} = 0.2$	$f_{2,\mathrm{out}}^{(3)} = 1$	$f_{3,\mathrm{out}}^{(4)} = 1$	$f_{4,\mathrm{out}}^{(2)} = 0.7$, $f_{4,\mathrm{out}}^{(5)} = 2$	No
External pulsed feeds maximal rates / mg /s	–	$F_{2,\mathrm{in}}^{(\mathrm{ext})} = 10$	$F_{3,\mathrm{in}}^{(\mathrm{ext})} = 10$	–	–

VIII.2.2 Transport Equations for Particles

We assume that the particles are mixed homogeneously and instantaneously upon arrival in each unit, so that a constant concentration $n_i^{(\mathrm{C})}$ (units / kg) of particles can be found throughout each unit. For the number of particles N_i^{P} (dimensionless number, $N_i^{\mathrm{P}} = n_i^{(\mathrm{C})} \cdot M_i^{\mathrm{C}}$) within each unit, the following equations result for the change of the number of particles due to the transport:

$$\frac{\mathrm{d}N_i}{\mathrm{d}t} = \sum_{j \neq i} \left(f_{i,\mathrm{in}}^{(j)} \cdot N_j - f_{i,\mathrm{out}}^{(j)} \cdot N_i \right) + F_{i,\mathrm{in}}^{(\mathrm{ext})} \cdot n_{\mathrm{F},i} \text{ for } j \neq 4 \,, \tag{VIII.3}$$

with the relative flows $f_{i,\mathrm{in}}^{(j)}$, $f_{i,\mathrm{in}}^{(j)}$ and absolute flows $F_{i,\mathrm{in}}^{(\mathrm{ext})}$ used in Eq. (VIII.1) and (VIII.2) and tabulated in Table VIII.1. The values for the particle concentrations $n_{\mathrm{F},i}$ within the feeds are listed in Table VIII.1. For the description of the screen (unit 4, $j = 4$), it is assumed, that the total outflow of the carrier mass $\left(f_{4,\mathrm{out}}^{(2)} + f_{4,\mathrm{out}}^{(5)}\right)$ corresponds to the correct decrease of the particle number, $N_i \cdot \left(f_{4,\mathrm{out}}^{(2)} + f_{4,\mathrm{out}}^{(5)}\right)$, but that the particles are either found in the stream to the second unit or to the fifth unit, depending on their volume v, resulting in the following modified particle flow rates:

$$f_{4,\mathrm{out}}^{\mathrm{P}(2)}(v) = \left(f_{4,\mathrm{out}}^{(2)} + f_{4,\mathrm{out}}^{(5)}\right) \cdot S(v)\ , \quad \text{and:}\quad f_{4,\mathrm{out}}^{\mathrm{P}(5)}(v) = \left(f_{4,\mathrm{out}}^{(2)} + f_{4,\mathrm{out}}^{(5)}\right) \cdot (1 - S(v))\ , \tag{VIII.4}$$

where $S(v)$ is a separation function describing the screening process. The resulting Eqs. (VIII.4) have to be used instead of $f_{4,\mathrm{out}}^{(2)}(v)$ and $f_{4,\mathrm{out}}^{(5)}(v)$ in Eq. (VIII.3) for the screen unit. In this work, the following simplified separation function is applied:

$$S(v) = \begin{cases} 1 & , \quad v < v_{\mathrm{S}} = \pi \cdot d_{\mathrm{S}}^3/6, & \text{with: } d_{\mathrm{S}} = 40\ \mathrm{nm}\,, \\ (v_{\mathrm{E}} - v)/(v_{\mathrm{E}} - v_{\mathrm{S}}) & , \quad v_{\mathrm{S}} < v < v_{\mathrm{E}} = v_{\mathrm{S}} + 2 \cdot (\pi \cdot d_{\mathrm{C}}^3/6 - v_{\mathrm{S}}), & \text{with: } d_C = 50\ \mathrm{nm}\,, \\ 0 & , \quad v > v_{\mathrm{E}} = \pi \cdot d_{\mathrm{E}}^3/6 & \text{with: } d_{\mathrm{E}} \approx 57.8\ \mathrm{nm}\,. \end{cases} \tag{VIII.5}$$

VIII.3 Simulation Methods

VIII.3.1 Transport of Weighted Monte Carlo (MC) Particles

The application of weighted MC particles allows to render the PSD in a more precise way [VIII.4]. Each MC particle in the unit is assigned an additional property, the statistical weight . This approach allows alternative formulations to the stochastic determination, which particles are selected to leave a compartment (or unit) and to be inserted into the next one (specific transport events are defined by [VIII.12, VIII.13] allows multiple simulation particles to leave within one time step and formulates binomial probabilities for these events).

If weighted MC particles are simulated, exact calculation of the removed weight becomes possible. The following simple Euler approach summarizes this for the MC particle k in the unit i:

$$W_k^{(i)}(t+\Delta t) = W_k^{(i)}(t) - W_k^{(i)}(t) \cdot \sum_{j \neq i} f_{i,\mathrm{out}}^{(j)} \cdot \Delta t = W_k^{(i)}(t) \cdot F, \qquad \text{with: } F = 1 - \sum_{j \neq i} f_{i,\mathrm{out}}^{(j)} \cdot \Delta t\,. \tag{VIII.6}$$

For each connected unit j which is connected to i, new MC particles are added with the same properties as particle k in the unit i and the statistical weight:

$$W_{\mathrm{new},k}^{(j)}(t + \Delta t) = f_{i,\mathrm{out}}^{(j)} \cdot \Delta t \cdot W_k^{(i)}(t)\,. \tag{VIII.7}$$

A scaling factor F can be used to keep track of the depleted statistical weight for all particles, if the flowrates are independent on the particle size, like proposed by [VIII.14]. However, in case of a unit operation like the screening process, the flow rates depend on the particle properties (the volume v according to Equation (VIII.4)), Equations (VIII.6) and (VIII.7) have to be evaluated for each individual particle. This might be computationally disadvantageous in the case of a serial implementation, but it is very efficient if a parallel implementation in combination with a graphic processing unit (GPU) is applied. The new particles with the weights $W_{\mathrm{new},k}^{j}$ can be inserted into the simulation by means of parallel merging algorithms or by the random removal of existing particles.

VIII.3.2 Merging

Following the approach presented in [VIII.6], two particles i and j with the statistical weights W_i, W_j and the volumes v_i and v_j are merged with each other to a new particle with W_{new} and v_{new} with the merge error E_{m} defined via:

$$W_{\mathrm{new}} = W_i + W_j, \qquad v_{\mathrm{new}} = (W_i \cdot v_i + W_j \cdot v_j)/(W_i + W_j), \qquad E_{\mathrm{m}} = \left(\left(v_i - v_j\right) / \min\left(v_i, v_j\right)\right)^2. \tag{VIII.8}$$

While the parallel algorithm in [VIII.6] dealt with the problem to include one nucleated particle into an existing particle population by finding merge partners with low statistic weights and the lowest

merge errors of a sample, the here presented work merges two entire particle populations with each other. This is done by a large number of parallel comparisons. The algorithm compares for two particles, whether the merging error is smaller than a predefined value E_{min}. The pair is merged if the condition is true. The value E_{min} is increased in the course of the simulation.[1]

VIII.3.3 Random Removal

The random removal algorithm has been introduced in the framework of a MC simulation of coagulation, in order to ascertain a constant number of simulation particles and avoid the decrease of computational accuracy [VIII.15]. We use this algorithm with some modifications for weighted simulation particles (like described in [VIII.6]). MC particles of the streams are included into the holdup by removing either the existing particles from the holdup or the particles from the stream and redistributing the removed mass on the rest of the particle population by multiplication with a constant factor. Random numbers are used for the selection of the particles which are to be removed.

VIII.3.4 Fixed Pivot Technique

For the validation of the transport code, a fixed pivot technique is used – although defined for the simulation of coagulation [VIII.16], it can be easily applied to the given problem. A fine one-dimensional grid of 1000 pivot points is set up, spanning particle sizes from 1 nm (first pivot point) to 10 μm (last pivot point), the sizes of two adjacent pivot points increase by a factor of $10^{(1/12)} \approx 1.028$. The pivot points are initiated with concentrations corresponding to the particle size distributions defined in Table VIII.1, and for each point the transport equation (VIII.3) is solved numerically.

VIII.4 Results

Figure VIII.2 shows exemplary PSDs resulting from the prolonged application of the merging technique as well as the random removal technique. The PSD in the disperser can be approximated by both methods exactly, hence no particles have to be inserted into this unit. It can be seen, that the random removal technique fails to predict the PSDs of the other units correctly. Both simulation techniques preserve the total mass of all particles in all units in the scope of the floating point precision, like it is shown in Figure VIII.3a. The total mass in all units resulting from the pivot method, M_{piv}, is compared in the Figure with the total mass M_{MC} resulting from MC simulations. Similar results can be seen for the number of particles (N_{piv} for the pivot method and N_{MC} for MC particles) in the screen unit, which is shown in Figure VIII.3. It can be seen, that the accuracy of the simulation can be tuned by the choice of the Euler step size and that this accuracy increases for smaller step sizes. Smaller step sizes lead, however to larger computational times, which are summarized in Table 3.

Table VIII.3: Computational times for 10 240 MC particles in seconds using a NVIDIA GTX 980 Ti GPU.

Euler step size (sec)	$\Delta t = 0.1$	$\Delta t = 0.01$	$\Delta t = 0.001$
Merging (10 parallel simulations)	198.9	2 012.7	19 928.6
Random Removal (100 parallel simulations)	49.5	128.7	1 181.5

It should also be mentioned, that the random removal methods exhibit a large amount of statistical noise. The arithmetic standard deviations for the values of the number-concentration of the particles (or the geometric mean diameter or the geometric standard deviations of the PSDs) are higher than 10% of the arithmetic mean of these values – this very high level of statistical noise disqualifies the here presented random removal technique for many flowsheet applications.

[1] An increase of E_{min} by a factor of 4 is done after every 64 parallel comparison steps – if the program is not terminated earlier because of the successful merging of all populations. During each parallel comparison step, 512 MC particles from each stream are compared with 512 MC particles in the hold up. The compared pairs change with each loop iteration, so that after 512 parallel loops (7 increments of E_{min}) each of the 512 MC particles in the holdup unit would have been compared with every particle from every stream, if no particles could have been merged. The data representing the particles is divided in blocks, where each block operates on its 512 particles for each stream and the holdup of the unit (if 10240 MC particles are used for the simulation, then 20 data blocks are used in parallel). We observed, that an initial setting of $E_{\text{min}} = 10^{-4}$ leads to the successful merging of all streams long before the end of the theoretically possible 512 loops – the last loop iteration would be done with the largest value for E_{min}, which is: E_{min} =1.64.

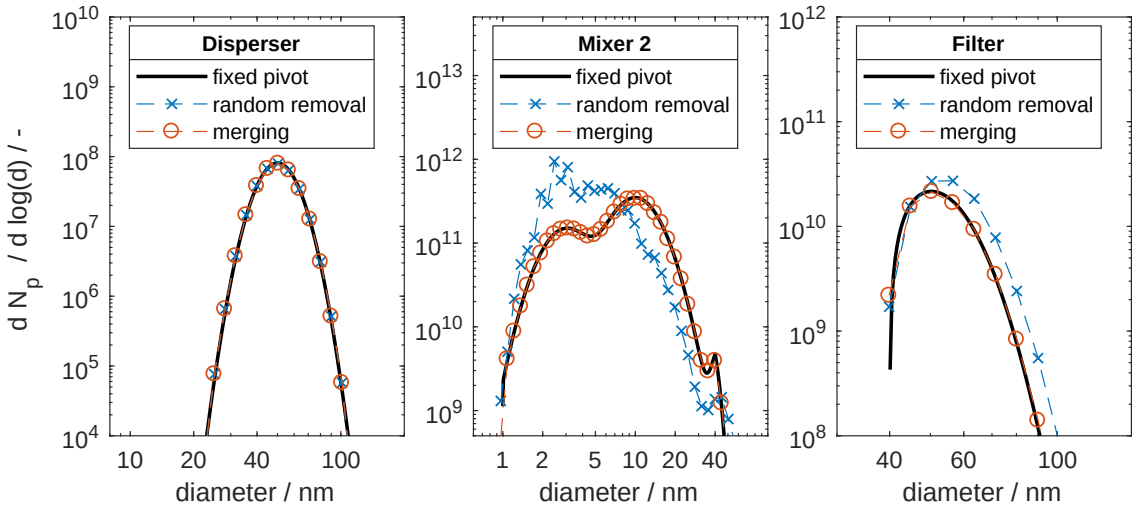

Figure VIII.2: PSDs for 3 units in Figure VIII.1 (the screen operates for particle ranges defined by Equation (VIII.5)) for a simulation time of 28 seconds, 10 240 MC particles and an Euler time step of $\Delta t = 0.1$ sec.

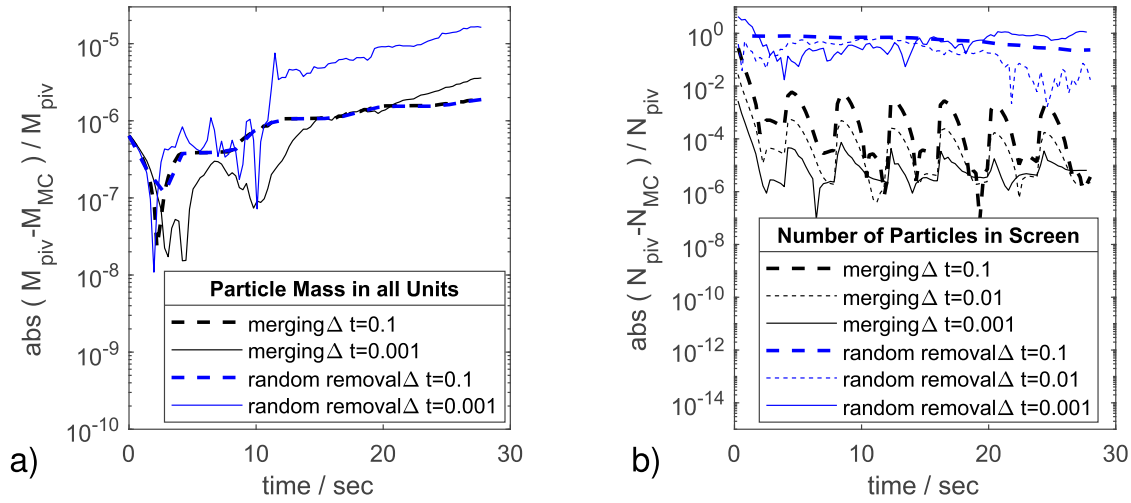

Figure VIII.3: The deviations of the MC simulations from the pivot results for different values of the Euler step Δt. a) the total mass of the system is compared. b) the number concentration in the screen unit is compared. The results are shown for 10240 MC particles.

VIII.5 Conclusions

We introduce and investigate Monte Carlo (MC) simulation techniques for the particulate transport in a network of units (or compartments). The techniques are benchmarked by comparison to simulations based on the fixed pivot method. The application of parallel algorithms, designed to run on graphic processor units (GPUs) has been tested for the simulation of an exemplary production setup with recycle streams, mixers and a screen unit. The simulation of the transport alone poses a challenging task, and it could be shown, that the simulation of a deterministic outflow of particles from single units coupled to a stochastically simulated inflow (simply termed 'random removal' in this work) is not able to reproduce the benchmark results with a high level of accuracy. A deterministic method, a massive parallel merge algorithm has been introduced, and the Euler step size has been identified as a parameter, which allows to tune the accuracy at the expense of the required computational time. This algorithm proves to reproduce the benchmark results with a high accuracy and is a promising candidate for a computationally efficient simulation of a multivariate flow-sheet problem, which also includes other non-linear particle processes, like coagulation, growth, evaporation, breakage, nucleation and

others.

Acknowledgments

This work is supported by the DFG (Deutsche Forschungsgemeinschaft) within the priority program SPP 1679 "Dynamic flowsheet simulation of interconnected solids processes".

References

[VIII.1] D. Ramkrishna and M. R. Singh. "Population balance modeling: Current status and future prospects". *Annual Review of Chemical and Biomolecular Engineering* 5 (2014), pp. 123–146. DOI: 10.1146/annurev-chembioeng-060713-040241.

[VIII.2] D. Ramkrishna. *Population balances: Theory and applications to particulate systems in engineering*. 1st ed. New York: Academic Press, 2000. ISBN: 9780125769709.

[VIII.3] Y. Xiong and S. E. Pratsinis. "Formation of agglomerate particles by coagulation and sintering-Part I. A two-dimensional solution of the population balance equation". *Journal of Aerosol Science* 24.3 (1993), pp. 283–300. DOI: 10.1016/0021-8502(93)90003-R.

[VIII.4] H. Zhao, F. E. Kruis, and C. Zheng. "Reducing statistical noise and extending the size spectrum by applying weighted simulation particles in Monte Carlo simulation of coagulation". *Aerosol Science and Technology* 43.8 (2009), pp. 781–793. DOI: 10.1080/02786820902939708.

[VIII.5] R. I. A. Patterson, W. Wagner, and M. Kraft. "Stochastic weighted particle methods for population balance equations". *Journal of Computational Physics* 230.19 (2011), pp. 7456–7472. DOI: 10.1016/j.jcp.2011.06.011.

[VIII.6] G. Kotalczyk and F. E. Kruis. "A Monte Carlo method for the simulation of coagulation and nucleation based on weighted particles and the concepts of stochastic resolution and merging". *Journal of Computational Physics* 340 (2017), pp. 276–296. DOI: 10.1016/j.jcp.2017.03.041.

[VIII.7] G. Kotalczyk, I. Skenderović, and F. E. Kruis. "A GPU-based monte carlo technique for the simulation of simultaneous nucleation, coagulation and growth based on weighted simulation particles". In: *AIChE annual meeting (2016)*. ISBN: 978-151083444-6.

[VIII.8] G. Kotalczyk, J. Devi, and F. E. Kruis. "A time-driven constant-number Monte Carlo method for the GPU-simulation of particle breakage based on weighted simulation particles". *Powder Technology* 317 (2017), pp. 417–429. DOI: 10.1016/j.powtec.2017.05.002.

[VIII.9] V. Skorych et al. "Novel system for dynamic flowsheet simulation of solids processes". *Powder Technology* 314 (2017), pp. 665–679. DOI: 10.1016/j.powtec.2017.01.061.

[VIII.10] M. Hillestad and T. Hertzberg. "Dynamic simulation of chemical engineering systems by the sequential modular approach". *Computers and Chemical Engineering* 10.4 (1986), pp. 377–388. DOI: 10.1016/0098-1354(86)87008-9.

[VIII.11] M. Celnik et al. "Coupling a stochastic soot population balance to gas-phase chemistry using operator splitting". *Combustion and Flame* 148.3 (2007), pp. 158–176. DOI: 10.1016/j.combustflame.2006.10.007.

[VIII.12] C. L. Marshall, P. Rajniak, and T. Matsoukas. "Multi-component population balance modeling of granulation with continuous addition of binder". *Powder Technology* 236 (2013), pp. 211–220. DOI: 10.1016/j.powtec.2012.01.027.

[VIII.13] R. Irizarry. "Fast compartmental Monte Carlo simulation of population balance models: Application to nanoparticle formation in nonhomogeneous conditions". *Industrial and Engineering Chemistry Research* 51.47 (2012), pp. 15484–15496. DOI: 10.1021/ie3011116.

[VIII.14] W. J. Menz, J. Akroyd, and M. Kraft. "Stochastic solution of population balance equations for reactor networks". *Journal of Computational Physics* 256 (2014), pp. 615–629. DOI: 10.1016/j.jcp.2013.09.021.

[VIII.15] M. Smith and T. Matsoukas. "Constant-number Monte Carlo simulation of population balances". *Chemical Engineering Science* 53.9 (1998), pp. 1777–1786. DOI: 10.1016/S0009-2509(98)00045-1.

[VIII.16] S. Kumar and D. Ramkrishna. "On the solution of population balance equations by discretization - I. A fixed pivot technique". *Chemical Engineering Science* 51.8 (1996), pp. 1311–1332. DOI: 10.1016/0009-2509(96)88489-2.

DOI: 10.17185/duepublico/78751
URN: urn:nbn:de:hbz:465-20230803-141636-9